



# Diamond-based heat spreaders for power electronic packaging applications

Thomas Guillemet

## ► To cite this version:

Thomas Guillemet. Diamond-based heat spreaders for power electronic packaging applications. Material chemistry. Université Sciences et Technologies - Bordeaux I; University of Nebraska, 2013. English. NNT : 2013BOR14841 . tel-01062919

**HAL Id: tel-01062919**

**<https://theses.hal.science/tel-01062919>**

Submitted on 11 Sep 2014

**HAL** is a multi-disciplinary open access archive for the deposit and dissemination of scientific research documents, whether they are published or not. The documents may come from teaching and research institutions in France or abroad, or from public or private research centers.

L'archive ouverte pluridisciplinaire **HAL**, est destinée au dépôt et à la diffusion de documents scientifiques de niveau recherche, publiés ou non, émanant des établissements d'enseignement et de recherche français ou étrangers, des laboratoires publics ou privés.

DIAMOND-BASED HEAT SPREADERS  
FOR POWER ELECTRONIC PACKAGING APPLICATIONS

By  
Thomas Guillemet

A DISSERTATION

Presented to the Faculty of  
The Graduate College at the University of Nebraska, United States, and  
The Graduate College at the University of Bordeaux, France

In Partial Fulfillment of Requirements  
For the Degree of Doctor of Philosophy

Major: Engineering (Materials Engineering)  
Major: Chemistry (Physical-Chemistry of Condensed Matter)

Under the Supervision of Professors Yongfeng Lu and Namas Chandra  
Under the Supervision of Professors Jean-François Silvain and Jean-Marc Heintz

Lincoln, Nebraska

August, 2013

# DIAMOND-BASED HEAT SPREADERS FOR POWER ELECTRONIC PACKAGING APPLICATIONS

Thomas Guillemet, Ph.D.

University of Nebraska – University of Bordeaux, 2013

Advisors: Yongfeng Lu, Namas Chandra, Jean-François Silvain, Jean-Marc Heintz

As any semiconductor-based devices, power electronic packages are driven by the constant increase of operating speed (higher frequency), integration level (higher power), and decrease in feature size (higher packing density). Although research and innovation efforts have kept these trends continuous for now more than fifty years, the electronic packaging technology is currently facing a challenge that must be addressed in order to move toward any further improvements in terms of performances or miniaturization: thermal management. Thermal issues in high-power packages strongly affect their reliability and lifetime and have now become one of the major limiting factors of power modules development. Thus, there is a strong need for materials that can sustain higher heat flux levels while safely integrating into the electronic package architecture. In such context, diamond is an attractive candidate because of its outstanding thermal conductivity, low thermal expansion, and high electrical resistivity. Its low heat capacity relative to metals such as aluminum or copper makes it however preferable for heat spreading applications (as a *heat-spreader*) rather than for dissipating the heat flux itself (as a *heat sink*). In this study, a dual diamond-based heat-spreading solution is proposed. Polycrystalline diamond films were grown through laser-assisted combustion synthesis on electronic substrates (in the U.S) while, in parallel, diamond-reinforced copper-matrix composite films were fabricated through tape casting and hot pressing (in France). These two types of diamond-based heat-spreading films were characterized and their microstructure and chemical composition were related to their thermal performances. Particular emphasize was put on the influence of interfaces on the thermal properties of the materials, either inside a single material (grain boundaries) or between dissimilar materials (film/substrate interface, matrix/reinforcement interface). Finally, the packaging potential of the two heat-spreading solutions invoked was evaluated.

This study was carried out within the framework of a French-American collaboration between the Electrical Engineering department of the University of Nebraska-Lincoln (United States, U.S.) and the Institute of Condensed Matter Chemistry of the University of Bordeaux (France). This study was financed by the Office of Naval Research in the U.S., and by the Région Aquitaine in France.

Thomas Guillemet, Ph.D.

Université du Nebraska – Université de Bordeaux, 2013

Advisors: Yongfeng Lu, Namas Chandra, Jean-François Silvain, Jean-Marc Heintz

Comme tout secteur de l'industrie des semi-conducteurs, l'électronique de puissance évolue suivant une augmentation constante des fréquence et puissance de fonctionnement, alors même que la taille du circuit intégré devant les supporter diminue. Tandis que les efforts du secteur en terme de recherche et de développement ont permis à ces tendances de se poursuivre sans discontinuer, les niveaux de densité de chaleur atteints actuellement par les circuits de puissance constituent un obstacle majeur à toute amélioration future. Dans ce contexte de contraintes thermiques limitantes, l'environnement direct des composants de puissance (ou leur *packaging*) a un rôle important à jouer dans la mesure où il constitue un terrain d'améliorations potentielles considérable, notamment du point de vue des matériaux utilisés. Dans cette étude, le diamant est considéré comme un candidat prometteur pour contribuer à l'évacuation de la chaleur. Ce matériau combine, en effet, de manière rare, une conductivité thermique exceptionnelle, une forte résistivité électrique, et un coefficient de dilatation thermique bas, ce qui le rend très intéressant pour jouer le rôle de drain thermique au sein d'un environnement électriquement actif. Il présente cependant une capacité thermique faible relativement à des métaux tels que le cuivre ou l'aluminium. Dans le cadre de cette étude, le diamant est donc préférentiellement appliqué à la *répartition* du flux de chaleur (sous forme d'un film mince) plutôt que dans un objectif de *dissipation* directe. Deux types de films diamantés ont été envisagés : des films de diamant polycristallins déposés sur substrat électronique (silicium) par combustion de flamme assistée-laser (aux Etats-Unis), et des films composites cuivre/diamant fabriqués par métallurgie des poudres (en France). Dans chacun des cas, l'utilisation de diverses techniques de caractérisation a permis d'établir des corrélations entre la microstructure des matériaux, leur composition chimique, ainsi que leurs performances thermiques respectives. L'importance de l'influence des interfaces sur les propriétés thermiques des deux types de systèmes a été soulignée, tant au sein d'un même matériau (joints de grains) qu'entre deux matériaux dissemblables (interface film/substrat, interface matrice/renfort). Enfin, le potentiel technologique des deux solutions envisagées a été évalué.

Ces travaux ont été menés dans le cadre d'un accord franco-américain de cotutelle de thèse entre l'Institut de Chimie de la Matière Condensée de l'Université de Bordeaux, en France, et le département d'Ingénierie Electrique de l'Université du Nebraska-Lincoln, aux Etats-Unis. Ils ont été financés, en France, par la Région Aquitaine, et aux Etats-Unis par le Bureau Américain de la Recherche Navale.



# ACKNOWLEDGEMENT

My gratitude first goes to my French and American advisors, Professor Jean-François Silvain and Professor Jean-Marc Heintz from the Institute of Condensed Matter Chemistry of Bordeaux, and Professor Yongfeng Lu and Professor Namas Chandra from the College of Engineering of the University of Nebraska-Lincoln. Their trust, support, and communicative optimism were constant from the very first day of our collaboration and kept still all along these four years. First under their direction, in the end by their sides, I learned, progressed, and matured in such a way that gives all its sense to the PhD program. Besides professional partnerships, I feel like solid friendships have also emerged from this collaboration.

I would like to thank the U.S. Office of Naval Research and the French Region Aquitaine for having financially supported this PhD program at the University of Nebraska-Lincoln and at the University of Bordeaux, respectively.

A four-year long dual PhD program between France and the United States with four advisors and height thousands kilometers between the two labs involved is far from being the most convenient way to get a doctorate, but it was the most exciting, challenging, and enriching human and scientific experience of my life so far. I am proud to have been the first student to be involved in such a challenging French-American dual PhD program, and proud to have contributed to build a strong academic partnership between our two universities. I deeply hope many other students will realize what an outstanding opportunity it is to be part of this international initiative and will pursue it in the coming years.

I would like to thank all the people in Bordeaux and Lincoln who made me feel at home in both places, while my repeated travels across the Atlantic ocean could have easily torn me apart.

My lab mates in Bordeaux, former and current: Matt Bardet, Guillaume Lacombe, Greg Hauss, Baptiste Buton, Julien Lesseur, Marion Gayot, Amélie Veillere, Yann Damon, Greg Lalet, Delphin Levasseur, Pierre Heijboer, Iona Moog, Guillaume Guery, Max Decain, Lionel Teule-Gay, Cecile Vincent, Rudy Guicheteau, Pierrick Richard, Erwan Plougonven, Evan Schumann, Hiroki Kurita, Emilien Feuillet, Marianne Le Troedec, Guy-Marie Valet, Thomas Alnasser, Cinta Pepin, Cedric Slotowski, Philippe Belanger. Thank you for infusing such a positive energy in the lab-life, it makes everyday-science even more appealing. I also thank the trainees who silently suffered under my direction at ICMCB for their hard work and dedication: Cynthia Guilbaud, Mellie Letheux, and Maud Guillois.

I also would like to thank all ICMCB staff for their work and efforts to run the lab and make it a pioneering research facility in France. Especially, I would like to thank Michel Lahaye, Christine

Labrugere, Melanie Majimel, and Eric Lebraud, for their great help and expertise in carrying out Auger, XPS and AFM, TEM, and XRD analyses at ICMCB, respectively. Anthony Rousseau, who never hesitated to help me out for PVD deposition. I also thank Christophe Toulin for providing me with countless literature references. My special thanks also goes to Lionel Teule-Gay, who dedicated a lot of his time to help me build the combustion deposition set-up at ICMCB. I also would like to thank Jean-Luc Battaglia and Andrzej Kusiak at Trefle laboratory, who let me work by their side and brought their long-time expertise in thermal science and characterization to serve this study. Their contribution was decisive in many aspects of this project. Finally, I would like to thank Claude Delmas and Mario Maglione, former and current head of ICMCB, for supporting me and letting me carrying out my PhD program in this lab.

My lab mates in Lincoln, former and current: Zhiqiang Xie, Yang Gao, Wei Xiong, Xiangnan He, Younshen Zhou, Masoud Mahjouri-Samani, Prem Kumar, Jongbok Park, Matt Mitchell, Lisha Fan, Lijia Jiang, Mengxiao Wang, Mengmeng Wang, Yutian Lei, Xi Huang, Hossein Rabiee, Dan Liang, Xuejian Li, Lianbo Guo, Xu, Ji, Wenjia Hou, Lei Liu, Zhe Ren, Jin Sun, Huifu Luo. Thank you for your friendship and for hosting me as a full-member of such a great research group. Working by your sides in the U.S. provided me with a different approach of scientific research, initiative spirit and entrepreneurship, and represents an inestimable experience. I also would like to thank Dennis Alexander, Lanping Yue, and Shah Valloppilly, for helping me out in carrying out SEM, AFM, and XRD analyses at UNL, respectively. I would especially like to thank Cheryl Wemhoff, Chelsea Hood, and Brian Robertson, from the University of Nebraska-Lincoln, who provided this program with precious help all along, especially on the administrative front, and strongly contributed to make this collaboration happen. A special thought also goes to the always-extending and vibrating French Sisporea of Lincoln, who makes the world an even smaller place.

I would like to address special thanks to my dear friend, lab mate, roommate, and sparring partner Sebastien Thomas. His friendship, wisdom, optimism and fighting spirit were of precious help. I hope his valuable qualities may have detained on me during the time we spent together.

I would like to thank my father Michel, without whom it would have been extremely difficult for me to pursue this French-American program. My thoughts also go to my mother, Régine, my brother Baptiste and my sister Camille, who supported and encouraged me under any circumstances.

Finally, and most deeply, I would like to thank Marion Ancessy, for her unconditional support during these four years, no matter the distance between us. Despite the hard times we have been through, she was always there. She made me learn a great deal, and I could not have achieved that much without her.

# TABLE OF CONTENTS

<b>ACKNOWLEDGEMENT .....</b>	<b>4</b>
<b>TABLE OF CONTENTS .....</b>	<b>6</b>
<b>LIST OF FIGURES .....</b>	<b>11</b>
<b>LIST OF TABLES .....</b>	<b>21</b>
<b>LIST OF ABBREVIATIONS .....</b>	<b>23</b>
<b>CHAPTER 1: INTRODUCTION.....</b>	<b>24</b>
1.1 Motivations.....	25
▪ Technological context: .....	25
▪ Passive cooling solutions: .....	28
▪ Active cooling solutions:.....	29
▪ Diamond-based heat-spreaders: .....	31
1.2 Overview of the dual PhD program .....	32
1.3 Dissertation outline.....	32
<b>CHAPTER 2: BACKGROUND AND REVIEWS.....</b>	<b>34</b>
2.1 Power electronic package architecture .....	35
▪ Electronic chip: .....	37
▪ Wire bonds: .....	37
▪ Solder joints: .....	38
▪ Ceramic substrate: .....	41
▪ Encapsulation and protective gels: .....	43
▪ Base plate and heat sink: .....	43
2.2 Main thermal management issues in power packages.....	44
2.3 Diamond: a unique material .....	50
2.3.1 Composition .....	51
2.3.2 Crystal structure and morphology .....	52
2.3.3 Properties.....	54
▪ Mechanical properties: .....	54
▪ Electrical properties: .....	54
▪ Optical properties: .....	55
▪ Thermal properties: .....	55
2.4 Diamond synthesis .....	57

▪ The (P, T) diagram of carbon: .....	57
▪ Nucleation and growth processes [50]: .....	58
2.4.1 Catalytic High-Pressure High-Temperature (HPHT) diamond synthesis .....	60
▪ Principles underlying catalytic HPHT diamond synthesis: .....	60
▪ A brief history of HPHT synthesis: .....	63
2.4.2 Chemical Vapor Deposition (CVD) of diamond at low pressures .....	64
▪ Principles underlying CVD diamond synthesis: .....	64
▪ Main routes for CVD diamond synthesis [4, 70, 71]: .....	68
▪ A brief history of CVD diamond synthesis: .....	70
2.5 Diamond-based heat-conductive materials in electronics .....	73
2.5.1 On the importance of interfaces on the heat conduction process .....	73
▪ Reactive and non-reactive bi-materials assemblies: .....	73
▪ Heat conduction in metals and diamond: .....	74
▪ Heat conduction across the metal/diamond interface: .....	78
2.5.2 CVD diamond films in electronics .....	85
2.5.3 HPHT diamond reinforced composite materials in electronics .....	87
2.6 Conclusion .....	93
<b>CHAPTER 3: COMBUSTION CVD DIAMOND FILMS .....</b>	<b>94</b>
3.1 Introduction .....	95
3.2 Laser-assisted combustion synthesis of diamond films .....	96
3.2.1 Combustion flame deposition: .....	96
3.2.2 Laser-resonant excitation of precursor molecules: .....	99
▪ Multienergy deposition process: .....	99
▪ Absorption of the laser energy by ethylene molecules in the flame environment: .....	100
3.2.3 Diamond deposition experimental set-up: .....	101
3.2.4 Diamond film microstructure: .....	103
▪ Top-surface microstructure: .....	103
▪ Cross-sectional microstructure: Van der Drift growth model .....	106
▪ Influence of laser excitation on diamond film microstructure: .....	107
3.3 Diamond film phase purity and residual stress analyses through Raman spectroscopy .....	109
3.3.1 Raman spectroscopy: background and underlying principles .....	109
3.3.2 Raman spectroscopy: experimental set-up .....	111
3.3.3 Phase purity analysis .....	112
3.3.4 Residual stress evaluation .....	114
3.3.5 Residual stress release through substrate laser-roughening .....	118
3.4 Thermal characterization through modulated photothermal radiometry .....	120
3.4.1 Background about thermal characterization of CVD diamond films .....	120

3.4.2 Modulated photothermal radiometry: underlying principles and equations.....	121
▪ Fundamental principle:.....	121
▪ Heat transfer geometry:.....	123
▪ Analytical heat transfer solution through thermal quadrupole method:....	125
▪ Thermal response of semi-infinite medium: .....	132
▪ Sensitivities: .....	133
▪ Influence of the roughness on the thermal response: .....	134
3.4.3 Photothermal radiometry: experimental set-up .....	135
3.4.4 Optical transducer.....	137
3.4.5 Results .....	138
3.5 Influence of the growth process and microstructure on the thermal properties of diamond films .....	141
▪ Levels of thermal conductivity and thermal resistance:.....	141
▪ Presence of foreign material at the diamond/Si interface: .....	142
▪ Influence of the microstructure of the diamond films:.....	143
▪ Theoretical estimation of interfacial thermal resistance through the diffuse mismatch (DM) model: .....	146
3.6 Deposition of combustion CVD diamond films on copper and copper/carbon composite substrates. ....	148
3.7 Conclusion.....	153
<b>CHAPTER 4: COPPER / DIAMOND COMPOSITE FILMS.....</b>	<b>154</b>
4.5 Investigations on the particles grown onto diamonds .....	154
4.6 Cu particles nucleation and growth process .....	154
4.1 Introduction .....	155
4.2 Starting materials.....	159
4.2.1 The copper matrix .....	159
4.2.2 The diamond reinforcements.....	160
4.3 The tape casting process.....	162
4.3.1 Background .....	162
4.3.2 Processing flowchart .....	164
4.3.3 Formulation .....	165
▪ Solvent:.....	166
▪ Dispersant agent: .....	166
▪ Binder: .....	167
▪ Plasticizer: .....	167
4.3.4 Shaping and drying.....	168
4.4 Heat treatments.....	171

4.4.1 Debinding .....	171
4.4.2 Nanowires growth .....	174
4.4.3 Hypotheses on the nanowires growth process.....	176
4.4.4 Reduction.....	178
4.5 Investigations on the particles grown onto diamonds .....	181
4.5.1 Surface chemistry of the diamond reinforcements.....	181
4.5.2 Particles sizes and populations .....	184
4.5.3 Particle composition and microstructure .....	186
4.5.4 Copper/diamond interface composition and microstructure .....	189
4.6 Cu particles nucleation and growth process .....	193
4.6.1 Conclusions drawn from chemical and microstructural characterizations.....	193
▪ Particles shape, size, and populations: .....	193
▪ Particles microstructure and composition: .....	193
▪ Interface between the particles and the diamond substrates: .....	193
4.6.2 Hypotheses on the nucleation and growth of the Cu particles .....	194
▪ CuO nanowires sublimation: .....	195
▪ CuO reduction in the vapor phase and Cu deposition onto the P-O-C nucleation sites: .....	195
▪ Cu particles growth following Wulff geometry: .....	196
4.7 The sintering process.....	199
4.7.1 Free sintering mechanism.....	199
▪ Free sintering driving force: .....	199
▪ The different microstructural stages of the sintering process: .....	202
4.7.2 Induction uniaxial hot pressing .....	203
4.8 Characterization of the Cu/D composite films .....	206
4.8.1 Density and microstructure .....	206
4.8.2 Thermal characterizations .....	209
▪ Thermal conductivity: .....	209
▪ Thermal expansion coefficient (CTE):.....	212
4.9 Comparison with traditional carbide-bonded Cu/D composites .....	215
4.9.1 Carbide forming materials.....	215
4.9.2 Boron and chromium-alloyed copper powders .....	219
4.9.3 Diffusion in Cu-Cr/D and Cu-B/D composite materials .....	222
▪ Diffusion modes: .....	222
▪ Diffusion mechanisms:.....	222
▪ Thermodynamic approach: Cu-Cr/D composites:.....	223
4.9.4 Sintering of carbide-bonded Cu/D composites .....	223
4.9.5 Influence of interfacial bonding on thermal performances of Cu/D composites.....	226
▪ Relative density: .....	226

▪ Thermal conductivity: .....	227
▪ Thermal expansion coefficient: .....	228
4.9.6 Thermal cycling.....	230
▪ Thermal cycle applied: .....	230
▪ Thermal conductivity evolution upon thermal cycling: .....	231
▪ Thermal boundary resistance at the Cu/D interface: .....	232
4.10 Conclusion.....	235
<b>CHAPTER 5: PROPOSITION OF NEW PACKAGING CONFIGURATIONS...</b>	<b>237</b>
5.1 Technological potential of diamond-based heat spreaders.....	238
▪ Technological considerations: .....	238
▪ CVD diamond films applicability: .....	239
▪ HPHT diamond reinforced composite films applicability: .....	240
▪ Packaging configurations considered: .....	241
5.2 Finite element simulations in operating module environment .....	242
▪ Definition of the geometry: .....	243
▪ Definition of the mesh: .....	244
▪ Definition of the boundary conditions: .....	245
▪ Calculation: .....	245
▪ Simulation of the temperature and shear stress distributions: .....	245
▪ Discussion about the simulation results: .....	248
▪ Proposition of novel packaging configurations: .....	249
5.3 Conclusion.....	252
<b>CHAPTER 6: SUMMARY &amp; OUTLOOK .....</b>	<b>253</b>
6.1 Summary .....	254
6.2 Future directions.....	255
<b>APPENDIX.....</b>	<b>257</b>
A.1 Main heat transfer modes .....	257
A.2 Characterization techniques.....	260
<b>LITERATURE REFERENCES .....</b>	<b>272</b>
<b>LIST OF JOURNAL PAPERS .....</b>	<b>284</b>
<b>LIST OF CONFERENCE PAPERS .....</b>	<b>285</b>

# LIST OF FIGURES

Figure 1.1: Timeline figuring Moore's law pace in CPUs, when replacing transistors by people.....	25
Figure 1.2: Trends in semiconductor industry as a function of time. (a) Clock speed, chip area, and chip power. (b) Chip heat flux density as a function of time.....	26
Figure 1.3: 3D view of a multi-chip power electronic module.....	27
Figure 1.4: Overview of how passive and active cooling solutions combine in a power module.....	28
Figure 1.5: Overview of the French-American dual PhD program between the University of Nebraska-Lincoln (UNL), in the US, and the University of Bordeaux (UB), in France .....	33
Figure 2.1: 2D cross-sectional architecture of a power electronic module .....	35
Figure 2.2: Photographs of a multi-chip power module: (a) Chips – ceramic – base plate; (b) Chips – ceramic – base plate – encapsulation (c) Chips – ceramic – base plate – encapsulation – protective gel.....	36
Figure 2.3: (a) SEM micrograph and (b) photograph of chip wire bonding.....	38
Figure 2.4: SEM micrographs of (a) Cu/Sn/Cu and (b) Cu/Au/Cu diffusion bonds .....	41
Figure 2.5: Cross-sectional view of an alumina DBC substrate .....	42
Figure 2.6: Thermal properties of the different materials composing a power package [5,10].....	44
Figure 2.7: Finite elements simulations: (a) Temperature distribution and (b) shear stress distribution at the solder joint / copper base plate interface in an operating power module .....	45
Figure 2.8: Schematic view of how CTE mismatches leads to compressive (yellow arrows) and tensile (green arrows) stresses in bi-materials assemblies: (a) $\alpha_1 > \alpha_2$ , (b) $\alpha_1 < \alpha_2$ . .....	45
Figure 2.9: Cross-sectional scanning electron micrograph of a cracked solder joint at the chip / metallic thin film interface.....	46
Figure 2.10: Thermal properties of diamond-based materials relative to other typical electronic packaging materials .....	49
Figure 2.11: Various natural diamond stones .....	51
Figure 2.12: 3D view of the diamond lattice .....	52
Figure 2.13: Crystal shapes produced in diamond nucleation and growth processes and associated growth parameter. The arrow indicates the direction of fastest crystal growth.....	53
Figure 2.14: (P, T) diagram of carbon.....	57



Figure 2.15: Schematic plot of free energy versus nucleus radius .....	59
Figure 2.16: Schematic plot showing growth rate, nucleation rate, and overall transformation rate versus temperature .....	60
Figure 2.17: (a) Sketch of cubic HPHT anvil apparatus. (b, c) HPHT diamonds .....	62
Figure 2.18: Schematic view of the three primary growth modes: (a) Wolmer-Weber (3D), (b) Franck Van der Merwe (2D), (c) Stranski-Krastanov (2D + 3D).....	66
Figure 2.19: SEM micrographs of (a) (100) textured and (b) randomly oriented CVD diamond films.....	68
Figure 2.20: (a) General scheme for CVD diamond growth from a CH <sub>4</sub> /H <sub>2</sub> gaseous mixture (b) HFCVD (c) TPCVD and (d) ASTeX-type MWCVD apparatus .....	69
Figure 2.21: Schematic view of reactive and non-reactive bi-materials assemblies .....	74
Figure 2.22: Schematic view of electronic band structures of metals, semiconductors, and insulators .....	76
Figure 2.23: Electron-phonon and phonon-phonon scattering processes: (a) Electron-phonon scattering, in which an electron emits a phonon. (b) Electron-phonon scattering, in which an electron absorbs a phonon. (c) Phonon-phonon scattering, in which a phonon decays into two phonons. (d) Phonon-phonon scattering, in which two phonons generate a phonon.....	79
Figure 2.24: Schematic illustrating pathways for the heat to flow across a metal/non-metal interface. (a) The electrons of the metal transfer their energy to the phonons of the non-metal through electron-phonon coupling. (b) The electrons of the metal transfer first their energy to phonons in the metal and then couple with phonons of the non-metal. $T_e$ , $T_p$ , $T'_e$ , and $T$ respectively stand for the electron and phonon temperatures of the metal, the equivalent temperature of the metal, and the temperature of the non-metal .....	80
Figure 2.25: (a) Schematic illustrating possible phonon reflection and transmissions in the framework of the acoustic mismatch model. (b) Incident and transmitted phonon angles at an interface between two materials with different phonon velocities .....	82
Figure 2.26: Schematic view of (a) hot-pressing, (b) Spark Plasma Sintering (SPS), and (c) pressure-assisted liquid infiltration processes for Cu/D composites fabrication.....	89
Figure 3.1: Schematic view of the structure of an oxyacetylene combustion torch.....	96
Figure 3.2: Schematic view of the diamond growth process through the addition of methyl radicals and etching of sp <sup>2</sup> hybridized carbon atoms by atomic hydrogen .....	98
Figure 3.3: Schematic of the different energy storage for a diatomic molecule .....	99
Figure 3.4: Optical absorption spectrum of the CO <sub>2</sub> laser excitation by the combustion flame .....	100

Figure 3.5: (a) Scheme of how the laser excitation affects the wagging mode of an ethylene molecule. (b) Vibration-rotation transitions of an ethylene molecule with CO <sub>2</sub> laser excitation at different wavelengths.....	100
Figure 3.6: Photographs of the combustion flame (a) without and (b) with 10.532 $\mu\text{m}$ laser excitation .....	101
Figure 3.7: Experimental set-up for laser-assisted combustion synthesis of diamond.....	102
Figure 3.8: Photographs of the laser-assisted combustion deposition process. The optical path of the laser beam is figured by the red dashed line.....	102
Figure 3.9: SEM micrographs of a diamond film grown onto a Si substrate through laser-assisted combustion synthesis .....	103
Figure 3.10: Typical (a) thickness and (b) roughness profiles of the diamond films obtained.....	103
Figure 3.11: SEM micrographs of diamond films grown onto Si substrates using 10.532 $\mu\text{m}$ laser excitation: (a) 5 minutes, (b) 15 minutes, (c) 30 minutes, (d) 40 minutes, (e) 60 minutes, (f) 120 minutes.....	104
Figure 3.12: SEM micrographs showing the early stages of the diamond film formation: (a) creation of diamond nuclei on the surface of the Si substrate (after 1 min deposition). (b) Diamond crystals coalescence (after 2 min deposition). (c) Continuous diamond film formation (after 5 min deposition).....	105
Figure 3.13: Influence of the substrate temperature on diamond crystal morphology.....	105
Figure 3.14: (a) Van der Drift growth model. The dash lines indicate the grain boundaries. The solid lines show the surface of the film at selected times. (b) Experimental cross-sectional SEM micrograph of diamond film grown through laser-assisted combustion synthesis .....	106
Figure 3.15: SEM micrographs showing the influence of the laser excitation onto the diamond film morphology: (a, b) no laser, (c, d) 10.22 $\mu\text{m}$ excitation, (e, f) 10.532 $\mu\text{m}$ excitation.....	107
Figure 3.16: (a) Energy level diagram showing the states involved in Raman spectroscopy. The line thickness is representative of the signal strength. (b) Light-matter interaction processes in Raman spectroscopy with Boltzmann distribution of different scattering effects .....	109
Figure 3.17: Typical Raman signature of diamond.....	110
Figure 3.18: Schematic of a conventional Raman spectrometer .....	111
Figure 3.19: Raman spectra of diamond films grown onto silicon substrates at various thicknesses: (a) without laser excitation, (b) with 10.532 $\mu\text{m}$ laser excitation.....	112
Figure 3.20: (a) sp <sup>3</sup> carbon content and (b) diamond quality parameter of diamond films grown with ( $\lambda = 10.532 \mu\text{m}$ ) and without laser resonant excitation.....	113

Figure 3.21: (a) Cross-sectional mapping and (b) evolution with respect to film thickness of FWHM of diamond peak for diamond films grown through 10.532 $\mu\text{m}$ laser excitation .....	114
Figure 3.22: Typical Raman shift of diamond films grown onto silicon (red line) and tungsten carbide (blue line).....	115
Figure 3.23: Raman shift and corresponding residual stress of diamond films grown onto silicon (red line) and tungsten carbide (blue line) as a function of film thickness .....	116
Figure 3.24: Raman mappings of diamond peak position obtained from diamond films grown on Si and WC-Co substrates .....	117
Figure 3.25: Intrinsic stress evolution with film thickness for diamond films grown on Si and WC-Co substrates .....	118
Figure 3.26: SEM micrograph and AFM surface profile of raw (a, b) and laser-roughened (c, d) WC-Co substrates. SEM micrographs of diamond films grown onto raw (e, f) and laser-roughened (g, h) WC-Co substrates during 30 minutes (e, g) and 60 minutes (f, h).....	119
Figure 3.27: Raman mapping of diamond peak shift on (a) raw and (b) laser-roughened WC-Co .....	119
Figure 3.28: Amplitude and phase of the infrared thermal response relative to the excitation signal.....	120
Figure 3.29: Uniform and Gaussian laser profiles in a modulated photothermal radiometry experiment.....	121
Figure 3.30: Heat transfer geometry in the deposit material as a function of excitation frequency .....	124
Figure 3.31: (a) 1D-wall heat transfer geometry. (b) Corresponding quadrupole representation.....	125
Figure 3.32: : Thermal impedance representation of the 1D heat transfer phenomena of Fig. 3.31.....	127
Figure 3.33: Thermal impedances network modeling the 1D heat transfer phenomenon in the tri-layered sample considered in infrared photothermal radiometry analysis .....	128
Figure 3.34: Modeling of the 1D heat transfer phenomenon in the tri-layered sample based on the thermal impedances formalism when the transducer absorbs the heat source on its whole thickness.....	128
Figure 3.35: Heat transfer model in the tri-layered assembly when the heat diffusion length is in the same range as the diamond film thickness (capacitive approach).....	129
Figure 3.36: Heat transfer model in the tri-layered assembly when the heat diffusion length is larger than the diamond film thickness (resistive approach).....	130
Figure 3.37: $e_d/l$ ratio with respect to excitation frequency for CVD diamond with $k_{dia} = 300 \text{ W.m}^{-1}.\text{K}^{-1}$ .....	131
Figure 3.38: : Typical (a) amplitude and (b) phase evolution in a semi-infinite media.....	132

Figure 3.39: Respective sensitivity of the thermal response (a) amplitude and (b) phase to $R_{dia/Si}^{th}$ .....	134
Figure 3.40: (a) SEM micrograph showing the roughness on the top surface of a diamond film. (b) Different optical paths induced by the roughness. (c) Isotherms propagating into a rough semi-infinite media.....	134
Figure 3.41: Scheme of the modulated photothermal radiometry experimental set-up.....	135
Figure 3.42: Photographs of the modulated photothermal radiometry experimental set-up .....	137
Figure 3.43: SEM micrographs of the diamond films analyzed through modulated PTR: (a) top surface, (b) cross-section in SE mode, (c) cross-section in BSE mode showing the Pt transducer.....	138
Figure 3.44: Fitting results between experimental and simulated (a) amplitude and (b) phase evolutions as a function of excitation frequency .....	139
Figure 3.45: SEM micrographs of the backside of a CVD diamond film delaminated from a Si substrate (a1, b1) and AES in-depth line profiles of the different areas detected (a2, b2).....	142
Figure 3.46: AES in-depth line profile on a Si substrate delaminated from a CVD diamond film.....	143
Figure 3.47: Raman spectra of 10 $\mu\text{m}$ -thick diamond films grown (a) 20 minutes and (b) 50 minutes through laser-assisted combustion synthesis with respect to film thickness .....	145
Figure 3.48: Schematic view of the composition of the Si/diamond interface.....	146
Figure 3.49: SEM micrographs of diamond nuclei onto a graphitized copper substrate.....	149
Figure 3.50: (a) Top surface and (b) cross section SEM micrographs of Cu/C composite substrates.....	149
Figure 3.51: SEM micrographs of a cracked and delaminated diamond film deposited onto a Cu/C composite substrate through laser-assisted combustion synthesis.....	150
Figure 3.52: SEM micrographs of a (a) raw and (b) Cr-coated Cu/C composite substrate.....	150
Figure 3.53: SEM micrographs of a CVD diamond-coated Cu/C composite substrate .....	151
Figure 3.54: TEM elemental analysis at the Cu/C/Cr/diamond interface. (a) Micrograph of the interface. (b) EDXS chemical mapping of the interface: C: red color, Cr: green color, Cu: blue color. (c) Line concentration profile across the interface.....	151
Figure 4.1: Schematic view of (a) a wetting ( $\theta < \pi/2$ ) and (b) a non-wetting ( $\theta > \pi/2$ ) liquid-solid system. Taking a surface tension balance in the plane of the solid leads to: $\gamma_{lg}\cos\theta + \gamma_{ls} = \gamma_{sg}$ (Young-Dupré equation).....	155
Figure 4.2: The binary copper-carbon phase diagram.....	156
Figure 4.3: (a) Cr-alloyed spherical copper powder and (b) Cr-coated diamond particle.....	157

Figure 4.4: EPMA Cr mapping of a Cu-Cr/30 vol.% C composite material, showing the chromium located at the Cu/C interfaces.....	158
Figure 4.5: Scanning electron micrographs and photograph (insert) of the dendritic copper powders employed as the matrix.....	159
Figure 4.6: X-ray diffraction spectrum of the dendritic copper powders employed as the matrix material.....	160
Figure 4.7: Scanning electron micrographs and photograph (insert) of the diamond powders employed as reinforcements.....	161
Figure 4.8: X-ray diffraction spectrum of the diamond powders employed as reinforcements.....	161
Figure 4.9: Scheme of the tape casting set-up and mechanism.....	162
Figure 4.10: Processing flowchart of the tape casting process.....	164
Figure 4.11: Schematic description of the dispersion mechanism.....	166
Figure 4.12: Photographs of (a) the planetary miller and (b) of a Cu/D slurry in a container.....	167
Figure 4.13: Photographs of (a) a green Cu/40 vol.% D composite after tape casting and (b) of the doctor blade.....	168
Figure 4.14: Photographs of a Cu/D green tape (a) straight after tape casting and (b) after 30 minutes drying.....	169
Figure 4.15: (a) Dimensions and (b) volume retraction of a Cu/D green tape upon drying.....	169
Figure 4.16: : Photograph of Cu/D green tapes containing (a) 70 vol.% and (b) 74 vol.% of solvent.....	170
Figure 4.17: Photographs showing the flexibility of the Cu/D green tape (a) longitudinally and (b) transversally; (c) shaped Cu/D green tape after drying and prior to debinding.....	170
Figure 4.18: Top surface scanning electron micrographs of a green copper/diamond composite tape .....	171
Figure 4.19: Photograph of (a) the debinding furnace and (b) debinded Cu/40 vol.% D composite tapes.....	171
Figure 4.20: SEM micrographs of a copper/diamond composite tape debinded one hour at 400°C under air.....	172
Figure 4.21: TGA analysis of a copper/diamond composite green tape upon debinding (under air).....	173
Figure 4.22: SEM micrographs showing the influence of temperature on the debinding process: (a) at T = 200°C, (b) at T = 300°C, (c) at T = 350°C, (d) at T = 400°C and t = 0 min.....	174

Figure 4.23: SEM micrographs showing the influence of holding time at 400°C on the nanowires growth process: (a) $t = 30$ min, (b) $t = 70$ min, (c) $t = 90$ min, (d) $t = 120$ min.....	175
Figure 4.24: (a) TEM micrograph of copper oxide nanowires grown onto copper dendrites upon air debinding; (b) corresponding diffraction pattern.....	175
Figure 4.25: Photographs of (a) the reduction furnace and (b) reduced Cu/40 vol.% D composite tapes.....	178
Figure 4.26: Scanning electron micrographs of a copper/diamond composite tape reduced 1h at 400°C under Ar/H <sub>2</sub> .....	178
Figure 4.27: TGA analysis of a debinded copper/diamond composite tape upon reduction under Ar/H <sub>2</sub> .....	179
Figure 4.28: X-ray diffraction patterns of (a) a debinded and (b) a reduced copper/diamond composite tape.....	180
Figure 4.29: SEM micrographs of particle-coated diamond reinforcements upon various reduction conditions. ....	181
Figure 4.30: (a) Chemical surface analysis of debinded diamond powders through XPS and its (b) P2p and (c) C1s decomposition. ....	182
Figure 4.31: AFM surface analysis of a Cu-coated diamond reinforcement. (a) 2D topographic image. (b) 2D phase image. (c) 3D topographic image... ..	185
Figure 4.32: AFM line profiles onto a Cu-coated diamond reinforcement.....	186
Figure 4.33: Chemical mapping of a Cu-coated diamond reinforcement through EDX spectroscopy.....	187
Figure 4.34: TEM micrographs of a Cu-coated diamond reinforcement .....	187
Figure 4.35: High-resolution TEM micrographs of a Cu-coated diamond reinforcement (a) before and (b) after exposure to the reductive electron beam.....	188
Figure 4.36: High-resolution TEM micrographs at the Cu/D interface of a Cu-coated diamond particle.....	190
Figure 4.37: High-resolution TEM micrograph at the Cu/D interface of a Cu-coated diamond reinforcement.....	191
Figure 4.38: SEM micrographs of a CVD diamond film grown through laser-assisted combustion synthesis and coated with copper dots.....	192
Figure 4.39: TEM micrographs showing the interface between a CVD diamond film and copper particles deposited onto its surface.....	192

Figure 4.40: (a) Possible (1-10) section through the $\gamma$ -plot of an fcc crystal. The length OA represents the free energy of a surface plane whose normal lies in the direction OA. Thus $OB = \gamma_{(001)}$ , $OC = \gamma_{(111)}$ , etc. Wulff planes are those such as that which lies normal to the vector OA. In this case, the Wulff planes are B, C, etc, give the inner envelope of all Wulff planes and thus the equilibrium shape. (b) The equilibrium shape in three dimensions showing (100) (square faces) and (111) hexagonal faces. (c) TEM micrograph of a faceted Cu particle grown onto a diamond reinforcement.....	197
Figure 4.41: Schematic description of the Cu/D interfacial bonding process developed.....	198
Figure 4.42: Schematic view of the equilibrium process of a grain boundary in a gas phase.....	201
Figure 4.43: Evolution of Laplace stress at the surface of a Cu particle as a function of particle diameter....	201
Figure 4.44: Schematic view of the different stages of the sintering process: (a) Creation and growth of bridges between particles (b) Elimination of the opened porosity (c) Elimination of the closed porosity.....	202
Figure 4.45: (a) Photograph and (b) scheme of the uniaxial hot pressing machine.....	204
Figure 4.46: Photographs of Cu/40 vol.% D composite materials with various shapes: (a) 6 mm diameter cylinder, (b) 20 mm diameter cylinder, (c) 6x10 cm <sup>2</sup> plate.....	205
Figure 4.47: Evolution of the relative density of the Cu/D composites as a function of the diamond volume fraction.....	207
Figure 4.48: (a) SEM micrograph of a hot-pressed and (b, c, d) fractured Cu/20 vol.% D composite material.....	208
Figure 4.49: (a) Photograph and (b) schematic description of the thermal diffusivity measurement device.....	210
Figure 4.50: Evolution of the experimental thermal diffusivity and conductivity of the Cu/D composites and comparison with respect to Maxwell's prediction as a function of the diamond volume fraction.....	211
Figure 4.51: Photographs of the horizontal dilatometer.....	212
Figure 4.52: Evolution of the experimental and theoretical coefficient of thermal expansion of the Cu/D composite as a function of the diamond volume fraction.....	214
Figure 4.53: Thermal conductivity comparison between Cu-X/42 vol.% D composite materials (where X stands for B, Cr, Al, Ti, Zr, and the percentages are atomic).....	216
Figure 4.54: The (a) Cu-B and (b) Cu-Cr binary phase diagrams [8].....	217
Figure 4.55: (a) The B-C and (b) Cr-C binary phase diagrams [8].....	218

Figure 4.56: SEM micrographs of (a) spherical Cu-Cr alloyed powders and (b) spherical Cu-B alloyed powders.....	220
Figure 4.57: Particle size distribution of spherical (a, b) Cu-B alloyed powders and (c, d) and spherical Cu-Cr alloyed powders in volume and number, respectively.....	221
Figure 4.58: (a) Interstitial and (b) lacunar diffusion mechanisms representations.....	222
Figure 4.59: EPMA chemical mapping of a hot-pressed Cu-Cr/40 vol.% D composite material: (a)BSE micrograph of the investigated area, (b) Cu mapping, (c) C mapping, (d) Cr mapping.....	224
Figure 4.60: AES line profile at the Cu/D interface in a Cu-Cr/D composite.....	225
Figure 4.61: Influence on interfacial bonding on the relative density of the Cu/D materials.....	227
Figure 4.62: Influence on interfacial bonding on the thermal conductivity of the Cu/D materials.....	227
Figure 4.63: Influence on interfacial bonding on the thermal expansion coefficient of the Cu/D materials.....	229
Figure 4.64: (a) Photograph of the thermal cycling machine and (b) thermal cycle applied.....	230
Figure 4.65: Evolution of the thermal conductivity of Cu/D composite materials upon thermal cycling, depending on the interfacial bonding solution adopted.....	231
Figure 5.1: Potential packaging architecture involving either Cu/D composite films, CVD diamond films, or a combination of both.....	241
Figure 5.2: Illustration of the different steps of an FEM simulation © through Comsol Multiphysics. (a) Definition of the mesh. (b) Definition of the boundary conditions. (c) Definition of the mesh. (d) Post-treatment.....	242
Figure 5.3: Illustration of the modeling of the initial packaging architecture.....	243
Figure 5.4: Propositions of new packaging configurations including CVD diamond and Cu/D composite films combined to Cu/C base plate, and their respective temperature and shear stress distributions.....	250
Figure 5.5: Heat flux streamlines (left) and isotherms (right) in the new packaging configurations proposed.....	251
Figure A1.1 One-dimensional heat transfer by conduction (diffusion of energy).....	259
Figure A2.1 Schematic of the Netzsch LFA-457 flash laser radiometry device.....	261
Figure A2.2 Schematic of the Netzsch DIL-402 horizontal dilatometer.....	261
Figure A2.3 Schematic of electron-matter interactions.....	262



Figure A2.4 (a) Schematic view of a scanning electron microscope and view of (b) secondary electron and (c) back-scattered electron emission processes.....	262
Figure A2.5 Schematic view of the Auger process.....	264
Figure A2.6 Schematic view of the photoelectric effect.....	265
Figure A2.7 Schematic view of an atomic force microscope.....	266
Figure A2.8 (a) Schematic view of a WDS spectrometer and (b) Bragg diffraction process.....	268
Figure A2.9 Schematic view of transmission electron microscope.....	270

# LIST OF TABLES

Table 2.1: Thermo-physical properties of different chip materials. ....	37
Table 2.2: Thermo-physical properties of different wire bonding materials. ....	38
Table 2.3: Thermo-physical properties of different soldering alloys. ....	39
Table 2.4: Thermo-physical properties of different ceramic substrates materials. ....	42
Table 2.5: Thermo-physical properties of different heat-dissipative materials. ....	47
Table 2.6: Thermo-physical properties of different reinforcement materials for thermal MMCs. ....	48
Table 2.7: The different types of natural diamond. ....	51
Table 2.8: Properties of natural diamond at room temperature. ....	56
Table 2.9: Typical process conditions employed for catalytic HPHT synthesis of diamond. ....	61
Table 2.10: Heat carriers mean free path and corresponding thermal conductivities of materials. ....	77
Table 3.1: Details of the roughness analysis carried out on the diamond films through AFM. ....	104
Table 3.2: CTEs of diamond, silicon, and tungsten carbide at ambient and deposition temperatures. ....	115
Table 3.3: Estimations of thermal conductivity and TBR of the diamond films analyzed through PTR. ....	140
Table 3.4: Estimations of thermal conductivity and TBR of the diamond films. ....	146
Table 4.1: Free surface energies of copper and diamond at room temperature. ....	156
Table 4.2: Typical process conditions for electrolytic synthesis of dendritic copper powders. ....	159
Table 4.3: AES elemental analysis of the diamond powders employed. ....	161
Table 4.4: Thermo-physical properties of the starting dendritic copper and diamond powders. ....	162
Table 4.5: Chemicals entering in the formulation of the slurry for the tape casting of a Cu/40 vol.% D composite tape. ....	165
Table 4.6: Molar masses of copper (Cu) and cupric oxide (CuO) [23]. ....	173
Table 4.7: XPS survey peak description. ....	183
Table 4.8: P2p signal decomposition. ....	184

Table 4.9: C1s signal decomposition. ....	184
Table 4.10: Crystallographic properties of copper, diamond, and cubic copper oxides [23]. ....	189
Table 4.11: Interplanar distances of cupric and cuprous oxides relative to that of the interphase [23]. ....	190
Table 4.12: Some carbides and their respective standard free enthalpy of reaction [22,23]. ....	215
Table 4.13: Respective volume and number $d_{50}$ of the Cu-B and Cu-Cr alloyed copper powders. ....	221
Table 4.14: Respective atomic radii of Cu, B, and Cr. ....	223
Table 4.15: Estimated Kapitza resistance at the Cu/D interface for different Cu/D composites. ....	233
Table 4.16: Bulk thermal conductivity of carbides and oxides [22,23]. ....	234
Table 5.1: Technological aspects of the potential diamond-based heat spreaders to be considered. ....	238
Table 5.2: Materials properties taken into account for the FEM simulations. ....	244
Table 5.3: FEM simulations of the temperature distribution in different packaging configurations. ....	246
Table 5.4: FEM simulations of the shear stress distribution in different packaging configurations. ....	247
Table A1.1 Typical values of the convection heat transfer coefficient ....	257
Table A1.2 Typical values of radiation heat transfer coefficients (emissivity). ....	258
Table A1.3 Summary of heat transfer processes. ....	259
Table A2.1 Summary of different characterization techniques. ....	271

# LIST OF ABBREVIATIONS

AES: Auger electron spectroscopy.	IMC: Intermetallic compound.
AFM: Atomic force microscopy.	IR: Infrared.
AMB: Active metal brazing.	LANE: Laser-assisted nano-engineering lab.
AMM: Acoustic mismatch model.	MCM: Multi-chip module.
BSE: Back-scattering electron.	MOSFET: Metal-oxide semiconductive field effect transistor.
CCVD: Combustion chemical vapor deposition.	MMC: Metal matrix composite.
CMC: Ceramic matrix composite.	MWCVD: Microwave assisted chemical vapor deposition.
CPU: Computing processing unit.	OES: Optical electron spectroscopy.
CTE: Coefficient of thermal expansion.	PCB: Printed circuit board.
CVD: Chemical vapor deposition.	PMC: Polymer matrix composite.
Cu/C: Carbon fiber-reinforced copper matrix.	PPS: Pulse plasma sintering.
Cu/D: Diamond-reinforced copper matrix.	PVD: Physical vapor deposition.
Cu/D(Cu): Copper-coated diamond-reinforced copper matrix.	RoHS: Restriction of the use of certain hazardous substances in electrical and electronic equipment.
Cu-B/D: Diamond-reinforced boron-alloyed copper matrix.	SAC: Tin (Sn) silver (Ag) copper (Cu)
Cu-Cr/D: Diamond-reinforced chromium-alloyed copper matrix.	SE: Secondary electron.
DBA: Direct bonded aluminum.	SEM: Scanning electron microscopy.
DBC: Direct bonded copper.	SOD: Silicon-on-diamond.
DMM: Diffuse mismatch model.	SPS: Spark plasma sintering.
EDXS: Energy dispersive x-ray spectroscopy.	TBR: Thermal boundary resistance.
FCC: Face centered cubic.	TEM: Transmission electron microscopy.
HFCVD: Hot filament assisted chemical vapor deposition.	TIM: Thermal interface material.
HPHT: High-pressure high-temperature.	TPCVD: Thermal plasma assisted chemical vapor deposition.
HIP: Hot isostatic pressing.	UB: University of Bordeaux.
IC: Integrated circuits.	UNL: University of Nebraska-Lincoln.
ICMCB: Institute of condensed matter chemistry of Bordeaux.	WEEE: Waste electrical and electronic equipment.
IGBT: Insulated gate bipolar transistor.	XPS: X-ray photoelectron spectroscopy.
	XRD: X-ray diffraction.

# **CHAPTER 1: INTRODUCTION**

---

## **1.1 Motivations**

## **1.2 Overview of the dual PhD program**

## **1.3 Dissertation outline**

---

## 1.1 Motivations

### ▪ *Technological context:*

In a context of industrial and transportation systems increasingly relying on electrical energy, the power electronics industry has known a rapid growth since the 1950s [1, 2]. Power electronics mainly consist of semiconductor devices acting as electrical energy convertors or switches in high-power systems. They are used to change the form of an electrical current from direct to alternative (or reverse), or to modify the potential and/or the current intensity. For instance, power electronic modules are integrated to engines or alternators for electrical energy management purposes. Therefore, power electronics are mainly found in embarked transportation systems (aeronautics, railway, automotive and, increasingly, hybrid vehicles), and more generally, in electricity production, conversion, and distribution systems. While microelectronics typically have to handle currents of less than one ampere and potentials of a few volts, power electronics frequently have to deal with tens of amperes and hundreds of volts.

The current technological trends place the power electronics industry in front of a challenging future. Indeed, the constant increase in electrical power raises concerns about technical limitations that have to be overcome in order to maintain a constant level of performances and lifetime. Especially, thermal aspects in electronic packages (either power electronic or microelectronic) are problematic. In 1965, Intel co-founder Gordon E. Moore noticed that the number of transistors per solid-state integrated circuits (ICs) (also called the *packing density* ( $\text{cm}^{-2}$ )) had doubled every two years since the invention of the ICs in 1958. He stated that this trend would last for at least ten more years. His intuition is still currently valid, partly because the semiconductor industry has used this statement as a basis to guide long-term planning and set research and development goals. Moore's law has been the driving-force for the miniaturization and performance improvement of IC-based devices, in terms for instance of clock speed and memory capacities, which roughly increase at an exponential rate since the 1960's. Figure 1.1 illustrates this trend in the fabrication of computing processing units (CPUs):

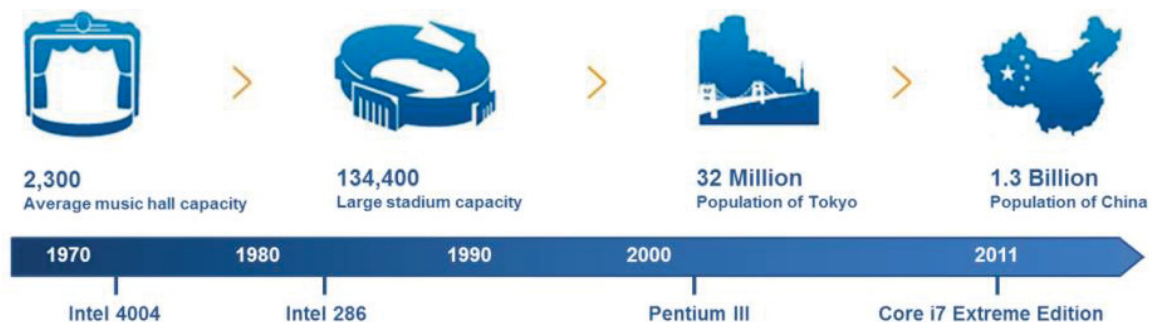
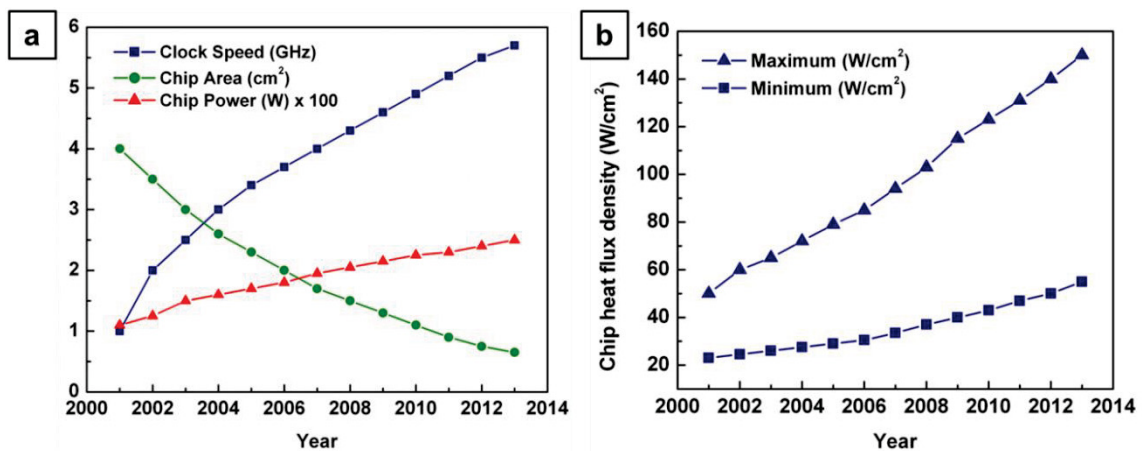


Figure 1.1: Timeline figuring Moore's law pace in CPUs, when replacing transistors by people [3].

Although such an exponential trend cannot continue indefinitely due to fundamental limits imposed by physics and technology, such barriers have to date been overcome through innovation. The continuous decrease of the size of a unit transistor has allowed a dramatic improvement of the overall circuit performance and an equally significant reduction of cost per manufactured component. In addition, the development of multichip modules (MCMs) and three-dimensional high-density packaging technologies, allowing mounting a large number of chips extremely close together, induce significant reductions in signal path length and contribute reaching higher operating frequencies [4-6]. In microelectronics, these trends are especially remarkable when considering the constant progresses of personal communication devices (laptops, cellphones, tablets, and other wireless devices). Power electronic industry, as any other semiconductor-based sector, is driven by the very same trends of increasing operating speed (higher frequency), increasing integration level (higher power), and decrease in feature size (higher packing density).

However, these trends unavoidably lead to an increase in power and heat flux densities generated by the active chips. Indeed, since the chips do not exhibit a 100% signal processing efficiency, a fraction of the electrical input is converted into heat and has to be dissipated. The dissipation of energy into heat has long been recognized as an issue that might limit electric signal processing. Nowadays however, this thermal barrier seems to be the most difficult to break to reach higher performance. While the chip power density was typically about  $0.5 \text{ W/cm}^2$  in the 1980's, it reached  $40 \text{ W/cm}^2$  in the early 2000's, and now frequently reaches  $150 \text{ W/cm}^2$ . In a same manner, chip heat flux density now frequently reaches  $100 \text{ W/cm}^2$ . Near-future projections anticipate maximum heat flux densities close to  $200 \text{ W/cm}^2$  in high-performance chips, which is equivalent to the heat dissipated by a nuclear reactor or a rocket entering the Earth's atmosphere. Figure 1.2 shows the current trends driving semiconductor industry, in terms of operating speed, chip size, and chip power and heat flux densities:



**Figure 1.2: Trends in semiconductor industry as a function of time. (a) Clock speed, chip area, and chip power (maximum estimations). (b) Chip heat flux density as a function of time [7, 8].**

These high levels of heat flux density raise concerns about the thermal management of the modules, which is critical to their reliability and lifetime. A rough estimate shows that high temperature is responsible for about 55% of the failures occurring in electronic components, while 6%, 19%, and 20% of these failures originate from dust, humidity, and vibration, respectively [8]. Consequently, thermal management has now become a major limiting factor to further development of power electronics technology and there is a strong demand for more efficient thermal management materials at a competitive cost [4, 5, 7-9].

Figure 1.3 provides a three-dimensional view of the architecture of a multi-chip power electronic module, where the chips are mounted together onto an insulating ceramic substrate, a copper base plate, and a heat sink. The active chips are bonded to thin films copper tracks through wire bonding. External metallic connections are also visible on the 3D view. A more detailed description of the structure of such module is given in chapter 2.

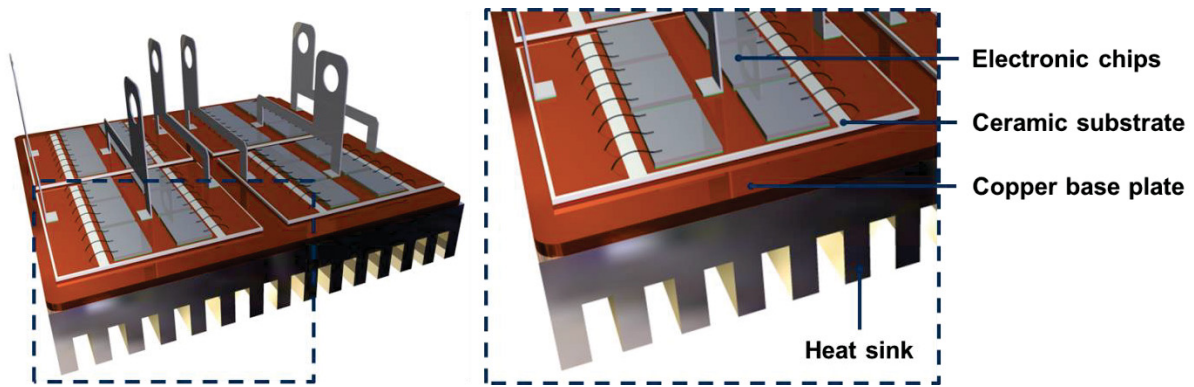


**Figure 1.3: 3D view of a multi-chip power electronic module [10].**

In a power electronic module, multiple substrate materials are attached to the active chips in order to conduct and dissipate the heat flux. The heat removal capacity of the package is limited by its total thermal resistance, which is the sum of the thermal resistances of each layer involved in the module architecture. In order to minimize the thermal resistance of the module, the cooling procedure of the device must be carefully analyzed by taking into account the different materials involved and their thermo-physical properties. In order to preserve the reliability of the active components, it is of critical importance to keep their temperature below their maximum operating temperature (also called *junction temperature*), which is typically located between 125°C and 175°C for a silicon chip. Above this temperature, the chip might become unstable and fail to short-circuit [10]. In addition, it is crucial to limit the creation of thermo-mechanical stresses induced by mismatches of coefficient of thermal expansion (CTE) between neighboring layered materials. Depending on the respective CTEs of the materials in the package, repeated tensile or compressive stresses are generated upon thermal cycling that might affect the mechanical integrity of the layered assembly, and lead to catastrophic failures [11].



Cooling methods for power electronic modules can be classified into two main categories: *passive* and *active*. Passive cooling solutions include heat-spreaders and heat-sinks that only rely on natural conduction and convection processes. Active cooling solutions on the contrary rely on electrical power to remove heat, and not only involve natural conduction and convection but also, and mainly, forced convection [8, 12].

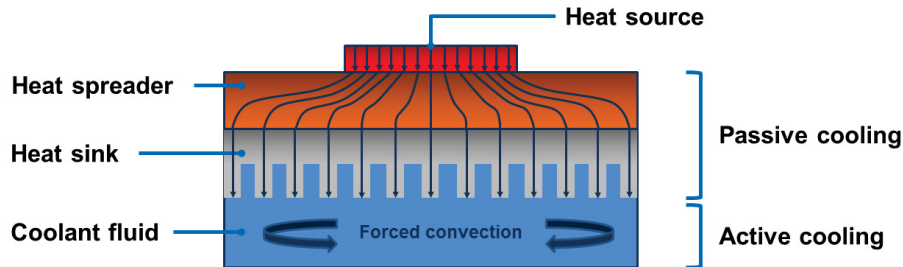


Figure 1.4: Overview of how passive and active cooling solutions combine in a power module [5].

- ***Passive cooling solutions:***

While active cooling devices and materials require electrical power to work, passive solutions, on the other hand, are self-sufficient. They mainly include metals and advanced composite materials with high thermal conductivity and adapted CTE, among them copper (Cu), aluminum (Al), copper/tungsten (Cu/W), copper/molybdenum (Cu/Mo), copper/carbon (Cu/C), and aluminum/silicon carbide (Al/SiC). Their main advantages are their simplicity, ready availability, relatively low costs, and ease of application.

Clear distinction between the respective roles of a heat sink and a heat spreader has to be made when dealing with passive heat dissipative materials. A thermal heat spreader material serves as an interface between a heat source and a heat sink. The primary function of the heat spreader is to collect heat from the source and spread it in a minimum amount of time onto the heat sink surface, which will eliminate the heat, as shown on Fig. 1.4. In other words, the heat spreader's role is to extract the heat rapidly from the source, where the heat is concentrated into a limited volume, and spread it over a large area. Therefore, the heat spreader allows preventing the creation of points of excessive temperature (*hot spots*) in the active chips, while the heat sink dissipates the heat [4, 5].

Showing a pin fin or plate fin architecture, the heat sink enables increasing the heat dissipation surface, thus enhancing convection heat transfer [13]. While a high heat capacity is needed for a material to be used as heat sink, a high in-plane thermal conductivity is the main characteristic to consider when selecting a heat spreading material. Heat sinks and heat spreaders are investigated in chapter 2. Passive cooling materials are sufficient to dissipate heat from certain products, especially small electronic devices with low heat output, such as MP3 players and mobile phones. It is also

adapted to other consumer electronic products such as televisions by providing sufficient vents on the product case to let the cool air enter and the heated air leave the case freely.

In a same manner, heat pipes constitute another passive cooling solution for electronic packages. Heat pipes provide a passive two-phase heat transfer method to transmit a large quantity of heat from a confined space to a condenser with minimum temperature drop. A classical heat pipe consists of a metallic vessel in which its inner walls are lined with a wick structure. The vessel is first vacuumed and charged with the coolant fluid (typically water, methanol, or liquid nitrogen) and hermetically sealed. When the heat is applied to one end of the metallic vessel, the working fluid vaporizes (phase change). The resulting pressure gradient forces the vapor to travel through the hollow core to the other end of the heat pipe, where it condenses back to liquid through a condenser, thus releasing latent heat. The liquid is finally pumped back to the original hot end by capillary action, completing the continuous evaporation/condensation cycle. The very same principle is employed in everyday-life refrigerators, coolers, and heat pumps. Heat pipes can help passive cooling of electronic packages by being included at the heat sink level or directly at the active chips level. Although providing an interesting passive cooling solution capable of dissipating large amounts of heat at low costs, the heat pipe technology suffer from depending on gravity for the capillarity to make the process work. Therefore, heat pipes still lack of applicability in airborne applications such as aeronautics and aerospace [5, 14].

- ***Active cooling solutions:***

Although passive cooling solutions can provide high heat removal rate, they solely cannot keep up with the thermal demands of high-performance and high-power electronics. Passive cooling solutions have to be teamed up with active cooling solutions to provide sufficient heat dissipation potential to a high-power electronic module. The main active cooling solutions involving forced convection are air cooling and liquid cooling, allowing convection heat transfer coefficients in the [25 – 250] and [100 – 20,000]  $\text{W.m}^{-2}.\text{K}^{-1}$  range, respectively [13].

Active air cooling relies on electric fans and blowers to induce air flow through the channels of the heat sink, thus increasing the coefficient of convection heat transfer and dissipating heat more efficiently than natural convection [13, 15]. Active liquid cooling solutions involves pumps to move the coolant fluid. They include liquid-cooled grooved and micro-channeled heat sinks, which are very promising cooling solutions to enhance heat dissipation in packages [16, 17]. In a same manner, immersion cooling and nucleate boiling, which brings the coolant in direct contact with the hot chips, allows the package architecture to be simplified by eliminating layers of substrate materials and their thermal resistance [18, 19]. Water is an excellent coolant fluid due to its desirable heat transfer characteristics, but is generally unsuitable for direct immersion cooling on account of its chemical characteristics. Indeed, chemical compatibility of the coolant fluid with the

chip and the other packaging materials exposed to the liquid is of primary consideration for the choice of a coolant fluid. Therefore, dielectric fluids (typically fluorocarbon coolants) are preferred fluids for direct immersion cooling at the chip level. In the same manner, liquid-jet impingement and spray cooling allow directing jets of coolant fluid onto the heat sink or directly onto the active chips, thus allowing the achievement of high-heat transfer rates but, again, raising concern about the chemical compatibility of the package materials with the fluid [20].

Finally, Peltier devices (or thermoelectric coolers) constitute another active cooling solution for electronic packages. The Peltier effect, or thermoelectrical effect, describes a heat transport phenomenon upon application of an electrical current, i.e. the conversion of an electrical current into a temperature variation. By circulating an electrical current in junctions between two different metals, electrons act as a coolant fluid, cooling one of the two metals while the other heats up. Therefore, Peltier devices are heat pumps that rely on the Peltier effect to transfer heat from one side of the device to another with consumption of electrical energy. The heat source must be located at one side, and a heat disposal device on the other. Thus, the heat from the heat source is dissipated through the two sides of the device. The main advantage of Peltier devices toward heat pipes is their compactness and low cost. Also, they do not include any circulating fluids or gases. Finally, their shape is more easily adapted to the structure to be cooled. However, the heat removal rate exhibited by Peltier devices is poor, far from those exhibited by heat pipes, while their electrical consumption is far from being negligible [21, 22].

Despite the fact that air cooling is by far the most employed cooling method for electronic packages, liquid active cooling can accommodate significantly higher heat fluxes due to higher specific heat and thermal conductivity of coolant liquids relative to gases. However, active liquid cooling involving pumps and jets tend to be more space-consuming relative to active air cooling systems which have demonstrated to be more compact. This is of critical importance given the miniaturization trends currently driving electronics and semiconductor industries and should have a key influence in future choices of active cooling solutions. Finally, liquid-based cooling systems may face reluctance from electronics industry which consider preferable to do not put liquids and active semiconductor chips in close contact.

Although the cooling architecture of power modules is expected to be more active-oriented in the next years for higher thermal efficiency, most of multi-chip power modules and discrete power electronic components only exhibit a base plate as the main heat dissipative element (Fig. 1.3). Therefore, passive cooling materials still have an important role to play in the thermal management strategy by quickly extracting the heat from the heat source, spreading it onto a larger surface, and dissipating it, thus preventing the active chips from excessive operating temperatures.

In this study, we will focus on the fabrication of passive solid-state heat spreaders to spread the heat quickly from the heat source to the heat sink, where the heat can be disposed more efficiently. Therefore, our primary objective is to create films materials (with thickness typically located in the [100 - 1000]  $\mu\text{m}$  range) with high in-plane thermal conductivity, suitable CTE with respect to the other materials of the module environment, limited weight impact, and high resistance to thermal cycling in operating environment.

▪ ***Diamond-based heat-spreaders:***

To do so, we will focus on diamond, which is a material of great interest for thermal application in electronics. Indeed, diamond combines in a very unique way an exceptional thermal conductivity (up to  $2000 \text{ W.m}^{-1}.\text{K}^{-1}$ ) to a high electrical resistivity (up to  $10^{13} \Omega.\text{cm}$ ), making it a material of primary choice for applications as heat conductive material in electrically active environments such as power packages [4].

Despite its exceptionally high thermal conductivity, diamond has a relatively low heat capacity ( $6.19 \text{ J.mol}^{-1}.\text{K}^{-1}$  at 300 K relatively to  $24.2 \text{ J.mol}^{-1}.\text{K}^{-1}$  for aluminum and  $24.5 \text{ J.mol}^{-1}.\text{K}^{-1}$  for copper). Consequently, in order to employ them to their best advantage, diamond-based materials should be used for heat-spreading purposes by incorporating it as an intermediate layer between a heat source and a heat sink. In addition, diamond exhibits a low CTE ( $[1-2] \times 10^{-6} \text{ }^{\circ}\text{C}^{-1}$ ), which makes it very stable from a dimensional aspect. Its CTE is also close to that of typical semiconducting materials such as silicon ( $2.6 \times 10^{-6} \text{ }^{\circ}\text{C}^{-1}$ ) and may also allow reducing the CTE of high thermal-expansion metallic matrix when used as a reinforcement material. Besides this promising combination of properties, diamond features the highest hardness of all materials, a high chemical inertness, and an extensive wear resistance [4].

Although natural diamonds have excellent properties for potential heat-spreading applications, their applicability is strongly limited by scarceness, thus prohibitive costs, and by variable composition from one sample to another. Furthermore, their physical dimensions severely limit the area to which they can be applied. To overcome these limitations, methods to synthesize diamond have been developed, among them high-pressure high-temperature (HPHT) synthesis, which allows producing synthetic diamond powders and crystals, and chemical vapor deposition (CVD) routes, which enable growing synthetic diamond films onto various substrate materials.

Two types of diamond-based heat-spreading films were investigated in this study:

- *Synthetic combustion CVD diamond films* deposited on electronic substrates through laser-assisted combustion synthesis;

- *Copper/diamond composite films* processed through tape casting and power metallurgy involving synthetic HPHT diamond powders.

In both cases, the microstructure of the final material, its chemical composition, the structure of the interfaces, and the influence of these factors on its thermal and thermo-mechanical performances were scoped. Especially, emphasis was put on the role played by bi-materials interfaces on the thermal properties of such systems, considering either interfaces between dissimilar materials (film/substrate interface, matrix/reinforcement interface) or that existing into the microstructure of a single material (grain boundaries).

Depending on the flexibility of each diamond-based heat spreading solution, especially in terms of thermal properties and thickness range, their packaging potential will be evaluated in order to employ them to their best advantage in the cooling procedure of a high-power package.

## 1.2 Overview of the dual PhD program

As described in Fig. 1.5, the thesis work described in this dissertation was carried out in the framework of a dual PhD program between two partners: the Laser-Assisted Nano-Engineering (LANE) lab, part of the department of Electrical Engineering of the University of Nebraska-Lincoln (UNL), in the U.S, and the Composite and Ceramics research group of the Institute of Condensed Matter Chemistry of Bordeaux (ICMCB), at the University of Bordeaux (UB), in France.

While my work in the U.S was focused on the combustion CVD diamond heat spreaders, my time in France was dedicated to copper/diamond composite films. The supervisors for these researches were Professor Yongfeng Lu and Professor Namas Chandra at UNL, and Professor Jean-François Silvain and Professor Jean-Marc Heintz at UB. Thermal characterizations of CVD diamond films were also carried out in France, at the Institute of Mechanics and Engineering, under direction of Professor Jean-Luc Battaglia. This four-year program was divided in two periods of time, each one two-year long. One was spent in the U.S; the other was spent in France.

A brief description of the dissertation outline is given in the next section, while deeper literature review of the characteristics of diamond, the ways to synthesize it, and how it can be useful for the thermal management of high-performance electronic packages is carried out in the next chapter of this dissertation.

## 1.3 Dissertation outline

The most significant contributions of this dissertation carried out at LANE lab – UNL are: 1) develop a laser-assisted combustion synthesis set-up to deposit CVD diamond films onto various substrates, 2) use scanning electron microscopy and transmission electron microscopy to investigate

the microstructure of the films and of its interfaces, 3) use Raman spectroscopy to quantify the phase purity and level of residual stress in the diamond films, 4) use an infrared photothermal radiometry set-up to investigate the thermal properties of the diamond films and to estimate the interface thermal resistances existing in diamond film/substrate assemblies, 5) investigate how bi-materials interfaces (both grain boundaries and film/substrate interface) impact their heat conduction potential.

The most significant contributions of this dissertation carried out at ICMCB – UB are: 1) develop a tape casting process to fabricate thin laminates of diamond dispersed copper matrix composite, 2) develop an innovative chemical bonding process for efficient heat transfer across copper/diamond interfaces, 3) use scanning electron microscopy and transmission electron microscopy to investigate the microstructure of the films and of its interfaces, 4) fabricate dense Cu/D composite products through hot pressing and power metallurgy, 5) evaluate the thermal performances of the copper/diamond composite films through flash laser radiometry, dilatometry, and thermal cycling, 6) evaluate the impact of the matrix/reinforcement interfaces on the heat conduction potential of the composite films.

This dissertation includes six chapters. In chapter 1, the motivations of this study are detailed and the dissertation outline is given. In chapter 2, fundamentals and recent development related to this study are reviewed. In chapter 3, the fabrication and the characterization of the heat-spreading CVD diamond films grown through laser-assisted combustion synthesis at UNL are explained and investigated. In chapter 4, the fabrication of copper/diamond composite films through tape casting and hot pressing and their characterization carried out at UB are described and studied. In chapter 5, the two diamond-based heat spreading solutions are compared from a technological prospective by using finite element simulation. Finally, a summary is given and future research directions are discussed in chapter 6.

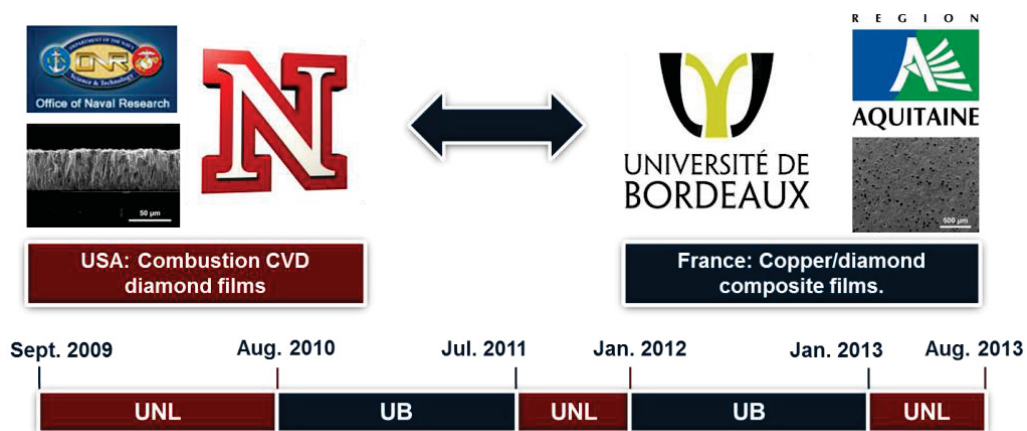


**Figure 1.5: Overview of the French-American dual PhD program between the University of Nebraska-Lincoln (UNL), in the U.S, and the University of Bordeaux (UB), in France.**

## **CHAPTER 2: BACKGROUND AND REVIEWS**

---

**2.1 Power electronic package architecture**

**2.2 Main thermal management issues in power modules**

**2.3 Diamond: a unique material**

**2.4 Diamond synthesis**

**2.5 Heat-conductive diamond-based systems**

**2.6 Conclusion**

---



## 2.1 Power electronic package architecture

The primary role of semiconductive power components is to act as switches in electrical energy conversion circuits [10, 23]. They typically consist in Schottky diodes, insulated gate bipolar transistor (IGBT), metal-oxide semiconductor field effect transistors (MOSFET), and thyristors. Since their appearance about sixty years ago, semiconductive power components have seen immense technology evolution, following the trends driving semiconductor industry described in chapter 1. These devices are now able to carry electrical currents of more than 100 A and are able to block voltages of several kilovolts. As a result, power on a single 1 cm<sup>2</sup> chip frequently reaches 150 W, leading to a heat flux of more than 100 W. Because a non-negligible fraction of this electrical power is converted into heat, its dissipation is of critical matter to the reliability and lifetime of power modules, which can contain multiple chips in the case of multi-chip packages (Fig. 1.3). In such context, the close environment of the power chips, also named as their *packaging*, plays a key role in their safety and reliability. Figure 2.1 describes the typical packaged architecture of a power electronic module:

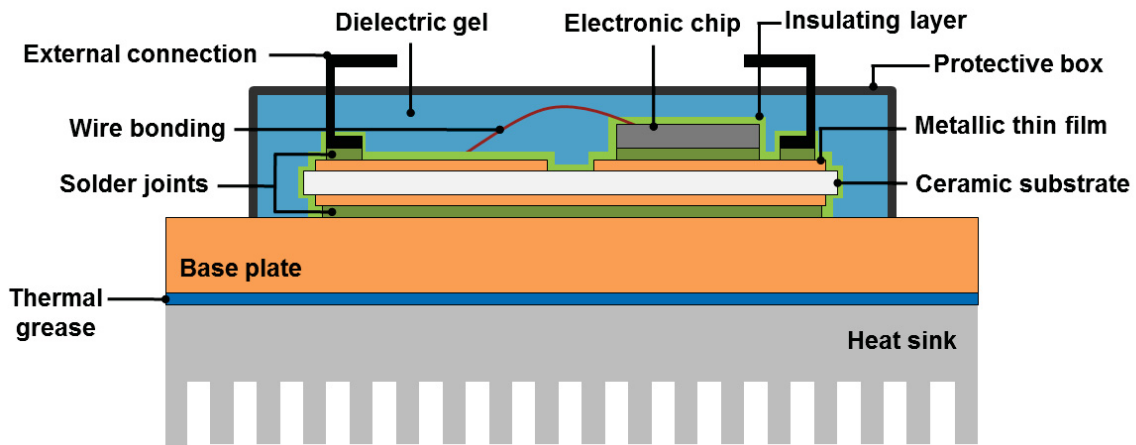


Figure 2.1: 2D cross-sectional architecture of a power electronic module [10].

The packaging has multiple functions [5, 10]:

- *Mechanical protection*: active chips being extremely sensitive to dust, humidity, and static electricity, the primary role of the packaging is to protect the chips from outside aggressive agents. This function is ensured by a solid protective box filled up with a dielectric gel;
- *Electrical connection*: electrical connections between the chips and the outside environment are ensured by external metallic pins located on the front side of the module; electrical connections between the chips and internal environment are ensured through wire bonding connecting the front side of the chips to conductive copper tracks coating the upper side of the ceramic substrate;



- *Electrical insulation*: the chips are mounted onto an dielectric ceramic substrate in order to electrically insulate the active components from the lower levels of the module; in addition, the chips are coated with a polymer film to protect them against electrical shocks;
- *Thermal dissipation*: the base plate and the heat sink are the two main elements providing heat dissipative potential to the assembly.

Figure 2.2 shows photographs of a power electronic module at different stages of the assembly process:

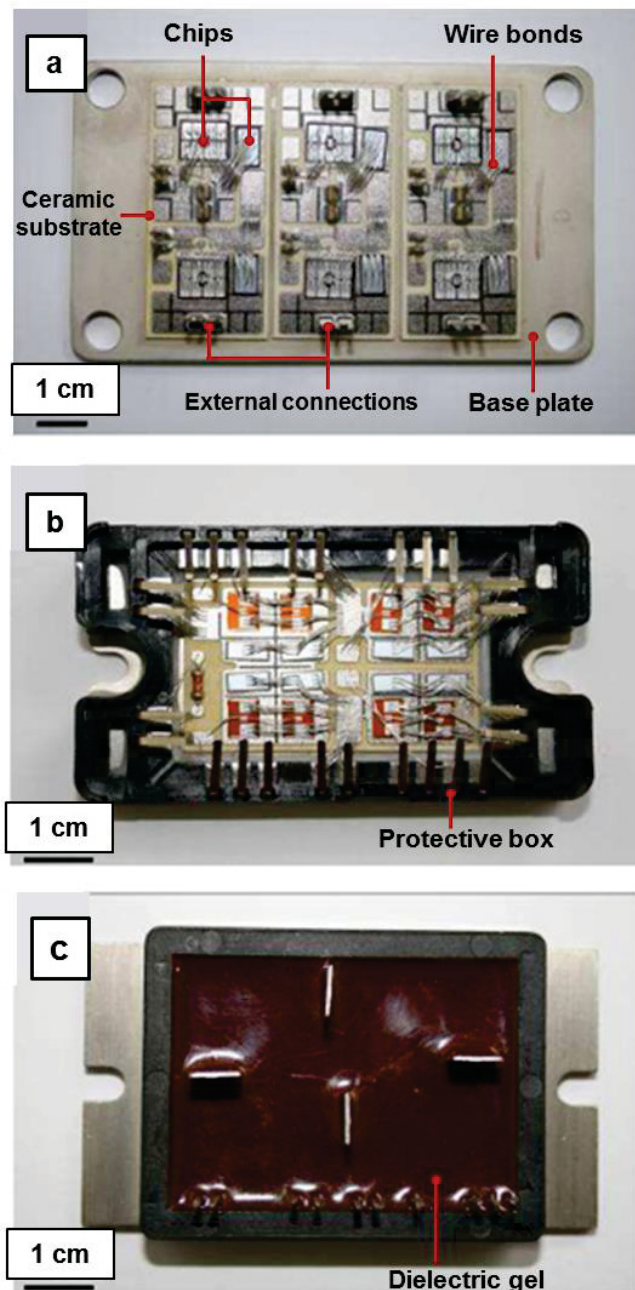


**Figure 2.2:** Photographs of a multi-chip power module: (a) Chips – ceramic – base plate; (b) Chips – ceramic – base plate – encapsulation (c) Chips – ceramic – base plate – encapsulation – protective gel.

Each component of the package has a specific function and the module cannot operate properly if one of them is missing or malfunctioning. The following paragraphs describe some of the packaging elements and the materials they typically involve.

- **Electronic chip:**

The electronic chips ensure the processing of the electric signal and are the only electrically active components of the module. Although a small percentage (1%) of power chips made of wide band-gap semiconductors such as silicon carbide (SiC) or gallium nitride (GaN) starts appearing for temperature applications up to 350°C [24-26], the very large majority (99%) of them is made of silicon (Si) due to its interesting band-gap and low production cost. It has now entirely replaced formerly-used gallium arsenide (GaAs) in ICs fabrication. Semiconductor materials such as Si, SiC, or GaN show limited intrinsic electrical conductivity but which can be improved by several orders of magnitude through n-type or p-type doping (introduction of electrons or holes in excess through the addition, for instance, of boron or phosphorous atoms, respectively). The physical properties of the electronic chip set the maximum operating temperature of the module (or maximum *junction temperature*), typically located around 150°C for a Si chip. The electronic chip is usually 600 μm thick [10,23]. A passivation layer in the form of a thermo-resistant polymer coating (typically polyimide) is applied to the chips in order to protect them against potential electrical shock.

**Table 2.1: Thermo-physical properties of different electronic chip materials [5,10].**

Material	Band Gap (eV)	$\alpha \times 10^{-6} (^{\circ}\text{C}^{-1})$	$k (\text{W.m}^{-1}.\text{K}^{-1})$	$\rho (\text{g.cm}^{-3})$	$T_{\text{max}} (^{\circ}\text{C})$
Si	1.1	2.6	[150-170]	2.33	150
SiC	2.4	4.3	[200-300]	3.21	350
GaN	3.4	3.2	150	6.1	350

In microelectronics, the electrically active parts of the chip are concentrated in a few micrometer thick area located at one side of the chip; the rest of the chip structure only serves as a mechanical support of the active area. In power electronics however, both sides of the chips are involved in the electric function, i.e. the whole volume of the semiconductive material is electrically active. This type of architecture is required by the high currents and voltages that the chip has to handle. Therefore, the soldering layer attaching the back side of the chip to the metallic film (Fig. 2.1) not only has to ensure mechanical bonding and thermal dissipation, but also electrical connection [5,10].

- **Wire bonds:**

Wire bonding consists in electrically connecting the active chips to the metallic film that acts as electronic conduction pathway on top of the ceramic substrate (Fig. 2.1). The high current existing

in power chips (up to 200 A for a 1 cm<sup>2</sup> chip) requires interconnections with minimum electrical resistivity. Gold is typically used in microelectronics due to its outstanding electrical conductivity [5]. In power electronics however, the large amount of metal used for interconnections make the cost of gold-based wire bonds prohibitive. Therefore, aluminum is preferred for power applications since it combines a sufficient electrical conductivity to affordable cost. In order to reduce the global electrical resistance of the interconnection, several wire bonds (up to ten) are assembled in parallel on a same chip. Typically, a 300  $\mu\text{m}$  diameter wire bond can handle a current of 20 A. The wire bonds are processed through ultrasonic welding. They can reach 500  $\mu\text{m}$  diameter [10].

**Table 2.2: Thermo-physical properties of different wire bonding materials [5,10].**

Material	$R_{elec}$ (n $\Omega$ .m)	$k$ (W.m <sup>-1</sup> .K <sup>-1</sup> )	Cost (\$·g <sup>-1</sup> ) (May 2013)
Au	22.1	320	54
Ag	15.9	430	32
Al	28.2	230	1.9

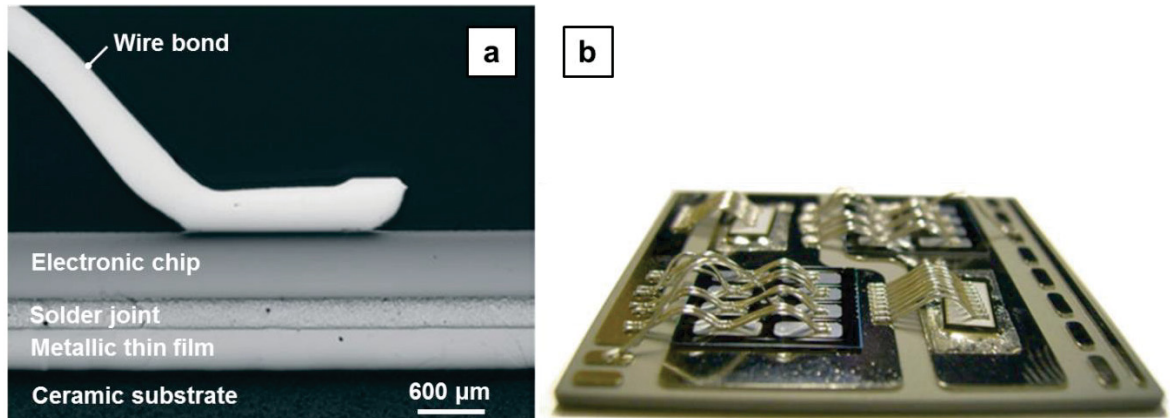


**Figure 2.3: (a) SEM micrograph and (b) photograph of chip wire bonding.**

- **Solder joints:**

Unlike microelectronics in which numerous techniques make it possible to bond the chips to their substrates (soldering, thermocompression, silver-loaded epoxy resin) [5], the very large majority of power chips are mounted onto their substrate through soldering. Soldering is an assembly technique that does not rely on the melting of the parts to be assembled (unlike welding), but only on diffusion phenomena and atomic migration. The main advantage toward welding is a lower processing temperature, which allows mitigating the microstructural degradation of the parts to be assembled. Also, the stresses and strains induced by the process are lowered. As shown in Tab. 2.3, a variety of soldering alloys is available. The soldering material has to exhibit a melting temperature lower than that of the parts to be bonded. It also has to capillary wet both parts and to

allow atomic diffusion upon heating. The resulting joint has to exhibit acceptable thermal and electrical conductivities and demonstrate sufficient mechanical strength to sustain the mismatch of coefficients of thermal expansion existing between the layers it bonds [5,10]. A solder joint between a chip and the metallic thin film of a ceramic substrate is visible on the micrograph of Fig. 2.3a.

Soldering is used in power modules at two locations: at the interface between the chip and the ceramic substrate, and at the interface between the ceramic substrate and the base plate. The fact that two different solder joints (chip/substrate and substrate/base plate) have to be processed in a single module implies that two different soldering alloys with two melting temperatures at least 40°C different have to be employed. Indeed, the chip/substrate joint (processed at first) should not melt when the ceramic substrate/base plate joint is processed. Also, the soldering alloys must have melting temperatures at least 10°C above the maximum operating temperature of the module (in order to resist in operating environment, typically 150°C), and below the maximum temperature that can be sustained by the chips (in order to do not degrade the chips during soldering, typically below 350°C). For instance, PbSn solder can be used to bond the chip to the ceramic, while SnAgCu solder is used for the ceramic/base plate bond. The solder joints are about 250 µm thick [10].

**Table 2.3: Thermo-physical properties of different soldering alloys [10].**

Solder composition (at.%)	T <sub>liquidus</sub> / T <sub>solidus</sub> (°C)	$\alpha \times 10^{-6}$ (°C <sup>-1</sup> )	Remarks
Sn <sub>63</sub> Pb <sub>37</sub>	183	25	Low melting temperature (eutectic composition), outstanding mechanical properties, good wettability toward copper, low cost. High toxic lead content.
Sn <sub>96.5</sub> Ag <sub>3.8</sub> Cu <sub>0.7</sub>	220/217	22	Recommended alloy to replace Sn/Pb alloys, many combinations with various copper contents.
Sn <sub>95</sub> Ag <sub>5</sub>	240/221	22	Excellent mechanical strength, but wide plastic domain which renders it hardly usable.
Au <sub>80</sub> Sn <sub>20</sub>	280	16	Alloy with high hardness and excellent thermal performances. High cost.

Although tin/lead alloy has been the predominant soldering choice for decades due to its excellent properties, lead is progressively banned from most of electronic products due to its high toxicity, as preconized by the European Restriction of Hazardous Substances (RoHS) [27] and Waste Electrical and Electronic Equipment (WEEE) [28] directives in the U.E. Similar law-enforcement have emerged in the U.S. and other industrialized countries such as Japan, although in a less-advanced fashion relative to the U.E. [29]. Therefore, electronic industries are urged to find alternative solutions to replace former lead-base soldering alloys, such as tin/silver/copper alloys (Sn/Ag/Cu, or SAC alloys).

Soldering alloys exist under two forms [10, 29]:

- *Solder pastes*: They consist in a mixture between the alloy, as a powder, and organics (a binder, which provides mechanical tenue to the paste, and a flux, which cleans the surfaces to be soldered and enhances their wettability toward the soldering alloy);
- *Solder preforms*. They consist in thin foils of the soldering alloy (without any additives) applied onto the surfaces to be soldered.

The soldering process is thermally activated. Various means are available (oven, laser, electric arc) but hot air flux is preferred in power electronics. While solder preforms lead to a soldering process that is cleaner (no organic compounds to be eliminated) and more precise (more accurate control of the soldered area and of the final joint thickness), solder pastes are cheaper, thus preferable for large area soldering, such as the one between the base plate and the ceramic substrate. Solder pastes are applied onto the areas to be soldered through serigraphy.

Despite the wide variety of soldering alloys available, the soldering technique shows limitations: the fact that the melting temperature of the soldering alloy has to be higher than the maximum operating temperature of the module imposes severe thermal stresses to the active components upon soldering. In addition, the need for soldering alloys with different soldering temperatures in a single package renders the process even more problematic. Therefore, new soldering solutions are investigated which do not imply the fusion of the bonding material. One of these is a solder paste developed by Semikron [30] which contains micrometric silver balls embedded in an organic binder. Bonding is achieved by heating up the paste to 240°C (thus way lower than the melting point of silver: 961°C) upon a pressure of 10 MPa which leads to the sintering of the silver particles, leading to a joint with thermal and electrical properties close to that of pure silver and stable up to 961°C, without resorting to the melting of the material.

Another non-melting emerging technology that is gaining increasing importance on the soldering market is diffusion bonding, involving alloys such as Sn/Cu or Cu/Au as bonding materials [31]. These metals make possible the chemical bonding of different parts of the module through exhaustive diffusion of a bonding metal into the parts to be assembled upon pressure and temperature and their transformation into intermetallic compounds (IMCs) and/or solid solutions (see Fig. 2.4). While the microstructure of classical solder joints are affected by thermal cycling (grain growth, diffusion phenomena), the diffusion bonding technique permits obtaining a joint with a microstructure that does not evolve upon future heating in operating environment since its microstructure has reached its final state at the end of the bonding process. Therefore, while the maximum temperature of safe-operation of a classical solder joint is limited by the diffusion phenomena and microstructural changes triggered upon heating [32], a diffusion bond can operate at higher temperature (400°C to 600°C) thanks to its microstructural stability. Diffusion bonding is therefore especially interesting for high temperature applications. The diffusion bonding material



(typically tin (Sn, Fig. 2.4a) or gold (Au, Fig. 2.4b)) is electrodeposited onto the parts to be assembled.

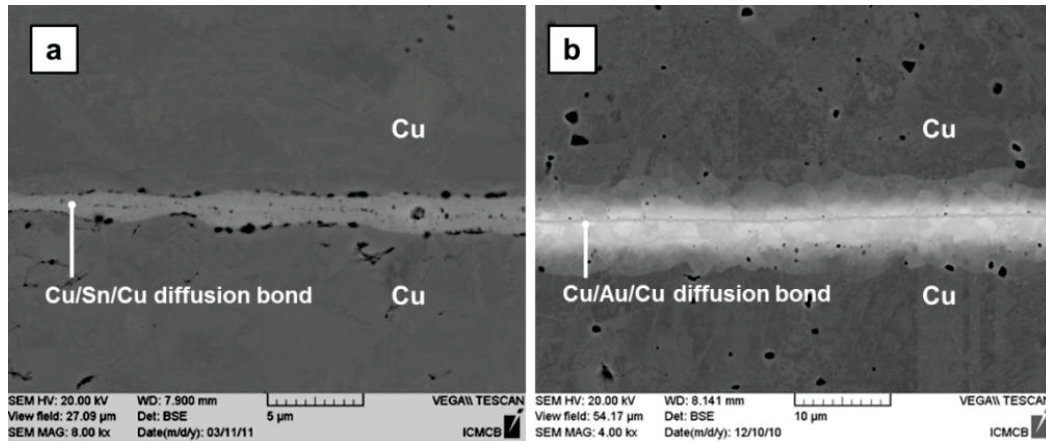


**Figure 2.4: SEM micrographs of (a) Cu/Sn/Cu and (b) Cu/Au/Cu diffusion bonds [31].**

However, the brittleness of the IMCs formed upon diffusion bonding constitutes a key issue to its application, since diffusion bonds cannot handle large thermal stresses. Therefore, this technique is especially interesting when bonding the ceramic substrate to the heat sink, where a copper-to-copper joint has to be created, thus involving the same metal on both sides of the joint and therefore limited CTE mismatch.

#### ▪ ***Ceramic substrate:***

In microelectronics, the active chips are mounted onto a printed circuit board (PCB) which simultaneously ensures their electrical interconnection, their mechanical assembly, and their electrical insulation from the backside of the package. Microelectronics PCBs typically consist in composite substrates made of an organic epoxy matrix reinforced with glass fibers and coated with a metallic thin film through electrodeposition (typically copper). However, PCBs are not suitable for power electronics applications because of their low thermal conductivity (below  $1 \text{ W}\cdot\text{m}^{-1}\cdot\text{K}^{-1}$ ), high thermal expansion coefficient ( $60 \times 10^{-6} \text{ }^\circ\text{C}^{-1}$ ), and limited maximum operating temperature ( $200^\circ\text{C}$ ) [5].

Therefore, power electronic chips are mounted onto a substrate made of a ceramic plate coated on both sides with thin metallic films. Similar to PCBs, this ceramic substrate has several technical purposes: ensure electrical insulation between the active chips and the external environment, provide mechanical stability to the assembly, and conduct heat to the lower parts of the module for heat dissipation. The ceramic material used is generally alumina ( $\text{Al}_2\text{O}_3$ ), although aluminum nitride (AlN) or silicon nitride ( $\text{Si}_3\text{N}_4$ ) are sometimes preferred for higher temperatures applications due to their superior thermal conductivity (Tab. 2.4). AlN and  $\text{Si}_3\text{N}_4$  also offer the advantage to have CTEs closer to that of chip materials (Tab. 2.1) relative to  $\text{Al}_2\text{O}_3$ . In addition,  $\text{Si}_3\text{N}_4$  exhibits very

interesting flexion strength that may allow the fabrication of power packages without resorting to a base plate to ensure mechanical stability, thus lightening the package architecture and getting rid of a certain number of interfacial thermal resistances. Finally, beryllium oxide (BeO) offers excellent heat conduction performances, but is left over by the electronics industry due to its high toxicity. These materials are good electrical insulators and at the same time, enable sufficient heat conduction. The dielectric ceramic substrate is coated on both sides with a thin metallic film that plays the role of electronic conduction pathway connected to the electronic chip on one side, and on the other side of contacting layer for soldering with the base plate. The ceramic substrate is typically 650  $\mu\text{m}$  thick, while the metallic coatings are usually 250  $\mu\text{m}$  thick [10]. The coated metal is either Cu or Al.

**Table 2.4: Thermo-physical properties of different ceramic substrates materials [5,10].**

Material	$\alpha$ ( $10^{-6} \text{ }^{\circ}\text{C}^{-1}$ )	$k$ ( $\text{W.m}^{-1}.\text{K}^{-1}$ )	$\rho$ ( $\text{g.cm}^{-3}$ )	Flexion strength (MPa)	$R_{elec}$ ( $\Omega.\text{m}$ )
$\text{Al}_2\text{O}_3$	7.2	[20 – 35]	3.90	345	$10^{19}$
AlN	4.6	[150 - 180]	3.26	360	$10^{12}$
$\text{Si}_3\text{N}_4$	3	[60 – 70]	3.44	932	$10^{12}$
BeO	7.5	[220 – 270]	3	250	$10^{15}$

In power electronics, the metal coatings are processed by bonding metallic foils to the ceramic substrate through two main methods.

- *The direct bonding method*: when using copper, this technique consists in heating a copper/ceramic/copper layered assembly at a temperature located below the melting temperature of copper (typically 1060°C when  $T_{\text{melting Cu}} = 1084^{\circ}\text{C}$ ) but above the melting temperature of oxidized copper (eutectic in the Cu-O phase diagram). Therefore, a thin layer of the copper foils in contact with the ceramic melt, thus creating a spinel with the ceramic. This process is typically employed for  $\text{Al}_2\text{O}_3$  substrate, but may also be applied to AlN substrates if the surfaces of the ceramic are preliminary oxidized. The as-processed copper/ceramic/copper assemblies are labeled as *Direct Bonded Copper* (DBC) substrates (Fig. 2.5) [33]. When aluminum is coated on the ceramic instead of copper, the substrates are labeled as *Direct Bonded Aluminum* (DBA) substrates. Aluminum coatings are especially interesting when the employed ceramic substrate is AlN.

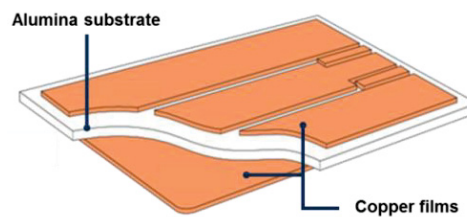


**Figure 2.5: Cross-sectional view of an alumina DBC substrate.**

- *The Active Metal Brazing (AMB)*: the AMB technique consists of brazing the copper foils onto the ceramic substrate through an Ag-Cu soldering alloy. This method usually requires lower temperatures relative to the direct method and is mainly used for AlN and Si<sub>3</sub>N<sub>4</sub> substrates.

The upper copper film is patterned as-desired to act as an electrical conduction track through a classical serigraphy process (masking, exposure, chemical etching, cleaning). The metallized surfaces are finally protected against oxidation using gold or nickel thin layers.

- ***Encapsulation and protective gels:***

Prior to being encapsulated, the active components are coated with a polyimide layer (1 to 10 µm thick) in order for them to be electrically insulated. The module is then encapsulated and filled out with a dielectric encapsulation gel which allows electrical insulation and provide sufficient mechanical tenue to the chips and wire bonds. However, if the gel is too rigid it will degrade the wire bonds. The gel has to recover the holes that may exist in the assembly, thus providing protection toward the external environment (air, light). The gel must also be chemically compatible with the chips, not affected by humidity (since it leads to a drop in dielectric potential) and able to sustain the operating temperature of the module without being degraded. Silicone gels and epoxy resins fill these requirements and are typically chosen as encapsulation materials. Silicone is more attractive from a chemical point of view due to its lower toxicity relative to epoxy. However, epoxy provides higher stiffness. Silicone and epoxy are sometimes associated in a two-layer fashion, a lower silicone level softly encapsulating the chips and wire bonds, and an upper epoxy level strengthening the encapsulation and providing high mechanical tenue to the packaging. Finally, the box containing the whole assembly, either made of plastic or metal, provides mechanical strength and shock resistance to the module [10].

- ***Base plate and heat sink:***

As mentioned in chapter 1, the ceramic substrate on which are mounted the power chips is soldered onto a base plate. This base plate has both thermal and mechanical functions. It first plays the role of a heat exchange surface between the hot upper parts of the module where the heat is generated and the cooling lower part of the package (heat sink, active cooling system). Secondly, its thickness (typically 3 to 5 mm), by far the largest in the assembly, allows mitigating the thermo-mechanical stresses that develop between the different layers upon thermal cycling and providing mechanical stability to the package. Therefore, metals are preferentially employed as base plate materials, as detailed in section 2.2. The base plate can be assembled onto a finned heat sink through clamping. In this case, a thermal interface material (or TIM, such as a thermal grease with  $k \sim 1 \text{ W.m}^{-1}.\text{K}^{-1}$ ) is usually employed to fill out the voids and gaps that may exist at the interface between the two parts, thus mitigating the contact heat transfer losses between the two elements



[34]. The base plate can also be directly associated to an active cooling system (liquid circulation, air blowers) to promote heat dissipation (see chapter 1). Nevertheless, in case of many power devices, either single or multi-chip packages, the base plate is directly clamped to an electronic rack, thus no presence of finned heat sink or active cooling solutions. Therefore, the base plate becomes the main element to be relied on for heat dissipation. In such context, diamond-based heat spreading films ([100 - 1000]  $\mu\text{m}$  thick) with high thermal conductivity and adapted CTE could be helpful to cool high-power packages by teaming up with the base plate. These films, depending on their properties, could either be located on top of the base plate or in the vicinity of the active chips.

The heat spreader should quickly extract the heat flux from the upper layers of the module and spread it onto the larger surface of the base plate, which would actually dissipate the heat. A suitable combination of properties is critical for the heat spreader in order to contribute the module lifetime. A high in-plane thermal conductivity is required in order to maintain the active components into their safe operating temperature area. In addition, the contacts between the heat spreader and its surroundings are critical. Defective thermal or mechanical contacts between two layers in close contact will critically affect the overall behavior of the operating package. Therefore, the heat spreader must have a CTE that is compatible with its neighboring layers. Also, flatness is required for solderability purposes. In section 2.2, we will explore in depth the materials employed for heat dissipation purposes and the specific thermal failures occurring in power packages.

If accessible in terms of thickness and fabrication, one could also consider using diamond-based materials to substitute the traditional alumina substrate (650  $\mu\text{m}$  thick) or even the copper base plate (3 mm thick), thus upgrading the package architecture. Various packaging configurations involving diamond-based materials such as those fabricated in this study are possible. They are more deeply explored in chapter 5.

## 2.2 Main thermal management issues in power packages

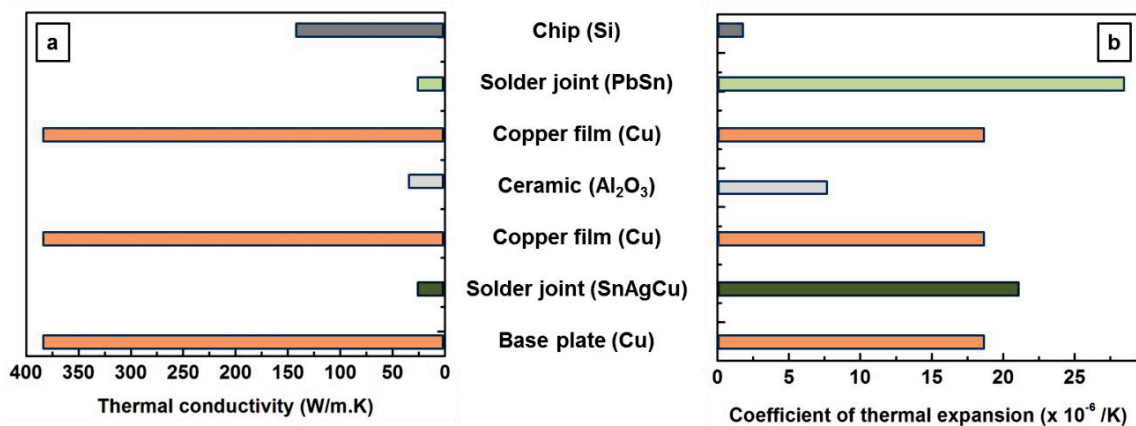
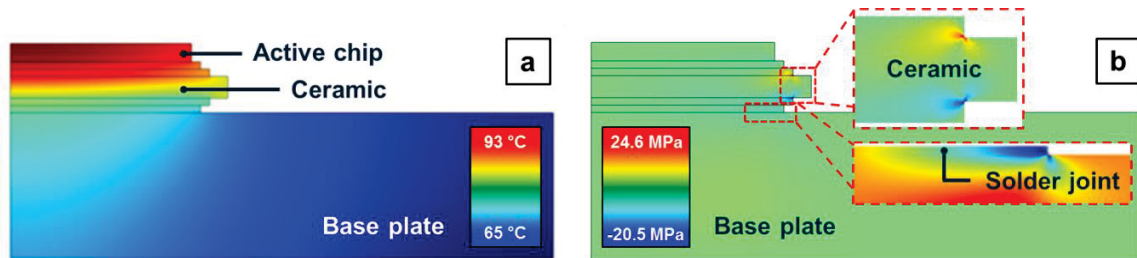


Figure 2.6: Thermal properties of the different materials composing a power package [5,10].

Section 2.1 provided a description of the architecture of a power electronic module as a layered structure made of different materials intimately mounted onto each other, each one having a precise role to play in order for the module to operate properly. Thermal management issues in power electronic modules precisely result from the fact that these assembled materials exhibit different thermo-physical properties, and especially different thermal conductivities and thermal expansion coefficients, as shown in Fig. 2.6.

Since the active chips act as heat sources and the package exhibits a global thermal resistance due to the finite thermal conductivities of the different layers, temperature gradients are created in the module structure, as shown on Fig. 2.7a where the active chip exhibits a temperature of about 93°C while the lower parts of the module exhibit a temperature of 65°C. The temperature level of the chips must be carefully bounded in order to prevent the creation of *hot-spots* (overheating), which affect the chip performances through unwanted atomic migration and oxidation phenomena.



**Figure 2.7: Finite elements simulations: (a) Temperature distribution and (b) shear stress distribution at the solder joint / copper base plate interface in an operating power module.**

The heat generated in the operating module leads to the creation of temperature gradients in the package structure. This makes the different layered materials expand differently upon temperature with respect to their CTEs. CTE mismatches between dissimilar neighboring materials lead to the creation of thermo-mechanical stresses that progressively affect the mechanical and thermal integrity of the assembly, and are likely to end up in catastrophic failures of some parts of the module upon repeated thermal cycles. Depending on the respective CTEs of the layers in vicinity, the stress can be either compressive or tensile, as shown in Fig 2.8.

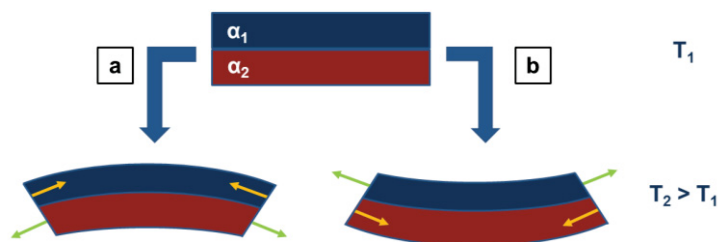


**Figure 2.8: Schematic view of how CTE mismatches leads to compressive (yellow arrows) and tensile (green arrows) stresses in bi-materials assemblies: (a)  $\alpha_1 > \alpha_2$ , (b)  $\alpha_1 < \alpha_2$ . [10]**

Thermal stresses jeopardize the reliability of the device, thus reducing its lifetime, and therefore have to be minimized. Especially, the CTE mismatch between the PbSn solder joint and the silicon chip ( $\Delta\alpha_{Si-PbSn} = 26.6 \times 10^{-6} \text{ }^{\circ}\text{C}^{-1}$ ) and that between the SnAgCu solder joint and the ceramic substrate in the lower level of the package ( $\Delta\alpha_{Alumina-SnAgCu} = 14.8 \times 10^{-6} \text{ }^{\circ}\text{C}^{-1}$ ) are large. Thus, solder joints are particularly sensitive areas and are great sources of fatigue rupture upon thermal cycling [11, 32, 35]. Fig. 2.9 shows a SEM micrograph of a solder joint between a chip and the metallized upper part of a ceramic substrate in which cracks have propagated upon repeated thermal cycles. Similarly, Fig. 2.7b shows a shear stress simulation where the maximum compressive stress is located in the solder joint between the base plate and the ceramic substrate. Simulations have demonstrated that the shear stress in the solder joint between the ceramic substrate and the base plate would be minimized with a base plate CTE of  $10 \times 10^{-6} \text{ }^{\circ}\text{C}^{-1}$  [36]. Finally, another well-known failure cause in power modules is the static rupture of the ceramic substrate that cannot sustain the CTE mismatch with the metallic thin films.

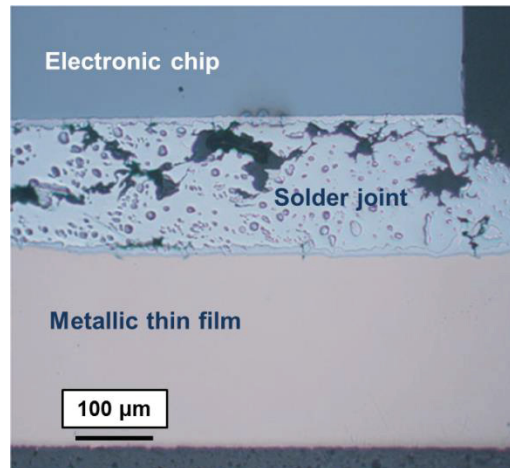


**Figure 2.9: Cross-sectional scanning electron micrograph of a cracked solder joint at the chip / metallic thin film interface [10].**

As a consequence, it is of primary importance to reduce the chances of module failure by employing heat conductive materials with high thermal conductivity but also coefficient of thermal expansion that is compatible with that of neighboring layers. Table 2.5 gathers some of the most common materials employed for heat conduction in power packages. Copper, aluminum, and silver are materials of primary choice due to their excellent thermal conductivity. Silver appears unqualified to any large-scale industrial application since its cost is prohibitive relative to copper and aluminum, although it exhibits fairly satisfying thermo-mechanical performances. Thus, its use is usually limited to specific niche applications. Aluminum features the strong advantage to have a density that is more than three times lower than that of copper, which makes aluminum a material of primary choice in applications for which weight is of particular importance, such as airborne systems in aeronautics and aerospace. The base plate and heat sink are indeed the largest and the

heaviest elements of the module (the base plate dimensions can reach 5 mm in thickness and 14×20 cm<sup>2</sup> in area). Nevertheless, the thermal performances of aluminum may appear too low for certain high heat-flux applications relative to copper. On the other hand, copper features an excellent thermal conductivity and a lower CTE relative to aluminum. Although more costly, its excellent thermal performances are of strong interest for the application we are aiming. Its high density makes however copper preferable for ground transportation systems such as automotive and railway comparative to airborne applications.

**Table 2.5: Thermo-physical properties of different heat-dissipative materials [5,10].**

Material	$\alpha (\times 10^{-6} \text{ }^{\circ}\text{C}^{-1})$	$k (\text{W.m}^{-1}.\text{K}^{-1})$	$\rho (\text{g.cm}^{-3})$
Cu	17	400	8.95
Al	23	230	2.70
Ag	19.7	430	10.50
W/[10-25] wt.% Cu	[5.6 – 8.2]	[180 – 240]	17
Mo/[30-50] wt.% Cu	[7.8 – 10.7]	[190 – 250]	[9.4 – 13.1]
Cu/40 wt.% C (vertical / in-plane)	17 / 10	160 / 250	6 / 11
Al/63 wt.% SiC	8	165	3
Cu/[70-40] vol.% SiC	[8 - 12]	[115 – 320]	[4.9 – 6.7]

Pure metals such as copper or aluminum exhibit extensive CTEs, which are too far from the CTEs of ceramic substrate materials such as alumina or aluminum nitride (Tab. 2.4) to prevent the creation of large thermo-mechanical stresses at the ceramic/base plate interface, thus jeopardizing the lifetime of the assembly. In order to decrease the CTE of bulk metallic materials, metal matrix composites (MMCs) have been developed.

A composite material is a multiphase material made from the heterogeneous assembly of two or more components in intimate contact at the atomic scale. At the macro scale however, it can be considered as a homogeneous material. Composite materials provide combination of properties that cannot be met by the different phases taken separately. Composite materials are made of a matrix and of reinforcements, the matrix being a continuous phase that surrounds the dispersed reinforcement phase. The reinforcements can either be particles, fibers, whiskers, nanofibers, or nanotubes. Finally, the zone located between the matrix and the reinforcements is called the interface. Depending on the nature of the matrix material, the different classes of composite materials are: polymer matrix composites (PMCs), ceramic matrix composites (CMCs), and metal matrix composites (MMCs).

MMCs started growing in the 1970's upon the impulse of the aerospace industry which was aiming to increase the elasticity modulus and the tenue to high temperatures of light (Al, Mg) and semi-light (Ti) structural alloys. Upon aerospace efforts, the superior mechanical performances of

MMCs relative to that of unreinforced metals and alloys were found to be applicable in technological fields such as aircraft structures, aeroengine blades, automotive motor parts, and brake systems. In these applications, MMCs were either able to provide increased specific stiffness, increased specific strength, enhanced resistance to high temperatures, or high-cycle resistance.

Beyond their use for mechanical purposes, MMCs have been found useful to a wide range of industrial sectors for thermal management applications, especially because of the possibility to tailor their coefficient of thermal expansion through the addition of ceramic reinforcement while maintaining or even enhancing the thermal conductivity of the metallic primary phase. Thermal applications of MMCs focus on electronic packaging applications (heat sinks, electronic racks, hard drives substrates, etc) which then spread in various sectors such as aerospace and aeronautics, automotive, and railway industries, but also energy conversion and more generally, any high-power machining application that requires extensive heat dissipation potential [37, 38].

Copper, aluminum, and silver constitute the main matrix materials employed in thermal MMCs fabrication. Other metal matrix materials such as titanium (Ti), beryllium (Be), magnesium (Mg), iron (Fe), nickel (Ni), or zinc (Zn) have been investigated but are not considered here for conciseness purposes. The materials reinforcing the metallic matrix mainly consist of silicon carbide, tungsten, molybdenum, carbon fibers, and carbon nanotubes. Tab. 2.6 gathers some properties of reinforcements used in the fabrication of heat dissipative MMCs [37,38].

**Table 2.6: Thermo-physical properties of different reinforcement materials for thermal MMCs [37, 38].**

Material	$d$ ( $\mu\text{m}$ )	$\rho$ ( $\text{g.cm}^{-3}$ )	$k$ ( $\text{W.m}^{-1}.\text{K}^{-1}$ )	$\alpha \times 10^{-6}$ ( $^{\circ}\text{C}^{-1}$ )
SiC particles	[30 – 300]	3.2	[200 – 300]	4.3
W particles	[1 – 30]	19.3	[150 – 180]	4.4
Mo particles	[1 – 30]	10.2	[140 – 160]	4.9
C fibers	[0.1 – 100]	2.1	[100 – 900]	-1.0
C nanotubes	[0.01 – 0.1]	2.0	[3000 – 6000]	-1.0

The reinforcement materials involved in thermal MMCs fabrication are mostly ceramics since they provide a very desirable combination of low density, high thermal conductivity, and low thermal expansion. Molybdenum-reinforced copper matrix (Cu/Mo), tungsten-reinforced copper matrix (Cu/W), and silicon carbide-reinforced copper matrix (Cu/SiC) composites have been traditionally employed since they allow reaching lower CTEs than the primary metallic phase while maintaining satisfying heat conduction potential (Tab. 2.5). They also provide excellent mechanical properties. These materials consist of a large amount of ceramic reinforcements dispersed into a metal matrix (note that the ceramic material is majoritarian toward the metal matrix).

While the high densities exhibited by Cu/Mo and Cu/W composites may limit their attractiveness, Cu/SiC composites provide a very interesting combination of limited CTE and low weight impact. However, as any ceramic reinforcements, the SiC additives that reduce the CTE of the metal matrix also lead to a decrease of the thermal conductivity of the primary phase. Consequently, their heat conduction potential may become insufficient to handle the heat flux densities encountered in high-power packages. Therefore, the reinforcement of an Al matrix by SiC reinforcements generally leads to weight the benefit of lower density and tailorable CTE against reduced thermal conductivity. Nevertheless, Al/SiC composite materials are by far the most widely employed type of MMCs for mechanical or thermal applications because of the excellent balance between limited density and high mechanical and thermal performances they provide [37]. Finally, all ceramic additives strongly affect the machinability of the metal matrix (Al or Cu).

In such context of limited compatibility between high thermal conductivity and low CTE, diamond-based materials, either diamond films grown through chemical vapor deposition (CVD) or metal-matrix composites reinforced with high-pressure high-temperature (HPHT) diamonds, appear to be very promising heat-conductive candidates since they combine a high thermal conductivity, a low CTE, and a low density. Fig. 2.10 provides an overview of how diamond-based materials compare to other typical electronic package materials in terms of both thermal conductivity and CTE [39].

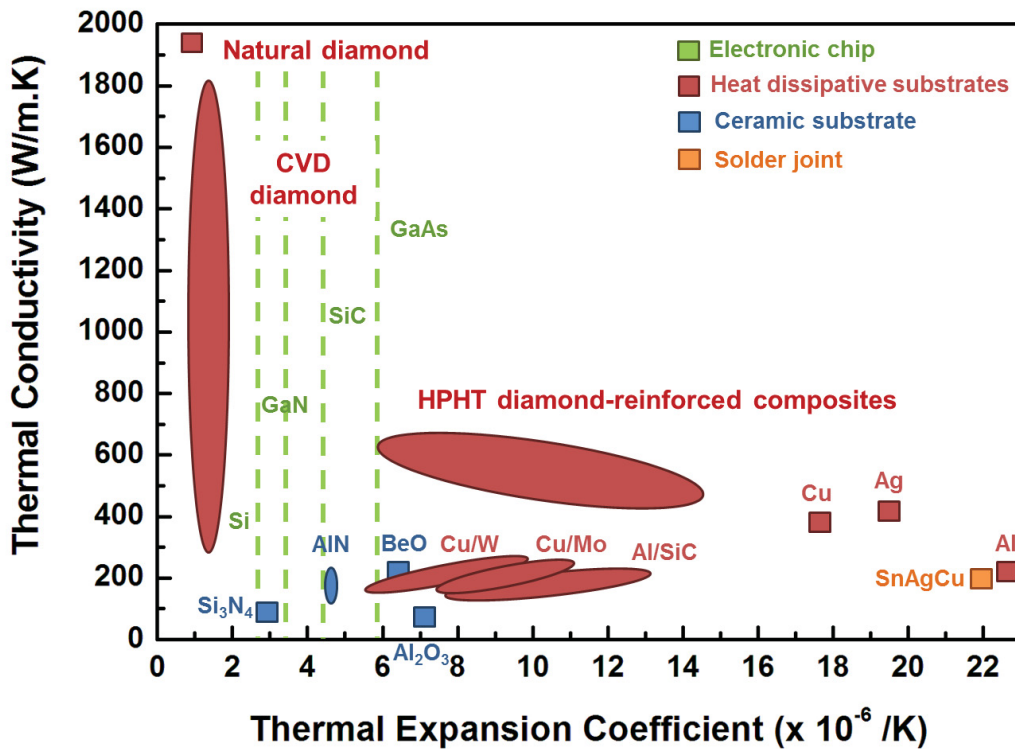


Figure 2.10: Thermal properties of diamond-based materials relative to other typical electronic packaging materials [39].



It is visible that diamond shows a very interesting combination of high thermal conductivity and low CTE relative to other packaging materials. Especially, CVD diamond shows high thermal conductivity, typically located between  $300 \text{ W.m}^{-1}.\text{K}^{-1}$  and  $1800 \text{ W.m}^{-1}.\text{K}^{-1}$  for the highest quality synthetic diamonds, and CTE that is close to that of semiconductive materials such as Si and SiC. Besides, the high electrical resistivity exhibited by CVD diamond can be a strong asset in the scope of an application as a heat spreading layer in an electrically active environment. More details about the use of CVD diamond in electronics are given in section 2.5.1 while section 5.1 deals with the possible packaging configurations involving CVD diamond films and substrates.

On the other hand, metal matrix composites reinforced with HPHT synthetic diamond powders also exhibit promising properties. While providing higher thermal conductivity relative to traditional metals and MMCs, their CTE is tunable and may be more adapted to a packaging close to ceramic substrates relative to CVD diamond. In addition, while reinforcements with high aspect ratio (length/diameter) such as fibers or whiskers allow to get enhanced load transfer from the matrix to the reinforcement, which is especially attractive to structural materials, low aspect ratio reinforcements such as diamond powders allows getting isotropic materials. Also, the use of diamond particles does not involve any deagglomeration of the reinforcements before processing, which, for instance, is a strong obstacle to the use of carbon nanotubes. Finally, the cost of diamond powders is observed to decrease, making diamond-based composites more and more competitive toward other reinforcements such as carbon fibers or carbon nanotubes. Examples of applications of diamond-reinforced MMCs to heat dissipation are given in section 2.5.2 while section 5.1 deals with potential packaging configurations involving Cu/D composite films and substrates.

In this study, we aim to improve the cooling process of power electronic modules by fabricating diamond-based heat-spreading films. Thanks to the exceptional thermal conductivity of diamond, diamond-based materials could help the cooling procedure by conducting the heat more efficiently from the hot upper layers of the package to the heat dissipative lower parts. Its low CTE can also be a strong advantage in order to mitigate inter-layers stresses. Section 2.3 investigates more deeply the composition, crystal structure, and properties of diamond.

## **2.3 Diamond: a unique material**

In a world where carbon is omnipresent, the unique and very rare carbon form of diamond has attracted the attention of the humankind for over two centuries. At first mostly appreciated for its beauty as a gem stone in jewelry, diamond has focused growing scientific interest as its outstanding properties were revealed. Indeed, diamond is also a unique material in the sense that it combines in a very unique way exceptional properties such as extreme hardness, high thermal conductivity, high electrical resistivity, low coefficient of thermal expansion, high degree of chemical inertness, high

wear resistance, and high optical transparency. Currently, the rare constellation of superlative properties of diamond makes it a very competitive material for a wide range of applications such as coating for cutting and drilling tools, optical windows and coatings, acoustic speakers, laser heat sink, active electronic devices, and of course, electronic packaging material [4]. The next paragraphs propose an overview of the crystalline structure, composition, morphology, and properties of diamond.

### 2.3.1 Composition

As graphite, pure diamond is only composed of the element carbon (C). However, deviations in its composition are frequent and impurities may exist in natural diamond. These impurities have a strong influence on the optical properties of diamond. This led to the creation of a classification of natural diamond into four types: Ia, Ib, IIa, IIb. The compositional characteristics of the different types of natural diamond are summed up in Tab. 2.7:

**Table 2.7: The different types of natural diamond [4].**

Diamond type:	Ia	Ib	IIa	IIb
Contains:	Nitrogen aggregates	Substitutional nitrogen	No impurities	Boron
Appearance:	Pale yellow	Gold yellow	Colorless	Blue

Although these four types of diamond exist in nature, type Ia is highly preponderant (98%), followed by type II (1.9%), and type Ib (0.1%). Type II diamonds are the purest natural diamonds. While colorless type IIa diamond offer the relative highest level of purity and are extremely rare (Fig. 2.11c), most natural diamonds contain impurities, the most common of which being nitrogen, typically found at levels ranging from 50 ppm to 2500 ppm. These impurities embedded in the diamond crystal structure impact its optical absorption spectra in the visible range and lead to various stone colors. Therefore, most natural diamond stones exhibit various shades of yellow and brown (Fig 2.11a).

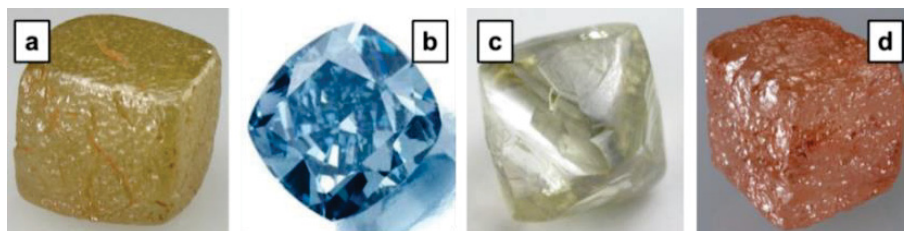


**Figure 2.11: Various natural diamond stones.**

Substitutional boron in type IIb diamond gives rise to absorption in the lower energy portion of the visible spectrum, thus resulting in a deep blue color of the crystal (Fig. 2.11b). Other colors found in nature include: orange, pink, mauve, green, red, and black. These colors also results from



the impact of different types of impurities embedded in the crystals on the absorption spectrum. Manganese, for instance, is known for a broad optical absorption at 550 nm that produces a pink or mauve color (Fig. 2.11d).

Synthetic HPHT diamond powders may exhibit dark green aspect due to the presence of nitrogen, while CVD synthetic diamond usually exhibit a dark grey aspect due to the existence of non-diamond carbon content into its microstructure. Although often considered as defects, for instance when acting as obstacles to the heat flux when thermal conduction is sought, these impurities may also be beneficial to diamond, especially from the optical viewpoint. In addition, isotopic composition of diamond may vary, i.e. carbon atoms with different numbers of neutrons but the same number of protons (and electrons) may exist in the same diamond material. At the natural state, diamond is made of 98.93% of  $^{12}\text{C}$  and 1.07% of  $^{13}\text{C}$ . However, the  $^{13}\text{C}$  content in diamond may change, depending on the gem stone.  $^{13}\text{C}$  isotopes were demonstrated to act as a phonon scatterers into diamond, thus decreasing the thermal and electrical conductivities of the material [40].

Similar to natural diamond, synthetic diamond is far from exhibiting a pure carbon composition. As discussed in chapters 3 and 4, diamond materials processed through synthetic methods, either HPHT or CVD routes, frequently include impurities and defects, the goal being for the scientific community to create a material as close as possible to natural diamond.

### 2.3.2 Crystal structure and morphology

Carbon atoms in diamond form a face-centered cubic (FCC) Bravais structure in which four of the eight tetrahedral sites are occupied and each carbon atom has four nearest neighbors, in the tetrahedral arrangement associated with  $\text{sp}^3$  covalent chemical bonds (Fig. 2.12).

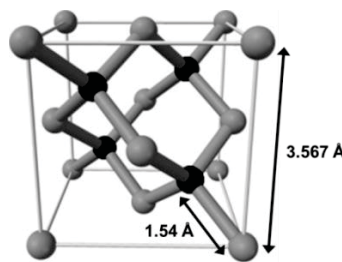


Figure 2.12: 3D view of the diamond lattice.

Diamond structure is similar to the zinc-blende structure, which consists in two interpenetrating face-centered cubic lattices of dissimilar atoms. Semiconductive materials such as silicon and germanium also exhibit a zinc-blende structure. In their cases as in the case of diamond, the structure is made up of only a single type of atom. Fig. 2.12 helps to visualize the two interpenetrating networks of carbon atoms of the diamond lattice (grey and black spheres). The

diamond cubic structure belongs to the  $Fd\bar{3}m$  space group. The nearest neighbor distance is 1.54 Å and the unit cell dimension (lattice parameter) is 3.567 Å at 298 K. There are eight atoms per unit cell, and  $1.77 \times 10^{23}$  atoms. $\text{cm}^{-3}$ , which make diamond the terrestrial material with the highest atomic density. Diamond exhibits a density of 3.515 g. $\text{cm}^{-3}$ . Diamond quantity is often expressed in carats, where one carat equals 200 mg, or about 57 mm<sup>3</sup> [4].

As explained in section 2.4, synthetic diamond crystals may exhibit various shapes, from cubic to cubo-octahedral and octahedral. The morphology of synthetic diamond crystals is strongly dependent on experimental parameters such as the temperature or carbon precursor concentration that affect the growth process. An interesting way to establish a relationship between the growth conditions and the resulting diamond morphology is the  $\alpha$  parameter (also called growth parameter), which is defined as the ratio of the growth rate in the (100) and (111) directions of the crystal (Fig. 2.13):

$$\alpha = \sqrt{3} \frac{v_{(100)}}{v_{(111)}} \quad (2.1)$$

It was demonstrated that the morphology of the diamond crystals could be influenced by manipulating this parameter, which in turn can be controlled by altering the growth environment. For instance, by fixing the concentration of carbon precursors, the crystal morphology can be changed by tuning the temperature [41,42].

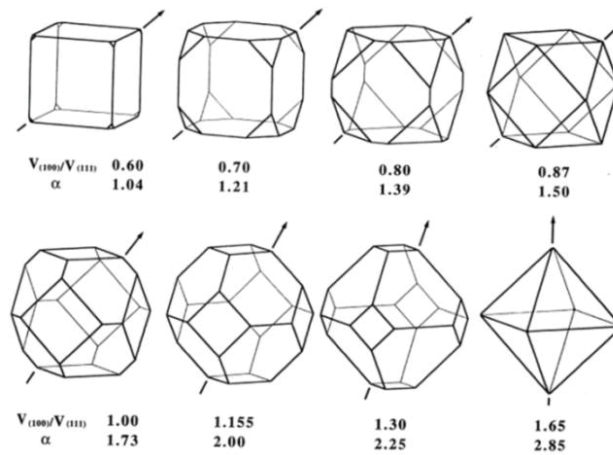


**Figure 2.13: Crystal shapes produced in diamond nucleation and growth processes and associated growth parameter. The arrow indicates the direction of fastest crystal growth.**

The crystallographic faces with the lowest growth rate produce the most important surface. An increase in growth temperature tends to transform the diamond crystallites to octahedral ( $\alpha = 1.65 \times \sqrt{3}$ ) to cubo-octahedral ( $\alpha = \sqrt{3}$ ) and finally to cubic shapes ( $\alpha = 0.6 \times \sqrt{3}$ ). At low temperatures, individual crystals develop as octahedral consisting of eight equivalent (111) faces. As the synthesis temperature increases, (100) faces start to appear at the corners of the octahedron (locations with

highest surface free energy). The faces keep growing as the temperature increases, making the crystallite evolve from an irregular cubo-octahedron with a majority of (111) surfaces ( $\alpha = [1.50 - 2.85]$ ), to a regular cubo-octahedron (where the (100) faces occupy the same area as (111) faces,  $\alpha = 1.50$ ), to an irregular cubo-octahedron with a majority of (100) surfaces ( $\alpha = [1.04 - 1.50]$ ), to finally end up on cubic shaped crystals ( $\alpha = 1$ ). At a fixed temperature, increasing the carbon precursor concentration has the same effect, changing the diamond crystal shape from octahedral to cubo-octahedral, and then cubic. Although the control of the growth parameter allows influencing the morphology of the final diamond crystallites, it is extremely complex, if not impossible, to control it in a HPHT process. Therefore, the resulting diamond powders typically exhibit various shapes in the range of the  $\alpha$  parameter fixed by the synthesis conditions. In CVD processes, growth of highly oriented (or textured) diamond films has been demonstrated to be possible by carefully controlling the substrate temperature and concentration of carbon precursors.

### 2.3.3 Properties

- ***Mechanical properties:***

Diamond is the hardest known terrestrial substance, which originates from the fact that diamond has the highest packing density. It was originally this characteristic of diamond that attracted the most the scientific community to use diamond as a coating material for wear protection. The degree of hardness is quantified in terms of both resistance to indentation and to abrasion (or scratch). Diamond also has the highest elastic modulus (or Young's modulus), which is the ratio of tensile stress to linear strain, in being equal to 1050 GPa, a value approximately five times higher than that of steel. The fact that diamond exhibits the highest elastic modulus also means that its compressibility is the lowest of any material. Similarly, it has a low Poisson's ratio (0.07). Because of its brittle nature, diamond is not particularly strong. Finally, diamond has the highest isotropic speed of sound (or phonon velocity:  $18,000 \text{ m.s}^{-1}$ ) of any known material [4].

- ***Electrical properties:***

Diamond exhibits an energy band structure with a 5.47 eV band gap between the valence band and the conduction band at 300 K. This makes diamond a strong electrical insulator with a dielectric constant of approximately 5.7. The electrical resistivity of diamond typically ranges between  $10^{13}$  and  $10^{16} \text{ } \Omega.\text{cm}$ , which makes it an ideal material for insulation in an electrically active environment such as a power module or a microelectronic package [4]. Nevertheless, it is also possible to p-dope diamond with boron. This introduces holes in the valence band such that the electrical conductivity increases substantially (down to  $0.1 \text{ } \Omega.\text{cm}$ ). As a consequence, diamond can also take the form of a p-type semiconductor and it has long been recognized as a promising material to be used as semiconductor in high-power active devices [43-45].

▪ ***Optical properties:***

Diamond has one of the largest optical transmission bandwidth of any solid material. It extends in wavelength from ultraviolet (225 nm) through the far infrared and into the microwave range. Throughout the entire visible region, pure diamond has essentially no optical absorption, thus a clear and transparent aspect. However, as detailed in section 2.3.1, impurities of various types can lead to a wide range of colors, and diamond contaminated with non-diamond carbon content is typically opaque. Diamond also has a large refractive index for a transparent material, of about 2.4 [4].

▪ ***Thermal properties:***

The thermal conductivity of diamond exceeds that of any other solid material, which is precisely the point why it is so interesting from a thermal management perspective. At room temperature, the thermal conductivity of high-purity natural single-crystalline IIa type diamond is approximately  $2200 \text{ W.m}^{-1}\text{.K}^{-1}$ , which is more than five times higher than the thermal conductivity of copper. Diamond's thermal conductivity increases with decreasing temperature, reaching a maximum value of  $4200 \text{ W.m}^{-1}\text{.K}^{-1}$  at 80 K. Besides, synthetic type I monocrystalline diamond powders processed through HPHT synthesis usually exhibit thermal conductivity located between 600 and  $1500 \text{ W.m}^{-1}\text{.K}^{-1}$ .

Synthetic polycrystalline CVD diamond films typically exhibit thermal conductivity ranging between  $300 \text{ W.m}^{-1}\text{.K}^{-1}$  and  $700 \text{ W.m}^{-1}\text{.K}^{-1}$  [46-48], which is higher than most of electronic packaging materials but considerably lower than the thermal conductivity values recorded for natural diamond. The thermal conductivity gap existing between CVD diamond films and bulk diamond is well-known to originate from the particular microstructure and composition exhibited by CVD diamond films. Phonons, which are the carriers of heat into diamond, may indeed be scattered in various ways. Point imperfections such as vacancies, impurities, interstitials and isotopes; line imperfections such as dislocations; and surface imperfections such as grain or twin boundaries are as many phonon scatterers that decrease the phonon mean free path, thus affecting the heat conduction process through diamond [40]. Type I diamonds with 0.1% nitrogen have, for instance, a thermal conductivity that is approximately 50% that of type II diamonds, which contain no nitrogen [4]. In a same manner, synthetic diamond crystals grown with pure  $^{12}\text{C}$  content have shown thermal conductivities 50% higher than those of natural diamond for which the atomic weight is 12.01 because the material contains 1.1%  $^{13}\text{C}$ .

The relatively lower thermal conductivity exhibited by synthetic CVD diamond films is also revealed by their typical black color, indicating a high-amount of non-diamond carbon content. Nevertheless, polycrystalline CVD diamond films were recorded to exhibit thermal conductivity as

high as  $1200 \text{ W.m}^{-1}.\text{K}^{-1}$  [48,49]. In addition, in-plane thermal conductivity of CVD diamond films is usually lower relative to vertical thermal conductivity (in the growth direction) due to the particular columnar microstructure of the deposit (see chapter 3). Finally, highly-oriented CVD diamond films with textured morphology, i.e. a preferred crystallographic orientation, are highly desirable for electronic applications since they permit reaching higher heat conduction performances due to enhanced phonon mean free path inside the film structure.

Diamond has also the lowest heat capacity of any solid in the temperature range between 0 and 800 K, since its value is  $6.19 \text{ J.mol}^{-1}.\text{K}^{-1}$  at 300 K (relatively to  $24.2 \text{ J.mol}^{-1}.\text{K}^{-1}$  for aluminum and  $24.5 \text{ J.mol}^{-1}.\text{K}^{-1}$  for copper). This makes CVD diamond to be preferably used for heat spreading purposes rather than for the dissipation of the heat flux itself [4]. Indeed, the temperature rise  $\Delta T$  (K) induced by a heat source  $Q$  (J) into a material of mass  $m$  (kg) and mass specific heat  $c_p$  ( $\text{J.kg}^{-1}.\text{K}^{-1}$ ) is given by:  $Q = mc_p\Delta T$ . Therefore, the higher the heat capacity of a material, the higher the heat flux it can sustain without temperature change, which is precisely the definition of the heat capacity. Therefore, a heat sink, which should sustain as much heat flux as possible while maintaining its temperature in order to dissipate the maximum amount of heat, should exhibit a high heat capacity.

Finally, the thermal expansion coefficient (CTE) of diamond is low, increasing from  $0.8 \times 10^{-6}$  to  $4.8 \times 10^{-6} \text{ }^{\circ}\text{C}^{-1}$  between 300 K and 1200 K, respectively. The low CTE of diamond makes the use of CVD diamond as a heat-spreader close to the silicon chips very appealing. Also, the low CTE of diamond powders will allow decreasing that of the copper matrix in a tunable fashion with respect to the diamond volume fraction in case of Cu/D composite materials. Table 2.8 sums up the main properties of natural diamond that are of interest to our study.

**Table 2.8: Properties of natural diamond at room temperature [4].**

Density	$3.51 \text{ g.cm}^{-3}$
Coefficient of thermal expansion	$[1 - 2] \times 10^{-6} \text{ }^{\circ}\text{C}^{-1}$
Thermal conductivity	$2200 \text{ W.m}^{-1}.\text{K}^{-1}$
Thermal diffusivity	$12.4 \text{ cm}^2.\text{s}^{-1}$
Heat capacity / Specific heat	$6.19 \text{ J.mol}^{-1}.\text{K}^{-1} / 0.54 \text{ J.g}^{-1}.\text{K}^{-1}$
Electrical resistivity	$[10^{13} - 10^{16}] \text{ } \Omega.\text{cm}$
Elastic modulus	1050 GPa
Bulk modulus	442 GPa
Poisson's ratio	0.07
Optical transmission at $\lambda = [514 - 1064] \text{ nm}$	100%

The next section focuses on the ways developed to synthesize diamond and their respective characteristics.

## 2.4 Diamond synthesis

### ▪ The (P, T) diagram of carbon:

Figure 2.14 shows a sketch of the (P, T) diagram of carbon. It displays the domains of existence of diamond and graphite, which are two allotropes of carbon. It also shows the (P, T) domains of the different techniques employed to fabricate synthetic diamond: High-Pressure High Temperature synthesis (HPHT), and Chemical Vapor Deposition (CVD) routes.

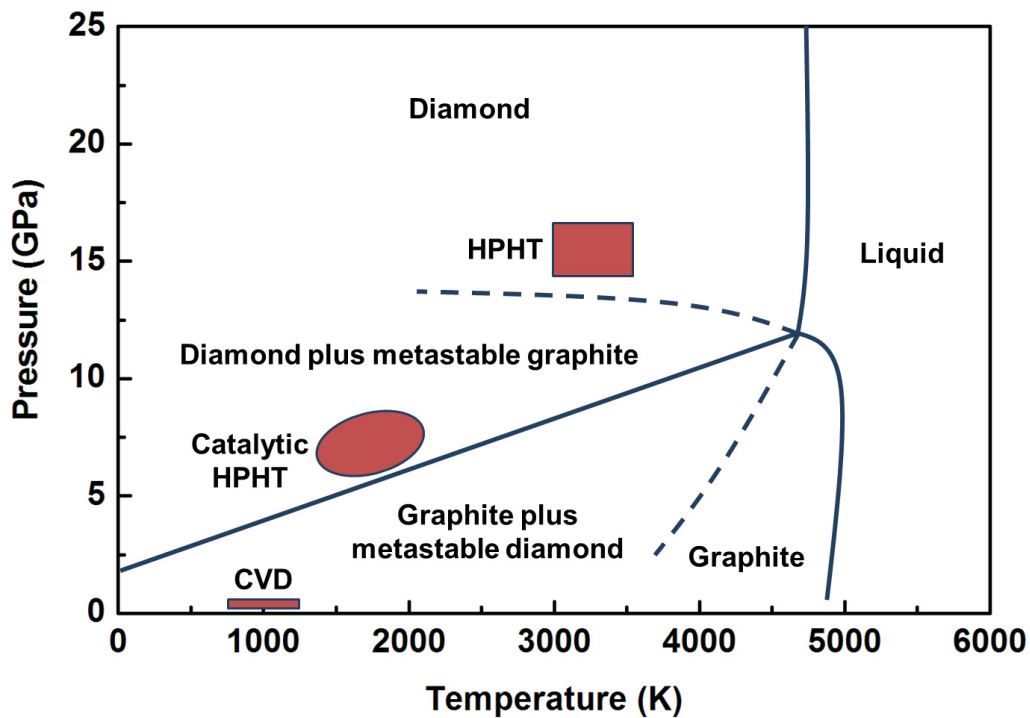


Figure 2.14: (P, T) diagram of carbon [4].

While diamond is the stable form of carbon at high pressures and high temperatures, graphite is the stable form of carbon under ordinary temperature and pressure conditions. As a matter of fact, one way to synthesize diamond is to submit graphite to high temperature and pressure conditions (about 55,000 atmospheres and 2000°C), known as the *High-Pressure High-Temperature* (HPHT) diamond synthesis. While basic HPHT synthesis attempts to reproduce in the lab the extreme geological conditions in which diamond forms 150 km below the Earth surface, catalytic HPHT allow softer processing conditions through the use of molten metals catalyzing diamond formation from graphite. This method is explored in section 2.4.1.

Although from a thermodynamic point of view, under standard temperature and pressure conditions, diamond is not the minimum energy state of carbon, it is neither an unstable form of carbon. When carbon atoms are in the diamond lattice spatial arrangement, the solid does not

spontaneously turns into graphite under low-pressure and low-temperature conditions, because of the extremely slow kinetics of such transformation. Such non-minimum energy arrangements are known as *metastable* states. Therefore, an alternative way to produce diamond is to synthesize it at pressures generally less than one atmosphere and temperatures less than 1000°C from gaseous carbon precursors. This approach of diamond synthesis is sometimes named the *new diamond technology* and gathers various methods of chemical vapor deposition (CVD) to grow diamond, which are reviewed in section 2.4.2.

▪ ***Nucleation and growth processes [50]:***

The synthesis of diamond crystals through HPHT routes or CVD techniques both rely on *nucleation* and *growth*, which are the processes underlying any phase transformation phenomena. Before moving forward, it is important to precisely define these concepts, which frequently appear in this study. Nucleation involves the appearance of very small particles, or *nuclei*, of the new phase (in our case: diamond, often consisting of only a few hundred atoms), which are capable of growing. During the growth stage, the nuclei increase in size, which results in the disappearance of some (or all) of the parent phase (carbon precursors). The transformation reaches completion if the growth of these new phase particles is allowed to proceed until the equilibrium fraction is attained. Two types of nucleation have to be distinguished, depending on the location at which nucleation occurs:

- *Homogeneous nucleation*: in which nuclei of the new phase form uniformly throughout the parent phase; homogeneous nucleation typically consists in the solidification of a liquid-phased material through the formation of stable solid-phased nuclei. Very limited attention has been focused by the research community on homogeneous nucleation of diamond. Although homogeneous diamond nucleation in a carbon precursor gas phase has been observed [4], the nucleation rate is extremely low, and the very large majority of diamond nucleation processes rely on heterogeneous nucleation.
- *Heterogeneous nucleation*: in which nuclei form preferentially at structural inhomogeneities, such as high-energy surfaces, impurities, grain boundaries, dislocations, and so on. The diamond nucleation processes further discussed in sections 2.4.1 and 2.4.2 are heterogeneous nucleation processes, as the very large majority of diamond nucleation phenomena reported in literature.

The notions of *critical radius* ( $r^*$ , nm) and *activation free energy* ( $\Delta G^*$ , J) are non-dissociable from nucleation phenomena. The critical radius represents the size above which a nucleated particle becomes stable and may be called a *nucleus*. The activation free energy represents the energy



barrier that has to be overcome in order to form a stable nucleus. In case of heterogeneous nucleation, they can be derived to the following expressions:

$$r^* = -\frac{2\gamma_{ab}}{\Delta G_v} \quad (2.2)$$

$$\Delta G_{het}^* = \left( \frac{16\pi\gamma_{ab}^3}{3\Delta G_v^2} \right) S(\theta) \quad (2.3)$$

Where  $\gamma_{ab}$  is the free energy of the surface of the formed nucleus ( $\text{J.m}^{-2}$ ), and  $\Delta G_v$  is the activation free energy (i.e. energy barrier) of the nucleation process (J).  $S(\theta)$  is a term that is dependent on the shape of the nucleus and has a numerical value between zero and unity. This term relates homogeneous and heterogeneous nucleations through the following relationship:

$$\Delta G_{het}^* = \Delta G_{hom}^* S(\theta) \quad (2.4)$$

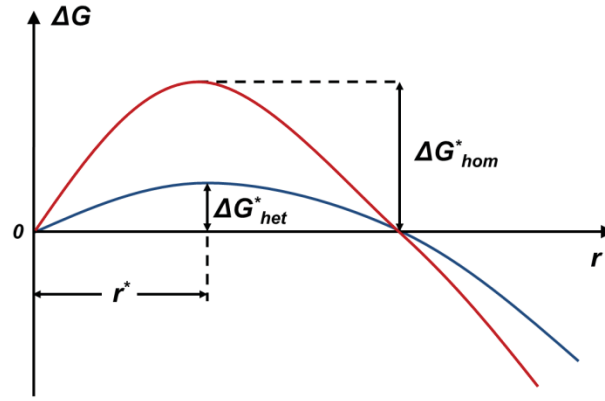


**Figure 2.15: Schematic plot of free energy versus nucleus radius.**

Practically, while critical radii are the same for homogeneous and heterogeneous nucleation of a same material, heterogeneous nucleation occurs more easily than homogeneous nucleation simply because the activation energy is lowered by an amount of  $S(\theta)$  when nuclei form onto preexisting surfaces or interfaces, as depicted in Fig. 2.15.

Once a nucleus has reached the critical size and become stable, the growth process starts. Nucleation keeps occurring simultaneously with growth of the new phase. As explained in the next sections, particle growth occurs following atomic diffusion phenomena. Therefore, the growth rate is determined by the rate of diffusion and is thermally activated. It can be estimated from the following expression, which is in the form of an *Arrhenius law* (exponentially dependent on temperature):

$$\dot{G} = C e^{\left( \frac{-E}{k_B T} \right)} \quad (2.5)$$



Where  $\dot{G}$  is the growth rate ( $\mu\text{m.s}^{-1}$ ),  $E$  is the activation energy (J),  $C$  is a preexponential factor,  $k_B$  is the Boltzmann constant ( $k_B = 1.38 \times 10^{-23} \text{ J.K}^{-1}$ ), and  $T$  is the growth temperature (K).

In a same manner as growth rate, the nucleation rate for both homogeneous and heterogeneous nucleation can be expressed through an Arrhenius law. Figure 2.16 schematically shows the curves of growth rate (blue) and nucleation rates (red) as a function of temperature. The green curve shows the overall transformation rate (green), which represents the combined effects of growth and nucleation rates. Several physical phenomena may be explained through Fig. 2.16. First, the size of the grown phase particles will depend on transformation temperature. Indeed, a transformation that occurs at a temperature where nucleation rate is low but growth rate is high will trigger the rapid growth of a few nuclei, thus leading to a microstructure made of few but relatively large grains. On the contrary, a transformation that occurs at a temperature where nucleation rate is high but growth rate is low will lead to a microstructure made of numerous but relatively small crystals.

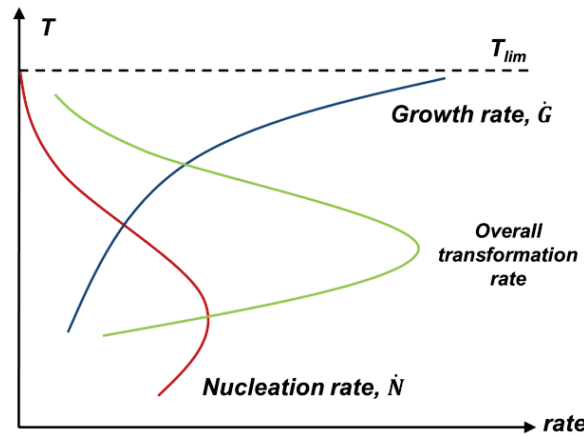


**Figure 2.16: Schematic plot showing growth rate, nucleation rate, and overall transformation rate versus temperature.**

These theoretical predictions will be illustrated in the rest of the dissertation, especially in chapter 3, in which the influence of the temperature on the size of the diamond grains formed through laser-assisted combustion CVD is demonstrated.

#### **2.4.1 Catalytic High-Pressure High-Temperature (HPHT) diamond synthesis**

##### **▪ Principles underlying catalytic HPHT diamond synthesis:**

Synthetic diamond powders are typically produced through *catalytic High-Pressure High-Temperature (HPHT) synthesis*. This technique consists in using high-purity graphite powders as carbon precursors and transition metals as solvent-catalysts to trigger the graphite-to-diamond conversion upon high pressure and high temperature conditions. The transition metals, which are usually powders, are employed as a molten medium to dissolve graphite and promote the

transformation of graphite into diamond. Indeed, upon high temperature, the graphite in the metal phase remains stable. However, when increasing the pressure, diamond becomes the stable allotrope of carbon (i.e., a different zone of the carbon (P, T) diagram is entered) and precipitates out from graphite into the molten metal. After cooling, the remaining graphite and catalysts metals embedding the diamond particles are dissolved in nitric acid, and diamond powders are obtained [4]. Table 2.9 sums up the typical process conditions used for HPHT synthesis of diamond:

**Table 2.9: Typical process conditions employed for catalytic HPHT synthesis of diamond.**

Carbon precursor	Catalyst metals	Temperature (°C)	Pressure (GPa)	Time (min)
Graphite	Fe, Ni, Co, Mn	[1300-2000]	[5-7]	[1-120]

The catalytic conversion of graphite into diamond under high pressure into a molten metal proceeds by heterogeneous nucleation and growth. Graphite will first be disintegrated into flakes by the invasion of liquid metal. These flakes are then puckered by the catalytic action of surrounding liquid metal that pulls every other carbon atoms away from the basal planes of graphite. From a crystallographic point of view, the puckering converts a  $sp^2$  bonded graphite flake into a  $sp^3$  hybridized diamond nucleus, which then grows by feeding through diffusion on either carbon atoms from graphite dissolved in the solvent metal, or graphite flakes suspended in the molten catalyst [51].

The ability of a transition metal catalyst to nucleate and grow diamond under high pressure strongly relies on its atomic size and electronic state. Indeed, a transition metal tends to react with carbon by overlapping its  $d$ -orbitals with graphite's  $p$ -orbitals. Therefore, it has to possess the right atomic size to cover every carbon atom on a graphite hexagon, and also has to have vacant  $d$ -orbitals to attract the  $\pi$ -carbon atoms of graphite. Consequently, the ability of a transition metal to catalyze the graphite-to-diamond conversion varies with its number of electron vacancies in  $d$ -orbitals. Elements with no  $d$ -vacancies, such as copper (Cu) or zinc (Zn), are inert relative to carbon and therefore have a minimal effect on the graphite-to-diamond transition. Elements with a limited number of  $d$ -vacancies, such as iron (Fe), nickel (Ni), manganese (Mn), or cobalt (Co), are effective carbon solvents and are able to strongly increase the transition rate. Finally, elements with many  $d$ -vacancies, such as titanium (Ti) or vanadium (V), tend to lock-up carbon atoms in carbides and therefore do not facilitate diamond formation.

Therefore, Mn, Fe, Co, and Ni (showing respectively five, four, three, and two vacancies in the  $d$ -orbital), are considered as the most powerful catalysts for graphite to diamond conversion. From a thermodynamic point of view, these metals all have a eutectic or peritectic relation to carbon, i.e. become reactive to carbon when they melt. Therefore, the melting temperature of the catalyst and its wettability toward graphite have a crucial influence on its catalytic effect for the conversion of

graphite into diamond. For instance, the diamond growth region of the (P, T) diagram is usually bounded by the catalyst melting temperature line and by the diamond / graphite equilibrium line (Fig. 2.14).

The reactivity of transition metals with carbon can be illustrated by the potential of diamond as a cutting tool. As explained in section 2.3.3, diamond exhibits the highest hardness of all terrestrial materials and is therefore chosen for numerous hard machining applications. However, the frictional force that develops during cutting increases with the number of vacancies in the *d*-orbitals of the cut metal. The frictional force triggers temperature raise that may lead to chemical wear (oxidation, dissolution, carbide formation, or graphitization) of diamond. That is the reason why diamond is used to machine transition metals with low *d*-vacancies such as copper (Cu) and zinc (Zn), rather than ferrous metals with numerous *d*-vacancies such as Fe or titanium (Ti, eight *d*-vacancies) which would lead to extensive frictional forces and extreme temperature levels [52].

The HPHT synthesis of diamond typically takes place in a diamond anvil cell (DAC) which is an apparatus that allows submitting a small amount of material to extreme pressures. A scheme of such a chamber is shown in Fig. 2.17a. The first anvil cells were developed by Professor Percy Bridgman, an American physicist at Harvard University who received the Nobel Prize in 1946 for his work on high pressures [53]. The graphite and catalysts powders are introduced into a ceramic mold embedded into a pyrophyllite container (aluminum silicate hydroxide). The heating is ensured by a graphite heater while the pressure is applied through steel pistons.

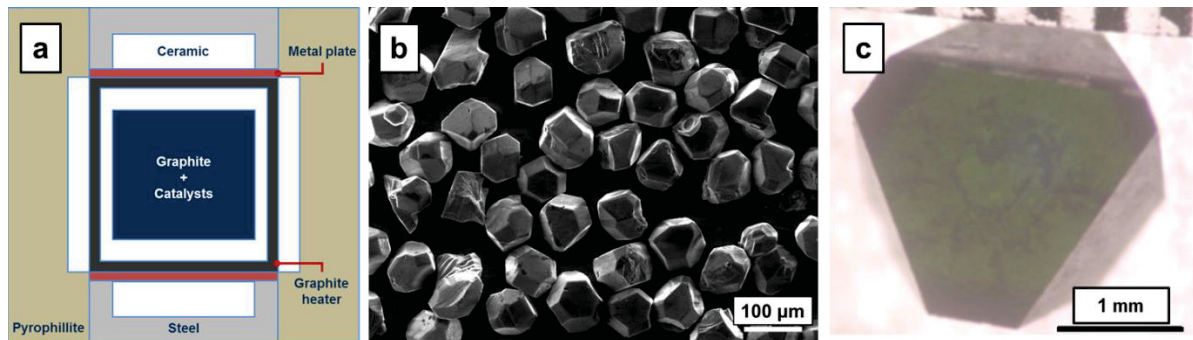


**Figure 2.17: (a) Sketch of cubic HPHT anvil apparatus. (b, c) HPHT diamonds [54-56].**

The resulting diamond powders typically exhibit cubic, cubo-octahedral, or octahedral shapes, as explained in section 2.3.2. Depending on the time of the HPHT treatment, a broad range of particles' size can be achieved. Typically, a HPHT treatment with a few minutes hold will lead to diamond powders with diameter in the micrometer range (Fig. 2.17b), while a longer time of pressurization can lead to the creation of centimeter scale diamond single crystals (Fig. 2.17c).

▪ *A brief history of HPHT synthesis:*

Once it was figured that diamond and graphite were both made of the sole element carbon, and that diamond was just a denser form of carbon than graphite (diamond is 56% denser than graphite ( $\rho_{dia} = 3.52 \text{ g.cm}^{-3}$ ,  $\rho_{gra} = 2.26 \text{ g.cm}^{-3}$ )), it was soon sensed that diamond could be formed by submitting graphite to extreme pressure. The first scientific efforts in that sense, although unsuccessful to create diamond from graphite, were endeavored by Bridgman in the 1940's [53]. Later, the first HPHT synthesis of an artificial diamond was achieved by Liljeblad and Lundblad from the Swedish company ASEA in 1953 [57]. They hot-pressed a mixture of iron carbide ( $\text{Fe}_3\text{C}$ ) and graphite in a complex high-pressure cubic apparatus at 7.5 GPa and 1500°C during three minutes to create the first man-made diamond. Despite the pioneering aspect of their work, they inexplicably did not report their success and the first public announcement of diamond HPHT synthesis was made in 1955 by Francis Bundy and his coworkers from the General Electric Company [58]. They had improved the anvils previously developed by Bridgman by employing tungsten carbide as the chamber material, and were able to submit graphite and metal catalysts to a pressure as high as 10 GPa and to a temperature of 2000°C into an innovative belt press developed by Hall.

Bundy, Strong, Hall, and other scientists from the General Electric Company strongly contributed to the development of the HPHT synthesis of diamond. They demonstrated the prominent role of iron (Fe), cobalt (Co), and nickel (Ni) as metal catalysts for diamond formation. Those three elements and their alloys remain, by far, the most employed solvent-catalysts today. They also demonstrated the catalytic influence of other molten transition metals such as ruthenium (Ru), thorium (Th), palladium (Pd), osmium (Os), iridium (Ir), and platinum (Pt). They also figured that manganese (Mn), chromium (Cr), and tantalum (Ta) could also effectively promote diamond formation [59-61]. In a same manner, Wakatsuki [62] reported that alloys of copper (Cu) with carbide forming elements such as titanium (Ti), molybdenum (Mo), tungsten (W), or zirconium (Zr) can act as solvent-catalysts for graphite conversion to diamond. These catalysts were also explored latter on by Kanda et al. [63]. Finally, compounds such as carbonates, oxides, sulfates, hydroxides, and silicates were also shown to enhance the conversion of graphite into diamond during HPHT synthesis, also through the work of Akaishi et al. [64].

In 1957, General Electric first introduced to the market man-made diamonds as super-abrasive materials. In 1961, while De Beer's Company joined General Electric in the industrial production of synthetic HPHT diamonds, Du Pont's scientists first achieved the direct conversion of graphite into diamond, without resorting to any catalytic material. The conversion was triggered by shock compression from an explosion that momentarily created an extreme pressure (350 Kb) and a temperature of about 770°C [65]. In 1963, Bundy and co-workers from the General Electric

Company also achieved the direct conversion of graphite into diamond, under a static pressure of about 12 GPa and a temperature of about 3000°C. This extreme temperature was created by flashing the sample with a pulse of current suddenly released from a high voltage capacitor [66].

Another milestone in HPHT synthesis of diamond was reached in 1972 when scientists from the General Electric Company announced they had successfully grown a synthetic diamond gem stone of a few carats by using, instead of graphite, small natural diamond crystals as the carbon source in a molten metal catalyst. The diamond was grown in very precisely controlled pressure and temperature conditions during an extensive period of time [67]. Since the first exciting results that emerged in 1950-60's, many others in the scientific community have documented the HPHT synthesis of diamond. More recently, Invar ( $\text{Fe}_{64}\text{Ni}_{36}$ ) [54] and Kovar ( $\text{Fe}_{59}\text{Ni}_{25}\text{Co}_{17}$ ) [55] alloys have been intensively employed as catalysts for diamond HPHT synthesis. Lately, efforts about HPHT synthesis have also focused on the study of the influence of new materials as catalysts, among them zinc (Zn) [56], aluminum (Al) [68], and boron (B) [69]. Chinese scientists, such as Jia et al. [55,56,68,69], are especially proactive in HPHT diamond research due to the leading position of China on the HPHT market.

All these efforts to develop HPHT synthesis of diamond were motivated at first by the extreme abrasive potential of diamond. Today, about twenty countries are engaged in the fabrication of HPHT synthetic diamonds, of which China produces the most in quantity. In terms of quality however, Ireland has a solid reputation in HPHT diamond synthesis due to the presence of General Electric and De Beers Companies on its soil. Each year, over three hundred tons of synthetic diamonds are produced through HPHT synthesis. These diamonds are indispensable to many industrial applications such as drilling, sawing, grinding, lapping, and polishing of various materials (ceramics, plastics, asphalts, non-ferrous metals). In addition, HPHT synthesis allows producing diamond powders typically employed for the fabrication of diamond-reinforced composite materials [4].

However, this type of process cannot lead to direct growth of diamond crystals and large-area deposition of diamond films onto a particular substrate. This is only possible through the CVD routes of diamond synthesis, which are explored in the next section.

#### **2.4.2 Chemical Vapor Deposition (CVD) of diamond at low pressures**

- ***Principles underlying CVD diamond synthesis:***

Unlike the HPHT route, Chemical Vapor Deposition (CVD) techniques allow synthesizing diamond crystals at low pressures, i.e. in the region of the (P, T) carbon diagram where diamond is in its metastable state. The region of metastability of diamond is most easily envisioned by

extending the diamond melting curve into the graphite-stable region (Fig. 2.14). In principle, diamond can be synthesized anywhere within this region of metastability if graphite formation is suppressed. One can also notice in Fig. 2.14 that a very little region of this region of metastability has been yet explored [4].

The term chemical vapor deposition implies that a chemical reaction occurs in a vapor phase, which then leads to the deposition of a material onto a solid surface. Indeed, CVD routes allow growing diamond onto various substrate materials from gaseous carbon precursors, i.e. to deposit an overlayer of diamond onto a crystalline substrate. When the deposit material is crystallographically organized in the same way as the substrate material (i.e. the preferred crystallographic orientation of the film and the substrate are the same), the deposition is termed *epitaxy*.

Then, *homoepitaxy* should be distinguished from *heteroepitaxy*, the former corresponding to the epitaxy of a diamond film onto a substrate of the same material or with the exact same crystal structure, while the latter corresponds to the epitaxy of a diamond film onto a substrate of foreign material. Homoepitaxial growth of diamond, typically on diamond itself or on cubic boron nitride (cBN, which only has a 1.3% lattice mismatch with diamond and similar surface energies ( $4.8 \text{ J}\cdot\text{m}^{-2}$  for the (111) plane)) single-crystal substrates, allows in certain conditions the deposition of single-crystal diamond films. However, deposition of diamond films on substrates other than diamond and cBN is desirable due to the difficulty in obtaining large-area single crystal substrates of either of these two materials. The primary difficulty associated with diamond epitaxy is the small number of materials available with suitable crystal structures and lattice constants. Some transition metals and ceramics, such as Ni, Cu, Fe, and cBN, constitute the few isostructural materials with sufficiently similar lattice constants. The lattice mismatch should typically be less than 5% to favor diamond epitaxy. In addition, the high surface energies exhibited by diamond (from  $5.3$  to  $9.2 \text{ J}\cdot\text{m}^{-2}$ , depending on the crystallographic plane considered) constitute further obstacles to diamond nucleation and growth. Therefore, the very large majority of diamond growth CVD processes consist in the deposition of diamond films on foreign substrates with no epitaxy. Yet, diamond has been successfully grown on a wide range of substrate materials since the inception of CVD routes: silicon (Si), tungsten carbide (WC), molybdenum (Mo), alumina ( $\text{Al}_2\text{O}_3$ ), and copper (Cu) [70, 71].

Nucleation and growth of diamond on a foreign surface may occur following three primary modes [50]:

- The first one is the *Volmer-Weber growth* mode, also called *island growth*, in which the interactions between the atoms reaching the surface of the substrate are stronger than the interactions between the arriving atoms and the surface itself, leading to the formation of three-dimensional atom clusters onto the surface, or “islands” (Fig. 2.18a);



- The second mode is the *Franck Van-der-Merwe growth* mode, which consists in a two-dimensional layer-by-layer film growth due to a higher chemical affinity between the atoms of the surface and the arriving atoms relative to the mutual chemical affinity between arriving atoms (Fig. 2.18b);
- The third and final growth mode is the *Stranski-Krastanov growth* mode, which combines 2D layer-by-layer growth with 3D island growth (Fig. 2.18c).



**Figure 2.18: Schematic view of the three primary growth modes:**

**(a) Volmer-Weber (3D), (b) Franck Van der Merwe (2D), (c) Stranski-Krastanov (2D + 3D).**

The appropriate conditions for achieving low-pressure growth of diamond can be obtained through a variety of methods. However, the different CVD routes all commonly combine three main elements: a gaseous feedstock of carbon precursors, a mean of providing energy that causes the gas components to dissociate, and a substrate on which the deposition takes place.

As further detailed in this chapter, various chemical vapor deposition (CVD) methods to grow diamond films on bulk substrates have emerged since the early 1950s, mostly differing by the mean employed to provide to the deposition system sufficient energy to dissociate the input gases. This can be done thermally through hot filament-assisted deposition (HFCVD, or thermally-assisted deposition), electrically through plasma jet-assisted deposition (or thermal plasma CVD: TPCVD) and microwave plasma-assisted deposition (MWCVD), or chemically through combustion flame deposition (or combustion CVD: CCVD) [4].

Although the energy sources of these CVD methods differ, the principle of the diamond growth process remains the same for all these techniques. It relies on the ability to set up a dynamic non-equilibrium system in which only  $sp^3$  carbon bonding can survive. This is first achieved by the presence of hydrocarbon radicals, and more importantly, by large quantities of atomic hydrogen in the deposition gas. Atomic hydrogen is indeed the key element to CVD deposition processes since it stabilizes the growing diamond surface by maintaining the diamond tetrahedral  $sp^3$  configuration while suppressing the  $sp^2$  atomic configuration, which leads to the growth of graphitic or amorphous carbon. By creating a plasma system where atomic hydrogen predominates, any graphitic bond is etched away, leaving only high-quality diamond [5].

The hydrocarbons radicals (such as methyl radicals  $\text{CH}_3$ ) originate from the breakdown of the input gas by the energy brought to the system and act as carbon precursors for diamond deposition on the substrate surface. They are generally formed from hydrocarbons (methane  $\text{CH}_4$ , acetylene  $\text{C}_2\text{H}_2$ , ethylene  $\text{C}_2\text{H}_4$ ) or carbon oxides (such as carbon monoxide  $\text{CO}$  or carbon dioxide  $\text{CO}_2$ ). Once the reactive species have been generated they can either adsorb on the surface, react with it, desorb from the surface and return into the gas phase, or diffuse onto the surface before finding an appropriate reactive site.

Atomic hydrogen employed in CVD diamond growth has several roles: it constitutes the main chemical species existing in the reaction environment and controls the chemical reactions in it; it prevents the formation of graphitic and amorphous carbons by saturating the bonds between the surface carbon atoms of diamond. Also, it activates the reactivity of the diamond surface by generating pending bonds and dissolves the graphite eventually formed, which appears thirty times faster than diamond. Atomic hydrogen used in CVD typically comes from  $\text{H}_2$  gas. Thus, the most commonly employed gas mixture for hot-filament or plasma-assisted CVD diamond growth is  $\text{CH}_4/\text{H}_2$ , with about 1 vol.%  $\text{CH}_4$ . The  $\text{C}_2\text{H}_2/\text{O}_2$  gas mixture is especially employed for combustion torch deposition, as detailed in chapter 3.

During the growth process, the diamond surface is almost entirely saturated with atomic radicals (hydrogen or oxygen, depending on the gas mixture employed), which limits the number of reactive sites where hydrocarbon radicals such as methyl radicals may adsorb. When a hydrogen atom from the vapor phase combines with a hydrogen atom adsorbed onto the surface to form an  $\text{H}_2$  molecule, a reactive site is created on the diamond surface. This reactive site is most likely to be neutralized by a new atomic radical and return to its initial state. However, occasionally, this reactive site can recombine with a methyl radical to create a  $\text{CH}_3$  site onto the diamond surface, thus incorporating a carbon atom to the diamond structure (see Fig. 3.2).

Similarly to HPHT synthesis, the temperature of the substrate and the concentration of carbon precursors are key parameters to the success or failure of the CVD process. The growth conditions must be carefully controlled in order to maintain the deposition of diamond and prevent the creation of graphite. Figure 2.19 shows SEM micrographs of diamond films grown on silicon substrates during this study. As it will be further explained in chapter 3, the substrate temperature and gas precursors' concentration windows required to grow diamond are narrow and these parameters should be carefully controlled. Finally, for many applications of diamond coatings (wear protection, heat dissipation), economics is an overriding issue and capital costs remain major obstacles to the scalability of CVD diamond processes. Therefore, high growth rates and large-area deposition while maintaining a satisfactory diamond quality level are strongly desirable to any industrial application [4].



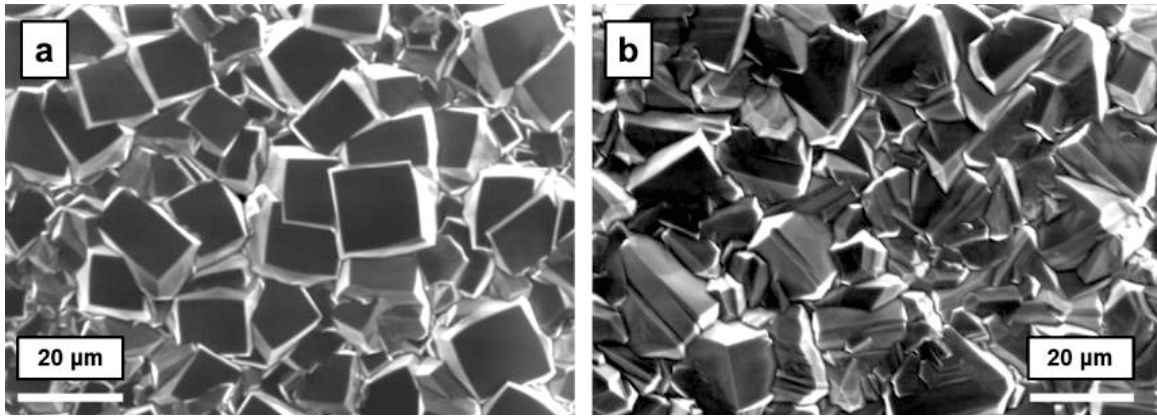


Figure 2.19: SEM micrographs of (a) (100) textured and (b) randomly oriented CVD diamond films.

▪ **Main routes for CVD diamond synthesis [4, 70, 71]:**

- *Hot-filament deposition (HFCVD):*

HFCVD (Fig. 2.20b) can be described as a light-bulb. In the same way a light bulb uses a refractory filament in a low-pressure environment, HFCVD uses a refractory filament (typically tungsten (W), tantalum (Ta), molybdenum (Mo) or rhenium (Re)) in a low-pressure environment to cause the filament to glow. The chamber is vacuumed to a tens of torr (20-30 Torr) while a gaseous mixture is introduced ( $\text{CH}_4/\text{H}_2$ , with about 1 vol.%  $\text{CH}_4$ ). The filament is activated through an electric current. At filament temperatures above 1700-1800°C, the hydrogen undergoes a thermal dissociation reaction, and atomic hydrogen can then interact with the small percentage of hydrocarbon gas to form methyl radicals ( $\text{CH}_3$ ) which leads to diamond growth. The substrate is placed a few millimeters from the filament and heated up to a temperature ranging from 700°C to 900°C. Most of inceptive research about diamond epitaxy was made on HFCVD reactors since they involve limited capital costs on the laboratory scale, are easy to use, and yet produce good-quality diamond films at growth rates ranging between 1 and 5  $\mu\text{m}/\text{h}$ . However, it is usually difficult to prevent the contamination of the diamond film by the filament material. Also, the filaments are particularly sensitive to oxidation and corrosive gases, which severely limits the variety of gaseous mixtures usable through this process.

- *Plasma jet-assisted deposition (TPCVD):*

TPCVD resorts to the use of a thermal plasma consisting of a mixture of argon and hydrogen in varying proportions providing a source of atomic hydrogen and of heat for dissociating the deposition precursors (typically methane  $\text{CH}_4$ ). Figure 2.20c shows a schematic of a typical TPCVD set-up consisting of a dc arc between a rod type cathode and a cylindrical nozzle-type anode. The plasma gas mixture is injected at high mass flow (several liters per minute) and enters the high-power arcing region from the base of the cathode, is heated and expanded by the arc discharge, and

finally leaves the anode nozzle to form a jet of active species at high temperature and supersonic velocity. The thermal plasma can either be generated by an electric arc or by a radio frequency induction discharge (rfi). Deposition precursors are usually added downstream of the nozzle because most hydrocarbons can form volatile compounds with cathode materials, thus leading to strong erosion. Arc powers can range from 100 W to 100 kW, and 40 to 90% of the electric power is transferred to the plasma, depending on the design and on the operating conditions. Argon-hydrogen ratios can also vary widely from 10% hydrogen to 100%. The deposition takes place in a chamber with a pressure between 100 Torr and 1 atmosphere. The thermal plasma features extreme levels of energy density (up to  $10^8 \text{ J/m}^3$ ) and temperature (typically between 1000 K and 5000 K), which allows rapid dissociation of any substance or gas and high-rate generation of deposition precursors. Therefore, deposition rates in the order of 100  $\mu\text{m/h}$  can be achieved through this technique, with a record in literature at 900  $\mu\text{m/h}$ .

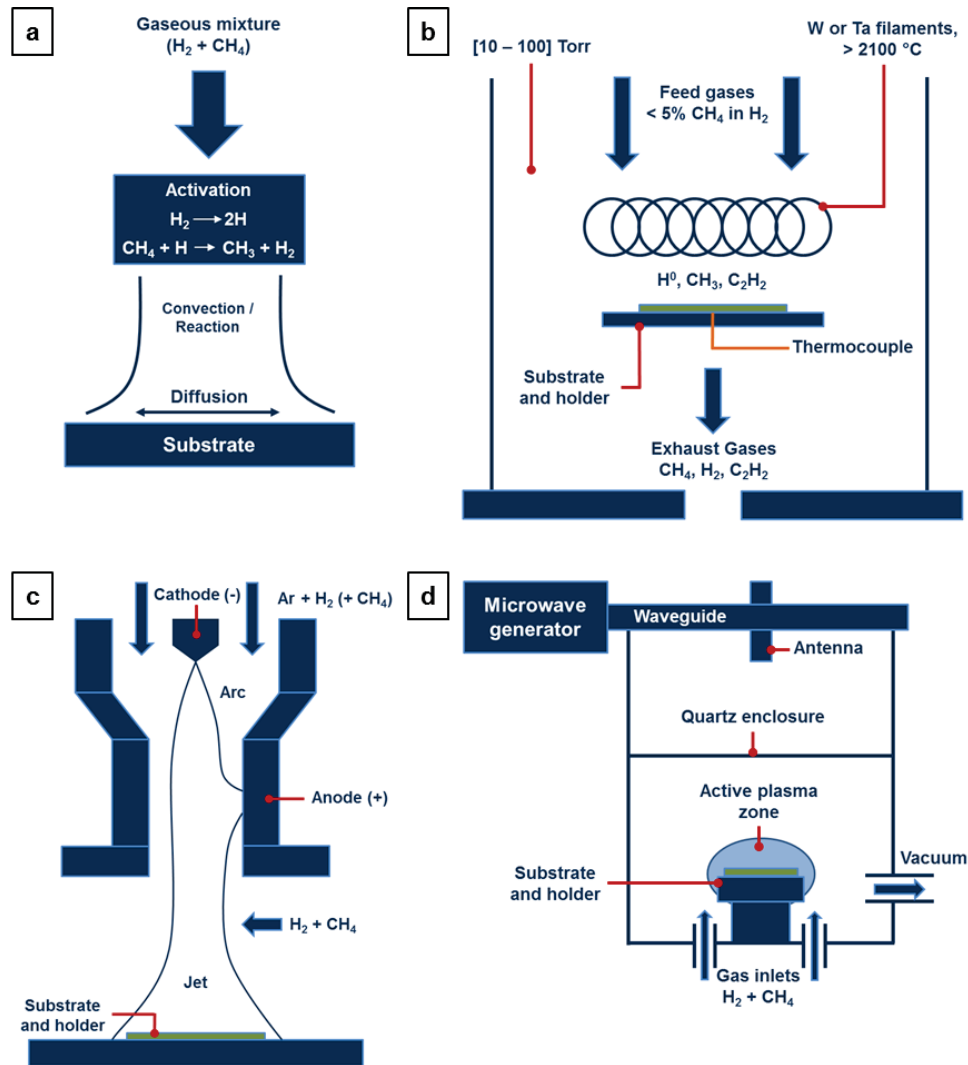


Figure 2.20: (a) General scheme for CVD diamond growth from a  $\text{CH}_4/\text{H}_2$  gaseous mixture (b) HFCVD (c) TPCVD and (d) ASTeX-type MWCVD apparatus [4].

- *Microwave assisted deposition (MWCVD):*

Likewise to plasma jet-assisted deposition, MWCVD (Fig. 2.20d) relies on the electrical activation of the gaseous carbon precursors. A magnetron generates microwaves (typically at a frequency of 2.45 GHz and a power from 600 W to 6000 W), whose energy is transferred to the gas phase. The gaseous species ( $H_2$ ,  $CH_4$ ) are thus heated up, making possible their dissociation and the formation of active radicals needed for diamond growth. MWCVD reactors employ experimental conditions that are very close to that of HFCVD reactors. The reaction chamber is maintained at low pressure (from 10 mtorr up to 200 torr). The electron temperature can reach 10,000 K while the gas temperature is usually located in the 1000-2000 K range. The microwave discharge varies in shape and behavior as a function of the chamber geometry and experimental parameters. It typically exhibits spherical shape located at the substrate emplacement. Diamond films grown through this technique do not suffer from contamination from any foreign materials, unlike HFCVD-grown diamond films. The MWCVD process is the most commonly used diamond growth process. It allows limited growth rate but lead to high-quality, possibly highly-oriented (textured), diamond film deposition when accurate control of the experimental parameters is achieved. Therefore, diamond films grown through MWCVD are of primary choice for applications requiring materials with a high degree of purity, such as the use of CVD diamond as an electronic substrate material.

Since it is a major topic of this study, especially about the work that has been done at the Electrical Engineering department in UNL, combustion is explored in more details in chapter 3.

▪ *A brief history of CVD diamond synthesis:*

The first conclusive scientific work about diamond growth at low pressures was reported by William G. Eversole, from the Linde Division of the Union Carbide Corporation, in the United States, in 1952-1953 [72,73]. He proposed and succeeded in precipitating diamond seed crystals onto diamond using carbon monoxide as a precursor. One can note that this achievement occurred simultaneously to that of the ASEA Company in Sweden, and precedes in time that of the General Electric Company in synthesis of diamond at high pressures, first accomplished in 1954 and publicly announced in 1955. Eversole, however, used preexisting diamond seeds to grow new diamond, while the General Electric and ASEA synthesized diamond from non-diamond carbon.

In parallel to their efforts on HPHT synthesis of diamond detailed in section 2.4.1, the General Electric Company devoted a lot of research time to grow diamond at low pressures from 1951 to 1956. Despite the exploration of numerous methods, these efforts did not end up successfully. At this time, and despite the achievement of Eversole, it was highly doubted that diamond could nucleate at all under metastable conditions and its growth was believed to be only possible at high-pressures, where it is the thermodynamically stable form of carbon. Nevertheless, some among the

research community, among them Bridgman [74], who strongly contributed to the HPHT synthesis of diamond, pointed out that metastable phases such as diamond could form from precursors if the activation barriers to more stable phases are sufficiently high. In other words, the formation of a metastable phase depends on selecting conditions under which the processes competing with diamond growth are not favored, i.e. spontaneous graphitization of the diamond surface and nucleation and growth of graphitic deposits.

A major step forward in low-pressure diamond synthesis was made when the scientific community started to gain understanding on the critical role played by atomic hydrogen on the diamond growth process. Lander and Morrison at Bell Laboratories provided a significant contribution by demonstrating through low-energy electron diffraction that there was a kinetic barrier to graphitization of a hydrogen-covered diamond surface combined with a significant mobility of carbon atoms in a certain temperature range [75]. Therefore, they stated that epitaxial growth of diamond on diamond was possible by using hydrogen to elevate the thermodynamic barriers to nucleation of the more stable phases such as graphite. Various U.S. patents by Hibshman [76], Vickery [77], or Angus [78] confirmed the critical role played by atomic hydrogen on diamond growth by suppressing the formation of graphitic carbons.

Another move forward was made when the molecular mechanism responsible for diamond growth became clearer. Based on thermodynamic computations, Angus and coworkers [79] suggested that free carbon atoms in the vapor phase may not be a major source of carbon for diamond growth. Instead,  $\text{CH}_4$  and other hydrocarbons appeared to be more likely involved in the reaction with the diamond surface leading to diamond growth. Based on their conclusions, Angus et al. proposed a three-step growth mechanism: (1) formation of mobile surface species containing a single carbon atom (such as methyl radicals  $\text{CH}_3$ ), (2) surface diffusion of the species onto the diamond surface, (3) addition to a vacant surface site. After discussions with major researchers such as Eversole, Lander, and Hibshman, Angus concluded that the chemical vapor deposition of hydrocarbons from gaseous carbon precursors was the method most likely to lead to diamond epitaxy. However, there was still skepticism about the possibility of growing diamond at rates that would allow any industrial applications.

Low-pressure diamond growth was subsequently confirmed by Angus et al. who succeeded in reproducing the work of Eversole in the mid-1960's [80]. In the meantime (1960's and 1970's), many efforts were devoted by researchers at the Physical Chemistry Institute of Moscow to grow diamond on non-diamond substrates at sub-atmospheric pressures. They reported in 1969 to have confirmed and improved the results previously obtained by Eversole. They had grown diamond on diamond seed crystals by using pure methane as a carbon precursor at pressures ranging from 0.1 to 0.3 torr and temperatures ranging from 950 to 1050°C [81]. Yet, despite the evidence brought to

light by U.S. researchers in the previous years, no mention of the use of atomic hydrogen in the diamond growth process was made in the reports of the Russian scientists. In spite of the tensed political climate between the U.S. and the Soviet Union at the time, Russian and American scientific communities found ways to communicate. Dmitri Fedoseev, a member of the research group in Moscow, became aware of the conclusions made by Angus et al. about the important role played by atomic hydrogen in the growth process at a conference in Kiev in 1971. Later on, he and his coworkers started using atomic hydrogen in their experiments. In 1976, a major achievement was made when the first formation of diamond crystals on non-diamond substrates at a sub-atmospheric pressure and a temperature of about 1000°C was reported by Deryagin and coworkers [82].

Finally, a major page in the book of low-pressure diamond synthesis was written by the work of Japanese scientists at the National Institute for Research in Inorganic Materials (NIRIM) in Tsukuba, which initiated a project on metastable diamond growth in 1974. They contributed to the field by providing technological solutions to rapid growth of diamond at low pressures on various substrate materials. Successful diamond synthesis was first achieved using a hot-filament to activate CH<sub>4</sub>-H<sub>2</sub> gas mixtures and reported in 1981. Thereafter, they presented papers reporting the growth of diamond at rates of several micrometers per hour [83,84]. Beneficiating from the understanding gained by their pairs in the U.S. and Russia about the diamond growth process, Japanese scientists among them Sato, Matsumoto, and Kamo, developed the first hot-filament assisted CVD and microwave-assisted CVD machines that are now very popular among researchers in the diamond community.

The NIRIM-type MWCVD machines developed by Kamo et al., with the ASTeX-type MWCVD machines developed later by Bachmann et al. at the ASTeX Corporation in the U.S. now represent the majority of apparatus used to grow diamond. Therefore, the NIRIM efforts strongly contributed to the development and scaling of the new diamond technology. In the late 1980's, still in Japan, Kurihara et al. [85] and Hirose et al. [86] respectively introduced and developed the plasma jet-assisted CVD and combustion flame-assisted CVD methods.

Since combustion CVD synthesis of diamond is of primary importance in this study, details about the inception of this technique are provided in chapter 3. Especially, focus is brought to the use of laser excitation and optical pumping techniques to enhance the diamond growth process through combustion flame synthesis. In the next sections of chapter 2, we will explore the literature looking for reported use of diamond based-materials, either CVD diamond films or HPHT diamond-reinforced composite materials, for heat dissipation purposes in electronic packages.

## 2.5 Diamond-based heat-conductive materials in electronics

After having pointed out the interest of using diamond for the thermal management of power electronic packages, followed by the principles and background of HPHT and CVD syntheses of diamond, we will now focus on a literature review of some of the existing reported fabrication and use of diamond-based materials, either CVD diamond films or HPHT diamond-reinforced composites, as heat conductive materials in electronic packages. Prior to discuss this matter, emphasis will be put on the importance of interfaces on the heat conduction process in bi-materials assemblies.

### 2.5.1 On the importance of interfaces on the heat conduction process

- ***Reactive and non-reactive bi-materials assemblies:***

When considering the fabrication of bi-materials assemblies, such as layered systems consisting of a diamond film grown onto a substrate or a composite material made of diamond particles dispersed into a copper matrix, one should especially be careful to the interface between the two materials. Indeed, the interface region governs the transfer of properties between the two materials considered and has a critical influence on the ultimate properties of the final assembly, such as its thermal conductivity or thermal expansion. The importance of the interface region comes from two main factors: interfaces occupy a large area in the assembly and, in general, the two materials assembled form a system that is not in thermodynamic equilibrium [87, 88].

It exists two possible types of bonding at the interface of a bi-materials assembly: *chemical bonding*, which involves a chemical reaction at the interface leading to the bonding process, and *mechanical bonding*, which strictly relies on mechanical gripping between the two materials. In the scope of heat spreading applications, interfaces, either existing between the heat-spreading film and its surrounding layers or inside the heat-spreading film itself, should allow an effective conduction heat transfer between the two materials, thus leading to a high thermal conductivity through the bi-materials assembly. The interface should also allow an efficient transfer of thermo-mechanical load upon thermal cycling, thus leading to a bi-materials system with enhanced lifetime and reliability. Therefore, an interface will be thermally efficient only if there is a strong chemical bonding between the two materials.

In crystallographic terms, ceramic-metals interfaces (such as diamond/silicon, diamond/tungsten carbide, or diamond/copper) are generally incoherent and exhibit high surface energies, which is a typical obstacle for chemical bonding and thus for the heat to flow from one material to another. Although mechanically-bonded heat sink materials (among them carbon fibers



dispersed copper matrix MMCs) have been reported to be efficient, pure mechanical bonding is generally detrimental to the heat conduction process between two materials.

Indeed, considering interfaces in bi-materials assemblies, two types of systems can be found [89]:

- *The reactive systems*: in which a chemical instability exists between the two materials, i.e. in which an interphase can be formed at the interface between the two materials. The chemical reactivity between the two materials is illustrated by similar surface energies. The interphase formed can be either beneficial or detrimental to the final properties of the assembly;
- *The non-reactive systems*: in which the two materials assembled are strictly stable from the chemical point of view, i.e. no interphase can be formed at the interface region separating them. In this type of system, the adhesion between the two materials is only mechanical. To improve the properties of non-reactive bi-materials assemblies, it is required to modify the surface chemistry of one of the two elements in order to allow the creation of chemical bonding at the interface between the two materials.

Figure 2.21 sums up the two interfacial configurations typically encountered in bi-materials assemblies. As detailed in chapters 3 and 4, both diamond/silicon and diamond/copper systems are non-reactive systems, thus requiring interface engineering solutions to implement chemical bonding at the interface.

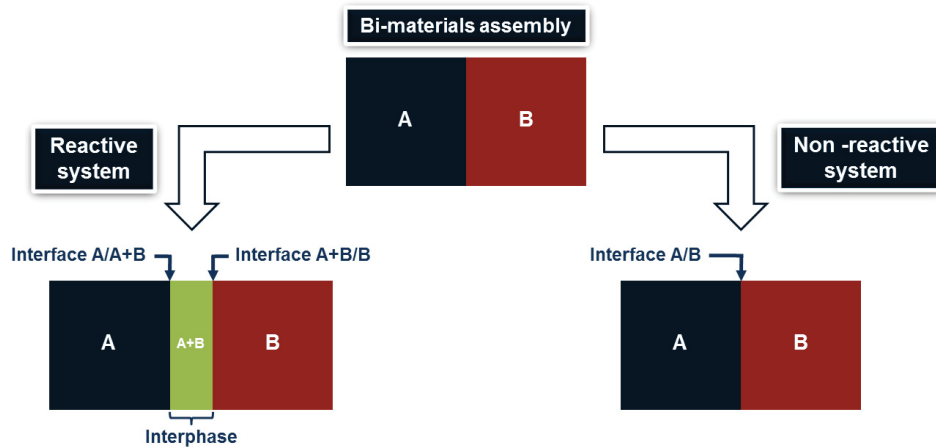


Figure 2.21: Schematic view of reactive and non-reactive bi-materials assemblies [89].

▪ ***Heat conduction in metals and diamond:***

In the modern view of materials, a solid may be considered as an assembly of atoms and free electrons bound in a periodic arrangement called the lattice. Accordingly, transport of thermal energy in a solid may be caused by two effects: the migration of free electrons or lattice vibrational



waves. When viewed as a particle-like phenomenon, the lattice vibration quanta are termed *phonons*. Therefore, when electrons and phonons carry thermal energy leading to conduction heat transfer in a solid, the thermal conductivity may be expressed as [13]:

$$k = k_e + k_{ph} \quad (2.5)$$

Where  $k_e$  and  $k_{ph}$  are the contributions of free electrons and phonons motion to the global thermal conductivity, respectively. The respective importance of the different contributions to the global thermal conductivity of a material can be related to its ability to conduct electrical current. The higher the electrical conductivity of a material, the larger  $k_e$ . Inversely, the higher the electrical resistivity of a material, the larger  $k_{ph}$ . Consequently, for pure metals such as copper, which exhibit a high electrical conductivity, the electron contribution to conduction dominates ( $k_e$  is larger than  $k_{ph}$ ), although phonons also contribute to the heat conduction process in metals. However, for nonconductive metals, semiconductors, or insulators, such as diamond or silicon, the phonon contribution is dominant ( $k_{ph}$  is larger than  $k_e$ ).

At the macro scale, the thermal conductivity of a material acts as a proportionality coefficient between the applied heat flux and the resulting temperature gradient in the material through Fourier's law:

$$q'' = -k\nabla T \quad (2.6)$$

Where  $q''$  is the heat flux density ( $\text{W}/\text{m}^2$ ),  $\nabla T$  is the temperature gradient ( $\text{K}.\text{m}^{-1}$ ), and  $k$  is the thermal conductivity ( $\text{W}.\text{m}^{-1}.\text{K}^{-1}$ ) [13]. Fourier's law also implies that the heat flux lines are perpendicular to isotherms lines since the heat flux temperature gradient vectors and collinear.

Thermal conductivity, which characterizes the ability of a material to conduct heat, should be distinguished from thermal diffusivity, which quantifies the speed at which heat diffuses into a material. The thermal diffusivity  $a$  ( $\text{m}^2.\text{s}^{-1}$ ) is defined by:

$$a = \frac{k}{\rho C_p} \quad (2.7)$$

Where  $\rho$  is the density of the material considered ( $\text{kg}.\text{m}^{-3}$ ),  $k$  its thermal conductivity ( $\text{W}.\text{m}^{-1}.\text{K}^{-1}$ ), and  $C_p$  its specific heat ( $\text{J}.\text{kg}^{-1}.\text{K}^{-1}$ ). While thermal conductivity may be seen as the stationary component of the heat conduction process, thermal diffusivity may be assimilated to its transient component. It has to be noticed that a high thermal diffusivity does not mean a high thermal conductivity since  $a$  is density-dependent. Thus, heat may diffuse as fast in an insulating material such as a plastic ( $k$  and  $\rho$  relatively small) as in a conducting material such as steel ( $k$  and  $\rho$  relatively large).

In terms of electronic band structure, metals can be regarded as materials whose valence and conduction bands are overlapping, making the conduction band partially empty and partially filled. Therefore, there is a large density of energetically available states that each electron can occupy. Consequently, electrons can move freely between energy levels without a high energy cost, which makes metals good electrical and thermal conductors. In terms of particle-like reasoning, metals can be viewed as made of a positively charged ionic solid structure embedded into an *electron gas* formed by negatively charged valence free electrons. These free electrons, whose energy levels are located in the metal conduction band, are the heat carriers since they conduct the vibrational energy coming from the heat source, and make metals especially efficient in conducting thermal energy [50].

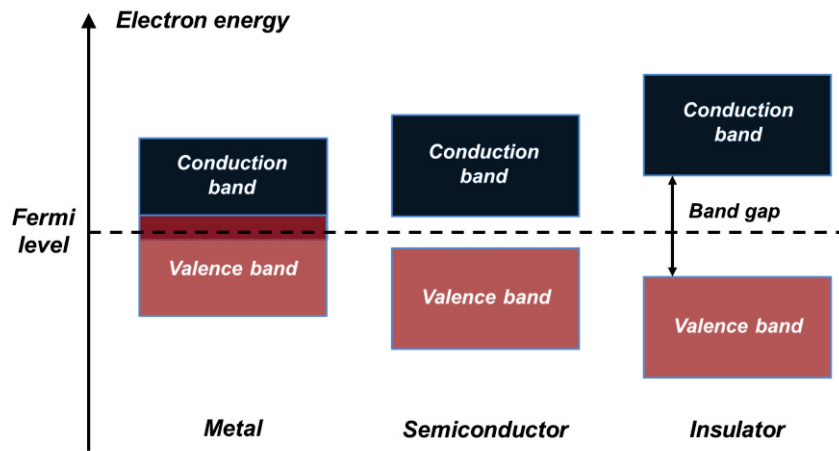


**Figure 2.22:** Schematic view of electronic band structures of metals, semiconductors, and insulators [50].

Diamond, on the other hand, shows an electronic band structure where the conduction and the valence bands are separated by a large energy gap (the *band gap*) which prevents electrons from the valence band to access the energetically free states of the conduction band that allow electrons motion, thus making diamond an electrically insulating material. Diamond exhibits a band gap that is especially large (5.47 eV at 300 K) which makes it useful for a wide range of insulating applications due to its large electrical resistivity, but which also makes possible the use of diamond as a p-type semi-conductive material through boron doping, as explained in section 2.3.3. Similarly, silicon exhibits an electronic band structure in which conduction and valence bands are separated but with a band gap of 1.11 eV at 300 K, which makes silicon a semiconductor material in which electronic conduction can be accurately controlled through the introduction of p-type (excess of holes) or n-type (excess of electrons) doped areas.

From a kinetic point of view, the thermal conductivity of a material can be expressed as:

$$k = \frac{1}{3} C v l_{mfp} \quad (2.8)$$

Where  $C$  is the electron/phonon specific heat per unit volume ( $\text{J.m}^{-3}.\text{K}^{-1}$ ),  $v$  is the mean electron/phonon velocity ( $\text{m.s}^{-1}$ ), and  $l_{mfp}$  is the electron/phonon mean free path (nm), i.e. the average distance traveled by an electron/a phonon before it collides with either an imperfection in the material or with a phonon. Whenever heat is conducted by free electrons or phonons, the thermal conductivity increases as the mean free path of the energy carriers (i.e. electrons or phonons) increases. In solids, the value of  $l_{mfp}$  decreases as the temperature increases, thus  $k$  decreases as the temperature increases. Table 2.10 gathers some values of mean free path and corresponding thermal conductivity for selected materials.

**Table 2.10: Heat carriers mean free path and corresponding thermal conductivities of materials [13].**

Materials	$l_{mfp}$ (nm)	$k$ ( $\text{W.m}^{-1}.\text{K}^{-1}$ )
Copper	35	400
Diamond (IIa)	315	2300
Gold	31	317
Silicon	43	148

In most of engineering problems, bulk thermal conductivity is accurate enough to describe the heat conductive behavior of a material. However, in certain technological fields such as microelectronics, the material's characteristic dimensions can be on the order of micrometers or nanometers, in which case care must be taken to account for the possible modifications of thermal conductivity that can occur as the physical dimensions become small. The influence of the microstructure of a material on its thermal conductivity is particularly important when considering ultra-thin films, with typical thickness in the [100 – 500] nm range.

When considering a material with characteristic dimension  $L$  (average grain size for instance), the influence of the medium scale on the heat conduction process can be estimated upon calculation of the  $L/l_{mfp}$  ratio. For a material exhibiting a large  $L/l_{mfp}$  ratio, the effect of the medium scale on reducing the average energy carrier path length is minor, and conduction heat transfer occurs as described at the bulk scale. However, as the medium scale reaches the average heat-carrier mean free path, the microstructure of the material may interfere with the average net distance traveled by the thermal energy carriers. This issue is especially relevant when considering the continuous shrinkage in size of individual active semiconductive components, in which heat transport phenomena at the nanometer scale are of critical importance. Following Moore's law pace described in chapter 1, current state-of-the-art field effect transistors shows channel lengths of 100 nm, with near-future projections down to 50 nm. This type of medium also questions the fundamental definition of temperature at such an atomic-level scale [90, 91].

In the case of electron-driven heat conduction as in the case of phonon-driven heat conduction, the physical defects existing in the material structure (such as grain boundaries, dislocations, voids, and impurities) act to *scatter* the energy carriers and redirect their propagation, which, in the end, affect the heat conduction process and decrease the thermal conductivity. The effect of the microstructure on the thermal conductivity of a material is also of major importance when considering interfaces between dissimilar materials such as interfaces between a film and its substrate or between the matrix and the reinforcements of a composite material. In this case, as in the case of the grain boundaries existing in diamond films, interfaces will play a critical role on the energy carriers responsible for the heat conduction process in the material [40].

▪ ***Heat conduction across the metal/diamond interface:***

Although the heat conduction processes in metals and diamond are well understood, one being driven by the motion of free electrons, the other by lattice vibrational waves (or phonons), accurate knowledge of the heat conduction process across metal/diamond interfaces remains an open challenge. Interfaces constitute interruption in the regular crystalline lattice in which heat carriers propagate. Thus, it is intuitively appealing that they should produce thermal resistances. Although it would be unrealistic to provide exhaustive understanding of the phenomena driving heat transport across metal/diamond interfaces, we will briefly review in this section some major concepts and ideas to help figuring out how thermal energy can be transferred from metal to diamond.

Phonons represent quanta of atomic lattice vibration in a periodically structured solid material (crystal). They are generally divided into two categories: optical phonons and acoustic phonons. Either optical or acoustic, phonons exhibit three main polarization modes: one longitudinal mode and two transverse modes.

Usually, lattice vibrations at different locations of a crystal show various frequencies and are at different stages of a periodic motion (they are at random phase, thus called incoherent phonons). It is these incoherent phonons, also termed *optical phonons*, corresponding to thermal lattice vibrations, which are studied through frequency-domain spectroscopy such as Raman spectroscopy (see chapter 3). Their name comes from the fact that they can be excited through optical excitation sources, such as infrared or visible lights. However, upon receiving an outside impulse (such as a heat flux), phonons initiate to keep pace with their neighbors, thus becoming in-phase. These coherent atomic motions are called *acoustic phonons* because they can interfere with each other in a wave-mechanics sense, thus carrying thermal energy in the material [13].

Thus, acoustic phonons are responsible for the heat transport process in diamond. Similarly to sound that propagates in air through a sequence of pressure waves, heat is carried into diamond through the propagation of coherent phonons.

Interfaces, as any localized non-uniformity, are known to *scatter* the thermal energy carriers (electrons and phonons), that is to affect their energy and direction of motion, thus leading to a discontinuity in the temperature when the heat flows from one material to the other. More generally, scattering originates from collisions of the heat carriers with local inhomogeneities or other particles. Interfacial thermal resistance was first observed by Kapitza in 1941 [92], who studied the heat conduction process at interfaces between solid copper and liquid helium. He gave his name to the general definition of the thermal boundary resistance, known as *Kapitza resistance*, involved in a variety of interfacial conduction heat transfer phenomena and given by:

$$R_{th} = \frac{\Delta T}{q''} \quad (2.9)$$

Where  $q''$  is the heat flux density ( $\text{W.m}^{-2}$ ) across the interface,  $\Delta T$  is the temperature difference between the two sides of the interface (K), and  $R_{th}$  the Kapitza resistance of the interface ( $\text{K.m}^2.\text{W}^{-1}$ ). The thermal conductance of the interface is simply equal to the inverse of the Kapitza resistance  $1/R_{th}$  ( $\text{W.m}^{-2}.\text{K}^{-1}$ ). The Kapitza resistance makes that a finite thermal boundary conductance exists at metal/diamond interfaces due to scattering of incident phonons and plays a critical role on the transport of thermal energy. To exploit the full thermal conductivity potential of a bi-materials assembly (diamond film/substrate system, or copper/diamond composite materials) as heat-dissipative materials, it is required to reduce the Kapitza resistance across the bi-materials interface to a minimum [93].

At the interface between a metal and a non-metal such as diamond, a transition from electron to phonon heat conduction is expected to take place. This is assumed to occur through various scattering phenomena between phonons and electrons in the vicinity of the interface, whom some are depicted in Fig. 2.23, where  $p$  and  $k$  represents electron and phonon wavevectors, respectively.

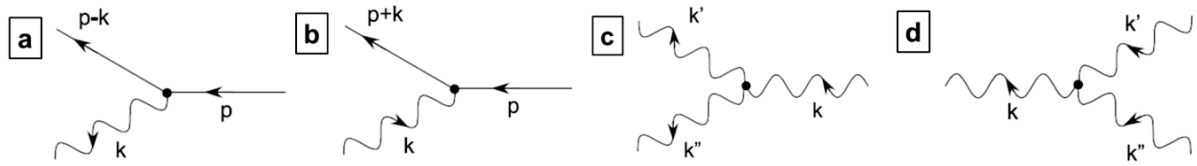


**Figure 2.23: Electron-phonon and phonon-phonon scattering processes: (a) Electron-phonon scattering, in which an electron emits a phonon. (b) Electron-phonon scattering, in which an electron absorbs a phonon. (c) Phonon-phonon scattering, in which a phonon decays into two phonons. (d) Phonon-phonon scattering, in which two phonons generate a phonon [94].**

Based on this premise that energy transfer must occur between electrons and phonons for the heat transfer to occur across metal-nonmetal interfaces, Majumder et al. [95, 96] postulated two main pathways for the heat transfer to be achieved through metal/diamond interfaces:

- *Coupling between electrons of the metal and phonons of the non-metal through anharmonic interactions at the metal-nonmetal interface* (Fig. 2.24a): in this case, an electron is scattered from the confining potential of the interface and emit a phonon, which moves from the interface into the diamond. Therefore, energy transfers directly from the metal electrons to the diamond phonons, and the Kapitza resistance is equal to:  $R_{th} = R_{e-p}$ . This mechanism is particularly significant for metals with strong electron-phonon interaction, or for an interface with a small value of phonon transparency;
- *Coupling between electrons and phonons within the metal in vicinity to the interface, and then subsequent coupling between phonons of the metal and phonons of the non-metal* (Fig. 2.24b): in this case, electrons first exchange energy with phonons within the metal, which are then coupled with the atomic vibrations in the dielectric material through interface bonds. The resulting Kapitza resistance may be expressed as:  $R_{th} = R_{e-p} + R_{p-p}$ . This mechanism is supposed to dominate in the case of metals with a weak electron-phonon interaction, such as copper.

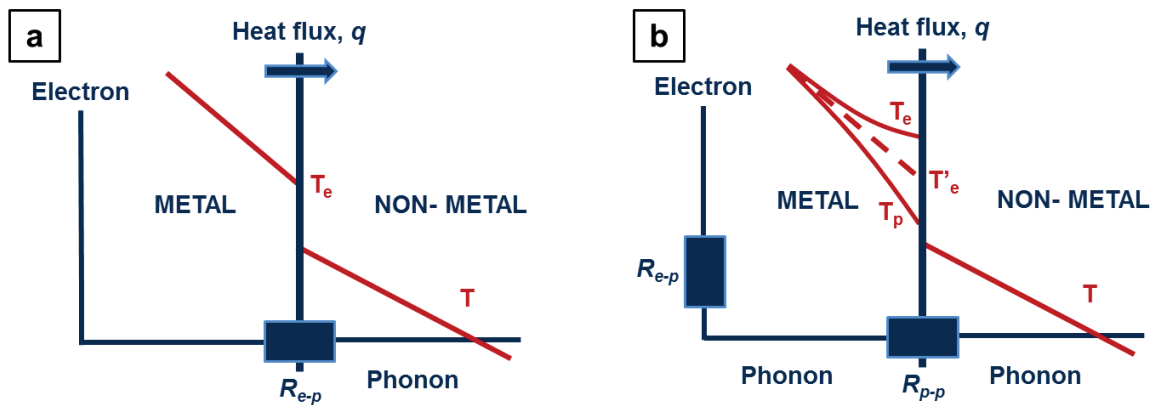


**Figure 2.24:** Schematic illustrating pathways for the heat to flow across a metal/non-metal interface. (a) The electrons of the metal transfer their energy to the phonons of the non-metal through electron-phonon coupling. (b) The electrons of the metal transfer first their energy to phonons in the metal and then couple with phonons of the non-metal.  $T_e$ ,  $T_p$ ,  $T'_e$ , and  $T$  respectively stand for the electron and phonon temperatures of the metal, the equivalent temperature of the metal, and the temperature of the non-metal [96].

The model assuming the existence of an electron-phonon coupling component in the metal (Fig. 2.23b) seems to gather more approbation from the scientific community. In order for the heat to be conducted across metal/non-metal interfaces, the heat flux has to overcome the thermal resistances represented by both electron-phonon and phonon-phonon coupling.

Two major models have been used to simulate phonon-phonon coupling phenomena through interfaces and estimate interfacial thermal resistances: the *acoustic mismatch* (AM) model, and the

*diffuse mismatch* (DM) model. These two models rely on the assumption that phonons undergo either reflection or transmission at the interface. They differentiate by considering either *specular* (*non-diffuse*, or *unscattered*) or *diffuse* (*scattered*) phonon reflection or transmission at the interface. When a phonon undergoes specular reflection or transmission at the interface, the angle of the incident phonon equals the reflected angle and the angle of the transmitted phonons can be determined by the laws of optical geometry. In contrast, when a phonon undergoes diffuse reflection or transmission, the event is completely independent of any preliminary information about the particle, such as the angle of incidence. Thus, the particle reflects or transmits with equal probability in all directions [93, 97, 98].

Although AM and DM models only consider phonon transmission or reflection through interfaces, they have been applied to metal/non-metal interfaces as well, assuming that phonon-phonon coupling resistance dominates over any electron-phonon coupling resistance. These models both assume strong chemical bonding at the interface, and are thus not applicable for interfaces relying on weak chemical bonds, such as hydrogen or Van der Waals bonds for example.

- *Acoustic mismatch (AM) model* [97,98]:

The AM model was developed by Khalatnikov [99] in 1952 to describe the thermal boundary resistance observed by Kapitza at the interface between solid copper and liquid helium. The AM model makes the simplifying assumption that phonons incident at an interface undergo specular (or non-diffuse) reflection or transmission at the interface and are governed by continuum acoustics. Thus, the interface is treated as a plane. Consequently, phonons are treated as plane waves and the materials in which they propagate as continua (no lattice).

For phonons with wavelength much greater than typical interatomic spacings, this continuum approximation is expected to be accurate. Given this approximation, there are only a few results possible when an incident phonon reaches the interface: the phonon can specularly reflect, reflect and mode convert, transmit, or transmit and mode convert (Fig. 2.25a). The final state is a superposition of these possibilities. The angles of reflection or transmission, with or without mode conversion, as well as the probability of each, are given by Snell's laws of optical geometry.

Assuming a longitudinal phonon from solid 1 incident on an interface at an angle  $\theta_{inc}$  from the normal of the interface, if the result is a transmitted longitudinal phonon in solid 2, the angle of transmission  $\theta_{trans}$  is given by Snell's laws as:

$$\sin \theta_{trans} = \frac{c_1^2}{c_2^2} \sin \theta_{inc} \quad (2.10)$$



Where  $c_l^i$  stands for the longitudinal phonon velocity (speed of sound,  $\text{m.s}^{-1}$ ) in material  $i$ . Equation 2.10 holds if the transmitted phonon is mode converted upon transmission, with the transverse phonon velocity  $c_t^2$  instead of the longitudinal one  $c_l^2$ .

In the AM model, the transmission angle cannot exceed  $90^\circ$ . Thus, for incident angles greater than that for which  $\sin \theta_{inc}$  equals  $c_l^1/c_l^2$  or  $c_l^1/c_t^2$ , the probability of transmission to a longitudinal or transverse phonon, respectively, vanishes. These are called the critical angles. The set of all angles less than the largest critical angle is called the critical cone. Only phonons incident from within the cone have a chance to be transmitted. On the side with greater phonon velocities, there is no critical cone: phonons with any incident angle have some chance for transmission.

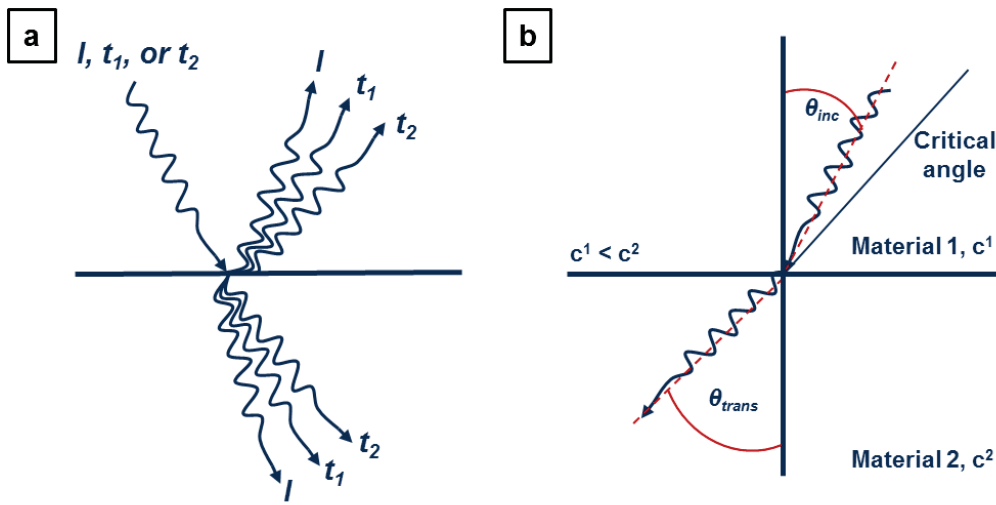


**Figure 2.25: (a) Schematic illustrating possible phonon reflection and transmissions in the framework of the acoustic mismatch model. (b) Incident and transmitted phonon angles at an interface between two materials with different phonon velocities [97].**

The AM model follows the principle of general detailed balance, i.e. if a phonon with incident angle  $\theta_{inc}$  transmits to a phonon with transmitted angle  $\theta_{trans}$  with probability  $\tau$ , then a phonon from the other side incident on the interface with incident angle  $\theta_{trans}$  transmits with the same probability  $\tau$  back into a phonon with transmitted angle  $\theta_{inc}$ . Also, the AM model relies on the fact that phonons can only undergo specular (or unscattered) transmission or reflection, and assumes that no scattered reflection or transmission, either elastic or inelastic, takes place at the interface.

Thus, the AM model describes the interface between dissimilar materials as a mismatch in acoustic impedances resulting from different densities and speeds of sound, which is similar to the refractive index mismatch of two optically different materials. The effect that this impedance mismatch has on phonon transmission is captured in the AM model.

For instance, the AM model gives the transmission probability (equivalent to the total fraction of energy transmitted through the interface) for phonon energy in material 1 incident normal ( $\theta_{inc} = 0^\circ$ ) to the interface with material 2 as:

$$\tau_{12} = \frac{4Z_1Z_2}{(Z_1+Z_2)^2} \quad (2.11)$$

Where  $Z_i = \rho c_s$  is the acoustic impedance of material  $i$  ( $\text{kg.m}^{-2}.\text{s}^{-1}$ ), with  $\rho$  and  $c_s$  being its density ( $\text{kg.m}^{-3}$ ) and speed of sound ( $\text{m.s}^{-1}$ ), respectively.

The AM model has been shown to predict relatively well TBR at low temperatures ( $T < 7$  K) and at ideal interfaces where specular reflection and transmission probable. However, this represents a very limited population of actual interfaces, which may have to be considered at room or higher temperatures and which in many cases show disordered regions that could induce diffuse phenomena. For instance, Eisenmenger et al. [100] demonstrated, using phonon pulses and liquid/solid interfaces, that the assumption of non-diffuse phonon transmission and reflection was not valid for high-frequency phonons ( $> 100$  GHz), because the roughness of the interface can become on the order of the wavelength of the phonons, which may thus be affected diffusely.

- *Diffuse mismatch (DM) model* [97,98]:

The limits of the AM model led Swartz and Pohl [97] to propose the DM model in order to predict interfacial thermal resistances in a more realistic way. The DM model assumes diffuse reflection and transmission, that is, a phonon “loses” its memory after reaching the interface and thus the probability of reflection from one side equals the probability of transmission from the other. The probability that a phonon will reflect or transmit into a given side of the interface is thus independent of where it came from but only proportional to the density of phonon states on the side considered. To apply the DM model in its simplest form, the following assumptions must be made: (i) phonons are elastically scattered at the interface, i.e. a phonon from one side with frequency  $\omega$  can only emit from the interface a phonon with the same frequency  $\omega$ ; (ii) phonon reflection or transmission is completely diffuse, i.e. a reflected or transmitted phonon has no memory of the mode (longitudinal or transverse) or direction of the incident phonon; (iii) materials on both sides of the interface are elastically isotropic, i.e. the longitudinal and transverse acoustic velocities (speeds of sound) are constant in all crystallographic directions.

In the DM model, the linear Debye approximation of the phonon dispersion is used to calculate the phonon density of states. Indeed, accurate calculation of the TBR at an interface requires detailed knowledge of the phonon dispersion relationship in the Brillouin zone of the material (lattice in the reciprocal crystallographic network). The Debye model relies on the assumption that this relationship is linear (Debye approximation).

The Debye model, which is the base for the DM model, originates from an attempt by Peter Debye to estimate the phonon contribution to the heat capacity of a solid and its evolution with respect to temperature ( $T$ ). Thus, Debye demonstrated that the heat capacity followed a  $T^3$  evolution law, also known as Debye law, at low temperature. In Debye theory, the Debye temperature  $\Theta_D$  is the temperature of a crystal's highest normal mode of vibration, i.e. the highest temperature that can be achieved due to a single normal vibration. The Debye temperature is given by:

$$\Theta_D = \frac{h\nu_m}{k_B} \quad (2.12)$$

Where  $h$  is the Planck's constant ( $h = 6.62 \times 10^{-34}$  J.s),  $k_B$  is the Boltzmann constant ( $k_B = 1.38 \times 10^{-23}$  J.K<sup>-1</sup>), and  $\nu_m$  is the Debye frequency (Hz, or s<sup>-1</sup>). The Debye frequency is a function of the number of atoms in the solid considered and of the speed of sound in the material.

Due to the assumption of diffuse reflection and transmission, the probability of transmission from side 1 to side 2 is the same as probability of reflection from side 2 to side 1, i.e.  $\tau_1(\omega) = 1 - \tau_2(\omega)$ . Therefore, the phonon transmission probability from side 1 to side 2 is calculated in the DM model from:

$$\tau_{1/2}(\omega) = \frac{\sum_{s=l,t} \nu_{s,2}^{-2}}{\sum_{s=l,t} \nu_{s,1}^{-2} + \sum_{s=l,t} \nu_{s,2}^{-2}} \quad (2.13)$$

Where  $\nu_l$  and  $\nu_t$  denote the longitudinal and transverse phonon velocity (m.s<sup>-1</sup>) and  $c_d$  is the Debye velocity (speed of sound, m.s<sup>-1</sup>) in material at side  $i$ , defined by:

$$c_{d,i} = \frac{(\nu_{l,i} + 2\nu_{t,i})}{3} \quad (2.14)$$

Although Debye model well predicts the heat capacity at low and elevated temperatures, it shows limited accuracy at intermediate temperatures. The Debye model was the base for the establishment of the DM model. More details about the underlying equations of the DM model are available in section 3.5 where it is used to estimate the thermal resistance at the diamond/Si interface.

Despite the fact that it improves the previous AM model, the DM model still assumes that the fraction of phonon energy transmitted is independent of the structure of the interface itself. Also, while the AM and DM models provide useful reference calculations against which to compare experimental results, and in many cases give rather similar predictions, neither captures the complexity of the interaction between phonons and real interfaces.

## 2.5.2 CVD diamond films in electronics

Although thermal performances of natural single-crystalline diamond exceeds by far that of polycrystalline diamond films grown through CVD routes (see also section 2.3.3), it is possible to achieve diamond films with high heat conduction potential through these techniques. Indeed, CVD diamond has been shown to exhibit superior properties relative to other packaging materials in terms of thermal conductivity, thermal expansion coefficient, mechanical strength, and electrical resistivity. Therefore, it has long been recognized as a promising electronic substrate material. The only obstacles to a more widespread use of CVD diamond substrates in such application have been its limited availability in large sizes, stress-free, of uniform thickness, and at competitive costs. CVD synthesis methods described in section 2.4.2 allowed widening the scope of potential diamond films applications by decreasing the capital cost of diamond synthesis, increasing its scalability and manufacturability, and providing diamond films with high phase purity and a high heat dissipative potential. Therefore, CVD synthesis has opened promising perspectives for diamond films to be applied as thermal management materials in high-power electronic packaging [4,5].

As in any other high-power electronic package, the temperature rise in laser-diode arrays is proportional to the thermal resistance between the active and coolant areas. Instead of the traditional approach that consists in using silicon, Goodson et al. [101] proposed to use a CVD diamond micro-channeled heat sink to help cooling laser-diode arrays by using epitaxial lift-off and grafting to bond a CVD diamond heat sink to the active areas of the package. They demonstrated that the new configuration they proposed allowed the reduction of its thermal resistance by 75% relative to a conventional configuration based on micro-channels in silicon.

Another approach consists in directly sandwiching CVD diamond heat spreading films between the active areas and a heat sink. Sakamoto et al. [102] safely increased the output power level of laser-diode arrays from 75W to 120W by embedding a CVD diamond substrate between active diodes and a copper heat sink. Similarly, Lin et al. [103] demonstrated that a 50  $\mu\text{m}$ -thick CVD diamond heat film could remarkably decrease the temperature rise in high-power laser diode arrays and the temperature difference between the different layers of the package.

Jagannadham et al. [104,105] fabricated multilayered CVD diamond/ $\text{AlN}$ /CVD diamond heat spreaders for high-power electronic packages through successive steps of microwave plasma-assisted CVD and laser physical vapor deposition (PVD). The total thickness of the heat spreader was less than 20  $\mu\text{m}$ . They used a gold/tin eutectic solder to bond the as-fabricated multilayered heat spreading substrates to Si and GaAs active chips after having metalized the CVD diamond surface with various metals. The multilayered diamond/ $\text{AlN}$ /diamond heat spreaders were proven mechanically resistant to thermal cycling, thus possibly enhancing module lifetime and reliability.

More recently, Su et al. [106] reported the fabrication of bi-layered diamond/alumina substrates by using a hot-filament assisted CVD process onto  $\text{Al}_2\text{O}_3$  substrates. They used a carbon ions implementation procedure to effectively reduce the residual stress between the alumina substrate and the diamond deposit. With a 100  $\mu\text{m}$  thick diamond over layer, the diamond/alumina substrates showed superior dielectric properties and a thermal conductivity of about  $400 \text{ W}\cdot\text{m}^{-1}\cdot\text{K}^{-1}$ , thus combining both electrical insulation and thermal conduction potentials. This approach with first suggested by Mo et al. [107]. In a similar fashion, Aleksov et al. [108] proposed the silicon-on-diamond (SOD) technology as an promising alternative to the conventional silicon-on-insulator ( $\text{Al}_2\text{O}_3$ , AlN) approach using textured CVD diamond films with [75-100]  $\mu\text{m}$  thickness.

As it will be explored in chapter 3, polycrystalline CVD diamond films exhibit a typical columnar microstructure, made of few but relatively larger grains in the upper layers of the deposit while lower levels are made of numerous but relatively smaller diamond crystal. It was previously stated in section 2.3.3 that point imperfections such as vacancies, impurities, interstitials and isotopes; line imperfections such as dislocations; and surface imperfections such as grain or twin boundaries are as many phonon scatterers in the diamond film structure that decrease the phonon mean free path, thus affecting the heat conduction process through diamond [40,109]. Thus, polycrystalline CVD diamond films typically exhibit high thermal conductivity in the growth direction relative to the direction parallel to the substrate. Therefore, it is highly desirable for using diamond as an electronic substrate material that the diamond growth shows preferential orientation, i.e. that a particular crystallographic orientation (especially the (100) direction as far as diamond films are concerned) is preferred during the growth process. This allows ordering the microstructure of the CVD diamond film in a way that orient grain boundaries parallel to the growth direction, thus allowing high phonon mean free path in the direction vertical to the film/substrate interface.

Fox et al. [110] grew both highly oriented (100)-textured and randomly oriented diamond films on silicon substrates through MWCVD using in-situ biasing. They demonstrated that the highly-oriented diamond films exhibited heat carriers mobility about three times that of the randomly oriented diamond films. In a similar manner, Stoner et al. [111,112] developed an in-situ carburization and bias-enhanced nucleation technique in which diamond was deposited on silicon and 100% of the diamond grains were oriented relative to the (100) Si substrate. Similar work involving nucleation enhancement through the application of a negative bias voltage to achieve oriented diamond growth was reported by Jiang et al. [113,114] through MWCVD and by Chen et al. through HFCVD [115]. This type of highly-oriented diamond films has been demonstrated to exhibit superior heat conduction performances. Wolter et al. [48] showed that (100)-oriented diamond films epitaxially grown through this type of process led to thermal conductivity up to 1100

$\text{W.m}^{-1}.\text{K}^{-1}$ , while the similar non-epitaxial diamond films exhibited thermal conductivity of about  $550 \text{ W.m}^{-1}.\text{K}^{-1}$ .

Finally Zhang et al. [116] provided an interesting contribution to the use of CVD diamond in electronics by combining a passive CVD diamond substrate coated with micro-pillars with an active water circulating system to cool down high-power electronic devices. The copper micro-pillars were fabricated through a process involving metallization of the CVD diamond substrate, photoresist coating and development, and finally copper electro-deposition onto the metallized back side of the diamond substrate. The micro-pillars allowed the enhancement of convection heat exchange by increasing the exchange surface between the diamond substrate and the circulating coolant fluid. The cooling capacity of this structure was shown to be about  $650 \text{ W.cm}^{-2}$  at a junction temperature of  $120^\circ\text{C}$ , which represent a considerable improvement relative to existing technology. In a different approach, Chen et al. [117] investigated the thermal stresses and heat transfer characteristics of a copper/diamond/copper heat spreading system. They demonstrated that an increasing diamond thickness led to higher thermal conductivity but also to larger thermal stresses. They also showed that the heat spreading efficiency starts decreasing when the diamond film thickness reaches  $100 \mu\text{m}$ , thus no need thicker films when aiming this type of applications.

CVD diamond films and substrates may be applicable at various locations in an electronic high-power package. Besides the role of heat spreader coupled to a base plate/heat sink that CVD diamond may endorse due to its superior thermal conductivity (see also sections 2.1 and 2.2), its high electrical resistivity makes it a material of primary choice to be substituted to the dielectric substrate insulating the chips from the rest of the module. Therefore, a free-standing thick CVD diamond substrate can also be attached to semiconductor active chips through soldering, thus ensuring both heat spreading and electrical insulation functions in a more efficient manner relative to  $\text{Al}_2\text{O}_3$  or  $\text{AlN}$  substrates usually employed. This would allow more efficient heat flow through the package structure. However, thermal stresses in the CVD diamond substrate environment must be limited. In the past years, CVD diamond films have been proven efficient as passive heat dissipative materials for optoelectronics, microelectronics, and high-power electronics.

### **2.5.3 HPHT diamond reinforced composite materials in electronics**

After having focused on the use of CVD diamond materials, we will now have a closer look at the other major way to use diamond for the thermal management of electronic packages, which consists in embedding diamond powders into a metallic matrix to create a composite material. Depending on the process conditions and on parameters such as the size or the quality of the diamond reinforcements, diamond-reinforced composite materials offer the possibility to achieve materials with tailorable properties, thus being adaptable to various packaging environments. In this

section, we will mostly focus on diamond-particles reinforced copper matrix (Cu/D) composites since this type of material is a major research topic in this study.

There exists two major ways of fabricating Cu/D composite materials [5]:

- *Liquid-state methods:*

They rely on the melting of the copper matrix to achieve diamond-reinforced copper matrix composites. Liquid-state routes mainly consist in capillary infiltration or pressure-assisted liquid infiltration techniques, such as gas pressure assisted infiltration or squeeze casting. They consist in the infiltration, under pressure or not (if no pressure, one can speak of *capillary infiltration*), of a close-packed preform of diamond powders by molten copper. The processing temperature is usually located in the [1100-1200] °C range, while pressure may vary from below 100 MPa for capillary infiltration, to above 1 GPa for ultrahigh-pressure infiltration.

Due to the use of a molten matrix material, infiltration processes allow fabricating Cu/D materials with diamond volume fraction as high as 90%. Thus, the thermal conductivity of the material created can reach [700-1200] W.m<sup>-1</sup>.K<sup>-1</sup> with thermal expansion coefficient located in the [3-12]×10<sup>-6</sup> °C<sup>-1</sup> range. Also, liquid-phased copper shows high chemical reactivity which can enhance interfacial bonding with diamonds if a foreign material is introduced at the interface. Besides these advantages, infiltration methods rely on heavy machinery and extreme processing conditions, thus showing extensive capital costs and energy consumption levels. The cost of liquid-state methods is mitigated by their net-shape capability.

- *Solid-state methods:*

They rely on the sintering of solid copper and diamond powders mixed together to achieve Cu/D composites. These powder metallurgy routes (see section 4.7) include hot pressing, spark plasma sintering (SPS), pulse plasma sintering (PPS), and shock wave consolidation. Plasma sintering shows the advantage to directly heating the powders to be sintered through the application of a DC pulsed current that directly passes through the powders, while hot pressing methods rely on indirect heating (typically induction heating of a graphite mould) of the powders, thus showing lower sintering efficiency. The pressure applied in solid-state methods may vary from below 100 MPa for hot pressing to above 1 GPa for hot isostatic pressing (HIP) or shock wave consolidation.

They provide efficient solid-state methods to create Cu/D composites without resorting to the melting of the copper matrix, which allows lower processing temperatures ([500-700] °C), thus inflicting less damage to the diamond reinforcements and showing lower energy consumption. Sintering also allows the production of near net shaped products, thus no need for additional work on the fabricated pieces and economic efficiency. This softer way of processing allows fabricating



Cu/D materials with thermal conductivity located in the  $[400-900]$   $\text{W.m}^{-1}.\text{K}^{-1}$  range and thermal expansion coefficient in the  $[5-12] \times 10^{-6} \text{ } ^\circ\text{C}^{-1}$  range.

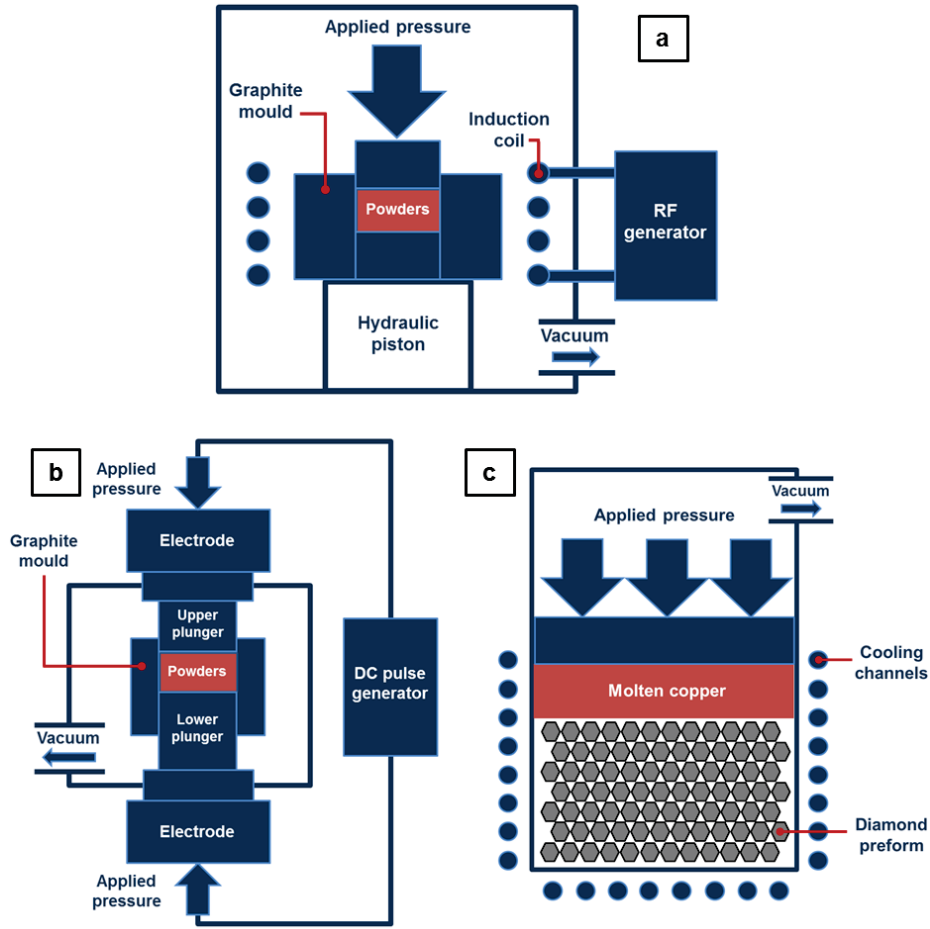


**Figure 2.26: Schematic view of (a) hot-pressing, (b) Spark Plasma Sintering (SPS), and (c) pressure-assisted liquid infiltration processes for Cu/D composites fabrication.**

As explained in section 2.5.1, metal/diamond interfaces are generally incoherent from a crystallographic perspective and exhibit high surface energy, which is problematic when considering the fabrication of diamond particle reinforced metal matrix composite materials for thermal management application, for which an intimate bonding at the matrix/reinforcement interface is critical to the load transfer between the two materials. The copper/diamond and silver/diamond systems are especially not chemically reactive, while the aluminum/diamond system is highly reactive and lead to the creation of carbides at the interface (see section 2.4.1).

Therefore, a major concern when fabricating Cu/D composites, either through high-pressure or low-pressure routes, is to find a way for the diamond reinforcements to chemically adhere to the matrix, thus allowing strong interfacial bonding and efficient transfer of properties between the two materials. The use of carbide forming additives to create chemical bonding at the Cu/D interface has been long recognized as an efficient way to interfacial bonding between the two materials, and

many among the diamond-composites research community used this technique to fabricate thermally performing Cu/D materials. The carbide forming additives can either be alloyed to the copper matrix or be directly coated onto the diamond powders through deposition techniques. However, all carbide-forming materials oxidize rapidly in air, and bonding to oxide surfaces is difficult. Therefore, a strong vacuumed environment is required when employing these additives.

Some work proposed to fabricate Cu/D composites without any carbide-forming additives. Burnham and Sussmann [118] from Amoco Corporation in the U.S. had realized the potential impact of using diamond reinforced MMCs for the cooling of high-power laser diode arrays. They patented the fabrication of a diamond-reinforced composite heat sink through hot pressing using various metal matrices (copper, silver, aluminum). However, no carbide forming additives were used for chemical bonding at the Cu/D interface in their invention. Similarly, Sun et al. [119] followed a shock wave consolidation route to fabricate Cu/D composites with diamond volume fractions ranging from 10% to 70% and no carbide-forming materials to optimize interfacial bonding. The obtained CTEs ranged from  $10 \times 10^{-6} \text{ }^{\circ}\text{C}^{-1}$  to  $13 \times 10^{-6} \text{ }^{\circ}\text{C}^{-1}$  but bonding at the Cu/D interface was shown to be weak.

One of the first commercial applications of Cu/D composites has been reported by Sun Microsystems and Lawrence Livermore National Laboratory, who have jointly developed a copper/diamond composite material called Dimalloy [120, 121] through pressurized infiltration. Dimalloy composite combines in a very interesting way a thermal conductivity of  $420 \text{ W.m}^{-1}.\text{K}^{-1}$  and an adjustable CTE of  $5.5 \times 10^{-6} \text{ }^{\circ}\text{C}^{-1}$ , which is compatible with the CTEs of semiconductor materials such as silicon and gallium arsenide. It involves commercially available type I diamond powders coated through physical vapor deposition with a carbide forming layer of tungsten-rhenium (W-Rh) alloy of about 10 nm. Dimalloy is the first commercial Cu/D composite involving carbide forming additives for interfacial bonding. Since then, many different processing techniques have developed and the thermal performances of Cu/D composites have kept being improved.

Yoshida et al. [39] also on focused high-pressure liquid infiltration and demonstrated the importance of parameters such as the size and volume fraction of the diamond reinforcements employed for Cu/D composites processing. They showed that larger diamond reinforcements are beneficial to the thermal conductivity of the composite by decreasing the total surface area of interfaces in the material. Hanada et al. [122] endeavored the same type of efforts focusing on powder metallurgy processing of Cu/D composites.

Still through infiltration, Abyzov et al. [123] reported the fabrication of Cu/D composites with a diamond reinforcement volume fraction of 63% exhibiting thermal conductivity ranging from 500 to  $900 \text{ W.m}^{-1}.\text{K}^{-1}$  and thermal expansion coefficient of about  $6 \times 10^{-6} \text{ }^{\circ}\text{C}^{-1}$  at  $25^{\circ}\text{C}$  through capillary infiltration of molten copper into a diamond powders bed at  $1150^{\circ}\text{C}$ . They used high-quality

diamond powders and coated them with a tungsten (W) layer with thickness between 100 and 500 nm through a diffusion method at 900-1100°C. These properties are extremely interesting for electronic substrate applications. In a similar liquid-phase approach, Wu et al. [124] fabricated diamond reinforced copper-aluminum matrix (Cu-Al/D) composites through squeeze casting, achieving materials with thermal conductivity of 330 W.m<sup>-1</sup>.K<sup>-1</sup> and tailorable CTE ranging from 6 to 13×10<sup>-6</sup> °C<sup>-1</sup>.

Webert et al. [125] investigated the influence of chromium (Cr) and boron (B) additives alloyed to the copper matrix on the properties of Cu/D composites prepared through gas pressure-assisted liquid infiltration. They observed a transition from weak to strong matrix/diamond bonding with increasing carbide-forming content alloyed to the matrix and the existence of an optimal carbide forming content. The resulting composites exhibited a very promising combination of thermal conductivity (600 W.m<sup>-1</sup>.K<sup>-1</sup>) and CTE (10×10<sup>-6</sup> °C<sup>-1</sup>).

On the powder metallurgy front, Schubert et al. [126-128] provided highly valuable input to the research on carbide forming additives by studying the influence of various carbide formers (Cr, B, Al, Ti, and Zr) on the final thermal performances of Cu/D composites prepared by rapid hot pressing. They used sputtering to pre-coat diamond powders and rated the performances of the final composites and reached thermal conductivity up to 640 W.m<sup>-1</sup>.K<sup>-1</sup> combined with a CTE of 11×10<sup>-6</sup> °C<sup>-1</sup> with a diamond volume fraction of 40%. They demonstrated the critical importance of the intrinsic thermal conductivity (and thus thermal resistance) of the interphase formed at the Cu/D interface on the final thermal conductivity of the composite. They also showed the superior potential of Cr and B relative to other carbide forming additives as chemical bonding agents at the Cu/D interface to enhance thermal conductivity and CTE of the composites. Xia et al. [129] carried out similar type of study on SPS fabricated Cu/D materials using diamond powders coated with a copper alloy containing small amounts of various carbide formers through magnetic sputtering.

Chu et al. [130] also used the SPS technique to sinter Cu/D composites using 100 µm diameter diamond powders coated with a 1 µm thick chromium (Cr) layer through vacuum evaporation. The diamond volume fraction ranged from 40% to 65%. They demonstrated the importance of the chromium coating on increasing the relative density of the Cu/D composites. SEM observations also showed the good integrity of the bond at the Cu/Cr/D interface while uncoated Cu/D composites exhibited voids and cavities in the interface region. They reached only limited thermal conductivities ([200-300] W.m<sup>-1</sup>.K<sup>-1</sup>) and ascribed this phenomenon to the poor thermal conductivity of Cr carbides formed at the interface and to the large thickness of the carbide interlayer formed. Rosinski et al. [131] also investigated the use of Cr additives at the Cu/D interface in powder metallurgy through the PPS process.

More recently, Chu et al., again, investigated the use of zirconium (Zr) for bonding at the Cu/D interface [132] and demonstrated that a careful optimization of the amount of carbide formed at the interface is critical to the final thermal conductivity of the composite. They interestingly achieved  $615 \text{ W.m}^{-1}.\text{K}^{-1}$  with a 55% volume fraction of 500 nm Zr-coated diamond reinforcements through hot pressing.

In a similar manner, Zhang et al. [133] used diamond powders coated with a 300 nm titanium (Ti) layer to enhance the heat transfer process in Cu/D composites. They achieved thermal conductivities of  $500 \text{ W.m}^{-1}.\text{K}^{-1}$  with diamond volume fractions ranging from 45% to 60% through SPS. Dong et al. [134] also chose Ti to improve Cu/D bonding through capillary infiltration. Despite a diamond volume fraction of 70%, they only reached a thermal conductivity of  $385 \text{ W.m}^{-1}.\text{K}^{-1}$  due to the extensive thickness of the Ti-carbide layer at the interface ( $2.5 \mu\text{m}$ ).

Finally, Mizuuchi et al. [135] reported the fabrication of Cu/D composites with excellent thermal performances through SPS using electroplated Cu-coated diamond powders. They reached a thermal conductivity of  $650 \text{ W.m}^{-1}.\text{K}^{-1}$  and a CTE of  $10 \times 10^{-6} \text{ }^{\circ}\text{C}^{-1}$  at a diamond volume fraction of 45% without any carbide bonding solution at the interface. Despite the fact that the Cu-coating of diamond powders does not circumvent at all the intrinsic non-wettability of diamond by copper, the authors explained this achievement by the fact that no molten copper was employed in their work, thus preserving the intrinsic quality of the diamond powders used relative to a liquid-phase route.

Despite the widely spread use of carbide-forming additives in the processing of Cu/D composites and the clear demonstration that it improves both thermal conductivity and CTE of Cu/D composites, the understanding of how the carbide interphase act to couple electronic conduction in the copper matrix and phonic conduction in diamonds is not clear yet. Also, the resistance of carbide-bonded Cu/D composites to thermal cycling is rarely investigated in the mentioned studies, although this aspect is critical to any application in real-operating environment. Due to their intrinsic brittleness, carbide interphases may indeed show poor tenue to thermal fatigue. Finally, one can notice that no other solution than carbide forming additives has been brought to light yet to chemically bond copper matrix and diamond reinforcements. Therefore, it might be interesting to explore other possible ways, which might offer different advantages.

While a variety of techniques is available to process Cu/D composite materials, none of those presented in this chapter allows the fabrication of thermally efficient Cu/D films at a large scale and limited costs. In chapter 4, we will combine the principles of tape casting, a technique mostly employed for the fabrication of ceramic thin sheets, with the principles of hot pressing to process in an innovative way Cu/D composite films with accurate thickness control and smooth surface finish. We finally aim to use these films as heat spreaders in electronic packages.

## 2.6 Conclusion

Power electronic packages consist of a complex multilayered architecture composed of various materials with different thermal and mechanical properties. The constant increase in operating speed (higher frequency), integration level (higher power), and packing density of ICs drive a strong market demand for efficient thermal management materials at acceptable costs. Diamond can help through the rare combination of high thermal conductivity, high electrical resistivity and low thermal expansion it features.

The objective when fabricating heat spreading films is to fabricate a material that can sustain high heat flux levels while safely integrating into the electronic package architecture. Thus, a high in-plane thermal conductivity and a CTE that match those of the surrounding materials are of primary concern to limit the temperature rise of active components and mitigate thermo-mechanical stresses that develop in the module upon thermal cycling. Also, the heat spreader should have limited weight impact and moderate fabrication costs.

Two major ways to use diamond as a heat spreading film material is either to grow diamond films through CVD synthesis or to use HPHT diamonds as reinforcements in a package substrate material such as copper to form a composite material. These two routes were reviewed in terms of principles and background. While electronic heat conduction dominates in metals such as copper or semi-metals such as silicon, phonon transport phenomena rule heat conduction in diamond. As electron-based as phonon-based heat conduction processes suffer from imperfections in the material microstructure such as grain boundaries, voids and cavities, and impurities, which act as many heat-carriers scatterers, thus affecting the thermal conductivity of the material.

The critical role played by interfaces in the heat conduction process through bi-materials assemblies was emphasized. Besides the intrinsic properties of the two materials involved, the thermal performances of bi-materials assemblies (such as CVD diamond films deposited onto a substrate or HPHT diamond-reinforced copper-matrix (Cu/D) composites) critically depend on the thermal resistance of the bi-material interface (or Kapitza resistance). Therefore, it is required to engineer chemical bonding solutions in order to couple electronic and phonic heat conductions, thus improving interfacial heat transfer. This is achieved, for instance, through the use of carbide forming additives in the processing of Cu/D composite materials.

Finally, the main routes for CVD and HPHT synthesis of diamond and the physical-chemical principles they rely on were presented. Also, brief literature reviews about the fabrication and implementation of diamond-based materials as technological solutions to cool high-power electronic packages were carried out.

## **CHAPTER 3: COMBUSTION CVD DIAMOND FILMS**

---

### **3.1 Introduction**

### **3.2 Laser-assisted combustion synthesis of diamond films**

### **3.3 Diamond films phase purity and residual stress analyses through Raman spectroscopy**

### **3.4 Thermal characterization through modulated photothermal radiometry**

### **3.5 Influence of the growth process and microstructure on the thermal properties of diamond films**

### **3.6 Deposition of combustion CVD diamond films on copper/carbon composite substrates**

### **3.7 Conclusion**

---

### 3.1 Introduction

The objective of CVD diamond synthesis is to achieve deposition of uniform diamond films and growth of self-standing diamond substrates with high quality and sufficient growth rate without compromising the economic efficiency of the process. Consequently, all CVD routes lead to neglect one of three aspects in order to promote the two others. Hot-filament CVD enables the growth of high-quality diamond at affordable costs but shows limited growth rates. In addition, it may lead to contamination from the filament material. Similarly, microwave-plasma assisted diamond deposition allows growing high-quality material but is in the meantime expensive and hardly scalable [71].

Combustion CVD is a particular diamond synthesis route relative to the methods mentioned above since it is the only technique that enables growing diamond in an open-air environment, i.e. at atmospheric pressure. Indeed, HFCVD as TPCVD and MWCVD rely on the existence of a confined low-pressure environment to achieve diamond growth. Besides, it provides interesting features such as high growth rate, scalability, low capital costs, and high flexibility. However, the quality of combustion CVD diamond films is usually lower than those achieved through conventional CVD routes due to contamination from the open-air environment [4, 136].

All CVD processes, including combustion flame deposition, rely on near-equilibrium effects to induce reactions in the gas phase leading to diamond growth. Therefore, it is not possible to exercise selectivity among the various chemical processes competing for diamond growth. In such context, lasers have been long recognized as a unique means of activating molecules in the growth medium through fast heating and selective optical pumping of the reactive chemical species. Thus, lasers offer potential for reduced growth temperature and limited deposition of nondiamond carbon content by selectively driving only the specific chemical channels that lead to diamond formation.

The laser-assisted combustion CVD route explored in this chapter originates from an initiative of the U.S. Office of Naval Research, who was seeking to develop a way to coat parts of military equipment (aircrafts, boats, submarines) with diamond in order to enhance their wear resistance. Thus, the diamond synthesis route developed in this study was not aimed, at first, to grow electronic-quality diamond materials. Nevertheless, we will see that the multienergy deposition process developed at the University of Nebraska-Lincoln showed promising capabilities in depositing heat spreading CVD diamond onto various substrates. This work was carried out under direction of Professor Yongfeng Lu from the Electrical Engineering department and Professor Namas Chandra from the Materials and Mechanical Engineering Department. Professor Jean-Luc Battaglia at the Institute of Mechanics and Engineering of the University of Bordeaux provided help, technical support, and expertise, to thermally characterize the diamond films.



## 3.2 Laser-assisted combustion synthesis of diamond films

### 3.2.1 Combustion flame deposition:

Combustion synthesis was first discovered in 1988 by Hirose and Kondo [86, 137, 138], who realized that acetylene flames produce copious amounts of atomic hydrogen and hydrocarbon radicals required for diamond growth. Combustion CVD (CCVD) synthesis of diamond shows numerous advantages relative to conventional plasma-assisted methods such as MWCVD or TCVD, among them scalable nature, minimal utility requirements, high growth rates, and significantly reduced capital costs, which make combustion synthesis one of the most flexible CVD alternatives for diamond growth. The main drawback of combustion synthesis is that it produces diamond films with moderate quality due to the diffusion of oxygen, impurities, and non-diamond carbon content upon atmospheric operation. Also, combustion diamond films exhibit radial inhomogeneity in terms of both diamond crystal size and film thickness. However, the latter issue can be addressed through the use of flat burners or multiple-torch configurations which allow large-area diamond coatings with uniform morphology.

Most of the studies on combustion synthesis have been carried out on oxygen-acetylene (or *oxyacetylene*) flames [4, 139, 140]. Figure 3.1 shows the typical structure of an atmospheric oxyacetylene torch in the configuration used for diamond deposition:

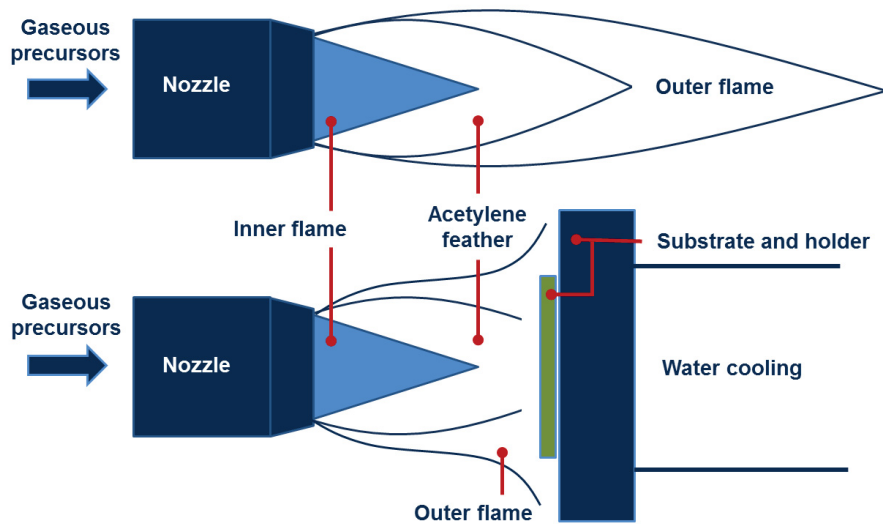


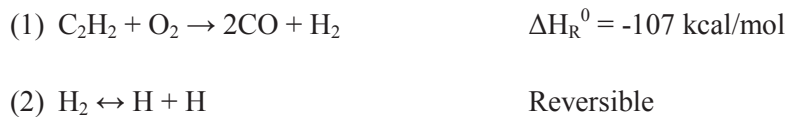
Figure 3.1: Schematic view of the structure of an oxyacetylene combustion torch [4].

The flame is composed of three distinct regions: (1) the inner flame, (2) the acetylene feather, and (3) an outer diffusion flame. The substrate is located in the feather region for diamond growth to occur. A critical parameter in combustion synthesis of diamond is the oxygen-to-hydrocarbons ratio ( $R$  defined as  $O_2:C_xH_y$ ), which strongly affects the flame shape, the diamond growth rate, and

the achieved quality of potential diamond. While a neutral flame is obtained at  $R = 1$ , in which the acetylene feather disappears because all the acetylene is consumed in the primary flame, the highest diamond quality has been shown to be achieved in hydrocarbons-rich flame, with  $R$  typically located in the  $[0.5 - 1]$  range. The optimal  $R$  ratio depends of course of the design of the nozzle and on the mass flow controllers employed.

Although acetylene is usually preferred for combustion synthesis of diamond due to the high flame temperature and velocity it allows, its high cost makes attractive the use of alternative fuels for diamond growth. Diamond has been effectively synthesized through the combustion of ethylene ( $C_2H_4$ ) [141] and propylene ( $C_3H_6$ ) [142]. In this study, a combustion torch made from a mixture of oxygen, acetylene, and ethylene, was used. The flame shape and chemistry are similar in both cases of  $O_2/C_2H_2$  and  $O_2/C_2H_2/C_2H_4$  torches. As further detailed in section 3.2.2, ethylene was added to the flame composition in order to achieve a multienergy deposition process through the combination of the flame energy with a laser excitation source.

Although the composition of acetylene flames is much different from the  $CH_4/H_2$  mixtures used in hot-filament or plasma-assisted CVD routes, the chemistry and the mechanism of diamond growth in combustion CVD is similar to that of other diamond deposition processes. The essence of the chemistry of acetylene flames may be distilled to the following two reactions [4]:



At first, the oxygen and acetylene are rapidly consumed, producing carbon monoxide and hydrogen, as indicated by reaction (1). The highly exothermic nature of the reaction leads to flame temperatures higher than 3000 K. At such temperatures, a significant fraction of hydrogen molecules are dissociated into atomic hydrogen, as expressed by reaction (2). Carbon monoxide is thermally stable and not expected to affect the growth process under these conditions. Also, a small reaction of the acetylene is converted into hydrocarbon radicals species such as methyl radicals ( $CH_3$ ), leading to the incorporation of carbon atoms to the growth surface when combining with the effect of a high concentration of atomic hydrogen, as depicted on Fig. 3.2 and detailed in section 2.4.2 describing the principles underlying diamond CVD synthesis.

Other reactive species such as CH and  $C_2$  are believed to be helpful to the diamond growth process, while OH radicals are assumed to play a role as critical as atomic hydrogen by etching the surface-bond hydrogen and stabilizing the  $sp^3$  hybridized surface carbon bonds. Where filament and plasma systems employ thermal or electrical energy to create atomic hydrogen, combustion systems rely on the chemical energy stored in the acetylene molecules to generate heat and atomic radicals.

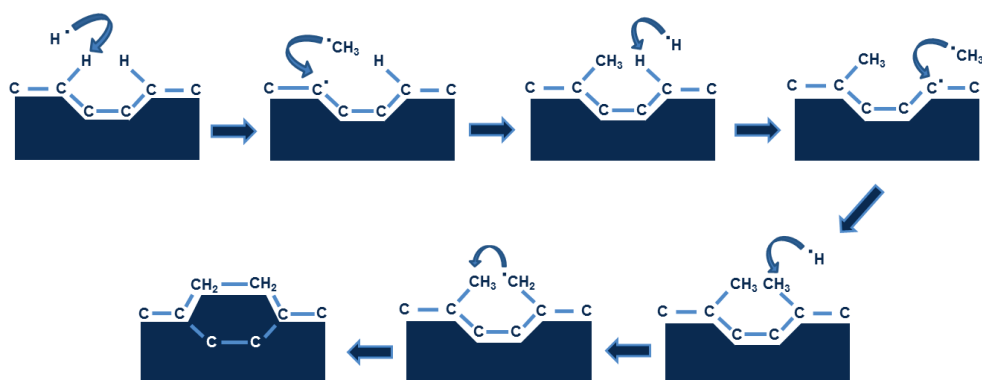


**Figure 3.2: Schematic view of the diamond growth process through the addition of methyl radicals and etching of  $sp^2$  hybridized carbon atoms by atomic hydrogen [71].**

Substrate temperature is the second most critical parameter to diamond growth through combustion synthesis. It typically ranges between 900 K and 1600 K, depending on the design of the combustion apparatus employed. Because of these high substrate temperatures, the substrate material must be carefully chosen to not be degraded upon exposure to the combustion flame. Diamond growth through combustion synthesis has been successfully reported on silicon (Si) [110-115, 143], molybdenum (Mo) [140], tungsten carbide (WC) [144, 145], tungsten copper (WCu) [146], and alumina [106], but also on materials with lower melting points such as copper [147, 148]. Evaluating the substrate temperature is difficult in all CVD environments, but especially in combustion synthesis due to the extreme heat fluxes present. Two techniques commonly used are optical pyrometry and thermocouples placed on the back side of the substrate. On one hand, pyrometry provides a good measure of the relative temperature of the substrate, but absolute values may be off by as much as 100 K due to uncertainties in emissivities. On the other hand, back-side thermocouples are affected by both quality of the contact and the steep thermal gradients present.

Substrate temperature has a dramatic effect on two major properties: diamond growth rate and morphology. As the substrate temperature increases, the growth rate reaches a maximum. Increasing the substrate temperature beyond this point leads to a rapid decline in both diamond growth rate and quality, which is believed to be due to a potential oxidation or graphitization of the diamond surface. Also, while the morphology of most diamond films grown through combustion synthesis is dominated by (111) (triangular-shaped) and (100) (square-shaped) facets due to lower growth rate relative to (110) facets, it is known that an increase in the substrate temperature increases growth rates by enhancing chemical reactions on the diamond surface [4]. This temperature effect especially promotes (111) facets growth rate, thus leading to preferentially (100)-oriented diamond films at high substrate temperatures. Thus, as substrate temperature increases, the diamond crystals morphology changes from octahedron to cubic. The temperature where (100) faceting occurs is usually near the temperature where maximum growth rate is observed.

### 3.2.2 Laser-resonant excitation of precursor molecules:

- **Multienergy deposition process:**

Particles, molecules, and molecular ions existing in the combustion flame environment store energy in various forms: molecular translations, rotations, vibrations, and electronic excitations (Fig. 3.3). Chemical reactions in CVD diamond growth proceed through bond breaking and rearrangements, which directly result from vibrational excitations of molecules or molecular ions [149]. Therefore, it is believed that vibrational excitations of gaseous precursors in the combustion flame environment are critical for chemical reactions in CVD processes [150]. Most of CVD routes only rely on translational energy provided by heating as a way to achieve the CVD process. Indeed, translational energy may be converted to vibrational energy through collisions. However, the number of collisions required for such energy conversion to occur is tremendous, in contrast with conversion of translational energy to rotational energy which only takes tens of collisions. Thus, sole heating appears as a limited way to succeed in CVD growth.

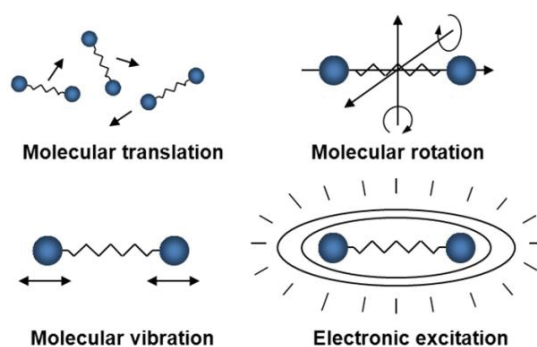


**Figure 3.3: Schematic of the different energy storage for a diatomic molecule [4].**

In this study, *multienergy deposition* refers to the use of multiple energy forms to achieve chemical reactions in the flame environment, including translational and vibrational energy. While the combustion process provides the species in the flame environment with translational energy (heating), a laser source is shined through the torch to provide them with vibrational energy. Most of frequencies of molecular vibrations are in the infrared (IR) range. Therefore, IR lasers are ideal energy sources to achieve resonant excitation of molecular vibrations [151]. However, the vibrational modes of acetylene ( $C_2H_2$ ) molecules show very low IR activity, unlike ethylene ( $C_2H_4$ ), which shows several active vibrational modes in the infrared range. The  $CH_2$ -wagging mode, which is one of the twelve active modes of  $C_2H_4$  molecules, fall in the range of the wavelength tunable  $CO_2$  laser used in this study ( $[9.2 - 10.9] \mu m$ ). Therefore, in this study,  $C_2H_4$  molecules were added to a  $C_2H_2/O_2$  mixture and a  $CO_2$  laser which wavelength matches the frequency of this vibrational mode was shined through the flame in order to resonantly excite the ethylene molecules, thus achieving a multienergy diamond deposition process through combustion synthesis.

▪ *Absorption of the laser energy by ethylene molecules in the flame environment:*

CO<sub>2</sub> laser is a typical energy source used in laser chemistry due to its high energy efficiency and high output power. However, common CO<sub>2</sub> lasers only produce a fixed wavelength of 10.591  $\mu\text{m}$ , which cannot match the wavelength required for effective resonant vibrational excitation. Thus, a wavelength tunable CO<sub>2</sub> laser with a [9.2 – 10.9]  $\mu\text{m}$  range was used in this study to promote chemical reactions and creation of active species into the flame environment by inducing resonant excitation of ethylene precursor molecules. Figure 3.4 shows the optical absorption spectrum of the CO<sub>2</sub> laser energy by the C<sub>2</sub>H<sub>4</sub>/C<sub>2</sub>H<sub>2</sub>/O<sub>2</sub> combustion flame with respect to laser wavelength. The spectrum was obtained from optical emission spectroscopy (OES) analysis:

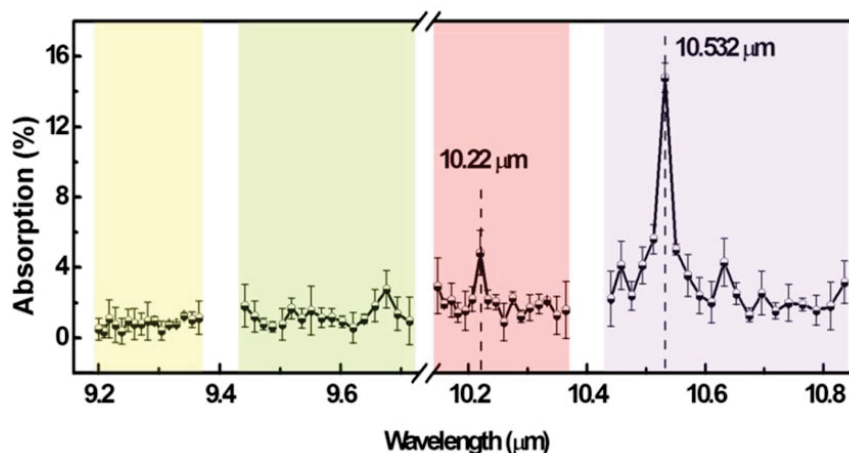


Figure 3.4: Optical absorption spectrum of the CO<sub>2</sub> laser excitation by the combustion flame.

Two absorption peaks were clearly detected from OES analysis of the laser absorption by the flame: (1) an absorption peak located at a wavelength of 10.22  $\mu\text{m}$ ; (2) an absorption peak located at 10.532  $\mu\text{m}$ . The strongest absorption peak at 10.532  $\mu\text{m}$  was ascribed to the Q branch ( $\Delta J = 0$ ) of a fundamental vibration mode of the ethylene molecules: the CH<sub>2</sub>-wagging mode, located at 10.534  $\mu\text{m}$  or 949.3  $\text{cm}^{-1}$ .

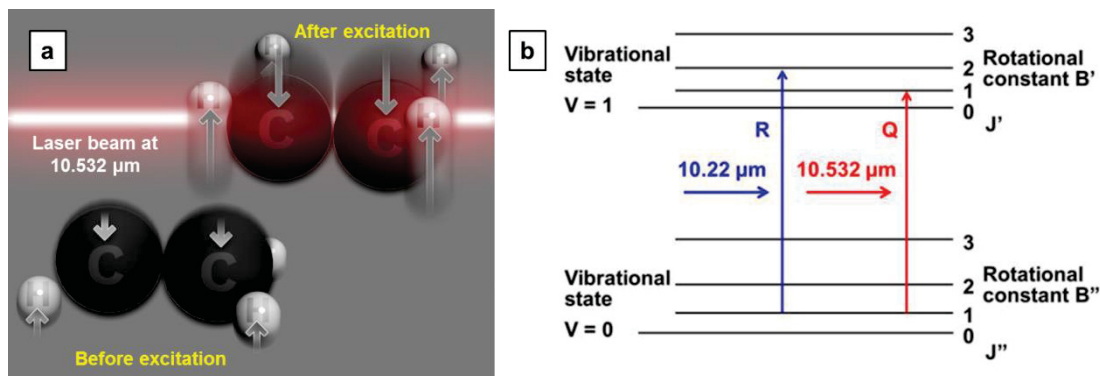
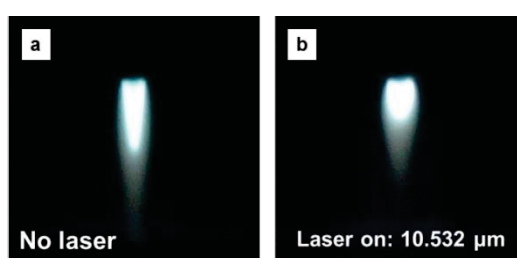


Figure 3.5: (a) Scheme of how the laser excitation affects the wagging mode of an ethylene molecule. (b) Vibration-rotation transitions of an ethylene molecule with CO<sub>2</sub> laser excitation at different wavelengths.

The other absorption peak located at 10.22  $\mu\text{m}$  was identified as the R branch ( $\Delta J = 1$ ) of the same  $\text{CH}_2$ -wagging mode, which means that the ethylene molecules were excited to a higher level of vibrational state and with a higher level of rotation energy (Fig. 3.5b). While at ground state, the  $\text{C}_2\text{H}_4$  molecule vibrates like a butterfly, its wagging vibration mode is resonantly excited by absorbing laser energy at 10.532  $\mu\text{m}$  (Fig. 3.5a). Thus, two laser wavelengths leading to maximum optical absorption by the flame have been employed to achieve a multienergy deposition process by combining the thermal energy of the combustion flame to the electromagnetic energy of the laser source. By tuning the laser wavelength to match that of the branches of the wagging vibrational mode of ethylene precursor molecules, the multienergy deposition process can help us by promoting diamond film morphology, increasing growth rate, and enhancing diamond quality [152-156].



**Figure 3.6: Photographs of the combustion flame (a) without and (b) with 10.532  $\mu\text{m}$  laser excitation.**

The absorption of the laser energy by the flame could also be visually noticed through a change in the flame shape when the laser was on. The irradiation of the laser beam into the flame induced an increase in the flame velocity and shrinkage of the flame size, as shown on Fig. 3.6, which reveals enhanced chemical reactions into the flame environment and increased flame temperatures.

### 3.2.3 Diamond deposition experiment al set-up:

The diamond deposition set-up is shown in Fig. 3.7. It consists of a wavelength tunable  $\text{CO}_2$  laser (XL1000, PRC Laser Corporation) with a [9.2 – 10.9]  $\mu\text{m}$  wavelength range associated to a combustion system. A combustion torch with a diameter of 1.5 mm was used. A gas mixture containing acetylene ( $\text{C}_2\text{H}_2$ , 99.999%), ethylene ( $\text{C}_2\text{H}_4$ , 99.6%) and oxygen ( $\text{O}_2$ , 99.996%) was used as gas precursors with a volume ratio of 1:1:2, respectively (600:600:1200 sccm, thus a  $R$  oxygen-to-hydrocarbons ratio of 0.5). The laser beam was guided through the combustion flame using a ZnSe convex lens with a focal distance of 25.6 cm. The distance between the lens and the nozzle was 30 cm. The distance between the flame inner cone and the top of the substrate was maintained around 0.8 mm.

The laser was operated in a continuous wave mode. Its output power was 800 W and its wavelength was set to 10.22  $\mu\text{m}$  or 10.532  $\mu\text{m}$  in order to match the branches of the vibrational wagging mode of ethylene molecules previously described (Fig. 3.4 and 3.5), thus achieving the



resonant excitation of the ethylene molecules. The substrate temperature was monitored using an infrared pyrometer (OS3752, Omega Engineering, Inc.) and regulated using a water-cooling stage. The stage was attached to an X-Y-Z translation system to position the substrate toward the torch. The substrate temperature was maintained in the [750 – 800] °C range during diamond deposition.

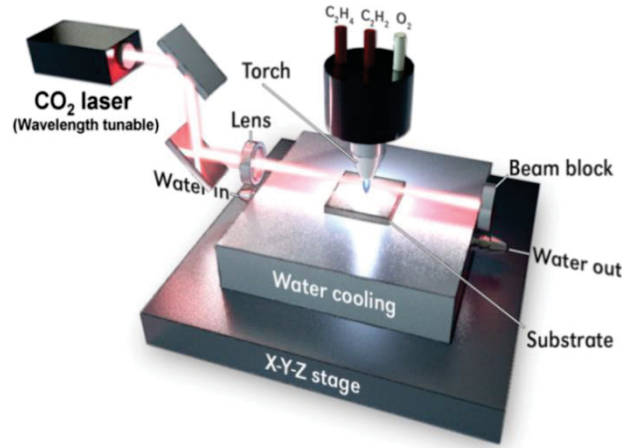


**Figure 3.7: Experimental set-up for laser-assisted combustion synthesis of diamond [156].**

Diamond films were deposited on commercial silicon substrates (Si(100)). Silicon was chosen as substrate material since it allowed us to investigate the thermal properties of the diamond films through infrared photothermal radiometry, and especially the potential thermal resistance existing at the film/substrate interface. Subsequently, the diamond films will be deposited onto materials of higher importance from a heat-spreading prospective, such as copper and copper/carbon substrates. The dimensions of silicon were  $10 \times 10 \times 0.6 \text{ mm}^3$ . The substrates were ultrasonically cleaned for 20 minutes in acetone prior to diamond deposition. Silicon substrates were seeded using ultrafine diamond powder (average diameter of 250 nm) through ultrasonic treatment in a mixture of diamond/ethanol solution, with 0.1 g diamond powder dispersed in 10 mL ethanol, to enhance the nucleation of diamond crystals on the Si(100) surfaces. Fig. 3.8 shows some photographs of the diamond deposition set-up.

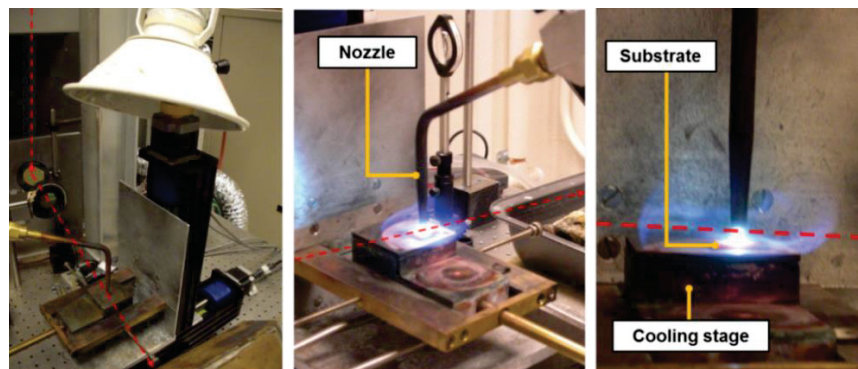


**Figure 3.8: Photographs of the laser-assisted combustion deposition process.**

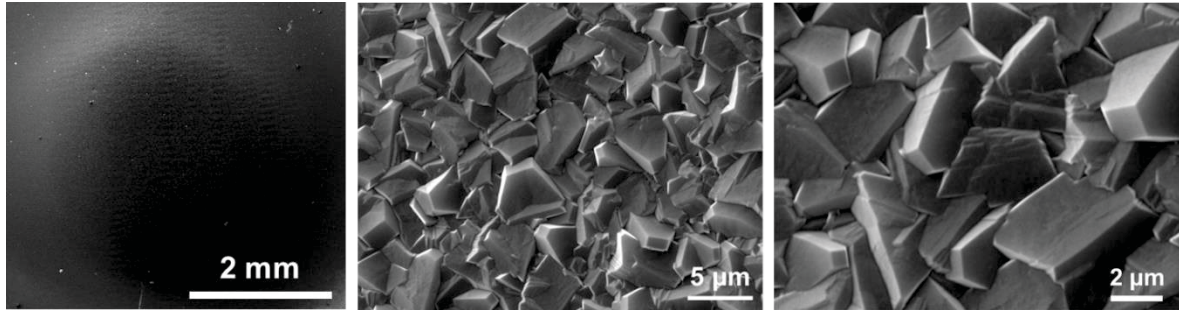
The optical path of the laser beam is figured by the red dashed line.



### 3.2.4 Diamond film microstructure:

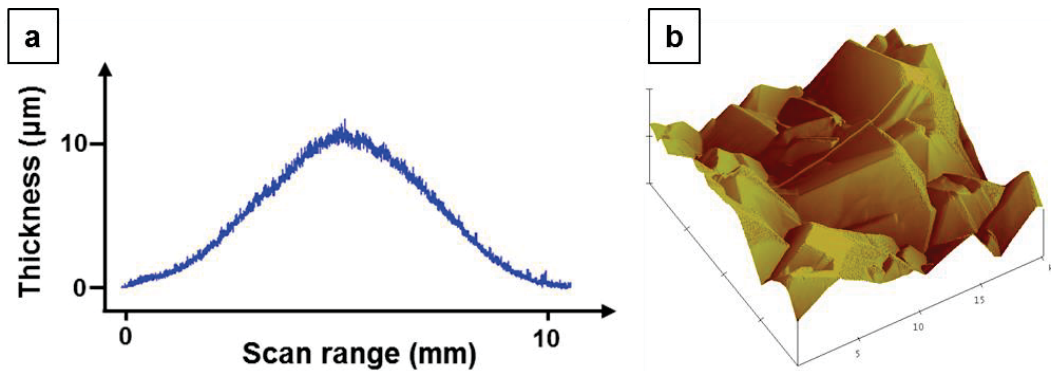
#### ▪ *Top-surface microstructure:*

Diamond films were deposited on the substrates as circular spots of about 1 cm in diameter for one hour deposition. Figure 3.9 show SEM micrographs of a diamond film deposited during 30 minutes onto a Si substrate through laser-assisted combustion synthesis with a laser excitation wavelength tuned at  $10.532\ \mu\text{m}$  to match the frequency of the  $\text{CH}_2$ -wagging vibrational mode of ethylene molecules:



**Figure 3.9: SEM micrographs of a diamond film grown onto a Si substrate through laser-assisted combustion synthesis.**

SEM micrographs of Fig. 3.9 show that the laser-assisted deposition process enabled fast deposition of thick diamond films on silicon substrates. The obtained materials are dense and homogeneous polycrystalline diamond films, consisting of randomly oriented diamond crystals. (111), (110), and (100) facets are visible on top of the diamond film. The recorded growth rate was about  $31\ \mu\text{m/h}$  on silicon substrates, which is higher than that of conventional vacuum-based CVD techniques [113, 115]. This is of significant importance since low growth rate in diamond CVD techniques is one of the critical limiting factors for diamond films applications. Figure 3.10 shows the typical thickness and roughness profiles of the obtained diamond films. These profiles were recorded using a stylus profiler (Ambios Technology) and an atomic force microscope.



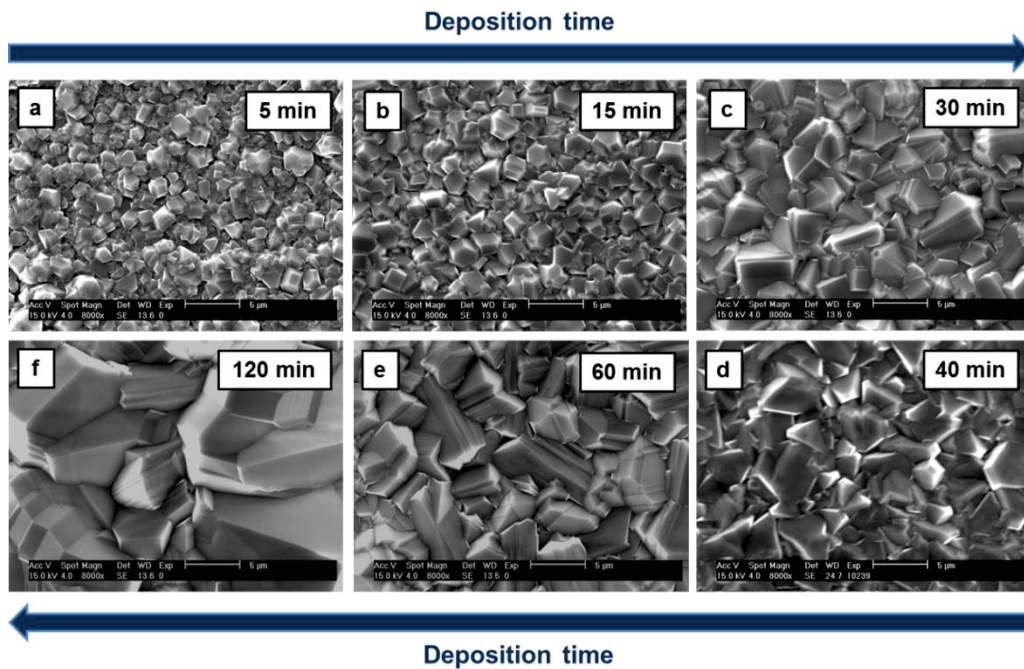
**Figure 3.10: Typical (a) thickness and (b) roughness profiles of the diamond films obtained.**

Figure 3.10a reveals the non-uniform thickness profile of our diamond films, which is a clear drawback when considering a technological application of these films as heat spreading materials in electronic packages. However, this issue can be addressed by using multiple torch configurations or flat burners, or by scanning the whole area of the substrate using a motorized stage. Nevertheless, the substrate area coated with diamond approaches 1 cm<sup>2</sup> with a single torch deposition system. Figure 3.10b reveals the rough profile of the diamond films obtained, which is also a concern in electronic packaging, where flatness and solderability are key factors to any diamond film applications. Table 3.1 shows the details of the quantitative study of the roughness.  $R_q$  and  $R_a$  respectively stand for the root mean square roughness and the mean roughness, both expressed in nanometers.

**Table 3.1: Details of the roughness analysis carried out on the diamond films through AFM.**

Film thickness ( $\mu\text{m}$ )	Surface analyzed ( $\mu\text{m}^2$ )	$R_q$ (nm)	$R_a$ (nm)
10	1000	560	381
60	400	753	628

AFM analysis demonstrates that the diamond films exhibit increasing roughness with film thickness and suggests average roughness close to the micrometer when film thickness approaches 100  $\mu\text{m}$ . Thus, a film polishing method should be used to flatten the films before any use as a heat spreading material [157]. Figure 3.11 shows the growth of diamond films onto Si substrates with different deposition times to enlighten its influence on diamond grain size:



**Figure 3.11: SEM micrographs of diamond films grown onto Si substrates using 10.532  $\mu\text{m}$  laser excitation: (a) 5 minutes, (b) 15 minutes, (c) 30 minutes, (d) 40 minutes, (e) 60 minutes, (f) 120 minutes.**

SEM micrographs of Fig. 3.11 demonstrate that the nucleation and growth process of the diamond films grown follow the Volmer-Weber mode described in chapter 2 (three-dimensional island growth mode): after an induction period, the nucleation of germs onto the surface occurs; these germs grow in three dimensions and finally coalesce to form a continuous film, as shown on Fig. 3.12, showing the early stages of the diamond growth process:

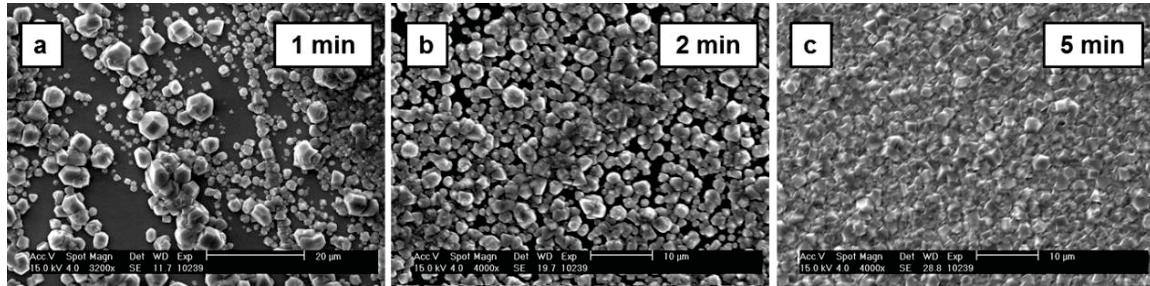


**Figure 3.12:** SEM micrographs showing the early stages of the diamond film formation: (a) creation of diamond nuclei on the surface of the Si substrate (after 1 min deposition). (b) Diamond crystals coalescence (after 2 min deposition). (c) Continuous diamond film formation (after 5 min deposition).

The growth process of the diamond film is discussed in more detail in the next section, dealing with the cross-sectional microstructure of the films. Finally, the influence of the substrate temperature on the diamond growth process should be enlightened. Figure 3.13 shows how this parameter affects the morphology of the diamond films at a fixed deposition time of 30 minutes:

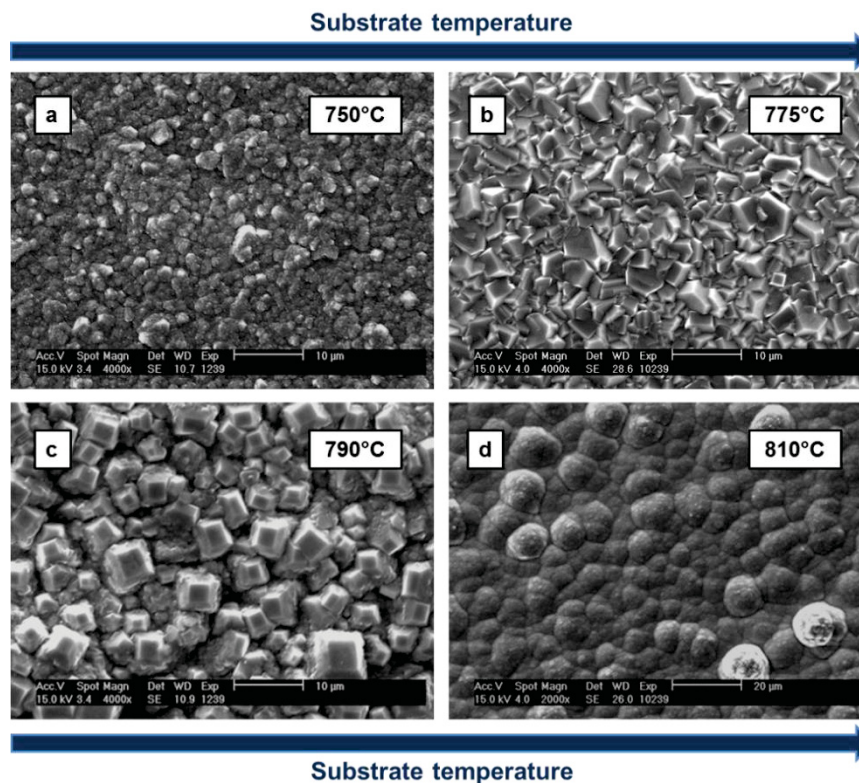


**Figure 3.13:** Influence of the substrate temperature on diamond film morphology.



From Fig. 3.13, it can be assessed that the substrate temperature critically affects the diamond film morphology. It also demonstrates how narrow is the temperature window allowing the growth of diamond films with repeatable microstructural characteristics. Indeed, at 750°C, the growth rate is low and diamond crystals appear relatively small after 30 minutes deposition (Fig. 3.13a). At 775-780°C, the growth rate is at its maximum and the diamond film morphology is consistent (Fig. 3.13b). However, a substrate temperature of 790°C leads to a faster diamond growth in the (111) direction thus leading to (100)-oriented diamond facets (Fig. 3.13c). When the temperature increases more (810°C), the diamond growth is annihilated by oxidation and ball-like shaped structures of graphite and amorphous carbon form onto the substrate (Fig. 3.13d). Thus, substrate temperature should be carefully kept around 780°C during film deposition, which was made difficult by the extreme heat fluxes and thermal inertia of the water-cooled stage.

▪ ***Cross-sectional microstructure: Van der Drift growth model***

In the early stage of the diamond growth process, the isolated diamond germs have different crystallographic orientations. However, after the grains have coalesced to form a continuous film, the diamond grains which fastest growth direction is normal to the substrate take the lead and grow preferentially. These grains keep growing parallel to each other and normally to the substrate along the process to form columnar grain structures. These grains are the only ones to subsist at the surface of the diamond film, which leads to a textured diamond surface. This selective growth process is only possible if no secondary nucleation processes are induced once the continuous diamond film is formed. This is called the Van der Drift growth model, named after Van der Drift who first described it in 1967 [158]. Figure 3.14 shows on the left a scheme of the columnar growth process described by the Van der Drift model (Fig. 3.14a), and on the right a cross-sectional SEM micrograph of a diamond film grown through laser-assisted combustion synthesis (Fig. 3.14b) in this study. One can notice that the experimental architecture of the diamond film cross-section is remarkably similar to the one described by the model.

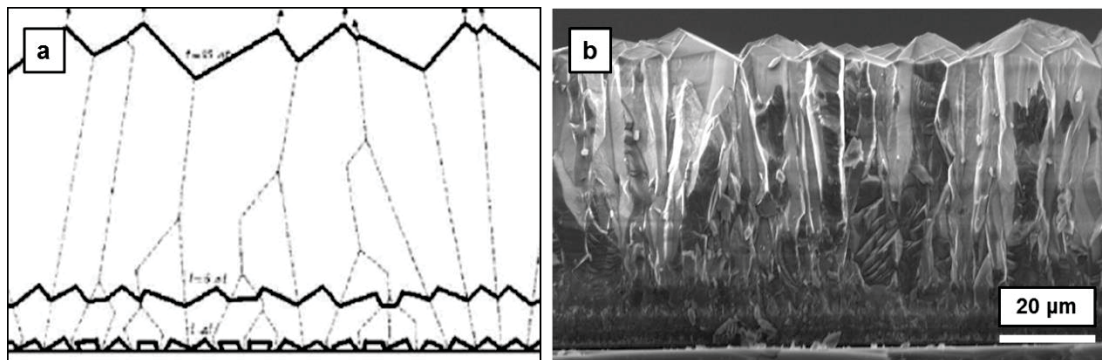


**Figure 3.14: (a) Van der Drift growth model. The dashed lines indicate the grain boundaries. The solid lines show the surface of the film at selected times. (b) Experimental cross-sectional SEM micrograph of diamond film grown through laser-assisted combustion synthesis.**

The Van der Drift growth model assumes microstructural evolution of the diamond film in the vertical direction. In the lower part of the film that is close to the interface, the diamond film is made of numerous but randomly oriented and relatively small diamond crystals with a high amount of grain boundaries. Grain boundaries being surface of high energy, they constitute preferential locations for impurities incorporations. As the deposition process goes on, columnar growth dominates, forming few but relatively larger diamond crystals with preferential growth direction normal to the substrate. Therefore, imperfections such as grain boundaries and impurities exist in large quantity close to the interface while the upper parts of the film are made of large single diamond crystals. The columnar microstructure of the film, which leads to a gradient in diamond crystal size in the vertical direction, may therefore also induce gradients for other parameters such as diamond phase purity and thermal conductivity, as it will be further explored.

▪ ***Influence of laser excitation on diamond film microstructure:***

SEM micrographs showing the influence of the wavelength of the CO<sub>2</sub> laser shined through the combustion flame on the resulting morphology of the diamond films are displayed in Fig. 3.15.

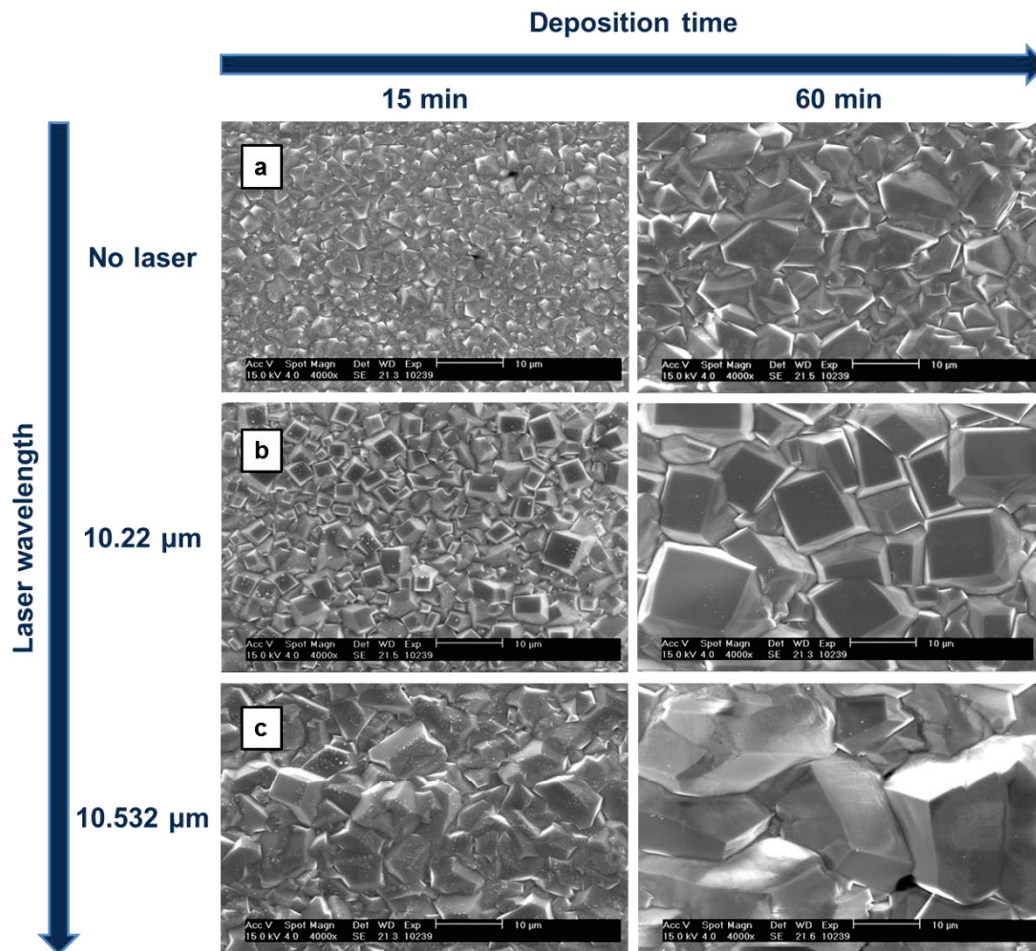


**Figure 3.15: SEM micrographs showing the influence of the laser excitation onto the diamond film morphology: (a, b) no laser, (c, d) 10.22  $\mu\text{m}$  excitation, (e, f) 10.532  $\mu\text{m}$  excitation.**

Consistently with the objective of the multienergy deposition process endeavored in this study, the laser excitation wavelength was shown to have a strong influence on the top surface morphology of the deposited diamond films. While the absence of laser excitation through the flame leads to typical randomly oriented polycrystalline diamond films (Fig. 3.15a), the laser excitation of ethylene molecules at the 10.22  $\mu\text{m}$  wavelength was demonstrated to increase the growth rate of (111) facets, thus resulting in preferentially (100)-textured diamond films (Fig. 3.15b). In a similar fashion, the use of the 10.532  $\mu\text{m}$  laser excitation wavelength results in a dramatic enhancement of the film growth rate and diamond crystal size relative to no laser (Fig. 3.15c) [159].

It was demonstrated through mass spectrometry that the  $\text{CO}_2$  laser excitation tuned at 10.22  $\mu\text{m}$  excited the ethylene molecules to a higher vibrational state with higher rotational energy, thus increasing the concentration of the  $\text{CH}_x\text{O}$  and  $\text{C}_2\text{H}_x\text{O}$  active species into the flame environment. Theoretical simulation of the reaction pathways indicated that these species react more easily with (111) diamond surfaces than with (100) surfaces, leading to a fast growth of the (111) surfaces of diamond, thus resulting in a (100)-oriented diamond film texture. This demonstrates the high potential of laser-assisted deposition techniques in achieving selectivity into the flame environment by promoting chemical reactions that lead to highly-oriented diamond films with superior properties [159].

These results enlighten the strongly beneficial influence of the laser excitation onto the diamond growth process, which allows enhancing both film growth rate and texture. These features are very promising when aiming applications of CVD diamond materials as electronic-packaging substrates, where high growth rate and preferential crystallographic orientation of diamond films are sought.

However, despite the evidence that 10.22  $\mu\text{m}$  excitation of ethylene molecules promotes the preferential growth of (100) diamond facets, it was unclear for some samples if the (100)-texture of the diamond film originated from the 10.22  $\mu\text{m}$  laser excitation or from an unusually elevated substrate temperature. In addition, the (100)-textured diamond morphology was typically located at the center of the diamond film (in a 500  $\mu\text{m}$ -diameter region), while the outer regions of the deposit showed randomly oriented morphology.

Therefore, for the sake of repeatability and microstructure homogeneity, the 10.532  $\mu\text{m}$   $\text{CO}_2$  laser excitation wavelength will be used in the rest of this study. Thus, the samples further analyzed through Raman spectroscopy and infrared photothermal radiometry have been grown through a multienergy process combining the chemical energy of the combustion flame and the electromagnetic energy of the 10.532  $\mu\text{m}$  laser excitation. The next sections will focus on phase purity and residual stress investigations of the films through Raman spectroscopy.

### 3.3 Diamond film phase purity and residual stress analyses through Raman spectroscopy

As mentioned in chapter 2, phase purity and residual stress are two key parameters in integrating CVD diamond films with non-diamond substrates and major limiting factors in diamond film applications in electronics [4, 5]. In order to integrate the as-deposited diamond films into devices, clear understanding about their crystal quality and level of stress level is required. In the following sections, Raman spectroscopy will be employed to quantify the levels of residual stress and phase purity of the diamond films grown through laser-assisted combustion synthesis.

#### 3.3.1 Raman spectroscopy: background and underlying principles

Raman spectroscopy consists in using the *Raman scattering*, an inelastic scattering effect, for the detection of vibrational modes of molecules and lattice vibration in solids (optical phonons described in chapter 2). The technique employs a laser (visible, near infrared, or near ultra-violet) to stimulate vibrational modes of the sample. Depending on the investigated material, the incident photons will be shifted up or down (also known as *Raman shift*). The Raman shifts are recorded in a *Raman spectrum*, which provides information about the vibrational mode of the sample. In the case of diamond, Raman spectroscopy provides key information about the phase purity and level of residual stress. Many different Raman spectroscopic techniques exist. However, we will focus in this study on *spontaneous Raman spectroscopy*, in which no device is used to enhance the Raman scattering effect. Indeed, spontaneous Raman scattering shows low efficiency: 1 in  $10^7$  incident photons is Raman scattered [160].

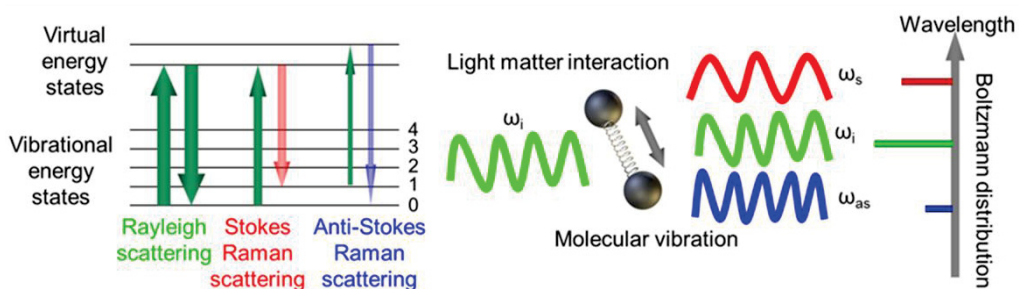


**Figure 3.16: (a) Energy level diagram showing the states involved in Raman spectroscopy. The line thickness is representative of the signal strength. (b) Light-matter interaction processes in Raman spectroscopy with Boltzmann distribution of different scattering effects.**

In spontaneous Raman spectroscopy, the solid lattice is excited from the ground state to a virtual energy state by an incident photon. After relaxing from the virtual energy state, it will emit a photon with different energy (inelastic scattering or Raman scattering) or with the same energy (elastic scattering or Rayleigh scattering). The Raman shift originates from the difference in energy



between the original state and the new state. If the final vibrational state of the solid lattice is higher in energy than the initial state, the emitted photon will be shifted to a longer wavelength (or lower frequency), known as *Stokes Raman scattering*. On the other hand, when the final vibrational state is lower in energy than the initial state, then the emitted photon will be shifted to a shorter wavelength (higher frequency), known as *anti-Stokes Raman scattering*.

Raman shifts are expressed in wavenumbers, or inverse centimeters ( $\text{cm}^{-1}$ ). The difference in wavelength between the incident and the scattered signal is converted into a Raman shift through the following formula [160]:

$$\Delta\omega = \left[ \frac{1}{\lambda_{\text{incident}}} - \frac{1}{\lambda_{\text{scattered}}} \right] \times 10^7 \quad (3.1)$$

Where  $\Delta\omega$  is the Raman shift ( $\text{cm}^{-1}$ ), and  $\lambda_{\text{incident}}$  and  $\lambda_{\text{scattered}}$  are the wavelengths of the incident and scattered photons.

Raman spectroscopy is a fast, non-destructive, and widely-employed method to characterize diamond films and evaluate their phase purity and residual stress. Diamond has a highly recognizable signature in Raman scattering with a sharp peak at  $1332 \text{ cm}^{-1}$  ( $\text{sp}^3$  carbon) [161, 162]. The full width at half maximum (FWHM) of the diamond line is representative of the diamond phase purity (pure diamond exhibits a FWHM of  $3 \text{ cm}^{-1}$ ), while its shift can be related to the level of residual stress in the film. A compressive or tensile stress induces a shift of the diamond peak to higher or lower wavenumbers, respectively [163, 164]. Also, representative of  $\text{sp}^2$ -hybridized carbon features, such as D-band (disordered graphite, at  $1375 \text{ cm}^{-1}$ ), G-band (ordered graphite, at  $1580 \text{ cm}^{-1}$ ) and the broad band of amorphous carbon (around  $1500 \text{ cm}^{-1}$ ) provide information about the non-diamond carbons existing in the film [161, 165].

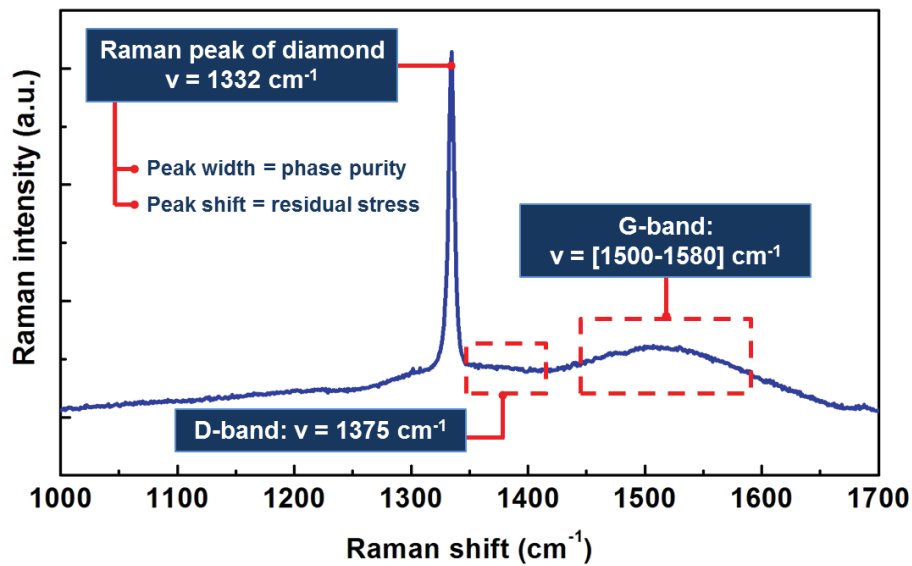


Figure 3.17: Typical Raman signature of diamond.

### 3.3.2 Raman spectroscopy: experimental set-up

In conventional spontaneous Raman spectrometer, laser light (usually continuous-wave) is focused by an objective lens and then illuminated onto a sample (usually on a microscope frame). The scattered light from the illuminated spot is collected with the same lens and then sent through a monochromator and finally detected with a charge-coupled device (CCD) camera. The light with wavelengths close to the laser light wavelength (from elastic Rayleigh scattering) is filtered out using a notch filter (or long-pass filters). For Raman imaging, the detector can also be replaced by an avalanche photodiode (APD) or a photomultiplier tube (PMT) [160].

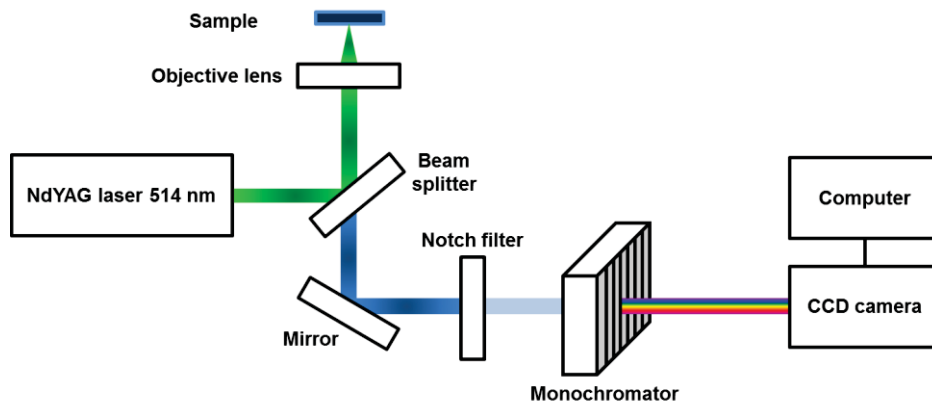


Figure 3.18: Schematic of a conventional Raman spectrometer.

Raman spectroscopic investigations were performed using a micro-Raman spectrometer (inVia H 18415, Renishaw) with a 514.5 nm argon ion laser as the excitation source. A point-focus mode was used during the diamond peak width evaluation. A line-focus mode was used during the diamond peak shift evaluations in order to decrease the bulk power density in the sample and avoid unwanted tensile-like peak shift due to local heating [166]. The laser power was 50 mW. The point-shaped spot was about 1  $\mu\text{m}$  in diameter. The probed volume of a point measurement was about 1  $\mu\text{m}^3$ . The line-shaped spot showed dimensions of about 40  $\mu\text{m}$  in length and 1  $\mu\text{m}$  in width. The grating used was 3000 lines/mm in order to achieve the highest resolution. By coupling with a 1014 pixels charge-coupled camera, a resolution of 0.31  $\text{cm}^{-1}/\text{pixel}$  was obtained.

Raman spectroscopy is a localized measurement collecting information only from the laser spot covered regions. In order to get more accurate values of peak widths and peak shifts, a mapping technique was used to scan a large area of the sample. Each mapping was about 5000  $\mu\text{m}^2$  in area, including about 250 individual scans. These scans provide an average value for the as-mapped parameter (either diamond peak width or diamond peak shift), thus more representative values for the diamond films studied. The diamond peak position was determined automatically using the curve-fitting option integrated in the operation software. All Raman spectra were taken at the center of the deposited diamond films.

### 3.3.3 Phase purity analysis

Low diamond purity due to defects, impurities, and non-diamond carbon contents drastically affects diamond thermal conductivity [40]. Diamond phase purity is revealed through Raman spectroscopy by the ratio between the intensity of the  $sp^3$ -hybridized carbon signal (diamond peak located at  $1332\text{ cm}^{-1}$ ) and that of the  $sp^2$ -hybridized carbon signal (D-band located at  $1375\text{ cm}^{-1}$  and amorphous carbon-band located around  $1500\text{ cm}^{-1}$ ). Fig. 3.18 shows the Raman spectra obtained from diamond films grown onto Si substrates with ( $10.532\text{ }\mu\text{m}$ , Fig. 3.19b) and without (Fig. 3.19a) laser resonant excitation of ethylene molecules with respect to various film thicknesses:

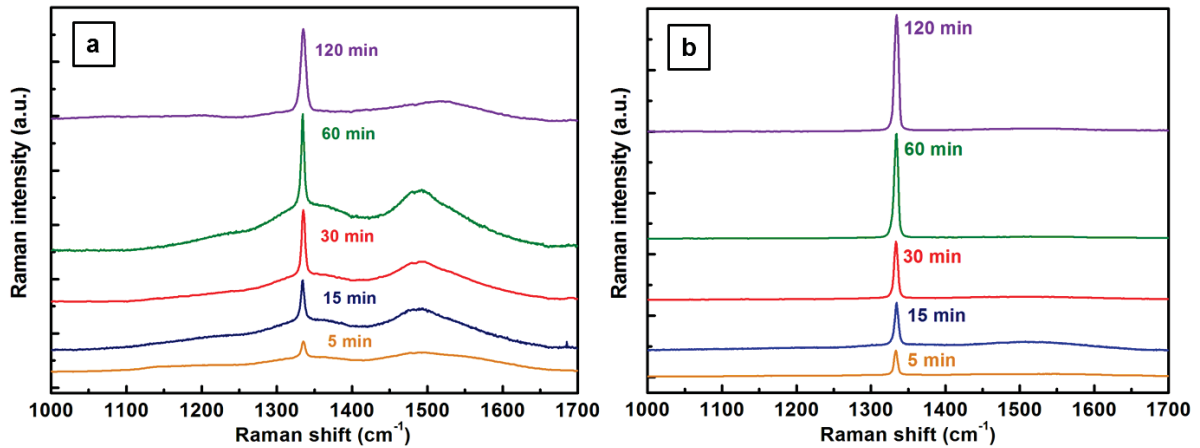


**Figure 3.19: Raman spectra of diamond films grown onto silicon substrates at various thicknesses: (a) without laser excitation, (b) with  $10.532\text{ }\mu\text{m}$  laser excitation.**

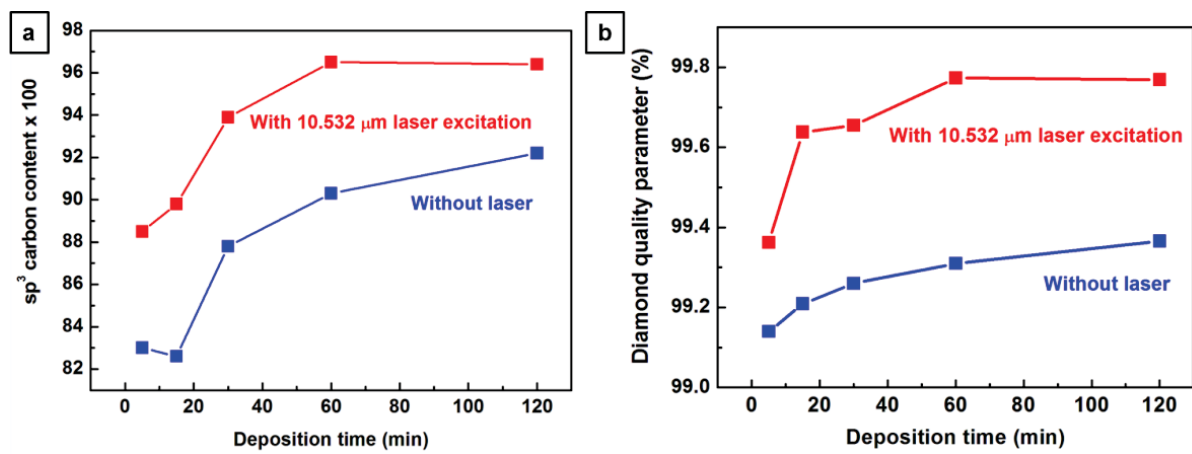
All of the films exhibited sharp diamond peaks located around  $1332\text{ cm}^{-1}$ . D-band ( $1375\text{ cm}^{-1}$ ) and amorphous carbon broad band ( $1500\text{ cm}^{-1}$ ) are also observed from diamond films grown with the combustion flame only, revealing a consistent level of impurities and non-diamond carbon content embedded in the films. The Raman spectra also clearly reveal the superior phase purity of the diamond films grown through the multienergy deposition process combining the laser resonant excitation and the combustion flame energy. These films show almost no D-band or amorphous carbon broad-band signal, except at low thicknesses, thus revealing an increased  $sp^3/sp^2$  carbon ratio relative to the films deposit without laser excitation. Moreover, to consider the respective scattering efficiency of diamond, graphite, and amorphous carbon (1, 50, and 233, respectively) [167], growth of high-phase purity diamond films could be concluded. Also, intensities of the diamond peak and amorphous carbon broad-band increased and decreased, respectively, with an increasing film thickness, suggesting a phase purity enhancement with increasing film thickness.

Diamond phase purity may be quantified in several ways: (1) by evaluating the  $sp^3/sp^2$  carbon ratio through the intensity ratio of diamond peak and cumulated D-band, G-band, and amorphous

carbon broad-band; (2) by calculating the diamond quality parameter through the following formula [168]:

$$Q_{[514\text{ nm}]} = \frac{I_{\text{Diamond}}}{(I_{\text{Diamond}} + \frac{I_{\text{a-carbon}}}{233})} \times 100 \quad (3.2)$$

Where  $I_{\text{Diamond}}$  is the intensity of the diamond line, and  $I_{\text{a-Carbon}}$  is the sum of the intensities of the observed non-diamond carbon features. The 233 factor corresponds to the relative Raman scattering efficiency from amorphous carbon to diamond. Figure 3.20 shows the  $sp^3$  carbon content and diamond quality parameter for diamond films grown with ( $10.532\text{ }\mu\text{m}$ ) and without laser resonant excitation:



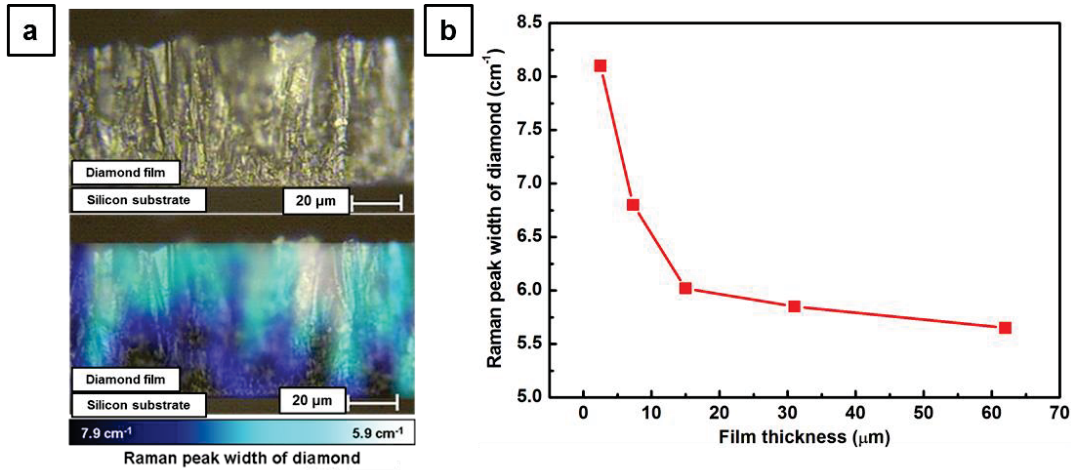
**Figure 3.20: (a)  $sp^3$  carbon content and (b) diamond quality parameter of diamond films grown with ( $\lambda = 10.532\text{ }\mu\text{m}$ ) and without laser resonant excitation.**

Figure 3.20 clearly quantitatively demonstrates the superior phase purity of the diamond films grown through the multienergy processing route relative to those deposit with the only action of the combustion flame. This was ascribed to the laser-resonant excitation process, in which efficient laser energy coupling stimulated the decomposition of the gaseous precursors and significantly increased concentration of atomic hydrogen and OH radicals. The increased atomic hydrogen and OH radical concentrations generated an etching environment for removing non-diamond carbon species [4, 139]. The laser-induced vibrational excitation of ethylene molecules thus improves the purity of the deposited diamond films.

In addition, it enlightens the fact that diamond phase purity increases with increasing film thickness, which is ascribed to the columnar structure of the film described through the Van der Drift model (see section 3.2.4). Upon thickness increase, the film structure turns from multiple but small randomly oriented diamond crystals to relatively larger but fewer grains growing normal to the substrate, thus fewer grain boundaries in the top layers of the film relative to the bottom part, close to the interface with the Si substrate. Since grain boundaries are surface of high energies, they

are ideal hosts for impurities and non-diamond carbon content. Therefore, the  $sp^3$  carbon content, and thus phase purity of the diamond film, increase from the bottom to the top, following the microstructure evolution.

The existence of a phase purity gradient inside the diamond film microstructure was also confirmed through Raman mapping of the diamond film cross-section (Fig. 3.21a) and plot of widths of diamond Raman peak with respect to film thickness (Fig. 3.21b):



**Figure 3.21: (a) Cross-sectional mapping and (b) evolution with respect to film thickness of FWHM of diamond peak for diamond films grown through 10.532  $\mu m$  laser excitation.**

Average diamond peak widths obtained from Raman mappings were located between 5.6 and 8.1  $cm^{-1}$  on Si, with minimum peak widths of 4  $cm^{-1}$ , which was close to that of high-quality type IIa diamond (3.1  $cm^{-1}$ ) [4]. The plotted points represent the centers of the distributions obtained from large area top surface mappings.

### 3.3.4 Residual stress evaluation

In this study, Raman spectroscopy was also used to measure the level of residual stress existing in the diamond films through the Raman shift of the diamond peak. A compressive or tensile stress induces a shift of the diamond peak to higher or lower wavenumbers, respectively [163, 164]. Residual stress in CVD diamond films leads to cracks, poor adhesion, and even delamination, thus strongly degrading the mechanical reliability of diamond films. Residual stress in a diamond film consists of two major parts. One is the thermal stress, caused by the mismatch of thermal expansion coefficients (CTEs) between diamond and the substrate material, which develops during cooling from deposition temperature. The other is the intrinsic stress (also called *growth stress*) which is the cumulative result of grain boundary formation and impurities incorporation into the film during deposition [163, 164, 169]:

$$\sigma_{residual} = \sigma_{thermal} + \sigma_{intrinsic} \quad (3.3)$$

Diamond films generally exhibit a lower CTE relative to conventional substrate materials. Therefore, thermal stress in diamond films is often compressive. On the other hand, the intrinsic stress is often revealed to be tensile. To investigate the level of residual stress in the diamond films, two types of substrate materials were employed: silicon (Si) and cemented tungsten carbide (WC-Co, BS-6S, 6 wt% Co, Basic Carbide Corp.). The WC-Co substrates were employed to provide a comparison with the Si substrates. WC-Co is a typical hard material that may be associated to diamond for cutting tools and drilling applications. The dimensions of the WC-Co substrates were  $12.7 \times 12.7 \times 1.6 \text{ mm}^3$ . Due to the intrinsic roughness of the WC-Co substrates, no seeding was needed to grow diamond on it. The diamond films were all grown through laser-assisted combustion synthesis using the  $10.532 \text{ }\mu\text{m}$  laser excitation.

Figure 3.22 shows the typical Raman shift obtained from diamond films deposited onto Si and WC-Co substrates. The Raman peak shift of stress-free diamond is  $1332 \text{ cm}^{-1}$ .

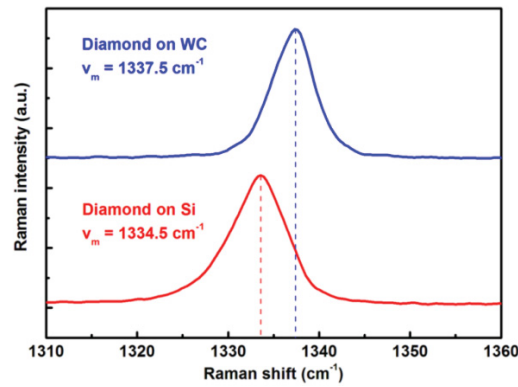


**Figure 3.22:** Typical Raman shift of diamond films grown onto silicon (red line) and tungsten carbide (blue line).

Diamond films deposited on both types of substrates exhibited peak shifts to higher wave numbers compared to stress-free diamond at  $1332 \text{ cm}^{-1}$ , revealing that the residual stress in the diamond films was compressive on both types of substrates. For diamond films deposited on both substrates under similar conditions, larger diamond peak shifts were observed on the diamond films deposited on WC-Co than that deposited on Si, with typical shifts at  $1337.5 \text{ cm}^{-1}$  on WC-Co and  $1334.5 \text{ cm}^{-1}$  on Si. These results are consistent with individual CTEs of diamond, silicon and WC-Co shown in Tab. 3.2.

**Table 3.2:** CTEs of diamond, silicon, and tungsten carbide at ambient and deposition temperatures.

Material	Diamond	Silicon (Si)	Tungsten carbide (WC-Co)
$\alpha$ at 293K ( $\times 10^{-6} \text{ }^{\circ}\text{C}^{-1}$ )	1.0	2.61	4.42
$\alpha$ at 1073K ( $\times 10^{-6} \text{ }^{\circ}\text{C}^{-1}$ )	4.58	4.45	6.50
Lattice parameter ( $\text{\AA}$ )	3.51	5.43	2.91
Lattice mismatch with diamond (%)	n.a.	52	-18.5

Since diamond has a lower CTE than Si and WC-Co, a compressive thermal stress is expected. Also, the respective amplitudes of residual stress in diamond films deposited on WC-Co and Si substrates are consistent with the higher CTE mismatch between diamond and WC-Co compared to that between diamond and Si.

The degrees of shift and splitting of the diamond Raman line are proportional to the level of biaxial residual stress inside the diamond films. Ager and Drory developed a general model relating singlet and doublet phonon scattering to the internal stress [164, 165, 170]. We used this model to calculate the level of residual stress in the deposited diamond films through the following relationship:

$$\sigma_{residual} = -0.567 \times (v_m - v_0) \quad (3.4)$$

Where  $v_m$  is the observed peak position and  $v_0$  is the Raman peak shift for an unstressed diamond film ( $1332 \text{ cm}^{-1}$ ). Therefore, if  $v_m < v_0$ , the residual stress is tensile ( $\sigma_{residual} > 0$ ). On the contrary, if  $v_m > v_0$ , the residual stress is compressive ( $\sigma_{residual} < 0$ ), as observed from the diamond films grown onto Si and WC-Co substrates.

Figure 3.23 represents the diamond peak shift measured in diamond films of various thicknesses deposited on silicon and WC-Co substrates. The corresponding residual stress (compressive) calculated using equation 3.4 is shown on a parallel scale. The total residual stress decreases with increasing film thickness on both silicon and WC-Co substrates, which demonstrates the existence of a vertical residual stress gradient in the film. This was ascribed to an increase in intrinsic stress due to the formation of grain boundaries and growth strains during the diamond deposition process, thus decreasing the total residual stress. It confirms that the intrinsic stress is a tensile stress.

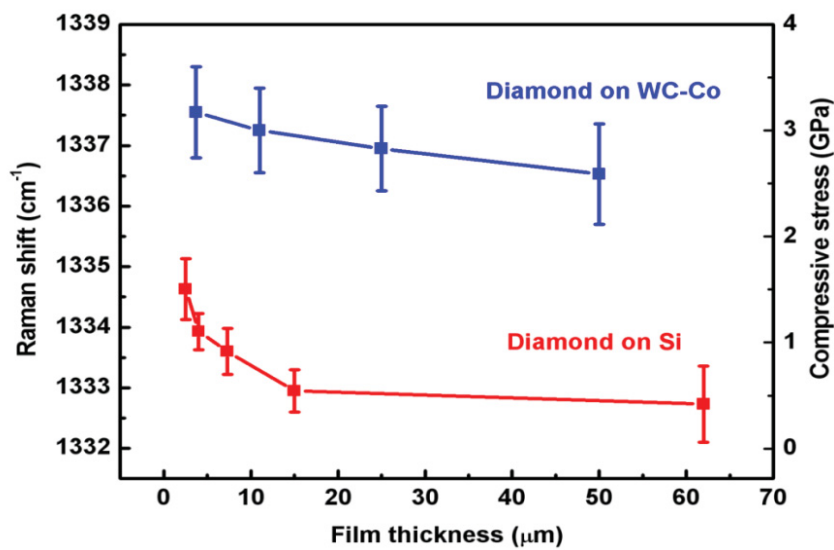
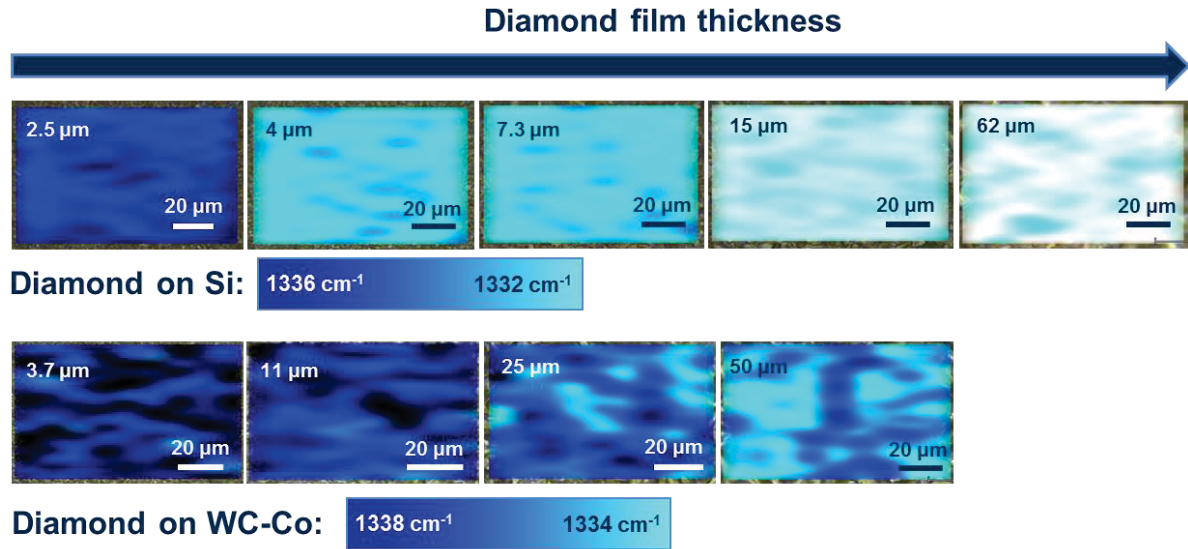


Figure 3.23: Raman shift and corresponding residual stress of diamond films grown onto silicon (red line) and tungsten carbide (blue line) as a function of film thickness.



The decrease in residual stress with increasing film thickness may also be visualized through the color evolution of the Raman peak shift mappings of the diamond films (Fig. 3.24):



**Figure 3.24: Raman mappings of diamond peak position obtained from diamond films grown on Si and WC-Co substrates.**

The thermal stress ( $\sigma_{\text{thermal}}$ , GPa) induced by the thermal expansion mismatch between the diamond film and the substrate can be calculated using the following equation [145, 163]:

$$\sigma_{\text{thermal}} = \left( \frac{E_{\text{Diamond}}}{1-\nu_{\text{Diamond}}} \right) \times \int_{T_0}^T (\alpha_{\text{Film}} - \alpha_{\text{Substrate}}) dT \quad (3.5)$$

Which leads to:

$$\sigma_{\text{thermal}} = \left( \frac{E_{\text{Diamond}}}{1-\nu_{\text{Diamond}}} \right) \times (\alpha_{\text{Film}} - \alpha_{\text{Substrate}}) \times (T - T_0) \quad (3.6)$$

Where  $E_{\text{Diamond}}$  is the Young's modulus of diamond ( $E_{\text{Diamond}} = 1150$  GPa),  $\nu_{\text{Diamond}}$  is the Poisson's ratio of diamond ( $\nu_{\text{Diamond}} = 0.07$ ),  $\alpha_{\text{Film}}$  and  $\alpha_{\text{Substrate}}$  are the thermal expansion coefficients of the diamond film and the substrate material, respectively, and  $T$  and  $T_0$  are the deposition and room temperatures, respectively ( $\Delta T = T - T_0 = 780$  K). A positive or negative sign stands for a tensile or compressive thermal stress, respectively. In order to take into account the variation of CTE with temperature, the following equation was used for each material:  $\alpha = (\alpha_{T_0} + \alpha_T)/2$ ,  $\alpha_{T_0}$  being the CTE at room temperature (293 K),  $\alpha_T$  being the CTE at deposition temperature. Although it is a thin-film approximation, equation 3.4 provides an estimation of the thermal stress induced by the CTE mismatch.

The corresponding calculated thermal stresses are  $-0.70$  GPa and  $-2.52$  GPa in diamond films deposited on silicon and WC-Co, respectively. The measured residual stresses at low film thickness

(2.5  $\mu\text{m}$  on Si and 3.7  $\mu\text{m}$  on WC-Co) are respectively  $-1.49$  GPa and  $-3.14$  GPa on Si and WC-Co substrates. The respective signs and amplitude of thermal stresses calculated are consistent with the residual stresses measured by Raman spectroscopy. The gap between the theoretical values and the measured values is ascribed to the domain size effect observed in Raman spectroscopy [171]. Assuming that the intrinsic stress is close to zero for thinner films, the intrinsic stress in diamond films was plotted. Figure 3.25 shows the increase of intrinsic stress with increasing film thickness.

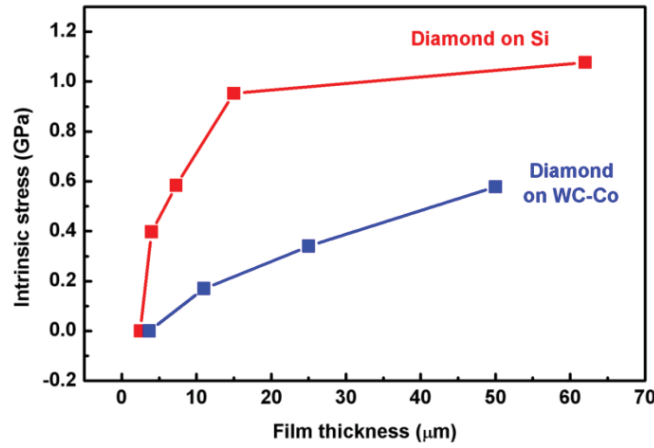


**Figure 3.25: Intrinsic stress evolution with film thickness for diamond films grown on Si and WC-Co substrates.**

Maximum intrinsic stresses of 1.1 and 0.6 GPa in diamond films deposited on Si and WC-Co were calculated, respectively. The respective intrinsic stresses observed on Si and WC-Co substrates are consistent with the lattice mismatches of Si and WC-Co with diamond calculated in Tab. 3.2 (the lattice mismatch  $\Delta l$  is given by:  $\Delta l = 100 \times (a_{\text{substrate}} - a_{\text{diamond}})/a_{\text{diamond}}$ , where  $a_{\text{diamond}}$  and  $a_{\text{substrate}}$  respectively stand for the lattice parameters of diamond and the substrate material considered). Although intrinsic stress is lower in diamond films deposited on WC-Co substrates than on silicon substrates, the diamond films were observed to delaminate much more easily from WC-Co substrates during the experiments. It is believed that the high thermal expansion mismatch and the observed diffusion of cobalt particles into the film [144] strongly affect the adhesion strength between the film and the substrate, thus being responsible for the peeling-off of the diamond films from WC-Co substrates. Finally, the residual stress in thick diamond films deposited on silicon is close to zero, which could be responsible for the good adhesion of the diamond films to Si substrates.

### 3.3.5 Residual stress release through substrate laser-roughening

Residual stresses in diamond films constitute a critical obstacle to their applicability. Therefore, it is important to provide solution for stress release in CVD diamond films and substrates. In this study, an innovative laser-roughening process was exercised to roughen the substrate surface prior

to diamond film deposition in order to induce elastic relaxation of the stress. The following results were obtained through laser-roughening of WC-Co substrate but it was also shown to be efficient on Si substrates.

The laser-roughening process was carried out at the University of Nebraska-Lincoln with help from Dr. Dennis Alexander and his co-workers from the Electrical Engineering department. The surface roughness of the WC-Co substrates was modified using a Ti sapphire femtosecond (fs) laser that was focused into a line onto the surface of the sample. Details about the experimental procedure are available in [172]. Figure 3.26 shows SEM micrographs and AFM profiles of raw and laser-roughened WC-Co substrates, accompanied with SEM micrographs of diamond films grown on raw and laser-roughened WC-Co substrates:

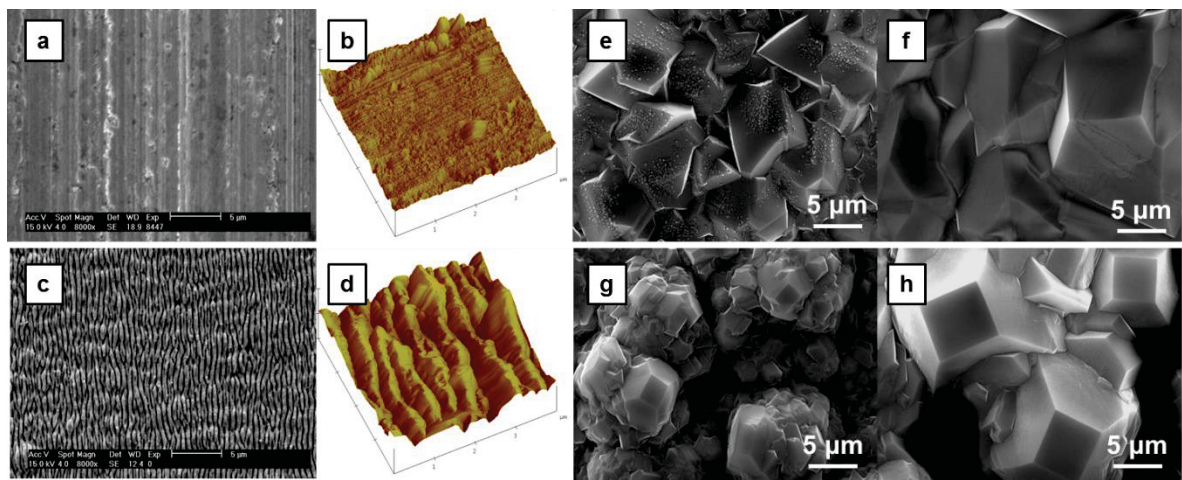


**Figure 3.26:** SEM micrograph and AFM surface profile of raw (a, b) and laser-roughened (c, d) WC-Co substrates. SEM micrographs of diamond films grown onto raw (e, f) and laser-roughened (g, h) WC-Co substrates during 30 minutes (e, g) and 60 minutes (f, h) [172].

Figure 3.27 shows the resulting Raman mapping of the diamond peak position on the top surface of two diamond films grown under the same conditions onto raw and laser-roughened WC-Co substrates and the resulting average peak shifts and residual stress levels:

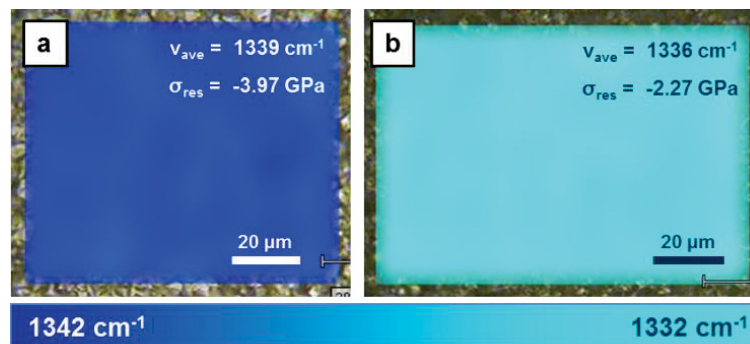


**Figure 3.27:** Raman mapping of diamond peak shift on (a) raw and (b) laser-roughened WC-Co.

From these results, it is clear that the laser-roughening of the substrate leads to a downshift of the diamond peak, representative of a strong residual stress release (more than 1.5 GPa) through elastic relaxation into the diamond film. However, the film morphology is affected by the roughness of the substrate since island growth seems to be promoted, thus leading to discontinuity in the film structure. Nevertheless, this stress release solution is very promising for CVD diamond applications and could be helpful for mitigating the thermal stress resulting from CTE mismatch between diamond and various types of electronic substrate materials, such as copper, silicon, and alumina.

### **3.4 Thermal characterization through modulated photothermal radiometry**

#### **3.4.1 Background about thermal characterization of CVD diamond films**

The design of an efficient electronic package involving CVD diamond as heat-spreading material requires accurate knowledge of its thermal properties. Numerous techniques have been used to determine the thermal conductivity of CVD diamond films, among them joule-heating thermometry [48], photoacoustic method [46], simple thermocouple routes [47], photothermal microscopy [173], or holographic interferometry [174]. Most of the thermal conductivity data gathered about diamond films concerns deposits obtained either through microwave-plasma assisted or hot filament techniques, and diamond films grown through combustion flame synthesis suffer from a lack of thermal conductivity characterization in literature.

Indeed, unlike combustion CVD, which is an open-air process, hot-filament and microwave-assisted CVD routes involve vacuum environments that are highly desirable when seeking to grow electronic-quality materials. Indeed, diamond films grown through combustion CVD usually suffer from a moderate quality due to their high non-diamond carbon content. Nevertheless, combustion CVD provides noteworthy features such as low capital costs and high growth rates which are key assets to diamond films applicability. Moreover, laser-assisted combustion CVD may allow, at certain laser excitation wavelengths, exercising selectivity from among the various competing chemical processes for diamond growth in the flame environment, thus possibly leading to the deposition of highly-oriented diamond films which would be strongly advantageous for electronic applications.

While thermal conductivity is extensively examined when characterizing diamond films under a thermal prospective, very few studies focused on the estimation of the thermal boundary resistance (TBR) existing at the diamond film/substrate interface, despite the critical role it plays in the heat conduction process through such layered assemblies [87, 175]. Goodson et al. [176] pointed out the shortage of existing data on thermal resistances at the boundaries of CVD diamond films. They

developed a pulsed laser-heating measurement technique to investigate the heat conduction process normal to metallized diamond films grown on Si substrates through microwave-plasma assisted deposition at 830°C, and determined the thermal resistance at the diamond/Si interface. They reported TBR values of  $1.7 \times 10^{-8} \text{ K.m}^2.\text{W}^{-1}$  for a 0.2  $\mu\text{m}$ -thick diamond film and up to  $3.5 \times 10^{-8} \text{ K.m}^2.\text{W}^{-1}$  for a 2.6  $\mu\text{m}$ -thick diamond film. Finally, they established that the details of the diamond deposition process had a great influence on the vertical heat conduction through diamond/Si assemblies, especially in terms of nucleation density and grain size. Verhoeven et al. [177] measured TBRs of  $1.1 \times 10^{-8} \text{ K.m}^2.\text{W}^{-1}$  for diamond films deposited at low temperature ( $\sim 500^\circ\text{C}$ ) on silicon using microwave-plasma-assisted CVD and  $2.0 \times 10^{-7} \text{ K.m}^2.\text{W}^{-1}$  for diamond films deposited through electron cyclotron resonance enhanced microwave-plasma-assisted CVD. In a same manner, Stoner and Maris [178] evaluated the thermal resistance at the interface between diamond and some metals at room temperature. The measured TBRs were reported to be  $3.33 \times 10^{-8} \text{ K.m}^2.\text{W}^{-1}$  at the diamond/Pb interface,  $4.0 \times 10^{-8} \text{ K.m}^2.\text{W}^{-1}$  at the diamond/Au interface,  $4.6 \times 10^{-8} \text{ K.m}^2.\text{W}^{-1}$  at the diamond/Al interface, and  $1.0 \times 10^{-7} \text{ K.m}^2.\text{W}^{-1}$  at the diamond/Ti interface.

In this study, infrared photothermal radiometry will be used to thermally characterize the diamond films, to estimate both thermal conductivity and thermal resistance at the film/substrate interface. The following sections enlighten the underlying equations and the principles of this technique.

### 3.4.2 Modulated photothermal radiometry: underlying principles and equations

- ***Fundamental principle:***

Photothermal radiometry (PTR) is a contactless thermal metrology technique relying on the measurement of infrared radiations emitted by a surface in response to a transient photothermal excitation. Its principles were stated by Cowan [179] before Nordal [180] developed the technology of the method. Extensive description of PTR and its principles is given in [181]. The principle of this technique relies on the use of a light source as a thermal excitation precursor. That excitation may be either pulsed or modulated (periodic), and the profile of its spatial distribution may be either uniform or Gaussian. The excitation radiation is absorbed by a surface initially at a temperature  $T_0$  and with an emissivity  $\varepsilon$ , which results in a temperature rise  $\Delta T$ . The heat flux thus emitted is a function of the temperature  $T$  and may be expressed through Stefan-Boltzmann law's:

$$M = \varepsilon \sigma T^4 \quad (3.6)$$

Where  $M \text{ (W.m}^{-2}\text{)}$  is the surface emittance and:

$$T = T_0 + \Delta T \quad (3.7)$$

Thus:

$$M_0 + \Delta M = \varepsilon \sigma (T_0 + \Delta T)^4 \quad (3.8)$$

With  $\sigma = 5.67 \times 10^{-8} \text{ W.m}^{-2}.\text{K}^{-4}$ , the Stefan-Boltzmann constant.

The aim of PTR analysis is to express the variation of surface temperature of the material  $\Delta T$  as a linear function of the variation of emittance  $\Delta M$ . To do so, it is required that the temperature variation induced by the laser excitation is small (a few Kelvins), thus leading to a variation of emittance which can be expressed as:

$$\Delta M \approx 4\varepsilon \sigma T_0^3 \Delta T \quad (3.9)$$

And therefore:

$$\Delta M \propto \Delta T \quad (3.10)$$

$\Delta M$  is measured by a thermal radiation detector and converted into an electrical signal. The temperature variations measured through PTR being small, typically in the order of 1 K, the electrical signal obtained from the temperature variation is noisy. Thus, the analysis is carried out in the frequency domain instead of the time domain for more accurate data analysis. This is especially relevant since the time frames we are dealing with in PTR are in the order of the microsecond.

The approach that best fits these requirements is the photothermal radiometry modulated in amplitude: a lock-in amplifier measures the amplitude and phase lag between the photothermal excitation signal and the infrared thermal response of the sample, as shown on Fig. 3.28:

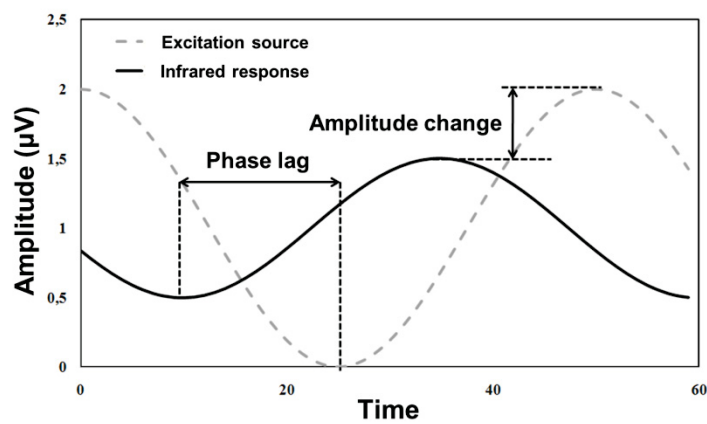


**Figure 3.28: Amplitude and phase of the infrared thermal response relative to the excitation signal.**

The voltages measured through PTR are small and drawn into electrical noise ( $< 1 \text{ mV}$  for a signal/noise ratio of about 1/1000). Thus, for an excitation flux modulated in amplitude expressed by:



$$\varphi = \varphi_0 \cos(2\pi ft) \quad (3.11)$$

The infrared thermal response measured is of the form:

$$A = A_0 \cos(2\pi ft + \Phi) \quad (3.12)$$

A function of transfer is thus established by scanning the frequency range considered. This function depends on the dimensions of the deposit considered and on the geometry of the heat flux at the surface of the material. In radiometry experiments, the characteristic thermal response time is in the order of the microsecond. Consequently, the devices measuring  $A$  and  $\Phi$  usually work in the [10 Hz – 100 kHz] frequency range.

The optical excitation sources employed in radiometry analysis are preferentially laser beams since they present surfacic energy distributions that are easily controlled. Figure 3.29 depicts the two main laser beam energy distribution modes:

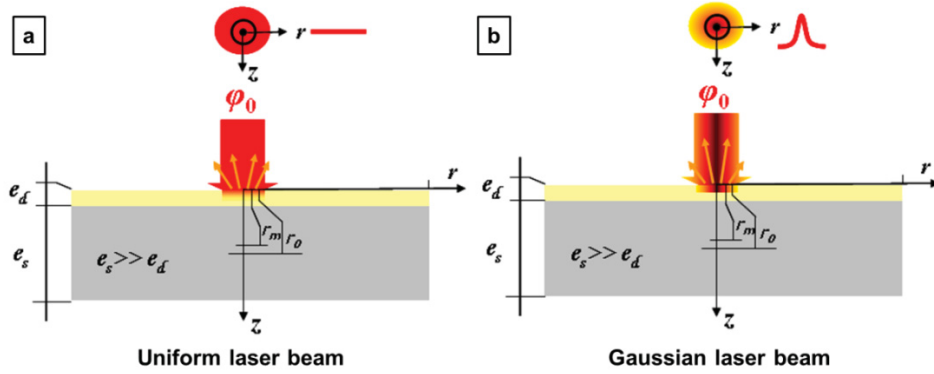


**Figure 3.29: Uniform and Gaussian laser profiles in a modulated photothermal radiometry experiment [181].**

The laser source employed in this study shows a Gaussian beam profile. The detectors employed to measure the radiations emitted by the sample only scope a limited area of the sample, usually circular and centered on the laser excitation spot (labeled as  $r_m$  on the scheme of Fig. 3.29). Thus, the excitation beam ( $r_0$ ) and the scoped emission area ( $r_m$ ) present a cylindrical symmetry centered on the axis of the laser spot (*axisymmetry*).

#### ▪ **Heat transfer geometry:**

The geometry of the laser beam allows modeling the heat transfer phenomenon following a two-dimensional (2D) axisymmetric geometry. However, the geometry of heat transfer adopted depends on the excitation frequency. Indeed, the *heat diffusion length*  $l$  ( $\mu\text{m}$ ), i.e. the depth at which the heat flux wave diffuses in the deposit, is defined by [182]:

$$l = \sqrt{\frac{a_d}{\pi f}} \quad (3.13)$$



Where  $f$  is the frequency (Hz), and  $a_d$  is the thermal diffusivity of the deposit defined as:

$$a_d = \frac{k_d}{\rho_d C_{p,d}} \quad (3.14)$$

Where  $k_d$  is the thermal conductivity of the deposit ( $\text{W.m}^{-1}.\text{K}^{-1}$ ),  $\rho_d$  is its density ( $\text{kg.m}^{-3}$ ) and  $C_{p,d}$  its specific heat ( $\text{J.kg}^{-1}.\text{K}^{-1}$ ).

On one hand, if the heat diffusion length is in the same range as the diameter of the laser excitation spot, the heat transfer can be assumed two-dimensional (2D) axisymmetric (Fig. 3.30a). On the other hand, if the heat diffusion length is small relative to the diameter of the laser excitation spot, the heat transfer geometry can be considered as only one-dimensional (1D) (Fig. 3.30b). While 1D heat transfer enables modeling the system by only considering the axial component of the deposit thermal conductivity ( $k_{d,z}$ ), 2D axisymmetric heat transfer requires that both axial ( $k_{d,z}$ ) and radial ( $k_{d,r}$ ) thermal conductivity components are taken into account.

Therefore, the heat transfer geometry may vary with frequency, and it is possible in case of certain materials with high thermal diffusivity or excitation sources with small dimensions to have to consider the heat transfer as 2D-axisymmetric at low frequencies (where the heat diffusion length is maximum, thus close to the size of the excitation spot) and 1D at higher frequencies (where the heat diffusion length becomes negligible relative to the diameter of the laser excitation spot), as shown on Fig. 3.30:

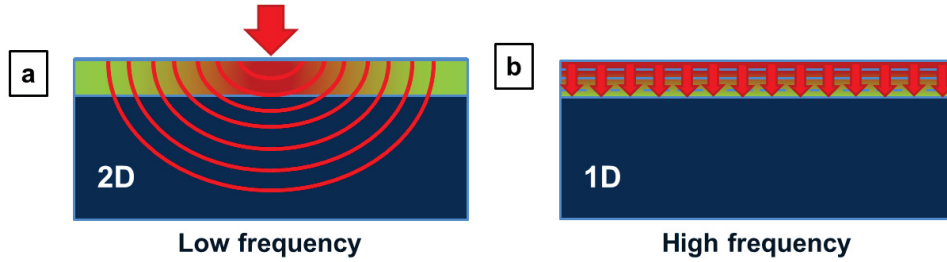


**Figure 3.30: Heat transfer geometry in the deposit material as a function of excitation frequency [181].**

Thus, the limit between 1D and 2D axisymmetric heat transfer is set by the ratio between the diameter of the laser spot and the heat diffusion length. Considering a CVD diamond film showing a thermal conductivity of  $300 \text{ W.m}^{-1}.\text{K}^{-1}$ , a density of  $3500 \text{ kg.m}^{-3}$ , and a specific heat at room temperature of  $520 \text{ J.kg}^{-1}.\text{K}^{-1}$ , eq. 3.14 leads to a thermal diffusivity of  $1.65 \times 10^{-4} \text{ m}^2.\text{s}^{-1}$ . Thus, the resulting heat diffusion length is  $700 \text{ }\mu\text{m}$  at  $100 \text{ Hz}$ ,  $230 \text{ }\mu\text{m}$  at  $1 \text{ kHz}$ , and  $23 \text{ }\mu\text{m}$  at  $100 \text{ kHz}$ , while the diameter of the laser spot used in this study is  $3 \text{ mm}$ .

Therefore, assuming that the CVD diamond films of this study exhibit similar thermal diffusivity, the heat diffusion length can be considered negligible relative to the diameter of the

laser spot as soon as the frequency reaches 100 Hz. Thus, the heat transfer geometry in the diamond films should be preferentially assumed to be 1D in the whole frequency ranged considered in our experiment ([0.7 - 21] kHz) in order to estimate the thermal conductivity and interfacial thermal resistances of diamond films. However, as it will be explained later, the 2D axisymmetric model will be shown to estimate more accurately the thermal properties of the CVD diamond deposits.

In addition, if the heat diffusion length is small relative to the thickness of the substrate, the substrate can be considered as a semi-infinite medium with known thermal properties. Given the thickness of the Si substrate used in this study ( $e_{Si} = 0.6$  mm) and the maximum heat diffusion lengths expected ( $l = 700$   $\mu$ m at 100 Hz), this assumption will be made to estimate the thermal properties of the diamond films.

▪ **Analytical heat transfer solution through thermal quadrupole method:**

The quadrupole method lets us provide analytical solutions used in non-destructive thermal characterization of materials to model heat transfer phenomena and estimate the thermal properties of materials. Analytical methods feature numerous advantages relative to numerical methods, such as shorter calculation times and high adaptability to various heat transfer geometries, either 1D or 2D axisymmetric. In addition, the quadrupole method relies on integral calculations and thus allows manipulating the temperature field in Laplace space, consequently leading to an extensive data processing capability.

While detailed explanations about the quadrupoles method can be found elsewhere [181, 183, 184], we will simply provide here a brief example of such a procedure to relate the temperature and heat flux on one face of a sample to the same parameters on the other face in a 1D heat transfer geometry. Similar calculations are possible for 2D axisymmetric heat transfer, however requiring heavier calculations in cylindrical coordinates.

Let us consider a one-dimensional wall of material  $i$  with thickness  $e_i$ , axial thermal conductivity  $k_i$ , and thermal diffusivity  $a_i$ . The wall surface located at  $z = 0$  is submitted to a uniform heat flux  $\Phi_0(t)$ .

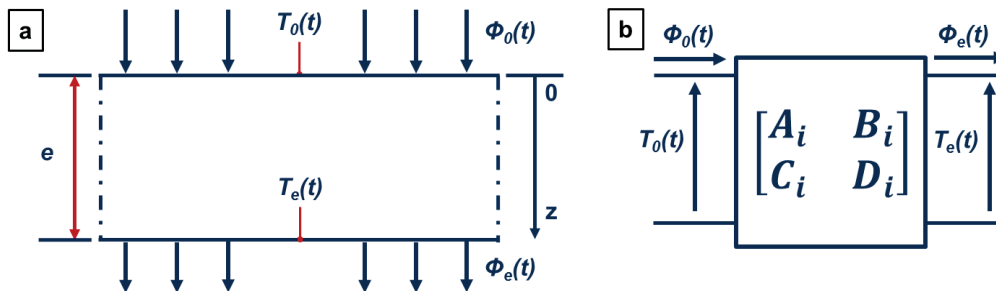


**Figure 3.31: (a) 1D-wall heat transfer geometry. (b) Corresponding quadrupole representation.**

According to the heat equation, the one-dimensional heat transfer may be described by:

$$\frac{\partial^2 T(z, t)}{\partial z^2} - \frac{1}{a} \frac{\partial T(z, t)}{\partial t} = 0$$

Where:  $\{0 < z < e, \quad t > 0\}$ .

The boundary conditions are the following:

$$\{z = 0, t > 0\} \rightarrow -k_i \frac{\partial T(z, t)}{\partial z} = \Phi_0(t)$$

$$\{z = e, t > 0\} \rightarrow -k_i \frac{\partial T(z, t)}{\partial z} = \Phi_e(t)$$

$$\{0 \leq z \leq e, t > 0\} \rightarrow T(z, t) = 0$$

By applying Laplace transforms with respect to time to the previous equations, a quadrupole formulation is obtained which relates the transformed heat flux and temperature on front face to the heat flux and temperature on the back face:

$$\begin{bmatrix} \bar{T}_0(p) = \bar{T}(z = 0, p) \\ \bar{\Phi}_0(p) = \bar{\Phi}(z = 0, p) \end{bmatrix} = \begin{bmatrix} A & B \\ C & D \end{bmatrix} \begin{bmatrix} \bar{T}_e(p) = \bar{T}(z = e, p) \\ \bar{\Phi}_e(p) = \bar{\Phi}(z = e, p) \end{bmatrix}$$

Where  $\bar{T}(p)$  and  $\bar{\Phi}(p)$  respectively correspond to the Laplace transforms of the temperature  $T(t)$  and heat flux  $\Phi(t)$ , defined by:

$$\bar{T}(z, p) = \int_0^{\infty} T(z, t) e^{-pt} dt$$

$$\bar{\Phi}(z, p) = \int_0^{\infty} \Phi(z, t) e^{-pt} dt$$

The components of the matrix are functions of the properties of material  $i$ :

$$A_i = D_i = \cosh(\gamma_i e_i)$$

$$B_i = \frac{\sinh(\gamma_i e_i)}{k_i \gamma_i}$$

$$C_i = \sinh(\gamma_i e_i) k_i \gamma_i$$

$$\text{Where: } \gamma_i = \sqrt{\frac{p}{a_i}} = \sqrt{\frac{p \rho_i c_{p,i}}{k_i}}$$

Therefore, the matrix relationship between heat fluxes and temperatures on the front face and back face of the wall is represented through the thermal quadrupole of Fig. 3.31b. Considering a layered system such as a deposit ( $d$  subscript) onto a substrate ( $s$  subscript), the very same reasoning may be applied, leading to the following matrix expression:

$$\begin{bmatrix} \overline{T_0}(p) \\ \overline{\Phi_0}(p) \end{bmatrix} = \begin{bmatrix} A_d & B_d \\ C_d & D_d \end{bmatrix} \begin{bmatrix} A_s & B_s \\ C_s & D_s \end{bmatrix} \begin{bmatrix} \overline{T_e}(p) \\ \overline{\Phi_e}(p) \end{bmatrix}$$

From that relationship, it is possible to obtain the equation relating the temperature on the back face with respect to the heat flux at the same location:

$$\overline{T_0}(p) = H_{1D}(p) \overline{\Phi_0}(p)$$

Where  $H_{1D}(p)$  represents the Hankel transform of the quadrupole. Thus, the heat transfer model is solved analytically using Laplace transforms for the time variable and Hankel transforms for the space variable. Therefore, the average measured temperature on the front face of the sample is obtained with respect to the heat flux in the frequency domain. This formalism, by knowing the temperature and heat flux fields, allows gaining access to the thermal properties of the deposit such as the vertical thermal conductivity or the thermal resistance existing at the film/deposit interface.

Subsequently, Maillet et al. [184] demonstrated that a thermo-electrical equivalent representation of the thermal quadrupole of Fig. 3.31b could be obtained through the use of thermal impedances as:

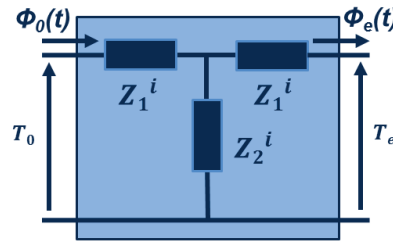


**Figure 3.32: Thermal impedance representation of the 1D heat transfer phenomena of Fig. 3.31.**

Where: 
$$Z_1^i = \frac{A_i - 1}{C_i} = \frac{\cosh(\gamma_i e_i) - 1}{\sinh(\gamma_i e_i) k_i \gamma_i}$$

And: 
$$Z_2^i = \frac{1}{C_i} = \frac{1}{\sinh(\gamma_i e_i) k_i \gamma_i}$$

In the thermo-electrical analogy of Fig. 3.32, the heat fluxes ( $\text{W.m}^{-2}$ ) are equivalent to current density ( $\text{A.m}^{-2}$ ) while the thermal potential (temperature) differences are assimilated to electrical potential (voltage) differences (V). The thermal impedances are functions of the thickness and the thermal properties of the material (thermal conductivity, density, specific heat).

In a similar manner, it can be shown that the heat transfer phenomenon in the tri-layered assembly considered in this study composed of the optical transducer (see section 3.4.3), the diamond film, and the silicon substrate can be modeled through the assembly in series of three reference cells as that displayed in Fig. 3.32, where each impedance is a function of the properties of the material considered:

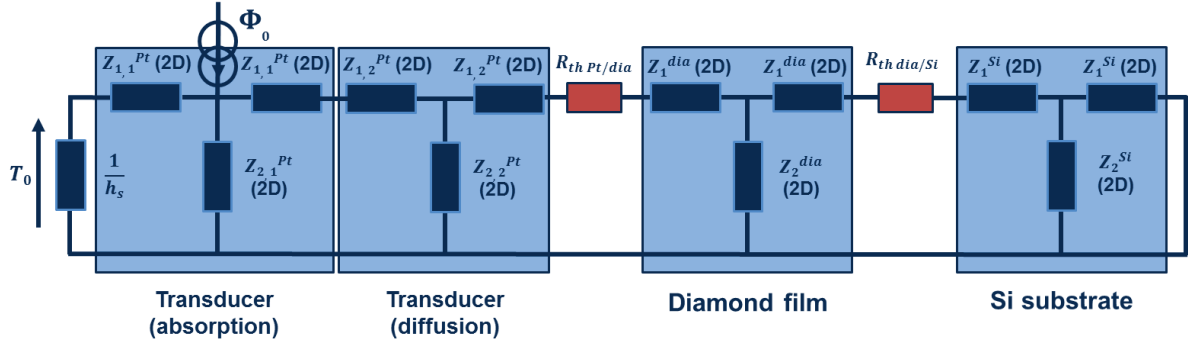


**Figure 3.33: Thermal impedances network modeling the 1D heat transfer phenomenon in the tri-layered sample considered in infrared photothermal radiometry analysis.**

In representation of Fig. 3.33, a source term has been added to represent the heat flux incident onto the sample surface and its absorption by the transducer. The thermal impedance cells corresponding to the heat flux diffusion in the transducer, the diamond film, and the silicon substrate are separated by resistive terms representing the interface thermal resistances at the transducer/diamond and diamond/silicon interfaces.

The source term may be included in the transducer cell by optimizing the transducer thickness in order for it to exhaustively absorb the incident heat flux, thus leading to a simplification of the thermal impedances representation as that of Fig. 3.34:

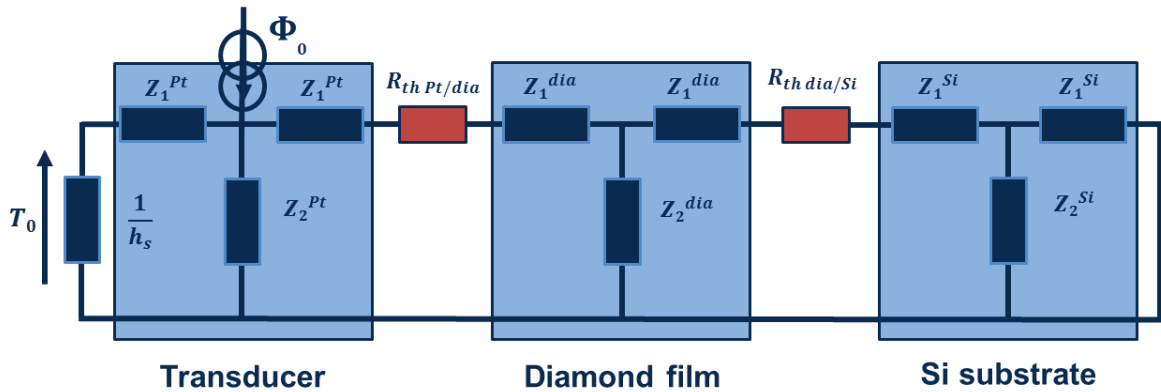


**Figure 3.34: Modeling of the 1D heat transfer phenomenon in the tri-layered sample based on the thermal impedances formalism when the transducer absorbs the heat source on its whole thickness.**

Subsequently, the thermal impedance network modeling the heat transfer phenomenon in the tri-layered assembly may be simplified by considering parameters such as the thermal excitation frequency range. Especially, given the frequency, it can be either necessary to take into account the influence of the heat capacity of the deposit on the heat transfer (thus adopting a *capacitive approach*) or to consider the deposit as a thermal resistance (*resistive approach*).

The validity of either approach depends on the ratio between the heat diffusion length  $l$  and the thickness of the deposit  $e_d$  considered. While the capacitive approach should be used when  $e_d$  is in the same range as  $l$ , the resistive approach is accurate when  $l$  is large relative to  $e_d$ . Therefore, the resistive approach is especially valid at low frequencies, where the thickness of the deposit is small relative to the heat penetration depth. Thus, the influence of the bulk heat capacity of the deposit can be neglected. Its validity decreases when the frequency increases, i.e. when the heat penetration depth decreases and the thermal response is more affected by the heat capacity of the bulk deposit, which leads preferentially to a capacitive approach. The capacitive approach is particularly valid when dealing with resistive material with low thermal diffusivity or showing extensive interfacial thermal resistances.

As previously mentioned, the silicon substrate is considered in this study as a semi-infinite medium due to the fact that the substrate thickness  $e_s$  is much larger than maximum heat diffusion length  $l$  expected. In addition, due to its very low thickness (typically 30 nm), the absorption of the laser excitation by the transducer is considered surfacic, and its temperature is considered uniform. Thus, the source term of Fig. 3.34 is replaced by a heat flux applied onto the surface of the transducer.

When the heat diffusion length is in the same range as the thickness of the diamond film (thus  $e_d/l \sim 1$ , typically at high frequencies), the capacitive approach leads to the following simplification of the thermal impedances network of Fig. 3.34:

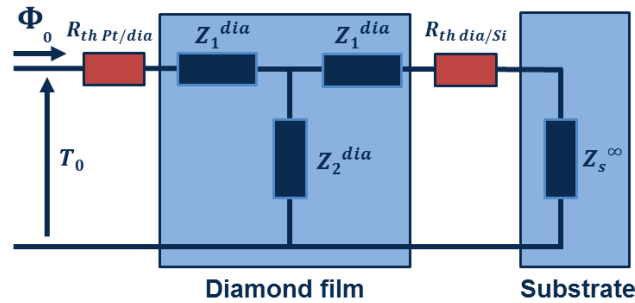


**Figure 3.35: Heat transfer model in the tri-layered assembly when the heat diffusion length is in the same range as the diamond film thickness (capacitive approach).**

Where the thermal impedance of the substrate, expressed as a semi-infinite medium, is:

$$Z_s^\infty = \frac{1}{\gamma_s k_s}$$

$$\text{And: } \gamma_s = \sqrt{\frac{p}{a_s}} = \sqrt{\frac{p \rho_s c_{p,s}}{k_s}}$$

Similarly to the thermal impedances involved in the representation of Fig. 3.32:

$$Z_1^d = \frac{\cosh(\gamma_d e_d) - 1}{\sinh(\gamma_d e_d) k_d \gamma_d} \quad \text{and} \quad Z_2^d = \frac{1}{\sinh(\gamma_d e_d) k_d \gamma_d}$$

In contrast, when the heat diffusion length is much larger than the thickness of the diamond film (thus  $e_d/l \ll 1$ , at low frequencies), the resistive approach leads to the following simplification of the thermal impedances network of Fig. 3.34:

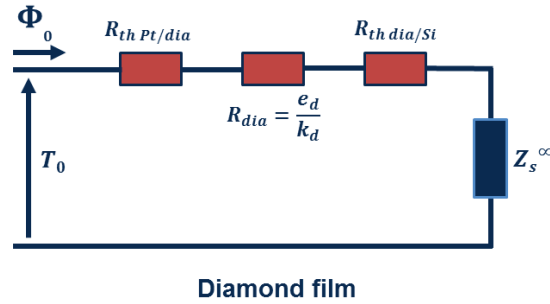


**Figure 3.36: Heat transfer model in the tri-layered assembly when the heat diffusion length is larger than the diamond film thickness (resistive approach).**

In the resistive model, the volume properties of the diamond film such as bulk heat capacity are assumed to have little influence on the thermal response relative to the interface thermal resistance, and the whole system is approximated as an association of thermal resistances in series. Thus, the total thermal resistance is given by the sum:

$$R_{th} = R_{Pt/dia}^{th} + R_{dia} + R_{dia/Si}^{th} \quad (3.15)$$

Where  $R_{Pt/dia}^{th}$ ,  $R_{dia}$  and  $R_{dia/Si}^{th}$ , respectively stand for the thermal resistance at the transducer/diamond interface, the thermal resistance of the diamond film, and the thermal resistance at the diamond/silicon substrate interface.

$$\text{Since: } R_{dia} = \frac{e_{dia}}{k_{dia}} \quad (3.16)$$

$$\text{We have: } R_{th} = R_{Pt/dia}^{th} + \frac{e_{dia}}{k_{dia}} + R_{dia/Si}^{th} \quad (3.17)$$



Where  $k_{dia}$  and  $e_{dia}$  are the thermal conductivity ( $\text{W.m}^{-1}.\text{K}^{-1}$ ) and thickness (m) of the diamond deposit, respectively.

In this study, the quadrupole method and subsequent thermal impedances representation previously described are implemented in a Levenberg-Marquard algorithm (minimization algorithm) used to process the data obtained from photothermal radiometry experiments (Matlab is used as data processing software). The thermal properties of the deposit are estimated through an inverse method: the vertical thermal conductivity of the diamond film, as well as the thermal resistances at the interfaces between the transducer and the diamond film and between the diamond film and the Si substrate, are obtained by minimizing the gap between the measured phase and amplitude and the calculated ones through the algorithm.

Depending on the thermal properties and of the geometry of the layered assembly, various models may be adopted to fit experimental data with theoretical predictions and estimate the thermal conductivity and interfacial thermal resistances of the deposit. Either 1D or 2D approaches, embedding or not a capacitive term from the deposit, can be considered. However, it is possible, as an illustration, to calculate the ratio between the thickness of the deposit and the heat diffusion length with respect to the excitation frequency for a 10  $\mu\text{m}$ -thick diamond film with a thermal conductivity of  $300 \text{ W.m}^{-1}.\text{K}^{-1}$ :

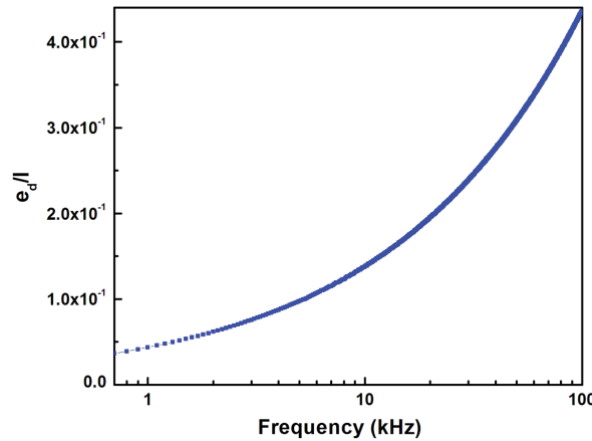


**Figure 3.37:  $e_d/l$  ratio with respect to excitation frequency for CVD diamond with  $k_{dia} = 300 \text{ W.m}^{-1}.\text{K}^{-1}$ .**

The ratio value ranges from 0.036 to 0.436 in the [0.7 – 100] kHz frequency range. Therefore, it can be concluded that the thickness of the diamond film is small relative to the heat diffusion length, even at high frequency. Thus, a resistive approach should be preferentially adopted to model the thermal behavior of such diamond films.

In this study, various models have been tested in order to achieve the best fit between experimental phase and amplitude data obtained from the thermal response of the diamond films to

theoretical predictions. Details about the models preferred in the case of our samples are given in further sections.

▪ **Thermal response of semi-infinite medium:**

When establishing the transfer function of the resistive model, it is possible to predict that the phase and amplitude evolutions as a function of the frequency in a semi-infinite media are as following:

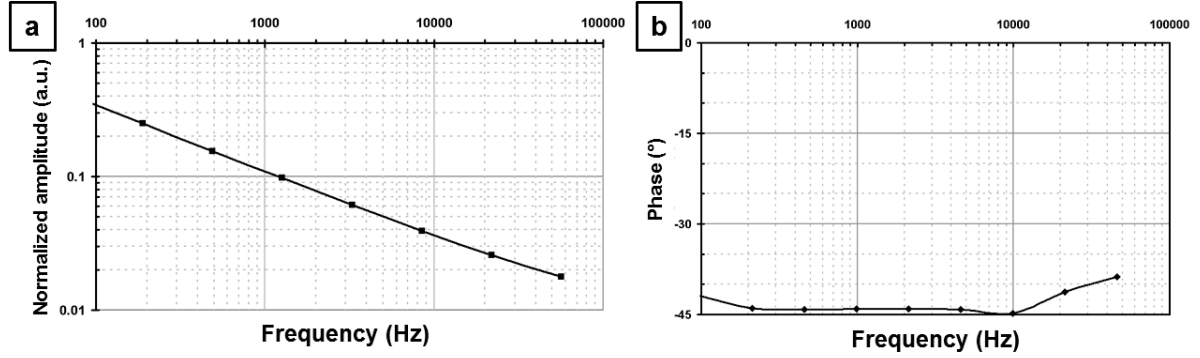


**Figure 3.38: Typical (a) amplitude and (b) phase evolution in a semi-infinite media.**

Indeed, it can be shown [181] that the transfer function of a semi-infinite media in a resistive approach may be written as:

$$Z = \frac{1}{E\sqrt{p}} + R_{th} \quad (3.18)$$

Where:  $p = j\omega$

And:  $E = \sqrt{\lambda\rho C_p}$  is the thermal effusivity of the material ( $J.s^{-1/2}.m^{-2}.K^{-1}$ ).

Thus:  $Z = \frac{1}{E\sqrt{j\omega}} + R_{th}$

Also:  $\frac{1}{\sqrt{j}} = j^{-1/2} = e^{-j\frac{\pi}{4}}$

Therefore:  $Z = \frac{1}{E\sqrt{\omega}} e^{-j\frac{\pi}{4}} + R_{th}$

Which is equivalent to:  $Z = \frac{1}{E\sqrt{\omega}} \left( \cos\left(\frac{\pi}{4}\right) - j\sin\left(\frac{\pi}{4}\right) \right) + R_{th} = \frac{1}{E\sqrt{2\omega}} (1 - j) + R_{th}$

Or:  $Z = \left[ \frac{1}{E\sqrt{2\omega}} + R_{th} \right] - j \frac{1}{E\sqrt{2\omega}}$

Thus, the module (amplitude) of the transfer function  $Z$  is equal to:

$$|Z^2| = \sqrt{\left( \left[ \frac{1}{E\sqrt{2\omega}} + R_{th} \right]^2 + \frac{1}{E^2 2\omega} \right)} \quad (3.19)$$

And its phase may be deduced from:

$$\tan \varphi = -\frac{(1/E\sqrt{2\omega})}{\left(\frac{1}{E\sqrt{2\omega}} + R_{th}\right)}$$

Which leads to:

$$\varphi = \tan^{-1} \left[ -\frac{(1/E\sqrt{2\omega})}{\left(\frac{1}{E\sqrt{2\omega}} + R_{th}\right)} \right] \quad (3.20)$$

Therefore, the limits of phase and amplitude at low and high frequencies are as following:

- When  $\omega \rightarrow 0$ :  $|Z^2| \rightarrow \infty$  and  $\varphi \rightarrow -\frac{\pi}{4} = -45^\circ$
- When  $\omega \rightarrow \infty$ :  $|Z^2| \rightarrow 0$  and  $\varphi \rightarrow 0^\circ$

These trends are in agreement with those displayed in Fig. 3.33.

#### ▪ **Sensitivities:**

The sensitivity of the phase to the thermal boundary resistance at the Si/diamond interface can be calculated from the following equations:

$$S_\varphi(R_{dia/Si}^{th}) = \frac{\partial \varphi}{\partial R_{dia/Si}^{th}}$$

In order to compare the sensitivity functions, we define the reduced sensitivity (without dimension):

$$S_\varphi^+(R_{dia/Si}^{th}) = R_{dia/Si}^{th} \frac{\partial \varphi}{\partial R_{dia/Si}^{th}}$$

Practically, the sensitivity is calculated using the following derivation:

$$S_\varphi^+(R_{dia/Si}^{th}) \sim R_{dia/Si}^{th} \frac{\Delta \varphi}{\Delta R_{dia/Si}^{th}} = R_{dia/Si}^{th} \frac{\varphi(R_{dia/Si}^{th} + \Delta R_{dia/Si}^{th}) - \varphi(R_{dia/Si}^{th})}{\Delta R_{dia/Si}^{th}} \quad (3.22)$$

Similar equations are used to derive the sensitivity of the amplitude to the TBR at the diamond/Si interface. This leads to the following sensitivity plots of phase (Fig. 3.39a) and amplitude (Fig. 3.39b) toward  $R_{dia/Si}^{th}$  at different temperatures. It is deduced from these plots that the sensitivity of the amplitude to  $R_{dia/Si}^{th}$  is extremely weak relative to that of the phase toward this parameter (a factor  $10^{10}$  separates the two sensitivities). This is especially due to the fact that the deposits considered in this study are made of CVD diamond, a material with a high thermal conductivity. Therefore, the estimation of  $R_{dia/Si}^{th}$  through the algorithm strongly relies on the phase

variations, while the amplitude variations with frequency provide little information due to a lack of sensitivity toward this parameter.

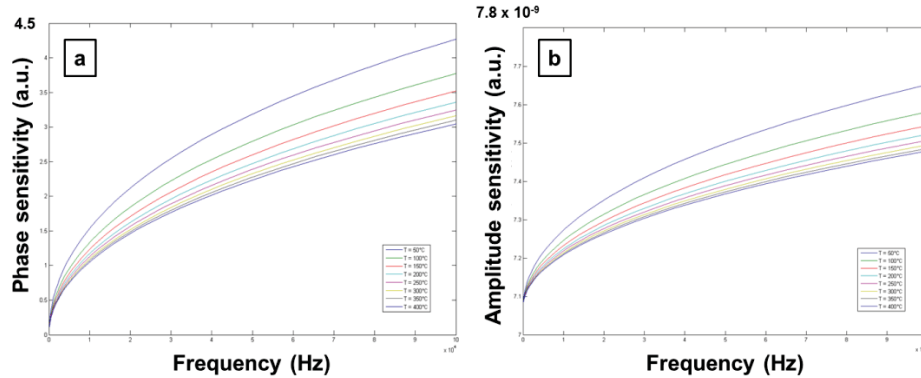


Figure 3.39: Respective sensitivity of the thermal response (a) amplitude and (b) phase to  $R_{dia/Si}^{th}$ .

Similarly, it can be demonstrated that, for deposit materials with high thermal conductivity (such as diamond), the thermal conductivity has little influence on phase variations, unlike the thickness of the deposit which strongly influences them. Finally, the specific heat of the deposit can be shown to affect phase variations but with limited impact and only at high frequencies where the  $e_d/l$  ratio is minimum [181, 182].

▪ ***Influence of the roughness on the thermal response:***

It was previously shown that the diamond films grown through laser-assisted combustion synthesis exhibited mean roughness close to 400 nm for a 10  $\mu\text{m}$ -thick diamond film and close to 700 nm for a 60  $\mu\text{m}$ -thick diamond film (see Fig. 3.10 and Tab. 3.1). This roughness is far from being negligible and may affect the heat transfer process through the diamond film in several ways: the roughness may either interfere between the incident excitation source and the resulting heat flux in the material through undesired optical reflections (Fig. 3.40b) or isotherms contrition (Fig. 3.40c), or between the resulting heat flux inside the material and the external thermal response.

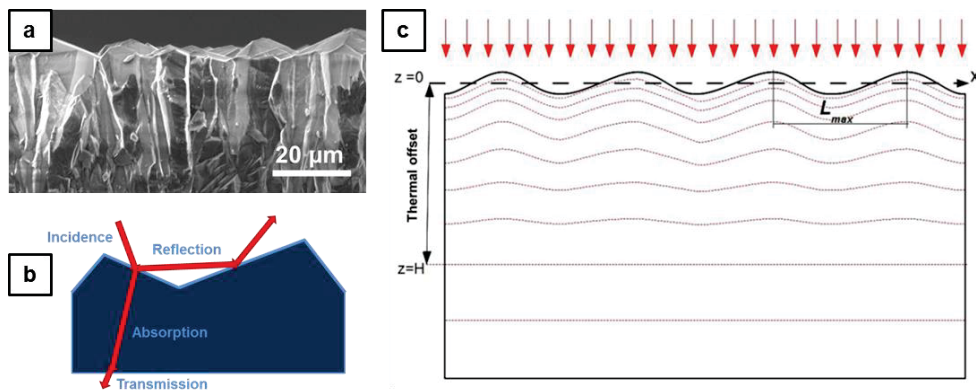


Figure 3.40: (a) SEM micrograph showing the roughness on the top surface of a diamond film. (b) Different optical paths induced by the roughness. (c) Isotherms propagating into a rough semi-infinite media.

Therefore, the roughness of the diamond films may induce additional thermal resistance on the top surface of the diamond layer. This would result in an increase in the interface thermal resistance between the diamond film and the optical transducer located on the top surface (see section 3.4.4). Figure 3.40c shows isotherms propagating into a semi-infinite solid from a rough surface with a sinusoidal profile. If the surface is at constant temperature, the isotherms will strictly fit to the surface profile. The disturbed profile of the isotherms will become more plane as the heat wave progresses through the material (once the thermal offset has been overcome). The required depth for the isotherms to become planar is a function of the heat diffusion length  $l$  (eq. 3.13).

No plane-surface equivalent profile was adopted in this study to model the roughness of the diamond film. However, estimation of the additional thermal resistivity induced by the roughness of the diamond films is carried out in section 3.5.

### 3.4.3 Photothermal radiometry: experimental set-up

The excitation source used in the experiment is a laser which spatial distribution is known and that may be easily collimated. The continuous laser beam is periodically modulated in intensity by an acousto-optic modulator allowing tuning the frequency of the optical signal from the hertz up to the megahertz without deteriorating the geometric profile of the laser beam. The excitation photothermal signal comes heat up the surface of the sample, and the resulting thermal response under the form of infrared emissions is collected and focalized by a set of parabolic mirrors onto the objective of an infrared detector.

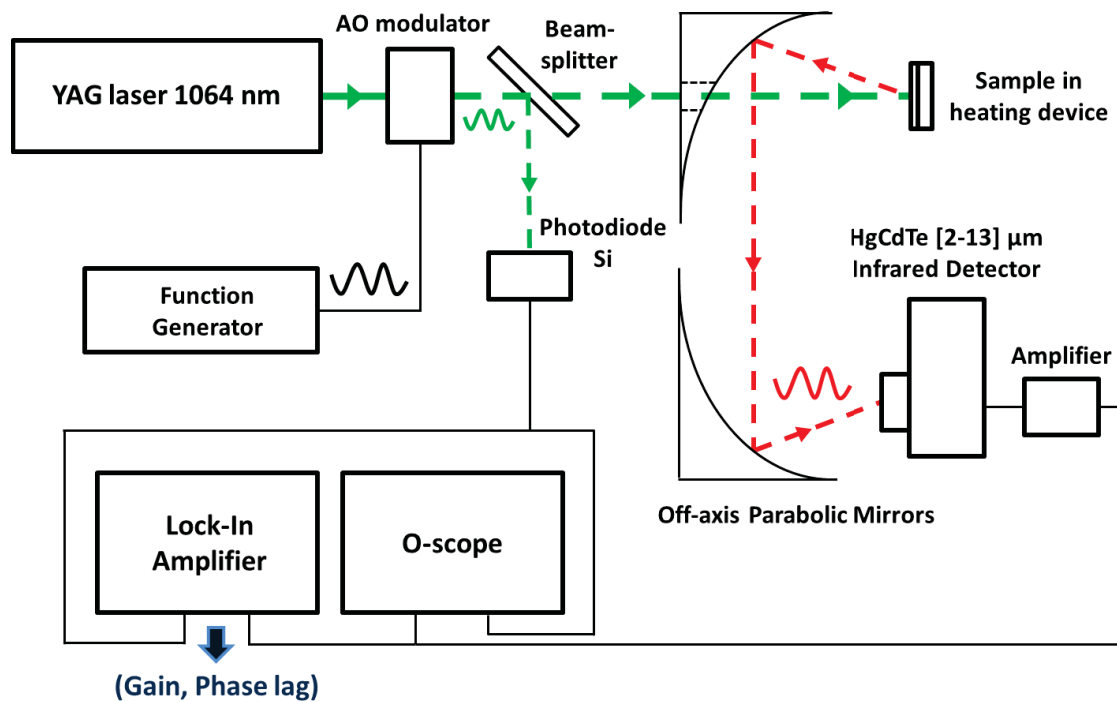
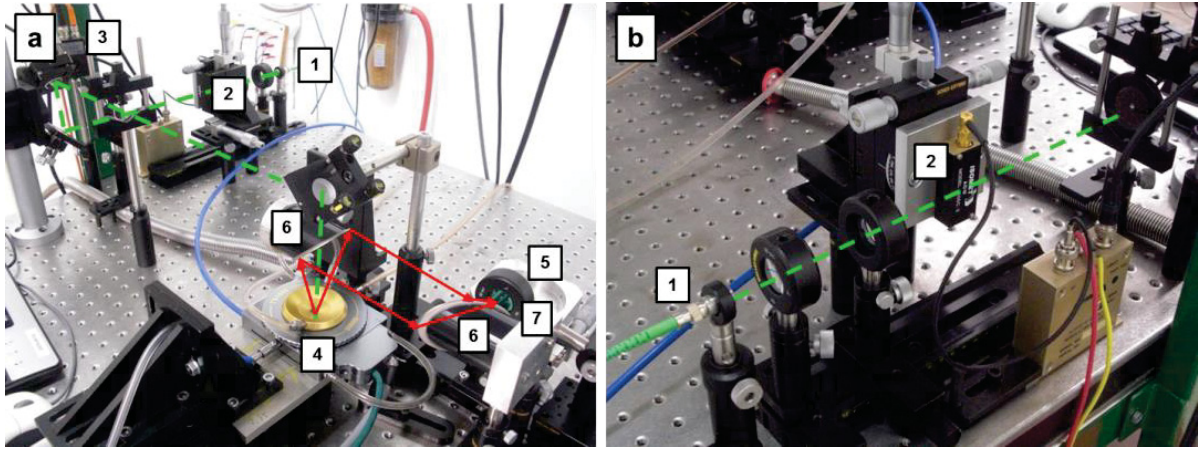


Figure 3.41: Scheme of the modulated photothermal radiometry experimental set-up [182, 185].

Besides, a high-speed photodiode (showing a responding time in the order of the nanosecond) records the laser signal exiting the acousto-optic modulator in order to provide a reference for the measure of the phase and amplitude of the response signal. The photodiode is located after the acousto-optic since this one may induce a delay on the laser signal, thus adding a potential phase lag varying with frequency, which has to be recorded.

The PTR experimental set-up depicted in Fig. 3.41 is composed of the following elements:

1. A continuous fiber-optics YAG laser (1 in Fig. 3.42) of 1064 nm and 5 W maximum power. The laser beam was modulated in intensity by an acousto-optic modulator in the range and is brought to the sample surface by a set of mirrors. The laser beam had a Gaussian profile of power distribution on the spot of 3 mm in diameter at  $1/e^2$ ;
2. An acousto-optic modulator (2 in Fig. 3.42; Isomet 1205C with a  $\text{PbMoO}_4$  crystal) driven by a function generator Agilent 33120A scanning the  $f = [0.7 - 21]$  kHz frequency range and modulating the laser beam in intensity, and thus in frequency, through a square signal;
3. A fast photodiode (3 in Fig. 3.42; ThorLabs DET10A/M with a silicium detector (showing a response time of 10 ns, sensitive in the [200-1100] nm spectral range)) measures the excitation signal. It is connected to the reference port of a lock-in amplifier from Stanford Research which records it;
4. A sample-holding chamber (4 in Fig. 3.42; Linkam TS 1200) that can heat up the sample up to 1200°C in a controlled vacuum atmosphere (down to  $10^{-6}$  mbar). The window of the chamber is made of a  $\text{BaF}_2$  and is transparent to visible and infrared light on the whole operation range of the laser and infrared detector;
5. A photoconductor detector (5 in Fig. 3.42; HgCdTe Judson J15D12) calibrated in phase for the measure of the thermal response variations at the surface of the sample. The detector is only sensitive to flux variation thus not to the temperature set by the chamber environment  $T_0$ . It detects the heat flux variation through the infrared radiation change and converts it into an electrical signal. The detector is sensitive in the  $[2 - 12]$   $\mu\text{m}$  spectral range and is equipped with an AMTIR-1 window (7 on Fig. 3.42) which filters the visible component of the excitation laser beam through a  $[0.7 - 11]$   $\mu\text{m}$  transmission range. The area in the scope of the IR detector corresponds to the circle of 0.5 mm in diameter of the excited zone of the sample;
6. Two off-axis parabolic mirrors (6 in Fig. 3.42) which collect and focus the infrared radiations emitted from the sample surface onto the infrared detector. The mirrors are covered with a thin film of rhodium for optimal infrared detection (rhodium presents a reflection rate over 90% in the  $[2 - 12]$   $\mu\text{m}$  spectral range);



**Figure 3.42: Photographs of the modulated photothermal radiometry experimental set-up.**

7. A lock-in amplifier Stanford Research SR 830 is used to measure the phase and amplitude of the thermal response using the photodiode signal as a reference. This device allows detecting a signal surrounded by a noise with an amplitude 1000 times higher. The integration time of measurement is set to 1 s; Due to an additional delay induced by the amplifier intern to the infrared detector, the phase has to be corrected for frequency above 10 kHz according to:  $\Phi_{cor} = 2.83 \times 10^{-4} f + \Phi_{mes}$ .
8. A Labview interface automatically records the phase and amplitude curves as a function of the frequency and temperature of the chamber.

### 3.4.4 Optical transducer

Given the thicknesses of the CVD diamond films considered ([2-15]  $\mu\text{m}$ ), the absorption of the laser excitation into the sample is considered as a surfacic phenomenon since the thickness of the deposit is small relative to the heat penetration depth. As mentioned in chapter 1, diamond is optically transparent on a large wavelength domain, and in particular at 1064 nm (its optical extinction coefficient  $\kappa$  is close to zero on the [0.7 - 12]  $\mu\text{m}$  spectral range). Thus, diamond does not absorb the laser excitation signal at the wavelength we use. Indeed, the absorptivity  $\beta$  of a material toward a light source with wavelength  $\lambda$  is given by:

$$\frac{1}{\beta} = \frac{\lambda}{4\pi\kappa} \quad (3.23)$$

Where  $\kappa$  is the coefficient of optical extinction of the material considered.

The optical extinction coefficient of diamond being close to zero at 1064 nm, it shows an absorptivity close to zero. Therefore, it is necessary to use an optical transducer, under the form of a thin (30 nm) metallic film coating the diamond surface, in order for the sample to absorb the laser excitation, i.e. to convert the flux of photons into a heat flux.



The optical transducer has to fulfill several criteria:

- High-temperature stability: in order not to be degraded by measurement at elevated temperatures;
- Low reflectivity and high emissivity toward the laser source;
- Low thickness relative to the thickness of the deposit. Its thickness must be high enough to convert 90% of the optical flux into a heat flux.

Platinum (Pt) fulfills these requirements. It presents a coefficient of optical extinction  $\kappa$  of 2.7 and a reflectivity of 60% at 1064 nm. It also shows a high melting temperature ( $T_{m, Pt} = 1768^\circ\text{C}$ ). A 30 nm-thick Pt film is thus coated onto the top surface of the diamond film through physical vapor deposition (PVD), as shown onto Fig. 3.43. By applying Beer-Lambert's law, it can be demonstrated that a 30 nm thick Pt layer is enough to absorb 90% of the optical flux [182].

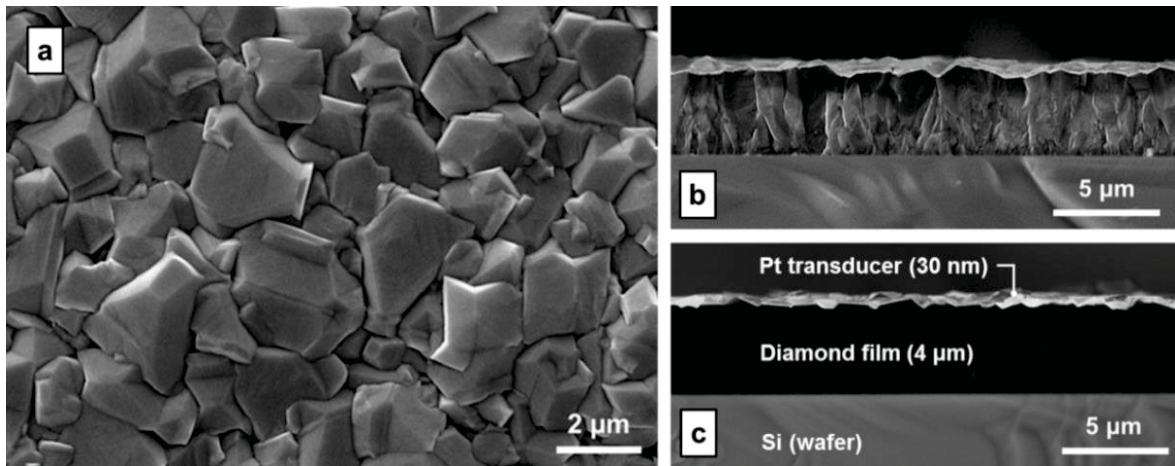


**Figure 3.43: SEM micrographs of the diamond films analyzed through modulated PTR:**

**(a) top surface, (b) cross-section in SE mode, (c) cross-section in BSE mode showing the Pt transducer.**

On Figure 3.43a, the typical polycrystalline morphology of a diamond film grown through laser-assisted combustion synthesis and coated with a 30 nm Pt layer is visible. One can see that the Pt-film sticks to the morphology variation of the film and is not affected by the roughness of the surface. Figure 3.43b shows the columnar grain structure of the films from a cross-sectional perspective, while Fig. 3.43c allows observing the Pt transducer film coating the top-surface of the diamond film through BSE imaging.

### 3.4.5 Results

Modulated PTR was successfully carried out onto diamond films with thicknesses of 5  $\mu\text{m}$ , 10  $\mu\text{m}$ , 12.5  $\mu\text{m}$ , and 15  $\mu\text{m}$ , respectively. The diamond films were grown under the same conditions (substrate temperature set to  $780^\circ\text{C}$ , flame-to-substrate distance set to 0.8 mm,  $\text{O}_2/\text{C}_2\text{H}_2/\text{C}_2\text{H}_4$  gas

ratio set to 1.2/0.6/0.6) through laser-assisted combustion synthesis using the 10.532  $\mu\text{m}$  laser excitation in order to induce the resonant excitation of the  $\text{CH}_2$ -wagging mode of ethylene molecules, thus promoting both growth rate and diamond phase purity. Their deposition times were 10 minutes, 20 minutes, 40 minutes, and 50 minutes, respectively.

Despite the presumption that heat transfer in the diamond films should be modeled using the resistive approach due to the expected high thermal diffusivity of the films, the capacitive approach was shown to provide the best fits between experimental data and theoretical predictions. This was ascribed to the presence of extensive thermal resistances in the samples, as detailed in Tab. 3.3. In addition, the heat transfer geometry was shown to be more accurately modeled as 2D instead of 1D, despite the fact that the laser spot diameter is much larger than the maximum heat diffusion length in our samples.

The fits between the measured and theoretical amplitude and phase of thermal infrared responses obtained from the diamond films are plotted as a function of frequency on Fig. 3.44a and 3.44b, respectively. The fits were recorded in the [0.7 – 21] kHz frequency range. At frequency higher than 21 kHz, the intensity of the thermal response of the samples was insufficient to be recorded. The experimental phase and amplitude evolutions fit remarkably well the evolutions simulated through the theoretical model.

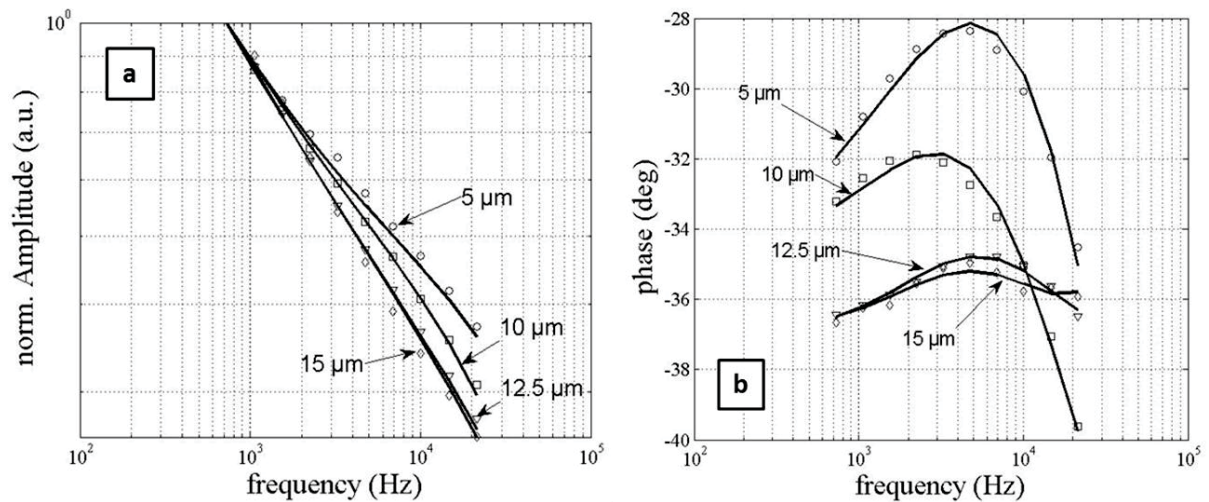


**Figure 3.44: Fitting results between experimental and simulated (a) amplitude and (b) phase evolutions as a function of excitation frequency.**

Table 3.3 gathers the estimations of the thermal conductivity of the diamond films and of the thermal resistances at the Pt/diamond ( $R_{Pt/dia}^{th}$ ) and diamond/Si ( $R_{dia/Si}^{th}$ ) interfaces. In addition, Tab. 3.3 shows roughness estimations gathered from the samples in order to support the estimations of  $R_{th Pt/dia}$ . It was estimated from the fits of Fig. 3.34 that the bulk thermal conductivity of the diamond film was located in the [450 – 500]  $\text{W.m}^{-1}.\text{K}^{-1}$  range for all the samples, which is

consistent with the range of thermal conductivity estimations of CVD diamond films provided in previous studies [46-48]. Finally, Tab. 3.3 shows estimations of the thermal conductivity of an affected diamond layer, corresponding to the very first growth layers of the diamond films, and assumed to show strong resistance to the heat flux. This concept is detailed in the discussion section (section 3.5).

**Table 3.3: Estimations of thermal conductivity and TBR of the diamond films analyzed through PTR.**

$e_d$ ( $\mu\text{m}$ )	5	10	12.5	15
$k_{dia}$ ( $\text{W.m}^{-1}.\text{K}^{-1}$ )	[450 - 500]			
$R_a$ (nm)	210	380	420	450
$R_{Pu/dia}^{th} \times 10^{-7}$ ( $\text{K.m}^2.\text{W}^{-1}$ )	0.51	0.91	0.97	1.10
$R_{dia/Si}^{th} \times 10^{-7}$ ( $\text{K.m}^2.\text{W}^{-1}$ )	3.69	3.09	1.72	1.71
$k_{a-dia}$ ( $\text{W.m}^{-1}.\text{K}^{-1}$ )	1.023	1.286	3.117	3.150

Accordingly to the trend predicted by the transfer function of the semi-infinite media model, the amplitude of the thermal response was observed to decrease for all samples as the excitation frequency increases. This is due to the fact that, as excitation frequency increases, the volume of material probed through PTR decreases, thus leading to a reduction of the temperature elevation induced in the sample. Therefore, the amplitude of infrared radiations tends to decrease with increasing frequency.

The phase signals do not start at  $-45^\circ$  due to the thermal resistivities existing in the samples, which induces a deviation from the model of the semi-infinite media. However, similarly to the amplitude, the phase of the thermal response tends to follow the trend predicted by the transfer function of the semi-infinite media by increasing with frequency between 0.7 kHz and 5 kHz. In the [5 - 21] kHz range, the heat diffusion length becomes smaller as the frequency increases, and the influence of the thermal resistance  $R_{th}$  becomes larger, thus leading to an additional deviation of the system from the semi-infinite media model, and to a decrease in the phase signal.

Finally, one can also notice the higher sensitivity to  $R_{th}$  of the phase signal relative to the amplitude signal. While almost no difference can be made between the amplitude signals of the 12.5 and 15 m thick diamond films, their respective phase signals show significant difference, due to the different interfacial thermal resistance they exhibit, even though this difference is small.

In the next section, we will try to interpret the results obtained from PTR analysis in terms of relationships between the microstructure and chemical composition of the diamond films and their thermal conductivity. Also, an architecture of the silicon/diamond interface will be proposed and the contribution of its different components to the diamond/Si thermal resistance will be theoretically estimated through the diffuse mismatch (DM) model.

### 3.5 Influence of the growth process and microstructure on the thermal properties of diamond films

#### ▪ *Levels of thermal conductivity and thermal resistance:*

The results obtained from PTR analysis of the diamond films demonstrate that, despite the open-air process conditions propitious to non-diamond content incorporation into the film microstructure, the diamond films grown through laser-assisted combustion synthesis are remarkable heat conductors, with thermal conductivity ranging between 450 and 500 W.m<sup>-1</sup>.K<sup>-1</sup> for each sample. This promising thermal conductivity is in agreement with the high phase purity demonstrated by the films through Raman spectroscopy in section 3.3.3. The thermal conductivities obtained from the diamond films are comparable to those reported for diamond films deposited through hot-filament assisted CVD or microwave-plasma assisted CVD [46-48]. This is ascribed to the beneficial effects of the multienergy deposition process in which inputs from the laser couple with those of the combustion flame, leading to enhanced diamond phase purity.

On the other hand, the estimations of the thermal resistance at the diamond/Si interface ( $R_{dia/Si}^{th}$ ) range from  $1.7 \times 10^{-7}$  K.m<sup>2</sup>.W<sup>-1</sup> to  $3.7 \times 10^{-7}$  K.m<sup>2</sup>.W<sup>-1</sup>. These estimation of  $R_{dia/Si}^{th}$  are about ten times higher relative to those typically reported for other diamond deposition processes such as hot-filament and microwave plasma-assisted CVD [177, 178]. As an enlightening comparison, section 3.4.1 provides examples of previous works carried out to estimate the thermal resistance at the interface between diamond films and various substrate materials. It appears from these previous studies that the thermal resistance at the diamond film/substrate interface is typically in the order of  $10^{-8}$  K.m<sup>2</sup>.W<sup>-1</sup>, thus ten times lower than that exhibited by the diamond films grown through laser-assisted combustion synthesis. This shows that, unlike the thermal conductivity of the bulk diamond film which is affected in a very limited way by the open-air environment and shows promising level, the diamond/Si interface strongly suffers from the open-air processing conditions and exhibits high level of heat flux resistance relatively to diamond/Si assemblies grown through classical vacuum-based CVD routes.

In addition, the thermal resistance at the Pt/diamond interface  $R_{Pt/dia}^{th}$  has been estimated to range from  $0.51 \times 10^{-7}$  K.m<sup>2</sup>.W<sup>-1</sup> to  $1.10 \times 10^{-7}$  K.m<sup>2</sup>.W<sup>-1</sup>. In agreement with the heat flux lines contrition effect depicted in Fig. 3.40, the thermal resistance at the Pt/diamond interface is measured to increase as the diamond film thickness and roughness increase. Despite  $R_{Pt/dia}^{th}$  is one order of magnitude lower than  $R_{dia/Si}^{th}$ , the thermal resistance at the Pt/diamond interface is shown to be far from being negligible.

Finally, these results demonstrate that the diamond/Si interface is about ten times more thermally resistive than either Pt/diamond interface or the bulk diamond film, enlightening the critical role played by the film/substrate interface in the heat diffusion process through bi-layered assemblies. Indeed, the thermal resistance of a 10  $\mu\text{m}$  thick bulk diamond film with a thermal conductivity of 500  $\text{W}\cdot\text{m}^{-1}\cdot\text{K}^{-1}$  is equal to:  $R_{dia} = e_{dia}/\lambda_{dia} = 2 \times 10^{-8} \text{ K}\cdot\text{m}^2\cdot\text{W}^{-1}$ , thus ten times lower than the recorded values for  $R_{dia/Si}^{th}$ .

▪ **Presence of foreign material at the diamond/Si interface:**

Due to the high temperature of the deposition process used in this study, it was expected to find compounds such as SiC and SiO<sub>2</sub> on the form of additional interfacial layers between the diamond film and the silicon substrate. The existence of foreign materials responsible for the high thermal resistance at the diamond/Si interface was sought to be detected through SEM and AES analyses. However, no thick interphase was detected through none of these techniques. Figure 3.45 shows SEM micrographs and AES in-depth line profiles of the back face of a diamond film grown through laser-assisted combustion synthesis on a Si substrate and then delaminated:

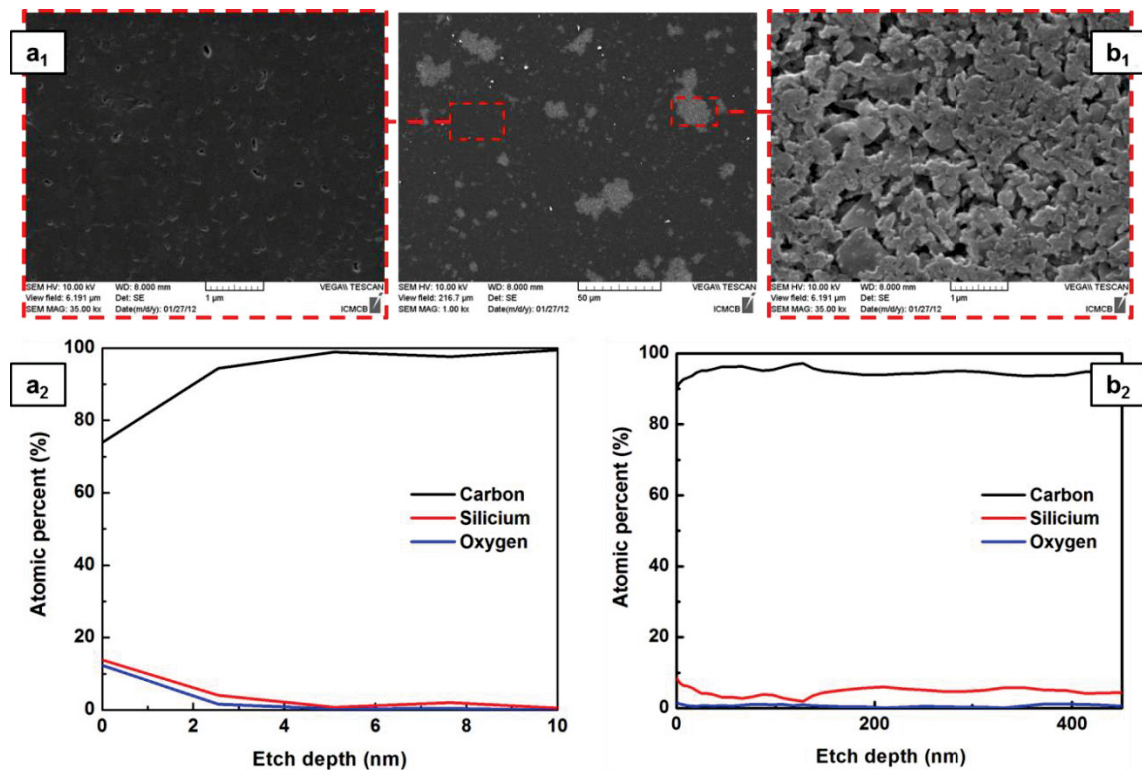


Figure 3.45: SEM micrographs of the backside of a CVD diamond film delaminated from a Si substrate (a<sub>1</sub>, b<sub>1</sub>) and AES in-depth line profiles of the different areas detected (a<sub>2</sub>, b<sub>2</sub>).

In agreement with the Auger analysis, no thick interphase material is observed through SEM. However, it was detected through SEM and AES that Si-rich areas existed on the back face of the delaminated diamond film. These areas were distinguishable through their white color (Fig. 3.45b<sub>1</sub>)



and showed consistent content of Si up to 400 nm in depth of the diamond film structure (Fig. 3.45b<sub>2</sub>). This type of Si-rich areas was similarly observed in previous studies [186].

However, no clear conclusion about the composition of these Si-rich areas of the diamond/Si interface could be made. It was demonstrated in previous studies that cubic silicon carbide ( $\beta$ -SiC) and amorphous silicon carbide (a-SiC) could form at the diamond/Si interface upon diamond growth [187], but no conclusion could be drawn on the fact that silicon carbide exists in the diamond film, since the white areas detected through SEM and AES could originate from the diffusion of Si atoms into the diamond film with no carbide formation (thus leading to a Si/C solid solution). Nevertheless, the interfacial Si/C mixed areas revealed through Auger analyses are assumed to be responsible for the chemical anchorage of the diamond grains to the Si substrate.

Likewise, the presence of an oxygen-rich layer on the top surface of a Si substrate from which a CVD diamond film had been delaminated was sought through in-depth AES line-profiling:

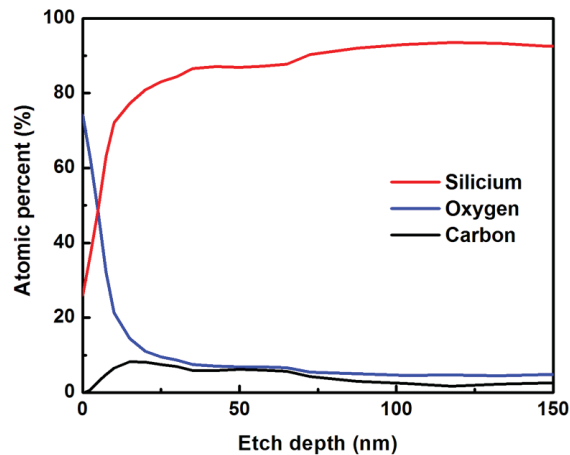


**Figure 3.46:** AES in-depth line profile on a Si substrate delaminated from a CVD diamond film.

The AES analysis demonstrated that oxygen was present in the Si substrate up to a depth of about 100 nm. This oxygen layer may form amorphous silica (a-SiO<sub>2</sub>) within the substrate or consist of a silicon/oxygen solid solution. The presence of an oxygen-rich layer in the upper layers of the Si substrate was ascribed to the open-air process environment and to the strongly oxidizing flame environment. Upon exposure to oxygen and high temperature, it is known that Si oxidized, leading to the creation of silicon oxide (SiO<sub>2</sub>). Thus, the oxygen-rich layer detected on top of the Si substrate was assumed in this study to be composed of SiO<sub>2</sub>.

▪ ***Influence of the microstructure of the diamond films:***

Rather than originating from the presence of a thermally resistive interphase of foreign material, which is not detected through SEM or Auger analyses, the relatively high level of thermal resistance measured at the diamond/Si interface may have several sources.

One of them is the presence of foreign materials such as those detected through AES:  $\text{SiO}_2$  originating from Si substrate oxidation, and Si/C compounds formed through interatomic diffusion of Si and C.

The second factor that affects the thermal resistance of the diamond/Si interface is the initial roughness of the Si substrate. Indeed, the Si substrates were laser-roughened prior to diamond deposition in order to promote diamond nucleation (see section 3.3.5). Thus, we introduce an additional roughness at the diamond/Si interface, which increases its thermal resistance.

Finally, the columnar structure of the films contributes to increase the thermal resistance at the diamond/Si interface. Indeed, in the lower layers of the film, the diamond film is made of numerous but randomly oriented and relatively small crystals with a high amount of grain boundaries. Grain boundaries being surface of high energy, they constitute preferential locations for impurities incorporations. As the deposition process goes on, columnar growth dominates, forming fewer but relatively larger diamond crystals with fastest crystallographic growth direction oriented normal to the substrate. Therefore, imperfections such as grain boundaries and impurities exist in large quantity in the layers neighboring the interface, while the upper parts of the film are made of large single diamond crystals. The phonon mean free path in the normal direction is longer in the columnar grains of the upper layers of the film relative to that in the smaller grains in the vicinity of the interface. This contributes to explain the strong resistance to the heat flux exhibited by the diamond/Si interface. This also means that the diamond/Si interface considered in this study not only consists in the physical interface separating the film and the substrate, but also includes the very first layers (up to 1  $\mu\text{m}$  thick) of the diamond deposit, which are made of a fine grain structure in which a-SiC,  $\beta$ -SiC, but also amorphous carbon (a-C) may be embedded.

Moreover, it is remarkable that, while the volume thermal resistance of the diamond films is estimated to keep in the same range for all samples, the thermal resistance between the diamond film and the silicon substrate is measured to decrease as the diamond film thickness increases. This is consistent with the fact that, at constant excitation frequency, the amplitude of IR emissions from the films decreases when the films get thicker, as shown on Fig. 3.44a. Since the level of IR radiations resulting from the laser excitation is proportional to the temperature of the layered sample (according to Planck's law of radiation), and that the Si substrate is the same for all the samples tested, we can state that the temperature raise of the sample induced by the laser excitation decreases when the film gets thicker. This means that the heat flows more easily through the diamond/Si assembly when the diamond film thickness increases, which is consistent with the decrease of TBR at the diamond/Si interface with increasing film thickness. This trend also confirms that the diamond/Si interface considered in this study includes the first layers of the diamond deposit.



Therefore, the decrease in thermal resistance at the diamond/Si interface with increasing thickness must inevitably be due to modifications either in the chemistry or in the microstructure of the downer layers of the diamond films. Indeed, the thicker samples having been exposed to the flame environment during a longer time, it is possible that thermally-activated diffusion and grain growth phenomena have influenced the structure and composition of the diamond film in the vicinity of the interface with the Si substrate.

This assumption was supported by Raman spectroscopic investigations of diamond films with equivalent thicknesses but different times of exposure to the flame environment (20 minutes and 50 minutes, respectively). At similar thickness, the diamond film exposed 50 minutes to the laser-assisted combustion deposition process showed strongly enhanced  $sp^3/sp^2$  carbon ratio relative to the film grown during 20 minutes, as shown on Fig. 3.47. Figure 3.47 also displays the full width at half maximum (FWHM) of the diamond peak of each spectrum, indicating the diamond phase purity. At equivalent thicknesses, the Raman peak width of diamond is observed to decrease from  $7.5\text{ cm}^{-1}$  to  $5.9\text{ cm}^{-1}$  for a 20-minutes grown film, and from  $4.9\text{ cm}^{-1}$  to  $3.9\text{ cm}^{-1}$  for a 50-minutes grown film.

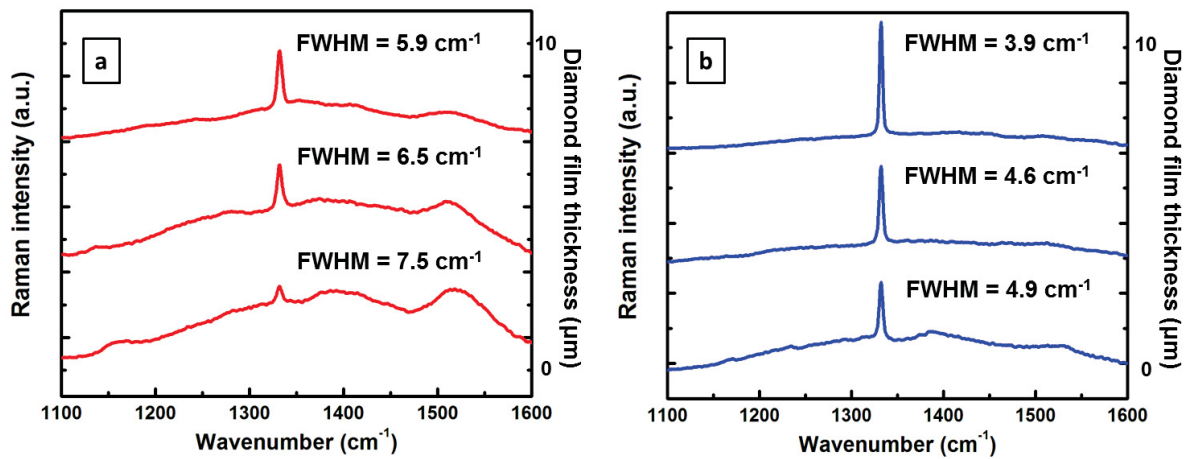


**Figure 3.47: Raman spectra of  $10\text{ }\mu\text{m}$ -thick diamond films grown (a) 20 minutes and (b) 50 minutes through laser-assisted combustion synthesis with respect to film thickness.**

This first confirms an increase in diamond phase purity with film thickness, and an enhancement of diamond phase purity with exposition time to the flame environment. This trend is observed on the whole thickness of the diamond film, and is especially remarkable in the lower diamond layers close to the Si substrate. The phase purity enhancement of the highly-resistive lower layers of the film with increasing deposition time is assumed to be responsible for the decrease in the thermal resistance at the diamond/Si interface with increasing film thickness recorded though PTR experiments.

Based on the AES analyses demonstrating the presence of silicon-rich zones in the lower parts of the diamond film and oxygen-rich zones in the upper parts of the silicon substrate, the diamond/Si interface can be viewed as a layered assembly as that shown in Fig. 3.48. The interface region is viewed as composed of the superposition of a thermal  $\text{SiO}_2$  layer on top of the Si substrate (labeled as  $a\text{-SiO}_2$ ), of an affected diamond film region in which small diamond crystals,  $a\text{-SiC}$ ,  $\beta\text{-SiC}$ , and  $a\text{-C}$  coexist (which is further assimilated to an amorphous silicon carbide region and labeled as  $a\text{-dia}$ ), and a top layer made of the first layers of the columnar-structured diamond film.

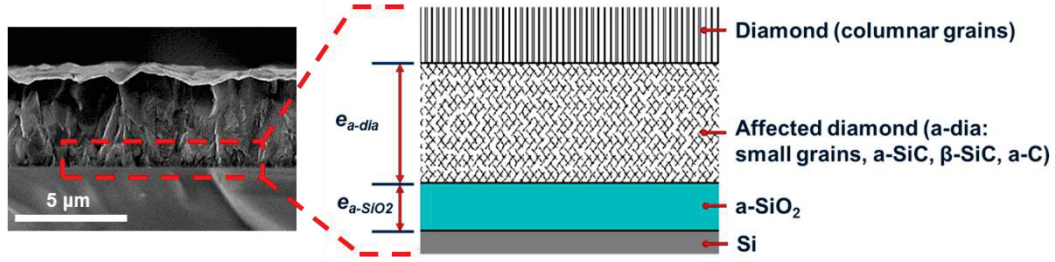


Figure 3.48: Schematic view of the composition of the diamond/Si interface.

Based on AES analyzes, the thicknesses of the  $a\text{-SiO}_2$  and affected diamond layers are assumed to be independent of the thickness of the diamond film deposited and respectively equal to  $e_{a\text{-SiO}_2} = 100 \text{ nm}$  and  $e_{a\text{-dia}} = 300 \text{ nm}$ . In the next section, the diffuse mismatch (DM) model will be used to theoretically estimate the respective contribution of the different layers to  $R_{dia/Si}^{th}$ .

▪ **Theoretical estimation of interfacial thermal resistance through the diffuse mismatch (DM) model:**

The parameters gathered in Tab. 3.4 will be used to theoretically estimate the different interfacial thermal resistances existing in the Pt/diamond/Si layered samples and thus provide an estimation of their respective contributions to the global thermal resistance.  $\Theta_D$ ,  $\rho$ ,  $C_p$ ,  $k$ ,  $v_l$ , and  $v_t$  respectively stand for the Debye temperature, the density, the specific heat, the thermal conductivity, and the longitudinal and transversal phonon velocity:

Table 3.4: Physical parameters of platinum, CVD diamond, amorphous silicon carbide, amorphous silica, and silicon used for DMM calculations.

Material	$\Theta_D$ (K)	$\rho$ (g.cm <sup>-3</sup> )	$C_p$ (J.kg <sup>-1</sup> .K <sup>-1</sup> )	$k$ (W.m <sup>-1</sup> .K <sup>-1</sup> )	$v_l \times 10^6$ (cm.s <sup>-1</sup> )	$v_t \times 10^6$ (cm.s <sup>-1</sup> )
Pt	240	24.45	130	71.6	0.4174	0.1750
dia (CVD)	2240	3.51	540	-	1.467	1.281
a-SiC	600	3.05	640	1.2	0.720	0.425
a-SiO <sub>2</sub>	246	2.20	787	1.43	0.834	0.590
Si	674	2.33	700	148	0.663	0.404

The diffuse mismatch (DM) model first allows theoretical estimation of the thermal resistance existing at the interface between the diamond film and the platinum transducer. Since  $\Theta_{D,d} \gg \Theta_{D,Pt}$ , the thermal resistance at the diamond/platinum may be approximated by [97]:

$$R_{Pt/dia}^{th} = \frac{4}{\tau_{Pt/dia} c_{p,Pt}(T) c_{D,Pt}} \quad (3.24)$$

Where the phonon transmission probability at the platinum/diamond interface  $\tau_{Pt/dia}$  is defined as:

$$\tau_{Pt/dia} = \frac{\sum_{s=l,t} v_{s,dia}^{-2}}{\sum_{s=l,t} v_{s,Pt}^{-2} + \sum_{s=l,t} v_{s,dia}^{-2}}$$

And the phonon velocity (Debye velocity,  $\text{m.s}^{-1}$ ) in the platinum transducer  $c_{D,Pt}$  is given by:

$$c_{D,Pt} = \frac{(v_{l,Pt} + 2v_{t,Pt})}{3}$$

Using the data of Tab. 3.4, eq. 3.24 leads to an estimation of the thermal resistance at the interface between the diamond film and the optical transducer of:  $R_{Pt/dia}^{th} = 2.125 \times 10^{-8} \text{ K.m}^2.\text{W}^{-1}$ . This value is remarkably consistent with the experimental value of  $R_{Pt/dia}^{th}$  measured through PTR on the 5  $\mu\text{m}$ -thick diamond film and reported in Tab. 3.3 ( $R_{Pt/dia}^{th} = 5.1 \times 10^{-8} \text{ K.m}^2.\text{W}^{-1}$ ). However, the agreement between the theoretical estimation and the experimental values of  $R_{Pt/dia}^{th}$  is affected as the diamond film thickness and roughness increase. Indeed, as film roughness increases, the contrition of the heat flux lines (Fig. 3.40) is accentuated, thus leading to a stronger thermal resistance at the interface between the platinum transducer and the diamond film.

Based on the view of Fig. 3.48, the thermal resistance of the interface region between the diamond film and the Si substrate may be decomposed as:

$$R_{dia/Si}^{th} = R_{dia/a-dia}^{th} + \frac{e_{a-dia}}{k_{a-dia}} + R_{a-dia/a-SiO_2}^{th} + \frac{e_{a-SiO_2}}{k_{a-SiO_2}} + R_{a-SiO_2/Si}^{th} \quad (3.25)$$

Where  $R_{dia/a-dia}^{th}$ ,  $R_{a-dia/a-SiO_2}^{th}$ , and  $R_{a-SiO_2/Si}^{th}$  are estimated through eq. 3.24 and using the parameters given in Tab. 3.4, similarly to  $R_{Pt/dia}^{th}$ .

Knowing that the respective Debye temperatures of diamond, SiC, SiO<sub>2</sub>, and Si are as  $\Theta_{D,Dt} > \Theta_{D,Si} > \Theta_{D,a-SiC} > \Theta_{D,a-SiO_2}$ , the DM model allows estimating the contribution of the different layers of Fig. 3.47 to the thermal resistance  $R_{dia/Si}^{th}$ . Eq. 3.24 leads to the following theoretical estimations of interfacial thermal resistances:

$$R_{dia/a-dia}^{th} = 3.419 \times 10^{-9} \text{ K.m}^2.\text{W}^{-1},$$

$$R_{a-dia/a-SiO_2}^{th} = 9.976 \times 10^{-10} \text{ K.m}^2.\text{W}^{-1},$$

$$R_{a-SiO_2/Si}^{th} = 1.424 \times 10^{-9} \text{ K.m}^2.\text{W}^{-1}.$$

Finally, assuming that those values are independent of the diamond film thickness, and given the measured and assumed values, respectively, of  $R_{dia/Si}^{th}$  and of the thicknesses of the  $\text{SiO}_2$  and affected diamond regions, one finds the theoretical thermal conductivity of the affected diamond layer reported in Tab. 3.3. ( $k_{a-dia}$ ). It appears clearly that the affected diamond region has a very low thermal conductivity, thus representing a strong thermal resistance to the heat flux at the diamond/Si interface. Of course,  $k_{a-dia}$  is estimated to increase with increasing diamond film thickness.

### **3.6 Deposition of combustion CVD diamond films on copper and copper/carbon composite substrates.**

Although it allows the investigation of their thermal properties through infrared photothermal radiometry, the deposition of diamond films onto silicon substrates only represent a limited interest from a thermal management prospective. Indeed, although diamond/Si assemblies have been long-time recognized as promising alternatives to the traditional Si/ceramic assemblies to provide the package with electrical insulation, thermal conductivity, and mechanical support, the growth of diamond films upon the temperature levels encountered in processes such as laser-assisted combustion CVD synthesis would catastrophically affect the microstructure of the active chip.

Thus, in the scope of heat spreading diamond films, it is of great interest to transpose the diamond films deposition process presented in this chapter to heat dissipative substrate materials, such as copper and copper/carbon composites. In this study, attempt was made to achieve the fabrication of hybrid thermal management substrates combining a heat-spreading CVD diamond film and a heat-sinking substrate either made of copper or copper-matrix composite.

Figure 3.49 shows SEM micrographs resulting from an attempt to grow diamond onto pure copper using a graphite spray interlayer to promote the nucleation process. Because of the large CTE mismatch between copper ( $\alpha_{Cu} = 17 \times 10^{-6} \text{ }^\circ\text{C}^{-1}$  at 293 K) and diamond ( $\alpha_{dia} = [1-2] \times 10^{-6} \text{ }^\circ\text{C}^{-1}$  at 293 K), this approach was shown to suffer from critical delamination and cracking issues, even after low deposition times, due to the extensive thermal stress generated in the diamond film upon cooling.



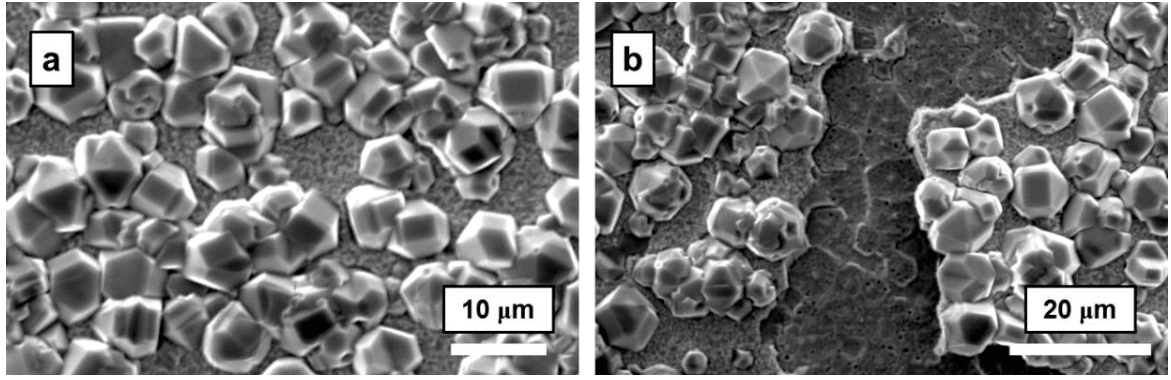


**Figure 3.49: SEM micrographs of diamond nuclei onto a graphitized copper substrate.**

Consequently, it was required to decrease the CTE of the substrate material in order to mitigate the thermal stress induced by the deposition process. Ceramic-reinforced copper matrix composite materials offer ideal solution for tuning the thermal expansion coefficient of the substrate. In this study, carbon fiber-reinforced copper matrix (Cu/C) composites were used as substrate materials (Fig. 3.50). The substrates were fabricated through powder metallurgy and hot pressing under the following processing conditions: 650°C, 30 bars, 20 minutes (see section 4.7.2). The carbon fibers used were commercial Teijin carbon fibers with longitudinal thermal conductivity of  $600 \text{ W}\cdot\text{m}^{-1}\cdot\text{K}^{-1}$ . The reinforcement volume fraction was set to 40%. A  $10\times 6 \text{ cm}^2$  Cu/C composite plate with thickness of 4 mm was fabricated and individual cylindrical substrates with diameter of 6 mm were subsequently machined. The choice of attempting to deposit CVD diamond onto Cu/C substrates instead of Cu/D substrates is driven by both cost and machining considerations.

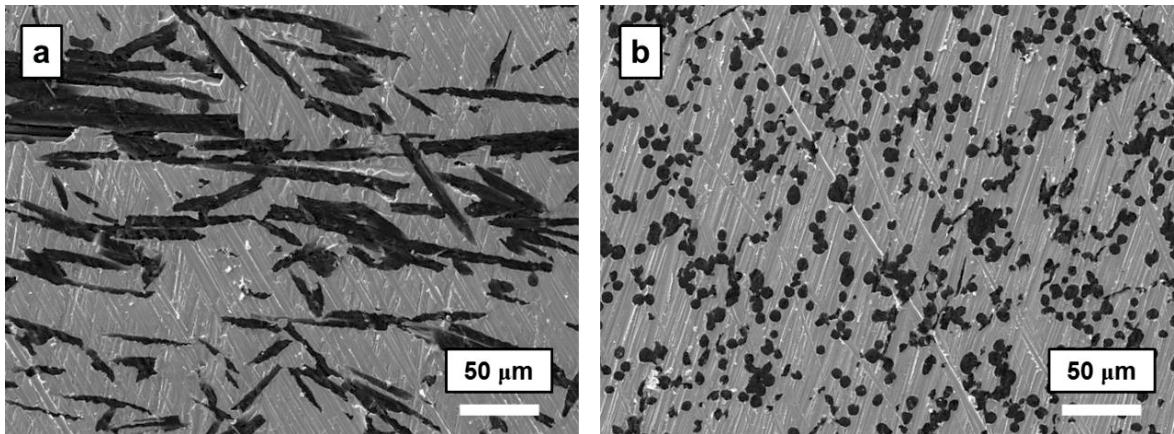


**Figure 3.50: (a) Top surface and (b) cross section SEM micrographs of Cu/C composite substrates.**

The carbon fibers were observed to be preferentially orientated perpendicularly to hot pressing direction. The Cu/C substrates were shown to exhibit a CTE of  $9\times 10^{-6} \text{ }^{\circ}\text{C}^{-1}$  in the longitudinal sense (parallel to the fibers direction, thus parallel to the diamond deposition surface). On the other hand, the CTE in the transverse direction (perpendicular to the diamond deposition surface) was shown to be the same as that of pure copper:  $17\times 10^{-6} \text{ }^{\circ}\text{C}^{-1}$ . As for pure Cu substrates, a graphite spray layer

was employed on Cu/C substrates to enhance diamond nucleation. However, despite the decrease in substrate CTE brought by carbon fiber reinforcements, the deposition of diamond films onto Cu/C still suffers from crack propagation, as shown on Fig. 3.51, which shows a diamond film grown during 20 minutes on a Cu/C substrate:

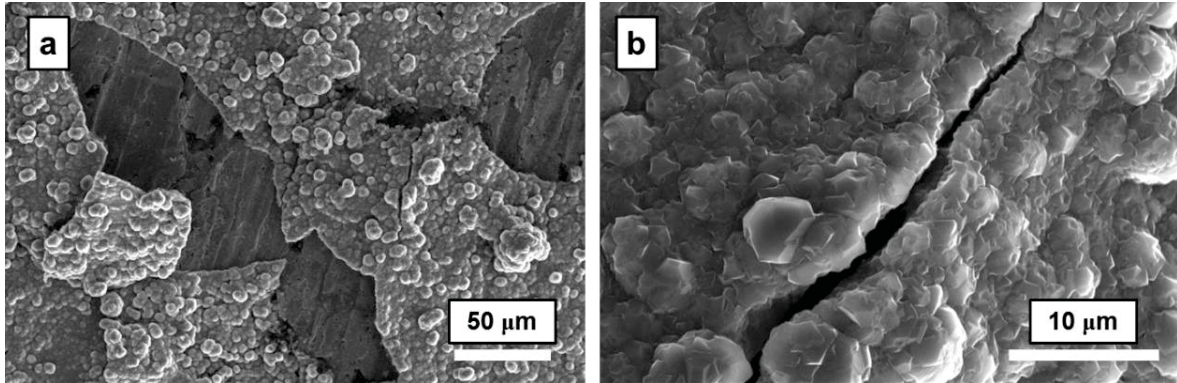


**Figure 3.51: SEM micrographs of a cracked and delaminated diamond film deposited onto a Cu/C composite substrate through laser-assisted combustion synthesis.**

In order to circumvent to the critical CTE mismatch between the diamond deposit and the Cu/C substrate, a 500 nm-thick chromium (Cr) layer was deposit onto the Cu/C substrate. Cr showing an intermediate CTE between diamond and the Cu/C substrate ( $\alpha_{Cr} = 4.9 \times 10^{-6} \text{ }^{\circ}\text{C}^{-1}$ ), it is expected to act as a thermo-mechanical buffer layer between the diamond film and the substrate. The Cr layer was deposited onto the Cu/C substrates through physical vapor deposition (PVD). Figure 3.52 shows top-surface SEM micrographs of the Cu/C substrate before (Fig. 3.52a) and after (Fig. 3.52b) Cr deposition. The Cr deposit is observed to fit the roughness of the substrate.

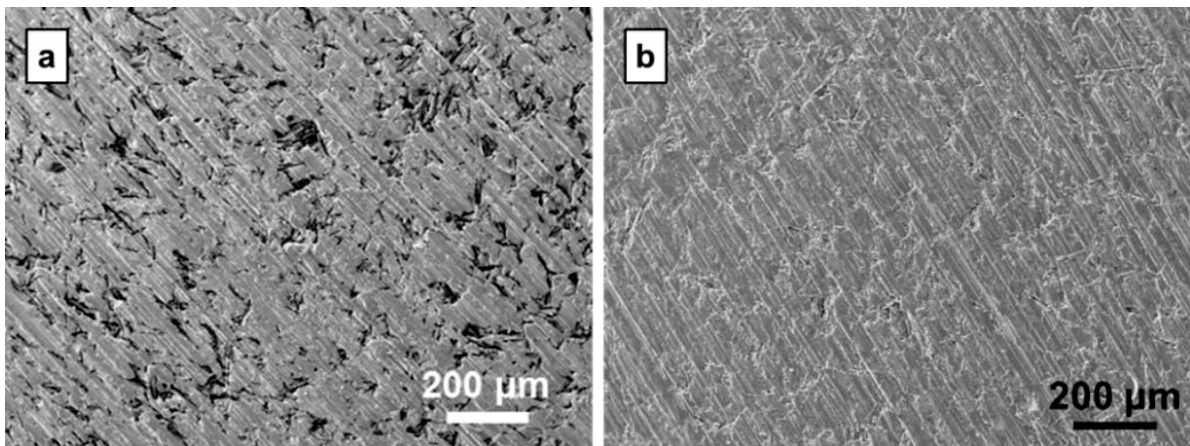


**Figure 3.52: SEM micrographs of a (a) raw and (b) Cr-coated Cu/C composite substrate.**

The 500 nm-thick Cr interlayer was shown to effectively act as a thermo-mechanical layer between the diamond deposit and the Cu/C substrate. Figure 3.53 shows SEM micrographs of a CVD diamond-coated Cu/C substrate with a 1 μm-thick interlayer:



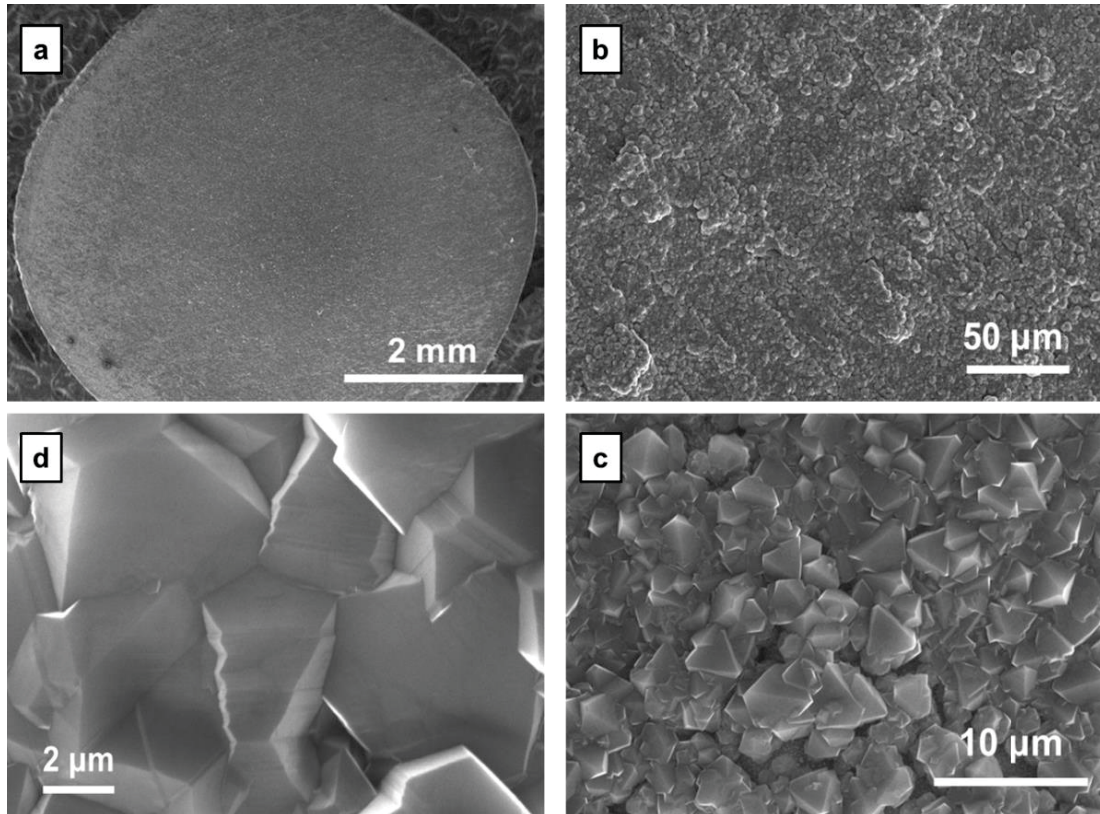


**Figure 3.53: SEM micrographs of a CVD diamond-coated Cu/C composite substrate.**

By comparing the deposition of combustion CVD diamond onto raw (Fig. 3.51) and Cr-coated (Fig. 3.53) Cu/C substrates, it clearly appears that the Cr interlayer effectively act as a thermo-mechanical buffer layer by mitigating the thermal stress generated at the film/substrate interface. Thus, it preserves the film from cracking and delaminating from the Cu/C substrate.

It should also be noticed that the CVD diamond film remarkably coat the substrate surface. This was made possible by the relatively small surface of the Cu/C substrates which was fitted entirely into the flame environment. However, due to the limited diameter of the combustion torch used in this study, the films as-grown still suffered from radial non-uniformity.

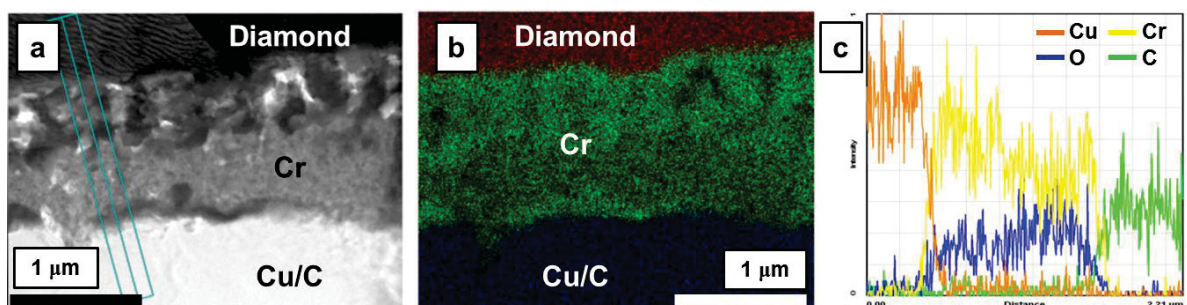


**Figure 3.54: TEM elemental analysis at the Cu/C/Cr/diamond interface. (a) Micrograph of the interface. (b) EDXS chemical mapping of the interface: C: red color, Cr: green color, C: blue color. (c) Line concentration profile across the interface.**



Moreover, TEM analysis at the interface between the Cu/C substrate, the Cr interlayer, and the diamond film shows that a high concentration of oxygen exists into the Cr layer. The presence of oxygen into the Cr interlayer is assumed to directly originate from the open-air deposition environment. Since oxides are poor thermal conductors, the oxidation of the Cr interlayer is strongly detrimental from the heat conduction aspect. The formation of Cr carbides would have been more beneficial due to higher thermal conductivity.

Since the interface structure of Cu/C/diamond assemblies is very different from that of diamond/Si samples, the estimation of thermal boundary resistance at the diamond/Si interface may be difficultly transposed to diamond films deposited onto other substrate materials. Nevertheless, the thermal conductivity data previously obtained from diamond films grown onto silicon is assumed to still be valid for diamond films grown through the same deposition process but onto different substrate materials.

This attempt to grow CVD diamond films onto heat-dissipative Cu/C composite substrates was successful and demonstrates that the combination of a CVD diamond heat-spreading film and a heat-sinking metal-matrix substrate is possible. It allows various electronic packaging configurations to be considered for combining heat-spreading CVD diamond to a heat-dissipating material.

### 3.7 Conclusion

It was demonstrated in this chapter 3 that fast deposition of high-quality diamond films onto various substrates (silicon, tungsten carbide) was made possible by laser-assisted combustion synthesis. The combustion synthesis technique shows numerous advantages toward traditional hot-filament and plasma-assisted deposition processes, among them high flexibility, low capital costs, and scalability. A multienergy diamond deposition process was achieved by coupling the energy of a CO<sub>2</sub> laser to that of a combustion flame. The laser resonant excitation of carbon precursors was achieved by tuning the laser wavelength to match a vibrational mode of ethylene molecules and shining it into the flame environment. This was shown to increase the concentration of active chemical species (hydrocarbons, OH radicals), thus promoting both growth rate and diamond phase purity relative to a traditional combustion flame process. The main drawbacks of the diamond deposition route proposed in this study are the limited deposition area, non-uniform thickness, and intrinsic roughness of the diamond films produces. Roughness is indeed redhibitory when considering electronic packaging applications where flatness and solderability are two key criteria for heat-spreader selection. Nevertheless, these issues may be addressed through technological solutions such as flat burners or multiple flames system to uniformly coat larger areas, and laser-polishing techniques to flatten the film surface. As an illustration, a laser-roughening procedure was successfully employed in this study to mitigate the residual stress existing in diamond films deposit onto tungsten carbide substrates.

The produced diamond films were demonstrated to exhibit high phase purity and high vertical thermal conductivity in the [450-500] W.m<sup>-1</sup>.K<sup>-1</sup> range. The thermal conductivity in the direction parallel to the substrate surface is assumed to be lower due to the columnar microstructure of the film. The laser-assisted deposition process was demonstrated to effectively overcome the issue of moderate quality typically exhibited by combustion torch deposition processes. However, the columnar microstructure of the film was shown to exhibit anisotropic properties, in terms of phase purity, level of residual stress, and thermal conductivity. The microstructure of the films, which was observed to evolve from a finely grained microstructure with relatively lower phase purity in the lower layers of the film to a structure made of relatively fewer but larger diamond grains with higher phase purity, led to purity, stress, and thermal conductivity gradients in the film microstructure, from the film/substrate interface to the top surface.

The diamond films produced in this study may provide efficient heat spreading solutions with high thermal conductivity and thermal expansion coefficient close to that of semiconductor materials such as silicon. However, the very first layers of the diamond films were shown to display high thermal resistance due to their composition and fine-grained microstructure. This aspect should be considered prior to any real-environment application of these combustion CVD diamond films.

## **CHAPTER 4: COPPER / DIAMOND COMPOSITE FILMS**

---

### **4.1 Introduction**

### **4.2 Starting Materials**

### **4.3 The Tape Casting Process**

### **4.4 Heat treatments**

### **4.5 Investigations on the particles grown onto diamonds**

### **4.6 Cu particles nucleation and growth process**

### **4.7 The Sintering Process**

### **4.8 Characterization of the Cu/D composite films**

### **4.9 Comparison with traditional carbide-bonded Cu/D composites**

### **4.10 Conclusion**

---

## 4.1 Introduction

Despite their promising properties, the applicability of CVD diamond films and substrates is narrowed by the cost per volume of these materials, which tend to reserve CVD diamond for niche thermal management applications because of limited availability in large sizes. Moreover, the low coefficient of thermal expansion (CTE) of diamond ( $[1-2] \times 10^{-6} \text{ }^\circ\text{C}^{-1}$ ), although being an advantage when located close the active components, is too far from the CTE of alumina ( $7.2 \times 10^{-6} \text{ }^\circ\text{C}^{-1}$ ) to avoid raising concern about excessive thermo-mechanical stresses when located at the DBC/base plate interface. This bi-materials interface is critical to the reliability of the module; thus, it is preferable to avoid a too large CTE mismatch between the two materials considered [5, 10, 11].

Therefore, it is interesting to consider the use of diamond as a reinforcing material embedded in a thermal package substrate material such as copper. Copper is widely used in the electronic industry because of its high thermal conductivity ( $k = 400 \text{ W.m}^{-1}\text{.K}^{-1}$ ), high electrical conductivity ( $\sigma = 6.48 \times 10^7 \text{ S.m}^{-1}$ ), and ductility. The thermal and mechanical properties of diamond and copper can this way be associated to obtain diamond reinforced copper matrix (Cu/D) composite heat-spreaders with thermal conductivity and CTE that can be tailored as a function of the fraction of reinforcements employed. In addition, the ductility of the copper matrix contributes to make the machinability of the final material easier. As a matter of fact, Cu/D composite heat-spreaders have attracted significant interest in the past years [125-135, 188, 189].

However, a permanent issue when considering the assembly of copper and carbon materials is the absence of mutual chemical affinity between these two elements, i.e. the copper/carbon system is a non-reactive system. Indeed, molten copper does not wet carbon. The non-wettability of carbon materials such as diamond by molten copper is a strong obstacle to the fabrication of heat-conductive Cu/D composites since interfacial bonding plays a key role on the heat conduction process at bi-materials interfaces. From a surface tension prospective, the low chemical affinity between copper and carbon can be depicted by Fig. 4.1b, where the wetting angle between liquid copper and solid carbon is larger than  $\theta = \pi/2$ .

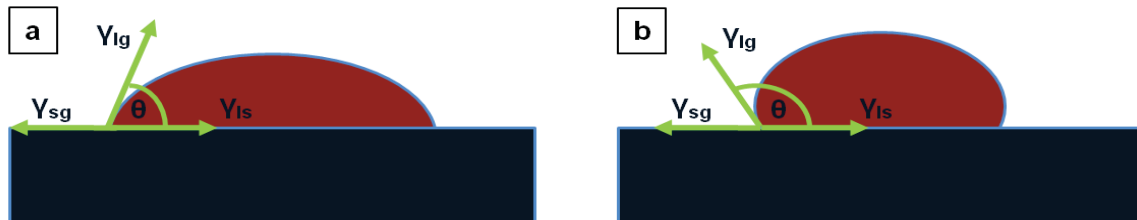


**Figure 4.1:** Schematic view of (a) a wetting ( $\theta < \pi/2$ ) and (b) a non-wetting ( $\theta > \pi/2$ ) liquid-solid system. Taking a surface tension balance in the plane of the solid leads to:  $\gamma_{lg}\cos\theta + \gamma_{ls} = \gamma_{sg}$  (Young-Dupré equation) [50].

The non-wettability of diamond by molten copper originates from the very dissimilar surface energies exhibited by these two materials as shown in Tab. 4.1 [190]:

**Table 4.1: Free surface energies of copper and diamond at room temperature.**

Material	Copper	Diamond
$\gamma_{sg} \text{ (J.m}^{-2}\text{)}$	1.72	[5.3 – 9.2]

From a thermodynamic point of view, the non-wettability of diamond by molten copper originates from the absence of chemical reaction between these two elements. As shown on the Cu-C phase diagram (Fig. 4.2), the Cu-C binary system is of the peritectic type ( $(\text{Cu})_{(s)} \rightarrow (\text{C})_{(s)} + L_{(l)}$ ), with the peritectic horizontal lying at a temperature just above the melting point of copper ( $T_{m \text{ Cu}} = 1084^\circ\text{C}$ ). The equilibrium phases are a liquid phase (L), a copper solid solution (Cu) with a very limited solubility of C of about 0.04 at.%, and a graphite-type solid solution (C) with no solubility of Cu.

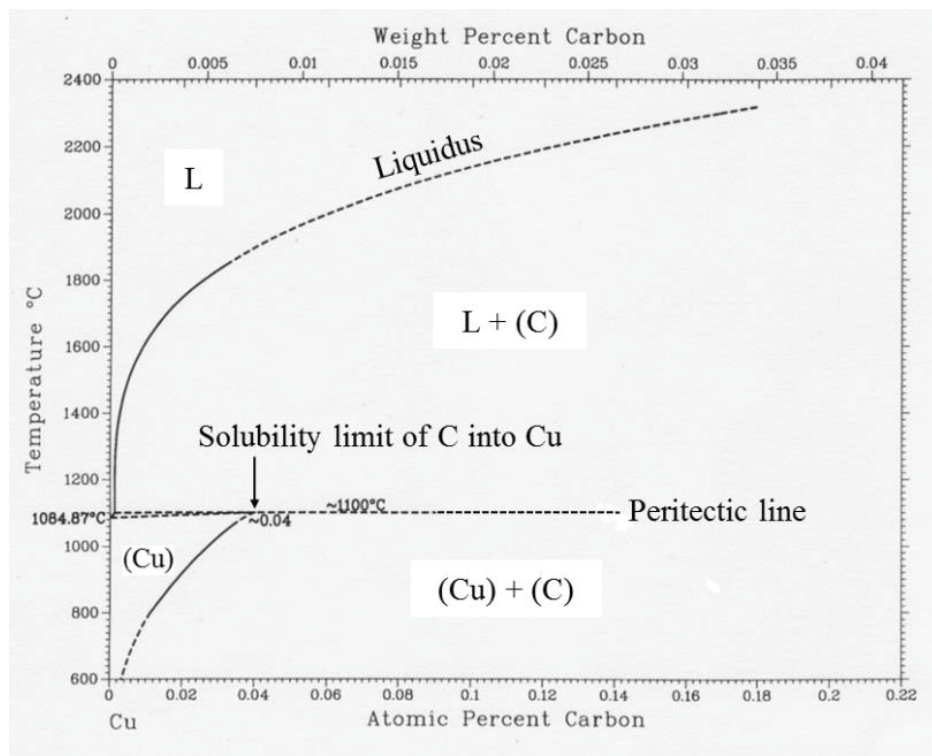


**Figure 4.2: The binary copper-carbon phase diagram [191].**

From an atomistic point of view, the non-reactivity between these two elements also originates from the lack of vacancies on the *d*-orbital of copper, which cannot interact with *p*-orbitals of carbon atoms, as explained in section 2.4.1. Although the preparation of  $\text{Cu}_2\text{C}_2$  and  $\text{CuC}_2$  compounds (termed *copper acetylides*) has been reported [192], these compounds exhibited extreme instability and are highly explosive when dried. Therefore, the Cu/C system exhibits a strong non-

chemical reactivity. The non-reactivity of the Cu/C system prevents the creation of any intermetallic compound or solid solution that would lead to a chemical interphase between the copper matrix and carbon-based reinforcements such as diamonds. Therefore, without providing any bonding solution, interfaces in copper/carbon composites strictly relies on mechanical bonding, which is detrimental to the transfer of properties in the composite, especially from a thermal prospective. Indeed, heat conduction in composites relies on an intimate bonding at the atomic scale between the matrix and the reinforcements, which is mainly possible when strong chemical bonds exist between the two material components [87].

In order to create a chemical bonding between the copper matrix and carbon-based reinforcements (either carbon fibers or diamond particles), a well-known solution consists in adding carbide-forming additives to the system. Carbide-forming additives (X) exhibit a high chemical affinity with carbon, thus allowing the creation of strong C-X chemical bonds through carbide interphases. Another critical aspect of carbide-forming additives is that they must possess a high solubility in the matrix material. Among carbide-forming additives, chromium (Cr) [130], boron (B) [128], titanium (Ti) [134], tungsten (W) [123], and zirconium (Zr) [132], are the most employed for copper/carbon composite processing. The carbide-forming additives are either pre-alloyed to the matrix material, as show on Fig. 4.3a, or directly coated onto the reinforcements through, for example, vapor phase deposition, as displayed on Fig. 4.3b:

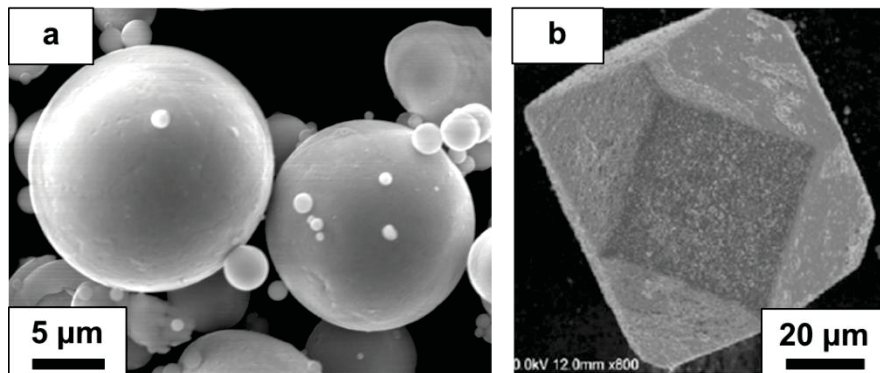


**Figure 4.3: (a) Cr-alloyed spherical copper powder and (b) Cr-coated diamond particle [130].**

The carbide-forming additives introduced into the binary copper/carbon system diffuse and react during the sintering process and further post-sintering heat treatments. They lead to the formation of carbides that will chemically bond the reinforcements to the copper matrix at the interface between the two materials. Figure 4.4 shows an example of chromium carbide location in a carbon fibers dispersed chromium-alloyed copper matrix composite material where the chromium, mapped in red color, surrounds the carbon fibers.

Carbide-bonding solutions in copper/carbon composites have been largely studied in the past years. Carbide interphases lead to a strong chemical bonding between copper and carbon and



strongly improves the transfer of properties at the matrix/reinforcement interface. From a thermal perspective, they have been proven to drastically increase the thermal conductivity and decrease the CTE of the resulting copper/carbon composites [123-135].

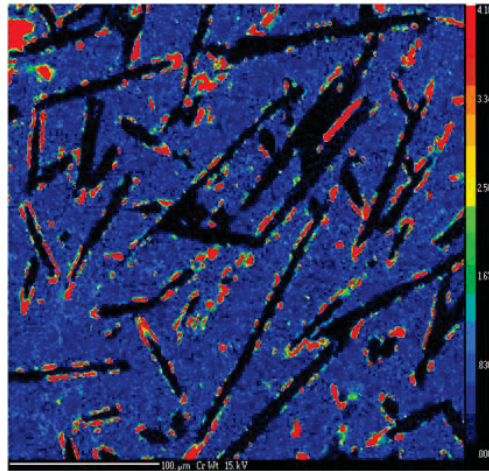


**Figure 4.4: EPMA Cr mapping of a Cu-Cr/30 vol.% C composite material, showing the chromium located at the Cu/C interfaces [89].**

However, from a mechanical perspective, carbide interphases are major obstacles to achieve high strength composite materials because they are brittle. Therefore, these phases critically affect the global mechanical behavior of the composite. For instance, the  $\text{Al}_3\text{C}_4$  aluminum-carbide phase is notorious for degrading the mechanical properties of Al/C MMCs [193, 194]. As a matter of fact, carbide-based bonding solutions reveal their limits upon thermal cycling since the mechanical integrity of the carbide interphase may be degraded upon the repeated thermal cycles endeavored in the operating environment of a power module.

This chapter deals with the fabrication of Cu/D composite heat-spreading films for power electronic applications through tape casting and hot pressing (powder metallurgy). Cu/D composites technology was explored in parallel to the study of CVD diamond films carried out in chapter 3 as an alternative way to use diamond for heat dissipation purposes. An innovative solution to chemically bond the copper matrix to diamond reinforcements into Cu/D materials was developed and patterned. This method is based on the coating of the surface of the diamond reinforcements by copper particles through functionalization of the diamond surface and heat treatments with copper powders. This solution was demonstrated to be as efficient as carbide bonding in terms of achieved thermal conductivity and CTE, and more efficient than carbide bonding in terms of tenue to thermal cycling in operating environment.

The fabrication, characterization, and simulation of the Cu/D materials considered were carried out at the Institute of Condensed Matter Chemistry of the University of Bordeaux, under direction of Doctor Jean-Francois Silvain and Professor Jean-Marc Heintz.

## 4.2 Starting materials

### 4.2.1 The copper matrix

Dendritic copper powders from Eckart Granules Poudmet Company (Germany) were used as the matrix material. Unlike spherical copper powders, which are typically produced through atomization (see section 4.9.2), dendritic copper powders (also called *electrolytic copper powders*) are fabricated following an electrolytic route which consists in reducing metallic copper ions ( $\text{Cu}^{2+}$ ) provided by various precursors (oxides, sulfates) in an aqueous media through an electrical current, thus obtaining metallic copper (Cu). The electrolytic synthesis of copper powders mainly relies on a high cathodic current density, a low concentration in cations  $\text{Cu}^{2+}$ , a low pH (acidic media), a low temperature (60°C maximum), and no convection effects into the reaction bath [195]. Table 4.2 sums up the typical process conditions employed for electrolytic Cu powders synthesis:

**Table 4.2: Typical process conditions for electrolytic synthesis of dendritic copper powders.**

$[\text{Cu}^{2+}]_{\text{aq}}$ (g/l)	$[\text{H}_2\text{SO}_4]_{\text{aq}}$ (g/l)	$d_A$ (A/m <sup>2</sup> )	$d_C$ (A/m <sup>2</sup> )	T (°C)	U (V)	Electrodes
30 g/l	[150-250]	[300-600]	[600-4000]	[40-60]	[1-2]	Pb/Sb (88/12)

The cathodic depot is then collected, water-washed, dried under air at 100°C, milled, and reduced. The as-produced powders exhibit typical dendritic shapes and a high purity rate. However, this process is more costly relative to the atomization process leading to spherical Cu powders. Figure 4.5 provide SEM micrographs of the copper powders used:

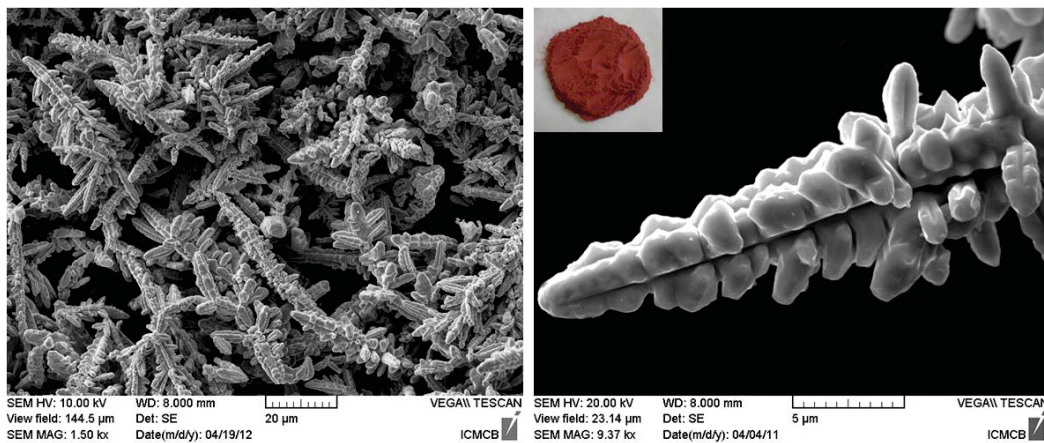


**Figure 4.5: Scanning electron micrographs and photograph (insert) of the dendritic copper powders employed as the matrix.**

SEM observations confirm the dendritic shape of the powders. It also shows that the copper powders have dendrite lengths between 20 and 40 μm. However, as shown by Fig. 4.6, no impurities were detected through XRD analysis of the powders, although this characterization

technique has a low detection resolution. Three diffraction peaks at  $43^\circ$ ,  $51^\circ$ , and  $74^\circ$  are detected through XRD analysis of the powders. These three peaks are typical of the diffraction pattern of copper. The broad band detected around  $18^\circ$  is due to the aluminum sample holder.

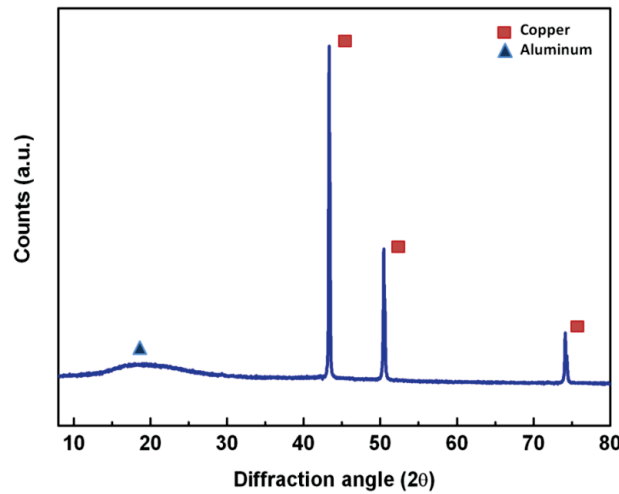


**Figure 4.6: X-ray diffraction spectrum of the dendritic copper powders employed as the matrix material.**

Dendritic copper powders were employed instead of spherical copper powders since these powders, due to their particularly high aspect ratio (surface/volume), require a lower sintering temperature and/or pressure to be densified. Indeed, a theoretical study of the sintering process enable to demonstrate that the densification process is less energy-consuming, thus possible at lower temperature, when the particles to be sintered have a high aspect ratio (as in the case of dendrites) rather than when the particles aspect ratio is low (as in the case of spherical particles) (see section 4.7.1 for more details).

#### 4.2.2 The diamond reinforcements

Single crystal diamond powders from Henan Zhongxing Corporation (China) were used as reinforcements. The diamond powders were MBD6 quality grade diamonds. SEM micrographs displayed on Fig. 4.7 show that the diamond powders were faceted with hexagonal or cubo-octahedral shapes and an average diameter of  $50\text{ }\mu\text{m}$ . The diamond powders exhibited a dark-green color. This type of diamond powders is well-known to be processed through High-Pressure High-Temperature (HPHT) synthesis. Details about this route to synthesize diamond are given in section 2.4.1. Although no impurities could be detected in the diamond powders through XRD analysis, as shown on Fig. 4.8, where a sharp x-ray diffraction diamond peak is displayed, traces of metallic elements employed for diamond synthesis (mainly nickel (Ni), manganese (Mn), and copper (Cu), but also traces of iron and cobalt) were revealed through Auger electron spectroscopic surface analysis, as detailed in Tab. 4.3. These elements are typically used as metal catalysts for the synthesis of the diamond powders, as explained in section 2.4.1.

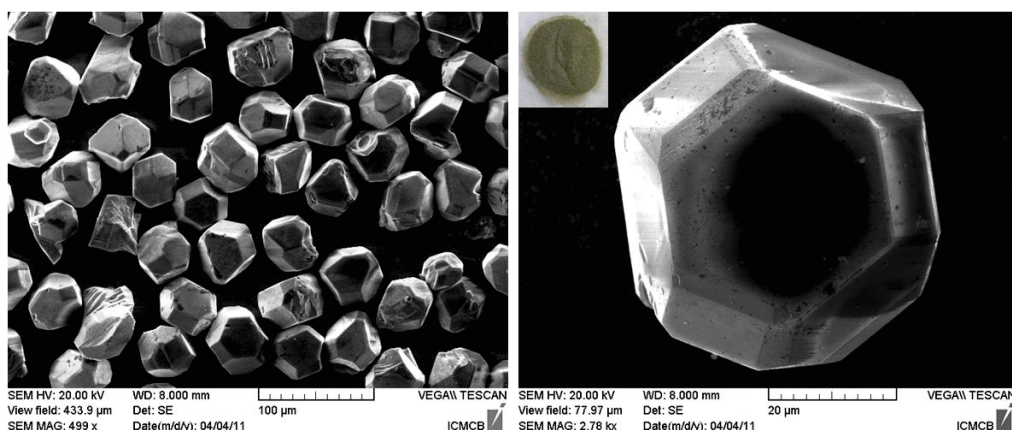


**Figure 4.7: Scanning electron micrographs and photograph (insert) of the diamond powders employed as reinforcements.**

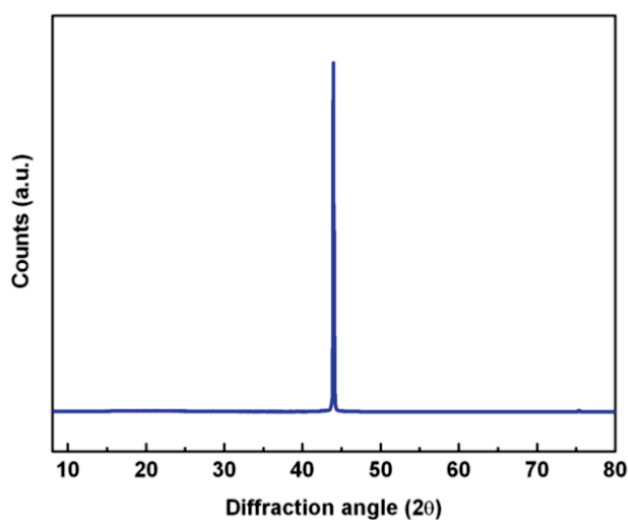


**Figure 4.8: X-ray diffraction spectrum of the diamond powders employed as reinforcements.**

The existence of residues of metal catalysts into the diamond grains is of course a drawback since they tend to decrease the thermal conductivity of the powder by acting as phonon scatterers [40], but also decrease the temperature of graphitization of the diamond powders [196].

**Table 4.3: AES elemental analysis of the diamond powders employed.**

Element	Weight percentage (%)	Atomic percentage (%)
Manganese (Mn)	0.0676	0.0148
Nickel (Ni)	0.0444	0.0091
Copper (Cu)	0.0165	0.0031
Iron (Fe)	0.0072	0.0016
Cobalt (Co)	0.0025	0.005
Carbon (C)	99.8618	99.9711

Table 4.4 gathers some properties of the copper and diamond powders employed in this study.

**Table 4.4: Thermo-physical properties of the starting dendritic copper and diamond powders.**

Materials	Copper	Diamond
Particle shape	Dendritic	Hexagonal / Cubo-octahedral
Mean particle length / diameter ( $\mu\text{m}$ )	30	50
Density ( $\text{g.cm}^{-3}$ )	8.95	3.51
Thermal conductivity ( $\text{W.m}^{-1}.\text{K}^{-1}$ )	385	1000
Coefficient of thermal expansion ( $\times 10^{-6} \text{ }^{\circ}\text{C}^{-1}$ )	17	1
Specific heat at $70^{\circ}\text{C}$ ( $\text{J.kg}^{-1}.\text{K}^{-1}$ )	391.9	681.1
Bulk modulus (GPa)	130	442
Shear modulus (GPa)	48.3	-

The specific heats of the powders were measured through differential scanning calorimetry (DSC). The mean particle length and diameter of dendritic copper powders and diamond powders, respectively, were evaluated through scanning electron microscopy (SEM). The thermal conductivity and CTE of the dendritic copper powders were measured through flash laser radiometry and dilatometry, respectively. The other properties indicated in table 4.4 were obtained from the literature [197-199].

## 4.3 The tape casting process

### 4.3.1 Background

We have seen in chapter 2 that most of the processes developed to produce Cu/D composites consist spark plasma sintering (SPS) [130, 135], pulse plasma sintering (PPS) [127, 131], infiltration [123, 134], and powder metallurgy [125, 126]. However, none of the techniques reported allow the fabrication of thin sheets of composite at low cost. *Tape casting process* offers an original solution to fabricate thin sheets (essentially two-dimensional) of any material that can be produced as a powder, such as copper/diamond composites. Figure 4.9 shows a schematic view of the tape casting process.

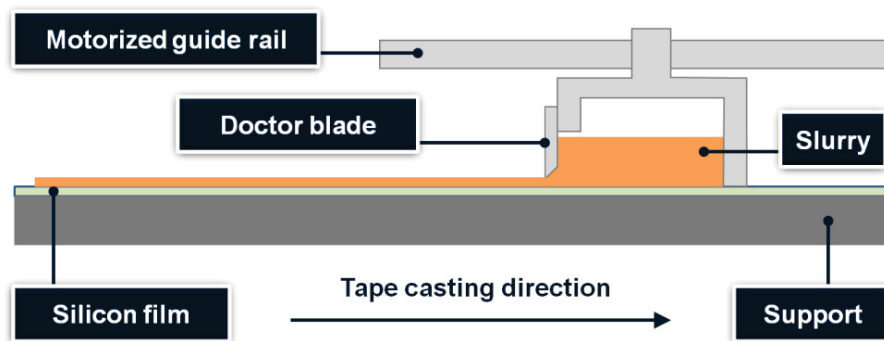


**Figure 4.9: Scheme of the tape casting set-up and mechanism.**

The tape casting process features three main components: a doctor blade, a carrier support, and a drying zone. It consists in spreading a slurry onto the carrier support by means of the doctor blade, which is a scraping blade for the removal of excess slurry from the carrier film being coated. Depending on the casting machine, either the blade can be moving and the carrier stationary, or the blade stationary and the carrier moving. In the case of this study, the doctor blade is motorized and the carrier support is fixed [200].

Although the heart of the system may appear very simple, the design of the doctor blades and casting machines as the formulation of the slurry to tape cast are not as intuitive. Tape casting process relies on the preparation of a suspension of the inorganic powders in an aqueous or non-aqueous system. Most of the solvents employed in tape casting are non-aqueous since the drying process is evaporative rather than absorptive. However, tape casting of aqueous-based systems has also being demonstrated to be successful and shows advantageous that cannot be neglected such as non-toxicity and non-flammability [201]. The slurry is a complex multicomponent system typically containing: powders (metallic and/or ceramic), solvent, binder, dispersant agent, and plasticizer. Each one of these components has a critical influence on the final slurry. The suspension must be stable, homogeneous and with a suitable rheological behavior according to the tape casting process. After tape casting, and after the solvent is evaporated from the tape, the obtained dried tape, or *green tape*, is cut to the desired shape. The composite tape is then heat treated, and sintered.

Tape casting emerged during World War II from the urgent need to find a substitute for mica as a capacitor material. Glenn Howatt initially described the process and published the first articles and patents dealing with tape casting [202, 203]. From Howatt's first works on tape casting of ceramic capacitors, the process has matured to become one of the most employed techniques for the formation of thin sheets of ceramic materials at an industrial scale. Also known as *doctor blading*, or *knife coating*, the tape casting process is currently industrially used to produce thin or multilayered ceramic structures for various applications: electronic packages ( $\text{Al}_2\text{O}_3$ , AlN) [204], capacitors ( $\text{BaTiO}_3$ ) [205], solid electrolytes for sensors or fuel cells [206], separators for batteries [207], piezoelectric ceramics for actuators and transducers [208]. The tape casting process is also familiar to other industries, such as the paper, plastic, and paint industries, in which it has long been employed to test the covering power of new formulations.

Tape casting features numerous advantages: (i) thickness control, (ii) easy handling, (iii) low capital cost, (iv) fastness, (v) smooth surface finish, (vi) scalability, and (vii) net shaping capability. Based upon powder metallurgy technology, tape casting of metal matrix composites offers a decrease of the machining cost due to its net-shaping capability (economical aspect) and a decrease of power consumption due to the low processing temperatures it involves relative to foundry processes (environmental aspect). The chief advantage of the tape casting process is that it is the



best way to form large-area, thin, flat, ceramic or metallic parts which would be very difficult, if not impossible, to press or extrude. Also, punching holes and slots into green metallic or ceramic tapes is easy and essential to the multilayered ceramic packages being designed and manufactured today. In terms of thickness control, tapes as thin as 5  $\mu\text{m}$  were reported to be manufactured. Typical dried tape thickness is generally accepted to range from 0.025 mm to 1.3 mm. Finally, in a specific addition to Cu/D composite materials, it enables a uniform dispersion of diamond particles into the copper matrix, which prevents eventual segregations due to the difference of density between copper and diamond powders during the mixing step [200].

#### 4.3.2 Processing flowchart

Figure 4.10 provides a detailed step-by-step description of the processing flowchart for the fabrication of copper/diamond composite films:

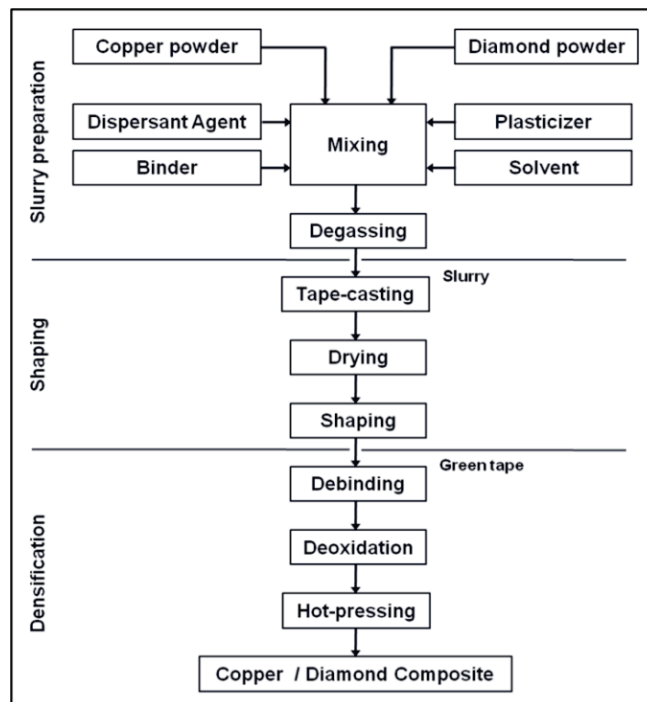


**Figure 4.10: Processing flowchart of the tape casting process [209].**

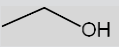
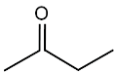
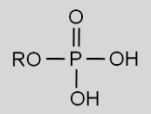
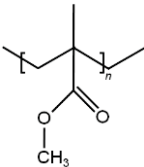
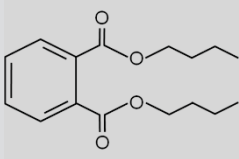
As shown on Fig. 4.10, the fabrication process is divided in three main steps:

- The slurry preparation: which consists in formulating a mixture of the matrix and the reinforcements with organics in order to create an homogeneous slurry with the suitable viscosity;
- The shaping: which consists in giving to the slurry a tape shape that is suitable for further processing steps and for the desired application (e.g. electronic substrate dimensions);
- The densification: which consists in heat treating and sintering the copper/diamond composite tape in order to create a densified final product.

### 4.3.3 Formulation

Table 4.5 provides a detailed description of the chemicals entering in the composition of the slurry:

**Table 4.5: Chemicals entering in the formulation of the slurry for the tape casting of a Cu/40 vol.% D composite tape.**

Chemical	Role	Topologic formula	Aspect	Degradation point (°C)	Mass / Volume
Dendritic copper powder	Matrix	Cu (metallic)	Solid powders Red color	Melts at 1084°C	39.66 g
Diamond powder	Reinforcements	C (sp <sup>3</sup> )	Solid powders Green color	Melts at 3550°C	10.34 g
Ethanol	Solvent		Liquid Transparent	Boils at 78°C	14.07 ml
2-Butanone	Solvent		Liquid Transparent	Boils at 79°C	27.30 ml
Phosphate ester	Dispersant agent		Viscous liquid Honey-like	-	0.25 g
PMMA	Binder		Solid powders White color	Boils at 200°C	4.65 g
DiButylPhtalate	Plasticizer		Viscous liquid Transparent	Boils at 340°C	3.15 g

The next paragraphs provide brief descriptions of each chemical involved in the slurry formulation and the role it plays. For more details about the formulation, shaping, and drying steps of the tape casting process, one can refer to [200, 209-211].

▪ **Solvent:**

The solvent must have a low temperature of vaporization and wet both copper and diamond powders. In addition, the powders must not react with the solvent. Based upon these requirements, an azeotropic mixture of ethanol and 2-butanone (Methyl ethyl ketone) (40/60) was chosen (an azeotrope is a mixture of two liquids whom evaporation produces vapors with the exact same composition as the initial liquid mixture). It indeed offers a low boiling point ( $T_{boiling} = 74.8\text{ }^{\circ}\text{C}$ ) and a low dielectric constant that is beneficial to the wettability of the powders by the solvent. The tape casting slurry contains 74 vol.% of solvent.

▪ **Dispersant agent:**

A dispersant agent is needed in order to uniformly disperse the powders into the slurry by developing repulsive forces between particles using electrosteric mechanisms (another type of dispersant uses electrostatic mechanisms for repulsion). The dispersant agent used is a phosphate ester (CP213, Cerampilot, France). Because of its acidic character, the phosphate ester partially dissociates to give protons that adsorb onto the surface of the ceramic particles (diamond reinforcements, copper powders). Therefore, the surface of the powders is positively charged. The counter-ion resulting from the dissociation of the phosphate ester is then attracted to the surface of the powders through electrostatic forces. The radicals bonded to the phosphorous atom (R) are hydrophobic (lipophilic) chains which will deploy into the organic solvent, thus preventing the powders from agglomerating through steric impeachment. The dispersion mechanism is summed up on Fig. 4.11:

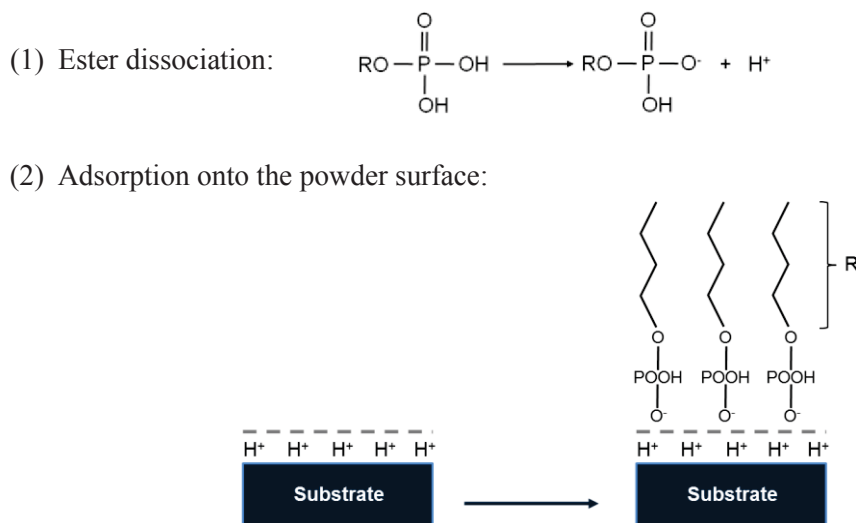


Figure 4.11: Schematic description of the dispersion mechanism.

It was demonstrated in previous studies that CP213, selected among several dispersant agents, led to the best deagglomeration and dispersion of copper and diamond powders. It was also shown that the optimum viscosity (1 Pa.s) was obtained with a dispersant concentration of 0.5 wt.% on the dry powder basis [209-211].

▪ **Binder:**

The binder ensures the cohesion of the green tape for both handling and to avoid crack propagation during tape drying. After solvent evaporation, the binder molecules bond to each other, thus providing green tape rigidity. Both nature and intensity of these bonds depend on the ramifications existing on the carbon chain of the binder. The structure of acrylate groups suggests that hydrogen bonds (rather than Van der Waals bonds) are involved in the bonding of PMMA chains. The binder has to be easily removed at low temperature without residues. We use here PolymethylMethacrylate (PMMA) with a molecular weight ranging between 120,000 and 150,000 g.mol<sup>-1</sup> and a boiling point of 200°C (Degalan 51/07, Degussa Hüls, Germany).

▪ **Plasticizer:**

An efficient plasticizer of the PMMA binder is the DibutylPhtalate with a molecular weight of 300 g.mol<sup>-1</sup> and a boiling point of 340°C (Fisher Scientific, France). The plasticizer confers a suitable flexibility to the green tape for good handling because of the insertion of plasticizer chains between the chains of PMMA. This leads to a decrease in the glass transition temperature of the polymeric skeleton from 110°C (for PMMA alone) to about 65°C (for the PMMA/DBP mixture) and reduces the tape rigidity. It was demonstrated that a binder/plasticizer ratio of 1:2 leads to an optimal compromise between green tape flexibility and mechanical strength [209-211].

The tape casting suspension was prepared in one step by mixing the powders, the organics, and the solvent using planetary milling during 15h at 20 rpm. Figure 4.12 shows photographs of a copper/diamond composite slurry and of the planetary miller employed for slurry preparation:

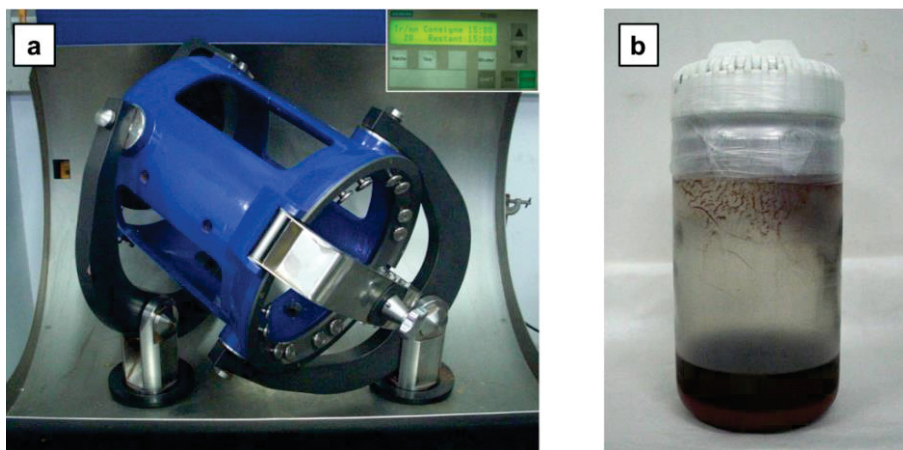


Figure 4.12: Photographs of (a) the planetary miller and (b) of a Cu/D slurry in a container.

As shown on Fig. 4.12b, when the slurry has been formulated but not mixed yet, the diamond reinforcements (on the top of the mixture) clearly segregate from the copper matrix powders (at the bottom of the mixture) because of the difference in density. The 15 hour-long mixing step allows homogenizing the Cu/D slurry before tape casting. Particular care had to be taken to limit as much as possible solvent evaporation during the formulation since solvent percentage is critical to the viscosity of the final slurry and solvent evaporation was quite fast. Parafilm (Company, USA) was employed to seal the slurry container prior to mixing through planetary milling.

#### 4.3.4 Shaping and drying

After homogenization, the mixture was degassed 30 minutes and then directly casted onto a silicone Mylar carrier film with a doctor blade. The doctor blade width was 10 cm and its speed was fixed at  $2 \text{ cm.s}^{-1}$  with a blade gap of 1.5 mm, which corresponds to a shear rate of  $13 \text{ s}^{-1}$ , the shear rate being given by the following formula:

$$\frac{dy}{dt} = \frac{v}{h} \quad (4.1)$$

Where  $v$  is the velocity of the moving blade ( $\text{m.s}^{-1}$ ),  $h$  is the gap between the moving blade and the support, and  $dy/dt$  is the shear rate ( $\text{s}^{-1}$ ). Figure 4.13 shows a photograph of a copper/diamond composite tape after the slurry has been spread onto the silicone film.

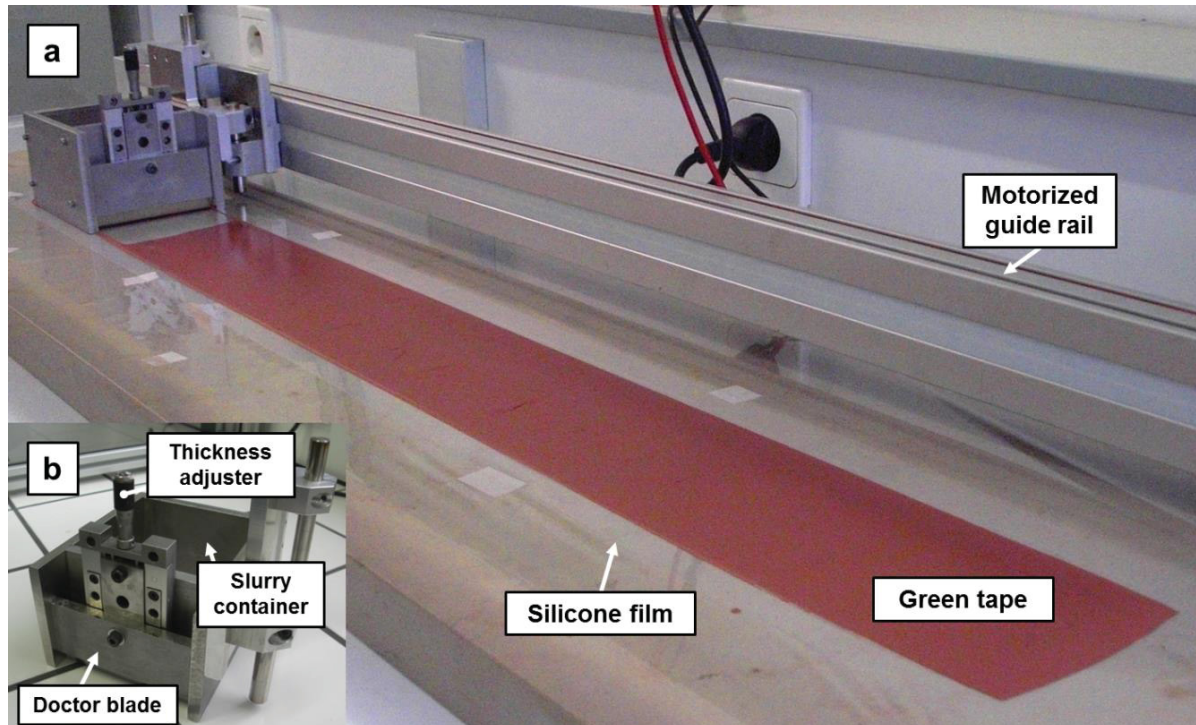
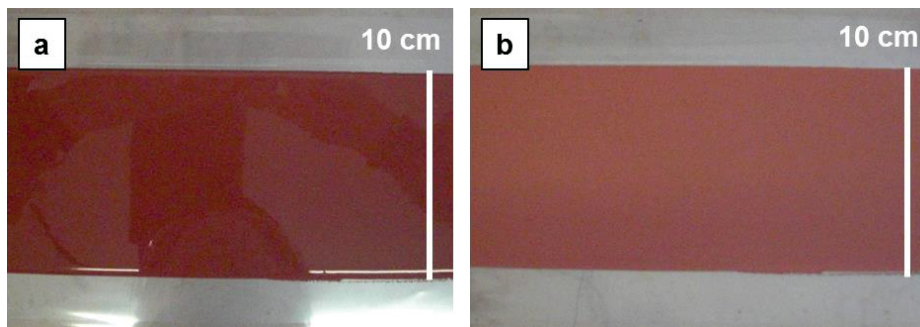


Figure 4.13: Photographs of (a) a green Cu/40 vol.% D composite after tape casting and (b) of the doctor blade [209].



The tape casting chamber is saturated with vapors of solvent (ethanol/2-butanone) prior to slurry spreading in order to prevent the evaporation of the solvents embedded into the tape from being too fast, which would lead to cracks creation during the drying step. Straight after the slurry has been spread onto the support, the evaporation of the solvents starts. This phenomenon triggers tape shrinkage and leads to the reduction of the dimensions of the composite tape. Figure 4.14 shows photographs of Cu/D tapes straight after slurry spreading (Fig. 4.14a) and after 30 minutes of drying (Fig. 4.14b). After tape casting, the tape initially exhibits a shiny aspect due to the presence of solvents. However, after only 30 minutes upon solvent evaporation, the tape's aspect is matt and its dimensions have started to shrink.



**Figure 4.14: Photographs of a Cu/D green tape (a) straight after tape casting and (b) after 30 minutes drying.**

Figure 4.15 shows the reduction in volume of the green tape as a function of time upon the drying process:

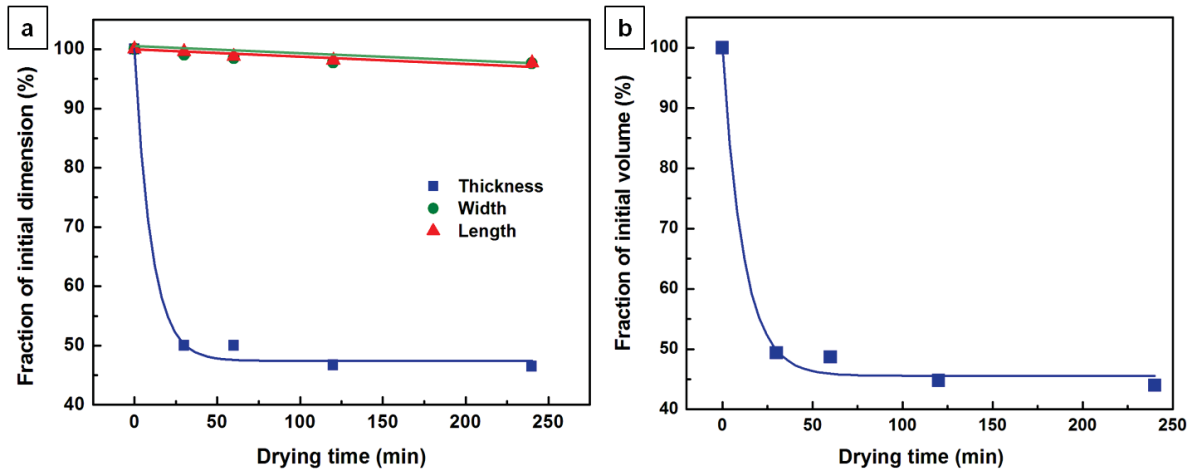


**Figure 4.15: (a) Dimensions and (b) volume retraction of a Cu/D green tape upon drying.**

It shows that the dimensions of the tape strongly decrease upon drying. The dimensional reductions were especially important from the aspect of thickness of the tape. On the contrary, its length and width suffer very limited change upon drying and kept almost constant. Mainly due to solvent evaporation through the surface of the tape, the green tape has its volume reduced by about 50% only after 30 minutes of solvent evaporation. After 4 hours upon drying, its volume has shrunk



by almost 55%. The volume shrinkage would reach 74% when the solvent evaporation is complete. However, the exhaustive evaporation of the solvents would take several days. Therefore, a drying time typically ranging between 6h and 12h was chosen in order to handle the tape with sufficient mechanical tenue while moving to the next processing steps. The rest of the solvents remaining in the tape will be easily eliminated upon the further heat treatments.

The viscosity of the slurry has a critical impact on the success or failure of the shaping step. On one hand, a slurry that is too viscous will be difficult to spread onto the support which leads to cracks creation (Fig. 4.16a) and to a tape with a lack of plasticity. On the other hand, a slurry that is too fluid will lead to a tape with a lack of consistency and mechanical strength. In one case as in the other, the viscosity of the slurry governs the efficiency of the tape casting step. In such context, and as mentioned in section 4.3.1, the chemicals involved in the slurry formulation and their respective quantities are of critical importance to the success or the failure of the tape casting process.

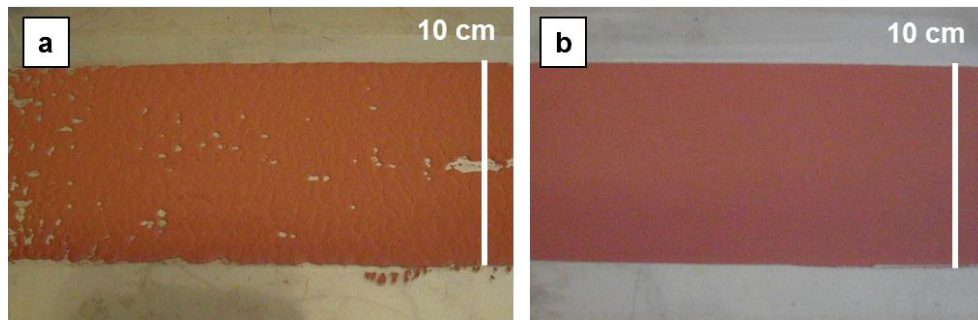


**Figure 4.16: Photograph of Cu/D green tapes containing (a) 70 vol.% and (b) 74 vol.% of solvent.**

The tapes were stored into the tape casting chamber during 12 hours in order to evaporate the maximum amount of solvents before further processing. Once the drying step completed, the Cu/D composite tape exhibits a “leather-like” aspect and can be easily handled and shaped, as shown on Fig. 4.17.

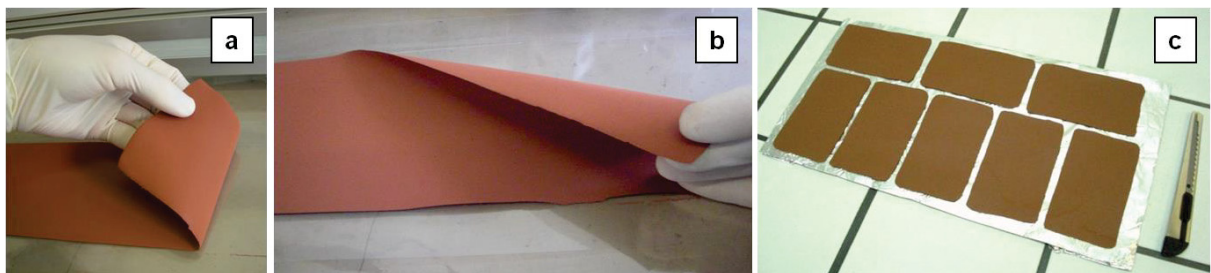


**Figure 4.17: Photographs showing the flexibility of the Cu/D green tape (a) longitudinally and (b) transversally; (c) shaped Cu/D green tape after drying and prior to debinding.**

SEM micrographs of a copper/diamond composite green tape are displayed on Fig. 4.18. These micrographs were taken after solvent evaporation from the composite tape. It is visible that the

diamond reinforcements and the dendritic copper powder matrix are embedded into the organics remaining into the tape (i.e. binder, plasticizer, dispersant agent).

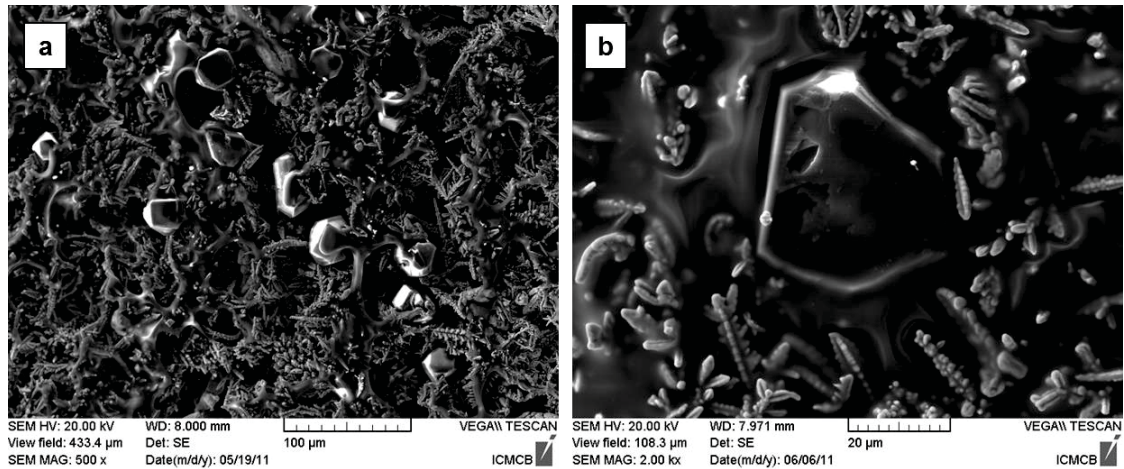


**Figure 4.18:** Top surface scanning electron micrographs of a green copper/diamond composite tape.

These organics have to be eliminated through thermal treatments before any further processing. Therefore, the green composite tapes were submitted in a first time to a debinding heat treatment under air atmosphere.

## 4.4 Heat treatments

The organics remaining in the green tape after shaping (i.e. binder, plasticizer, and dispersant agent) are removed under air through a debinding step, which triggers the oxidation of the copper matrix. As a matter of fact, a second thermal treatment under reducing Ar/H<sub>2</sub> atmosphere is then required to reduce the copper matrix.

### 4.4.1 Debinding

Following the shaping step, the Cu/D composite tapes were submitted to a two-hour long debinding heat treatment at 400°C under air in order to eliminate the remaining organics, thus having only the powders left.

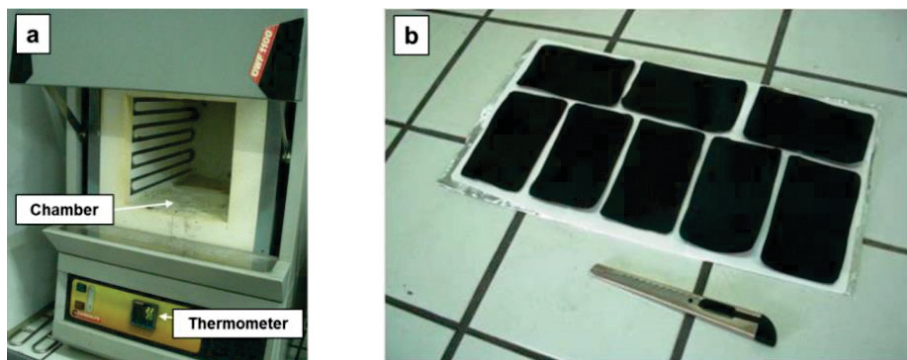


**Figure 4.19:** Photograph of (a) the debinding furnace and (b) debinded Cu/40 vol.% D composite tapes.

SEM micrographs of a debinded copper/diamond composite tape are shown on Fig. 4.20. SEM micrographs tend to demonstrate the efficiency of the debinding process since no organics is observed to remain in the tape after the heat treatment under air. Air atmosphere was chosen to get rid of the organics since it allows an exhaustive elimination of the organics in a faster manner relative to a neutral gas atmosphere, such as argon (Ar) or nitrogen (N<sub>2</sub>) [210, 211]. At a finer scale, it is observable that the debinding process triggers the formation of nanosized wire-shaped (or *nanowires*) structures onto the surface of the dendrites, as shown on Fig. 4.20c and 4.20d. This is discussed in more details in further sections of the dissertation.

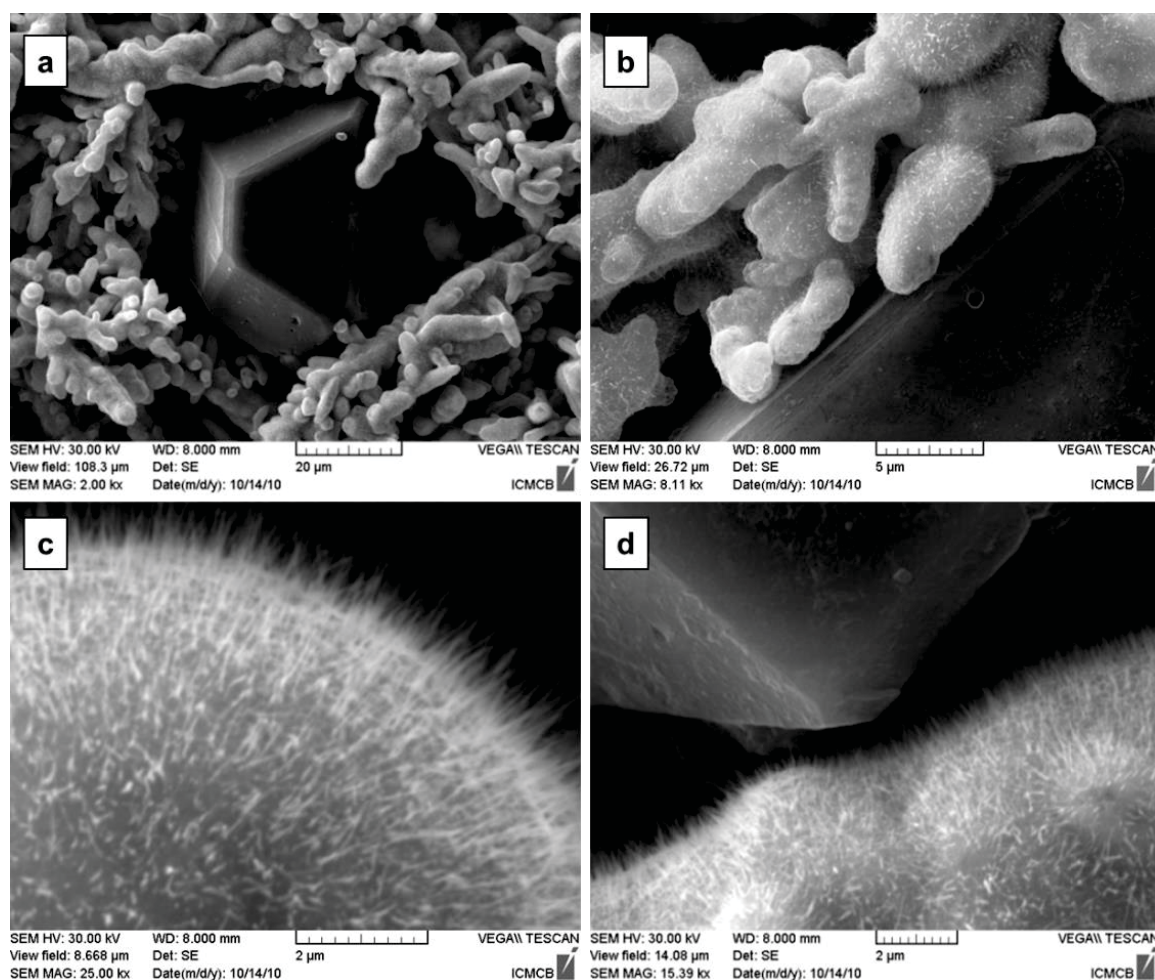


**Figure 4.20:** SEM micrographs of a copper/diamond composite tape debinded one hour at 400°C under air.

XRD analysis shown on Fig. 4.28a demonstrated that the oxidized copper matrix was composed of both cupric oxide (CuO, also called *tenorite*, with Cu in its +II oxidation state) and cuprous oxide (Cu<sub>2</sub>O, also called *cuprite*, with Cu in its +I oxidation state). The formation of cupric oxide was also remarkable at the naked eye through the black coloration of the Cu/D composite tapes after debinding, as shown on figure 4.19b, which is typical of CuO, whereas Cu<sub>2</sub>O typically exhibits a red color. Thermo-gravimetric analysis (TGA) was carried out in order to confirm the efficiency of the debinding process.



Figure 4.21 shows the TGA of a green Cu/D composite tape under air (red curve) and nitrogen atmosphere (dark blue curve) from room temperature to 500°C. In parallel is shown the TGA of the oxidation of copper powders under air (bright blue curve):

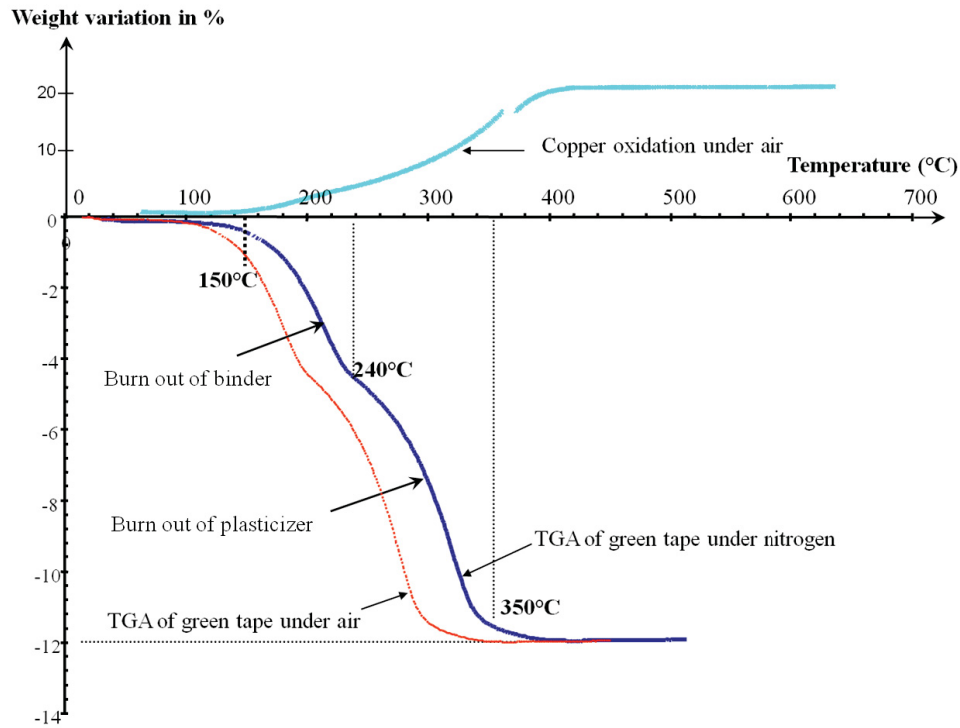


**Figure 4.21: TGA analysis of a copper/diamond composite green tape upon debinding (under air) [210].**

On the red and dark blue curves, the first and second mass losses respectively correspond to the burn out of the binder (PMMA:  $T_{melting} = 160^{\circ}\text{C}$ ) and plasticizer (DBP:  $T_{boiling} = 340^{\circ}\text{C}$ ). Under air atmosphere as under neutral atmosphere, TGA analysis demonstrated that the elimination of the organics is exhaustive when the temperature reaches 400°C. The debinding treatment is therefore effective under both types of atmosphere. However, it is clear from the thermo-gravimetric analysis that the elimination of the organics from the green tape is faster under air than under neutral atmosphere, which drove the choice for air atmosphere in this study.

The bright blue curve reveals the mass gain resulting from cupric oxide formation starting at 150°C, which originates from the fact that copper oxides (both CuO and Cu<sub>2</sub>O) have higher molar masses relative to pure copper, as shown in Tab. 4.6. One should notice that the global mass gain resulting from copper oxide formation is about 20%. An equivalent mass loss should result from the reduction process in order for it to be exhaustive.

**Table 4.6: Molar masses of copper (Cu) and cupric oxide (CuO) [198].**

Material	Cu	CuO	Cu <sub>2</sub> O
Molar mass (g/mol)	63.54	79.54	143.09

#### 4.4.2 Nanowires growth

SEM analysis carried out onto the debinded tape showed that nanowires had grown onto the oxidized copper dendrites. For clearer understanding of the growth process, it is interesting to go deeper into the investigation of their microstructure and growth conditions. Figure 4.22 shows the influence of the temperature on the organics burn out and on the growth of the nanowires:

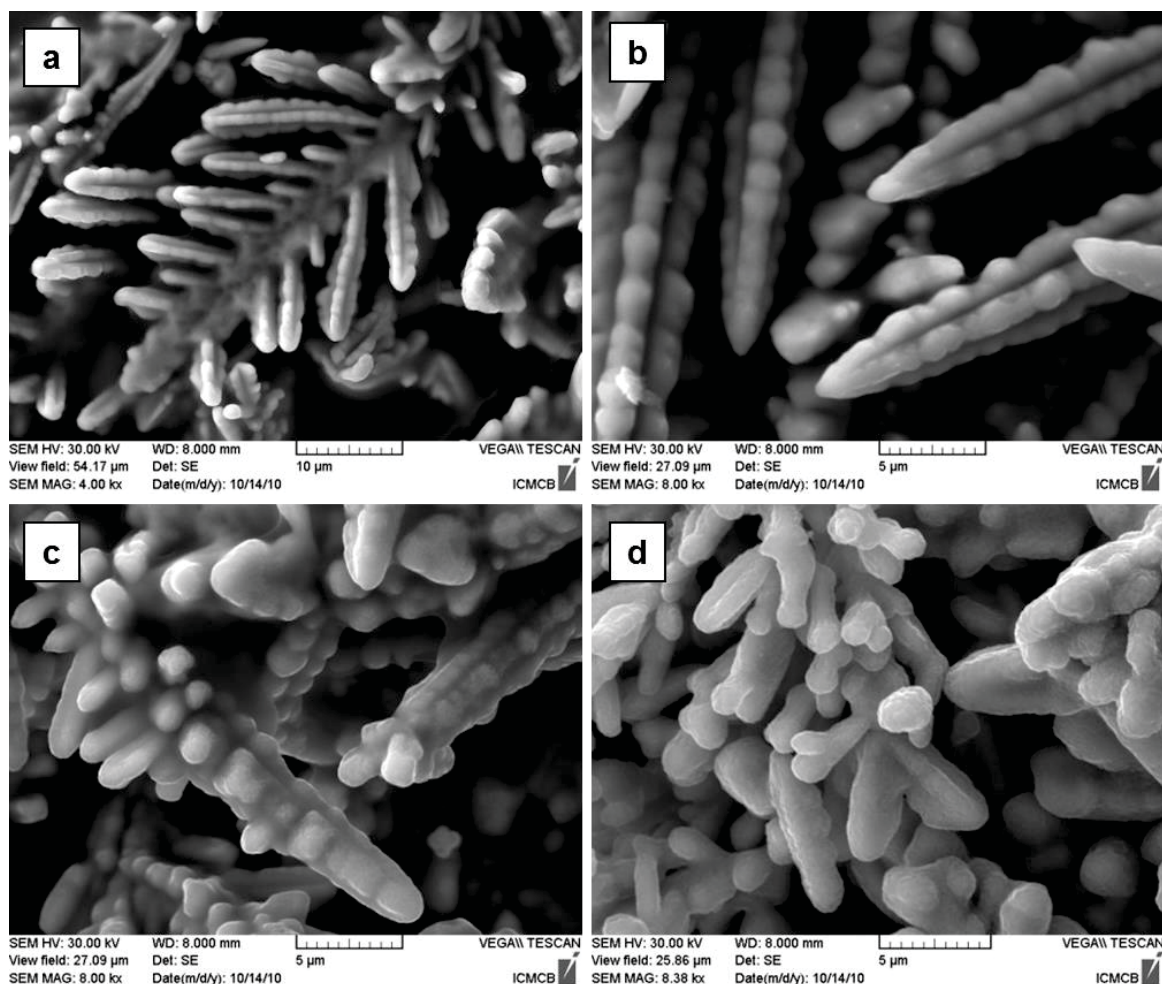


**Figure 4.22: SEM micrographs showing the influence of temperature on the debinding process:**

**(a) at  $T = 200^{\circ}\text{C}$ , (b) at  $T = 300^{\circ}\text{C}$ , (c) at  $T = 350^{\circ}\text{C}$ , (d) at  $T = 400^{\circ}\text{C}$  and  $t = 0$  min.**

SEM analysis showed that the nanowires start growing when the temperature reaches  $400^{\circ}\text{C}$ . One can also notice that, consistently with TGA analysis (Fig. 4.21), organics are observed to exist in the tape until the temperature reaches  $350^{\circ}\text{C}$  and are eliminated between  $350^{\circ}\text{C}$  and  $400^{\circ}\text{C}$ . However, copper oxidation under air starts much earlier, typically around  $100^{\circ}\text{C}$ . Therefore, mass gain starts with copper oxidation. The nanowires growth onto the copper dendrites is observed to start after 10 minutes at  $400^{\circ}\text{C}$ , and the nanowires keep growing as the holding time at  $400^{\circ}\text{C}$  increases, as shown on Fig. 4.23.

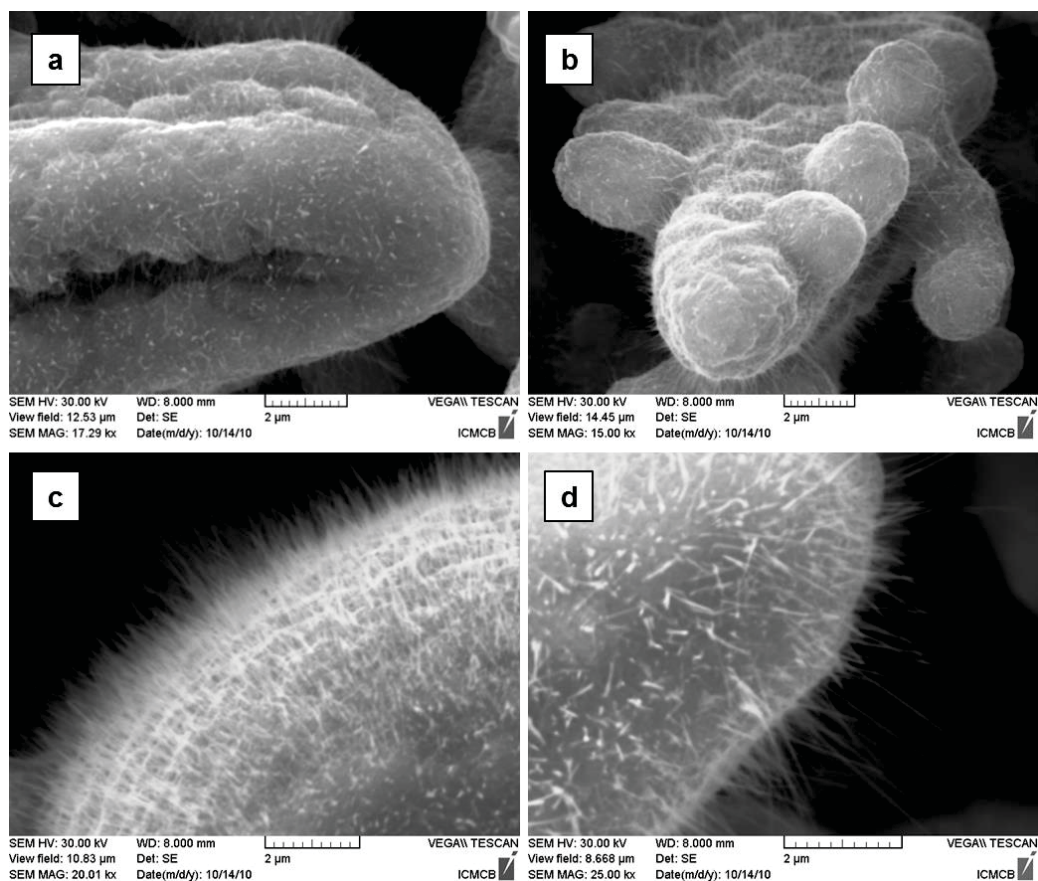


**Figure 4.23: SEM micrographs showing the influence of holding time at 400°C on the nanowires growth process: (a)  $t = 30$  min, (b)  $t = 70$  min, (c)  $t = 90$  min, (d)  $t = 120$  min.**

TEM analysis was employed to observe the nanowires structure and to determine their chemical nature (Fig. 4.24). After 120 minutes at 400°C, the nanowires exhibit lengths ranging between 500 nm and 3  $\mu\text{m}$ , and diameters typically below 100 nm. The lengths of these nanowires could be conveniently controlled by changing the oxidation time.

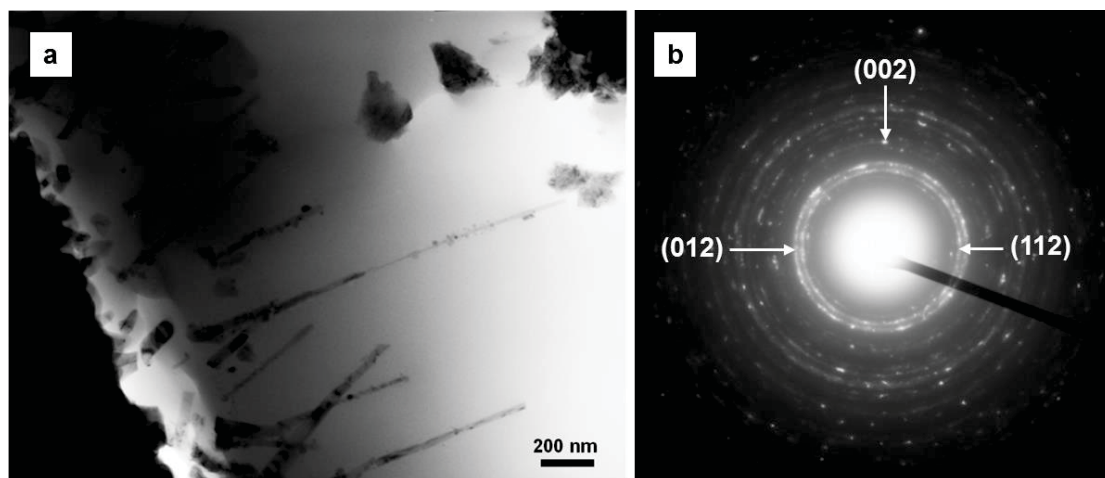


**Figure 4.24: (a) TEM micrograph of copper oxide nanowires grown onto copper dendrites upon air debinding; (b) corresponding diffraction pattern.**



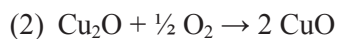
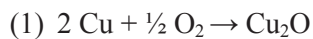
The ring-shaped diffraction pattern shown on Fig. 4.24b demonstrated that the nanowires were polycrystalline. Although no clear conclusion could be drawn so far about the elemental composition of the nanowires, the diffraction pattern suggests that the nanowires are made of CuO. Indeed, the rings of the pattern were indexed to the (112), (002), and (012) diffraction peaks of monoclinic CuO rather than cubic cuprous oxide (Cu<sub>2</sub>O).

#### 4.4.3 Hypotheses on the nanowires growth process

Materials of interest such as silicon (Si) [212, 213], tin (Sn) [214], germanium (Ge) [215], gallium arsenide (GaAs) [216], and gallium nitride (GaN) [217] have been reported to be synthesized in the form of nanowires. Although the vapor-liquid-solid (VLS) mechanism is the most commonly accepted nanowire growth process in gas phase [212], various other mechanisms have been proposed, such as vapor-solid-solid (VSS) [213], vapor-solid (VS) [214], oxide-assisted growth (OAG) [217, 218], and screw dislocations growth [219]. VLS processes typically involve metal catalyst particles that end at the tips of the finally grown nanowires. Such morphology was not observed on the nanowires formed, plus no liquid phase could be formed at the debinding temperature. Therefore, the VLS mechanism was excluded. In addition, no apparent built-in screw dislocations were observed in the as-grown CuO nanowires. Thus, it is not likely that CuO nanowires growth originates from screw-dislocations.

Given the oxygen-rich atmosphere in which the CuO nanowires was observed to occur, it is believed that the copper oxides formed upon debinding are involved in the CuO nanowires growth process. Therefore, the hypothesis of an *oxide-assisted vapor-solid* growth mechanism was emitted in order to explain the growth of the CuO nanowires. The VS mechanism has been applied to account for the growth of a variety of metal oxides [214]. However, the process considered in this study differs from typical VS mechanisms in that a precursor is involved, rather than originating from the direct oxidation of the metal [220].

Indeed, when copper is oxidized in air, the major resulting product is cuprous oxide (Cu<sub>2</sub>O). Cupric oxide (CuO) is only formed slowly through a second step of oxidation. Indeed, at 600 K: the free enthalpies of formation of Cu<sub>2</sub>O and CuO through Cu oxidation are respectively:  $\Delta_r G^\circ_{\text{Cu}_2\text{O}} = -124.944 \text{ kJ.mol}^{-1}$  and  $\Delta_r G^\circ_{\text{CuO}} = -100.851 \text{ kJ.mol}^{-1}$ . Therefore, Cu<sub>2</sub>O acts as a precursor to CuO formation. The oxidation process of the copper matrix can be summed up through the following reaction pathway, with reaction (2) acting as the rate-determining step for CuO vapor formation:



From a kinetic point of view, Cu<sub>2</sub>O formation is privileged since its standard free energy of formation is lower. However, from a thermodynamic point of view, CuO is the more stable copper oxide compound.

The supersaturation ratio of the condensing species in the gas phase plays a key role in the growth of one-dimensional nanostructures through the VS mechanism [214, 219]. It is defined as:

$$\alpha = \frac{p}{p_0} \quad (4.2)$$

Where  $\alpha$  stands for the supersaturation ratio,  $p$  for the vapor pressure of condensing species at the surface, and  $p_0$  is the equilibrium vapor pressure. For anisotropic growth of nanowires, the supersaturation ratio of CuO must be maintained below a certain critical value, above which two-dimensional or even isotropic growth occurs. Therefore, a low supersaturation ratio is necessary for anisotropic growth to happen, while a medium supersaturation ratio leads to growth of bulk crystals. At high supersaturation ratio, homogeneous nucleation in the gas phase results in powder formation. The slow formation rate of CuO through reduction of Cu<sub>2</sub>O ensures a sufficiently low vapor pressure for this material in the reaction chamber, thus a continuous growth mode for the CuO nanowires. At the beginning of the nanowires growth process, CuO vapors must have been generated through the thermal debinding process at 400°C. The CuO vapors then condensate onto the copper dendrites and crystallize. A competition in growth rate among different crystallographic planes then starts in the early stage of the crystallization process. Once the condition at which one-dimensional anisotropic growth is favored occurred, the CuO particles start to strike on a specific advancing plane to induce a continuous one-dimensional growth, leading to the formation of nanowires. Crystallographic planes possessing relatively higher surface energies are thermodynamically more unstable, and more vulnerable to attack of external atoms. Therefore, growth of CuO nanowires preferentially occurs in planes with the highest surface energies.

Cupric oxide exhibits interesting properties of superconductivity. It has also been known as a p-type semiconductor that exhibits a narrow band-gap (1.2 eV), and belongs to a particular class of materials called Mott insulators, who are electrical insulators while their electronic structure suggests that they are electrical conductors. This originates from the particular electronic band structure they exhibit, which cannot be described through the conventional band theory. Therefore, CuO nanowires are of strong interest for a variety of electronic and magnetic applications.

The presence of copper oxide in the composite powder mixture being critically detrimental to the forthcoming sintering process, a second reductive heat treatment is required prior to densification.

#### 4.4.4 Reduction

After debinding, the copper oxide/diamond composite tape is heat treated at  $+6.3^{\circ}\text{C}/\text{min}$  up to  $400^{\circ}\text{C}$  under  $\text{Ar}/\text{H}_2$  (5 vol.%) flux with a 60 minutes hold at  $400^{\circ}\text{C}$ . Figure 4.25 shows photographs of the reduction furnace and of reduced copper/diamond composite tapes.

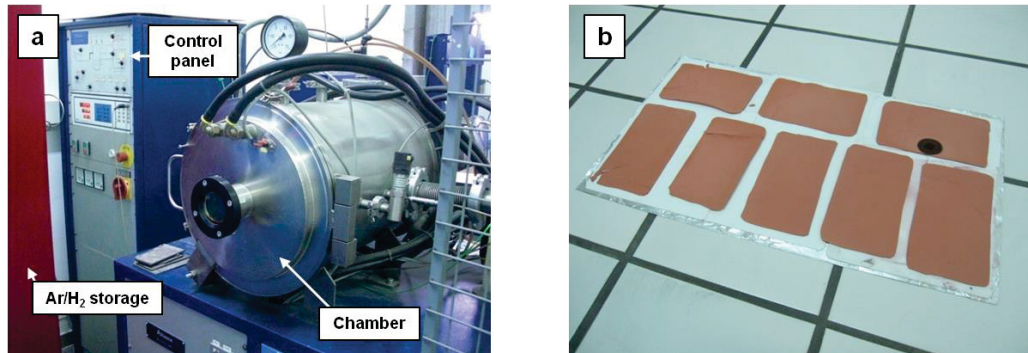


Figure 4.25: Photographs of (a) the reduction furnace and (b) reduced Cu/40 vol.% D composite tapes.

Figure 4.26 shows SEM micrographs of a reduced copper/diamond composite tape:

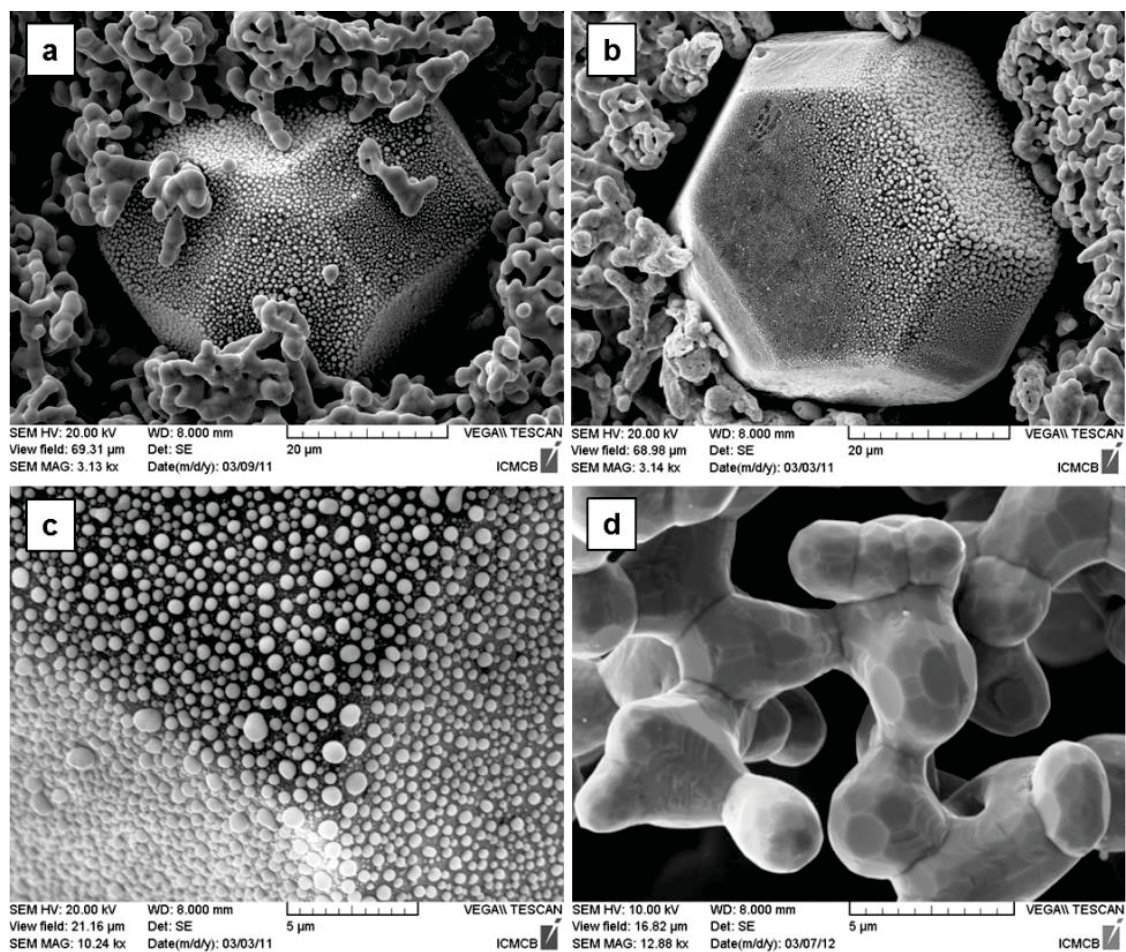
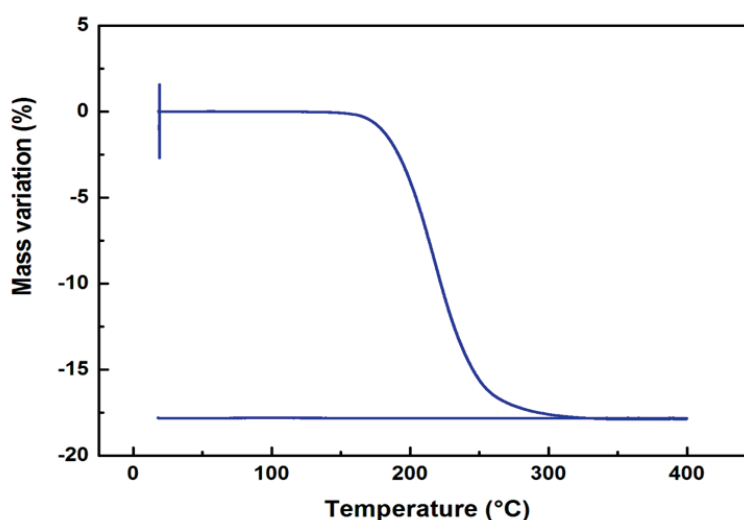


Figure 4.26: Scanning electron micrographs of a copper/diamond composite tape reduced 1h at  $400^{\circ}\text{C}$  under  $\text{Ar}/\text{H}_2$  [209].

It is visible on Fig. 4.25b that the tapes have recovered the color of metallic copper, although a dark zone which has not been properly reduced remains. This tape would be retreated under Ar/H<sub>2</sub> to be exhaustively reduced prior to further processing. In Fig. 4.26, we observe that the diamond reinforcements are embedded into the reduced copper matrix (Fig. 4.26a and 4.26b). Figure 4.26d demonstrates that the wire-shaped copper oxide nanostructures that were observed onto the oxidized copper dendrites after debinding (Fig. 4.20, 4.23) are no longer present, as a consequence of the dendrites reduction. In addition, the copper dendrites are observed to be faceted after reduction (Fig. 4.26d).

Moreover, it is remarkable on Fig. 4.26b and 4.26c that the diamond reinforcements of the composite tape are coated with spherical particle after reduction. After 1 h at 400°C, the size of these particles range from 100 nm to 1 µm. The coverage of the diamonds surface by the particles is remarkably uniform on each crystallographic facet of the reinforcements. However, various sizes of particles are observed to coexist onto the surface of the diamond reinforcements. Deeper structural and chemical investigations of the deposited particles are carried out in section 4.5.

Figure 4.27 shows the thermo-gravimetric analysis of a debinded composite tape under the conditions of the reducing heat-treatment:



**Figure 4.27: TGA analysis of a debinded copper/diamond composite tape upon reduction under Ar/H<sub>2</sub>.**

It demonstrates that the copper/diamond composite tape experiences a mass loss of about 18% upon reduction under Ar/H<sub>2</sub>, thus leading to the conclusion that the copper matrix is exhaustively reduced during the reductive heat-treatment. Indeed, the mass gain upon debinding had been measured to be of about 20% (Fig. 4.21). X-ray diffraction analysis also suggested that this reductive heat treatment was effective in reducing the copper oxides into metallic copper, as shown on Fig. 4.28, which shows the diffraction pattern of a copper/diamond composite tape after

debinding (Fig. 4.28a) and after reduction (Fig. 4.28b). Diffraction peaks of both cuprous and cupric oxides are detected in the tape after debinding. Only signals of metallic copper are detected after the reductive heat-treatment, which means that the copper matrix has been exhaustively deoxidized.

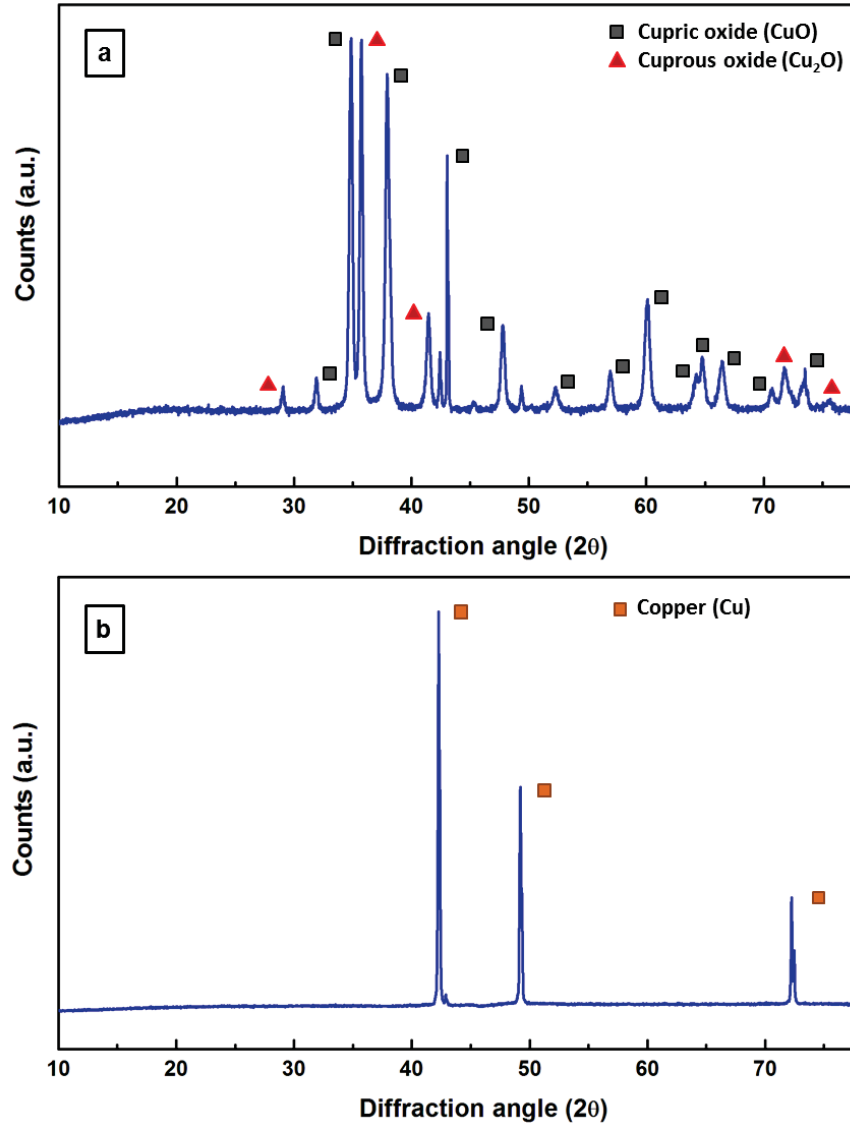


**Figure 4.28: X-ray diffraction patterns of (a) a debinded and (b) a reduced copper/diamond composite tape.**

Finally, it was demonstrated that the size of the particles deposited onto the diamond substrates could be adjusted by tuning the reduction time and temperature. Figure 4.29 shows SEM micrographs of particle-coated diamond reinforcement reduced upon different conditions: the diamond reinforcements are coated with particles whose sizes range from 100 nm to 400 nm (after 1 minute at 350°C under Ar/H<sub>2</sub>, Fig. 4.29a), from 300 to 800 nm (after 5 minutes at 400°C under Ar/H<sub>2</sub>, Fig. 4.29b), and from 400 nm to 1 μm after 60 minutes at 400°C under Ar/H<sub>2</sub> (Fig. 4.29c). However, the influence of the size of the Cu particles deposited on the final thermal properties of the composites has not been established yet. Deeper investigation is needed on this topic.



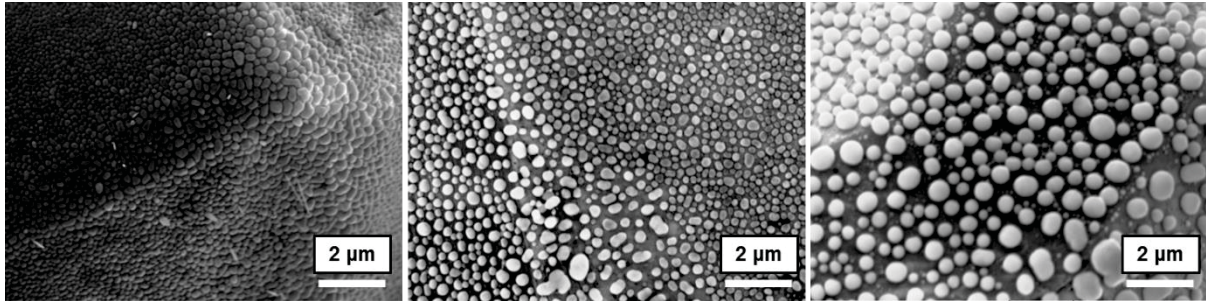


Figure 4.29: SEM micrographs of particle-coated diamond reinforcements upon various reduction conditions.

Hot pressing was then employed to obtain dense copper/diamond composite materials. However, prior to focus on the sintering step, it is interesting to more closely examine the particles deposited onto the diamond reinforcements surface, especially from the chemical and microstructural points of view.

## 4.5 Investigations on the particles grown onto diamonds

In this section, we will try to gain more understanding about the nucleation and growth of the particles observed onto the diamond surface after reduction. Our objectives are the following:

- Investigate the surface chemistry of the diamond reinforcements after debinding to understand how the particles can nucleate onto the diamond surface; X-ray Photoelectron Spectroscopy (XPS) will be used to do so;
- Study the different populations of particles existing onto the surface and their respective size; Atomic Force Microscopy (AFM) will be employed in this aim;
- Analyze the chemical composition of the particles and the existence or not of an interphase at the interface between the particles and the diamond substrates; Transmission Electron Microscopy (TEM) and Energy Dispersive X-ray Spectroscopy (EDXS) will be helpful to this task.

Details about the physical and technical principles underlying each of these techniques are provided in the annex section. Based on the conclusions drawn for these investigations, a growth mechanism will be proposed.

### 4.5.1 Surface chemistry of the diamond reinforcements

XPS analysis is a surface chemical analysis method which allows getting information about the chemical nature of the elements existing onto the surface and their chemical environment by measuring the binding energy of the electrons to the nucleus. The analyzed depth typically ranges between 2 nm and 10 nm. The first step consists in obtaining a global energy spectrum of the surface which shows the elements existing on the surface. In a second time, one can focus on some



peaks of this spectrum to obtain particular spectra with higher resolution, thus providing information about the chemical environment of the elements considered. XPS analysis was carried out onto the surface of diamond reinforcements after formulation and debinding (thus prior to reduction and Cu particles deposition). Figure 4.30 shows the resulting spectrum (Fig. 4.30a) and the decomposition of P2p and C1s peaks (Fig. 4.30b and 4.30c, respectively). Table 4.7 shows a detailed peak description of the XPS survey.

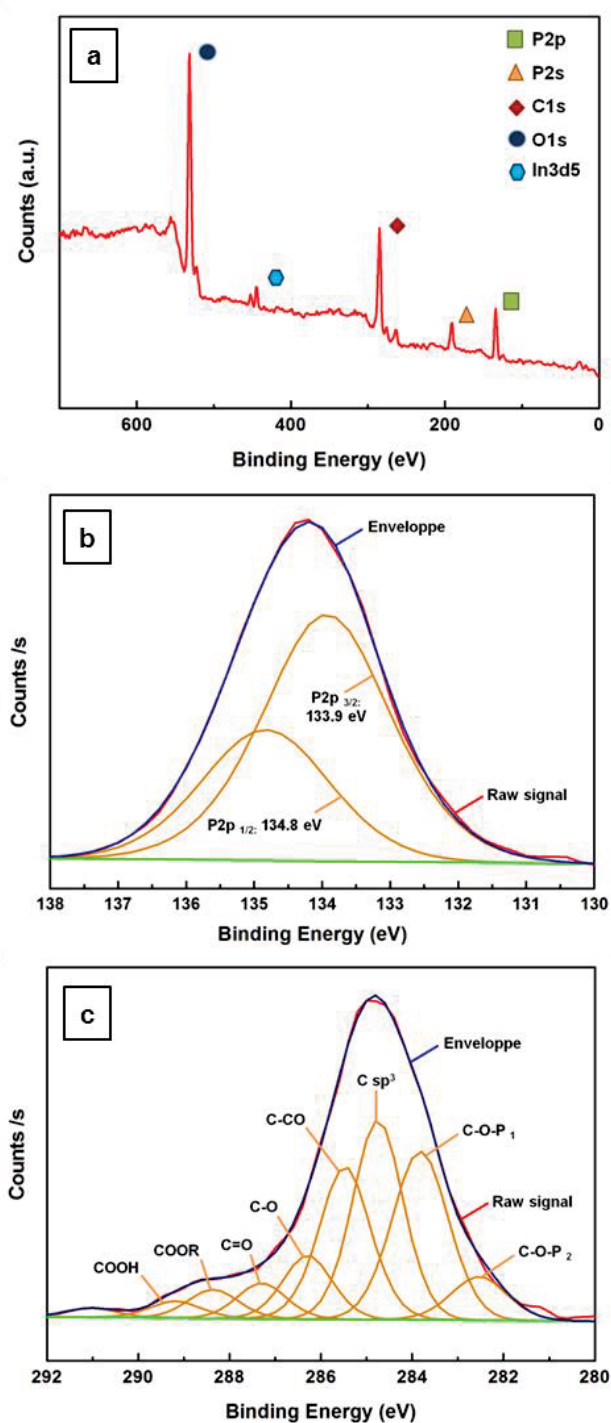


Figure 4.30: (a) Chemical surface analysis of debinded diamond powders through XPS and its (b) P2p and (c) C1s decomposition.

**Table 4.7: XPS survey peak description.**

Peak	Binding energy (eV)	Atomic percentage (%)
P2p	134.22	11.98
C1s	284.84	42.24
O1s	531.24	42.45
In3d	444.15	0.59
Si2p	102.79	1.02
N1s	398.98	1
Ca2p	346.55	0.45
Na1s	1070.58	0.28

The surface analysis of the diamond powders carried out through XPS clearly demonstrates that, apart from carbon, phosphorus (P peaks located at 134.2 eV (P2p) and 191.4 eV (P2s)) and oxygen (O peak located at 531.2 eV) are the two main chemical elements detected onto the surface of the debinded diamond powders. It is clear from the XPS global spectrum that the surface of the diamond powders has been functionalized through the use of the phosphate ester dispersant agent, which is rich in phosphorus and oxygen (see Tab. 4.5). The indium signal (In peak located at 444.1 eV) observed results from the use of an indium foil as sample-holding layer during XPS characterization. Finally, the Si, Na, Ca, and N signals are understood to come from the ceramic crucible in which the diamond powders were heat treated.

The atomic number of P is 15 and its electronic configuration is  $1s^2 2s^2 2p^6 3s^2 3p^3$ . XPS allows the binding energies of the core electrons of the 2s and 2p orbitals to be measured. However, when considering a single element showing multiple peaks, only the peak of highest intensity is valuable in XPS. Therefore, the P2s signal will not be considered in further analysis. The 2p orbital of phosphorous splits into two energy levels with a gap of 1 eV: a low energy level  $P2p_{1/2}$ , which hosts 4 electrons, and a high energy level  $P2p_{3/2}$ , which hosts 2 electrons. A finer analysis of the P2p signal allows confirming this theoretical prediction, showing the  $P2p_{1/2}$  and  $P2p_{3/2}$  peaks at 134.8 eV and 133.9 eV respectively, thus separated by a gap of 1.1 eV.

The most common compound encountered when combining phosphorus and oxygen is  $P_2O_5$ . The oxidation number of phosphorus in the  $P_2O_5$  environment is +5. The P2p signal of our diamond powders is located at 134.2 eV, which corresponds to an intermediate binding energy between the P2p signal of phosphorus in its  $P^{5+}$  configuration ( $P2p_{P^{5+}} = [134.9 - 135.2]$  eV) and the P2p signal of phosphorus in its  $P^{3+}$  configuration ( $P2p_{P^{3+}} = 132.4$  eV), as shown in Tab. 4.8. Therefore, it is probable that multiple bonding configurations between P, C, and O, exist at the surface of the diamond powders which combine  $P_2O_5$  structures to other C-O-P assemblies.

**Table 4.8: P2p signal decomposition.**

	Peak	Binding energy (eV)
Recorded signal	P2p	134.22
P2p configurations:	P2p <sub>P3+</sub>	132.4
	P2p <sub>P5+</sub>	[134.9 – 135.2]

Table 4.9 shows the main peaks resulting from the decomposition of the C1s signal, thus providing information about the chemical environment of the carbon atoms of the surface:

**Table 4.9: C1s signal decomposition.**

Peak	Binding energy (eV)	Atomic percentage (%)
C1s (C sp <sup>3</sup> )	284.75	10.98
C1s (C-O-P <sub>1</sub> )	283.82	10.29
C1s (C-O-P <sub>2</sub> )	282.54	2.69

From the decomposition of the C1s signal, it can be seen that two C-O-P configurations are detected through XPS. The sum of the atomic percentage of the two corresponding signals is equivalent to the atomic percentage of the P2p signal, meaning that the very large majority of phosphorus existing onto the surface is bonded to oxygen.

One of these configurations (C-O-P<sub>2</sub> located at 282.54 eV) is close in energy to a C-P bond. Therefore, C-P chemical bonds might exist onto the diamond surface, however in lesser quantity relative to C-O-P bonds since the atomic percentage of C-O-P<sub>1</sub> configuration is higher relative to the atomic percentage of C-O-P<sub>2</sub> configuration. C-P bonds have been investigated for a long time by researchers, but these investigations were met by little success. We provided in this study an interesting contribution to the probable existence of such chemical bonds in nature. Finally, a large amount of oxygen existing at the surface of the diamond particle (about 30 at.%) remains unbounded to phosphorus, thus being available for bonding with other chemical elements. This amount of free oxygen is believed to be involved in the bonding process between diamond and copper, as explained further.

AFM will be employed in the next section to investigate the sizes of the Cu particles deposited and the various populations existing onto the diamond surface.

#### 4.5.2 Particles sizes and populations

AFM is a local scanning technique relying on the interaction between the atoms of the surface and the atoms of a very sharp tip mounted on a cantilever to obtain a topographical mapping of a surface and, hence, to quantify parameters such as surface feature sizes and roughness. While the

classical tapping mode allows mapping the topography of the surface, phase imaging provides higher sensitivity toward the surface morphology, and frequently allows the observation of features barely visible in classical topographic imaging. Two-dimensional and three-dimensional images obtained through AFM analysis of a Cu-coated diamond particle are shown on Fig. 4.31.

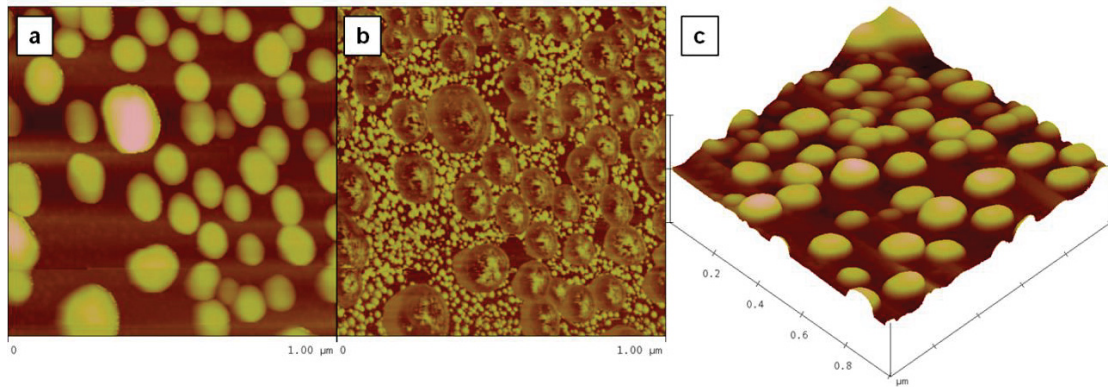


**Figure 4.31: AFM surface analysis of a Cu-coated diamond reinforcement. (a) 2D topographic image. (b) 2D phase image. (c) 3D topographic image.**

The AFM images obtained confirm the almost-spherical shape of the Cu particles deposited. The phase image obtained from AFM analysis (Fig. 4.31b) visibly shows that nanosized copper particles, which are barely detected through the topographical analysis of the surface, exist among the submicronic particles. This smaller particle population coexisting with the larger particle population contributes to enhance the chemical bonding of the copper matrix with the diamond reinforcements during sintering.

The three-dimensional topographic image (Fig. 4.31c) revealed that the average roughness ( $R_a$ ) of the investigated area was 20 nm. AFM analysis also enlightened that the bonding between the copper particles and the diamond surface is resistant to the tapping mode analysis since no delamination of the copper dots was observed during or after AFM analysis. Line profiles analyses carried out on Cu-coated diamond surface enables getting an idea of the variety of the sizes of the Cu particles existing onto the surface: the largest ones are about 120 nm high while the smallest copper particles reach only 3 nm of height (Fig. 4.32).

The large distribution of sizes existing onto the surface explains why the average measured roughness is 20 nm, a value located at an average position between the biggest and the smallest particles. This average roughness value could be considered similar to the  $d_{50}$  value of a particle size distribution, which splits the particle distribution into two equals populations (see section 4.9.2). This means that the number of small particles (between 3 and 20 nm diameter) is much larger than the number of large particles (between 20 and 120 nm). The line profiles confirm the existence of nanosized copper substructures among the micro-sized copper particles observed through SEM.

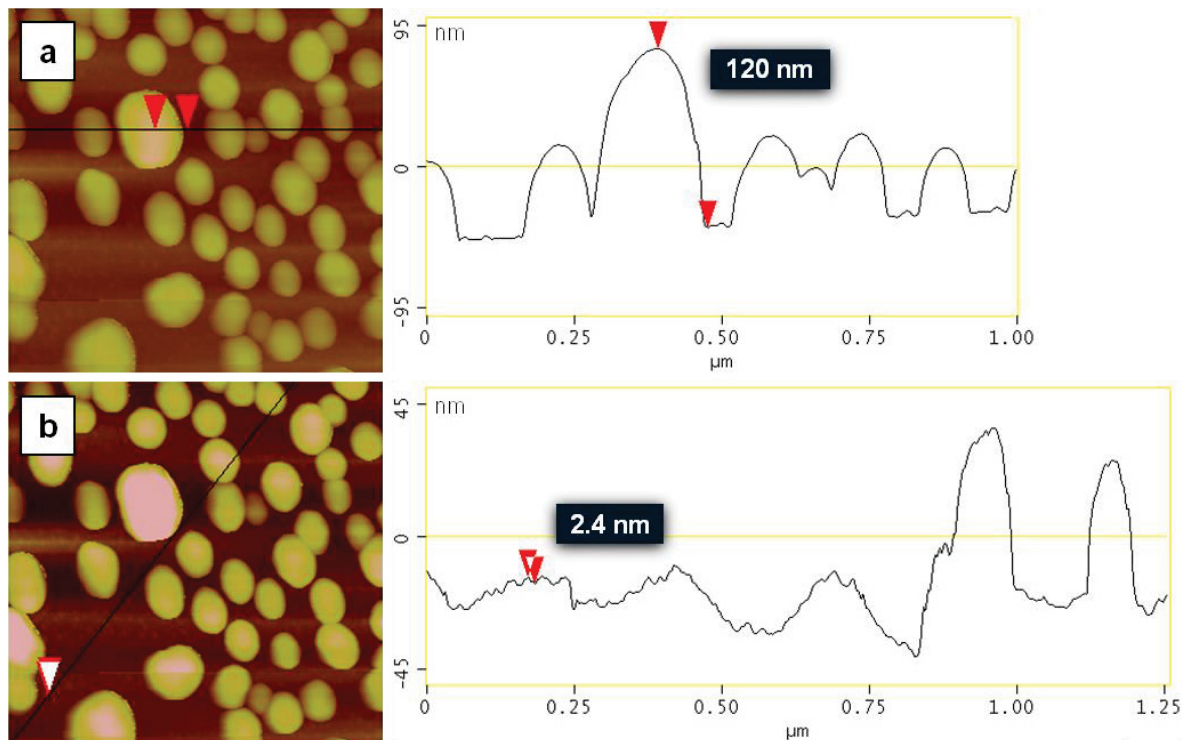


**Figure 4.32: AFM line profiles onto a Cu-coated diamond reinforcement.**

The two populations of Cu particles existing onto the surface of the diamond reinforcements both contribute to obtain a strong chemical bonding between the copper matrix and the diamond reinforcements through the creation of Cu-Cu metallic bonds upon densification. However, the chemical nature of the bonds binding the diamond reinforcements to the copper dots is still in lack of understanding. TEM analysis has been employed to enlighten the structure of the Cu/D interface.

TEM will be employed in the next section to investigate the chemical nature of the deposited particles and the structure of their interface with the diamond substrates.

#### **4.5.3 Particle composition and microstructure**

Energy dispersive x-ray spectroscopy (EDXS) is an analytical technique used for elemental characterization of a sample. Similar to x-ray diffraction (XRD), it relies on the fact that each fundamental element exhibits a unique atomic structure, leading to a unique set of x-ray diffraction peaks. By measuring the X-ray energy resulting from electronic transitions into the atom structure, EDXS provides information about the elemental composition of the sample. Either elemental point investigation or mapping can be carried out through this technique.

EDXS elemental mapping analysis was carried out onto the particles deposited onto the diamond reinforcements in order to reveal their chemical nature (Fig. 4.33).



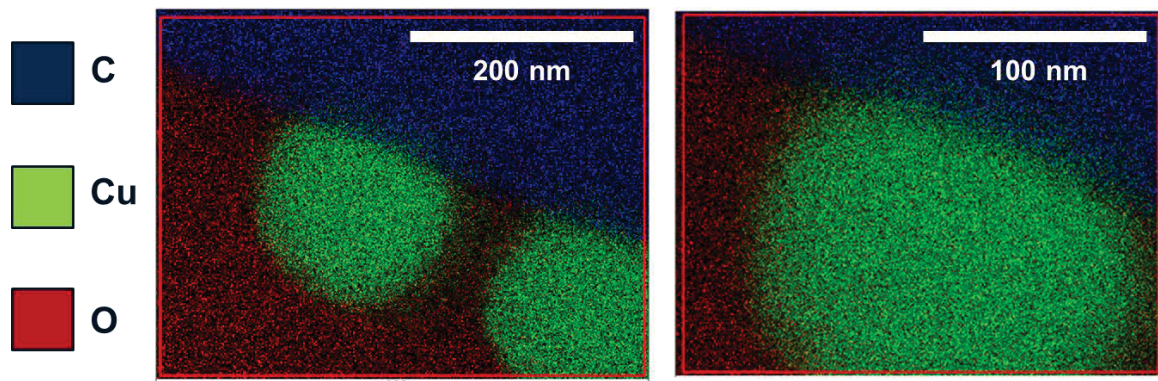


**Figure 4.33: Chemical mapping of a Cu-coated diamond reinforcement through EDX spectroscopy.**

The EDXS mapping clearly demonstrates that the particles coating the diamond reinforcements are metallic copper particles (the copper appears in green color). Neither an interphase at the interface between the copper particle and the diamond reinforcement nor an oxide layer covering the particle can be detected through EDXS analysis. The diamond substrate (carbon) clearly appears in blue color. The red color surrounding the copper particle corresponds to oxygen and is due to the presence of a TEOS ( $\text{SiO}_2$ ) layer embedding the Cu-coated diamond sample for TEM observation. The sample was prepared through focused ion beam (FIB) in collaboration with Serma Company (Grenoble, France).

Transmission Electron Microscopy (TEM) allows the fine microstructure of an ultra-thin specimen to be inspected by interacting a focused beam of electrons with the atoms of the sample. An image is formed from the interaction of the electrons with the atoms of the specimen and then detected by a CCD camera. More details about TEM analysis can be found in the annex section. TEM cross-sectional micrographs of a Cu-coated diamond reinforcement are shown in Fig. 4.34a and 4.34b. The samples for TEM observations were prepared through focused ion beam (FIB) cutting in collaboration with Serma Technology company (Grenoble, France).

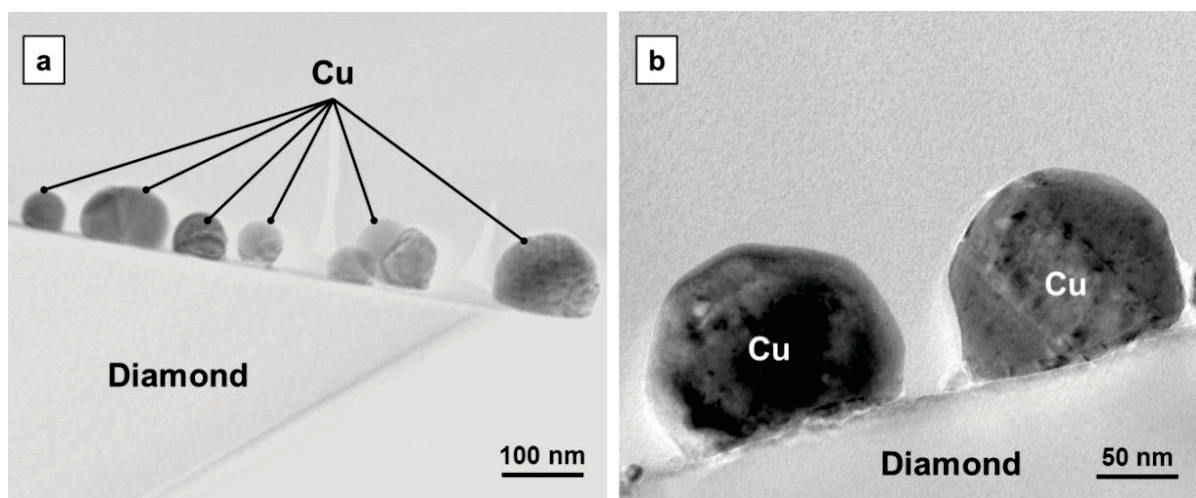


**Figure 4.34: TEM micrographs of a Cu-coated diamond reinforcement.**



TEM analyses show that the largest Cu particles deposited are observed to be mainly polycrystalline, meaning that several crystallographic orientations coexist into a single particle. Grains separated by twin boundaries are visible in the structure of some of the Cu particles grown onto the diamond surface (Fig. 4.34b). A twin boundary is a special type of grain boundary across which there is a specific mirror lattice symmetry.

On Fig. 4.34b, the Cu dots seem to be faceted. This observation corroborates the faceted aspect of the copper dendrites due to the reductive heat treatment upon Ar/H<sub>2</sub> (Fig. 4.26d) and demonstrates the high crystallinity of the Cu particles grown onto the diamond surface. Smaller single crystal particles around 10 nm diameter are also observed through TEM analysis. Therefore, the TEM observations confirm the AFM analyses which enlightened the existence of two populations of Cu particles onto the surface of the diamond reinforcements (Fig. 4.31 and 4.32).

Fig. 4.35 shows high-resolution TEM micrographs of a small Cu particle grown onto a diamond reinforcement substrate. The Cu particle is shown at the early stage of the exposure to the electron beam (Fig. 4.35a) and after having been exposed to the electron beam during several minutes (Fig. 4.35b). On Fig. 4.35a, Moiré fringes are clearly detected from the Cu particle, meaning that two crystalline networks interact. The Fourier transform of the image of the particle shows that only one orientation is highlighted while the displayed spots are clearly doubled. This demonstrates that two networks with the same symmetry but different lattice dimensions interact together. Upon exposure to the reductive electron beam, the copper oxide layer reduces to metallic copper, as shown on the resulting Fourier transform where doubles spots are now clearly defined single spots (Fig. 4.35b).

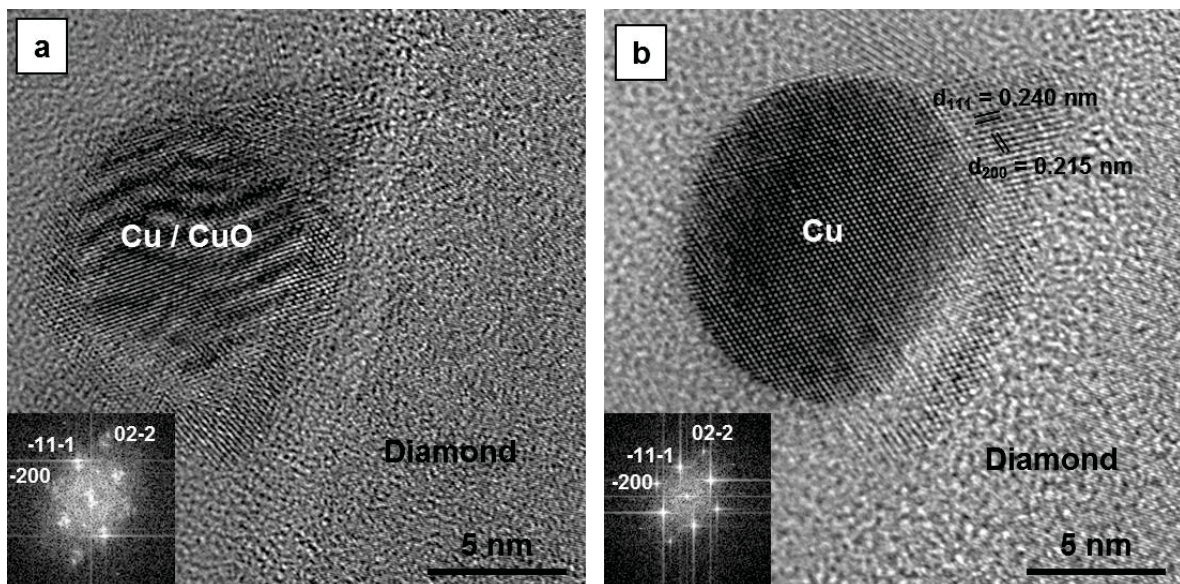


**Figure 4.35: High resolution TEM micrographs of a Cu-coated diamond reinforcement (a) before and (b) after exposure to the reductive electron beam.**

Table 4.10 gathers the crystallographic properties of various known copper oxides, metallic copper, and diamond. It suggests that cubic cupric oxide (CuO) is responsible for the Moiré fringes when interacting with the copper network. Indeed, cubic CuO is the closest compound to copper in terms of both space group (Cu and cubic CuO both belong to the Fm-3m group with FCC unit cell) and lattice parameter. Moreover, Cu and cubic CuO both present a [110] zone axis which could explain the Moiré fringes. Although not being its most commonly found allotrope as bulk material, cubic copper oxide is a stable crystalline form of copper oxide. In addition, it is known that when considering objects as small as the copper nanoparticles considered, an impact of the decrease in the size of the objects on their structure (due to a high surface area over volume ratio) has to be taken into account, i.e. nano-objects may display different configuration relative to bulk-objects of the same nature. Nevertheless, it cannot be excluded that Cu<sub>2</sub>O was responsible for interfering with the Cu network. Indeed, Cu<sub>2</sub>O is the compound that spontaneously forms onto metallic copper upon air oxidation, as explained in section 4.4.3.

**Table 4.10: Crystallographic properties of copper, diamond, and cubic copper oxides [198].**

Material	Crystal structure	Space group	Lattice parameters (Å)
Cu	Cubic	Fm-3m	a = 3.613
D	Cubic	Fd-3m	a = 3.566
CuO	Cubic	Fm-3m	a = 4.245
Cu <sub>2</sub> O	Cubic	Pn-3m	a = 4.2676

Therefore, the Cu particle is understood to be initially coated with a copper oxide layer due to the air exposure of the sample between the processing steps and its preparation for TEM observation.

#### 4.5.4 Copper/diamond interface composition and microstructure

Despite the oxide layer reduction upon electron beam exposure, the interphase observed between the Cu particle and the diamond substrate, which is about 2 nm thick, is not affected, which reveals that its structure is consistent enough to not being modified by the electron beam, as shown on Fig. 4.35b. In addition, such interphase is repeatedly observed through high-resolution TEM micrographs, as shown on Fig. 4.36.

The micrographs of Fig. 4.36 was obtained at the interface between a large copper particle and the diamond reinforcement on which it was grown. This micrograph clearly confirms that an interphase exists between the copper dots and the diamond. This interphase is polycrystalline and about 7 nm large (+/- 2 nm). Moreover, the Moiré fringes first observed to cover the Cu particles (Fig. 4.35a) are now detected in the interphase structure, suggesting that two crystallographic networks with same symmetry, but different lattice parameters, interact together at the interphase location. Therefore, copper oxide is understood to be located at the interphase.

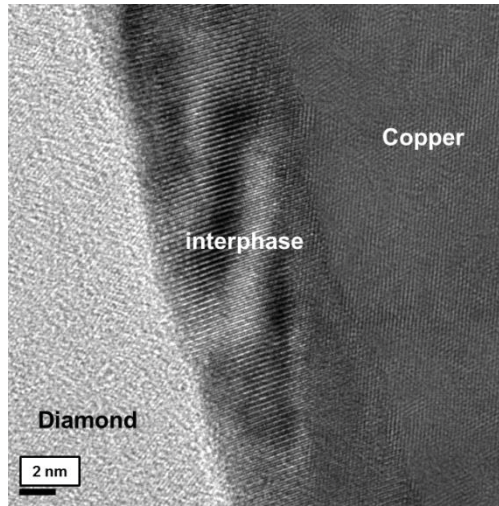


**Figure 4.36: High-resolution TEM micrographs at the Cu/D interface of a Cu-coated diamond particle.**

The fact that copper and oxygen are the only two reactive elements in the reducing furnace also suggests that they are involved in the creation of this interphase. XPS analysis has demonstrated that a large amount of oxygen exists on the diamond surface after debinding. This oxygen is understood to be available for chemical bonding with metallic copper during the reduction process. The measurement of interplanar distances of the interphase on Fig. 4.35b tends to confirm that the interphase is made of cubic copper oxide. Indeed, close correspondence was found between the interplanar distances measured and the (111) and (200) planes of cubic CuO and Cu<sub>2</sub>O. However, no clear distinction can be definitively made between cupric (CuO) and cuprous (Cu<sub>2</sub>O) oxide in the interphase. Also, the fact that the interphase between two FCC cubic networks (copper and diamond) is made of the same network symmetry would be consistent.

**Table 4.11: Interplanar distances of cupric and cuprous oxides relative to that of the interphase [198].**

Interplanar distances (nm)	Interphase	CuO	Cu <sub>2</sub> O
<111>	0.240	0.2451	0.2464
<200>	0.215	0.2123	0.2134

Slight distortions in the distances were observed. These were assumed to be due to a size-effect brought by the nanometric size of the object considered. Finally, one should notice that this copper oxide interphase was not detected through EDXS chemical mapping analysis (Fig. 4.33) due to the detection resolution of this characterization technique which is too low to detect such thin layers of oxide. Figure 4.37 shows a high-resolution TEM micrograph where the crystallographic planes are defined clearly enough so that we were able to record and index the Fourier transforms of the copper and diamond phase. Some dislocations are observed in the copper oxide interphases to accommodate the lattice deformation between the CuO and diamond networks. One dislocation out of fifteen crystallographic plans was detected. This resulted in an experimental network distortion of about 3.2% while the theoretical one between diamond and cubic CuO is about 6.6%, which tends



to confirm the existence of a cubic CuO interphase at the Cu/D interface. The slight gap between measured and theoretical distortions was assumed to originate from a size-effect brought by the nanometric size of the objects considered.

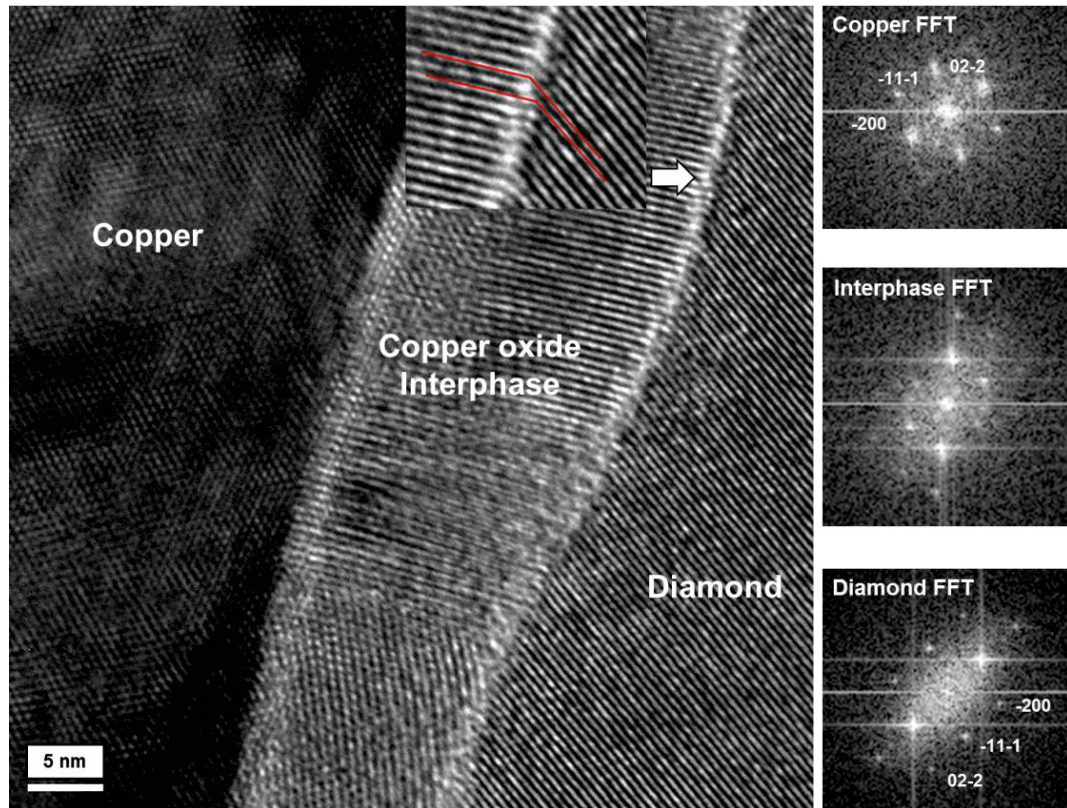


**Figure 4.37: High-resolution TEM micrograph at the Cu/D interface of a Cu-coated diamond reinforcement.**

It has to be pointed out that phosphorous-based compounds may also be involved in the composition of the interphase. However, XPS analysis suggested that a major amount of phosphorous atoms were chemically bonded to oxygen through  $P_2O_5$  structures. In addition, the evidence we gathered from TEM investigations strongly suggest that copper oxide (CuO) is the observed interphase material. Finally, it has been previously observed that copper oxide was responsible for the chemical bonding between copper and carbon surface such as epoxy resins and polymers [221]. This even more supports our understanding of the interphase composition.

Besides, the Cu particles coating process was shown to be also effective on CVD diamond films such as that grown in chapter 3. Figure 4.38 shows in a similar fashion as Fig. 4.26 and Fig. 4.29 SEM micrographs of a CVD diamond film grown through laser-assisted combustion synthesis on which Cu particles have been deposited. The very same process such as that developed for the HPHT diamond powders (functionalization, debinding with copper powders, reduction) was employed to grow Cu dots onto CVD diamond. One can see that the Cu coating remarkably fits to the film morphology.

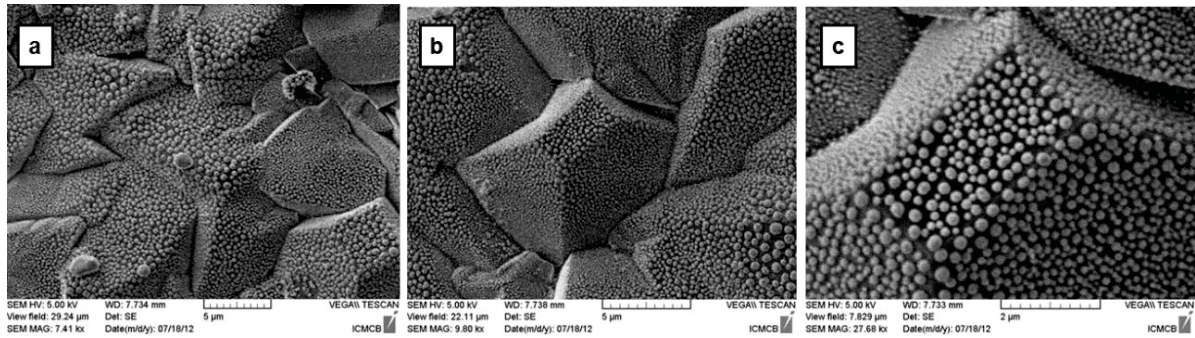


**Figure 4.38: SEM micrographs of a CVD diamond film grown through laser-assisted combustion synthesis and coated with copper dots.**

It is worth notice that the Cu particles deposited onto the surface of the CVD diamond film showed similar interphase at the copper/diamond interface than that revealed between the Cu dots and the diamond reinforcements in Cu/D composites. Figure 4.39 shows TEM micrographs obtained at the interface between CVD diamond and the deposited Cu particles.

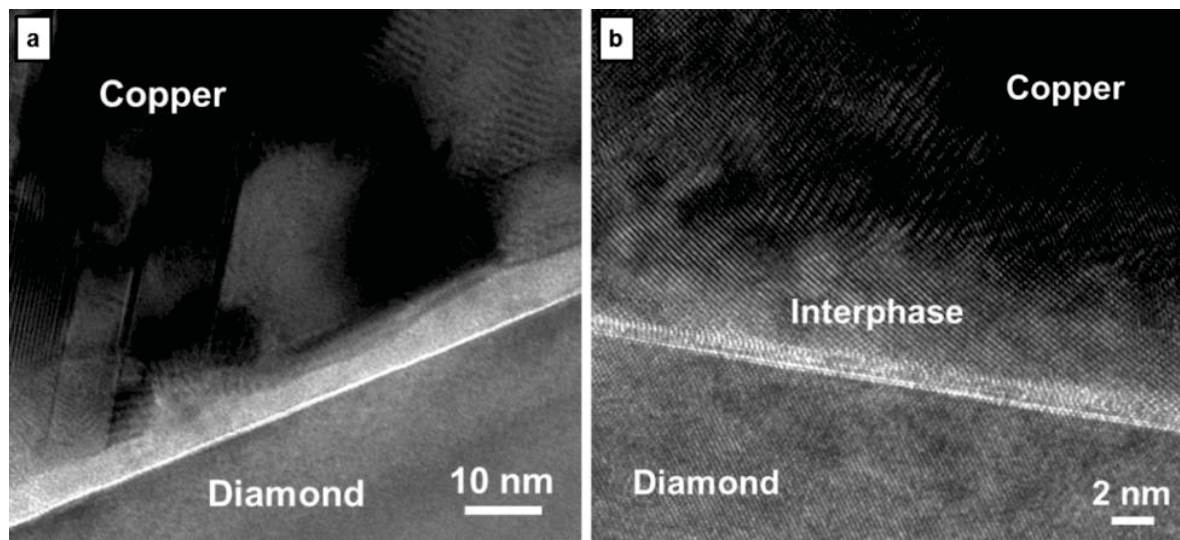


**Figure 4.39: TEM micrographs showing the interface between a CVD diamond film and copper particles deposited onto its surface.**

The Cu particles deposited onto diamonds is thus expected to allow the formation of an adhesive interface between the copper matrix and the diamond reinforcements through strong chemical bonding without requiring any carbide forming materials. The as-deposited copper particles constitute an innovative and very promising bonding process alternative to traditional carbide forming bonding additives for heat conduction across copper/diamond interfaces. The next paragraphs try to bring understanding on the nucleation and growth process of the copper particles onto the diamond surface from the characterizations carried out so far and by making hypotheses on the growth process. Finally, the potential of the Cu-coating process of diamond (both HPHT and CVD) will be studied from an electronic packaging prospective in the next chapter.

## 4.6 Cu particles nucleation and growth process

### 4.6.1 Conclusions drawn from chemical and microstructural characterizations

Chemical and microstructural characterizations carried out in section 4.5 provide us valuable information about the Cu particles deposition process onto diamond reinforcements and bring understanding about the nucleation/growth process leading to the coating of the diamond grains with copper particles. It allows us to draw some conclusions about how this Cu-coating process actually works.

- ***Particles shape, size, and populations:***

The numerous SEM analyses carried out on Cu-coated diamond reinforcements during this study showed that the particles uniformly coated the entire surface of the diamond grains, without any preference for particular crystallographic facets. It also demonstrated that the deposited particles were almost sphere-shaped, and that various populations of Cu particles, with different diameters, coexisted onto a single diamond grain. Finally, it was shown through SEM analysis that it was possible to adjust the size and coverage effect of the Cu particles by tuning the reduction time and temperature. The AFM analyses confirmed the almost-spherical shape of the grown particles and also showed that the distribution of sizes of the Cu particles deposited on the diamond surface was large, meaning that several populations of particles coexist, with diameter ranging from the nanometer to the micrometer.

- ***Particles microstructure and composition:***

EDXS analysis demonstrated that the particles deposited onto the diamond reinforcements were metallic copper particles. No thick ( $> 1\ \mu\text{m}$ ) interphase could be detected at the copper/diamond interface through this technique. TEM analyses showed that the largest particles (100 to 200 nm in diameter) were polycrystalline and faceted, demonstrating the high phase purity and crystallinity of the particles grown. Smaller particles (10 to 30 nm in diameter) exhibited single crystal structure. Twin boundaries were observed in some particles. Finally, a very thin copper oxide layer (nanometer scale) was observed to exist on the surface of the grown particles.

- ***Interface between the particles and the diamond substrates:***

XPS analysis of the surface of the diamond reinforcements after formulation and debinding demonstrated that the surface was functionalized with phosphorus and oxygen. These elements are understood to come from the use of the phosphate ester dispersant agent during the formulation process and to be responsible for the chemical bonding between the diamond reinforcements surface and the copper particles deposited upon further reduction. The analysis of the chemical



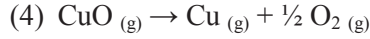
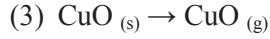
environments of the P and O atoms of the surface suggests that C-O-P and C-P bonds exist. Phosphorous, which exists in a large amount onto the diamond surface (about 12 atomic percent), is mainly combined to oxygen through  $P_2O_5$  structures, although other configurations are detected to exist onto the diamond surface. Therefore, the C-O-P structures are believed to act as heterogeneous nucleation sites for the growth of the Cu particles. Finally, XPS showed that a large amount of oxygen (30 at.%) is not bonded to phosphorus onto the diamond surface, and remains therefore available onto the surface after debinding.

TEM analyses carried out onto the grown Cu particles confirmed the prominent role played by oxygen atoms in the bonding process between the diamond surface and the Cu particles. They suggested that copper oxide ( $CuO$ ,  $Cu_2O$ ) is the main compound that first nucleate onto the C-O-P sites and that it forms an interphase responsible for the chemical bonding between the diamond substrate and the growing Cu particles. The interphase was shown to be between 2 nm thick (for the smallest particles grown) and 15 nm thick (for the largest particles grown). However, no definitive conclusion about the nature of the copper oxide that forms the interphase could be drawn from the TEM analyses carried out. Finally, the implication of phosphorus into the interphase formation cannot be excluded, since (C, O, P) compounds may be created in the early stages of the interphase formation.

#### **4.6.2 Hypotheses on the nucleation and growth of the Cu particles**

The conclusions drawn from the chemical and microstructural investigations carried out in section 4.6.1 allow us to formulate hypotheses on the different steps of the Cu-particles deposition process, and therefore to propose a nucleation and growth mechanism.

The phosphorus and oxygen detected onto the surface of the diamond reinforcements after debinding is understood to come from the phosphate ester employed as a dispersant agent during the formulation step (see section 4.3.3). Upon mixing the powders with the organics for tape casting slurry preparation, the P-side of the chains of phosphate ester are adsorbed onto the carbon surface. Upon debinding, the organic side of the chains is burned out while P-O-C structures remain anchored to the surface, as detected through XPS analysis. These P-O compounds will then act as nucleation sites for the growth of the Cu particles onto the diamond powders. The Cu particles deposition is inferred to originate from a solid-vapor process that sees the  $CuO$  whiskers sublimating, reducing into the gas phase, and metallic copper condensating onto the functionalized diamond surface to form the Cu particles. The very same type of process was involved in the formation of the whiskers during the debinding step (see section 4.4.1). The sublimation of the  $CuO$  whiskers can be described by the following reaction pathway:



Where *s* and *g* subscripts stand for solid phase and gas phase, respectively. We understand the Cu particles nucleation and growth process occurring upon reduction of the Cu/D tape as being made of the following steps.

▪ ***CuO nanowires sublimation:***

In a first time, solid cupric oxide from the CuO nanowires sublimates to its gaseous form through a solid-vapor process similar to that described in section 4.4.1 which leads to the formation of the CuO nanowires. The fact that the CuO whiskers are able to sublime at such low temperature (400°C) is due to the very high aspect ratio they exhibit. Indeed, the influence of the radius of curvature *r* on the sublimation temperature can be estimated using the following formula [190]:

$$\frac{T_{sub\ r} - T_{sub\ CuO}}{T_{sub\ CuO}} = \frac{\Delta T_{sub\ CuO}}{T_{sub\ CuO}} = \frac{2\gamma}{r} \frac{V^{s\ CuO}}{\Delta H_{sub}} \quad (4.3)$$

Where  $T_{sub\ r}$  and  $T_{sub\ CuO}$  are the sublimation temperatures of nanometric CuO and bulk CuO, respectively (°C),  $\gamma$  is the surface free energy of CuO (J.m<sup>-2</sup>), *r* is the radius of curvature (m),  $V^{s\ CuO}$  is the molar volume of CuO (l.mol<sup>-1</sup>), and  $\Delta H_{sub}$  is the sublimation free enthalpy of CuO (kJ.mol<sup>-1</sup>). What we are looking for here is the  $\Delta T_{sub\ CuO}$  in order to estimate the influence of the radius of curvature of CuO whiskers on their sublimation temperature.

Bulk cupric oxide exhibits a sublimation temperature of 1000°C and a surface free energy of 1 J.m<sup>-2</sup>. Its molar volume is 1.257 x 10<sup>-3</sup> l.mol<sup>-1</sup> and the enthalpy of sublimation is about 305 kJ.mol<sup>-1</sup> at 400°C. Therefore, when estimating that the radius of curvature of a CuO whisker is of the order of 10 nm (10<sup>-8</sup> m), its sublimation temperature would be dropped by 824°C, meaning that nanosized CuO structures would sublime at a temperature of 176°C instead of 1000°C for bulk CuO. As a matter of fact, it is possible that CuO whiskers sublime under the reducing heat treatment at 400°C [197-199].

▪ ***CuO reduction in the vapor phase and Cu deposition onto the P-O-C nucleation sites:***

In a second time, gaseous CuO is reduced in the Ar/H<sub>2</sub> atmosphere (vapor phase) to form gaseous metallic copper. Our hypothesis on the nucleation and growth process of the Cu particles suggests that metallic copper in the vapor phase resettles again onto the phosphorus-oxygen sites of the diamond substrates which are believed to act as heterogeneous nucleation sites for the growth of the observed Cu dots. According to the results obtained from XPS analysis, C-O-P-O-Cu and/or C-P-O-Cu chemical bonds would be involved in the bonding between the diamond substrate and the copper particles. P is mainly combined with O through P<sub>2</sub>O<sub>5</sub> structures but is also inferred to be

directly bonded to the diamond substrate through C-P bonds. Other C-O-P structures are also believed to exist onto the diamond surface. Moreover, the Cu diffusing from the gas phase and adsorbing onto the diamond surface is understood to combine in a first time with the oxygen existing onto the surface, thus forming the copper oxide interphase detected through TEM investigations. Then, Cu keeps diffusing from the vapor phase and the Cu particle keeps growing. It was attempted to confirm the presence of phosphorous at the interface between the copper particles and the diamond substrates through in-depth Auger electron spectroscopic (AES) analysis of a deposited copper particle. However, no phosphorus could be detected through this experiment, the amount of phosphorous being too low to be detected through AES.

▪ ***Cu particles growth following Wulff geometry:***

Given the morphology of the Cu particles grown onto diamond, it is obvious that they originate from a process involving 3D growth. It is also possible that a first step of 2D growth precedes the growth of the 3D Cu structures. In such case, the primary 2D atomic layer would only be a few nanometers thick and could not be detected through the characterization techniques we used. However, the strong lack of chemical affinity between the surface atoms (carbon) and arriving atoms (copper) suggests that the growth follows an island growth mode (Volmer-Weber mode).

The facets observed on the copper dendrites and on the copper dots grown onto the diamond surface originate from the minimization by the grown structures of their surface free energy  $\gamma$  ( $\text{J}\cdot\text{m}^{-2}$ ). Surface free energy is investigated in more details in section 4.7.1, dealing with the sintering process. However, it can be said that the origin of the surface free energy is that atoms in the crystal layers nearest the surface are without some of their neighbors, i.e. without some metallic bonds. Therefore, each of the surface atom without a certain amount of nearest neighbors exhibit an excess internal energy proportional to the number of nearest neighbors missing relative to the atoms of the bulk material. For instance, copper has a surface free energy of  $1.72 \text{ J}\cdot\text{m}^{-2}$ . Typically, the higher the melting temperature of a metal, the higher the bonding energy of its atoms, and thus the higher its surface energy.

A convenient method for plotting the variation of  $\gamma$  with surface orientation in three dimensions is to construct a surface about an origin such that the free energy of any plane is equal to the distance between the surface and the origin when measured along the normal to the plane in question. A section through such a volume is shown in Fig. 4.40. This type of polar representation of  $\gamma$  is known as a  $\gamma$ -plot and has the useful property of being able to predict the equilibrium shape of an isolated single crystal.

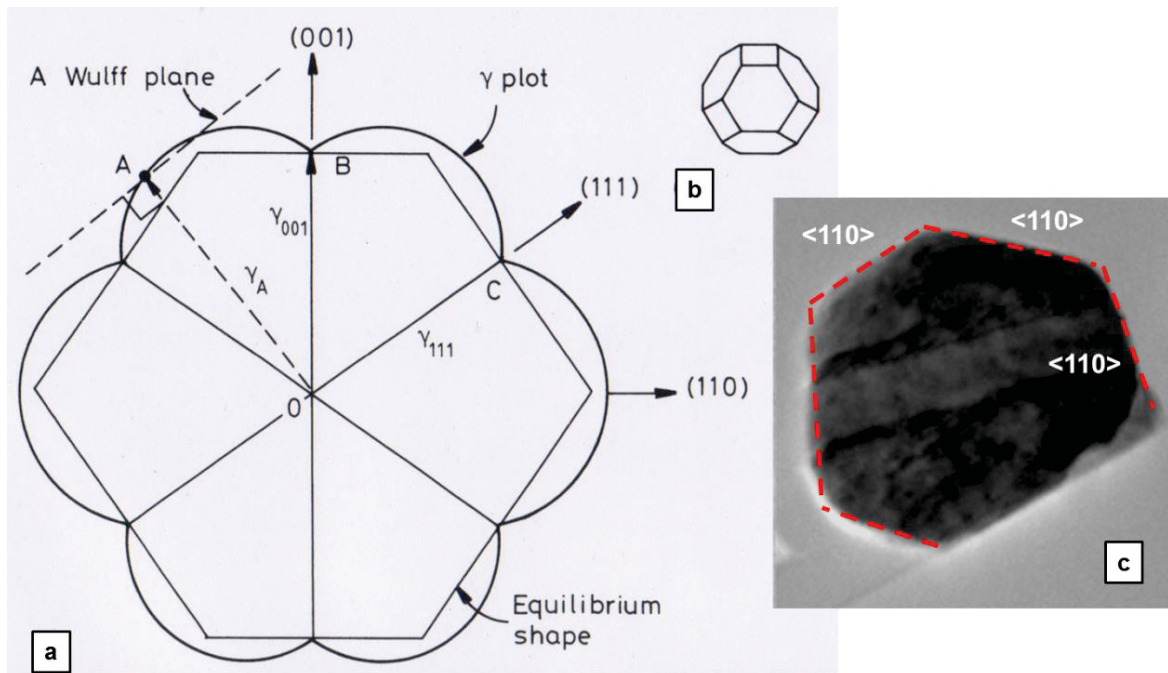


**Figure 4.40:** (a) Possible (1-10) section through the  $\gamma$ -plot of an fcc crystal. The length OA represents the free energy of a surface plane whose normal lies in the direction OA. Thus  $OB = \gamma_{(001)}$ ,  $OC = \gamma_{(111)}$ , etc. Wulff planes are those such as that which lies normal to the vector OA. In this case, the Wulff planes are B, C, etc., give the inner envelope of all Wulff planes and thus the equilibrium shape. (b) The equilibrium shape in three dimensions showing (100) (square faces) and (111) hexagonal faces. (c) TEM micrograph of a faceted Cu particle grown onto a diamond reinforcement [190].

For an isolated crystal bounded by several planes  $A_1, A_2$ , etc. with energies  $\gamma_1, \gamma_2$ , etc. the total surface energy will be given by the sum  $A_1 \gamma_1 + A_2 \gamma_2 + \dots$ . The equilibrium shape has the property that  $\sum A_i \gamma_i$  is a minimum and the shape that satisfies this condition is given by the following, so-called *Wulff construction*. For every point on the  $\gamma$  surface, such as A in Fig. 4.39, a plane is drawn through the point and normal to the radius vector OA. The equilibrium shape is then simply the inner envelope of all such planes. Therefore when the  $\gamma$ -plot contains sharp features, the equilibrium shape is a polyhedron with the largest facets having the lowest surface free energy. It is obvious when observing the structure of the Cu particle coating the diamond surface that it follows the growth of a typical Wulff construction.

As a conclusion, it can be stated that the chemical bonding between the copper matrix and the diamond reinforcements relies on the following steps:

- The surface functionalization of the diamond surface through C-O-P and C-P bonds and the creation of (C, O, P) structures, among them  $P_2O_5$  compounds;
- The nucleation of copper onto the oxygen-rich nucleation sites of the diamond surface leading to the creation of a copper oxide (CuO or  $Cu_2O$ ) interphase; this interphase is

assumed to originate from the combination of metallic copper reduced in the vapor phase to atomic oxygen existing at the diamond surface in the very early stages of the nucleation and growth process;

- The further growth of copper particles onto the copper oxide interphase through the diffusion of Cu atoms from the gaseous feedstock following Wulff geometries;
- The creation, upon sintering, of metallic copper-to-copper chemical bonds between the copper particles coating the diamond reinforcements and the copper powders which will form the matrix of the composite material.

Therefore, the copper coating process can roughly be depicted as following:

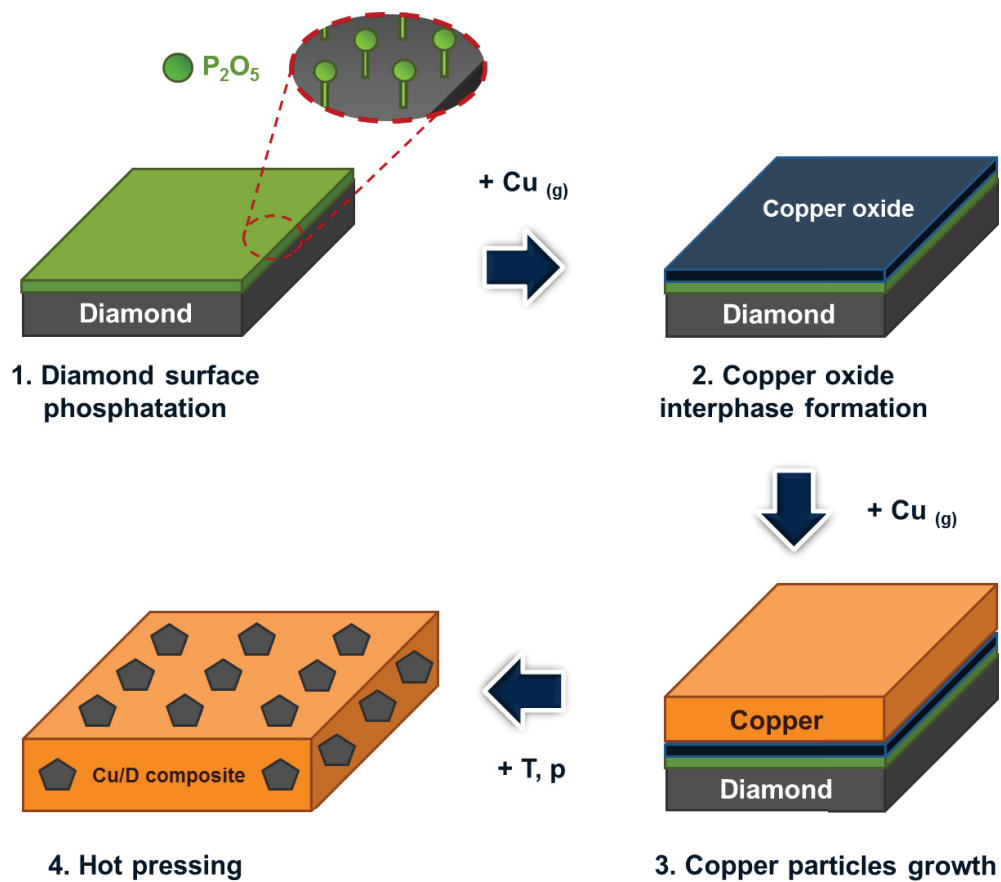


**Figure 4.41: Schematic description of the Cu/D interfacial bonding process developed.**

In further sections of the dissertation, we will evaluate the ability of this innovative bonding process to conduct the heat flow and transfer the thermo-mechanical load across the copper/diamond interface through thermal conductivity, thermal expansion, and thermal cycling investigations. We will now move to the next step of the processing of our Cu/D composite materials, which consists in sintering the composite tapes in order to obtain dense and thermally efficient final products.

## 4.7 The sintering process

The fabrication process relying on powder metallurgy technology, it has to go through a sintering step which will allow the transformation of the copper/diamond composite powder mixture into a dense material. Since it does not involve melting, powder metallurgy offers numerous advantages relative to classical foundry such as the decrease of the machining cost (economical aspect) and of power consumption (environmental aspect). In addition, powder metallurgy exhibits a yield close to 100% since a very limited amount of matter is lost through this process. Finally, powder metallurgy is well adapted to large scale production of standard pieces, since the investments costs are compensated by the simplicity and reliability of the process. We will first focus on the physical phenomena governing the sintering processes, both free and pressure-assisted, since they have a direct influence on the microstructure of the material, and therefore on its final properties [195].

### 4.7.1 Free sintering mechanism

- ***Free sintering driving force:***

The sintering process allows transforming cold-compacted powders into a dense material through a heat treatment where the powders remain in the solid state, thus without resorting to melting. Free sintering is understood as a sintering process where no additional pressure is applied to the material. Sintering originates from the creation of grain boundaries and from the elimination of the porosity existing into the powder-based material. It results in a retraction of the material (i.e. a reduction in the dimensions of the sample) and, therefore, in its densification (i.e. a reduction in the volume of the sample). The higher the porosity in the material, the bigger the retraction. The driving force of sintering mechanism is the reduction of the interface energy of a material. In a solid-state material such as the copper powder matrix, the global interface energy  $E$  (J) involves two components: a solid-gas interface component (powders surface) and a solid-solid interface component (grain boundaries), as shown by eq. 4.4:

$$E = \gamma_{sg}A_{sg} + \gamma_{ss}A_{ss} \quad (4.4)$$

Where  $\gamma_{sg}$  and  $\gamma_{ss}$  are the interface free energies of the solid-solid and solid-gas interfaces, respectively (J.m<sup>-2</sup>); and  $A_{sg}$  and  $A_{ss}$  are the areas they respectively occupy in the solid considered (m<sup>2</sup>). From a thermodynamic point of view, sintering originates from the replacement, upon heating, of solid-gas interfaces by solid-solid interfaces, which exhibit lower free energy. Therefore, the growth of the grain boundaries, which allows the material to decrease its global free energy, goes



with the reduction of the porosity of the material, thus leading to a retraction of the sample at the macro scale.

Consequently, the driving force  $F_{sint}$  ( $\text{J.m}^{-3}$ ) of the sintering process can be written as:

$$F_{sint} = -\left(\frac{dE}{dV}\right) \quad (4.5)$$

Where  $dE$  is the variation in interface energy of the material (J) and  $dV$  the variation of its volume upon retraction ( $\text{m}^3$ ). The reduction in the interface energy of a solid requires an evolution of its microstructure. This evolution relies on the existence of stress gradients at the micro scale. In the vicinity of a curved interface between two media 1 and 2 (for instance, solid copper and the surrounding atmosphere), the interface free energy (which is equivalent to an interface stress) imposes a pressure between the two sides of the interface, which can be translated by eq. 4.6:

$$(P_1 - P_2) = \frac{2\gamma}{r} \quad (4.6)$$

Where  $P_i$  is the effective pressure in medium  $i$  (Pa),  $\gamma$  the interface free energy ( $\text{J.m}^{-2}$ ), and  $r$  is the radius of curvature of the surface element considered (m). This equation is called the *Laplace equation*. If the two media 1 and 2 are different, this pressure difference leads to an excess of chemical potential in the solid material, thus increasing the equilibrium pressure in the gas, and favoring the creation of solid/solid interfaces at the detriment of solid/gas interfaces. More generally, in the case of solid copper with radius of curvature  $r$  in equilibrium with its surrounding atmosphere, the excess pressure in the solid phase (or *Laplace stress*)  $\Delta P_s$  can be written:

$$\Delta P_s \approx \frac{2\gamma_{sg}}{r} \quad (4.7)$$

The fact that the pressure difference is inversely proportional to the radius of curvature explains why dendritic copper powders require lower temperatures (typically  $600^\circ\text{C}$ ) to be sintered relative to spherical copper powders, which require higher temperatures (typically  $850^\circ\text{C}$ ). Indeed, dendritic copper powders, due to their particular shape, exhibit lower radius of curvature, which leads to higher Laplace stress values in the solid copper phase relative to spherical copper powders, thus ending up on a less energy-consuming sintering process. The fact that the pressure gradient is inversely proportional to the radius of curvature also explains why nanosized powders have lower sintering temperature relative to micro-sized powders, which exhibit higher  $r$  values, thus lower Laplace stress values  $\Delta P_s$  (for nanosized powders, the Laplace stress can reach hundreds of MPa).

When considering a triple line system made from three surfaces, for instance two grains of copper surrounded by a gas, the equilibrium angle between a grain boundary and the surrounding atmosphere can be written:

$$\gamma_{ss} = 2\gamma_{sg} \frac{\cos\psi_e}{2} \quad (4.8)$$

Where  $\gamma_{ss}$  and  $\gamma_{sg}$  are the interface free energies of the solid/solid and solid/gas interfaces, respectively ( $\text{J.m}^{-2}$ ) and  $\psi_e$  is the equilibrium angle between the grain boundary and the surrounding atmosphere.

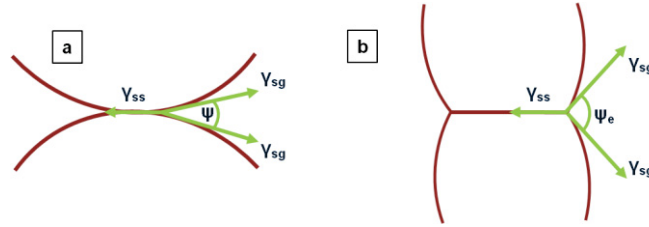


**Figure 4.42: Schematic view of the equilibrium process of a grain boundary in a gas phase [195].**

Since  $\gamma_{ss}$  is lower than  $\gamma_{sg}$ , when  $\psi$  is lower than the equilibrium angle  $\psi_e$ , the sintering driving force acts on the triple line that leads to the growth of the grain boundary until  $\psi$  has reached its equilibrium value  $\psi_e$ . As the temperature increases, the value of  $\gamma_{sg}$  relative to  $\gamma_{ss}$  increases as well, forcing the equilibrium angle to increase too, which leads to the disappearance of the solid/gas interfaces.

The critical role played by the curvature radius into Laplace equation can also be applied to our material in explaining why we were able to adjust the size of the grown Cu particles by tuning the reduction time and temperature. Indeed, the enlargement of the Cu particles coating the diamond surface with reducing time and temperature originates from a phenomenon called *Oswald ripening*. This phenomenon is due to the fact that the pressure gradient existing at the surface of the particles is inversely proportional to the curvature radius. Therefore, considering a certain diameter, the stress gradient at the surface of the particle becomes intolerable from a certain temperature. Therefore, Oswald ripening forces them to coalesce in order to form larger and more thermodynamically stable particles, as visible on Fig. 4.29a, b, and c.

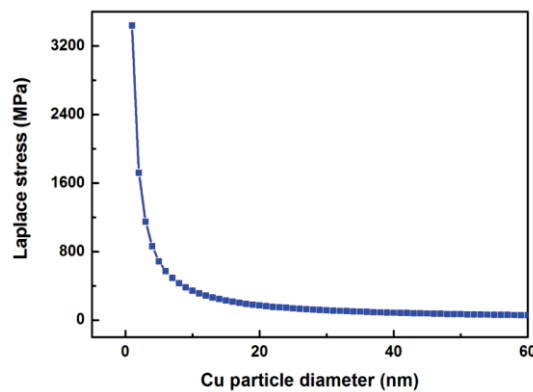


**Figure 4.43: Evolution of Laplace stress at the surface of a Cu particle as a function of particle diameter.**

Figure 4.43 shows the evolution of the Laplace stress at the surface of a Cu particle at room temperature as a function of the particle diameter. It is visible on Fig. 4.43 that Laplace stress exceeds 3400 MPa for a 1 nm diameter Cu particle and drops to 69 MPa for Cu particles exhibiting diameters of 50 nm. Therefore, any Cu particle with diameter below 50 nm will be forced to coarsen at while being maintained at 400°C. This explains why we observe larger particles when increasing the temperature of the reducing heat treatment (since for a single material,  $\gamma_{sg}$  increases with temperature) or when holding the heat treatment at 400°C during a longer time (see Fig. 4.29).

▪ ***The different microstructural stages of the sintering process:***

From a microstructural point of view, the different stages of the sintering process can be schemed as following:

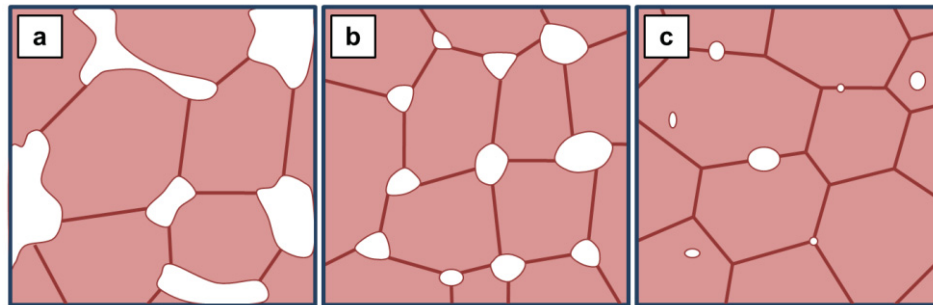


**Figure 4.44: Schematic view of the different stages of the sintering process: (a) Creation and growth of bridges between particles (b) Elimination of the opened porosity (c) Elimination of the closed porosity [195].**

- *1<sup>st</sup> stage: Creation and growth of bridges between the particles*

The first stage of the sintering process consists, when the temperature is high enough, in the creation of *solid bridges* at the contacts between particles (Fig. 4.44a). This results in the existence of stress gradients between the surface of the bridge (in tension) and the bulk material (in compression) in order to balance the surface tension. These stress gradients trigger the creeping of the copper matrix, leading to the growth of the solid bridges (Fig. 4.44b).

For polycrystalline solids, Laplace stress rarely exceeds a few MPa (no plastic deformation of the bridges), and the bridges are grown through a process called *atomic diffusion creeping*, which consists in a lacunar diffusion process in the solid phase, either from the surface of the grains (*surface diffusion*), from the grain boundaries (*inter-granular diffusion*) from the bulk material (*volume diffusion*) (see section 4.9.3). As the bridges grow, the curvature gradients at the surface of the grains decrease. The first stage ends when the curvature gradients are uniform between two neighbor grains. At this stage, the pores are still *opened*, i.e. with a large length/radius ratio.

- *2<sup>nd</sup> stage: Elimination of the opened porosity*

At the second stage of the sintering process, the material is made of a network of inter-connected pores. The curvature of the surfaces is determined by the equilibrium angles of the triple lines and by the pores environment. If the pore is stable, mass transfer keeps going from the grain boundaries or from the bulk material to the pore. Below a certain length/radius ratio, the pores become unstable and end up by being *closed* (typically with a spherical shape).

- *3<sup>rd</sup> stage: Elimination of the closed porosity*

At the third stage of the sintering process, the pores are closed and keep shrinking because of the mass transfer from the grain boundaries and the bulk of the grains. Grains migration may then trigger *grain growth*.

#### 4.7.2 Induction uniaxial hot pressing

In this study, induction uniaxial hot pressing was employed to sinter the Cu/D composite materials after they have been reduced. Although the sintering process described above consists in free sintering, the very same principles govern the hot-pressing process, which is a pressure-assisted sintering technique. The main difference between free sintering and the pressure-assisted methods consists in the fact that the applied pressure helps the sintering process by increasing the contact surface between the grains, thus decreasing the time needed for the porosity to be eliminated. Indeed, the external pressure is transmitted to the material through the continuous contacts existing between the grains through the complex randomly organized network they form.

▪ ***Plastic deformation and creeping processes:***

The application of a constant pressure upon sintering of a ductile material such as copper leads to two main phenomena that enhance the densification process: plastic deformation and creeping. Plastic deformation consists in a non-reversible deformation of the powders by the application of a pressure to the bed of powders that exceeds the limit of elasticity of the material at the considered processing temperature. The minimum pressure to be applied in order to plastically deform the powders is given by:

$$P_{min} = \frac{3\sigma_y}{4\pi R^2} Z a d \quad (4.9)$$

Where  $\sigma_y$  is the limit of elasticity of the material,  $Z$  the average number of contacts between particles,  $a$  the surface area of a contact,  $R$  the particles radius, and  $d$  the relative density.

However, plastic deformation typically only enables reaching compaction levels below 0.9, but it is difficult to fully densify a material by only resorting to this process. In order to approach the fully-dense state (equivalent to a relative density of 1), creeping must be combined to plastic

deformation. Creeping is a temperature-activated phenomenon that consists in a non-reversible deformation of the powders by the application of a constant pressure lower than the limit of elasticity of the considered material. Creeping occurs upon heating when the pressure and processing time are sufficiently high. Therefore, the pressure parameter is critical to achieve a fast and effective densification process. By applying pressure to the ductile powders, plastic deformation combine with creeping lead to composite materials with satisfying relative density.

▪ **Hot-pressing machinery:**

The hot pressing technique shows three degrees of freedom: time, pressure, and temperature. By tuning these parameters, one can adjust the microstructure of the final material. A photograph and a scheme of the hot pressing device are shown on Fig. 4.45:

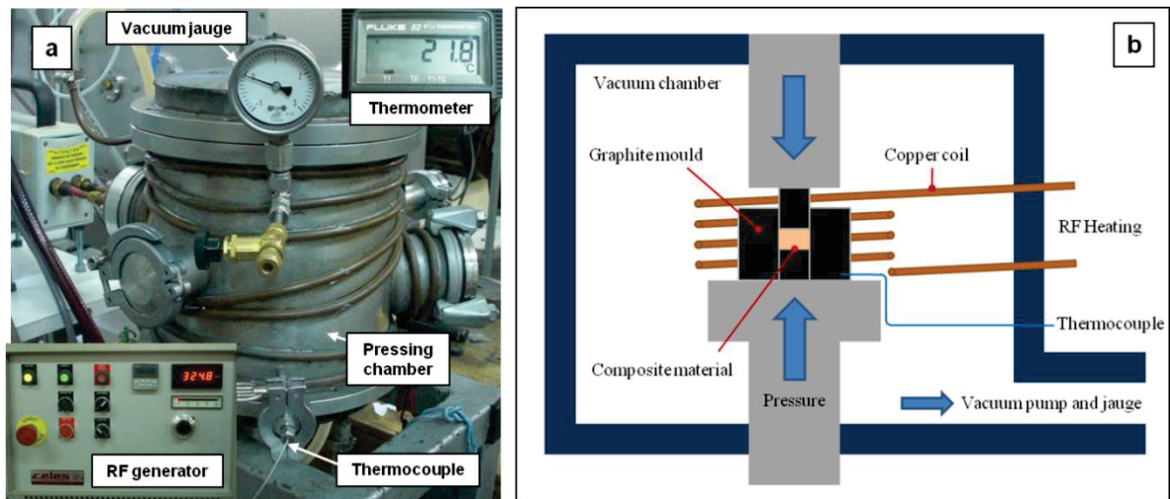


Figure 4.45: (a) Photograph and (b) scheme of the uniaxial hot pressing machine [209].

The uniaxial hot pressing machine relies on the combination of an induction heating system with a hydraulic pressing jack. Induction heating consists in heating an electrically conductive material through electromagnetic induction: high-frequency alternative currents are generated by a high-power radio-frequency generator and passed through a copper coil. The high-frequency alternative currents passed through the copper coil trigger the creation of eddy currents (also called *Foucault currents*) inside the coil, which induce free electron motion inside the structure of the graphite mould. The resistance to electron motion in the graphite heats up the mould, which itself heats up the material inside the mould.

The induction heating technique is a widely spread heating method in powder metallurgy. It has the advantage to allow heating of the material without any direct contact with the heat source. Hot pressing also features the advantages of being a sintering technique that is fast, with low capital

cost, and low energy consumption, relative to other processes employed to fabricate copper/diamond composite materials such as liquid infiltration, SPS, or PPS [122-135].

▪ ***Hot pressed samples:***

Multilayer systems made from 30 net-shaped 6 mm diameter tapes were hot-pressed in order to reach suitable sample thickness for thermal measurements. The stacks were introduced between two pistons into a mould which was heated to 650°C under vacuum ( $10^{-3}$  Pa) and maintained under hot pressure during 30 minutes using an induction system and a regulation monitor. Graphite and steel have been used as mould and pistons materials. Steel is an interesting mould material because of its mechanical tenue upon hot pressing. However, steel shows its limits when required to hot press at elevated temperatures. Indeed, it was not possible to heat up the steel mould above 650°C without modifying its microstructure and affecting its mechanical properties. On another hand, graphite shows lower mechanical tenue but can be heated up to 1000°C under controlled temperature if needed.

The effective applied pressure on the pistons was 50 MPa. The temperature was controlled through a thermocouple placed into the graphite mould combined to a thermometer. Composite films as thin as 100  $\mu\text{m}$  could be processed. Thick samples up to 10 mm could also be fabricated depending on the number of 200  $\mu\text{m}$  thick tapes hot pressed together. For further dilatometry characterization purposes, samples height had to be located between 3.6 mm and 4.4 mm, while minimum height for thermal conductivity measurements was 2 mm. Therefore, Cu/D samples with thickness around 4 mm (+/- 0.6 mm) were processed. Cu/D composites with diamond volume fraction ranging from 0 to 50 vol.% were fabricated through the combination of the tape casting and hot pressing processes. For each volume fraction of diamond (from 0 to 50%), 8 to 10 samples were fabricated and evaluated.

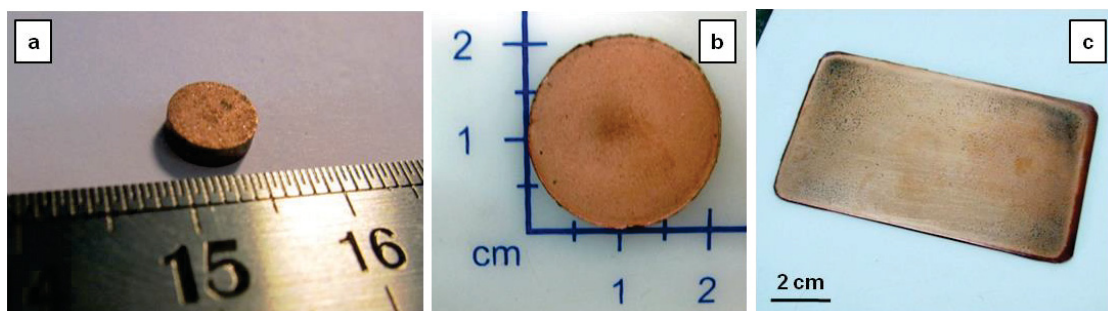


**Figure 4.46: Photographs of Cu/40 vol.% D composite materials with various shapes:**  
**(a) 6 mm diameter cylinder, (b) 20 mm diameter cylinder, (c) 6x10 cm<sup>2</sup> plate. [209]**

Thanks to the net-shaping capability of the tape casting process, composite samples of various shapes and dimensions could be fabricated, as shown on figure 4.46, showing cylindrical samples of



6 mm (Fig. 4.46a) and 20 mm (Fig. 4.46b) and a rectangular Cu/D composite piece of 6×10 cm<sup>2</sup> (Fig. 4.46c).

The type of Cu/D composite product shown on Fig. 4.46c can be used as-fabricated as a heat spreading substrate in a power electronic package. For solderability purposes, commercial layers of pure copper with smooth surface finish were hot pressed on both sides of the composite material so that it can easily be soldered, for instance, to a DBC substrate, thus overcoming the rough surface finish of the raw Cu/D samples (Fig. 4.46a, b). The net-shaping potential of the powder metallurgy process also allows addressing the strong issue raised by the very limited machinability of copper/diamond composite materials due to the high wear resistance of diamond. By fabricating products at desired dimensions, there is no need for reworking the pieces. However, precise control of the retraction phenomenon upon sintering is required in the meantime.

## 4.8 Characterization of the Cu/D composite films

### 4.8.1 Density and microstructure

Density is of primary importance for thermal management materials since porosity is a major obstacle to heat conduction in a solid (air being a first quality thermal insulating material:  $k_{air} = 0.0262 \text{ W.m}^{-1}.\text{K}^{-1}$ ). Densities of the composites were measured through the Archiméd's method (detailed in section 4.1) and formula:

$$\rho_A = \frac{m_{air}}{m_{air}-m_{water}} \times \rho_{Water} \quad (4.10)$$

Where  $m_{air}$  and  $m_{water}$  are the masses of the sample measured in the water and in the air, respectively (g);  $\rho_{Water}$  is the density of water ( $\rho_{Water} = 1 \text{ g.cm}^{-3}$ ); and  $\rho_A$  is the density of the composite ( $\text{g.cm}^{-3}$ ).

The as-measured densities were compared to the theoretical densities calculated through the rule of mixture (ROM):

$$\rho_c = V_m \rho_m + V_r \rho_r \quad (4.11)$$

Where  $\rho_m, \rho_r$ , and  $\rho_c$  are the densities of the copper matrix, of the diamond reinforcements, and of the composite, respectively ( $\text{g.cm}^{-3}$ );  $V_m$  and  $V_r$  are the volume fractions of the copper matrix and diamond reinforcements, respectively. The experimental densities were related to the theoretical ones by using the relative density parameter, which corresponds to the percentage of the full density that is reached by a composite sample, as shown on Fig. 4.47.

We reach relative densities ranging from 99% to 95.9% for diamond volume fractions ranging from 0% to 50%, respectively, which confirms that the obtained materials are dense and that the copper coating effectively acts as an interfacial chemical bonding agent. We observe a decrease of the composite density with diamond volume fractions of 40% and 50%, which is due to the detrimental effect of an increasing reinforcement volume fraction on the creeping process of the copper matrix. From a thermal prospective, one can consider that a porosity level of 4% or more (96% or less of relative density) is critically detrimental to the heat flow conduction in the composite material. It is therefore expected that Cu<sub>50</sub>D<sub>50</sub> composite materials provide poor thermal conduction performances.

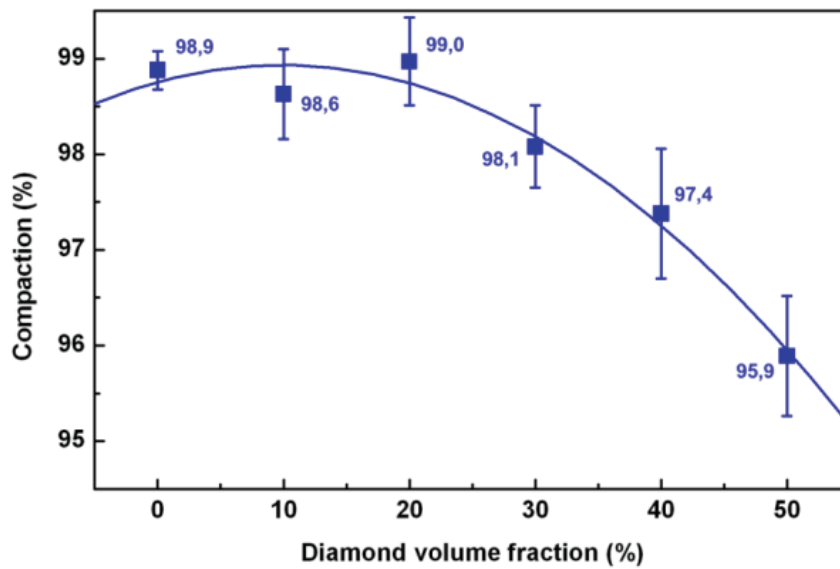


**Figure 4.47: Evolution of the relative density of the Cu/D composites as a function of the diamond volume fraction.**

Figure 4.48 shows SEM micrographs of Cu/D composite materials after hot pressing. Figure 4.46a shows that the diamond reinforcements exhibit a remarkably uniform dispersion into the copper matrix. This is a strong advantage of the tape casting process since it limits the segregation issues thanks to the stabilized dispersion of copper and diamond powders into solvents through the use of dispersant upon slurry formulation. Therefore, the fabricated Cu/D composite materials are isotropic, which is a critical advantage when considering applications as heat spreading or heat sinking substrates. As a matter of fact, we will consider for thermal characterization (sections 4.8.2 and 4.8.3) that the thermal conductivity and the CTE of the processed materials are isotropic. After densification, we observe neither delamination nor distinction between the layers hot-pressed together. The shear induces by the tape casting process does not influence the dispersion of the reinforcements. However, it has to be remarked that the polishing of the Cu/D composites was made difficult due to the hardness and wear resistance of the reinforcements. Consequently, scratches, due to the SiC polishing paper, are visible on the copper matrix surface.

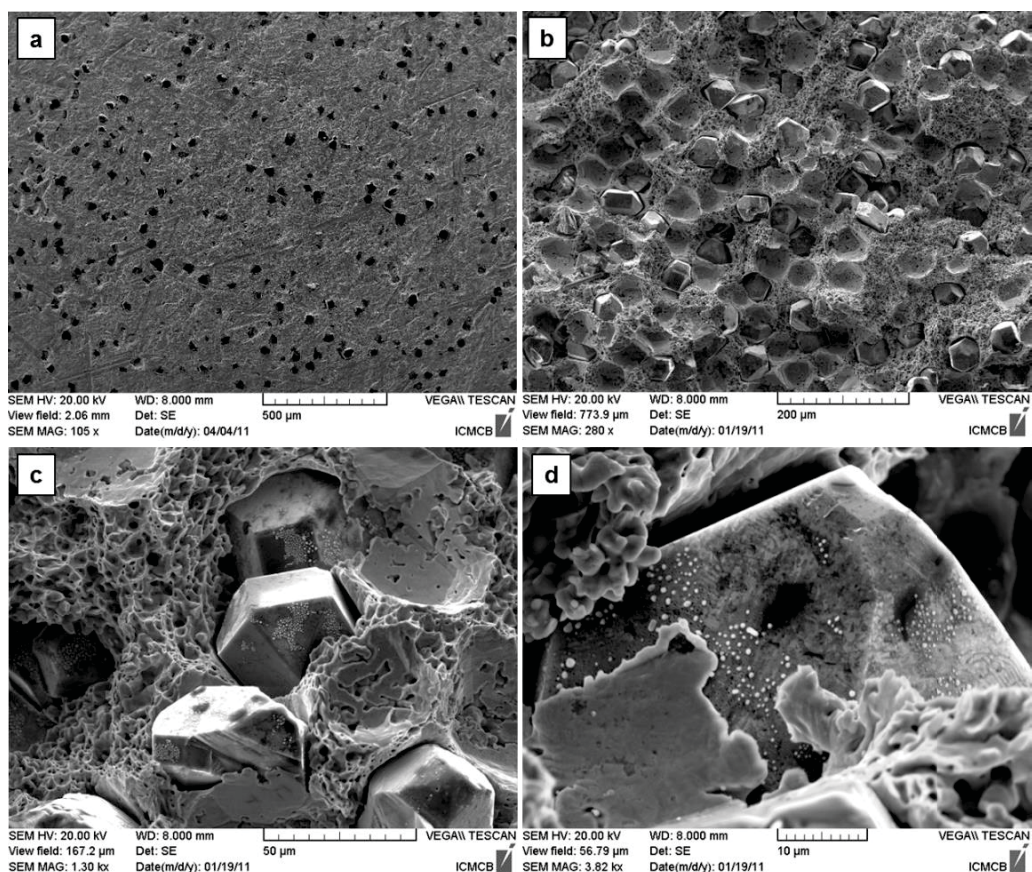


**Figure 4.48:** SEM micrograph of a (a) hot-pressed and (b, c, d) fractured Cu/20 vol.% D composite material.

Figure 4.48b and 4.48c show fractures of hot-pressed Cu/D composites, revealing a typical ductile fracture profile from the copper matrix. The voids reveal the grain boundaries of the copper matrix. On Fig. 4.48c, a fracture profile shows diamond reinforcements embedded into the copper matrix. It reveals that the chemical bonding between the diamond reinforcements and the copper matrix through the diamond copper-coating process we developed critically suffers from the fracture process, which was expected due to the extreme solicitation induced by the fracture procedure.

It is also interesting to observe that some copper particles coating the diamond reinforcements remain onto the diamond surface after the fracture process while some have been delaminated through that step. However, this provides us with no information about the adhesion strengths of the Cu-coating to the diamond surface and to the copper matrix.

Finally, no degradation of the diamond particles was observed after densification, and no product of an eventual chemical reaction between copper and diamond was detected, in agreement with the Cu-C phase diagram. As mentioned in chapter 2, diamond is a metastable allotrope of carbon under room temperature and atmospheric pressure. The diamond structure remains stable only because of a kinetic difficulty in rebuilding the graphite lattice, which is the stable form of carbon under usual conditions. However, this difficulty decreases with an increasing temperature.

The transformation of diamond to graphite (or *graphitization*) is also made easier by the presence of impurities into the diamond lattice, such as the catalysts detected onto the diamond powders surface through AES in section 4.2.2 (mainly nickel, cobalt, and manganese) since they decrease the graphitization temperature of diamond. Under vacuum, the partial pressure of oxygen is very low and diamond only experiences *surface graphitization* between 700 and 1400°C. It is only when the temperature goes above 1400°C that *bulk graphitization* (or volume graphitization) of diamond occurs [196].

However, no graphitization was observed onto the surface of the diamond reinforcements through SEM observations after the different heat treatments (debinding, reduction, hot pressing) of the fabrication process.

#### 4.8.2 Thermal characterizations

##### ▪ *Thermal conductivity:*

Thermal conductivity is a major property for heat dissipation material since the higher the thermal conductivity, the faster the heat will be spread onto the heat dissipation surface. Thermal conductivity was calculated from thermal diffusivity measurement using the following formula:

$$k_c = a_c \rho_c C_{p_c} \quad (4.12)$$

Where  $k_c$  is the thermal conductivity of the composite ( $\text{W.m}^{-1}.\text{K}^{-1}$ ),  $a_c$  the thermal diffusivity of the composite ( $\text{m}^2.\text{s}^{-1}$ ),  $\rho_c$  the density of the composite ( $\text{kg.m}^{-3}$ ), and  $C_{p_c}$  the specific heat of the composite ( $\text{J.kg}^{-1}.\text{K}^{-1}$ ) calculated using the ROM:

$$C_{p_c} = V_m C_{p,m} + V_r C_{p,r} \quad (4.13)$$

Where  $C_{p,m}$  and  $C_{p,r}$  are the specific heats of the copper matrix and diamond reinforcements, respectively (Tab. 4.4);  $V_m$  and  $V_r$  are the volume fractions of the matrix and the reinforcements, respectively. Thermal diffusivity of the composites was measured through flash laser method in axial direction of small cylinders of 6 mm diameter and 4 mm height using a Netzsch LFA 457 device. Figure 4.49 shows a schematic description and a photograph of the thermal diffusivity measurement device.

Thermal diffusivity evaluation relies on De Giovanni's formula:

$$a_c = 0.1388 \times \frac{e^2}{t_{1/2}} \quad (4.14)$$

Where:  $e$  is the thickness of the evaluated sample (m) and  $t_{1/2}$  is the time of half-maximum of the recorded signal (s). Thermal diffusivity was measured at 70°C for reasons of measurement stability. The faster the sample diffuses heat, the shorter  $t_{1/2}$ , thus the higher the diffusivity. Therefore, thermal diffusivity can be considered the transient component of the heat conduction properties of a material, while thermal conductivity its continuous component.

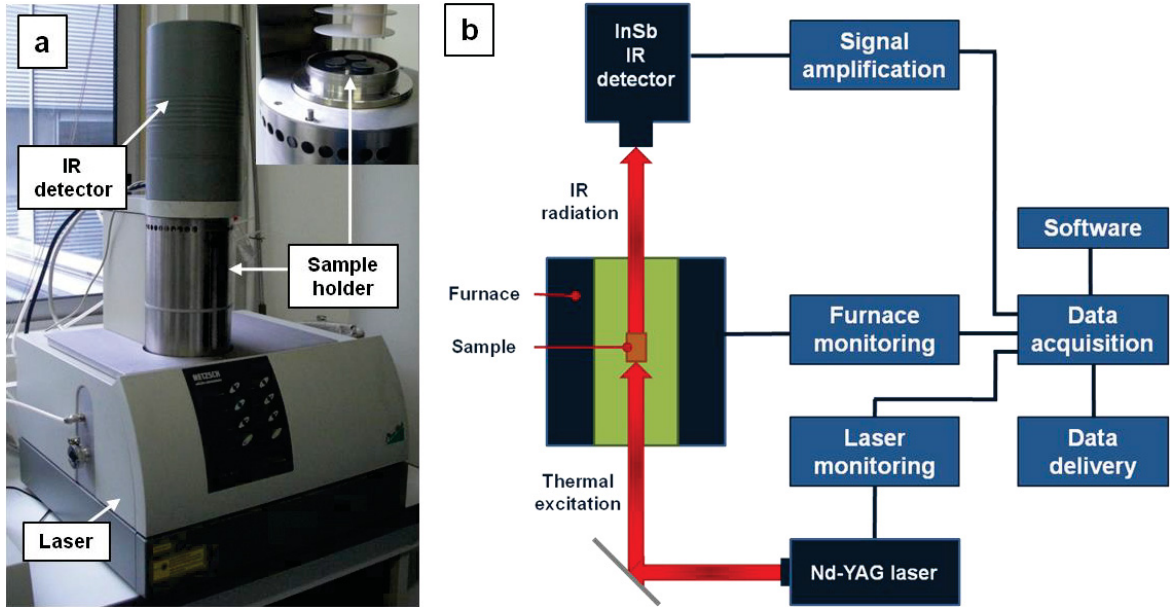


**Figure 4.49: (a) Photograph and (b) schematic description of the thermal diffusivity measurement device.**

Experimental thermal conductivity measured were compared to theoretical values predicted by Maxwell's model [189]:

$$k_c = k_m \frac{[2(\frac{k_d}{k_m} - 1)V_d + (\frac{k_d}{k_m} + 2)]}{[(1 - \frac{k_d}{k_m})V_d + (\frac{k_d}{k_m} + 2)]} \quad (4.15)$$

Where  $k_m$ ,  $k_d$ , and  $k_c$  are the thermal conductivities of the copper matrix, the diamond reinforcements, and the composite material, respectively; and  $V_d$  is the volume fractions of diamond reinforcements.

Thermal conductivity results obtained from Cu/D composites fabricated through tape casting and hot pressing with diamond volume fraction ranging from 0% to 50% are shown on Fig. 4.50. The average thermal conductivity of composites increases regularly from 365 W.m<sup>-1</sup>.K<sup>-1</sup> to 457 W.m<sup>-1</sup>.K<sup>-1</sup> with respect to diamond volume fractions ranging from 0% to 40%, which confirms that the copper particles deposited onto the diamond reinforcements prior to sintering effectively act as chemical bonding agents between diamond and the copper matrix and enable efficient interfacial heat transfer between electronic and phonon conduction.



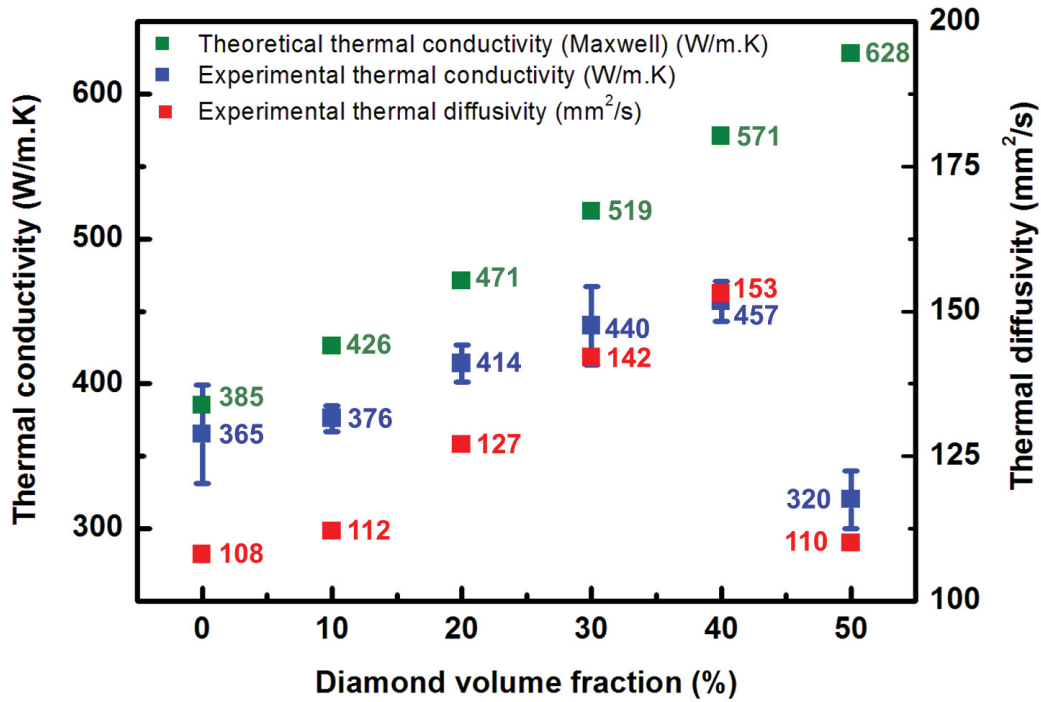


Figure 4.50: Evolution of the experimental thermal diffusivity and conductivity of the Cu/D composites and comparison with respect to Maxwell's prediction as a function of the diamond volume fraction.

However, we observe a drop of thermal conductivity to  $320 \text{ W.m}^{-1}.\text{K}^{-1}$  with a diamond volume fraction of 50% due to the low compaction of the  $\text{Cu}_{50}\text{D}_{50}$  composite, which is critically detrimental to the thermal conductivity. This decrease in thermal conductivity means that the percolation threshold (i.e. the reinforcement volume fraction at which it exists a continuous path between reinforcements into the composite) has been reached. The percolation threshold is thus located between 40% and 50% in diamond volume fraction. Once reached, the percolation threshold prevents the densification process from being completed, thus leading to composite materials with a high porosity level, therefore critically affecting its thermal properties. Finally, it is also interesting to notice that the increase in thermal conductivity slows down relatively to thermal diffusivity increase between 10% and 40% diamond volume fraction. This is due to the fact that thermal conductivity is density-dependent, while thermal diffusivity is not affected by a decreasing relative density.

Maxwell's model predicts the thermal conductivity of a composite material assuming that:

- The reinforcements are strictly spherical;
- The reinforcement volume fraction is low (dilute medium);
- No thermal boundary resistance exists at the copper/diamond interface.

The significance of the theoretical values predicted by Maxwell's model is also affected by the fact that the precise thermal conductivity of the diamond powders is unknown in this study; it was



assumed to be equal to  $1000 \text{ W.m}^{-1}.\text{K}^{-1}$  (Tab. 4.4). Despite this uncertainty, the evolution of experimental thermal conductivities follows that of the theoretical thermal conductivities predicted by Maxwell's model. However, the gap between the measured thermal conductivities and those calculated is important. It has two sources: one is the interfacial thermal resistances of layer interfaces in stack; another is the interfacial thermal resistance between diamonds and copper.

The thermal conductivity measured with a pure copper sample is only  $364 \text{ W.m}^{-1}.\text{K}^{-1}$  instead of the theoretical value of  $385 \text{ W.m}^{-1}.\text{K}^{-1}$ . It is assumed that interfacial thermal resistances between the tapes pressed together likely lead to a decrease in the global thermal conductivity of the stack. Although no distinction can be made between the layers through electronic micrograph, it was measured that the thermal conductivity of the stack decreases when the number of tapes by stack increases.

The interfacial thermal resistance between diamond particles and the copper matrix may also contribute to decrease the thermal conductivity. The existence of porosity or voids at the matrix/reinforcement interface would also degrade the thermal properties of the composites. In addition, the non-spherical shape of diamond particles is likely favorable to increase the gap between experimental and Maxwell's model values. Finally, we observe that the deviation from Maxwell's prediction increases with diamond volume fraction since the validity of the dilute medium assumption is affected when the diamond volume fraction increases.

Nevertheless, we reach an average thermal conductivity of  $455 \text{ W.m}^{-1}.\text{K}^{-1}$  and a maximum thermal conductivity of  $480 \text{ W.m}^{-1}.\text{K}^{-1}$  with a diamond volume fraction of 40%, which is a significant improvement (+ 25%) relative to pure copper ( $k_{Cu} = 385 \text{ W.m}^{-1}.\text{K}^{-1}$ ).

#### ▪ *Thermal expansion coefficient (CTE):*

Although a high thermal conductivity is critical to any material used as a heat-spreader, the CTE is often the limiting factor for heat-spreading material selection in electronic industry. Indeed, it is critical to limit the thermo-mechanical stresses due to CTE mismatch in the layered structure of the module in order to maximize the lifetime of the module (see chapter 2).

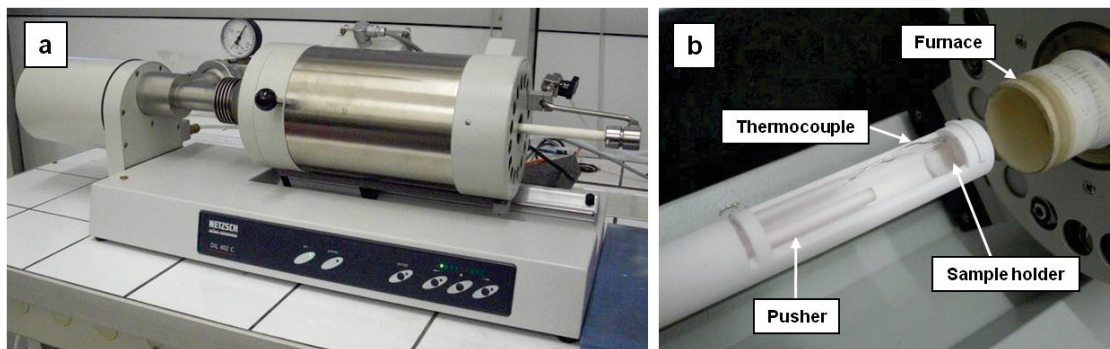


Figure 4.51: Photographs of the horizontal dilatometer.

Thermal expansion coefficients of the composites were measured on cylindrical samples of 6 mm in diameter and 4 mm in height (+/- 0.6 mm) using a horizontal Netzsch dilatometer DIL402C. More details of the structure of the apparatus are provided in the annex section. Figure 4.51 shows photographs of the CTE measurement apparatus.

The measurement method consists in heating up a sample of which initial length is known ( $L$ ) and in measuring its length variation ( $\Delta L$ ) upon thermal cycling. Indeed, the isobaric thermal expansion coefficient is defined as:

$$\alpha = \frac{1}{V} \left( \frac{\partial V}{\partial T} \right)_p \quad (4.16)$$

Which at constant pressure leads to:

$$\alpha = \frac{\Delta V}{V} \frac{1}{\Delta T} \quad (4.17)$$

If the material is considered to isotropically expand, the coefficient of thermal expansion can be evaluated upon one direction only, and equation 4.14 becomes:

$$\alpha = \frac{\Delta L}{L} \frac{1}{\Delta T} \quad (4.18)$$

Which leads to:

$$\Delta T = \frac{1}{\alpha} \frac{\Delta L}{L} \quad (4.19)$$

Therefore, the slope of the evolution of  $\Delta L/L$  as a function of the temperature makes it possible to get the CTE of the material. Two thermal cycles going from room temperature and 250°C were applied. It is required to calibrate the device using an alumina sample prior to the actual sample investigation in order to evaluate the impact of the dilatation of the different parts of the chamber (alumina sample, sample holder, pusher) to the global dilatation measured and to affranchise of these components during the actual measurement.

Kerner's model is a thermo-elastic model frequently used to predict CTE of composite materials [189]:

$$\alpha_c = \alpha_m V_m + \alpha_d V_d + \frac{V_d(1-V_d)(\alpha_d - \alpha_m)(K_d - K_m)}{K_m(1-V_d) + K_d V_d + \left( \frac{3K_d K_m}{4G_m} \right)} \quad (4.20)$$

Where  $\alpha_m$ ,  $\alpha_d$ , and  $\alpha_c$ , are the CTEs of the copper matrix, the diamond reinforcements, and the composite material, respectively;  $V_m$  and  $V_d$  are the copper matrix and diamond reinforcements respective volume fractions;  $K_m$  and  $K_d$  are the bulk modulus of the copper matrix and the diamond reinforcements, respectively;  $G_m$  is the shear modulus of the copper matrix (Tab. 4.4).

Theoretical and experimental CTE results obtained from Cu/D composites fabricated through tape casting and hot pressing with diamond volume fraction ranging from 0% to 50% are shown on Fig. 4.52.

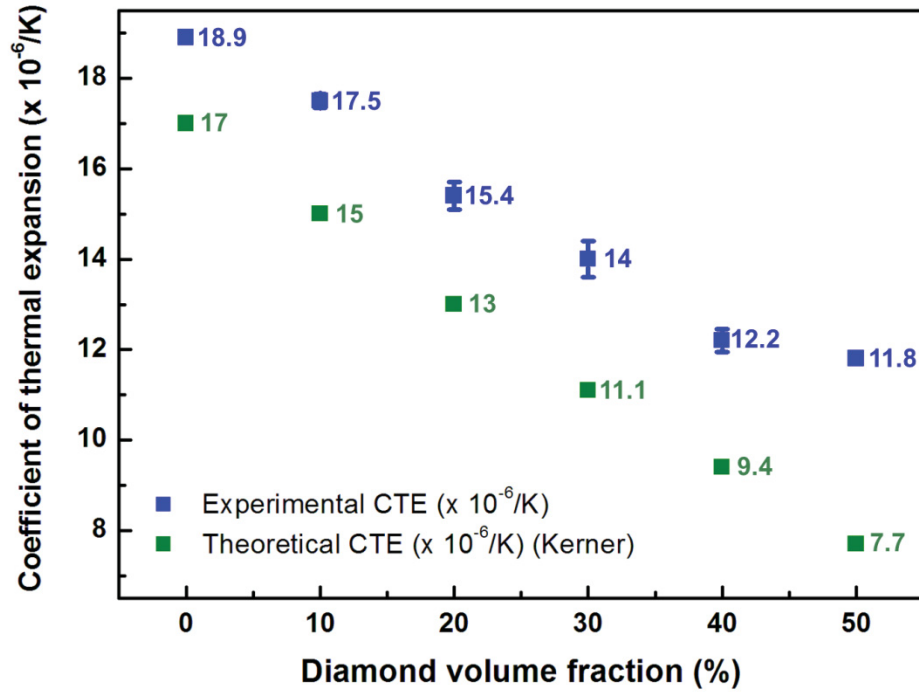


**Figure 4.52: Evolution of the experimental and theoretical coefficient of thermal expansion of the Cu/D composite as a function of the diamond volume fraction.**

The average measured CTEs of composites decrease linearly from  $18.9 \times 10^{-6} \text{ }^{\circ}\text{C}^{-1}$  to  $11.8 \times 10^{-6} \text{ }^{\circ}\text{C}^{-1}$  with diamond volume fractions ranging from 0% to 50% and evolve with the same slope as the theoretical values. Unlike thermal conductivity, CTE is not affected by the low compaction exhibited by the Cu<sub>50</sub>D<sub>50</sub> composites since it keeps decreasing between 40% and 50%, although its decrease is less pronounced between these two volume fractions.

The deviation between experimental and theoretical CTE values is clearly noticeable. The CTE of pure copper samples fabricated by tape casting and hot pressing is measured to be  $18.9 \times 10^{-6} \text{ }^{\circ}\text{C}^{-1}$ , which is higher than the theoretical value ( $\alpha_{Cu} = 17 \times 10^{-6} \text{ }^{\circ}\text{C}^{-1}$ ). The source of this deviation cannot be ascribed to the multilayered structure of the samples, and its origins are not understood since the device was preliminary calibrated with an alumina sample.

Nevertheless, a minimum CTE of  $12 \times 10^{-6} \text{ }^{\circ}\text{C}^{-1}$  with a diamond volume fraction of 40% is reached, which represents a strong reduction (- 30%) relative to pure copper. In power packages, it was previously demonstrated that a minimum level of thermo-mechanical stress in the solder joint between the DBC substrate and the heat sink could be achieved by having a heat sink with a CTE of  $10 \times 10^{-6} \text{ }^{\circ}\text{C}^{-1}$ . Thus, the Cu/D composite heat-spreaders are very close to satisfy this industrial

requirement. These results demonstrate that the deposition process of copper submicronic particles leads to a strong interfacial bonding, thus enabling an efficient thermal expansion load transfer at the matrix/reinforcement interface.

## 4.9 Comparison with traditional carbide-bonded Cu/D composites

In order to compare the innovative Cu-particles bonding process we developed to the carbide-bonding method traditionally employed to bond copper to diamond, carbide-bonded Cu/D composites were fabricated. Chromium (Cr) and boron (B) were used as carbide-forming additives. The composite samples investigated in this section of the dissertation were all fabricated through a simple powder metallurgy route (powders mixture and hot pressing), thus not involving the tape casting process. The Cu-bonded composite samples were prepared by pre-coating the diamond reinforcements with Cu particles through chemical and heat treatments and then through the same powder metallurgy route. The properties of the Cu/D(Cu) composites detailed in this section were obtained from a different set of samples than that used in section 4.8 and were fabricated through a simple powder metallurgy route, thus without resorting to tape casting. Cu/D composite materials made from pure powder mixture, thus without neither Cu-coating nor carbides for interfacial bonding, were processed in order to provide a reference value for comparison purposes. The volume fraction of diamond was 40% for all the composite samples.

For each type of composite (no bonding, Cr-carbide-bonded, B-carbide-bonded, and Cu-bonded), the density, thermal conductivity, thermal expansion coefficient, and resistance to thermal cycling were evaluated and compared. Therefore, this part of the study brings understanding on how the interfacial bonding (mechanical or chemical) impacts the microstructure and the thermal performances of the Cu/D composites.

### 4.9.1 Carbide forming materials

Thermodynamically, the ability of a particular element to form carbides can be quantified through its standard free enthalpy of reaction. Table 4.9 gathers some of the most common carbides employed to process copper/carbon composite materials and their respective standard free enthalpy of reaction:

**Table 4.12: Some carbides and their respective standard free enthalpy of reaction [197,198].**

Carbide	Cr <sub>3</sub> C <sub>2</sub>	TiC	ZrC	Mo <sub>2</sub> C	VC	WC	B <sub>4</sub> C	NbC
$\Delta_r G^\circ_{298.15K}$ (kJ.mol <sup>-1</sup> )	-22.1	-90.4	-96.5	-15.6	-53.1	-19.2	-14.2	-69.2

The lower the standard free enthalpy of reaction, the most favorable is the formation of the carbide from a thermodynamic point of view. Therefore, in standard pressure and temperature conditions, the carbide-forming elements can be ranked from the most to the least carbide-forming as following:  $Zr > Ti > Nb > V > Cr > W > Mo > B$ .

L. Weibert et al. [125] and Schubert et al. [127, 128] have fabricated Cu/D composite materials with various carbide-forming additives through infiltration. They have shown that the addition of carbide-forming elements could be drastically beneficial to the thermal properties of the final materials, especially when adding chromium and boron to the copper matrix (Fig. 4.53).

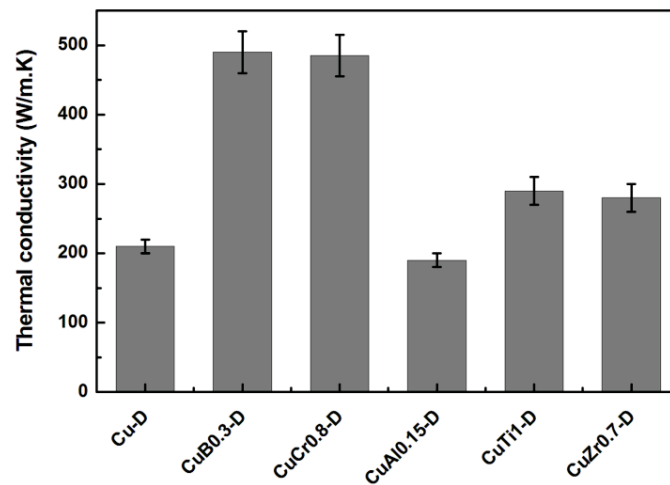


**Figure 4.53: Thermal conductivity comparison between Cu-X/42 vol.% D composite materials (where X stands for B, Cr, Al, Ti, Zr, and the percentages are atomic) [128].**

Another criterion for the selection of a carbide-forming additive is its solubility into copper, i.e. its ability to diffuse into the matrix material. Indeed, it is crucial that no other stable phase which would inhibit or prevent the diffusion of the carbide-forming element toward the matrix/reinforcement interface forms upon sintering. Finally, it is crucial to keep the quantity of carbide-forming elements added to the copper/diamond system as low as possible. Indeed, it was demonstrated that an increase in the quantity of foreign material elements such as carbide-forming additives led to a decrease of the global thermal conductivity of the Cu/D composites [89].

Based upon these criteria, chromium (Cr) and boron (B) were selected for carbide-bonding of copper/diamond composite materials. Although lower than that of other elements such as Zr, Ti, or Nb, their ability to form carbides is interestingly combined with their solubility into copper and with an acceptable cost. Moreover, Cr and B have been proven thermally efficient as bonding materials for Cu/D composite materials processing. Lastly, B has also the advantage to be an element with a low atomic radius, which allows it to diffuse interstitially into the copper matrix, as explained in section 4.9.3.

The Cu-B and Cu-Cr binary phase diagrams are displayed in Fig. 4.54 to illustrate the solubility of boron and chromium into the copper matrix. As shown on Fig. 4.54, Both Cu-B and Cu-Cr phase diagrams are of the eutectic type:

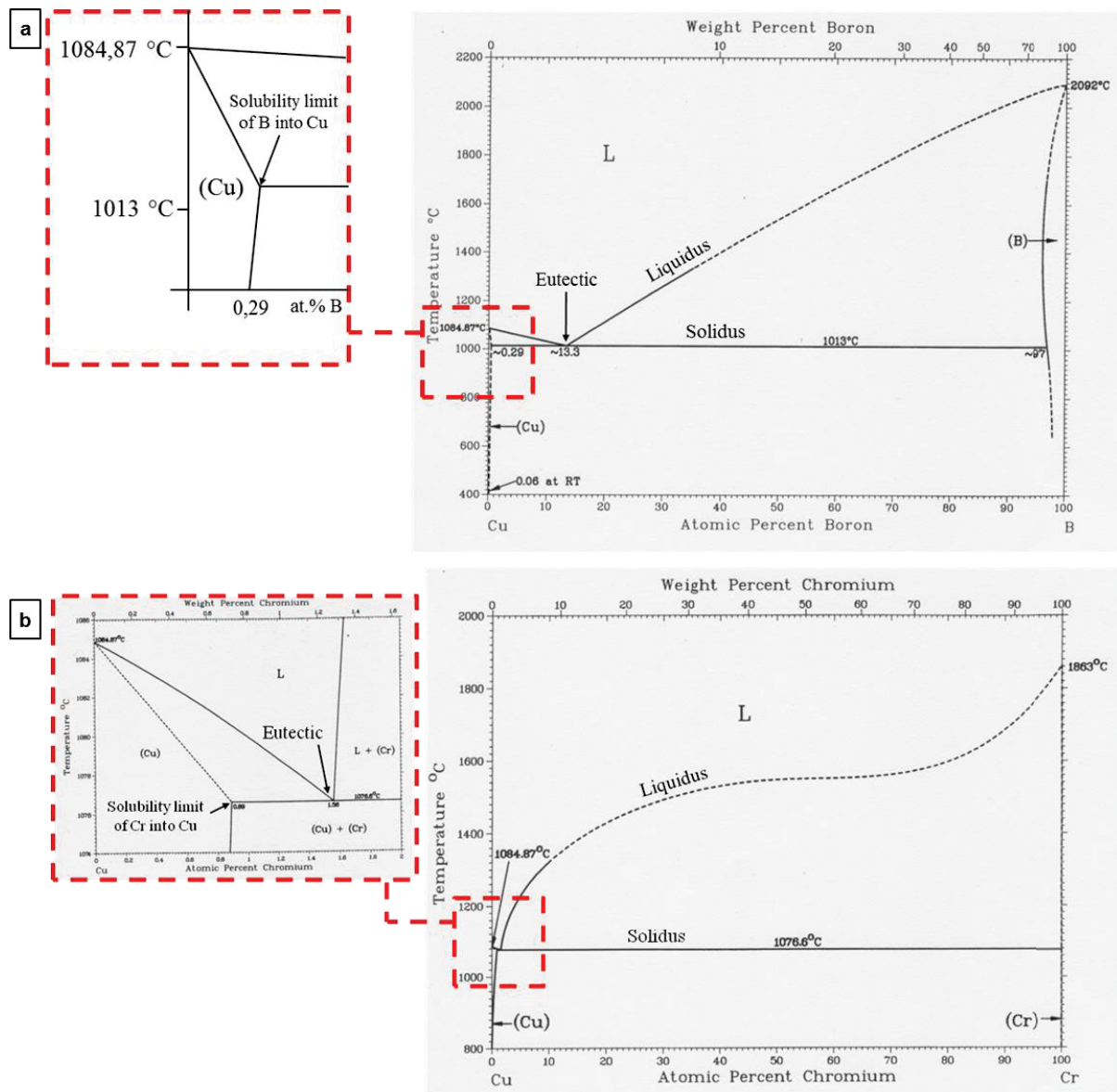
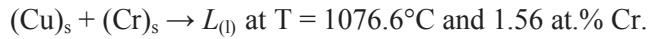
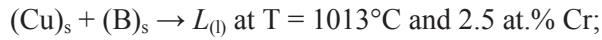


Figure 4.54: The (a) Cu-B and (b) Cu-Cr binary phase diagrams [191].

The equilibrium phases visible on the Cu-B phase diagram are a liquid phase (L), a FCC copper-rich solid solution (Cu) with a limited maximum solubility of boron of 0.29 at.% at 1013°C, and a boron-rich solid solution (B) with a maximum recorded solubility of copper between 3.65 and 4.17 at.%. Various allotropic forms of boron are observed in the (B) domain. However, no intermediate phases exist.



The equilibrium phases visible on the Cu-Cr phase diagram are a liquid phase (L), a FCC copper-rich solid solution (Cu) with a maximum solubility of chromium of about 0.89 at.% at 1077°C and a bcc chromium-rich solid solution (Cr) with no solubility of copper. Similarly to the Cu-B binary system, no intermediate phase is observed on the Cu-Cr phase diagram.

As demonstrated by the Cu-B and Cu-Cr phase diagrams, the respective solubility limits of Cr and B in copper are 0.89 at.% and 0.29 at.%. The solubility limit of an additive into the matrix corresponds to the maximum amount of this additive that can be dissolved into the matrix in order to form a single-phased solid solution. Above the solubility limits, two phases are formed, through precipitates inside the matrix material for instance, which would critically affect the diffusion of the carbide-forming additive and the creation of a chemical Cu/D interface. Therefore, it is required to use alloyed-copper powders with carbide-forming additives content lower than their respective solubility limits into copper.

In a same manner, the B-C and Cr-C binary phase diagrams are displayed in Fig. 4.55 to illustrate the ability of chromium and boron to form carbides:

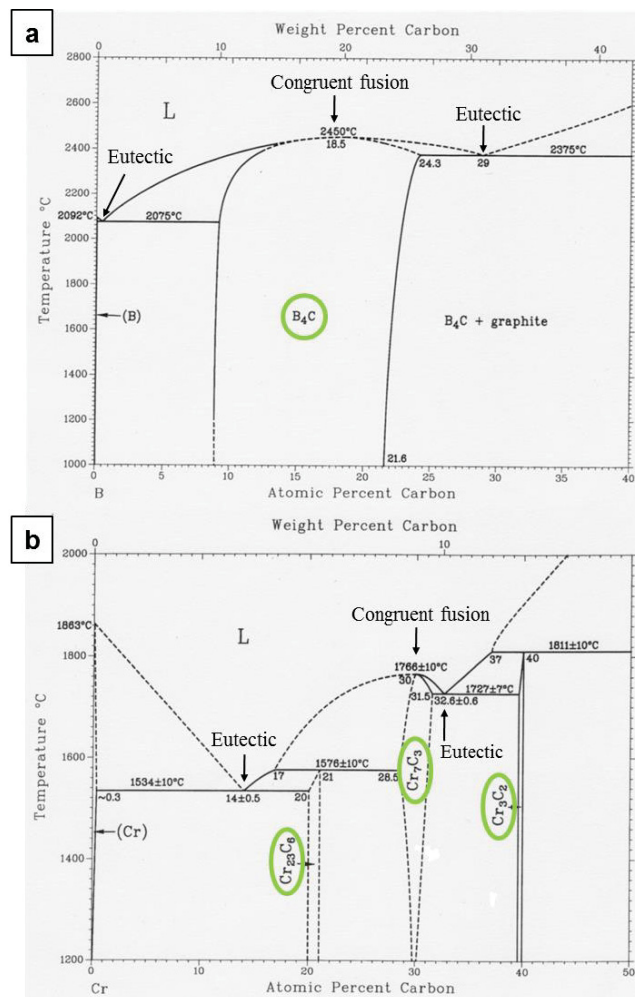


Figure 4.55: (a) The B-C and (b) Cr-C binary phase diagrams [191].

The equilibrium phases visible on the B-C phase diagram are a liquid phase (L), a boron-rich solid solution (B) with no solubility of carbon, a carbon-rich graphitic phase with no solubility of boron, and an intermediate phase  $B_4C$  between 8 at.% and 21.6 at.% carbon and in a large range of temperature. The existence of this intermediate phase is the most interesting point of the C-B system from the point of view of interface bonding since it is suitable to create chemical bonding at the Cu/D interface. Eutectic points located on isotherms  $T = 2075^\circ\text{C}$  ( $(B)_s + B_4C_{(s)} \rightarrow L_{(l)}$ ) and  $T = 2375^\circ\text{C}$  ( $(C)_s + B_4C_{(s)} \rightarrow L_{(l)}$ ) are also visible. One can finally notice that the  $B_4C$  phase melts congruently at  $2450^\circ\text{C}$  (i.e. without any alterations of the composition).

In a same manner, the equilibrium phases visible onto the Cr-C phase diagram are a liquid phase (L), a chromium-rich solid solution (Cr) with a limited solubility of carbon of 0.3 at.% at  $1534^\circ\text{C}$ , a carbon-rich graphitic phase with no solubility of boron, and intermediate phases  $Cr_{23}C_6$ ,  $Cr_7C_3$ ,  $Cr_3C_2$ . These intermediate phases have narrow homogeneity ranges but are stable upon elevated temperatures and will be involved in the chemical bonding at the interface between diamond reinforcements and Cr-alloyed copper matrix. The  $Cr_3C_2$  compound is known to be the most stable chromium carbide. Eutectic points located on isotherms  $T = 1534^\circ\text{C}$  ( $(Cr)_s + Cr_{23}C_{6(s)} \rightarrow L_{(l)}$ ) and  $T = 1727^\circ\text{C}$  ( $Cr_7C_{3(s)} + Cr_3C_{2(s)} \rightarrow L_{(l)}$ ) are also visible. At last, one can notice that the  $Cr_7C_3$  phase melts congruently at  $1766^\circ\text{C}$ .

Consequently, when present in lower amounts relative to their solubility limits into copper, and processed in the suitable temperature ranges, boron and chromium additives can lead to the formation of intermediate carbide phases in the vicinity of the diamond reinforcements. Therefore, the carbide-forming additives existing into B-alloyed and Cr-alloyed copper powders should allow chemical bonding at the Cu/D interface. The as-processed Cu-Cr/D and Cu-B/D composites will then be compared to the Cu/D(Cu) composites in terms of relative density and thermal performances.

#### 4.9.2 Boron and chromium-alloyed copper powders

Spherical Cr and B-alloyed copper powders from Nanoval GmbH (Germany) were used as matrix materials for the fabrication of carbide-bonded Cu/D composites. The B-alloyed copper powders contained 0.05 at.% of boron, while Cr-alloyed copper powders contained 0.6 at.% of chromium, the carbide-forming additive contents being thus compatible with the solubility limits established from the Cu-B and Cu-Cr phase diagrams. These contents in carbide-forming additives are consistent with the solubility limits previously established from the Cu-Cr and Cu-B phase diagrams (section 4.9.1). SEM micrographs of the alloyed copper powders confirmed the spherical shape of the powders (Fig. 4.56). X-ray diffraction analysis confirmed that the powders were effectively made of metallic copper. Cr or B additives existing in the powders could not be detected through this XRD analysis since their respective quantities are too low for being traced.

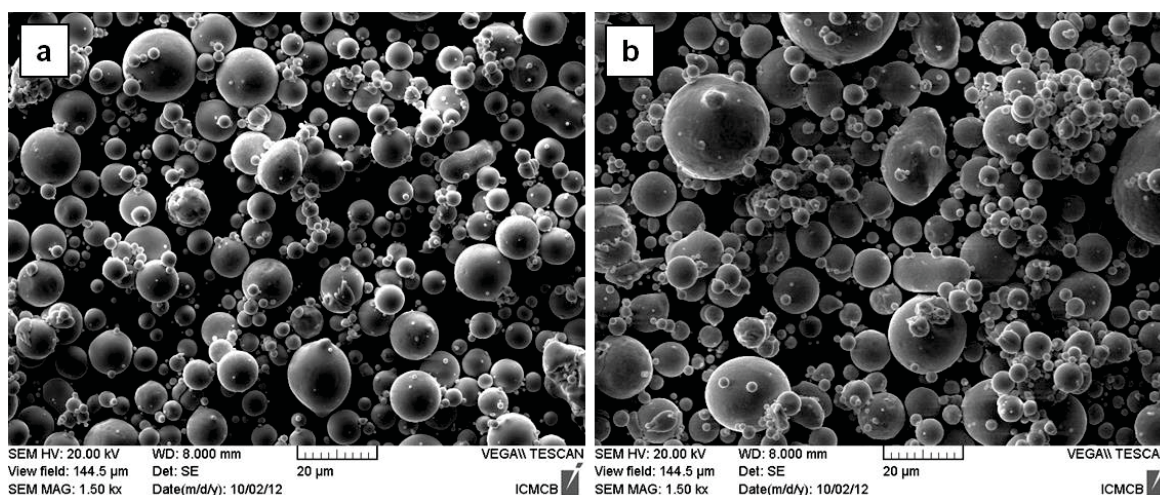


**Figure 4.56: SEM micrographs of (a) spherical Cu-Cr alloyed powders and (b) spherical Cu-B alloyed powders.**

Unlike dendritic copper powders that are produced through electrolysis, the spherical copper powders are fabricated through atomization. The atomization process consists in fractionating a spray of molten metal into extremely fine droplets using the impact energy of high-pressurized fluids (water, oil, or gases). The liquid droplets then solidify and will constitute the final spherical powder particles. The powder diameters are typically below 150  $\mu\text{m}$ . However, the powders produced through atomization generally exhibit lower purity relative to those produced through electrolysis because of the very confined and protective environment provided by the electrochemical synthesis in liquid solution [195].

Nevertheless, atomized powders represent more than 60 wt.% of the entire world powder production (the production of atomized metallic powders is estimated to one million tons a year). This success is due to the high yield of the atomization processes (up to 30 tons per hour for water atomization), which leads to low capital costs. In addition, atomization techniques provide high flexibility in terms of powder compositions, which only relies on the solubility of the different molten elements, allowing the achievement of a wide range of alloys.

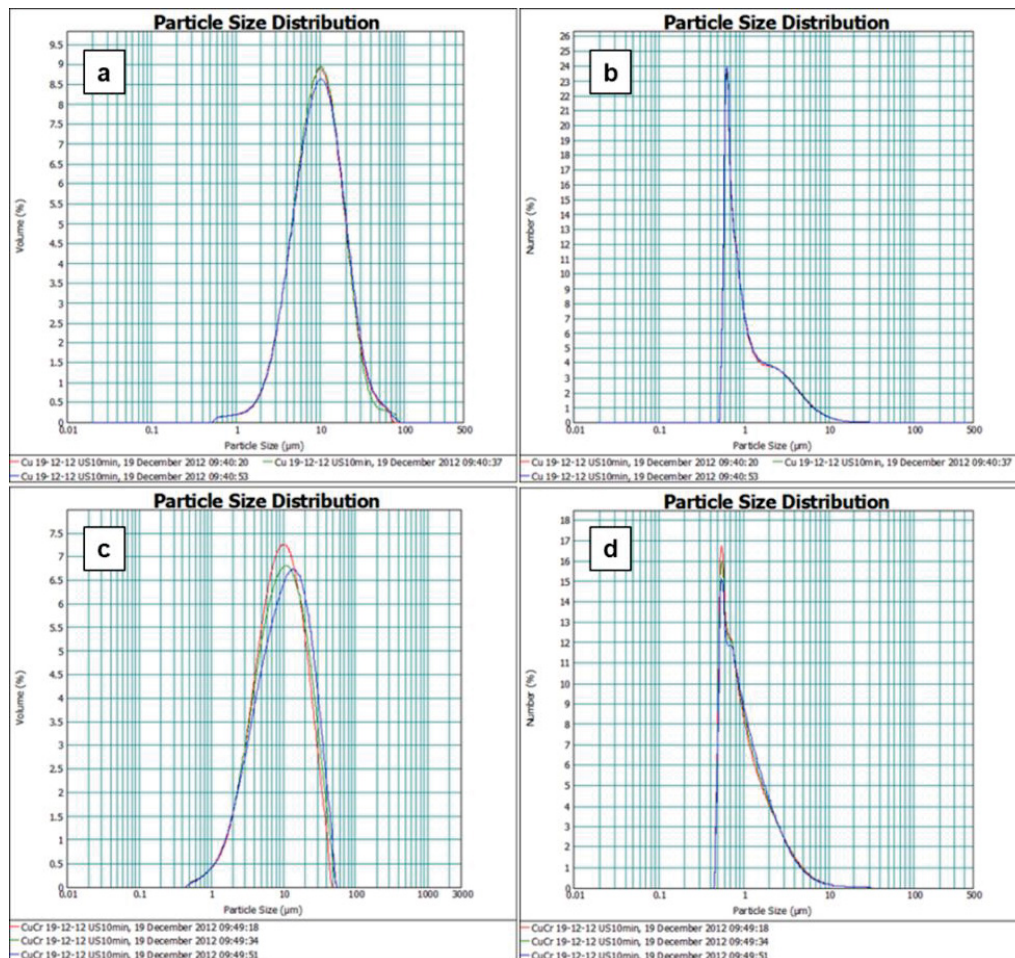
In order to evaluate the size of the powders, granulometric analyses of the Cr-alloyed and B-alloyed copper powders were carried out. Figure 4.57 shows the particle distribution of Cu-B and Cu-Cr alloyed powders in volume and in number, respectively. Table 4.10 gathers the  $d_{50}$  in volume and in number of the two types of spherical alloyed copper powders. The  $d_{50}$  diameter is the median particle diameter which splits the particle diameter distribution in two equal parts. Figures 4.57a and 4.57c show that the Cu-B and Cu-Cr powders are fairly well distributed around the diameter value of 10  $\mu\text{m}$ . However, when considering the distribution in number, one can notice that the particles with diameters below 1  $\mu\text{m}$  are far more numerous than particles with diameter above 1  $\mu\text{m}$ , which is also remarkable on the SEM micrographs of the alloyed copper powders (Fig. 4.56).

Table 4.13 also clearly enlightens the strong difference existing between the volume and the number distributions since we reach  $d_{50}$  located around  $9.7 \mu\text{m}$  for the particle distribution in volume while  $d_{50}$  located around  $0.9 \mu\text{m}$  are obtained from the particle distribution in number. There is therefore a factor of 10 between the two types of distribution, which has to be noticed.

**Table 4.13: Respective volume and number  $d_{50}$  of the Cu-B and Cu-Cr alloyed copper powders.**

Powders	$d_{50}$ in volume ( $\mu\text{m}$ )	$d_{50}$ in number ( $\mu\text{m}$ )
Cu-B	9.678	0.91
Cu-Cr	9.756	0.905

Carbide-bonded composite materials were fabricated through direct powder mixture between the alloyed-copper powders and the diamond reinforcements. The Cu-Cr/D and Cu-B/D composite powder mixtures were then densified through uniaxial hot pressing. The carbide forming additives (Cr, B) present in the powders will react upon pressure and temperature during sintering and allow the creation of a carbide interphase that will chemically bond the diamond reinforcements to the copper matrix, thus leading to enhanced heat transfer properties at the Cu/D interface.



**Figure 4.57: Particle size distribution of spherical (a, b) Cu-B alloyed powders and (c, d) spherical Cu-Cr alloyed powders in volume and number, respectively.**



#### 4.9.3 Diffusion in Cu-Cr/D and Cu-B/D composite materials

Although, for conciseness purposes, we will refrain from reminding here the fundamental laws governing the diffusion processes, it is important to make a brief statement about the basics of the diffusion phenomena that may occur in a solid-state material.

▪ **Diffusion modes:**

Diffusion in a polycrystalline solid-state material is mainly activated through temperature:

- At low temperature ( $T < 0.3T_m$ , where  $T_m$  is the melting temperature of the solid considered): atomic motion can only exist at the surface of the solid, where atomic bonds are cut;
- At intermediate temperature ( $0.3T_m < T < 0.5T_m$ ): atom diffusion occurs at the grain boundaries, an atom moving by exchanging its position with the defects of the grain boundaries. This phenomenon is called *inter-granular diffusion*;
- At elevated temperature ( $0.7T_m < T$ ): atom diffusion occurs in the volume of the grains as the number of defects inside the grains increases. This phenomenon is called *volume diffusion*.

These three phenomena can coexist at a same temperature in a single material.

▪ **Diffusion mechanisms:**

Atom motion in a solid requires the presence of punctual defects (vacancies) or interstitial sites. Therefore, the two fundamentals diffusion processes encountered in polycrystalline solids are:

- The *interstitial mechanism*: this mechanism concerns elements with small atomic radii located at interstitial sites into a lattice (Fig. 4.58a);
- The *lacunar mechanism*: this mechanism concerns atoms located at substitution sites into a lattice. Diffusion of such atoms can only occur if vacancies exist in the vicinity of these atoms (Fig. 4.58b).

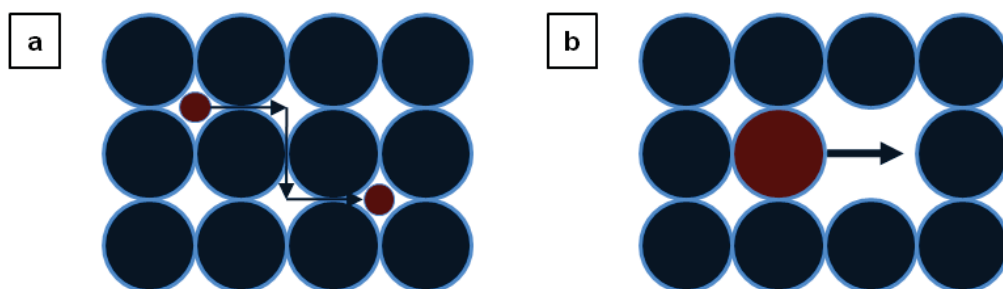


Figure 4.58: (a) Interstitial and (b) lacunar diffusion mechanisms representations.

**Table 4.14: Respective atomic radii of Cu, B, and Cr.**

Element	Cu	B	Cr
Atomic radius (nm)	0.128	0.098	0.128

In the case of Cu-Cr/D composite materials, the chromium additives are located into substitution sites of the copper matrix since Cu and Cr have similar atomic radii, thus forming a substitution solid solution with copper. Therefore, the diffusion of Cr atoms into the copper matrix occurs following a lacunar mechanism. Unlike chromium, boron has a very low atomic radius which allows it to be located interstitially into the copper matrix. As a consequence, the diffusion of boron into the copper matrix of Cu-B/D composite occurs following an interstitial mechanism.

▪ ***Thermodynamic approach: Cu-Cr/D composites:***

According to Fick's law, the diffusion of an element into the matrix can only occur if a concentration gradient of the element exists into the matrix. The chromium additives forming a solid solution with copper are uniformly dispersed into the copper matrix, thus without any concentration gradient. As explained in section 4.9.3, the diffusion of the chromium additives is temperature-activated upon the sintering process. The temperature elevation triggers the creation of vacancies into the copper matrix through atoms displacement but also the displacement of atoms to the neighboring vacancies, thus leading to the diffusion of chromium atoms into the copper matrix.

Without any force driving the displacement of the atoms, these move randomly into the copper matrix. The main concern is to know if the chromium additives will react with carbon at the Cu/D interface or stay in the copper-rich solid solution. The affinity of chromium with carbon is quantified by the standard Gibbs free energy of formation of the chromium carbide  $\text{Cr}_3\text{C}_2$  (see table 4.12). In order to evaluate the tendency of chromium additives either to form chromium carbides with the carbon of the diamond reinforcements or remaining into the copper solid solution as substitution elements, one can calculate the Gibbs free energy for both reactions and compare [89]. It results from these calculations that the formation of the chromium carbide will be favored toward the formation of the copper/chromium solid solution since the Gibbs free energy of formation of the Cu/Cr solid solution is higher than the Gibbs free energy of formation of the  $\text{Cr}_3\text{C}_2$  compound. Therefore, from a thermodynamic point of view, the creation of chromium carbides is favored toward the creation of a copper-rich solid solution with chromium.

#### **4.9.4 Sintering of carbide-bonded Cu/D composites**

The Cu-Cr/D and Cu-B/D composite powder mixtures were densified using the same uniaxial hot pressing system as the one described in section 4.7.2. However, the hot pressing parameters were different. Indeed, hot pressing temperature was higher since the spherical shape of the alloyed-



copper powders required more energy to be sintered (see section 4.7.1). Therefore, Cu-B/D and Cu-Cr/D composite powders mixtures were hot-pressed using a graphite mould and graphite pistons which were induction-heated to 850°C. Steel mould could not be used to process Cu-Cr/D and Cu-B/D composites since the hot pressing temperature was too high. Indeed, it was recommended to do not heat up the steel moulds above 650°C unless triggering microstructural changes in the alloy, thus affecting its mechanical properties and its tenue to hot pressing. As for Cu/D(Cu) composites, vacuum was set to  $10^{-1}$  mbar and the effective applied pressure on the pistons was 50 MPa. The materials were maintained under hot pressure during 30 minutes. 6 mm diameter cylindrical composite materials samples with height ranging from 2 to 4 mm were fabricated in order to fit the dimensional requirements of further thermal characterizations.

Electron Probe Micro Analysis (EPMA) allows determining the chemical composition of small volume of solid materials in a non-destructive manner. This technique works following the same principle as SEM or EDXS. The scoped volume of material is about  $1 \mu\text{m}^3$ . Figure 4.59 shows the results of the chemical mapping of a Cu-Cr/D composite through electron probe micro-analysis (EPMA).

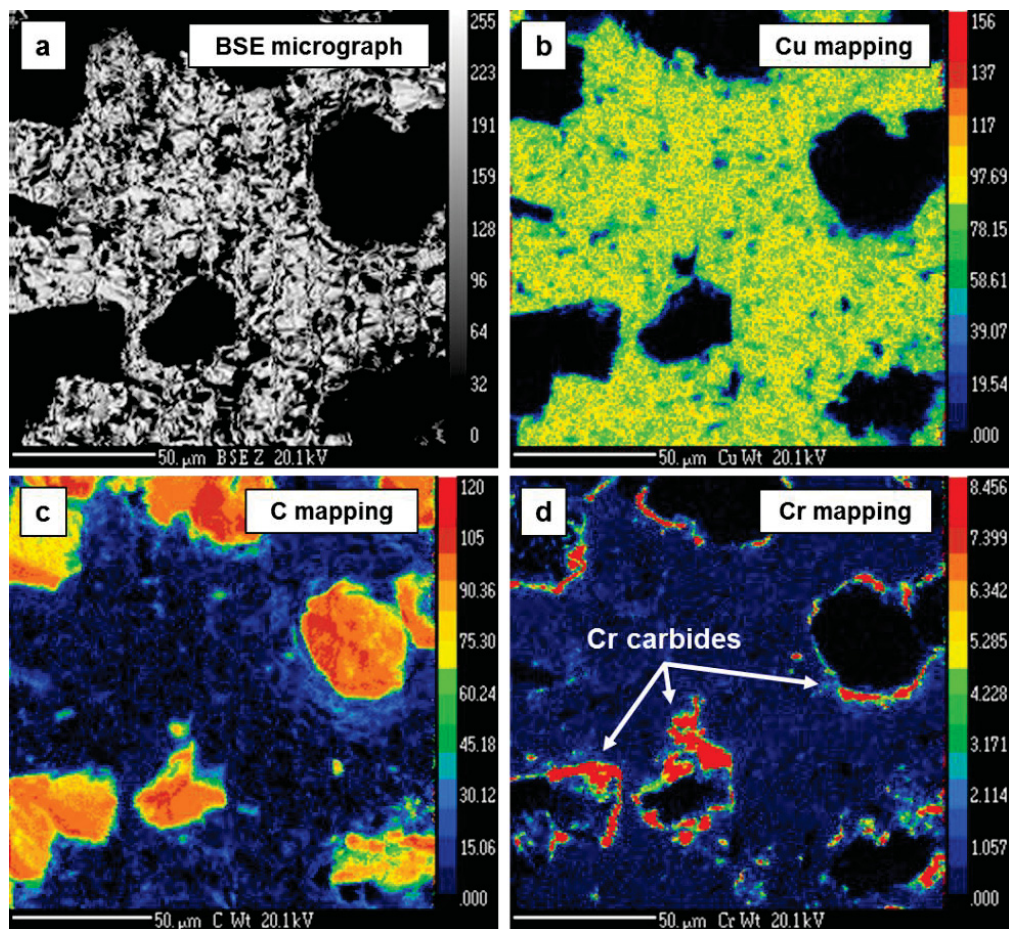


**Figure 4.59: EPMA chemical mapping of a hot-pressed Cu-Cr/40 vol.% D composite material: (a)BSE micrograph of the investigated area, (b) Cu mapping, (c) C mapping, (d) Cr mapping.**

The back scattering electron (BSE) micrograph of the analyzed area of the composite is shown on figure 4.59a. It reveals the different components of the composite through chemical contrast. The black areas correspond to the diamond reinforcements dispersed in the copper matrix (white area). Figures 4.59b, 4.59c, and 4.59d correspond to chemical maps of copper, carbon, and chromium, respectively.

The EPMA chemical mapping demonstrates that the chromium additives initially dissolved in the copper matrix have diffused during sintering and are located at the interfaces between the copper matrix and the diamond reinforcements after sintering. It is also visible on Fig. 4.57d that the chromium-rich interphase between the copper matrix and the diamond reinforcements may reach several micrometers in thickness. However, chromium carbide is not detected at all interfacial locations between copper and diamond. This may be due to the low detection resolution ( $1\text{ }\mu\text{m}^3$ ) of the EPMA technique. Finally, it has to be noticed that EPMA chemical analysis could not be efficiently carried out onto Cu-B/D composites since the boron content into the Cu-B alloyed powders was too low (0.05 at.% of B in Cu-B powders, instead of 0.6 at.% of Cr in Cu-Cr powders).

Although EPMA line profiling may enable determining the composition of the carbide located at the interface, no clear conclusion about the chemical nature of the chromium-based compounds existing at the Cu/D interfaces could be drawn from EPMA analysis. Therefore, AES analysis was coupled to EPMA for more understanding.

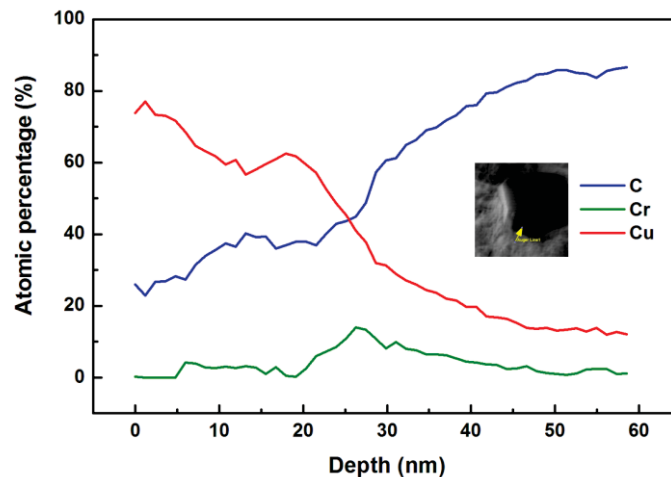


Figure 4.60: AES line profile at the Cu/D interface in a Cu-Cr/D composite.

Figure 4.60 shows an AES line profile recording the signals of C, Cu, and Cr carbide, at the matrix/reinforcement interface of a Cu-Cr/D composite material, going from the copper matrix to the diamond reinforcement. The analysis demonstrates that Cr carbide is detected at the Cu/D interface (green line). However, it is again difficult to be conclusive on the composition of the

carbide involved ( $\text{Cr}_2\text{C}_3$  or  $\text{Cr}_7\text{C}_3$ , as explained on the phase diagram (Fig. 4.53b)). Therefore, the chromium-rich areas lead to a chemical interfacial bonding through the creation of chromium carbide at the Cu/D interface. Nevertheless, it should be pointed out that, even through AES line profiling, Cr carbide was not detected at every location of the interface between diamond and copper of the Cu-Cr/D composite sample. This may be due to the limited chromium content of the Cr-alloyed copper powders.

The carbide-bonded composites (Cu-Cr/D, Cu-B/D) were then compared to the Cu/D composites fabricated without using any bonding solution (pure Cu/D materials) and to those processed through the innovative Cu-particle deposition process developed at ICMCB (Cu/D(Cu) composites). This will allow us to draw conclusions about the influence of the interfacial bonding on the thermal performances of the Cu/D composite materials.

#### 4.9.5 Influence of interfacial bonding on thermal performances of Cu/D composites

On the columnar graphs of Fig. 4.61, 4.62, and 4.63, the (a) column (blue) corresponds to the property of the Cu/D composite materials processed through pure powder mixture without providing any interfacial bonding solution (labeled Cu/D). The (b) and (c) columns (orange and purple) correspond to the property of boron carbide and chromium carbide bonded Cu/D composites (labeled Cu-B/D and Cu-Cr/D, respectively). The (d) column (red) corresponds to the property of the Cu/D composites processed through the innovative Cu-particle deposition process we developed (labeled Cu/D(Cu)). For each type of Cu/D composite, 8 to 10 samples were fabricated and evaluated. The diamond volume fraction is set to 40% for all the samples.

##### ▪ *Relative density:*

Average relative densities obtained from  $\text{Cu}_{60}\text{D}_{40}$  composite materials with different interfacial configurations were measured through the same Archimed's method as the one described in section 4.8.1 and are shown on Fig. 4.61.

Cu/D composites fabricated without any bonding additives exhibit an average relative density of 93.4% (Fig. 4.61a). Cu/D composite materials involving boron and carbide forming additives exhibit relative densities of 98.3% (Fig. 4.61b) and 95.8% (Fig. 4.61c), respectively. Cu/D composites fabricated through the Cu-coating process of diamonds exhibit an average relative density of 100% (Fig. 4.61d), which means that the fully-dense state has been reached. The fact that we repeatedly reach the fully-dense state through the Cu-coating process demonstrates that the Cu particles deposited onto diamond effectively acts as interfacial chemical bonding agents.

Composite materials involving carbide-forming bonding additives reach acceptable compaction levels (Fig. 4.61b (Cu-B/D composites): 98.3%, Fig. 4.61c (Cu-Cr/D composites): 95.8%). Finally,

and unsurprisingly, pure Cu/D composites exhibit the lowest compaction level (Fig. 4.61a: 93.4%). In agreement with the Cu-C phase diagram, copper and carbon exhibit a low mutual chemical affinity, which is responsible for the weak and non-reactive copper/diamond interface exhibited by these composites. Accordingly, their low compaction will critically affect their thermal performances.

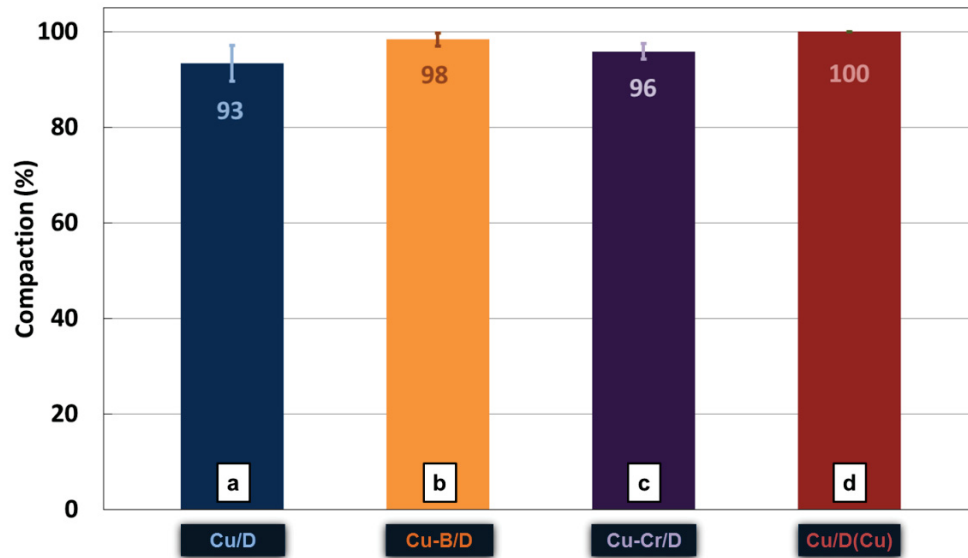
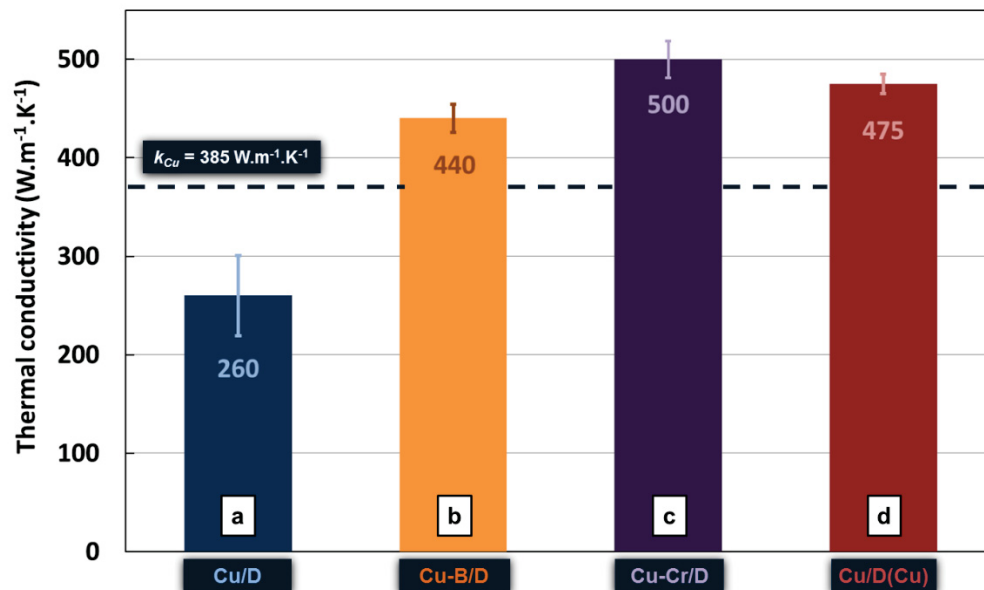


Figure 4.61: Influence on interfacial bonding on the relative density of the Cu/D materials.

▪ **Thermal conductivity:**

Average thermal conductivities obtained from Cu<sub>60</sub>D<sub>40</sub> composite materials with different interfacial configurations were measured through the same procedure as the one described in section 4.8.2 and are shown on Fig. 4.62.



**Figure 4.62: Influence on interfacial bonding on the thermal conductivity of the Cu/D materials.**

Pure Cu/D composites fabricated without any interfacial bonding solution exhibit a thermal conductivity of  $260 \text{ W.m}^{-1}.\text{K}^{-1}$  (Fig. 4.62a). Cu/D composite materials involving boron and chromium carbide forming additives respectively exhibit thermal conductivities of  $440 \text{ W.m}^{-1}.\text{K}^{-1}$  (Fig. 4.62b) and  $500 \text{ W.m}^{-1}.\text{K}^{-1}$  (Fig. 4.62c). Cu/D(Cu) composites fabricated through the Cu-coating process of diamonds exhibit an intermediate average thermal conductivity of  $475 \text{ W.m}^{-1}.\text{K}^{-1}$  (Fig. 4.62d).

Consistently with their low relative density, pure Cu/D composites exhibit low thermal conductivity. The high porosity level of these composites leads to heat transfer losses and critically degrades their heat conduction performances. Cu-B/D composites and Cu-Cr/D composites exhibit strongly enhanced thermal conductivities relative to pure Cu/D composites processed without any bonding solution. In a same manner, average thermal conductivity results obtained from Cu/D(Cu) composites fabricated through the innovative Cu-coating process confirm that the copper particles deposited onto the diamond reinforcements prior to sintering effectively act as chemical bonding agents between the diamonds and the copper matrix and allow efficient interfacial heat transfer and efficient coupling between electronic and phonon heat conductions.

Promisingly, Cu/D(Cu) composites exhibit thermal conductivity that is superior to that of the Cu-B/D composites, and comparable to that of the Cu-Cr/D composites. These results demonstrate the primary role played by interfacial chemical bonding, either through carbide interphases or copper coating, on the heat conduction process at interfaces of Cu/D composite materials. Indeed, the use of boron carbide, copper coating, and chromium carbide bonding solutions at the copper/diamond interface respectively lead to an increase in thermal conductivity of 70%, 82%, and 92% relative to the level reached by pure Cu/D composites ( $k_{\text{Pure Cu/D}} = 260 \text{ W.m}^{-1}.\text{K}^{-1}$ ). In addition, the respective average thermal conductivity of Cu-B/D, Cu/D(Cu), and Cu-Cr/D composites are higher by 14%, 25%, and 30% than the thermal conductivity of pure sintered copper ( $k_{\text{Cu}} = 385 \text{ W.m}^{-1}.\text{K}^{-1}$ ).

▪ ***Thermal expansion coefficient:***

In the same manner, average CTE obtained from  $\text{Cu}_{60}\text{D}_{40}$  composite materials with different interfacial configurations were measured through the procedure described in section 4.8.3 and are shown on Fig. 4.63. Pure Cu/D composites fabricated without any bonding additives exhibit a CTE of  $14.5 \times 10^{-6} \text{ }^{\circ}\text{C}^{-1}$  (Fig. 4.63a). Cu-B/D composites involving a boron carbide bonding interphase (Fig. 4.63b) and Cu/D(Cu) composites processed through the Cu-coating process of diamonds (Fig. 4.63d) both exhibit a CTE of  $12 \times 10^{-6} \text{ }^{\circ}\text{C}^{-1}$ . Cu-Cr/D composite materials involving a chromium



carbide bonding interphase exhibit the lowest thermal expansion coefficient value, with a CTE of  $11 \times 10^{-6} \text{ }^{\circ}\text{C}^{-1}$  (Fig. 4.63c).

The results obtained from the CTE evaluation demonstrate that the innovative diamond Cu-coating process we developed allows reaching similar thermo-mechanical performances relative to traditional carbide-bonded Cu/D materials. Indeed, Cu/D(Cu) composites exhibit a CTE of  $12 \times 10^{-6} \text{ }^{\circ}\text{C}^{-1}$  while Cu-B/D and Cu-Cr/D composites respectively exhibit CTEs of  $12 \times 10^{-6} \text{ }^{\circ}\text{C}^{-1}$  and  $11 \times 10^{-6} \text{ }^{\circ}\text{C}^{-1}$ . Therefore, it shows that the deposition process of copper submicronic particles leads to a strong interfacial bonding, thus enabling efficient thermal expansion load transfer at the matrix/reinforcement interface. The relatively high CTE exhibited by pure Cu/D composites is due to the lack of adhesion at the Cu/D interface.

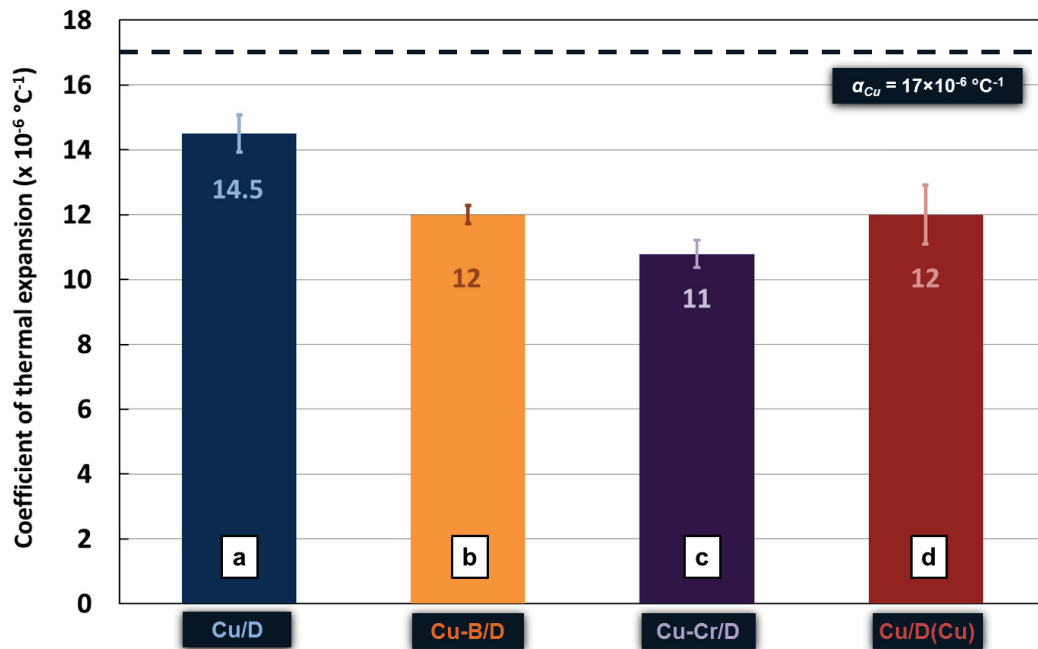


Figure 4.63: Influence on interfacial bonding on the thermal expansion coefficient of the Cu/D materials.

Although CTE mainly relies on mechanical bonding between the matrix and the reinforcements, the comparative CTE evaluation enlightens the influence of chemical bonding on the thermo-mechanical load transfer process: the use of boron carbide, copper coating, and chromium bonding solutions respectively lead to a decrease of CTE of 17%, 17%, and 24% relative to the level reached by pure Cu/D composites ( $\alpha_{\text{pure Cu/D}} = 14.5 \times 10^{-6} \text{ }^{\circ}\text{C}^{-1}$ ). The respective CTE decrease of Cu-B/D, Cu/D(Cu), and Cu-Cr/D composites are 30%, 30%, and 35% relative to the theoretical CTE of pure copper ( $\alpha_{\text{Cu}} = 17 \times 10^{-6} \text{ }^{\circ}\text{C}^{-1}$ ). Cu-Cr/D composite materials exhibit the lowest CTE of all samples, which is due to the strong carbide interphase present at the Cu/D interface in these materials.



However, the carbide interphase being composed of intermetallic compounds, it is intrinsically brittle. Therefore, it might be affected through thermal cycling, thus leading to degraded thermal performances of carbide-bonded composites along lifetime. This aspect, especially important when considering applications in an electronic module environment, is investigated in the next section.

#### 4.9.6 Thermal cycling

##### ▪ *Thermal cycle applied:*

When considering the fabrication of materials for heat dissipation purposes in power electronic modules, one should especially be attentive to their resistance to thermal cycling. Upon module operation, the selected materials will be submitted to repeated large-amplitude temperature variations that may source thermal stresses, thus fatigue, and, in the end, catastrophic failures of the package (see chapter 2). Therefore, it is critical to check the reliability and lifetime of the selected materials through thermal cycling prior to any applications in real operating module environment.

The composite materials were thermally cycled using a ClimaTemperatur System (Germany) machine (Fig. 4.64a). The thermal cycle applied was based on standard thermal cycles used in power electronics and aeronautics industries (Fig 4.64b).

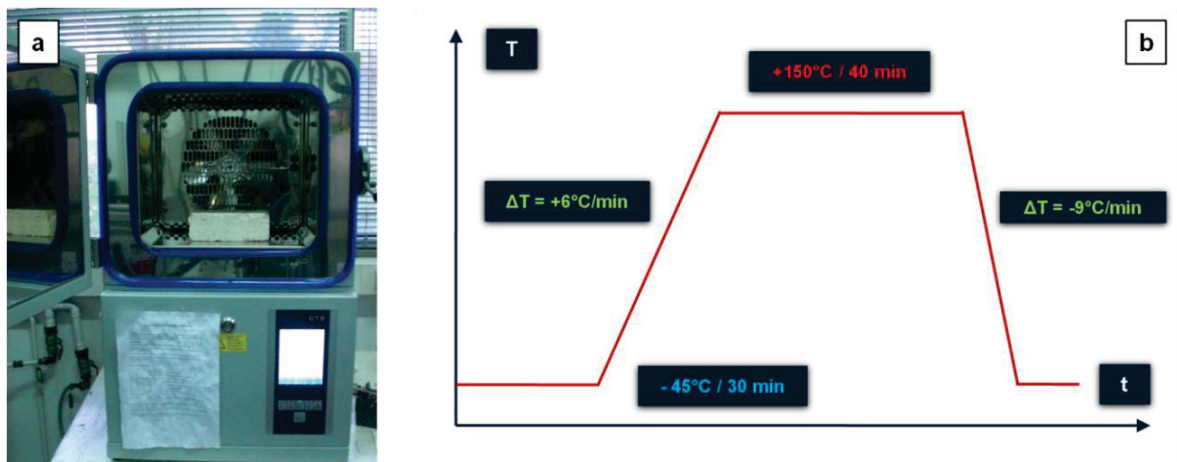


**Figure 4.64: (a) Photograph of the thermal cycling machine and (b) thermal cycle applied.**

The cycle started at  $-45^{\circ}\text{C}$ , the temperature then increased up to  $+150^{\circ}\text{C}$  following a ramp of  $+6^{\circ}\text{C}\cdot\text{min}^{-1}$ . The temperature was held at  $+150^{\circ}\text{C}$  during 40 minutes. The temperature then decreased to  $-45^{\circ}\text{C}$  following a ramp of  $-9^{\circ}\text{C}\cdot\text{min}^{-1}$  and the temperature was held at  $-45^{\circ}\text{C}$  during 30 minutes. A series of 100 cycles followed by a series of 400 additional cycles were applied to the samples. Therefore, the Cu/D composites were submitted to a total number of 500 thermal cycles. The thermal conductivity of the materials was evaluated after 0, 100, and 500 cycles in order to investigate their resistance to thermal cycling.

Although the cycling procedure endeavored will provide useful indication about the lifetime of the fabricated materials, it should be pointed out that these data should be taken with caution since the Cu/D composites are not cycled in the configuration they would have in an actual power module environment (namely soldered to the other layered materials of the package).

▪ ***Thermal conductivity evolution upon thermal cycling:***

Average thermal conductivities obtained from Cu/D composite materials with different interfacial configurations after 0, 100, and 500 thermal cycles are shown on figure 4.65. It demonstrates that Cu/D composites fabricated through the Cu-coating patterned process exhibit higher resistance to thermo-mechanical fatigue than carbide-bonded Cu/D composites.

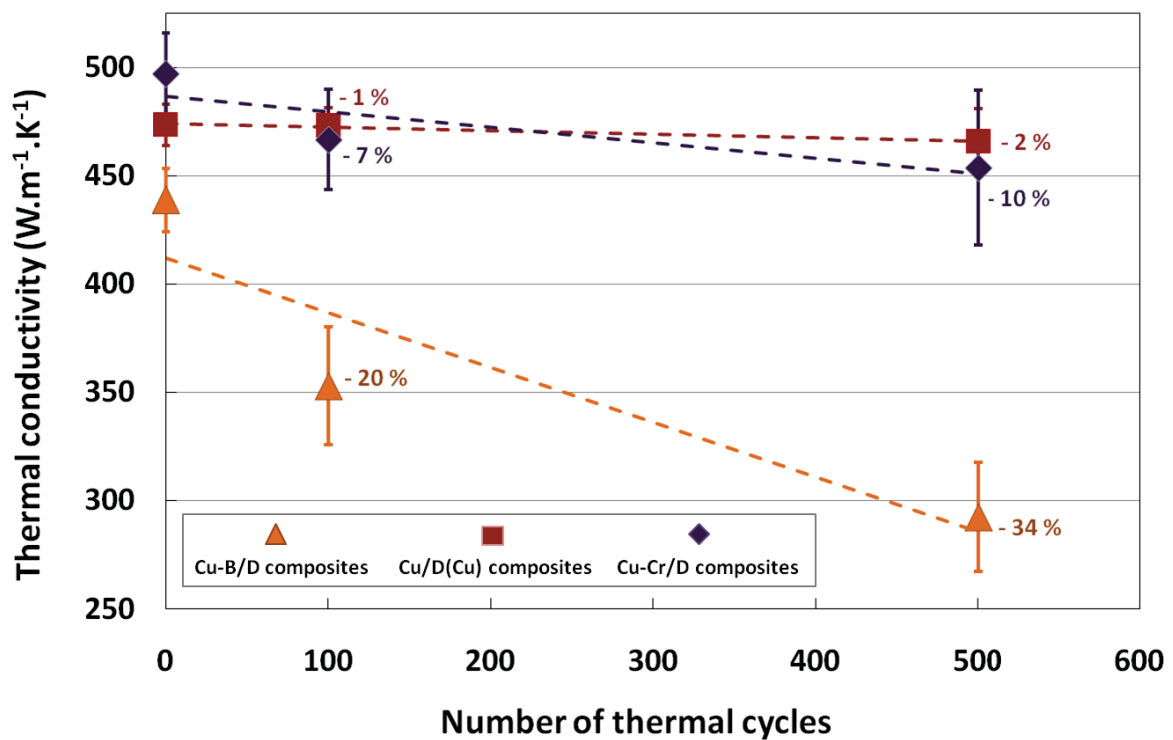


**Figure 4.65: Evolution of the thermal conductivity of Cu/D composite materials upon thermal cycling, depending on the interfacial bonding solution adopted.**

Indeed, Cu-Cr/D composites (500 W.m<sup>-1</sup>.K<sup>-1</sup>) experience drops of 7% (465 W.m<sup>-1</sup>.K<sup>-1</sup>) and 10% (450 W.m<sup>-1</sup>.K<sup>-1</sup>) after 100 and 500 cycles, respectively, while Cu-B/D composites (440 W.m<sup>-1</sup>.K<sup>-1</sup>) experience drops of 20% (350 W.m<sup>-1</sup>.K<sup>-1</sup>) and 34% (290 W.m<sup>-1</sup>.K<sup>-1</sup>) in their thermal conductivity after 100 and 500 cycles, respectively.

On the other hand, Cu/D(Cu) composites (475 W.m<sup>-1</sup>.K<sup>-1</sup>) only experience drops of 1% (470 W.m<sup>-1</sup>.K<sup>-1</sup>) and 2% (465 W.m<sup>-1</sup>.K<sup>-1</sup>) in their thermal conductivity after 100 and 500 thermal cycles, respectively, demonstrating that Cu/D(Cu) composite materials fabricated through the

innovative Cu-coating developed are remarkably stable upon thermal cycling and thermo-mechanical fatigue.

The larger thermal conductivity drops experienced by carbide-bonded Cu/D composites are understood to be due to the brittleness of the carbide interphase bonding the copper matrix to the diamond reinforcements. During thermal cycling, the composite repeatedly expands and retracts. Therefore, the CTE mismatch between the copper matrix, the diamond reinforcements, and the carbide interphase (either B or Cr carbide) lead to thermo-mechanical stresses that affect the mechanical integrity of the brittle carbide interphase. This consequently degrades the heat conduction performances of the cycled composite. Cu/D(Cu) composites, on the other hand, do not suffer from mechanical degradation of the Cu/D interface because no carbide bonding additives were used to process it. The Cu-coating bonding provides high resistance to thermal cycling since the bonding materials (copper oxide, copper) shows higher ductility, thus limiting the thermo-mechanical stresses at the interface due to CTE mismatches.

The high resistance to thermal cycling exhibited by Cu/D(Cu) composites relative to Cu-B/D and Cu-Cr/D composites is a key asset from an industrial point of view because the reliability and lifetime of the fabricated heat spreaders are critical. Relative to pure copper, the Cu/D(Cu) composites combine enhanced thermal conductivity, reduced CTE, reduced weight impact, and high resistance to thermal cycling. These composites are therefore very promising candidates for applications as heat spreading materials in high-power electronics packages.

▪ ***Thermal boundary resistance at the Cu/D interface:***

The Hasselman-Johnson model [189] was employed to estimate the Kapitza resistance, i.e. the thermal resistance at the matrix/reinforcements interfaces into the Cu/D composite materials, and to compare the resistance opposed by the different composites (Cu/D, Cu/D(Cu), Cu-B/D, Cu-Cr/D) to the heat flow. Hasselman and Johnson developed a model which allows the estimation of the Kapitza resistance of a metal/diamond composite material:

$$k_c = k_m \frac{\left[ 2\left(\frac{k_d}{k_m} - 1 - \frac{k_d}{ah}\right)V_d + \left(\frac{k_d}{k_m} + \frac{2k_d}{ah} + 2\right) \right]}{\left[ \left(1 - \frac{k_d}{k_m} + \frac{k_d}{ah}\right)V_d + \left(\frac{k_d}{k_m} + \frac{2k_d}{ah} + 2\right) \right]} \quad (4.21)$$

Where  $k_m$ ,  $k_d$ , and  $k_c$  are the measured thermal conductivities of the metal, diamond, and composite material, respectively ( $\text{W}\cdot\text{m}^{-1}\cdot\text{K}^{-1}$ ).  $V_d$  and  $a$  are the diamond volume content and radius (m).  $h$  is the interface thermal conductance, inverse of the Kapitza resistance ( $h = 1/R_{th}$ ,  $\text{W}\cdot\text{K}^{-1}\cdot\text{m}^{-2}$ ).

Equation 4.21 leads to the following expression for the interface thermal resistance in the composite:

$$R_{th} = a \frac{\left[ \frac{k_c k_d}{k_m} (V_d - 1) + k_d (2V_d + 1) + k_m (2 - V_d) - k_c V_d \right]}{[k_c k_d (V_d + 2) + k_d k_m (V_d - 2)]} \quad (4.22)$$

The Kapitza resistance obviously depends on the quality of the bonding at the copper/diamond interface: a chemically enhanced Cu/D bonding should decrease the Kapitza resistance, thus allowing higher heat conduction performances, while a Cu/D interface affected by the naturally low mutual chemical affinity between copper and carbon will suffer from a high Kapitza resistance and low heat conduction potential. Table 4.15 gathers the parameters employed and the estimation of  $R_{th}$  for each type of Cu/D composite fabricated:

**Table 4.15: Estimated Kapitza resistance at the Cu/D interface for different Cu/D composites.**

Material	$k_m$ (W.m <sup>-1</sup> .K <sup>-1</sup> )	$k_d$ (W.m <sup>-1</sup> .K <sup>-1</sup> )	$k_c$ (W.m <sup>-1</sup> .K <sup>-1</sup> )	$V_d$	$a$ (μm)	$R_{th}$ (× 10 <sup>-7</sup> m <sup>2</sup> .K.W <sup>-1</sup> )
Cu/D	400	1000	260	0.4	50	<b>2.95</b>
Cu-B/D	400	1000	440	0.4	50	<b>2.53</b>
Cu-Cr/D	400	1000	500	0.4	50	<b>2.39</b>
Cu/D(Cu)	400	1000	475	0.4	50	<b>2.44</b>

The brief estimation of  $R_{int}$  carried out first demonstrates that, no matter the interfacial bonding solution adopted, the Kapitza resistance at the interface of Cu/D composites is in the order of  $2 \times 10^{-7}$  m<sup>2</sup>.K/W. It is also noteworthy that the engineering of a chemical bonding solution at the Cu/D interface allows decreasing the Kapitza resistance at the matrix/reinforcement interface. The value of  $R_{int}$  is decreased by both carbide interphases and the diamond Cu-coating process, consistently with their respective thermal conductivity. Nevertheless, the values of thermal boundary resistance at the matrix/reinforcement interface of Cu-B/D, Cu-Cr/D, and Cu/D(Cu) composites remain relatively high. This is ascribed to the fact that foreign materials interphases have been introduced into the composites to create chemical bonding at the interface. Therefore, these foreign elements (chromium carbides Cr<sub>3</sub>C<sub>2</sub> and Cr<sub>7</sub>C<sub>3</sub>, boron carbide B<sub>4</sub>C, copper oxides CuO and Cu<sub>2</sub>O) also contribute to the global thermal resistance evaluated.

It is also interesting to notice that this thermal boundary resistance (TBR) is in the same range of order than the TBR estimated in chapter 3 at the interface between silicon substrates and CVD diamond films through infrared photothermal radiometry ( $R_{dia/Si}^{th} = [1.7 - 3.7] \times 10^{-7}$  m<sup>2</sup>.K.W<sup>-1</sup>).

Finally, it may be pointed out that Cu/D(Cu) composites and carbide-bonded Cu/D composites exhibit Kapitza resistances that are in the same range of order, despite the fact that the carbide interphases can be up to 1 μm thick, while copper oxide interphases observed are up to 20 nm thick. Therefore, the chemical nature of the bonding material has a critical impact on the thermal conductance of the interface. Indeed, it is known that carbides have usually high thermal conductivity, while oxide exhibit higher thermal resistance to the heat flow, as shown in Tab. 4.16.

**Table 4.16: Bulk thermal conductivity of carbides and oxides [197, 198].**

Material	Cr <sub>3</sub> C <sub>2</sub>	B <sub>4</sub> C	CuO
<i>k</i> (W.m <sup>-1</sup> .K <sup>-1</sup> )	19.1	[30-42]	[1-5]

Therefore, the process we developed to chemically bond copper to diamond is affected by the low thermal conductivity of the interphase employed. However, the extreme thinness of this copper oxide interphase allows strong chemical bonding at the interface and lets reach a thermal conductivity that is similar to that of carbide-bonded composites. In addition, the copper oxide interphase was demonstrated to be more resistant to repeated thermal cycles in operating module environment relative to brittle carbide interphases. That point makes a key difference when aiming to make Cu/D composites for heat spreading applications.

## 4.10 Conclusion

Diamond dispersed copper matrix composite films were fabricated through tape casting and hot pressing to be utilized as heat-spreading materials in power electronic packages. This composite route was investigated as an alternative way to use the exceptional thermal properties of diamond for heat dissipation purposes.

Suspensions of the copper and diamond powders were prepared and shaped through tape casting. The tape casting process features numerous advantages such as: accurate thickness control, smooth surface finish, net-shaping capability, scalability, and low capital cost. The composites tapes exhibited satisfactory aspect and could be easily handled. The process showed solid repeatability and could be easily transposed to large-scale production.

An innovative bi-materials bonding solution was developed and patterned in order to chemically bond the copper matrix and the diamond reinforcements and enhance the transfer of properties between the two materials, which is critical to achieve the desired highest thermal conductivity and suitable CTE. The bonding process developed consists first in coating the surface of the diamond reinforcements with copper submicronic particles, which will then act as bonding agents with the copper matrix upon sintering.

Chemical investigations demonstrated that phosphate groups were responsible for the surface functionalization of the diamonds. These phosphate groups originate from the use of a particular dispersant agent during formulation and are detected in a large amount onto the diamonds after formulation and heat treatment of the powders.

Nucleation and growth of the copper particles onto the surface of the diamond reinforcements occurred upon a reducing heat treatment under Ar/H<sub>2</sub>. The sublimation of copper oxide nanowires, formed upon a first debinding heat treatment, played a critical role into the coating process of diamonds by copper particles.

The growth involved a three-dimensional component, therefore allowed the island growth mode, so called Volmer-Webber. The copper particles were shaped similarly to Wulff structures. Microstructural investigations through high-resolution transmission electron microscopy allowed demonstrating that a copper oxide interphase was located at the interface between the diamond substrates and the copper particles. This interphase was between 2 nm and 20 nm thick, depending on the size of the Cu particle observed.

Thermal characterizations demonstrated that this innovative chemical bonding route between copper and diamond allowed reaching interesting performances: the Cu/40 vol.% D composites as-processed exhibit a thermal conductivity up to 480 W.m<sup>-1</sup>.K<sup>-1</sup> associated to a CTE down to



$11 \times 10^{-6} \text{ }^{\circ}\text{C}^{-1}$  and a density of  $6.6 \text{ g.cm}^{-3}$ . These performances are comparable to those achieved through traditional carbide interphases bonding routes involving chromium or boron as carbide forming materials. Therefore, the copper particles coated onto the diamond reinforcements were shown to be performing as chemical bonding agents leading to efficient heat flow across the Cu/D interface and efficient transfer of thermo-mechanical load upon thermal expansion.

In addition, the Cu-coating bonding process was demonstrated to be more resistant to thermal cycling in operating environment relative to carbide bonded Cu/D composites. This was ascribed to the intrinsic brittleness of the carbide interphases.

At last, the efficiency of the copper oxide interphase has to be contemplated with respect to its thickness. Although high thermal performances are achieved through this method, the extreme thinness of the CuO interphase might let us expect higher thermal conductivity. Although the heat flow path is much lower through a 10 nm CuO interphase than through a 1  $\mu\text{m}$  thick carbide interphase, the low thermal conductivity of oxides is believed to affect the electron-phonon coupling efficiency at the interface. Nevertheless, the thermal cycling resistance of the Cu/D(Cu) composites fabricated relative to traditional carbide-bonded composites makes a key difference in the scope of an application as heat-spreading layers in power modules.

# **CHAPTER 5: PROPOSITION OF NEW PACKAGING**

## **CONFIGURATIONS**

---

**5.1 Technological potential of the diamond-based heat spreaders**

**5.2 Finite element simulations in operating module environment**

**5.3 Conclusion**

---

In this chapter, we will investigate the potential applicability of the two types of diamond-based heat-spreading solutions considered in chapter 3 and 4, respectively: CVD diamond films, such as that grown through laser-assisted combustion synthesis, and diamond-reinforced copper matrix composite films, such as that processed through tape casting and hot-pressing. Finite element analysis will be employed to simulate the thermal and thermo-mechanical behavior of the considered materials in different packaging configurations of a power electronic module. Finally, the outlook and prospective of this chapter will conclude this dissertation.

## 5.1 Technological potential of diamond-based heat spreaders

We will review in this section the respective advantages and drawbacks of the two types of diamond-based heat spreading solutions previously considered. As previously mentioned, an ideal heat spreading film would combine a high in-plane thermal conductivity, a coefficient of thermal expansion that is compatible with that of the surrounding materials, and a limited weight impact on the package structure. Electrical insulation potential could be a plus. Its thickness control, net-shaping, and scalability potential should moderate the processing costs, while its solderability (thus limited roughness) should mitigate the cost of integration into the package.

### ▪ *Technological considerations:*

Table 5.1 gathers some aspects to be considered when selecting a material in the scope of a potential application as a heat spreading film.

**Table 5.1: Technological aspects of the potential diamond-based heat spreaders to be considered.**

Diamond based heat spreader:	CVD diamond films	Diamond-reinforced copper-matrix composite films
Property isotropy:	No	Yes
Property tunability:	No	Yes
Thermal conductivity ( $\text{W.m}^{-1}.\text{K}^{-1}$ )	[450-500] vertical [300-400] in-plane	480
Thermal expansion coefficient ( $\times 10^{-6} \text{ }^{\circ}\text{C}^{-1}$ )	[1-2]	11
Density ( $\text{g/cm}^3$ )	3.5	6.6
Thickness control ( $\mu\text{m}$ )	[0-3000]	[125-5000]
Electrical insulator:	Yes	No
Scalability:	Yes	Yes
Net-shaping capability:	Yes	Yes
Machinability:	No	No
Solderability:	No	Yes

▪ ***CVD diamond films applicability:***

CVD diamond films such as those processed through laser-assisted combustion synthesis show promising vertical thermal conductivity but their properties are non-isotropic due to columnar microstructure. Therefore, the in-plane thermal conductivity of the films, although not measured in this study because of experimental limitations, is expected to be lower. Also, the very low CTE of CVD diamond films may be a drawback in the vicinity of the base plate (which typically has a large CTE) due to excessive thermo-mechanical stresses but may also be an advantage close to the semiconductor active device (typically silicon) which shows small CTE mismatch with diamond. Moreover, CVD diamond films provide the advantage to be electrically insulating. This property can be employed to its best advantage by considering the replacement of the alumina enclosed in the DBC substrate by a free-standing CVD diamond substrate. By coating top and back surfaces of a CVD diamond substrate with Cu dots (see chapter 4), the bonding of copper films onto the substrate could be made possible. This would thus provide an interesting combination of heat conduction and electrical protection.

Furthermore, the low heat capacity of diamond ( $6.2 \text{ J.mol}^{-1}.\text{K}^{-1}$ ) makes the use of CVD diamond as a heat spreader instead of as a heat dissipation material strongly preferable. In addition, CVD deposition techniques allow reaching thicknesses in the  $[0 - 3000] \text{ }\mu\text{m}$  range, however with extensive deposition times, thus making the cost-per-volume of CVD diamond sensibly higher than that of Cu/D composite films. Therefore, in order to use CVD diamond to its best advantage and minimum cost, the optimal film thickness combining maximum heat spreading potential, minimum thermo-mechanical stresses, and minimum cost has to be found.

However, in this chapter, the technological potential of CVD diamond films is extrapolated assuming that limitations such as roughness and low scalability can be addressed. Laser-polishing techniques should be used to flatten the diamond films surface. Thus, the Cu-particles coating process presented in chapter 4 could be employed to coat the CVD diamond surface with Cu-dots, thus allowing to chemically bond a thin copper film to its top surface in the same manner as a DBC substrate. This would allow us to overcome the non-solderability issue presented by CVD diamond substrates and soldering the active chip to the CVD substrate through a copper interlayer. Also, the CVD diamond films are assumed to be scalable on the electronic-substrate scale by using, in case of combustion CVD for instance, flat flame burners or multiple flame configurations.

In addition, it is also possible to combine a CVD diamond film and a composite substrate, as shown in section 3.6, to create a composite heat-conductive architecture composed of a heat-spreading CVD diamond film on top of a heat-dissipative substrate. By depositing CVD diamond onto the surface of a composite base plate, thermal conduction and electrical insulation would be

combined in a way that allows getting rid of several interfaces, which represent as many additional thermal resistances.

The simulations carried out in the following section assume that free-standing, stress-free, electrically insulating and large scale CVD diamond substrates can be fabricated and may be included into the package architecture.

▪ ***HPHT diamond reinforced composite films applicability:***

On the other hand, Cu/D composite films made of Cu-coated HPHT diamond powders reinforcing a copper matrix provide interesting features such as high thermal conductivity (up to  $500 \text{ W.m}^{-1}.\text{K}^{-1}$ ), moderate CTE (down to  $11 \times 10^{-6} \text{ }^{\circ}\text{C}^{-1}$ ), and strong resistance to thermal cycling (only -2% thermal conductivity drop after 500 cycles).

The tape casting process was shown to make feasible the fabrication of Cu/D composite films with uniform properties, smooth surface finish, net-shaping capability, accurate thickness control, and easy handling, at a low cost and a large scale. All these advantages make Cu/D composite films superior to combustion CVD diamond films in terms of both scalability and cost-effectiveness, thus strongly advantageous from an industrial point of view. In addition, hot pressing was also shown to exhibit fastness, low costs, and moderate machinery requirements relative to other typical Cu/D composite fabrication routes such as spark plasma sintering (SPS) or pressure-assisted liquid infiltration.

While the tape casting process allows Cu/D composite films with thickness as low as  $120 \text{ }\mu\text{m}$  to be produced, a simple powder metallurgy route may also be exercised to fabricate Cu/D composite substrates with thickness up to  $[3 - 5] \text{ mm}$ . Consequently, although being primarily oriented to heat-spreading applications, the Cu/D composite solution may, to a certain extent, also show potential for heat sinking applications by substituting to the thick copper base plate traditionally used in power packages. This can also be supported by the fact that the low heat capacity of pure diamond has limited impact when using diamond as a reinforcement material in a metallic matrix with heat capacity.

However, this option may be strongly detrimental from an economic point of view. Indeed, the production costs of Cu/D composites through the presented route combining tape casting and hot pressing are low relatively to other processes such as liquid-infiltration. Therefore, the cost of the material is strongly dependent on the volume of diamond powders required to fabricate it (in this study, about  $1 \text{ }\text{€}.\text{g}^{-1}$ ). Consequently, the processing cost of a  $3 \text{ mm}$ -thick Cu/D substrate would be about six times higher than that of a  $500 \text{ }\mu\text{m}$ -thick Cu/D film. In addition, the simulations further presented in this chapter demonstrate that the thermal and thermo-mechanical advantages of using a Cu/D composite base plate are limited relative to the use of a thinner Cu/D film on top of a

traditional base plate. In addition, base plate materials with lower CTE but acceptable cost such as carbon fiber-reinforced copper matrix (Cu/C) composite can also be used as base plate.

▪ **Packaging configurations considered:**

One can imagine various packaging configurations including diamond-based materials as heat spreaders for the thermal management of power electronic modules. Some of them are depicted in Fig. 5.1. Configuration 1 is the basic architecture and serves as a reference to evaluate the potential improvements brought by the use of diamond-based heat spreading materials. Configuration 2 will include a Cu/D base plate and will allow us to compare the packaging potential of such a solution with respect to its cost. Configurations 3 and 4 respectively employ a Cu/D composite film and a CVD diamond film as a heat spreader on top of a copper base plate. Configuration 5 relies on substituting the alumina plate of the DBC substrate by a free-standing CVD diamond substrate to combine electrical insulation and thermal conduction. Similarly, configuration 6 combines this diamond-type DBC substrate to a Cu/D composite heat spreader with a copper base plate. Finally, configuration 7 and 8 get rid of the lower solder joint and copper film to directly deposit a CVD diamond substrate onto a pure copper or Cu/D coated base plate, respectively. As explained in chapter 1, no diamond-based base plate was considered due to the relatively low heat capacity of diamond and to the excessive capital costs of such an element. CVD diamond or Cu/D composite films included in the packaging configurations are 500  $\mu\text{m}$ -thick by default.

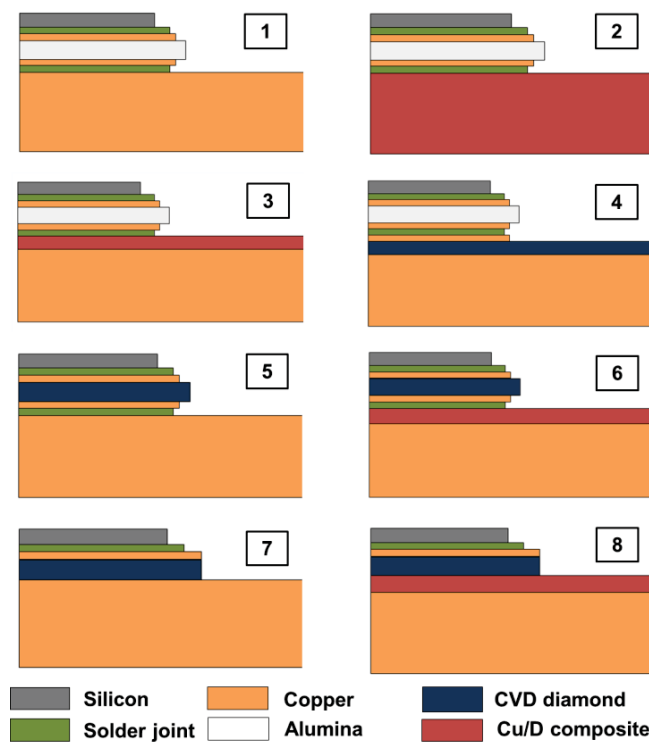


**Figure 5.1: Potential packaging architecture involving either Cu/D composite films, CVD diamond films, or a combination of both.**



In the next section, we will use the finite elements method to simulate the temperature and the thermo-mechanical stresses existing in the various package architecture described in Fig. 5.1. The potential of diamond-based materials to reduce the junction temperature and mitigate stresses in the structure, thus strengthening its reliability and prolonging its lifetime, will be discussed.

## 5.2 Finite element simulations in operating module environment

The © Comsol Multiphysics (version 3.5a) software was used in this study to simulate the thermal and thermo-mechanical performances of the diamond-based heat spreaders considered in this study into the packaging environment of a power electronic module. Especially, the distribution of temperature and shear stress into the package were investigated. The software relies on the finite elements method (FEM) to run the simulations. This technique consists in approaching the solution of a problem by discretizing it into a finite number of elements through a *mesh*. The finer the mesh, the more accurate the simulation (and the longer the calculation time). Figure 5.2 illustrates the different steps of a FEM simulation through © Comsol Multiphysics.

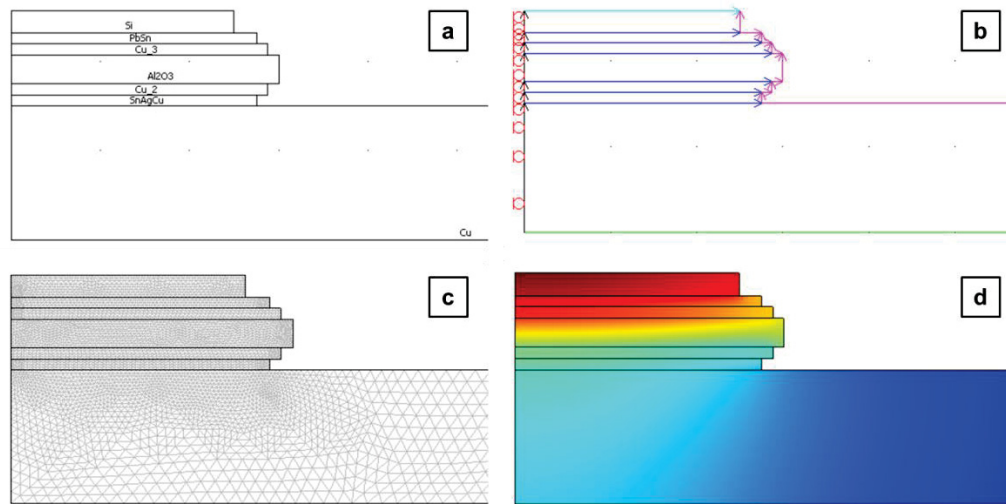


**Figure 5.2: Illustration of the different steps of an FEM simulation © through Comsol Multiphysics. (a) Definition of the mesh. (b) Definition of the boundary conditions. (c) Definition of the mesh. (d) Post-treatment [11, 32, 222].**

The definition of the geometry consists in modeling the shape of the different elements constituting the system, in the present case, the package of the electronic power module. In this study, the simulation was carried out in two dimensions (2D), but it is also possible in one dimension (1D), and three dimensions (3D). Similar to the mesh effect, the higher the number of dimensions taken into accounts, the longer the calculation. Any symmetry in the system represents a potential time saver by simulating only a part of the system with a similar mesh but more rapidly, or with a finer mesh through an equivalent calculation time. In this study, an axial symmetry is assumed in the package structure, thus only needing to simulate half of it.

The definition of the boundary conditions consists in implementing the initial parameters into the system, such as the properties of the volumes, interfaces, sides, and submits of the whole geometry. In our case, the volume conditions are the thermo-physical properties of the materials constituting the package such as thermal conductivity and thermal expansion coefficient.

The definition of the mesh consists in subdividing the geometry into an ensemble of elementary units. This division enables transposing the initial continuous problem to a discrete problem made of a finite number of elements. The different elements of the mesh do not necessarily have all the same size. Larger elements are used where the simulated functions show little variations while finer elements will be employed at locations of expected large variations.

The simulation of the problem consists in calculating a solution for each element of the mesh. Thus, the finer the mesh, the larger the number of elements, and the longer the calculation on the whole geometry. In addition, the calculated solution is not an exact one but an approached solution, more or less accurate depending on the calculation criteria fixed. Using Comsol, one can carry out stationary simulations or temporal simulations (thus adding a temporal dimension to the problem). Temporal simulations are especially interesting when focusing on the kinetics of the heat transfer phenomena. In this study, we will limit ourselves to stationary simulations, thus only focusing on the final state of the system with respect to initial parameters. Therefore, we mainly rely on Fourier's law to simulate the evolution of the system and the main parameters considered are the thermal conductivities instead of the heat capacities.

The post-treatment consists in representing data obtained from the solution calculated. By associating a color to each element of the mesh, it is possible to map the values taken by a variable on the whole studied geometry.

▪ ***Definition of the geometry:***

Figure 5.3 describes how the package architecture was modeled prior to running FEM simulations. The structure was modeled as 2D-axisymmetric, thus not necessary to model half of. The different materials involved in the layered package structure were investigated with more detail in chapter 2.

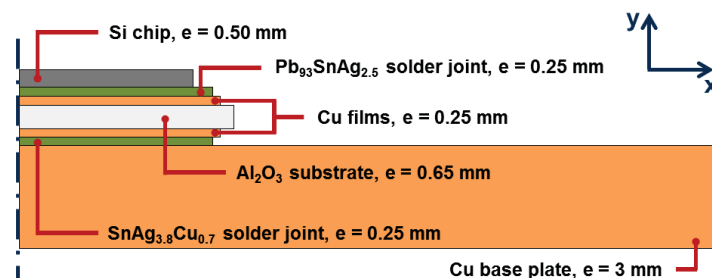


**Figure 5.3: Illustration of the modeling of the initial packaging architecture.**

This architecture is of course a basis for packaging modifications according to the architectures considered in Fig. 5.1, either by changing the nature of some materials, or by removing or adding additional layers to the package. When CVD diamond or Cu/D composite films were part of the configuration, their thickness was set to 500  $\mu\text{m}$ . Table 5.2 gathers the material properties taken into account to run the FEM simulations of temperature and shear stress distributions.  $k$ ,  $\alpha$ ,  $C_p$ ,  $\rho$ ,  $E$ , and  $\nu$ , respectively stand for the thermal conductivity, the thermal expansion coefficient, the specific heat, the density, the Young's modulus, and the Poisson's ratio. These properties were embedded into the materials library of the simulation software.

A wide variety of phenomena may be simulated through Comsol Multiphysics. We will focus on this study on the conduction heat transfer phenomenon and on the thermo-mechanical stresses this heat transfer induces into the package structure. More specifically, given a constant heat source, we will concentrate on the temperature and shear stress distributions. Indeed, as detailed in chapter 2, the over-heating of active components and the existence of excessive shear stresses between layers of dissimilar materials are key issues to the reliability of power modules. The objective here is to understand how the packaging configuration, and especially the inclusion of diamond-based materials such as CVD diamond films or Cu/D composites in this configuration, may influence the resulting maximum temperature of the active chip and the shear stress distribution in the package.

**Table 5.2: Materials properties taken into account for the FEM simulations.**

Material	$k$ (W.m <sup>-1</sup> .K <sup>-1</sup> )	$\alpha$ ( $\times 10^{-6}$ °C <sup>-1</sup> )	$\rho$ (g/cm <sup>3</sup> )	$E$ (GPa)	$\nu$
Silicon (Si)	163	4.1	2.3	112	0.27
Pb <sub>93</sub> SnAg <sub>2.5</sub>	35	29	11.3	25	0.44
Copper (Cu)	400	17	8.9	110	0.35
Alumina (Al <sub>2</sub> O <sub>3</sub> )	35	6.6	3.9	370	0.25
SnAg <sub>3.8</sub> Cu <sub>0.7</sub>	70	22	8.0	50	0.4
CVD diamond	500 (vertical) / 350 (in-plane)	2	3.5	1050	0.07
Cu/ 40 vol.% D	500	11	6.7	110	0.35
Cu/ 40 vol.% CF	250 (in-plane) 160 (vertical)	10 (in-plane) 17 (vertical)	6.25	110	0.35

▪ **Definition of the mesh:**

The mechanical stress phenomena that are to be enlightened in these simulations are highly localized. Thus, it is crucial to use a mesh that is fine enough to lead to simulations consistent enough to approach the real-operating environment situation. In this study, three steps of mesh refinement were used before running the simulations. The elements used to mesh the geometry were triangularly-shaped. An image of the mesh is shown in Fig. 5.2c.

- ***Definition of the boundary conditions:***

- *Thermal boundary conditions:*

The ambient temperature was chosen equal to 25 °C ( $T_{amb} = 298.15$  K). The electronic chip was described as a heat source whose heat flux density was tuned so that the maximum temperature of the chip was equal to 100°C in configuration 1 (Fig. 5.1). For information, the corresponding chip heat flux density was close to 100 W/cm<sup>2</sup>. The external environment of the module was assumed to be air ( $T_{air} = T_{amb}$ ), with a free-convection heat transfer coefficient of 15 W/m<sup>2</sup>.K. An exception was made at the lower surface of the base plate, where the external medium was assumed to be a liquid-cooling environment with a forced-convection heat transfer coefficient of 10,000 W/m<sup>2</sup>.K. Thus, these boundary conditions made the heat generated in the package to be preferentially evacuated from the top to the bottom of the structure. Thermal interfaces between dissimilar materials were assumed to be perfect.

- *Mechanical boundary conditions:*

The dimensions of each element of the architecture were defined for an ambient temperature of 25°C. Mechanical interfaces between dissimilar materials were assumed to be perfect. The segments of the structure on the symmetry axis do not have any degree of freedom outside the considered axis. The lower point of the module on the symmetry axis (thus on the back face of the base plate) is the origin of the geometry and does not have any degree of freedom (reference point).

- ***Calculation:***

The calculation procedure is composed of two steps: in a first step, the temperature distribution is calculated; then, based on the temperature distribution, the thermo-mechanical stress distribution is simulated.



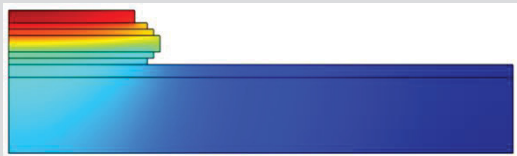





It has to be noticed that these simulations were ran in the case of ideal elasticity. Thus, plastic deformations are not taken into account in our model. In addition, thermally-activated phenomena such as diffusion or materials aging that could potentially modify the thermo-mechanical properties of the materials in time are also ignored. Therefore, the temperature and shear stress values calculated are not to be taken as exact in the physical sense. In this study, they are only useful to provide a comparison means between the different packaging configurations.

- ***Simulation of the temperature and shear stress distributions:***

Tables 5.3 and 5.4 gathers the temperature and shear stress distribution profiles obtained from FEM analysis of the different packaging architectures shown in Fig. 5.1. For all the temperature profiles displayed, the color scale is constant: [100 – 40] °C ([bright red - deep blue], respectively).

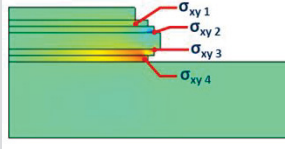
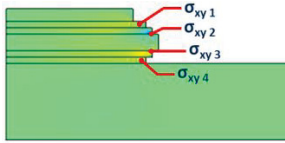
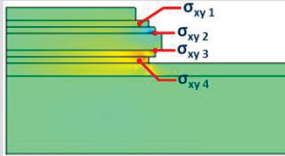
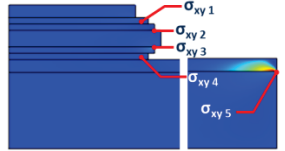
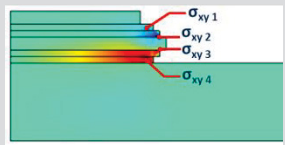
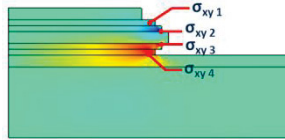
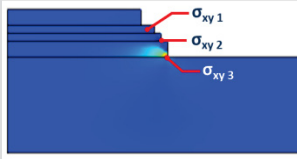
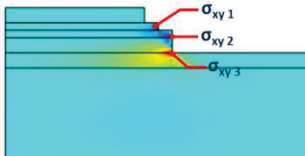
We focus in Tab. 5.3 on the maximum temperature reached by the active silicon chip.

Table 5.3: FEM simulations of the temperature distribution in different packaging configurations.

Packaging configuration:	Temperature distribution profile:	Maximum chip temperature:
1		100.7 °C
2		98.2 °C
3		99.4 °C
4		99.7 °C
5		80.5 °C
6		79.1 °C
7		76.8 °C
8		72.1 °C

We focus in Tab. 5.4 on the shear stresses developing between the layers of the package.

**Table 5.4: FEM simulations of the shear stress distribution in different packaging configurations.**

Packaging configuration:	Shear stress Distribution profile:	Shear stress values:
1		$\sigma_{XY1} = +8.5 \text{ MPa}$ ; $\sigma_{XY2} = -20.5 \text{ MPa}$ $\sigma_{XY3} = +24.6 \text{ MPa}$ ; $\sigma_{XY4} = +14.6 \text{ MPa}$
2		$\sigma_{XY1} = +10 \text{ MPa}$ ; $\sigma_{XY2} = -19.6 \text{ MPa}$ $\sigma_{XY3} = +21.6 \text{ MPa}$ ; $\sigma_{XY4} = +5.3 \text{ MPa}$
3		$\sigma_{XY1} = +9.1 \text{ MPa}$ ; $\sigma_{XY2} = -21 \text{ MPa}$ $\sigma_{XY3} = +24.2 \text{ MPa}$ ; $\sigma_{XY4} = +15.9 \text{ MPa}$
4		$\sigma_{XY1} = +8.1 \text{ MPa}$ ; $\sigma_{XY2} = -20.5 \text{ MPa}$ $\sigma_{XY3} = +21.3 \text{ MPa}$ ; $\sigma_{XY4} = -12.2 \text{ MPa}$ $\sigma_{XY5} = +95.6 \text{ MPa}$
5		$\sigma_{XY1} = +8.5 \text{ MPa}$ ; $\sigma_{XY2} = -25.7 \text{ MPa}$ $\sigma_{XY3} = +34.26 \text{ MPa}$ ; $\sigma_{XY4} = -8.5 \text{ MPa}$
6		$\sigma_{XY1} = -8.4 \text{ MPa}$ ; $\sigma_{XY2} = -25.4 \text{ MPa}$ $\sigma_{XY3} = +32.5 \text{ MPa}$ ; $\sigma_{XY4} = +14.6 \text{ MPa}$
7		$\sigma_{XY1} = -6.7 \text{ MPa}$ ; $\sigma_{XY2} = -43.9 \text{ MPa}$ $\sigma_{XY3} = +154 \text{ MPa}$
8		$\sigma_{XY1} = -12.7 \text{ MPa}$ ; $\sigma_{XY2} = -25.6 \text{ MPa}$ $\sigma_{XY3} = +41.9 \text{ MPa}$



▪ ***Discussion about the simulation results:***

Different conclusions can be drawn from the temperature distribution simulations. First it clearly appears that the use of a Cu/D 3 mm-thick composite heat-sinking base plate (configuration 2) does not provide any competitive advantage relative to the use of a 500  $\mu\text{m}$ -thick Cu/D composite heat-spreading film associated to a copper base plate (configuration 3) from the thermal point of view. Indeed, the maximum operating temperatures reached by the active silicon chip are sensibly the same in both configurations. However, it should be noticed from a thermo-mechanical perspective that the use of a Cu/D base plate allows a consistent reduction of the shear stress that develops in the solder joint between the DBC substrate and the base plate ( $\sigma_{XY4}$ ).

Furthermore, FEM simulations show that the use of a diamond-based heat-spreading film, either made of diamond-reinforced composite (configuration 3) or CVD diamond (configuration 4) and located on top of a copper base plate makes almost no difference on the maximum active chip temperature when the alumina substrate remains in the packaging structure. Indeed, a decrease of no more than 1°C is expected from these packaging configurations. In addition, the inclusion of a Cu/D heat-spreading film on top of base plate does not decrease the induced shear stresses in solder joints (configuration 4), while the use of a CVD diamond heat-spreading film at the same location induces unsustainable level of shear stress at the heat-spreader/base plate location (configuration 3).

However, the temperature distributions simulations also demonstrate the critical impact of low thermal conductivity-alumina on the heat conduction process and the strong potential of CVD diamond to replace it as an electrically insulating and thermally conductive material. The substitution of alumina by CVD diamond in the package architecture would lead, upon constant heat flux, to a decrease in the maximum chip temperature of more than 20°C, with maximum chip temperatures of 80.5°C and 79.1°C in configurations 5 and 6, respectively. The heat-spreading interest of a Cu/D composite film on top of the copper base plate is shown in configuration 6, where it allows the heat flux spreading surface to be enlarged (see Fig. 5.5). Aside from a critical advantage in terms of maximum temperature of the active chip, the substitution of alumina by CVD diamond also triggers an increase of the shears stresses developed in the layers due to the low CTE of CVD diamond ( $2 \times 10^{-6} \text{ }^\circ\text{C}^{-1}$ ). Nevertheless, the stress levels developed are of the same order of that which develop in configuration 1, and may be mitigated by judicious adjustment of the layer thicknesses or of the base plate material.

Finally, it can be interesting to directly bond CVD diamond to the base plate surface. Configurations 7 and 8 were designed following this idea. This type of architecture would allow reducing the number of interfaces in the package structure, thus decreasing its global thermal resistance and enhancing the heat conduction process. Temperature distribution simulations show indeed that these two configurations lead to the highest decrease in the hot-spots of the active chip,

with temperatures of 76.8°C 72.1°C, respectively. However, the direct bonding of CVD diamond onto the base plate leads to the creation of extensive shear stresses at the interface between the CVD diamond film and the base plate. The level of shear stress would be unsustainable in configuration 7 ( $\sigma_{XY4} = 154$  MPa). Thus, a Cu/D composite film with lower CTE and higher thermal conductivity is used in configuration 8 to mitigate the shear stress ( $\sigma_{XY4} = 41.9$  MPa).

▪ ***Proposition of novel packaging configurations:***

After simulating the temperature and shear stresses distributions induced by the different packaging configurations, and taking into account the aspects of technological feasibility and capital costs, configuration 6 and 8 are designated as the most promising potential packaging architecture involving CVD diamond and Cu/D composite films. However, solutions must be found to decrease the shear stress levels while maintaining minimum hot-spots on active components.

Configuration 6 is composed of the same elements as configuration 1, except that the 650  $\mu\text{m}$ -thick alumina substrate has been replaced by a 500  $\mu\text{m}$ -thick free-standing commercial CVD diamond substrate. The smooth CVD diamond surface has been coated with Cu particles on both sides through the process developed in this study (see chapter 4) in order to allow bonding copper thin films on both sides of the substrate in the same fashion as DBC substrates. This can be achieved through a simple diffusion bonding process upon moderate pressure and temperature. A 500  $\mu\text{m}$ -thick Cu/D composite film prepared by tape casting and hot pressing is combined to a copper base plate in order to enhance heat spreading. The Cu/Cu/D bonding can also be achieved through a simple hot pressing route. Finally, two types of solder are involved in the structure: PbSn eutectic at the Si/Cu interface and SnAgCu at the Cu/Cu/D interface.

Configuration 8 is similar to configuration 6, except that the copper thin film coating the back face of the CVD diamond substrate and the lower solder joints have been eliminated. Thus, it is possible to use a more advantageous soldering alloy between the Si chip and the top surface of CVD diamond, such as SnAgCu, which shows a lower CTE ( $\alpha = 22 \times 10^{-6} \text{ }^\circ\text{C}^{-1}$ ) and a higher thermal conductivity ( $k = 70 \text{ W.m}^{-1}.\text{K}^{-1}$ ) relative to PbSn ( $\alpha = 29 \times 10^{-6} \text{ }^\circ\text{C}^{-1}$ ,  $k = 35 \text{ W.m}^{-1}.\text{K}^{-1}$ ).

However, it should be notable in configuration 8 that the direct deposition of CVD diamond onto a copper-based substrate, whom section 3.6 provides an example, has been shown to be hardly possible without the incorporation of an intermediate thermo-mechanical buffer layer (such as chromium in this study). If the thermal conductivity of this interlayer is high enough, the additional thermal resistance induced will only have a limited impact on the heat conduction process. However, through combustion synthesis, this chromium layer was shown to be strongly oxidized into the flame environment, and is thus expected to show poor thermal conductivity. Therefore, the direct deposition of combustion CVD diamond on the base plate top surface is hardly feasible from an

industrial point of view. Thus, configuration 8 should be achieved through the direct bonding of a free-standing CVD diamond substrate to the base plate or through the growth of CVD diamond onto the base plate through vacuum-based deposition route, such as microwave plasma- assisted CVD or hot-filament CVD. In the latter case, masking methods (such as those used in photolithography) can be used to net-shape the CVD diamond coating. However, due to limited growth rate, the use of a commercial free-standing CVD diamond substrate would be preferred for fastness purposes.

In order to subsequently reduce shear stresses, configuration 6 can be improved by coating a 250  $\mu\text{m}$ -thick Cu/D composite film on the back side of the CVD substrate instead of pure copper in order to reduce CTE mismatch with base plate. However, the film on top surface must remain copper since serigraphy process must be used on it to design the chip electrical pathways. Similarly, in both configurations 6 and 8, copper can be replaced by carbon fiber-reinforced copper matrix (Cu/C) composite as base plate, which shows lower CTE ( $10 \times 10^{-6} \text{ }^\circ\text{C}^{-1}$ ), high thermal conductivity ( $250 \text{ W.m}^{-1}.\text{K}^{-1}$ ), and moderate cost. This type of base plate can be processed through a simple powder metallurgy route (hot pressing). Thus, the final two proposed configurations and their respective temperature and shear stress distribution profiles are the following:

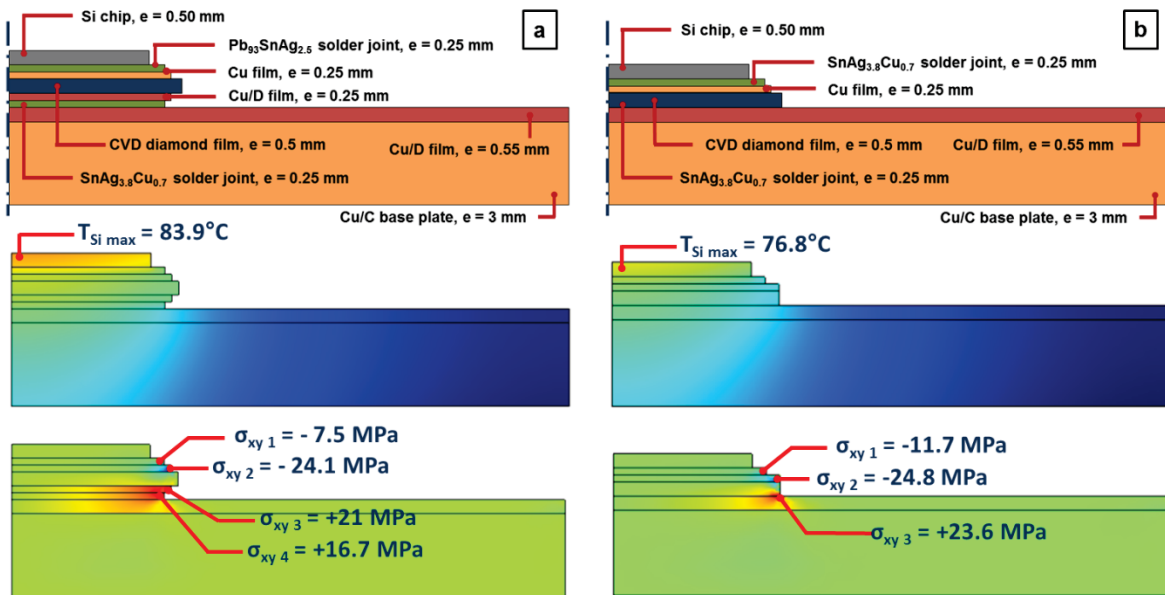


**Figure 5.4: Propositions of new packaging configurations including CVD diamond and Cu/D composite films combined to Cu/C base plate, and their respective temperature and shear stress distributions.**

It can be seen that both configurations combine sensitively lower maximum active chip temperature and same levels of shear stress as packaging configuration 1. Similarly to the DBC substrate in configuration 1, the highest levels of shear stress are located in the close vicinity of the CVD diamond substrate. While these shear stress levels are almost the same for both configurations 6 and 8 (typically 20 MPa, either compressive or tensile), configuration 8 provides lower chip

temperature (76.8 °C against 83.9 °C in configuration 6). However, it should be noticed that configuration 6 may be more accessible from a feasibility aspect due to the simplicity brought by the use of a solder joint at the interface between the base plate and the insulating substrate.

Figure 5.5 shows simulations of the heat flux streamlines (left) and isotherms (right) into the packaging configurations 1, 6, and 8, respectively.

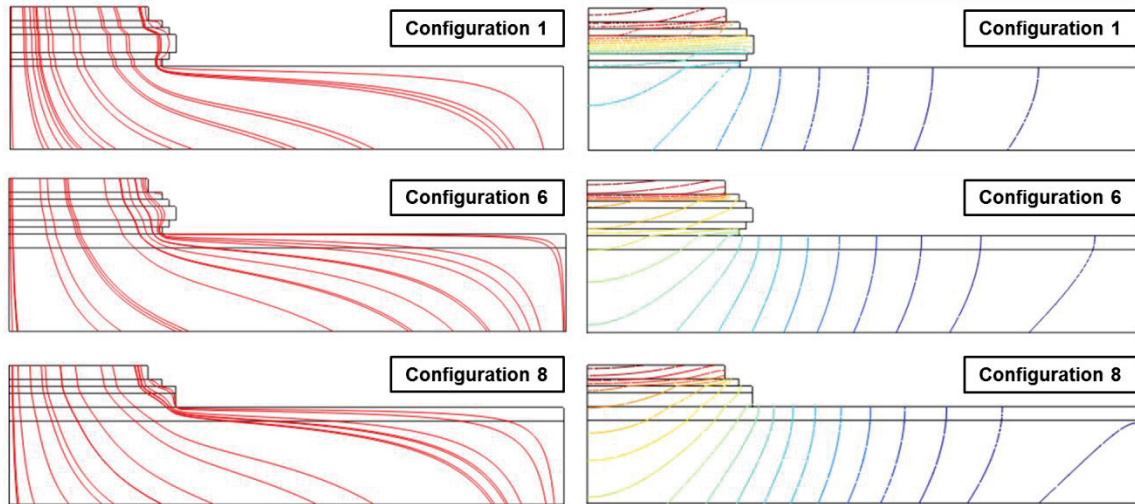


**Figure 5.5: Heat flux streamlines (left) and isotherms (right) in the new packaging configurations proposed.**

In agreement with Fourier's law, the isotherms are normal to the heat flux streamlines. We can observe from the streamline plots that the decrease in maximum chip temperature comes with an enlargement of the heat spreading surface which allows a higher volume of the heat sink to be used, thus mitigating the chip maximum temperature in a more efficient manner. Thus, the addition of CVD diamond and Cu/D composite into the package architecture is effective in enhancing heat spreading.

Although these novel packaging configurations show promising combination of limited maximum chip temperature and shear stress, it has to be highlighted that their cost may be substantially higher, especially when involving free-standing commercial CVD diamond substrates (about 38 USD.mm<sup>-3</sup> for commercial CVD diamond, relative to about 0.01 USD.mm<sup>-3</sup> for commercial alumina), thus potentially limiting CVD diamond to high added-value niche applications. Also, the low toughness (tenacity) of this type of diamond substrates was not taken into account in these simulations and may be problematic from a mechanical point of view, especially during the steps of coating the copper-based film on the sides of the CVD diamond substrate. However, it should also be reminded that commercial CVD diamond substrates would also show net-shape, high-quality surface finish, high phase purity, and thus consistently higher thermal conductivity than that considered in this study.

### 5.3 Conclusion

Although the FEM simulations carried out only take into account a limited number of parameters and anticipate ideal case scenarios, they provide a rough comparison of the temperature and shear stress distributions in electronic power packages with respect to the use, or not, of diamond-based materials such as CVD diamond and Cu/D composite films and substrates. These simulations tend to show that the precious combination of properties brought by diamond may be useful to the thermal management of power packages, especially to decrease the maximum temperature reached by active semiconductive components. However, the strong heat conduction potential brought by diamond-based materials frequently comes with an increase of thermo-mechanical stresses due to the low CTE of diamond itself.

Nevertheless, satisfying compromise combining consistently decreased maximum chip temperature and limited shear stresses may be found through the association of diamond-based heat-spreaders with heat-sinking materials showing more suitable CTE relative to pure copper, such as carbon fiber-reinforced copper matrix composite. In such attempt, two novel packaging configurations involving both CVD diamond and Cu/D composite films were proposed. While CVD diamond shows extremely promising potential to replace former alumina to create diamond DBC due to its electrical insulation and thermal conduction properties, Cu/D composite could be useful as heat-spreading films either located on top of base plate or back of diamond DBC thanks to their suitable CTE and high thermal conductivity. For both types of diamond-based materials, the copper coating process developed in this study can help facilitating chemical bonding between diamond and the other copper-based materials of the package structure.

Despite its promising potential, CVD diamond still suffers from a high cost due to limited large-scale availability. Nevertheless, the use of CVD diamond in power electronic packaging, especially to replace former alumina as a dielectric substrate, may be considered as a worthy investment in high-power and high-temperature applications regarding to the reliability and enhanced lifetime it could provide to the module architecture. On the other hand, the price of HPHT diamond powders is shown to becoming more and more competitive relative to other dispersed reinforcement materials such as carbon fibers, particularly due to the strong impulse brought to the market by Chinese hard-materials processing companies. Therefore, HPHT diamond-reinforced materials are also expected to tend toward high affordability.

In a context of constantly more challenging thermal issues in power electronic packages, diamond-based materials such as those considered in this study may be promising solutions to invest in for packaging materials with higher performances and reliability, thus following the trend of a more sustainable packaging technology.

## **CHAPTER 6: SUMMARY & OUTLOOK**

---

### **6.1 Summary**

### **6.2 Future directions**

---



## 6.1 Summary

In this study, diamond was considered as a potential promising candidate material to enhancing cooling procedure of power electronic packages. The objective was to fabricate diamond-based heat-spreading films with high in-plane thermal conductivity, suitable CTE with respect to the surrounding package environment, limited weight impact on the module structure, and acceptable cost in the scope of potential industrial applications.

A dual diamond-based heat-spreading solution was considered in the framework of a dual French-American PhD program between the College of Engineering of the University of Nebraska-Lincoln, in the U.S., and the Institute of Condensed Matter Chemistry of the University of Bordeaux, in France.

In the U.S., a laser-assisted combustion diamond synthesis set-up was developed in order to grow polycrystalline diamond films onto various substrate materials. A multienergy deposition process was achieved by coupling the chemical energy of a combustion flame to the energy of a laser beam. Laser resonant excitation of carbon precursor molecules allowed the growth of diamond film with enhanced phase purity, growth rate, and chemical selectivity. The deposition technique showed high flexibility, with limited capital costs and potential scalability. Despite the limited diamond phase purity that the open-air deposition environment suggested, the diamond films were shown to exhibit promising vertical thermal conductivity located in the  $[450 - 500] \text{ W.m}^{-1}.\text{K}^{-1}$ , thus suggesting a lower in-plane thermal conductivity due to columnar grain microstructure. The film/substrate interface was shown to present strong resistance to the heat flux, and its thermal resistance was quantified. The residual stresses existing into the films deposited onto different substrate materials were also investigated through Raman spectroscopy.

In France, a tape casting route was developed to fabricate thin laminates of HPHT diamond-reinforced copper matrix (Cu/D) composite films. The tape casting process demonstrated numerous advantages, among them: scalability, smooth surface finish, accurate thickness control, net shaping capability, low cost, and easy handling. The tape casting process was coupled to a simple powder metallurgy route to fabricate dense pieces of Cu/D heat-spreaders. A copper-particle deposition process was developed in order to Cu-coat the diamond reinforcements, thus allowing strong chemical bonding at the interface between the copper matrix and the diamond reinforcements upon sintering. The Cu-coating process provides an innovative alternative to traditional carbide-bonding processes at the Cu/D interface. A copper oxide interphase was demonstrated to be responsible for the Cu/D chemical bonding, although clear conclusion about its chemical composition could not be drawn. The interphase was shown to allow efficient coupling between electronic and phonic heat conduction processes at the metal/diamond interface (maximum thermal conductivity of

500 W.m<sup>-1</sup>.K<sup>-1</sup> at 40% diamond volume fraction) and efficient thermo-mechanical load transfer between the matrix and the reinforcements (minimum CTE of 11×10<sup>-6</sup> °C<sup>-1</sup> at 40% diamond volume fraction). Finally, the Cu/D heat spreaders were shown to exhibit higher resistance to thermal cycling relative to carbide-bonded Cu/D materials due to the softness of the copper oxide interphase compared to brittle carbide interphases (only -2% in thermal conductivity after 500 cycles).

The packaging potential of the two types of diamond-based heat spreaders was considered through finite element simulations. While its low CTE and relatively high cost limit the applicability of CVD diamond in packaging because of extensive thermo-mechanical stresses and limited scalability, the rare combination of electrical resistivity and thermal conductivity it allows may represent a worthy investment as a heat-spreader, especially in replacing tradition alumina substrate in close vicinity of the hot active chips. In addition, the Cu coating process may enhance the solderability of CVD diamond substrates. On the other hand, Cu/D composite films present a higher large scale potential and an interesting combination of moderate CTE and high thermal conductivity, which makes it useful as a heat-spreading film on top of a thicker base plate in order to limit shear stresses.

## 6.2 Future directions

From a scientific perspective, it would be helpful to gain more understanding on the chemical composition and microstructural evolution of the CVD diamond films in the very first stages of the deposition process. For example, TEM could be employed to detect the presence of SiC and other non-diamond phases in the film structure. This would help model the architecture of the diamond films and understand their thermal behavior in terms of both thermal conductivity and thermal resistance.

In a similar manner, deeper investigation (especially through TEM analysis) should be carried out on the growth of copper particles onto diamond in order to obtain clear enlightenment of the phases responsible for the copper/diamond bonding process. Although this study suggests that copper oxide is involved in the Cu/D bonding process, no clear conclusion on the chemical composition of the interphase could be drawn. Also, it could help enlightening how the interphase contributes to conduct the heat flux at the copper/diamond interface.

From a technological perspective, the performances achieved by the Cu/D composite films fabricated in this study are promising for applications as heat-spreading passive components in power electronic packages. The coating process developed to cover the diamond reinforcements with chemically bonded copper particles ensures efficient transfer of properties between the matrix and the reinforcements. The achieved thermal conductivity and its stability upon thermal cycling are especially remarkable.

Nevertheless, a lower coefficient of thermal expansion located around  $10 \times 10^{-6} \text{ }^{\circ}\text{C}^{-1}$  could be useful in order to minimize thermo-mechanical stresses at the DBC/heat-sink interface. A potential way to achieve a lower CTE while keeping the process unchanged is to use two different populations of diamond particles in order to create bi-populated diamond reinforced copper matrix composites. This way would allow reaching higher diamond volume fraction (up to 50%), thus decreasing the CTE of the resulting materials.

Potential ways to enhance the thermal conductivity of the composites would be to increase the size of the diamond reinforcements or use diamond reinforcements with enhanced purity. Being known for improving the thermal conductivity of Cu/D composites, these two factors were tested while working at ICMCB, but are not reported in this dissertation due to lack of relevant results. These two ways deserve deeper investigations.

Still considering the technological aspect, the Cu coating process opens interesting perspectives in bonding CVD diamond films or substrates with copper thin films and using such *diamond DBC* to replace alumina as an electrically insulating substrate in power package, as it is suggested in the packaging configurations proposed in chapter 5. Thus, this type of substrate would combine a high dielectric potential to a high thermal conductivity in a very promising way. By extension, the Cu coating process developed in this study might be useful to a variety of bi-materials bonding processes, involving, for instance, polymers or metals, and might be useful to a variety of applications. As an illustration, a company from the Netherlands showed interest in the Cu-coating process to help coat diamond onto tungsten carbide cutting tools for drilling and ground explorations applications.

Finally, an interesting issue to address would be the use of flat burners or multiple-flames configuration to grow diamond on the whole surface of a substrate, and see how the laser-excitation process could be part of such a deposition set-up. Also, it would be interesting to investigate how the diamond films, once integrated to a silicon substrate for example, sustain thermal cycling. This would enlighten any potential chemical, microstructural, or thermal evolution of the diamond film structure in real-operation environment, and would be helpful in the scope of any potential application in electronic packaging.

From an academic and human perspective, this French-American dual PhD initiative should be pursued in order to retain the strong partnership between our two universities, encourage sharing scientific knowledge and technical expertise from both sides, and provide other students with the same benefits as it did for me.

# APPENDIX

## A.1 Main heat transfer modes

Heat transfer (or heat) is thermal energy in transit due to a spatial temperature difference. Whenever there exists a temperature in a medium or between media, heat transfer must occur. Conduction heat transfer is one of the three existing heat transfer processes with convection and radiation. For conciseness purposes, we will not go into the details of convection and radiation heat transfers, since our interest here mainly focused on conduction heat transfer. However, the following paragraphs provide a short description of these heat transfer processes.

- **Convection heat transfer:**

Convection heat transfer combines the diffusion of thermal energy due to molecular motion plus the thermal energy transfer due to macroscopic motion (advection). Convection heat transfer is particularly important when considering the heat transfer occurring between a fluid in motion (liquid or gas) and a bounding surface when the two are at different temperatures. The resulting convective heat flux ( $q''_{conv}$ , W/m<sup>2</sup>) is a function of the temperatures of the bounding surface ( $T_s$ , K), of that of the moving fluid ( $T_\infty$ , K), and of a parameter called convection heat transfer coefficient ( $h$ , W/m<sup>2</sup>.K) which is specific to each fluid. A clear distinction between *heat flux* ( $q''$ ) and *heat rate* ( $q$ ) has to be stated: the *heat flux* is the rate of heat transfer per unit area:

$$q = q'' \cdot A \quad (A1.1)$$

where  $A$  is the area (m<sup>2</sup>). Typically, liquids have a greater convective heat transfer potential than gases, thus higher  $h$  values. Depending on if the convection is natural (free) or induced by external forces (forced), the  $h$  parameter also varies. Table A2.1 provides a few examples of convection heat transfer coefficient:

**Table A1.1: Typical values of the convection heat transfer coefficient.**

	Free convection		Forced convection	
	Gases	Liquids	Gases	Liquids
$h$ (W/m <sup>2</sup> .K)	[2-25]	[50-1000]	[25-250]	[100-20,000]

From a thermal management prospective, convective heat transfer is of major importance since finned heat sinks and fans are widely employed to enhance convective heat dissipation for cooling of electronic packages.

- **Radiation heat transfer:**

Radiation heat transfer occurs when thermal energy is emitted by matter that is at a nonzero temperature. From a thermal management prospective, radiation heat transfer is mostly considered from solid surfaces, although it may originate from liquids or gases, and may be attributed to changes in the electron configurations of the constituent atoms or molecules. Radiated thermal energy is transported by electromagnetic waves (or photons). While the transfer of energy by conduction or convection requires the presence of a material medium, radiation does not. In fact, radiation heat transfer occurs most efficiently in a vacuum. The radiative heat flux ( $q''_{rad}$ , W.m<sup>-2</sup>) between a surface and its surroundings is a function of the temperatures of the surface ( $T_s$ , K) and of the surroundings ( $T_{sur}$ , K), and on a radiation heat transfer coefficient called emissivity ( $0 < \varepsilon < 1$ ), which depends on the surface material and finish. If  $\varepsilon = 1$ , the surface is called an ideal radiator or *blackbody*, which constitutes the upper limit of radiative emissions. Finally, it involves a constant called the Stefan-Boltzmann constant ( $\sigma = 5.67 \times 10^{-8}$  W.m<sup>-2</sup>.K<sup>-4</sup>). Table A1.2 provides a few examples of emissivities.

**Table A1.2: Typical values of radiation heat transfer coefficients (emissivity).**

Material	Polished Al	Rough Cu	WC-Co	Brick	Rubber	Glass	Water
$\varepsilon$	0.05	0.75	0.85	0.85	0.93	0.92	0.98

▪ **Conduction heat transfer:**

Conduction heat transfer may be viewed as the transfer of energy from the more energetic to the less energetic particles of a substance. Higher temperatures are associated with higher molecular energies, and when neighboring particles collide, as they are constantly doing, a transfer of energy from the more energetic to the less energetic particles must occur. In the presence of a temperature gradient, energy transfer by conduction must then occur in the direction of decreasing temperature. The heat conduction phenomenon is described through *Fourier's law*, which express the conductive heat flux ( $q''_{cond}$ , W.m<sup>-2</sup>) as a function of the temperature gradient ( $dT/dx$ , K.m<sup>-1</sup>) and of a conductive heat transfer coefficient called thermal conductivity ( $k$ , W.m<sup>-1</sup>.K<sup>-1</sup>) which is specific to the medium considered.

The thermal conductivity is a transport property which provides an indication of the rate at which energy is transferred through the energy diffusion process into the material. It depends on the physical structure of matter at the atomic scale. In solids, heat conduction may be attributed to atomic activity in the form of migration of free electrons or lattice vibrations. In liquids and gases, in which particles are much more spaced, heat conduction is mostly the result of molecular interactions and collisions. As a consequence, solids typically exhibit a much greater heat conductive potential relative to liquids and gases. Finally, Tab. A1.3 briefly recaps the three main heat transfer processes and the physical mechanisms and equations they rely on.

**Table A1.3: Summary of heat transfer processes.**

Mode	Mechanism	Heat flux equation (W.m <sup>-2</sup> )	Transport property or coefficient
<b>Conduction</b>	Diffusion of energy due to random molecular motion	$q''_{cond} = -k \frac{dT}{dx}$ (Fourier's law)	$k$
<b>Convection</b>	Diffusion of energy due to random molecular motion plus energy transfer due to macroscopic motion	$q''_{conv} = h(T_s - T_\infty)$ (Newton's law)	$h$
<b>Radiation</b>	Energy transfer by electromagnetic waves	$q''_{rad} = \varepsilon \sigma (T_s^4 - T_{sur}^4)$ (Stefan-Boltzmann's law)	$\varepsilon$

▪ **Fourier's law:**

Although the conduction heat flux equation, Fourier's law, was introduced in section 3.1.3.1, it is interesting to consider its origin. Fourier's law was developed in 1822 by the French mathematician Jean-Baptiste Joseph Fourier (1768-1830). This law describing the heat conduction process is a phenomenological law (empirical) that was developed from observed phenomena rather than being derived from underlying principles. Considering a one-dimensional plane wall for which the temperature gradient is negative (Fig. A1.1), the expression of the conduction heat flux is written as follows:

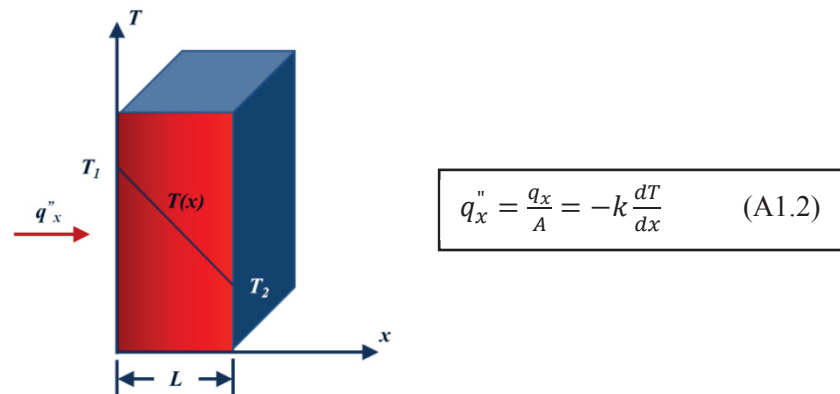


**Figure A1.1: One-dimensional heat transfer by conduction (diffusion of energy).**

Since the temperature distribution  $T(x)$  is linear, the temperature gradient may be expressed as:

$$\frac{dT}{dx} = \frac{T_2 - T_1}{L} \quad (\text{A1.3})$$

Therefore, the heat flux is equal to:

$$q''_x = k \frac{T_1 - T_2}{L} = k \frac{\Delta T}{L} \quad (\text{A1.4})$$



Equation A1.4 enlightens the importance of the minus sign in the expression of the conduction heat flux in order to have  $q_x''$  as a positive quantity. Indeed, the heat is always conducted in the direction of the decreasing temperature (thus from  $T_1$  to  $T_2$  on figure A1.1). Fourier's law, as written in equation A1.4, implies that the conduction heat flux is a directional quantity. In particular, the direction of heat flow is normal to the cross-sectional area  $A$ . More generally, the heat flow direction will always be normal to a surface of constant temperature called an isothermal surface (or isotherm). On figure A1.1, the isothermal surfaces are normal to the  $x$  direction. Being a directional quantity, the conduction heat flux can be expressed as a vector. Therefore, it is possible to write a more general statement of the conduction heat flux equation involving three space dimensions as follows:

$$q_{cond}'' = -k\nabla T = -k_x i \frac{\partial T}{\partial x} + k_y j \frac{\partial T}{\partial y} + k_z k \frac{\partial T}{\partial z} \quad (A1.5)$$

Which is equivalent to:  $q_{cond}'' = i q_x'' + j q_y'' + k q_z'' \quad (A1.6)$

Where:  $\left\{ q_x'' = -k_x \frac{\partial T}{\partial x} ; q_y'' = -k_y \frac{\partial T}{\partial y} ; q_z'' = -k_z \frac{\partial T}{\partial z} \right\} \quad (A1.7)$

And  $\nabla$  is the three-dimensional del operator,  $T(x, y, z)$  is the scalar temperature field, and  $k(x, y, z)$  is the scalar thermal conductivity field.

Each of the  $q_i''$  expression obtained from Fourier's law relates the conduction heat flux across a surface to the temperature gradient in a direction perpendicular to the surface through the thermal conductivity parameter. Equation A1.7 supposes that the thermal conductivity is different in each direction of space ( $k_x, k_y, k_z$ ), i.e. that the medium considered is non-isotropic. If the medium is considered isotropic (such as Cu/D composite material):  $k_x = k_y = k_z = k$ .

## A.2 Characterization techniques

The following paragraphs provide briefs description of some of the characterization techniques employed throughout this study. The physical principles and the major elements constituting the equipment are detailed. Raman spectroscopy is not mentioned here since more details about this technique can be found in sections 3.3.1 and 3.3.2.

### ▪ *Thermal diffusivity and dilatometry:*

Figures A2.1 and A2.2 provide detailed descriptions of the flash laser radiometry and dilatometry devices used in this study. They allow the measurement of the thermal diffusivity and thermal expansion coefficient of the Cu/D composite samples fabricated in chapter 4. The underlying principles of these two techniques are mentioned in sections 4.8.2.

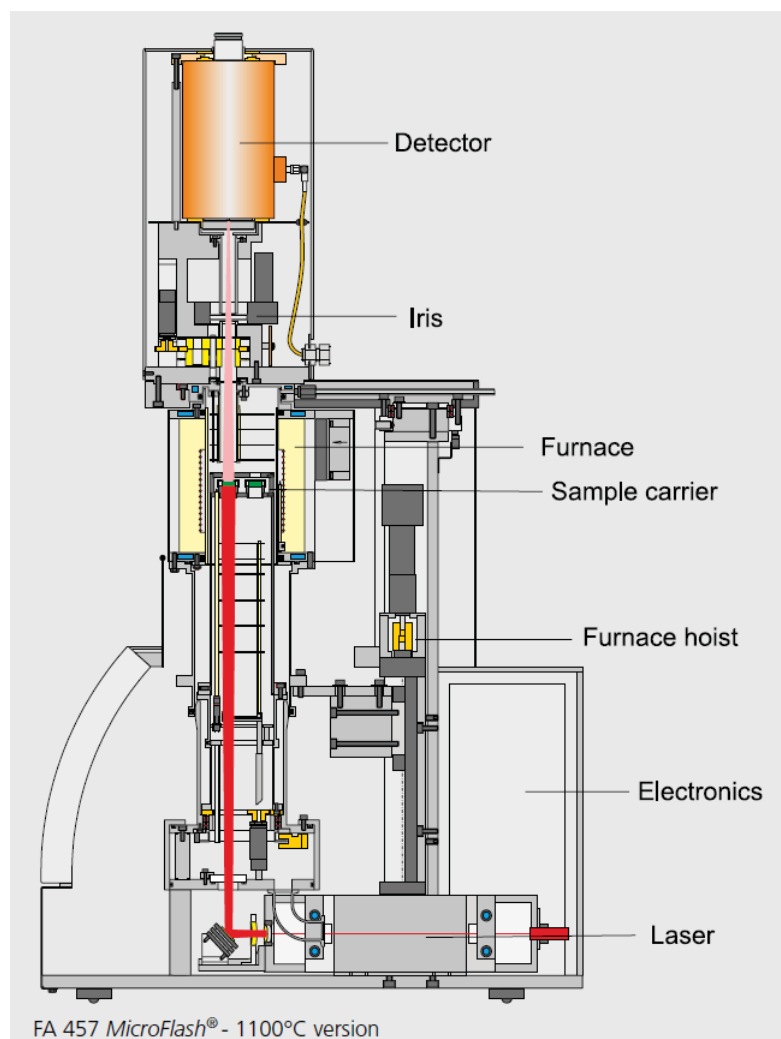


**Figure A2.1: Schematic of the Netzsch LFA-457 flash laser radiometry device.**

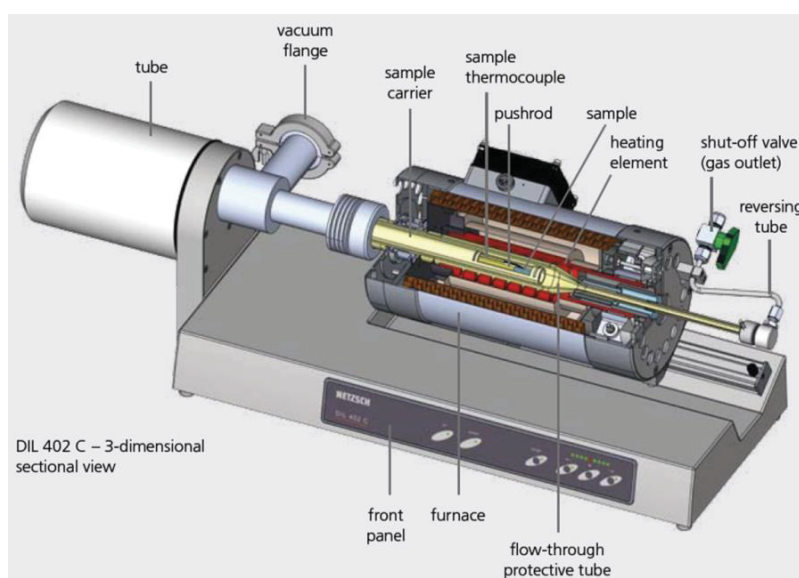


**Figure A2.2: Schematic of the Netzsch DIL-402 horizontal dilatometer.**

▪ **Scanning electron microscopy (SEM):**

Scanning electron microscopy (SEM) allows producing high-resolution image of a sample through electron-matter interactions. Figure A2.3 illustrates the main electron-matter interactions involved in microscopy and spectroscopy techniques:

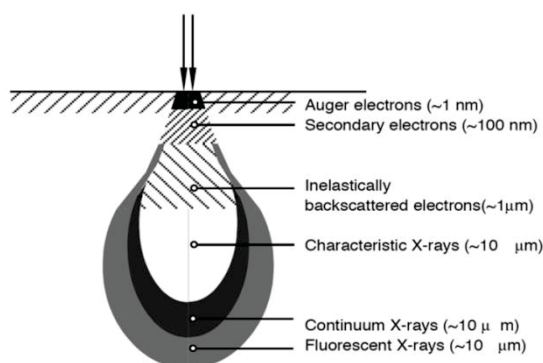


**Figure A2.3: Schematic of electron-matter interactions.**

By scanning a beam of primary electrons onto a sample's surface, the sample reemits certain particles, as described in Fig. A2.3. The sample must show sufficient electrical conductivity in order to prevent any charge accumulation onto the surface, which affects the imaging process. For insulating materials (dielectrics, ceramics), a metallic coating can be applied through sputtering onto the surface prior to SEM analysis. A SEM microscope is composed of a primary electron gun (usually a tungsten (W) or tantalum (Ta) glowing filament), of an electronic column, which consists in several electronic lenses and deflection coils, used to focus, direct, and stabilize the electron beam, of an automated sample holding stage, and of detectors to record the particles emitted from the sample's surface (Fig. A2.4a). The particles emitted from the sample and detected through SEM can either be secondary electrons (SE, Fig. A2.4b) or back-scattered electrons (BSE, Fig. A2.4c).

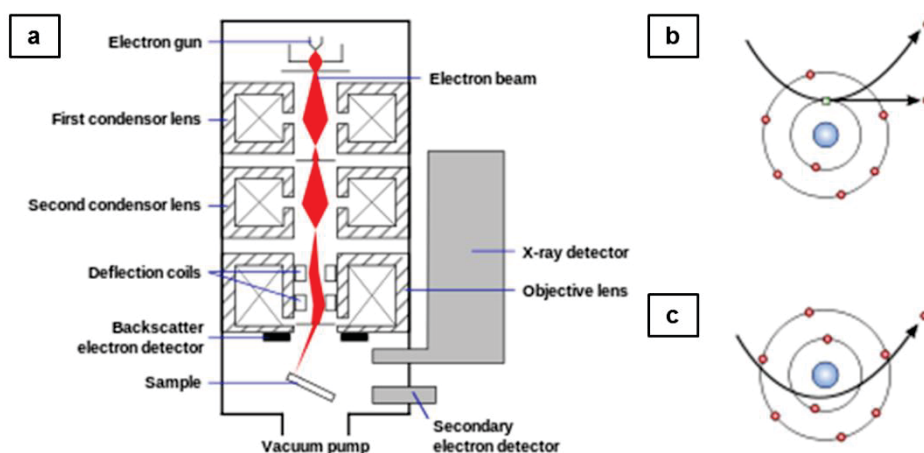


**Figure A2.4: (a) Schematic view of a scanning electron microscope and view of (b) secondary electron and (c) back-scattered electron emission processes.**

When a primary electron hits an atom from the sample's surface, it may transfer its kinetic energy to an electron with weak bonding energy to the nucleus (usually a valence electron from the outer shells of the atom) thus triggering the ejection of this electron from the atom and the ionization of the atom. The ejected electron is termed a *secondary electron*, since it originates from the interaction of a primary electron with the atom's structure. Secondary electrons usually have energy located around 50 eV (low energy) which makes these electrons easy to collect and record. It is worth notice that a single primary electron may lead to the creation of several secondary electrons.

As shown on Fig. A2.3, secondary electrons come from the superficial layers of the sample (typically from a depth located between 10 nm and 100 nm). Therefore, these electrons are strongly sensitive on the sample's surface structure since the intensity of the SE signal collected from one location of the sample depends on the surface morphology at this point. This makes possible the recording of topographical images of the sample through SE imaging.

Back-scattered electrons originate from the interaction of primary electrons with the atoms nuclei through quasi-elastic interactions. After interaction with the nucleus, a primary electron is back-scattered to a direction close to its initial direction and with a weak energy loss. Back-scattered electrons exhibit energies way higher than secondary electrons (typically 30 keV) and are emitted from deeper in the sample (up to 1  $\mu\text{m}$ ). Therefore, they only allow imaging with a limited resolution (usually [0.1 – 1]  $\mu\text{m}$ ).

Finally, back-scattered electrons are strongly sensitive to the atom's atomic number. Heavy atoms (with a relatively larger atomic number) emit a larger quantity of back-scattered electrons relative to light atoms (with a relatively smaller atomic number). Consequently, BSE imaging makes possible phase contrast imaging by distinguishing the brighter areas of the sample (which reveal atoms with high atomic numbers) from the darker ones (which reveal atoms with relatively lower atomic numbers) (see Fig. 3.43 for an example).

- ***Auger electron spectroscopy (AES):***

Auger electron spectroscopy (AES) is a surface analysis technique which provides access to the chemical composition of the very first atomic layers of the surface of a solid material (a few nanometers deep). AES analysis relies on the *Auger process* (Fig. A2.5): when a primary electron hits an atom, an electron from the inner shells (core electron, K level for example) may be ejected and make the atom enter an excited state. The atom will then desexcite to recover its fundamental state. This occurs through electronic transitions that will see an electron from a higher level ( $L_1$  for example) fills the gap left by the missing K level electron, thus releasing an energy  $E_K - E_{L1}$ . This energy may then be dissipated, either through the emission of x-ray photons (fluorescence X, see

the paragraphs on EPMA) with energy  $h\nu = E_K - E_{L1}$ , or by being transferred to an electron from a higher level ( $L_{2,3}$  for example), which will thus be ejected from the atom. The  $L_{2,3}$  level electron ejected from the atom is termed an *Auger electron*, and *Auger spectroscopy* is carried out by recording this type of particle. The energy of Auger electrons depends on the electronic level from which they are emitted. In the case of Fig. A2.5, its energy is equal to:

$$E_{Auger} = E_K - E_{L1} - E_{L2,3} \quad (A2.1)$$

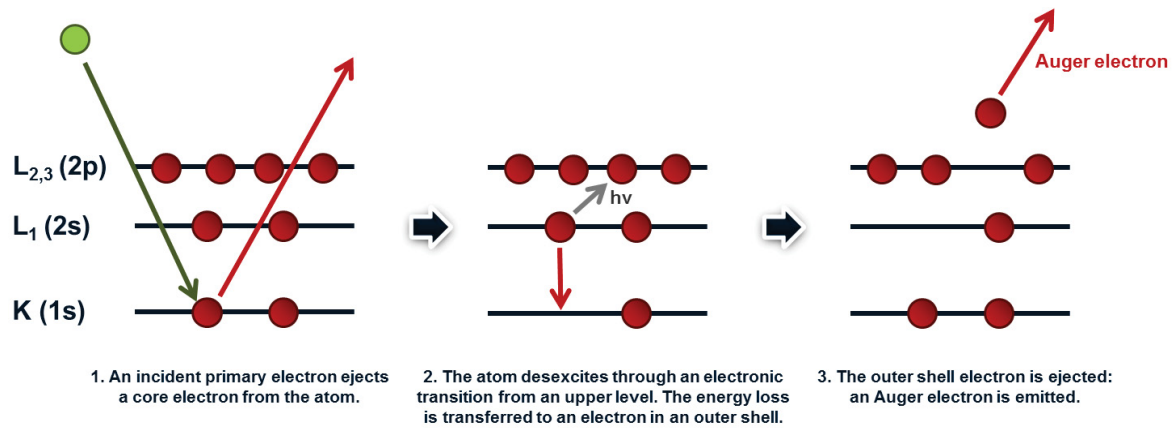


**Figure A2.5: Schematic view of the Auger process.**

The electronic transitions involved in the Auger process are characteristic of each chemical element. By analyzing the energy distribution of the Auger electrons emitted by a sample, one can establish its chemical composition. This makes Auger spectroscopy a technique of primary choice for surface elemental identification. However, very lights elements (such as H, He) only emit x-ray photons when desexciting, and thus are not detectable through Auger spectroscopy. In-depth chemical concentration profiling is also made possible through ionic etching ( $Ar^+$  ions) of the sample's surface and step-by-step local analyses. Chemical mapping of a surface is also accessible with certain AES devices by scanning the sample's surface.

While the primary electrons used in AES are high-energy electrons (in the order of several keV), Auger electrons exhibit weak energies (in the order of 100 eV). Of course, their energies are independent from the energy of the primary electrons beam. The low energy level of Auger electrons explains why this technique only gains access to the very first atomic layers of a sample (only a few nanometers). It is also the reason why AES requires a highly vacuumed environment to be carried out, in order to prevent any collisions of interfering particles from the environment with the Auger electrons to be recorded. Auger electrons are recorded by electronic lenses and then classified and counted with respect to their kinetic energies through an analyzer with cylindrical mirrors. The resulting spectrum allows analyzing the potential electronic transitions recorded and thus let access to the chemical composition of the sample.

The main advantages of AES toward XPS (see next paragraph) are: a higher resolution (typically [3 - 5] nm in depth and 50×50 nm<sup>2</sup> in surface), quantitative analysis capability, analysis speed, and in-depth atomic concentration profiling capability.

▪ **X-ray photoelectron spectroscopy (XPS):**

X-ray photoelectron spectroscopy (XPS) is a surface chemical analysis method which enables getting information about the chemical composition of a sample's surface and its chemical environment. XPS relies on the photoelectric effect: when irradiated by a single wavelength x-ray source (with energy  $E_{incident}$ ), an atom may be ionized through the ejection of some of its electrons, either from core or outer shells. The electrons ejected through this process are termed *photoelectrons*.

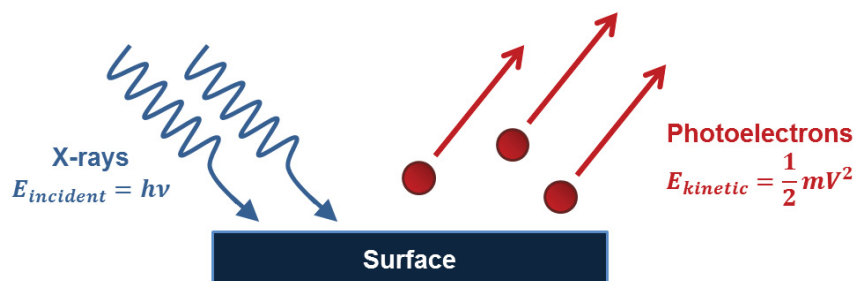


**Figure A2.6: Schematic view of the photoelectric effect.**

By recording the kinetic energies ( $E_{kinetic}$ ) of the photoelectrons emitted, XPS provides access to their initial binding energy ( $E_{binding}$ ) to the nucleus through the Einstein's equation:

$$E_{binding} = E_{incident} - E_{kinetic} = hv - \frac{1}{2}mV^2 \quad (A2.2)$$

where  $hv$  is the energy of the primary incident x-rays (eV) with  $h$  the Planck's constant ( $h = 6.62 \times 10^{-34} \text{ m}^2 \cdot \text{kg} \cdot \text{s}^{-1}$ ) and  $v$  the frequency of the light source (Hz), and  $E_{kinetic}$  is the kinetic energy of the photoelectrons recorded (eV) with  $m$  their mass (kg) and  $V$  their speed ( $\text{m} \cdot \text{s}^{-1}$ ).

A spectrum showing the binding energies of the recorded photoelectrons with respect to signal intensity is recorded. Each intensity peak corresponds to a specific binding energy, and thus to a specific chemical element, which leads to the chemical composition of the sample's surface.

The energy of the incident x-rays is in the order of the ionization energy of the core electrons of the atom. Emissions of photoelectrons from the core electrons provide the main XPS peaks revealing the chemical nature of the atom. On the other hand, emissions of photoelectrons from outer shells electrons lead to XPS peak shifts, which provide information about the chemical environment of the atom (potential chemical bonding to other atoms, degree of oxidation).



XPS grants access to the chemical composition of a sample on a depth of less than 1 nm. Surface mapping is also possible, typically onto a surface in the order of  $50 \times 50 \mu\text{m}$ . Not only qualitative but also semi-quantitative information can be obtained by analyzing the integral of the peaks. The main drawback of XPS toward AES is its limited resolution, while its main advantage remains its capability to provide information about the chemical environment of the surface's atoms.

▪ **Atomic force microscopy (AFM):**

Atomic force microscopy (AFM) is a local scanning technique relying on the interaction between the atoms of the surface and the atoms of a very sharp tip mounted on a cantilever to obtain a topographical mapping of the surface and, hence, to quantify parameters such as surface feature sizes and roughness or bonding strengths. When the tip is in close vicinity with the sample's surface, attractive and repulsive forces between the tip and the sample lead to a deflection of the cantilever. The cantilever's deflection is measured using a laser source reflected from the top surface of the cantilever into an array of photodiodes, which then provides feedback to a computer. The sample is mounted onto a piezoelectrically-activated stage which allows moving the sample. Figure A2.7 provides a schematic description of an AFM set-up:

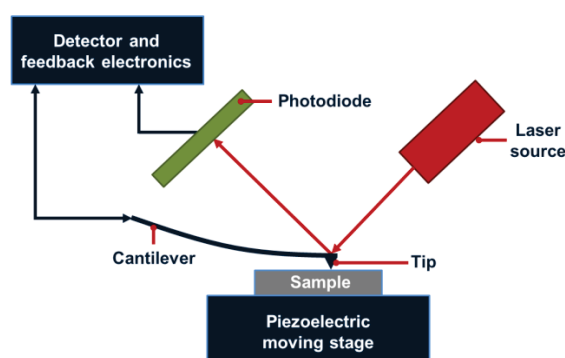


**Figure A2.7: Schematic view of an atomic force microscope.**

AFM proposes three primary scanning modes: the contact mode, the non-contact mode, and the tapping mode. The contact mode (or static mode) relies on repulsive forces to image the surface's topography. The tip is dragged across the surface of the sample, which leads to cantilever deviations with respect to surface's roughness, and provides feedback to the detectors. In this mode, the force between the tip and the surface is maintained constant while scanning by initially imposing a fixed cantilever deviation. This mode usually leads to extensive tip wearing due to constant contact with the surface.

In the non-contact mode (or dynamic mode), the cantilever's tip does not contact the sample's surface. The cantilever is oscillated at its resonance frequency (frequency modulation) or slightly

above (amplitude modulation) with amplitude of oscillation going from a few nanometers (typically  $< 10$  nm) down to a few picometers. In this mode, the tip-to-surface distance is adjusted with respect to the deviations in the oscillation frequency (or amplitude) in order to be kept constant. Any deviation in the tip-to-surface distance leads to interaction forces between the tip and the surface, which make the oscillation frequency or amplitude vary. The recording of frequency or amplitude changes thus provides a feedback to the detector in order to image the surface's topography. Amplitude modulation is the most common non-contact AFM mode. Changes in the oscillation amplitude or phase provide the feedback for surface imaging. Phase imaging can also be used in tapping mode (such as in this study, see section 4.5.2) and can provide a higher sensitivity toward the surface morphology relative to the contact mode. It frequently enables the observation of surface structures that are barely visible in contact or tapping modes. Non-contact AFM features some advantages: it does not suffer from tip degradation and it is especially useful for sensitive samples such as biological materials. However, the non-contact mode is highly sensitive to the environment and usually requires a vacuumed atmosphere to be carried out.

The alternative-contact mode (or tapping mode) is by far the most common AFM mode employed. In this mode also, the tip is vertically oscillated, at its resonant frequency, but at larger amplitudes relative to the non-contact mode (typically in the order of [100-200] nm). As interaction forces of the surface with the tip make the oscillation amplitude vary, a piezoelectric actuator adjusts the height of the tip above the sample in order to keep the oscillation amplitude constant. By recording the amplitude deviations induced by the intermittent contacts of the tip with the surface, a tapping topographical image is constructed. Similar to the non-contact mode, the tapping mode enables lesser damages to the tip, while showing high-resolution imaging capability in open-air environment.

AFM features several advantages toward SEM, among them open-air operation capability (no need for vacuumed environment), three-dimensional imaging capability, and higher resolution (down to 1 angstrom, close to that of a scanning tunneling microscope).

- ***Electron probe microanalysis (EPMA):***

Electron probe microanalysis (EPMA, or French *Microsonde de Castaing*) is a non-destructive in-situ chemical analysis technique enabling to record all the elements (starting at beryllium (Be)) existing in a volume of a few cube micrometers. EPMA relies on the detection of x-rays emitted by the core shells of an atom, and resulting from the interaction of the atom's structure with a high-energy primary electrons beam (from 5 keV to 40 keV). EPMA is based on the same desexcitation principle as that involved in AES, except that EPMA focus on the x-rays resulting from the desexcitation process rather than on the Auger electrons emitted.

Each chemical element exhibiting a characteristic x-ray spectrum, the spectral analysis of the x-ray emissions, i.e. the x-ray emission intensity distribution with respect to the x-ray wavelength (wavelength dispersive spectrometry, or WDS mode), or with respect to the x-ray energy (energy dispersive spectrometry, EDS or EDXS mode), provide information about the chemical composition of the excited volume.

A WDS spectrometer is composed of a monochromatic crystal (Lithium Fluoride (LiF), quartz) and of a proportional gas flux counter (pressurized Ar/CH<sub>4</sub> mixture). The X-rays source (the sample), the crystal, and the counter, must all be located on a focus circle (the Rowland's circle on Fig. A2.8). When, at a given X-ray wavelength  $\lambda$  (nm) emitted from the sample, the crystal is located in the Bragg position, i.e. when the angle  $\theta$  of the incident X-rays and the interplanar distance of the crystal  $d_{hkl}$  (nm) satisfy the following relationship:

$$n\lambda = 2d_{hkl} \sin \theta \quad (\text{A2.3})$$

(with  $n$  an integer), then the X-ray emission is diffracted by the crystal to the detector and recorded. The movement of the detector with the crystal following the Rowland's circle trajectory makes the angle between the sample and the crystal to vary. By selecting a crystal with a specific  $d_{hkl}$ , and by varying  $\theta$  between 20° and 70°, a large wavelength range can be analyzed.

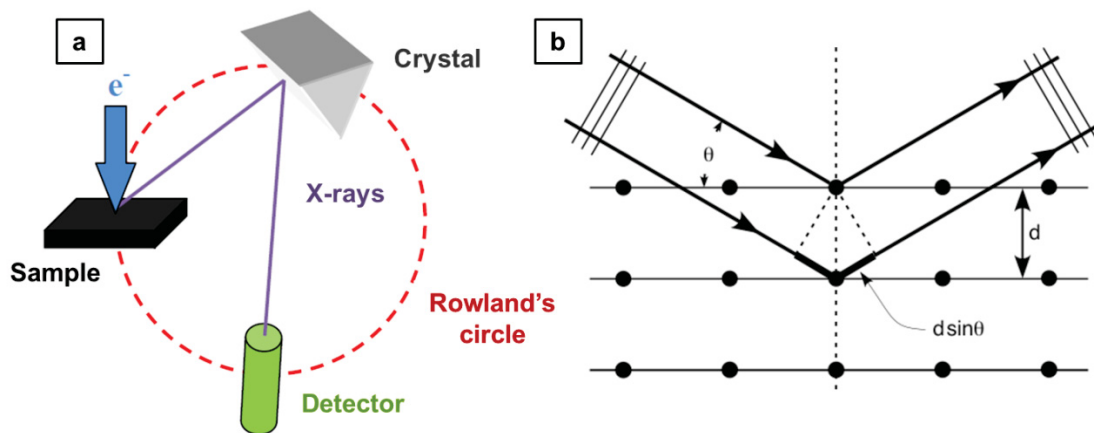


**Figure A2.8: (a) Schematic view of a WDS spectrometer and (b) Bragg diffraction process.**

In the EDS mode, the distinction of the different X-photons is based on their energies by using a silicon diode compensated with lithium (Si(Li)) as detector, which converts the energy of a photon by creating electron-hole pairs. The resulting voltage, function of the photon energy, is recorded in a multichannel analyzer. EDS spectrometers are sometimes associated to transmission electron microscope (TEM) in order to provide high-resolution chemical mapping capability (see section 4.5.3).

WDS and EDS spectrometers both feature advantages and drawbacks. WDS spectrometers show higher spectral resolution, higher signal/noise ratio, and a more extended range of X-ray emissions that can be analyzed relative to EDS spectrometers. However, the elements that can be detected by a crystal depend on its interplanar distances. Therefore, a single crystal provides access to a certain number of elements but not to all of them. Consequently, several crystals with different  $d_{hkl}$  have to be combined in order to exhaustively scan the chemical composition of a sample. This makes the WDS mode slower relative to EDS. EDS spectrometers gather a spectrum of all the elements at the same time within the probed volume of the sample and are therefore faster than WDS. However, they exhibit a lower spectral resolution and a lower signal/noise ratio relative to WDS spectrometers, which may lead to interferences between different chemical elements. In addition, Si(Li) diodes do not enable the detection of elements lighter than sodium (Na).

EPMA also enables quantitative and semi-quantitative local chemical analysis by comparing the recorded X-ray signal to that of samples with known elemental concentrations. Thus, EPMA makes possible chemical concentration mapping of a sample (see Fig. 4.59). EPMA is one of the most precise quantitative local chemical analysis techniques. This method is also remarkable by its fastness since an automated EPMA machine equipped with analysis and processing software may record the concentration of about ten elements in less than two minutes. The sensitivity of EPMA to the elemental concentration is also fine: 0.02 at.% for elements with atomic number  $Z \geq 11$  and 1 at.% for elements with atomic number  $Z \leq 10$ . However, the probed volume can go up to several cube micrometers, and the lateral resolution of EPMA is in the order of 1  $\mu\text{m}$ . Consequently, the large volume analyzed limits the spatial resolution of this method.

▪ ***Transmission electron microscopy (TEM):***

Transmission electron microscopy (TEM) is an imaging technique that makes possible microstructural observations at the nanometric scale by recording electrons transmitted through a sample. TEM analysis was especially useful in this study when aiming to study interfaces, either between the diamond reinforcements and the copper particles (see section 4.5.3) or between the CVD diamond film and Cu/C substrates (see section 3.6).

The sample first has to be made transparent to the electron beam by reaching a sufficiently low thickness. This is achieved through the combination of a first step of mechanical polishing (down to a thickness of 50  $\mu\text{m}$ ) with a second step of ionic etching using a focused ion beam (FIB, usually  $\text{Ar}^+$  ions). The as-prepared sample must show parallel faces. Ion-assisted polishing eliminates the potential defects and stresses that may have appeared upon mechanical polishing, and can be processed either longitudinally or transversally. In this study, the samples were prepared in collaboration with the Serma society, based in Grenoble, France.

A TEM microscope is composed of three major elements: the electron gun, the electronic lenses, and the collimators. The electron gun produces and accelerates the electron beam, the electronic lenses direct, stabilize, and focus the electron beam on the sample, and the collimators allow tuning the contrast and enlightening of the image. Figure A2.9 provides a schematic description of a TEM microscope:

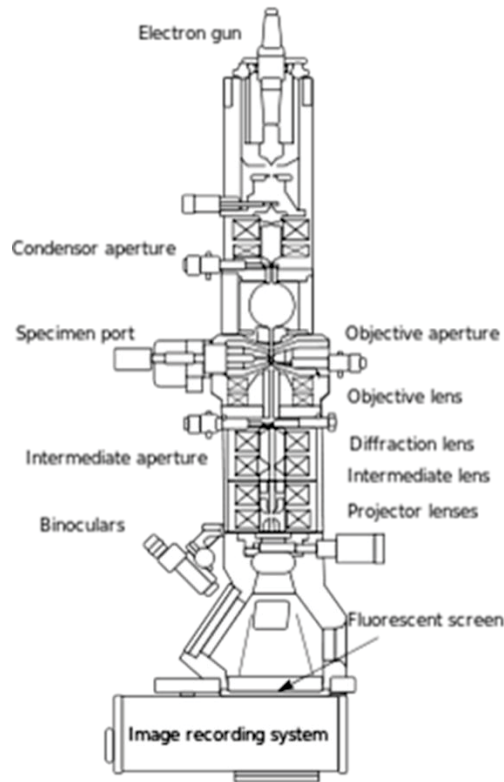


**Figure A2.9: Schematic view of transmission electron microscope.**

TEM imaging provides access to both the image of the enlightened area and to its diffraction pattern. Therefore, there are two major observation modes in TEM microscopy:

- The diffraction mode: Following Bragg's law (Fig. A2.8b), the interaction of the transmitted electron beam with a crystalline material leads to the formation of a diffraction pattern corresponding to the diffraction of the incident primary electron beam by the crystallographic structure of the material. By projecting this pattern onto a photographic film or imaging detector, one can directly observe the diffraction pattern of the material. Subsequently, the orientation of this organized network toward the incident beam and the nature of the material and different structural characteristics (symmetry, interplanar distances) may be determined by indexing this pattern with respect to known diffraction references;
- The imaging mode: Based on the diffraction pattern, and using contrast collimator, one can either select the central spot of the pattern (corresponding to the transmitted beam) or a

diffracted spot, and thus form images either in dark field or in bright field. These images constitute powerful tools to get precise knowledge of the fine microstructure of a material.

Table A2.2 provides a summary of the different characterization techniques reviewed in this appendix and their main characteristics:

**Table A2.1: Summary of different characterization techniques.**

Technique	Excitation source	Recorded signal	Type of analysis	Resolution limit	Information obtained
<b>SEM</b>	Electrons	Electrons (SE, BSE)	Imaging	SE mode: 100 nm BSE: 1 $\mu\text{m}$	Microstructure Topography Phase imaging
<b>TEM</b>	Electrons	Transmitted electrons	Imaging	< 1 nm	Microstructure Interfaces
<b>AES</b>	Electrons	Auger electrons	Surface chemistry In-depth chemistry	50 $\text{nm}^2$	Elemental composition, concentration profiles
<b>XPS</b>	X-rays	Photoelectrons	Surface chemistry	50 $\mu\text{m}^2$	Elemental composition, chemical environment
<b>AFM</b>	Mechanical	Mechanical deviation	Surface topography	< 1 nm	Surface morphology, roughness, bonding strength
<b>EPMA</b>	Electrons	X-rays (EDS, WDS)	Volume chemistry	1 $\mu\text{m}^3$	Qualitative and quantitative chemical composition
<b>Flash laser radiometry</b>	Photons	IR emissions	Thermal behavior	10 $\text{mm}^2 \cdot \text{s}^{-1}$	Thermal diffusivity
<b>Dilatometry</b>	Heat flux	Dimensional change	Thermo-mechanical behavior	1 $\times 10^{-6} \text{ } ^\circ\text{C}^{-1}$	Thermal expansion coefficient



# LITERATURE REFERENCES

- [1] World Energy Outlook, International Energy Agency, Paris, (2010).
- [2] M. Auzanneau, Oil Man Blog, hosted by LeMonde.fr, (2010) : <http://petrole.blog.lemonde.fr/2010/11/18/tout-va-bien-le-peak-oil-est-atteint-dit-lagence-internationale-de-lenergie/>
- [3] Intel Website: <http://www.intel.com/content/www/us/en/silicon-innovations/moores-law-technology.html>
- [4] J. Amussen, D. K. Reinhard, "Diamond Films Handbook", Ed. Marcel Dekker, New York, (2002).
- [5] X. C. Tong, "Advanced materials for thermal management of electronic packaging", Springer Series in Advanced Microelectronics, 30, (2011).
- [6] M. M. Sabry, D. Atienza, A. K. Coskun, "Thermal analysis and active cooling management for 3D MPSoCs", IEEE Int. Symp. on circuits and systems, 11, (2011).
- [7] M. J. Ellsworth, Int. Soc. Conf. on Ther. Ph., "Chip power density and module cooling technology projections for the current decade", (2004).
- [8] S.S. Anandan, V. Ramalingam, "Thermal management of electronics: A review of literature", Therm. Sc., 12 (2), 5, (2008).
- [9] R. Viswanath, V. Wakharkar, A. Watwe, V. Lebonheur, "Thermal performance challenges from silicon to systems", Intel Tech. J., Q3, (2000).
- [10] C. Buttay, "Modules et boitiers de puissance (packaging)", Editions Techniques de l'Ingénieur, D3 116, (2008).
- [11] P. M. Geffroy, J. D. Matthias, J. F. Silvain, "Heat sink material selection in electronic devices by computational approach", Adv. Eng. Mat., 10, 4, (2008).
- [12] S. Lee, "Optimum design and selection of heat sinks", IEEE Trans. on components packaging and manufacturing technology – Part A, 18, 4, (1995).
- [13] F. P. Incropera, D. P. DeWitt, T. L. Bergmann, A. S. Lavine, "Fundamentals of heat and mass transfer – Sixth edition", Springer, (2007).
- [14] Y. F. Maydanik, "Loop heat pipes", App. Therm. Eng., 25, 635, (2005).
- [15] C. Hilbert, S. Sommerfeldt, O. Gupta, D. J. Herrell, "High performance air cooled heat sinks for integrated circuits", IEEE Trans. on components hybrids and manufacturing technology, 13, 4, (1990).
- [16] J. Schulz-Harder, K. Exel, A. Meyer, "Direct liquid cooling of power electronic devices", 4<sup>th</sup> Int. Conf. on integrated power systems, (2006).
- [17] P. Wang, P. McCluskey, A. Bar-Cohen, "Hybrid solid-and-liquid cooling solution for isothermalization of insulated gate bipolar transistor power electronic devices", IEEE Trans. on components packaging and manufacturing technology, 1, (2012).
- [18] K. Kota, P. Hidalgo, Y. Joshi, A. Glezer, "A novel conduction-convection based cooling solutions for 3D stacked electronics", 26<sup>th</sup> annual IEEE semiconductor thermal measurement and management symposium, (2010).
- [19] A. F. Ali, M. S. El-Genk, "Spreader for immersion nucleate boiling cooling of a computer chip with a central hot spot", En. Conv. Man., 53, 259, (2012).

- [20] H. Y. Li, K. Y. Chen, M. H. Chiang, "Thermal-fluid characteristics of plate-fin heat sinks cooled by impingement jet", *En. Conv. Man.*, 50, 2738, (2009).
- [21] L. M. Goncalves, J. G. Rocha, C. Couto, P. Alpuim, J. H. Correia, "On chip array of thermoelectric Peltier microcoolers", *Sens. Act. A*, 145-146, 75, (2008).
- [22] A. Bar-Cohen, "Thermal management of on-chip hot spots and 3D chip stacks", *IEEE Int. Conf. on microwaves communications antennas and electronic systems*, (2009).
- [23] J.M. Dorkel, "Semi-conducteurs de puissance : Problemes thermiques – Partie 1", *Editions Techniques de l'Ingénieur*, D3 112, (2003).
- [24] J. Barcena, J. Maudes, M. Vellvehi, X. Jorda, I. Obieta, C. Guraya, L. Bilbao, C. Jimenez, C. Merveille, J. Coletto, "Innovative packaging solution for power and thermal management of wide-bandgap semiconductor devices in space applications", *Acta Astronautica*, 62, 422, (2008).
- [25] A. Akturk, S. Potbhare, N. Goldsman, A. Lelis, "Self-consistent thermal and electrical analysis of silicon carbide power DMOSFET heating and cooling", *IEEE Transactions*, 978-1-4244-6031-1, (2009).
- [26] R.W. Johnson, J. Williams, "SiC power device packaging technologies for 300 to 350°C applications", *Mat. Sc. Forum*, 483-485, 785, (2005).
- [27] European Commission. Directive 2008/35/EC of the European Parliament and of the Council of 11 March 2008 on restriction of the use of certain hazardous substances in electrical and electronic equipment (RoHS), (2008).
- [28] European Commission. Directive 2012/19/EU of the European Parliament and of the Council of 4 July 2012 on waste electrical and electronic equipment (WEEE), (2012).
- [29] H. Ma, J.C. Suhling, "A review of mechanical properties of lead-free solders for electronic packaging", *J. Mater. Sc.*, 44 (5), 1141, (2009).
- [30] C. Gobl, J. Faltenbacher, "Low temperature sinter technology die attachment for power electronic applications", *Proceedings of CIPS*, (2010).
- [31] G. Lacombe, PhD thesis, Universite de Bordeaux, Ecole Doctorale des Sciences Chimiques, (2012).
- [32] M. Ciappa, "Selected failure mechanisms of modern power modules", *Microelec. Rel.*, 42, 653, (2002).
- [33] J.F. Burges, C.A. Neugebauer, G. Flanagan, R.E. Moore, "The direct bonding of metals to ceramics and application in electronics", *Electrocomp. Sc. Tech.*, 2, 233, (1976)P. Gwinn, R.L. Webb, "Performance and testing of thermal interface materials", *Microelec. Rel.*, 34, 215, (2003).
- [34] J. P. Gwinn, R. L. Webb, "Performance and testing of thermal interface materials", *Microelec. J.*, 34, 215, (2003).
- [35] S. Ridout, C. Bailey, "Review of methods to predict solder joint reliability under thermo-mechanical cycling", *Fatigue Fract. Eng. Mater. Struct.*, 30, 400, (2006).
- [36] G. Lalet, PhD thesis, Université de Bordeaux, Ecole Doctorale des Sciences Chimiques, (2010).
- [37] C. Zweben, "Advances in composite materials for thermal management in electronic packaging", *JOM*, 50 (6), 47, (1998).
- [38] C. Zweben, "Advanced composites and other advanced materials for electronic packaging thermal management", *International symposium on advanced packaging materials*, (2001).

- [39] K. Yoshida, H. Morigami, "Thermal properties of diamond/copper composite material", *Microelec. Rel.*, 44, 303, (2004).
- [40] T.R. Anthony, J.L. Fleischer, J.R. Olson, D.G. Cahill, "The thermal conductivity of isotopically enriched polycrystalline diamond films", *J. Appl. Phys.*, 69, 8122, (1991).
- [41] P.M. Menon, R.E. Clausing, L. Heatherly, C.S. Feigerle, "The morphology of diamond grown by hot filament chemical vapor deposition", *Diam. Relat. Mat.*, 7, 1201, (1998).
- [42] S.G. Zhou, C.Y. Zang, H.A. Ma, Q. Hu, X.L. Li, S.S. Li, H.M. Zhang, X.P. Jia, "HPHT synthesis of different shape coarse-grain diamond single crystals", *Chin. Phys. Lett.*, 26 (4), 48102, (2009).
- [43] H.J. Looi, L.Y.S. Pang, Y. Wang, M.D. Whitfield, R.B. Jackman, "High-performance metal semiconductor field effect transistors from thin-film polycrystalline diamond", *Diamond Relat. Mat.*, 7, 565, (1998).
- [44] A.T. Collins, "Diamond electronic devices – a critical appraisal", *Semicond. Sci. Technol.*, 4, 605 (1988).
- [45] M. Willander, M. Friesel, Q. Wahab, B. Straumal, "Silicon carbide and diamond for high temperature device applications", *J. Mater. Sc. – Mat. In Electronics*, 17, 1, (2006).
- [46] N. Takabatake, T. Kobayashi, D. Sekine, T. Izumi, "Thermal characterization of CVD diamond film by photoacoustic method", *Appl. Surf. Sc.*, 159-160, 594 (2000).
- [47] H.P. Ho, K.C. Lo, S.C. Tjong, S.T. Lee, "Measurement of a thermal conductivity in diamond films using a simple scanning thermocouple technique", *Diamond Relat. Mat.*, 9, 1312 (2000).
- [48] S.D. Wolter, D.A. Borca-Tasciuc, G. Chen, N. Govindaraju, R. Collazo, F. Okuzumi, J.T. Prater, Z. Sitar, "Thermal conductivity of epitaxially textured diamond films", *Diamond Relat. Mat.*, 12, 61 (2003).
- [49] D.T. Morelli, C.P. Beetz, T.A. Perry, "Thermal conductivity of synthetic diamond films", *J. Appl. Phys.*, 64, 3063 (1988).
- [50] W. D. Callister Jr., "Materials Science and Engineering – An Introduction – Seventh Edition", John Wiley & Sons, Inc., (2007).
- [51] J. Sung, "Graphite to diamond transition under high pressure: a kinetic approach", *J. Mater. Sc.*, 35, 6041, (2000).
- [52] C.M. Sung, M.F. Taib, "Reactivities of transition metals with carbon: implications to the mechanism of diamond synthesis under high pressure", *Int. J. Refract. Met. Hard Mat.*, 15, 237, (1997).
- [53] P. Bridgeman, "The physics of high pressure", G. Bell and Sons Ed., London, (1952).
- [54] D.P. Yang, X.R. Ji, H.S. Liu, Y.A. Li, T.C. Zhang, P.W. Zhu, "The influence of Li-based catalysts/additives on cBN crystal morphologies synthesized under HPHT", *Diamond Relat. Mat.*, 20, 174, (2011).
- [55] Y.F. Zhang, C.Y. Zang, H.G. Ma, Z.Z. Liang, L. Zhou, S.S. Li, X.P. Jia, "HPHT synthesis of large single crystal diamond doped with high nitrogen concentration", *Diamond Relat. Mat.*, 17, 209, (2008).
- [56] X.B. Liu, H.A. Ma, Z.F. Zhang, M. Zhao, W. Guo, M.H. Hu, G.F. Huang, Y. Li, X.P. Jia, "Effect of zinc additive on the HPHT synthesis of diamond in Fe-Ni-C and Fe-C systems", *Diamond Relat. Mat.*, 20, 468, (2011).
- [57] H. Liander, *ASEA J.*, 28, 97, (1955).

- [58] F.P. Bundy, H.T. Hall, H.T. Strong, R.H. Wentorf, "Man made diamonds", *Nature*, 176 (4471), 51, (1955).
- [59] H.P. Bovenkerk, F.P. Bundy, H.T. Hall, H.M. Strong, R.H. Wentorf, "Preparation of diamond", 184 (4693), 1094, (1959).
- [60] F.P. Bundy, H.P. Bovenkerk, H.M. Strong, R.H. Wentorf, Diamond-graphite equilibrium line from growth and graphitization of diamond, *J. Chem. Phys.*, 35 (2), 383, (1961).
- [61] R.H. Wentorf, H.P. Bovenkerk, "On the origin of natural diamonds", *Astrophys. J.*, 134, 995, (1961).
- [62] M. Wakatsuki, "New catalysts for the synthesis of diamond", *Japan. J. Appl. Phys.*, 5, 337, (1966).
- [63] H. Kanda, M. Akaishi, S. Yamaoka, "New catalysts for diamond growth under high pressure and high temperature", *Appl. Phys. Lett.*, 65, 784, (1994).
- [64] M. Akaishi, H. Kanda, S. Yamaoka, "High pressure synthesis of diamond in the systems of graphite-sulfate and graphite-hydroxide", *Japan. J. Appl. Phys.*, 29 (7), 1172, (1990).
- [65] P.S. De Carli, J.C. Jamieson, *Science*, 133, 1821, (1961).
- [66] F.P. Bundy, *J. Chem. Phys.*, 38, 631, (1963).
- [67] H.M. Strong, R.H. Wentorf, *Naturwissenschaften*, 59, 1, (1972).
- [68] W.Q. Liu, H.A. Ma, X.L. Li, Z.Z. Zhang, R. Li, X. Jia, "Effects of additive Al on the HPHT diamond synthesis in an Fe-Mn-C system", *Diamond Relat. Mat.*, 16, 1486, (2007).
- [69] J.Q. Zhang, H.A. Ma, Y.P. Jiang, Z.Z. Liang, Y. Tian, X. Jia, "Effects of the additive boron on diamond crystals synthesized in the system of Fe-alloy and carbon at HPHT", *Diamond Relat. Mat.*, 16, 283, (2007).
- [70] R.J. Nemanich, "Growth and characterization of diamond films", *Mater. Sci.*, 21, 535, (1991).
- [71] S. Ferro, "Synthesis of diamond", *J. Mater. Chem.*, 12, 2843, (2002).
- [72] A.D. Kiffer, Report – Tonowanda Laboratories, Linde Air Products Co, "Synthesis of diamond from carbon monoxide", (1956).
- [73] W.G. Eversole, US Patents 3,060,187 and 3,060,188, (1962).
- [74] P.W. Bridgman, *Sc. Am.*, 193, 42, (1955).
- [75] J.J. Lander, J. Morrison, *Surf. Sc.*, 4, 241, (1966).
- [76] H.J. Hibshman, US Patent 3,714,334, (1973).
- [77] E.C. Vickery, US Patent 3,714,334, (1973).
- [78] J.C. Angus, N.C. Gardner, U.S. Patent 3,661,526, (1972).
- [79] S.P. Chauhan, J.C. Angus, N.C. Gardner, *J. Appl. Phys.*, 47, 4746, (1976).
- [80] J.C. Angus, H.A. Will, W.S. Stanko, *J. Appl. Phys.*, 39, 2915, (1968).
- [81] B.V. Deryagin, V.A. Ryabov, D.V. Fedoseev, B.V. Spitsyn, B.M. Lukyanovich, K.S. Uspenskaya, Second All-Union Symposium on Processes for Nucleation and Growth of Crystals and Films of Semiconducting Compounds, Novosibirsk, (1969).
- [82] B.V. Deryagin, B.V. Spitsyn, L.L. Builov, A.A. Klochkov, A.E. Gorodetski, A.V. Smolyaninov, *Dokl Akad Nauk SSSR*, 231, 333, (1976).
- [83] S. Matsumoto, Y. Sato, M. Kamo, N. Setaka, *J. Mater. Sc.*, 17, 3106, (1982).
- [84] S. Matsumoto, Y. Sato, M. Tsitsumi, N. Setaka, *J. Cryst. Growth*, 62, 642, (1983).
- [85] K. Kurihara, K. Sasaki, M. Kawarada, N. Koshino, *Appl. Phys. Lett.*, 52, 6, (1988).

- [86] Y. Hirose, N. Kondo, Program and Book of Abstracts, Japan Applied Physics 1988 Spring Meeting – Tokyo, Japanese Physical Society, 434, (1988).
- [87] M.D. Losego, M.E. Grady, N.R. Sottos, D.G. Cahill, P.V. Braun, “Effects of chemical on bonding on heat transport across interfaces”, *Nature Mat.*, 11, 502, (2012).
- [88] A.K. Roy, B.L. Farmer, S. Sihn, V. Varshney, S. Patnaik, S. Ganguli, “Thermal interface tailoring in composite materials”, *Diamond Relat. Mat.*, 19, 268, (2010).
- [89] A. Veillere, PhD thesis, Universite de Bordeaux, Ecole Doctorale des Sciences Chimiques, (2009).
- [90] D.G. Cahill, W.K. Ford, K.E. Goodson, G.D. Mahan, A. Majumdar, H.J. Maris, R. Merlin, S.R. Phillpot, “Nanoscale thermal transport”, *J. App. Phys.*, 93, 2, (2003).
- [91] P.M. Norris, P.E. Hopkins, “Examining interfacial diffuse phonon scattering through transient thermoreflectance measurements of thermal boundary conductance”, *J. Heat Trans.*, 131, 268, (2009).
- [92] P.L. Kapitza, *J. Phys. Moscow*, 4, 181, (1941).
- [93] M. Battabyal, O. Beffort, S. Kleiner, S. Vaucher, L. Rohr, “Heat transport across the metal-diamond interface”, *Diamond Relat. Mat.*, 17, 1438, (2008).
- [94] M. Hase, M. Kitajima, “Interaction of coherent phonons with defects and elementary excitations”, *J. Phys. Condens. Matter*, 22, 073201, (2010).
- [95] A. Majumdar, “Microscale heat conduction in dielectric thin films”, *J. Heat Transf.*, 115, 7, (1993).
- [96] A. Majumdar, P. Reddy, “Role of electron-phonon coupling in thermal conductance of metal-non-metal interfaces”, *App. Phys. Lett.*, 84, 4768, (2004).
- [97] E.T. Swartz, R.O. Pohl, “Thermal boundary resistance”, *Rev. Mod. Phys.*, 61, 605, (1989).
- [98] P. Reddy, K. Castelino, A. Majumdar, “Diffuse mismatch model of thermal boundary conductance using exact phonon dispersion”, *App. Phys. Lett.*, 87, 211908, (2005).
- [99] I.M. Khalatnikov, *Zh. Eksp. Fiz.*, 22, 687, (1952).
- [100] W. Eisenmenger, in “Phonon Scattering in Condensed Matter V”, Ed. Anderson and J.P. Wolfe, Springer, Berlin/Heidelberg/New York, (1986).
- [101] K.E. Goodson, K. Kurayabayashi, R.W. Pease, “Improved heat sinking for laser-diode arrays”, *IEEE Trans. on Components, Packaging, and Manufacturing Tech. – Part B*, 20 (1), 104, (1997).
- [102] M. Sakamoto, J.G. Endriz, D.R. Scifres, “120W CW output power from monolithic AlGaAs (800 nm) laser diode array mounted on diamond heat sink”, *Elec. Lett.*, 28 (2), 197, (1992).
- [103] Y. Lin, Z. Fang, “Thermal characteristics of semiconductor laser phase-locked arrays with diamond film heat sink”, *Elec. Lett.*, 27 (1), 18, (1991).
- [104] K. Jagannadham, “Multilayer diamond heat spreaders for electronic power devices”, *Sol. State Elec.*, 42 (12), 2199, (1998).
- [105] K. Jagannadham, T.R. Watkins, R.B. Dinwiddie, “Novel heat spreader coatings for high power electronic devices”, *J. Mater. Sc.*, 37, 1363, (2002).
- [106] Q.F. Su, J.M. Liu, L.J. Wang, W.M. Shi, Y.B. Xia, “Efficient CVD diamond film/alumina composite substrate for high density electronic packaging application”, *Diamond Relat. Mat.*, 15, 1550, (2006).
- [107] Y. Mo, Y.B. Xia, X.Q. Huang, H. Wang, “Dielectric properties of diamond film/alumina composites”, *Thin Sol. Films*, 305, 266, (1997).

- [108] A. Aleksov, T.X. Li, N. Govindaraju, J.M. Gobien, S.D. Wolter, J.T. Prater, Z. Sitar, “Silicon-on-diamond: An advanced silicon-on-insulator technology”, *Diamond Relat. Mat.*, 14, 308, (2005).
- [109] H. Verhoeven, J. Hartmann, M. Reichling, W. Müller-Sebert, R. Zachai, “Structural limitations to local thermal diffusivities of diamond films”, *Diamond Relat. Mat.*, 5, 1012, (1996).
- [110] B.A. Fox, B.R. Stoner, D.M. Malta, P.J. Ellis, R.C. Glass, F.R. Sivazlian, “Epitaxial nucleation, growth and characterization of highly oriented (100)-textured diamond films on silicon”, *Diamond Relat. Mat.*, 3, 382, (1994).
- [111] B.R. Stoner, G.-H.M. Ma, S.D. Wolter, T.J. Glass, “Characterization of bias-enhanced nucleation of diamond on silicon by in vacuo surface analysis and transmission electron microscopy”, *Phys. Rev. B*, 45 (19), (1992).
- [112] S.D. Wolter, B.R. Stoner, J.T. Glass, P.J. Ellis, D.S. Buhaenko, C.E. Jenkins, P. Southworth, “Textured growth of diamond on silicon via in-situ carburization and bias-enhanced nucleation”, *App. Phys. Lett.*, 62, 1215, (1993).
- [113] X. Jiang, C-P. Klages, “Heteroepitaxial diamond growth on (100) silicon”, *Diamond Relat. Mat.*, 2, 1112, (1993).
- [114] X. Jiang, C.L. Jia, “Diamond epitaxy on (001) silicon: an interface investigation”, *Appl. Phys. Lett.*, 67, 1197, (1995).
- [115] Q.J. Chen, J. Yang, Z.D. Lin, “Synthesis of oriented textured diamond films on silicon via hot filament chemical vapor deposition”, *Appl. Phys. Lett.*, 67, 1853, (1995).
- [116] Z.D. Zhang, H. Schneider, P. Tounsi, “A promising solution using CVD diamond for efficient cooling of power devices”, *Mater. Sc. Eng. B*, 177, 1358, (2012).
- [117] Y.J. Chen, T.F. Young, “Thermal stress and heat transfer characteristics of a Cu/diamond heat spreading device”, *Diamond Relat. Mat.*, 18, 283, (2009).
- [118] R.D. Burnham, R.S. Sussmann, US Patent 5,008,737, (1991).
- [119] Q. Sun, O.T. Inal, “Fabrication and characterization of diamond/copper composites for thermal management substrate applications”, *Mat. Sc. Eng. B*, 41, 261, (1996).
- [120] J.A. Kerns, N.J. Colella, D. Makowiecki, H.L. Davidson, “Dymalloy: a composite substrate for high power density electronic components”, *International Symposium on Microelectronics – Los Angeles*, (1995).
- [121] H.L. Davidson, N.J. Colella, J.A. Kerns, D. Makowiecki, “Copper-diamond composite substrates for electronic components”, *Proceedings of the 45<sup>th</sup> Electronic Components and Technology Conference*, 538, (1995).
- [122] K. Hanada, K. Matsuzaki, T. Sano, “Thermal properties of diamond particle-dispersed Cu composites”, *J. Mat. Proc. Tech.*, 153-154, 514, (2004).
- [123] A.M. Abyzov, S.V. Kidalov, F.M. Shakhov, “High thermal conductivity composite of diamond particles with tungsten coating in a copper matrix for heat sink applications”, *App. Therm. Eng.*, 48, 72, (2012).
- [124] J.H. Wu, K.L. Zhang, Y. Zhang, J.W. Li, X.T. Wan, “Effect of copper content on the thermal conductivity and thermal expansion of Al-Cu/diamond composites”, *Mat. Design*, 39, 87, (2012).



- [125] L. Weber, R. Tavangar, "On the influence of active element content on the thermal conductivity and thermal expansion of Cu-X (X = Cr, B) diamond composites", *Scripta Mat.*, 57, 988, (2007).
- [126] T. Schubert, L. Ciupinski, J. Morgiel, H. Weissmuller, T. Weissgarber, B. Kieback, "Advanced composite materials for heat sink applications", *Proceedings of the European Powder Metallurgy Conference*, 319, (2007).
- [127] T. Schubert, L. Ciupinski, W. Zielinski, A. Michalski, T. Weissgarber, B. Kieback, "Interfacial characterization of Cu/diamond composites prepared by powder metallurgy for heat sink applications", *Scripta Mater.*, 58, 263, (2008).
- [128] T. Schubert, B. Trindade, T. Weissgarber, B. Kieback, "Interfacial design of Cu-based composites prepared by powder metallurgy for heat sink applications", *Mater. Sci. Eng. A*, 475, 39, (2008).
- [129] Y. Xia, Y.Q. Song, C.G. Lin, S. Cui, Z.Z. Fang, "Effect of carbide formers on microstructure and thermal conductivity of diamond-Cu composites for heat sink materials", *Trans. Nonferrous Met. Soc. China*, 19, 1161, (2009).
- [130] K. Chu, Z.F. Liu, C.C. Jia, H. Chen, X.B. Liang, W.J. Gao, W.H. Tian, H. Guo, "Thermal conductivity of SPS consolidated Cu/diamond composites with Cr-coated diamond particles", *J. Alloys Comp.*, 490, 453, (2010).
- [131] M. Rosinski, L. Ciupinski, J. Grzonka, A. Michalski, K.J. Kurzydowski, "Synthesis and characterization of the diamond/copper composites produced by the pulse plasma sintering (PPS) method", *Diamond Relat. Mat.*, 27-28, 29, (2012).
- [132] K. Chu, C.C. Jia, H. Guo, W.S. Li, "On the thermal conductivity of Cu-Zr/diamond composites", *Mat. Design*, 45, 36, (2013).
- [133] Y. Zhang, H.L. Zhang, J.H. Wu, X.T. Wang, "Enhanced thermal conductivity in copper matrix composites reinforced with titanium-coated diamond particles", *Scripta Mat.*, 65, 1097, (2011).
- [134] Y.H. Dong, R.Q. Zhang, X.B. He, Z.G. Ye, X.H. Qu, "Fabrication and infiltration kinetics analysis of Ti-coated diamond/copper composites with neat net-shape by pressureless infiltration", *Mat. Sc. Eng. B*, 177, 1524, (2012).
- [135] K. Mizuuchi, K. Inoue, Y. Agari, S. Yamada, M. Tanaka, M. Sugioka, T. Takeuchi, J. I. Tani, M. Kawahara, J. H. Lee, Y. Makino, "Thermal properties of diamond-particle dispersed Cu-matrix composites fabricated by spark plasma sintering (SPS)", *Mat. Sc. Forum*, 638-642, 2115, (2010).
- [136] K. V. Ravi, "Combustion synthesis: Is it the most flexible of the diamond synthesis?", *Diamond Relat. Mat.*, 4, 243, (1995).
- [137] Y. Hirose, S. Anamuna, K. Komaki, "The synthesis of high-quality diamond in combustion flames", *J. App. Phys.*, 68, 12, (1990).
- [138] Y. Hirose, US Patent 4,938,940, (1990).
- [139] J. B. Donnet, H. Oulanti, T. Le Huu, M. Schmitt, "Synthesis of large single crystal diamond using combustion flame method", *Carbon*, 44, 374, (2006).
- [140] K. Kohse-Hoeinghaus, A. Loewe, B. Atakan, "Investigations of the gas phase mechanism of diamond deposition in combustion CVD", *Thin Sol. Films*, 368, 185, (2000).
- [141] J. S. Kim, M. A. Cappelli, "Diamond film growth in low pressure premixed ethylene-oxygen flames", *App. Phys. Lett.*, 65, 2786, (1994).

- [142] H. S. Shin, D. G. Goodwin, "Diamond growth in premixed propylene-oxygen flames", 66, 2909, (1995).
- [143] C. J. Tang, A. J. Neves, A. J. S. Fernandes, "Growth of high-quality large grained diamond films on mirror-polished silicon without surface pretreatment", *Diamond Relat. Mater.*, 12, 251, (2003).
- [144] J. B. Donnet, D. Paulmier, H. Oulamti, T. Le Huu, "Diffusion of cobalt in diamond films synthesized by combustion flame method", *Carbon*, 42, 2215, (2004).
- [145] Z. Q. Xu, L. Lev, M. Lukitsch, A. Kumar, "Analysis of residual stresses in diamond coatings deposited on cemented tungsten carbide substrates", *J. Mater. Res.*, 22, 4, (2007).
- [146] A. Glaser, H. G. Jentsch, S. M. Rosiwal, A. Ludtke, R. F. Singer, "Deposition of uniform and well adhesive diamond layers on planar tungsten copper substrates for heat spreading applications", *Mater. Sc. Eng. B*, 127, 186, (2006).
- [147] Y. X. Han, H. Ling, J. Sun, M. Zhao, T. Gebre, Y. F. Lu, "Enhanced diamond nucleation on copper substrates by graphite seeding and CO<sub>2</sub> laser irradiation", *App. Surf. Sc.*, 254, 2054, (2008).
- [148] L. Constant, F. Le Normand, "HF CVD diamond nucleation and growth on polycrystalline copper: a kinetic study", *Thin Sol. Films*, 516, 691, (2008).
- [149] F. F. Crim, "Making energy count", *Science*, 317, 1707, (2007).
- [150] D. R. Killelea, V. L. Campbell, N. S. Shuman, A. L. Utz, "Bond selective control of a heterogeneously catalyzed reaction", *Science*, 319, 790, (2008).
- [151] R. N. Zare, "Laser control of chemical reactions", *Science*, 279, 1875, (1998).
- [152] H. Ling, J. Sun, Y. X. Han, T. Gebre, Z. Q. Xie, M. Zhao, Y. F. Lu, "Laser-induced resonant excitation of ethylene molecules in C<sub>2</sub>H<sub>4</sub>/C<sub>2</sub>H<sub>2</sub>/O<sub>2</sub> reactions to enhance diamond deposition", *J. App. Phys.*, 105, 014901, (2009).
- [153] H. Ling, Z. Q. Xie, Y. Gao, T. Gebre, X. K. Shen, Y. F. Lu, "Enhanced chemical vapor deposition of diamond by wavelength-matched vibrational excitations of ethylene molecules using tunable CO<sub>2</sub> laser irradiation", *J. App. Phys.*, 105, 064901, (2009).
- [154] Z. Q. Xie, Y. S. Zhou, X. G. He, Y. Gao, J. B. Park, H. Ling, L. Jiang, Y. F. Lu, "Fast growth of diamond crystals in open air by combustion synthesis with resonant laser energy coupling", *Cryst. Growth Des.*, 10 (4), 1752, (2010).
- [155] Z. Q. Xie, X. G. He, W. Hu, T. Guillemet, J. B. Park, Y. S. Zhou, J. Bail, Y. Gao, X. C. Zeng, L. Jiang, Y. F. Lu, "Excitation of precursor molecules by different laser powers in laser-assisted growth of diamond films", *Cryst. Growth Des.*, 10 (11), 4928, (2010).
- [156] T. Guillemet, Z. Q. Xie, Y. S. Zhou, J. B. Park, A. Veillere, W. Xiong, J. M. Heintz, J. F. Silvain, N. Chandra, Y. F. Lu, "Stress and phase purity analyses of diamond films deposited through laser-assisted combustion synthesis", *App. Mat. Interf.*, 3, 4120, (2011).
- [157] M. Murakawa, S. Takeuchi, A. Alahelisten, M. Kasugai, "An efficient mechanical polishing method for diamond-coated inserts and testing of their performances", *Surf. Coat. Tech.*, 86, 686, (1996).
- [158] A. Van der Drift, *Philips Res. Rep.*, 22, 267, (1967).
- [159] Z. Q. Xie, PhD thesis, University of Nebraska-Lincoln, College of Engineering, 2012.
- [160] D. J. Gardiner, "Practical Raman spectroscopy", Springer-Verlag, (1989).

- [161] D. S. Knight, W. B. White, "Characterization of diamond films by Raman spectroscopy", *J. Mater. Res.*, 4 (2), 385, (1989).
- [162] J. Filik, "Raman spectroscopy: a simple, non-destructive way to characterize diamond and diamond-like materials", *Spectroscopy Europe*, 17 (5), 10, (2005).
- [163] Y. Nakamura, S. Sakagami, Y. Amamoto, Y. Watanabe, "Measurement of internal stresses in CVD diamond films", *Thin Sol. Films*, 308, 249, (1997).
- [164] Q. H. Fan, J. Gracio, E. Pereira, "Residual stresses in chemical vapour deposited diamond films", *Diamond Relat. Mat.*, 9, 1739, (2000).
- [165] A. Kromka, J. Breza, M. Kadlecikova, J. Janik, F. Balon, "identification of carbon phases and analysis of diamond/substrate interfaces by Raman spectroscopy", *Carbon*, 43, 425, (2005).
- [166] S. Kouteva-Arguirova, W. Seifert, M. Kittler, J. Reif, "Raman measurement of stress distribution in multicrystalline silicon materials", *J. Mater. Sc. Eng. B*, 102, 37, (2003).
- [167] S. M. Leeds, T. J. Davis, P. W. May, C. D. O. Pickard, M. N. R. Ashfold, "Use of different excitation wavelengths for the analysis of CVD diamond by laser Raman spectroscopy", *Diamond Relat. Mater.*, 7, 233, (1998).
- [168] G. W. Back, K. Fabisiak, L. Klimek, M. Kozanecki, E. Saryga, "Investigation of biaxial stresses in diamond films deposited on a silicon substrate by the HF CVD method", *Opt. Mater.*, 30, 770, (2008).
- [169] J. G. Kim, J. Yu, "Comparative study of residual stresses measurements methods on CVD diamond films", *J. Mater. Sci. Eng., B*, 57, 24, (1998).
- [170] J. Ager, M. D. Drory, "Quantitative measurement of residual biaxial stress by Raman spectroscopy in diamond grown on a Ti alloy by chemical vapor deposition", *Phys. Rev. B*, 48 (4), 2601, (1993).
- [171] R. J. Nemanich, Bergman L. Y. M. LeGrice, K. F. Turner, T. P. Humphreys, *Proceedings of SPIE*, (2), 1437, (1991).
- [172] A. Veillere, T. Guillemet, Z. Q. Xie, C. A. Zuhlke, D. R. Alexander, J. F. Silvain, J. M. Heintz, N. Chandra, Y. F. Lu, "Influence of WC-Co substrate pretreatment on diamond films deposition by laser-assisted combustion synthesis", *App. Mater. Interfaces*, 3, 1134, (2011).
- [173] K. Plamann, D. Fournier, B. C. Forget, A. C. Boccara, "Microscopic measurements of the local heat conduction in polycrystalline diamond films", *Diamond Relat. Mater.*, 5, 699, (1996).
- [174] K. M. Leung, A. C. Cheung, B. C. Liu, H. K. Woo, C. Sun, X. Q. Shi, S. T. Lee, "Measuring thermal conductivity of CVD diamond and diamond-like films on silicon substrates by holographic interferometry", *Diamond Relat. Mater.*, 8, 1607, (1999).
- [175] H. K. Lyeo, D. G. Cahill, "Thermal conductance of interfaces between highly dissimilar materials", *Phys. Rev., B*, 73, 144301, (2006).
- [176] K. E. Goodson, O. W. Kading, M. Rosler, R. Zachal, "Experimental investigation of thermal conduction normal to diamond-silicon boundaries", *J. Appl. Phys.* 1385, (1995).
- [177] H. Verhoeven, H. Reib, H. J. Fuber, R. Zachai, "Thermal resistance of thin diamond films deposited at low temperatures", *Appl. Phys. Lett.*, 69, 1562, (1996).
- [178] R. J. Stoner, H. J. Maris, "Kapitza conductance and heat flow between solids at temperatures from 50 to 300 K", *Phys. Rev., B*, 48, 16373, (1993).

- [179] R. D. Cowan, "Proposed method of measuring thermal diffusivity at high temperatures", *J. Appl. Phys.*, 32, 1363, (1961).
- [180] E. Nordal, O. Kanstad, P. E. Nordal, S. O. Kanstad, "Photothermal-radiometry", *Phys. Scr.*, 20 (5-6), 659, (1979).
- [181] A. Capella, PhD thesis, Université de Bordeaux, Ecole Doctorale des Sciences Physiques et de l'Ingénieur, (2012).
- [182] A. Kusiak, J. Marton, J.-L. Battaglia, R. Daniel, "Using pulsed and modulated photothermal radiometry to measure the thermal conductivity of thin films", *Thermoch. Acta*, 156, 1, (2013).
- [183] J. Pailhes, C. Pradere, J.-L. Battaglia, J. Toutain, A. Kuisak, A. W. Aregba, J.-C. Batsale, "Thermal quadrupole method with internal sources", *Int. J. Therm. Sci.*, 53, 49, (2012).
- [184] D. Maillet, S. Andre, J.-C. Batsale, A. DeGiovanni, « Thermal quadrupoles: solving the heat equation through integral transforms », Ed. Hardcover, (2000).
- [185] J.-L. Battaglia, A. Kusiak, V. Schick, A. Cappella, C. Wiemer, M. Longo, E. Varesi, "Thermal characterization of the  $\text{SiO}_2\text{-Ge}_2\text{Sb}_2\text{Te}_5$  interface from room temperature up to  $400^\circ\text{C}$ ", *J. Appl. Phys.*, 107, 044314, (2010).
- [186] S.-F. Wang, Y.-R. Wang, J.-C. Pu, J. C. Sung, "Interface study of diamond films grown on (100) silicon", *Thin Sol. Films*, 498, 224, (2006).
- [187] D. Wittorf, W. Jager, C. Dieker, A. Floten, H. Guttler, "Electron microscopy of interfaces in chemical vapour deposition diamond films on silicon", *Diamond Relat. Mater.*, 9, 1696, (2000).
- [188] L. Weber, R. Tavangar, "Diamond-based metal matrix composites for thermal management made by liquid-metal infiltration – Potential and limits", *Adv. Mat. Res.*, 59, 111, (2009).
- [189] S. V. Kidalov, F. M. Shakhov, "Thermal conductivity of diamond composites", *Materials*, 2, 2467, (2009).
- [190] D. A. Porter, K. E. Easterling, M. E. Sherif, "Phase transformation in metals and alloys – Third edition", CRC Press, (2009).
- [191] T. B. Massalski, "Binary alloy phase diagrams – Second edition", Vol. 1 & 2, (1990).
- [192] F. Cataldo, "From dicopper acetylide to carbene", *Polym. Int.*, 48, 15, (1999).
- [193] J. F. Silvain, Y. Le Petitcorps, M. Lahaye, M. Turner, "AES and EPMA studies of aluminum and aluminum-gold carbon composite interfaces", *Surf. Sc.*, 352-354, 839, (1996).
- [194] H. Kwon, D. H. Park, J. F. Silvain, A. Kawasaki, "Investigation of carbon nanotube reinforced aluminum matrix composite materials", *Comp. Sc. Tech.*, 70, 546, (2010).
- [195] D. Bouvard, "Metallurgie des poudres", Ed. Hermes Sciences, Paris, (2002).
- [196] W. Z. Shao, V. V. Ivanov, L. Zhen, Y. S. Cui, Y. Wang, "A study of graphitization of diamond in copper-diamond composite materials", *Mat. Lett.*, 58, 146, (2003).
- [197] Smithells Metals Reference Book, 8<sup>th</sup> edition, W. F. Gale & T. C. Totemeier.
- [198] Handbook of Chemistry and Physics, W. M. Haynes, 91<sup>st</sup> edition, (2010-2011).
- [199] NIST-JANAF, Thermodynamical tables. M. W. Chase Jr., 4<sup>th</sup> edition – Part II.
- [200] R. E. Mistler, E. R. Twinn, "Tape casting: theory and practice", The American Ceramic Society, (2000).

- [201] D. Hotza, P. Greil, "Review: aqueous tape casting of ceramic powders", *Mat. Sc. Eng. A*, 202, 206, (1995).
- [202] G. N. Howatt, R. G. Brecltenridge, J. M. Brownlow, "Fabrication of thin ceramic sheets for capacitors", *J. Am. Ceram. Soc.*, 30 (8), 237, (1947).
- [203] G. N. Howatt, "Method for producing high-dielectric high-insulation ceramic plates", U.S. Patent 2,582,993, (1952).
- [204] X. J. Luo, B. L. Zhang, W. L. Li, H. R. Zhuang, "Preparation of aluminum nitride green sheets by aqueous tape casting", *Cer. Int.*, 30, 2099, (2004).
- [205] D. H. Kim, K. Y. Lim, U. Paik, Y. G. Jung, "Effects of chemical structure and molecular weight of plasticizer on physical properties of green tape in BaTiO<sub>3</sub>/PVB system", *J. Eur. Cer. Soc.*, 24, 733, (2004).
- [206] P. Timakul, S. Jinawath, P. Aungkavattana, "Fabrication of electrolyte materials for solid oxide fuel cells applications by tape casting", *Cer. Int.*, 34, 867, (2008).
- [207] M. Zhang, K. Takahashi, I. Uechi, Y. Takeda, O. Yamamoto, D. Im, D. J. Lee, B. Chi, J. Pu, J. Li, N. Imanishi, "Water-stable lithium anode with Li<sub>1.4</sub>Al<sub>0.4</sub>Ge<sub>1.6</sub>(PO<sub>4</sub>)<sub>3</sub>-TiO<sub>2</sub> sheet prepared by tape casting method for lithium-air batteries", *J. Power Sources*, 235, 117, (2013).
- [208] K. H. Koh, S. J. Jeong, M. S. Ha, J. S. Song, "Electric field induced fracture mechanism and aging of piezoelectric behavior in Pb(MgNb)O<sub>3</sub>-Pb(Zr)TiO<sub>3</sub> multilayer ceramic actuators", *Cer. Int.*, 30, 1863, (2004).
- [209] T. Guillemet, P. M. Geffroy, J.-M. Heintz, N. Chandra, Y. F. Lu, J.-F. Silvain, "An innovative process to fabricate copper/diamond composite films for thermal management applications", *Composites Part A*, 43, 1746, (2012).
- [210] P. M. Geffroy, T. Chartier, J. F. Silvain, "Preparation by tape casting and hot pressing of copper carbon composite films", *J. Eur. Cer. Soc.*, 27, 291, (2007).
- [211] P. M. Geffroy, J. F. Silvain, T. Chartier, "Elaboration by tape casting and hot rolling of copper/silicon carbide composite thin films for microelectronic applications", *Mat. Sc. Forums*, 534-536, 881, (2007).
- [212] J. Bae, R. Thompson-Flagg, J. G. Ekerdt, C. K. Shih, "Pattern formation of nanoflowers during the vapor-liquid-solid growth of silicon nanowires", *Physica B*, 403, 3514, (2008).
- [213] H. Nagayoshi, H. Nordmark, S. Nishimura, K. Terashima, C. D. Marioara, J. C. Walmsley, R. Holmestad, A. Ulyashin, "Vapor-solid-solid Si nano-whiskers growth using pure hydrogen as the source gas", *Thin Sol. Films*, 519, 4613, (2011).
- [214] Y. J. Hsu, S. Y. Lu, "Vapor-solid growth of Sn nanowires: growth mechanism and superconductivity", *J. Phys. Chem. B*, 109, 4398, (2005).
- [215] L. P. Tan, Z. Lu, H. T. Tan, J. Zhu, X. Rui, Q. Yan, H. Hoon Hng, "Germanium nanowires-based carbon composites as anodes for lithium-ion batteries", *J. Power Sources*, 206, 253, (2012).
- [216] S. A. Dayeh, C. Soci, X. Y. Bao, D. Wnag, "Advances in the synthesis of InAs and GaAs nanowires for electronic applications", *Nano Today*, 4, 347, (2009).
- [217] W. S. Shi, Y. F. Zheng, N. Wang, C. S. Lee, S. T. Lee, "Microstructures of gallium nitride nanowires synthesized by oxide-assisted method", *Chem. Phys. Lett.*, 345, 377, (2001).

- [218] R. Q. Zhang, Y. Lifshitz, S. T. lee, "Oxide assisted growth of semiconducting nanowires", *Adv. Mater.*, 15 (7-8), 615, (2003).
- [219] S. S. Brenner, G. W. Sears, "Mechanism of whisker growth-III, Nature of growth sites" *Acta Metal.*, 4, 268, (1956).
- [220] X. Jiang, T. Herricks, Y. Xia, "CuO nanowires can be synthesized by heating copper substrates in air", *Nanolett.*, 2 (12), 1333, (2002).
- [221] J. J. Eisch, J. Laskowski, J. Bielinski, M. P. Boleslawski, "The deposition and adhesion of copper films on smooth polymer surfaces", *J. Mater. Sc. Lett.*, 14, 146, (1995).
- [222] J. D. Matthias, P. M. Geffroy, J. F. Silvain, "Architectural optimization for electronic packaging", *Appl. Thermal Eng.*, 29, 2391, (2009).



# LIST OF JOURNAL PAPERS

1. *Thermal characterization of diamond films through modulated photothermal radiometry*, **T. Guillemet**, A. Kusiak, L. Fan, Z.Q. Xie, J.M. Heintz, N. Chandra, Y.S. Zhou, J.Fr. Silvain, Y.F. Lu, and J.L. Battaglia. (in preparation)
2. *An innovative bonding solution for heat conduction at the copper/diamond interface*, **T. Guillemet**, M. Majimel, J.M. Heintz, N. Chandra, Y.F. Lu, J.F. Silvain. (in preparation)
3. *An innovative process to fabricate copper/diamond composite films for thermal management applications*, **T. Guillemet**, P.M. Geffroy, J.M. Heintz, N. Chandra, Y.F. Lu, J.F. Silvain, Composites Part A: Applied Science and Manufacturing, 43, 1746-1753, 2012.
4. *Stress and phase purity analyses of diamond films deposited through laser-assisted combustion synthesis*, **T. Guillemet**, Z.Q. Xie, Y.S. Zhou, J.B. Park, A. Veillère, W. Xiong, J.M. Heintz, J.F. Silvain, N. Chandra, Y.F. Lu, ACS Applied Materials and Interfaces, 3, 4120-4125, 2011.
5. *Influence of WC-Co substrate pretreatment on diamond film deposition by laser-assisted combustion synthesis*, A. Veillère, **T. Guillemet**, Z.Q. Xie, C. Zuhlke, D. Alexander, J.F. Silvain, J.M. Heintz, N. Chandra, Y.F. Lu, ACS Applied Materials and Interfaces, 3 (4), 1134-1139, 2011.
6. *Excitation of precursor molecules by different laser powers in laser-assisted growth of diamond crystals*, Z.Q. Xie, X.N. He, W. Hu, **T. Guillemet**, J.B. Park, Y.S. Zhou, J. Bai, Y. Gao, X.C. Zeng, L. Jiang, Y.F. Lu, Crystal Growth and Design, 10 (11), 4928-4933, 2011.
7. *Innovative process for submicronic Cu particles deposition onto various substrates*, J.F. Silvain, C. Vincent, **T. Guillemet**, A. Veillère, J. M. Heintz, Materials Research Bulletin, 47, 500-503, 2012.
8. *The role of controlled interfaces in the thermal management of copper/carbon composites*, J.F. Silvain, A. Veillère, J.M. Heintz, C. Vincent, **T. Guillemet**, G. Lacombe, Y.F. Lu, and N. Chandra, Emerging Materials Research, Volume 1, Issue 2, 75-87, 2012.
9. *Control of crystallographic orientation in diamond synthesis through laser resonant vibrational excitation of precursor molecules*, Z.Q. Xie, J. Bai, Y.S. Zhou, Y. Gao, J.B. Park, **T. Guillemet**, L. Liang, X.C. Zeng. (submitted)
10. *Mode-selective reactions in chemical vapor deposition of diamond through laser-vibrational excitations*, Z.Q. Xie, Y.S. Zhou, X.N. He, Y. Gao, **T. Guillemet**, J.B. Park, M.M. Wang, L. Jiang, and Y.F. Lu. (in preparation)

## LIST OF CONFERENCE PAPERS

1. *Investigation of interface thermal resistance of diamond films grown through laser-assisted combustion synthesis*, J.F. Silvain, **T. Guillemet**, J.L. Battaglia, A. Kusiak, A. Capella, J.M. Heintz, N. Chandra, and Y.F. Lu, International Conference on Advanced Laser Technologies, Budva, Montenegro, September 2013.
2. *Copper/diamond composite materials for thermal management applications*, **T. Guillemet**, G. Lacombe, J.L. Diot, M. Majimel, J.M. Heintz, N. Chandra, Y.F. Lu, J.F. Silvain, 8<sup>th</sup> European Advanced Technology Workshop on Micropackaging and Thermal Management, La Rochelle, France, February 2013.
3. *Influence of copper/matrix reinforcement interface on thermal performances of heat dissipative copper/diamond composite materials*, **T. Guillemet**, M. Majimel, J.M. Heintz, N. Chandra, Y.F. Lu, and J.F. Silvain, Journée Chimie Grand Sud-Ouest of the Société Chimique de France, November 2012.
4. *Fabrication by tape-casting and hot pressing of copper/diamond composite films for electronic packaging applications*, **T. Guillemet**, J.M. Heintz, N. Chandra, Y.F. Lu, J.F. Silvain, Powder Metallurgy World Congress and Exhibition, Yokohama, Japan, October 2012.
5. *Evaluation of thermal resistance at the silicon/diamond interface through infrared photothermal radiometry*, **T. Guillemet**, J.L. Battaglia, A. Kusiak, A. Capella, J.M. Heintz, N. Chandra, J.F. Silvain, and Y.F. Lu, 31<sup>st</sup> International Congress on Applications of Laser and Electro-Optics, Anaheim, CA, USA, September 2012.
6. *Fabrication of heat-spreading copper/diamond composite films for power electronic applications*, **T. Guillemet**, J.M. Heintz, N. Chandra, Y.F. Lu, and J.F. Silvain, Journée de l'Ecole Doctorale des Sciences Chimiques, University of Bordeaux, Bordeaux, France, April 2012.
7. *An innovative process to fabricate interphase-free copper diamond composite films*, **T. Guillemet**, J.M. Heintz, N. Chandra, Y.F. Lu, and J.F. Silvain, 7<sup>th</sup> European Advanced Technology Workshop on Micropackaging and Thermal Management, La Rochelle, France, February 2012.
8. *Fabrication by tape casting and hot pressing of copper diamond composite films*, **T. Guillemet**, J.F. Silvain, J.M. Heintz, N. Chandra, and Y.F. Lu, 18<sup>th</sup> International Conference on Composite Materials, Jeju, South Korea, August 2011.